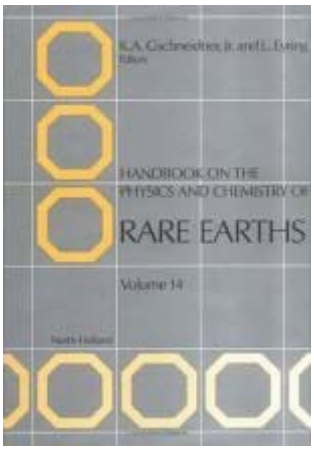

Handbook on the Physics and Chemistry of Rare Earths, **volume 14**

Elsevier, 1991

Edited by: Karl A. Gschneidner, Jr. and LeRoy Eyring
ISBN: 978-0-444-88743-6

Handbook on the Physics and Chemistry of Rare Earths, Vol. 14
Edited by K.A. Gschneidner, Jr. and L. Eyring

PREFACE

Karl A. GSCHNEIDNER, Jr., and LeRoy EYRING

These elements perplex us in our rearches [sic], *baffle us in our speculations, and haunt us in our very dreams. They stretch like an unknown sea before us – mocking, mystifying, and murmuring strange revelations and possibilities.*

Sir William Crookes (February 16, 1887)

This volume is a departure from our goal to combine and integrate as far as practical the physics and chemistry of the rare earth elements, in that there is a strong emphasis on the physical aspects, especially of intermetallic compounds. Integration is still our overall goal, but there are times when a particular volume by itself will have a strong emphasis on one aspect of the rare earth field – which is the case here.

Two of the chapters are concerned with relatively new experimental methods of studying rare earth metallic phases – high-energy neutron spectroscopy and light scattering. In these chapters (93 and 95, respectively) the authors explain the new kinds of information one obtains from these techniques and how this complements the knowledge previously gleaned from the more common measurements – such as NMR, heat capacities, magnetic susceptibility, transport and elastic properties. One of the remaining three chapters deals with NMR studies of rare earth intermetallics (94) and the other two are concerned, not so much with a particular experimental technique, but with physical phenomena that occur in these compounds: the electron–phonon interaction (96) and heavy Fermion behavior (97).In the first chapter (93) of this volume, Osborn, Lovesey, Taylor and Balcar describe a fairly new technique for probing the lanthanide 4f levels within metallic solids using high-energy neutrons from spallation sources to study transitions between different $^{2S+1}L_J$ multiplets. Intermultiplet spectroscopy is extremely useful in studying intermediate valence and heavy-fermion materials because it can be used to study the mixing of the two valence configurations in the former and to obtain information on the degree of hybridization of the 4f level in the latter. In studying mixed valent materials, the transition studied only involves the reorientation of the orbital and spin momenta of the 4f wave functions, rather than the removal of an electron from its shell as in optical studies, i.e., photoemis-

sion and X-ray absorption (see volume 11 of the HANDBOOK) and thus there are no problems of final state screening effects.

In the second chapter (94) of the present volume, Dormann reviews the advances that have been made in NMR spectroscopy over the past 12 years, since Barnes' overview on NMR, EPR and Mössbauer effect, in volume 2 of the HANDBOOK. Dormann's contribution is more specialized since it concentrates on NMR in intermetallic, magnetically ordered compounds. As Dormann points out, considerable progress has been made in experimental techniques which enable experimentalists to study materials and perform measurements that could not have been done ten years ago, and this has led to a much better understanding and comprehension of these magnetic lanthanide materials. These experimental advances allow the determination of the temperature dependence of spontaneous magnetization, direction of easy magnetization, and the electronic structure of intermetallic compounds with non-magnetic components.

Because metallic materials are opaque, the optical information obtainable is quite limited in comparison with what we know about transparent solids and liquids. There have been a number of recent developments in the past decade that has changed this situation. In chapter 95, Zirngiebl and Güntherodt describe how Raman and Brillouin light scattering has become a valuable complementary tool to neutron scattering. The advantages of these methods are high resolution, strict symmetry selection rules, small sample sizes and independence of the rare earth isotope. These optical studies have given us detailed information about crystalline electric-field excitations, spin–orbit split J multiplet excitations, and phononic and electric properties of rare earth intermetallic compounds including Kondo and intermediate valence materials.

In the last two reviews of this volume, a theorist (Thalmeier in chapter 96 and Grewe in chapter 97) and an experimentalist (Lüthi in chapter 96 and Steglich in chapter 97) combine their talents to present interesting and stimulating assessments of their areas of expertise – electron–phonon coupling and heavy Fermion phenomena, respectively.

The electron–phonon coupling, which can lead to many interesting phenomena at low temperatures, has been examined in chapter 96 by Thalmeier and Lüthi in connection with elastic or vibrational degrees of freedom (such as elastic constants, thermal expansion, and magnetostriction) in rare earth intermetallic compounds. The main emphasis in the Thalmeier–Lüthi compendium is on the interesting effects found in valence fluctuation, Kondo lattice, and heavy-electron materials. Although the nature of the electron–phonon interaction is not well understood in these types of materials, at least to the degree it is comprehended in rare earth materials with normal behaviors, the authors have done an admirable job in summarizing the state of the art and pointing out the problems that need to be solved in the future to bring us to a fuller understanding of these materials.

In the last review (chapter 97) of this volume, Grewe and Steglich present an overview of one of the most exciting areas of physics during the past 15 years – heavy fermion behavior. These phenomena occur primarily at the beginning of the lanthanide (and also actinide) series where the 4f electrons are strongly hybridized with the valence electrons, and many unusual effects are observed. One of the more interesting aspects, and probably the least understood, is the occurrence of supercon-

ductivity in materials which have extremely large effective electronic masses (≈ 1000 times larger than that in copper). These phenomena and other unusual but related behaviors of highly correlated electron systems have triggered much excitement in the scientific community, and in time, as we understand these systems, our knowledge of the electronic behavior of materials in general will be vastly improved, and its impact will be felt not only in physics, but also in chemistry and the biological sciences.

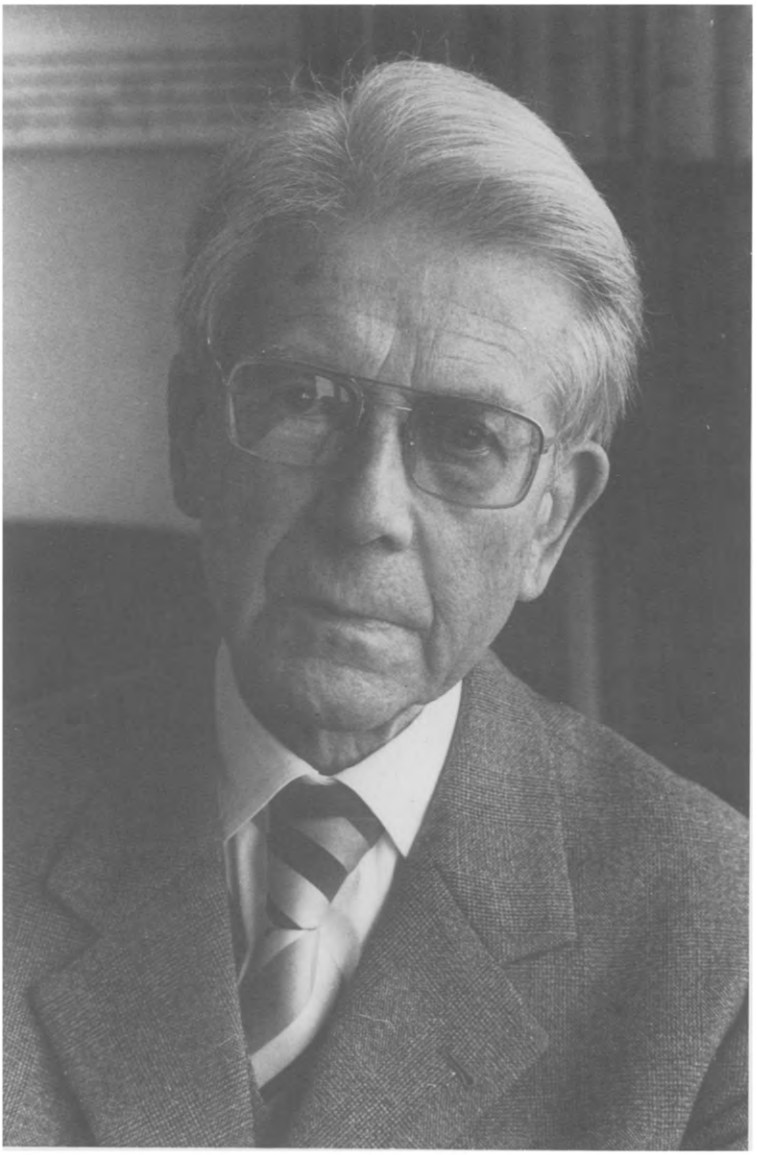

DEDICATION

The authors and editors dedicate this volume to Professor Friedrich Hund on the occasion of his 95th birthday, February 4, 1991.

Professor Hund's insight concerning the electronic structure of atoms led to his famous rules regarding the lowest energy state of bound electrons. These rules have had a profound influence on the whole of science and are one of the basic tenets of chemistry and physics. Hund's rules probably have no greater impact in all of the periodic table than on the lanthanide elements, especially with regard to: (1) *Aufbau* principle of atomic structure, which accounts for the special stability of half-filled and completely filled shells, which are quite evident in the divalent states of europium and ytterbium metals, relative to the normal trivalent rare earth metals; (2) assignment of energy levels of the spectra of the lanthanide atoms and ions in a wide variety of condensed matter substances and gases; and (3) the calculation of magnetic moments due to the 4f electrons in lanthanide materials, which are in excellent accord with experiment.

K.A. Gschneidner, Jr.
G. Güntherodt
B. Lüthi
F. Steglich

October 31, 1990

CONTENTS

CONTENTS OF VOLUMES 1–13

VOLUME 1: Metals

VOLUME 2: Alloys and intermetallics

VOLUME 3: Non-metallic compounds – I

VOLUME 4: Non-metallic compounds – II

VOLUME 5

VOLUME 6

VOLUME 7

VOLUME 8

VOLUME 9

VOLUME 10: High energy spectroscopy

VOLUME 11: Two-hundred-year impact of rare earths on science

VOLUME 12

VOLUME 13

Handbook on the Physics and Chemistry of Rare Earths, Vol. 14
edited by K.A. Gschneidner, Jr. and L. Eyring

Chapter 93

INTERMULTIPLET TRANSITIONS USING NEUTRON SPECTROSCOPY

R. OSBORN, S.W. LOVESEY and A.D. TAYLOR
ISIS Facility, Rutherford Appleton Laboratory Chilton, Didcot, Oxon, OX11 0QX, United Kingdom

E. BALCAR
Atominstitut der Österreichischen Universitäten Schüttelstrasse 115, A-1020 Vienna, Austria

Contents

1. Introduction

One of the most striking properties of lanthanide metals and compounds is the relative insensitivity of electrons in the unfilled 4f shell to the local environment, compared to non-f electron shells with similar atomic binding energies. Whereas the 5d and 6s electrons form itinerant electron bands in the metallic solids, the 4f electrons remain localised with negligible overlap with neighbouring ions. For the maximum in the 4f radial charge distribution lies within those of the closed 5s and 5p shells, so the 4f shell is well shielded from external perturbations on the atomic potential, such as the crystal field.

One consequence of this extreme localisation is that one-electron band theory cannot be used to describe the 4f-electron wavefunctions since the intra-atomic correlation energies are considerably larger than the band widths. For instance, photoemission and inverse photoemission data show clearly defined peaks representing different ionisation states of the 4f shell (Lang et al. 1981, Baer and Schneider 1987). On the basis of these results, the cost in Coulomb energy of adding an extra 4f electron to the unfilled shell is estimated to be about 6 eV for most of the lanthanides, and nearly 12 eV for the half-filled shell of gadolinium (Herbst and Wilkins 1987). This is compared with band widths estimated to be of the order of only 0.5 eV (Freeman et al. 1987). This suggests that the 4f shell is in the extreme Mott insulating limit.

It is well known that the atomic model, i.e., the approximation of the 4f states by atomic wavefunctions, has been extremely successful in describing the magnetic properties of lanthanide metals and compounds. In particular, the magnetic ground states, and those at low energies, are derived from a manifold with total angular momentum J, determined by Hund's rules, as in the free ion and the ionic solids. The evidence for this is found throughout the literature on lanthanides, and come from both bulk thermodynamic data (specific heat, magnetisation, susceptibility etc; Rhyne 1972, McEwen 1978) and microscopic measurements (neutron scattering, NMR, EPR, Mössbauer; Sinha 1978, Barnes 1979). Indeed, polarised neutron diffraction has provided direct measurements of 4f-electron magnetisation distributions in a wide range of lanthanide metallic systems and the results are in good agreement with relativistic Dirac–Fock calculations of atomic wavefunctions (Freeman and Desclaux 1972). The radial distribution of the 4f electrons are therefore accurately predicted within the atomic model. The only discrepancies are at small values of momentum transfer where there is evidence of a more diffuse contribution to the magnetisation density. This is assumed to arise from the polarisation of the band electrons through exchange interactions with the 4f electrons, and explains minor anomalies in the ordered moments of some systems (Sinha 1978).

It appears then from experimental data that not only do local atomic correlations persist in the metallic environment, but they dominate perturbations due to the crystalline lattice. Deviations from the atomic model are therefore going to be difficult to detect. Hund's rules are a consequence of the Coulomb and spin–orbit interactions within the 4f shell but, whilst their success confirms the importance of

these interactions, it gives no information on their strength, other than to show that the crystal field is a weak perturbation. In principle, the Coulomb and spin–orbit parameters can be obtained from atomic calculations but the evidence of optical spectroscopy, even on free ions, is that Dirac–Fock values, in particular of the Coulomb potential, are a substantial overestimate (Freeman and Watson 1962, Carnall et al. 1989). This is now believed to be a consequence of performing the calculations within a single $4f^n$ configuration, whereas interactions with other excited configurations gives rise to a significant screening effect (Rajnak and Wybourne 1963). In any case, atomic calculations are clearly unable to describe modifications to the potential due to the metallic environment. The only direct way of determing the intra-4f potential is to measure the high-energy excitation spectra not within the ground state J-multiplet, as in crystal-field studies, but between different multiplets.

The value of performing intermultiplet spectroscopy has been demonstrated by optical results on ionic systems. Well defined atomic spectra from intra-4f transitions have been measured up to 6 eV in all the trivalent lanthanides (except, of course, promethium) [Dieke (1968), Morrison and Leavitt (1982); see fig. 1 based on Carnall et al. (1989)]. Each level is characterised by the quantum numbers $|L, S, J, \Gamma\rangle$, where L and S are the combined orbital and spin angular momenta of the 4f electrons participating in the many-electron wavefunctions, and J is the vector sum of L and S. The quantum number Γ represents the other labels needed to specify the level fully. It is usually the label of an irreducible representation of the crystal field and we shall omit it. The Coulomb potential is responsible for separating the 4f states into Russell–Saunders terms of specific L and S, while the spin–orbit interaction is diagonal in J and so splits these terms into either $2S+1$ or $2L+1$ levels with $J = |L-S|$ to $L+S$. Provided the spin–orbit interaction is weaker than the Coulomb interaction, as is the case in the lanthanides, the resulting levels consist of relatively pure $|L, S, J\rangle$, or in spectroscopic notation $^{2S+1}L_J$, states. These $2J+1$ manifolds are then weakly split by departures from spherical symmetry in the potential, i.e., the crystal field. There are exceptions where L and S are no longer good quantum numbers. For instance, when levels with the same J but different L and S are relatively close in energy, they are strongly mixed by the spin–orbit coupling. The matrix elements of the intra-4f potential are mainly determined by four parameters; the Coulomb potential requires the three Slater integrals, $F^{(2)}$, $F^{(4)}$ and $F^{(6)}$ and the spin–orbit potential requires just one, ζ_{4f}. In analyses of optical results, they are treated as phenomenological parameters to be fitted to the data. The Slater integrals determined in this way are found to increase across the lanthanide series, as expected from the contraction of the radial wavefunctions, but also to depend on the type of ligand (Newman 1977). Measurements of intermultiplet transitions are therefore a sensitive probe of modifications to the intra-atomic correlations in solids.

It is, unfortunately, extremely difficult to obtain optical spectra on metals, although some Raman data is now available (Güntherodt et al. 1981, Zirngiebl et al. 1985) and, as the title of this chapter suggests, neutron inelastic scattering is

beginning to play a role (Taylor et al. 1988, McEwen 1988, Osborn 1989). Spectroscopic data are, however, of great interest particularly in metallic systems where the 4f moment is inherently unstable. These include intermediate valence compounds involving cerium, samarium, europium, thulium or ytterbium, where two nearly degenerate electronic configurations are hybridised (Lawrence et al. 1981), and heavy-fermion cerium compounds where the valence is nearly integral but strong band–4f hybridisation suppresses the 4f magnetism (Brandt and Moshchalkov 1984, Fulde et al. 1988). Similar phenomena are found in actinide compounds particularly involving uranium, neptunium and plutonium (Stewart 1984, Cooper et al. 1985). All these systems are near the threshold where the localised atomic model begins to break down because of increasing hybridisation with the conduction band.

Intermultiplet spectroscopy can throw light on two aspects of the problem. Firstly, in intermediate valence compounds, it is in principle possible to study the mixing of the two configurations. Neutrons have until recently only been able to measure the spin fluctuations of the ground state multiplet, which gives no information on its composition unless the absolute cross-section is determined very reliably. Intermultiplet transitions from different electronic configurations can be distinguished in neutron scattering by their energies and the dependence of the intensities on their wavevector transfers. This method of determining the ground state of fluctuating valence systems is not subject to the major corrections due to final-state effects or the surface sensitivity of the photoemission method (Campagna and Hillebrecht 1987) and X-ray absorption edge studies (Röhler 1987). The transition only involves the reorientation of the orbital and spin angular momenta of the 4f-electron wavefunctions, rather than the removal of an electron from its shell, so problems of final-state screening do not arise.

Secondly, intra-atomic spectra are sensitive to the degree of hybridisation of the 4f shell. This is because of the renormalisation of the intermultiplet transitions, and in particular the reduction in the Slater integral parameters as the degree of hybridisation increases. When the 4f electrons hybridise, they partially occupy more delocalised states so that the Coulomb correlations with other f electrons are reduced. This represents one mechanism for screening the Coulomb potential by the band states that is not available in the free ion. Reductions in the Slater integrals have been seen in ionic systems, and they are correlated to the polarisibility of the neighbouring ligands (Newman 1977), i.e., the ability of the ligand electron wavefunctions to screen the intra-4f potential. Such reductions have now been seen in metallic systems using neutrons (Taylor et al. 1988, Osborn 1989), and this forms a major part of the work covered in this chapter.

In spite of this established potential, neutron scattering has so far made only a limited contribution in the field of intermultiplet spectroscopy. This is for two reasons. Firstly, intermultiplet transitions have relatively low cross-sections. Only the $J \rightarrow J \pm 1$ transitions ($\Delta L = \Delta S = 0$) are magnetic dipole allowed, i.e., their cross-sections are non-zero at zero momentum transfer $\boldsymbol{\kappa}$, and even these are an order of magnitude weaker than the scattering within the ground state multiplet

(Balcar and Lovesey 1986). The remaining non-dipolar transitions can have cross-sections at non-zero κ, but these are usually weaker still. Such measurements therefore require extremely low instrumental backgrounds, and preferably, low nuclear scattering cross-sections in the sample. However, undoubtedly the main inhibiting factor has been the energy scale involved. With the exception of the Eu^{3+} and Sm^{2+} ions, all the intermultiplet transitions energies are greater than 100 meV and most exceed 200 meV (Martin et al. 1978). This energy range has not been generally accessible to neutron scattering until recently with the advent of high-intensity pulsed neutron sources.

Broadly speaking, spectrometers on reactor sources can be used to observe inelastic events in which there is a transfer of neutron energy of up to 150–200 meV. The performance of reactor-based spectrometers fades beyond this energy transfer, since the neutron flux has a Maxwellian energy distribution that decreases rapidly on the high-energy side of the maximum intensity. In contrast to this, the neutron spectrum from a pulsed spallation source is under-moderated and has a substantial epithermal component. The relatively high flux of energetic neutrons from a spallation source, taken together with the low backgrounds and intrinsically good resolution makes possible the measurement of excitations at energy transfers of greater than 1 eV with a sufficient signal-to-noise ratio. There are problems associated with the need to keep the momentum transfer reasonably low at the same time as increasing the energy transfer but they have not prevented the measurement of magnetic excitations at energies of up to 1.8 eV, much higher than had previously been thought possible [see, e.g., Loewenhaupt (1985a), for a discussion of the kinematic constraints of neutron inelastic scattering].

Since the science we describe has only been developing in the past few years, this chapter is not a review in the regular sense. However, the initial results are extremely promising and the theoretical apparatus for their analysis is well developed. It is now possible, therefore, to make an assessment of the potential contribution of neutron intermultiplet spectroscopy to the understanding of lanthanide (and actinide) metals. In the following section (2), we shall outline those aspects of the atomic model of lanthanide ions required in the interpretation of the results, and then introduce the theory of neutron scattering from atomic electrons (sect. 3). There then follow two sections (4 and 5) of experimental results, whose titles need some preliminary discussion. The first (4) is entitled *Spin–orbit transitions*. It covers measurements of the transitions in which the magnitudes of the orbital and spin angular momenta remain the same but their relative orientation changes; that is the total angular momentum, J, is changed. The transition energies are therefore only sensitive to the spin–orbit interaction, at least to first order, hence the name. The second experimental section (5) is entitled *Coulomb transitions* and deals with the measurements of transitions in which the orbital and/or spin angular momenta change. Their energies provide a measure of the Coulomb potential between the 4f electrons, as well as the spin–orbit interaction, and, as the current review shows, are far more sensitive to

the metallic environment of the lanthanide ion. This nomenclature is therefore based on the different physics that may be derived from the two sets of transitions and provides a convenient structure for the present review[a].

The final section (6) develops the Racah algebra required in the calculation of the cross-sections in more detail. Explicit expressions are derived for both the orbital and spin matrix elements involved in the scattering of neutrons by non-relativistic atomic electrons. The non-relativistic formulation allows the decoupling of the angular components from the radial components in the 4f wavefunctions. The results are given in terms of the coefficients of radial integrals tabulated in other publications. An appendix gives the values of these coefficients for all the transitions likely to be measurable by neutron scattering along with an example of how to use them in evaluating cross-sections.

2. Scientific background

2.1. *Atomic model of lanthanide ions*

The analysis of the atomic spectra of lanthanide ions has reached a high level of sophistication with remarkably good agreement between experiment and calculation. This is true for optical spectra on free ions and also ionic solids, where the same interactions apply but with the addition of the crystal-field potential. Detailed reviews of both theory and experiment may be found in Goldschmidt (1978), Morrison and Leavitt (1982) and Carnall et al. (1989). There is only space here to describe briefly those interactions to which the neutron spectra may be sensitive.

The atomic model of lanthanide ions consists of assuming that the $4f^n$ configuration is well separated in energy from other configurations so that the dominant interactions are within the 4f shell itself. The basis states for treating these interactions are Slater determinants made up of states of the form,

$$\psi_{nlm_lm_s}(r) = \frac{1}{r} R_{nl}(r) Y_{lm_l}(\theta, \phi) \chi_{m_s} \tag{1}$$

where $n = 4$ and $l = 3$ for the 4f shell. m_l and m_s are the z-components of the orbital and spin angular momenta respectively. The wavefunction of each 4f electron is therefore the product of a radial function, $R_{nl}(r)$, a spherical harmonic $Y_{lm_l}(\theta, \phi)$, representing the orbital state, and a two-component spinor χ_{m_s} repre-

[a] The generic description of all these transitions, spin–orbit and Coulomb, as *inter*multiplet transitions is widely used by specialists in the field of neutron scattering but may cause confusion to optical spectroscopists. The latter would call spin–orbit transitions *intra*multiplet since they are between states within the multiplet of J-levels derived from the same Russell–Saunders term. However, it seems useful, in the present context, to distinguish between transitions within the ground state Hund's rule J-multiplet (e.g., crystal-field excitations) and those between different $^{2S+1}L_J$ multiplets, the former being intramultiplet and the latter intermultiplet. This emphasises the fact that the former measure the relatively weak interactions of the 4f electrons with the surrounding lattice whilst the latter probe the much stronger interactions within the 4f shell itself.

senting the spin state. In a spherically symmetric potential, all these states are degenerate. Hartree–Fock estimates of the radial wavefunctions are obtained in the central-field approximation, where the Coulomb interactions with the nucleus and other electrons are combined self-consistently into a spherically averaged potential.

2.1.1. *The Coulomb interaction*

The strongest perturbation splitting the degeneracy of the $4f^n$ configuration arises from departures from this spherical averaging, principally due to the Coulomb repulsion between the 4f electrons (except, of course, in Ce^{3+} where there is only one electron in the f shell). The Coulomb matrix elements are diagonal in L and S, which are respectively the combined orbital and spin angular momenta of the f shell, and so split the $4f^n$ configuration into $(2S+1)(2L+1)$ degenerate Russell–Saunders terms ^{2S+1}L. The problem of finding the term energies of configurations of equivalent f electrons has been solved by Racah; extensive tabulations are given by Nielson and Koster (1963) and Condon and Odabaşi (1980). As a result of expanding the Coulomb interaction in Legendre polynomials, the term energies are given by linear combinations of Slater integrals $F^{(k)}$; for $l=3$ there are four integrals, $k=0$, 2, 4 and 6. Their definition is

$$F^{(k)} = e^2 \int_0^\infty \int_0^\infty \frac{r_<^k}{r_>^{k+1}} [R_{4f}(r_i) R_{4f}(r_j)]^2 \, dr_i \, dr_j \,, \tag{2}$$

where $r_<$ and $r_>$ are, respectively, the lesser and greater of r_i and r_j. The Slater integrals are often expressed as (Condon and Obadaşi 1980)

$$\begin{aligned} F_2 &= F^{(2)}/225 \,, \\ F_4 &= F^{(4)}/1089 \,, \end{aligned} \tag{3}$$

and

$$F_6 = 25F^{(6)}/184041 \,,$$

which simplifies the factors appearing in the matrix elements and gives a better idea of their relative contributions to the term energies. For 4f hydrogenic radial wavefunctions, $F_4/F_2 = 0.138$ and $F_6/F_2 = 0.0151$ (Judd 1963). It is interesting to note that Judd found similar ratios for 5f hydrogenic wavefunctions, 0.142 and 0.0161 respectively, as this illustrates that the ratios of the Slater integrals are much less sensitive to changes in the charge distribution than are their absolute values.

To provide a concrete example, the energies of the lowest three terms of the $4f^2$ configuration are given by,

$$\begin{aligned} E(^3\mathrm{H}) &= F_0 - 25F_2 - 51F_4 - 13F_6 \,, \\ E(^3\mathrm{F}) &= F_0 - 10F_2 - 33F_4 - 286F_6 \,, \\ E(^1\mathrm{G}) &= F_0 - 30F_2 + 97F_4 + 78F_6 \,. \end{aligned} \tag{4}$$

The energies of the first two excited terms with respect to the ^{3}H ground state are therefore $13.4F_2$ and $16.8F_2$ if the radial functions are hydrogenic. A crude estimate of F_2 for trivalent lanthanide ions is given by Judd (1955), $F_2 = 1.54(Z - 34)$ meV.

It might be thought that far better estimates of the Slater integrals would be obtained by ab initio calculations. In fact, it has been known for a long time that both non-relativistic and relativistic Hartree–Fock calculations substantially overestimate their values (Freeman and Watson 1962, Freeman and Desclaux 1979). When F_2, F_4 and F_6 are treated as phenomenological parameters to be fitted to the observed energy levels, they are found to be some 30–40% below the theoretical estimates, even in the free ion. This discrepancy shows that there is a screening mechanism reducing the bare intra-4f Coulomb potential that is largely independent of the local environment. The usual explanation is that the screening is the result of configuration interactions (CI). In other words, higher-lying electronic configurations are being mixed into the $4f^n$ configuration. The 4f electrons therefore spend part of their time in more delocalised states, so weakening their repulsion. This view is supported by the work of Rajnak and Wybourne (1963) which demonstrates that the contribution of the CI to the 4f Hamiltonian, when treated as a small perturbation, has the same symmetry as the Coulomb contribution, so that its effects can be absorbed into the Slater parameters. Unfortunately, calculations along these lines converge very slowly (Morrison and Rajnak 1971) suggesting that many different configurations make a contribution. It seems that an alternative method of modelling the screening is required. It is interesting to note that other contributions from the CI which have matrix elements of different symmetry to the Coulomb interaction, such as the Trees parameter, are given quite accurately by this calculation.

Although the predominant screening mechanism is present in the free ion, there is an extra reduction in the Slater integrals in ionic solids, of the order of 5%. Hybridisation with the ligand orbitals is a further means of reducing the effective interactions within the 4f shell, and correlations have been found relating the size of the Slater parameter reduction with the type of ligand (Newman 1977), $\Delta F(\mathrm{Pr{:}LaCl_3}) > \Delta F(\mathrm{Pr{:}LaF_3})$ etc. Newman (1977) has remarked that these reductions are found to be proportional to the polarisibility of the ligand ion and therefore presumably to its ability to screen any electrostatic potential in the lanthanide ion. As this chapter will show, even greater reductions are seen in metallic systems although not enough have been studied to establish any systematics, e.g., whether there is correlation with the density of states of the conduction band.

2.1.2. *The spin–orbit interaction*

For lathanide ions, the spin–orbit interaction is the next most important component in the atomic Hamiltonian. Within the $4f^n$ configuration, it is the sum over the 4f shell of $\xi(r)\boldsymbol{l}\cdot\boldsymbol{s}$ where $\boldsymbol{l}$ and $\boldsymbol{s}$ are the individual orbital and spin angular momenta of each electron. The spin–orbit parameter ξ is given by

$$\xi(r) = \frac{\hbar^2}{2m_e^2c^2}\,\frac{1}{r}\,\frac{\partial V(r)}{\partial r}\,, \tag{5}$$

where V is the spherical potential acting on the 4f electrons. In the $^{2S+1}L_J$ basis, it has the form $\zeta_{4f}\boldsymbol{L}\cdot\boldsymbol{S}$, where ζ_{4f} is a radial integral of $\xi(r)$, which is diagonal in J. Its effect is to lift the degeneracy of the ^{2S+1}L terms, producing a multiplet of J-manifolds, labelled $^{2S+1}L_J$, where J is between $|L-S|$ and $L+S$. For instance, in the f^2 configuration, the ^{3}H term is split into the $^3H_4$, $^3H_5$ and $^3H_6$ levels and the ^{3}F term is split into the $^3F_2$, $^3F_3$ and $^3F_4$ levels. Provided there are no other levels with the same value of J at similar energies, the level splittings follow the Landé interval rule,

$$E_J - E_{J-1} = \lambda\zeta_{4f}J\,, \tag{6}$$

where $\lambda = \pm\frac{1}{2}S$ for states of maximum multiplicity, i.e., $2S+1$. Therefore, since the ground state J-manifold always has maximum multiplicity by Hund's rules, the energies of the lowest spin–orbit excitations are $\zeta_{4f}(J+1)/2S$ for the $J\rightarrow J+1$ transitions in the first half of the lanthanide series (Ce to Eu) and $\zeta_{4f}J/2S$ for the $J\rightarrow J-1$ transitions in the second half (Tb to Yb).

Since the spin–orbit interaction mixes different $^{2S+1}L_J$ levels with the same J, this means that L and S are no longer good quantum numbers. In some cases, it can be difficult to assign a meaningful $^{2S+1}L_J$ label to a particular level, since several terms make nearly equal contributions. For instance, the nominal $^3F_4$ level contains an admixture of both $^1G_4$ and, to a lesser extent, $^3H_4$ character. It is normal to choose that term forming the largest component in this intermediate (as opposed to LS or Russell–Saunders) coupling wavefunction. This is not such a serious problem for the lowest lying multiplets of interest to neutron scattering, most of which have a dominant component from one ^{2S+1}L term, though the effects of intermediate coupling must be taken into account in evaluating transition matrix elements. The extreme limit in which the spin–orbit interaction dominates the Coulomb interaction is more appropriately treated in a jj-coupling basis, but this limit does not apply even to the actinides.

The spin–orbit interaction is largely determined by the form of the 4f wavefunctions close to the ionic core. This can be seen from the definition of ξ and is emphasised by the observation that, in a Coulombic field, ζ_{4f} is proportional to $\langle r^{-3}\rangle$. Like the Coulomb interaction, it is overestimated in Hartree–Fock calculations, though the discrepancy is less than 10%. Moreover, it is much less sensitive to the local environment. ζ_{4f} is only reduced by 2.5% in going from free Pr^{3+} ions to Pr:LaF_3 (Carnall et al. 1989). The spin–orbit interaction increases much faster across the lanthanide series than the Coulomb interaction because it is much more sensitive to the lanthanide contraction. Carnall et al. (1989) showed that ζ_{4f} increases from 80 meV in Ce^{3+} to over 360 meV in Yb^{3+}.

2.1.3. *Summary*

The multiplet structure of lanthanide ions is determined by the three Slater integrals F_2, F_4 and F_6, which describe the intra-4f Coulomb interaction, and the

spin–orbit parameter ζ_{4f}. Although, in principle, they are all calculable by Hartree–Fock methods, in practice, they are treated as phenomenological parameters, to be fitted to observed energy spectra. These are known accurately in free ions and ionic solids from optical studies. Figure 1 gives the energies of all the multiplets below 2 eV identified by analyses of optical spectra. Whereas the spin–orbit parameter is insensitive to the local environment, the Slater integrals are significantly shifted in going from the free ion to the ionic solid. As we shall see in sect. 5 even larger shifts are seen in metals showing that a more efficient screening process is at work. Such shifts appear to be larger still in the actinides, as would be expected given the more delocalised character of the 5f shell.

A number of other interactions are known to be significant from optical studies. These arise from the effect of configuration interactions (e.g., the Trees parameter mentioned above) and the couplings of the orbital and spin angular momenta of different electrons (orbit–orbit, spin–spin, spin–other-orbit). These produce nineteen free-ion parameters in all and require the measurements of level transitions over a very wide energy range if their values are to be meaningful (Carnall et al. 1989). Their combined effects are nevertheless much smaller than the Coulomb and spin–orbit interactions, and so given that neutron spectra are still confined to below about 2 eV we shall neglect them in this chapter.

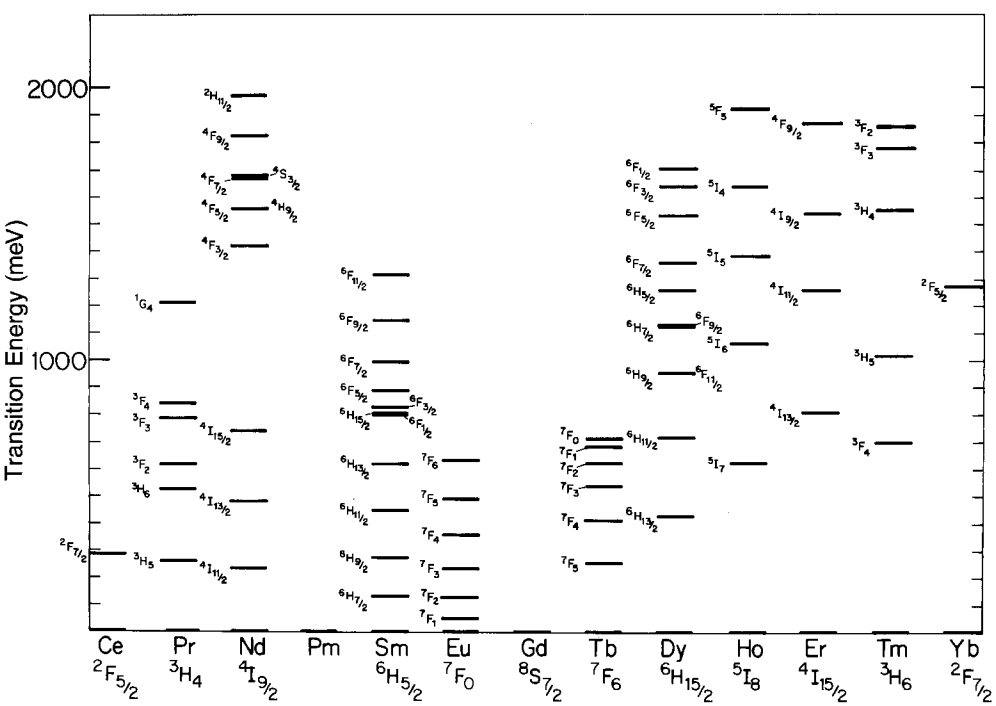

Fig. 1. Energies of intermultiplet transitions in trivalent lanthanide ions doped in LaF_3 (Carnall et al. 1989). The transitions are labelled by the final state of the transitions from the ground state level specified at the bottom of each column.

2.2. *Neutron scattering cross-sections from atomic states*

The precise form of the neutron–electron interaction is obtained from the relativistic (one-particle) Hamiltonian in which an anomalous magnetic moment is attributed to the neutron. In the non-relativistic limit, which is adequate for slow-neutron scattering experiments, the interaction with the electric and magnetic fields generated by atomic electrons is the sum of a direct magnetic interaction between the neutron magnetic moment and the magnetic field created by the electrons, and an electrostatic interaction. The latter is smaller than the magnetic interaction by a factor m_e/m_n, where m_e and m_n are the electron and neutron masses, respectively, and for this reason it is not significant in subsequent discussions of inelastic events.

For the purpose of our discussion of neutron electron spectroscopy, the neutron interaction with the target sample is taken to be the sum of the nuclear and magnetic interactions. The magnetic field generated by atomic electrons derives from two processes. Firstly, a dipole-like field is created by the spin of the electrons. Secondly, a moving charge creates a magnetic field. Hence, the sources of the magnetic field are the microscopic electron spin and momentum current densities. What actually appears in the neutron scattering amplitude is essentially the spatial Fourier transform of the magnetic field. The Fourier transform arises because the scattering event is well described by the Born approximation, in which the initial and final neutron wavefunctions in the transition matrix elements are taken to be simple plane-wave states (Balcar and Lovesey 1989).

Let us label the atomic electrons by the index ν, and denote the classical electron radius multiplied by the neutron gyromagnetic ratio γ by the symbol

$$r_0 = \gamma e^2/m_e c^2 = -0.54 \times 10^{-12}\ \text{cm}\,. \tag{7}$$

The interaction potential describing the magnetic scattering of neutrons, which is to be added to the nuclear potential, is formed by the operator

$$\boldsymbol{T}(\boldsymbol{\kappa}) = \sum_{\nu} \exp(\mathrm{i}\boldsymbol{\kappa}\cdot\boldsymbol{r}_\nu)\,\frac{1}{\kappa^2}\left[\boldsymbol{\kappa}\times\left(\boldsymbol{s}_\nu\times\boldsymbol{\kappa} - \frac{\mathrm{i}}{\hbar}\,\boldsymbol{p}_\nu\right)\right]. \tag{8}$$

Here, $\boldsymbol{\kappa}$ is the change in the wavevector of the neutron and $\boldsymbol{r}$, $\boldsymbol{s}$ and $\boldsymbol{p}$ are the electron position, spin and momentum operators, respectively. If $\frac{1}{2}\boldsymbol{\sigma}$ is the neutron spin operator, the magnetic interaction potential is

$$V_{\mathrm{M}}(\boldsymbol{\kappa}) = r_0\,\boldsymbol{\sigma}\cdot\boldsymbol{T}(\boldsymbol{\kappa})\,. \tag{9}$$

The magnetic amplitude is obtained from this potential by forming the appropriate matrix elements.

2.2.1. *Neutron scattering matrix elements*

We form matrix elements of V_{M} taken between many-electron atomic states, drawing on the extensive algebra of atomic and nuclear spectroscopy calculations based on work by Racah. The application to f electrons is reviewed by Judd (1963).

Let the atomic electrons be non-relativistic, and belong to one atomic shell. In this limit, all electrons possess the same radial wavefunction $R_{4f}(r)$, and an electron wavefunction is given by expression (1). The restriction of our theoretical work to non-relativistic electrons in a single shell brings a considerable simplification to the mathematics, as the reader can verify by consulting papers that discuss more complicated but limited cases (Lovesey 1978). The simple model is physically realistic, as we have mentioned, and for this we can obtain complete results with which to confront experimental data. One consequence of using the single-shell non-relativistic model is that the matrix element of $\boldsymbol{T}$ is expressed solely in terms of Racah tensors which have an odd rank. If the unit tensor is denoted by $W^{(\kappa,k)}$, where κ and k are the ranks of the spin and spatial parts of the tensor, $W^{(\kappa,k)}$ is termed odd if $\kappa + k$ is an odd integer. The reduced matrix elements of an odd tensor have some remarkable properties which were discovered by Racah (1943). Firstly, it is diagonal with respect to the seniority quantum number v used to label states with the same total spin S and angular momentum L. Secondly, the matrix element is independent of the number of equivalent electrons n in the atomic shell with angular momentum l.

The properties of the odd tensors that have been mentioned appear in the identity,

$$(l^n, v, S, L \| W^{(\kappa,k)} \| l^n, v', S', L') = \delta_{v,v'} (l^v, v, S, L \| W^{(\kappa,k)} \| l^v, v, S', L') \,. \tag{10}$$

The result also provides a relation between matrix elements for the conjugate states l^n and l^{4l+2-n}. Such states have the same quantum numbers, including the same seniority. We observe that the matrix elements of an odd tensor are the same for conjugate states, i.e., for lanthanide and actinide ions we need the tensors evaluated for $l = 3$ and $n = 1, 2, \ldots, 7$.

Let us précis the content of the foregoing discussion. The magnetic amplitude that enters the cross-section for an isolated ion is a weighted sum of spin and spatial (orbital) Racah tensors. The weighting factors are proportional to appropriate combinations of vector coupling coefficients – Clebsch–Gordan or $3j$ symbols – and the actual form is given in sect. 6. Only odd tensors are involved. These satisfy certain useful relations, and an extensive tabulation of values for f-electron configurations is presented in the appendix.

2.2.2. *Forward scattering cross-sections*

By way of introduction to a complete theory of scattering by atomic electrons we consider the limiting case where the wavevector transfer $\boldsymbol{\kappa}$ is vanishingly small. In this instance, the magnetic interaction reduces to the form

$$V_{\mathrm{M}}(\boldsymbol{\kappa}) = r_0 \boldsymbol{\sigma} \cdot \frac{1}{2\kappa^2} \{\boldsymbol{\kappa} \times [(\boldsymbol{L} + 2\boldsymbol{S}) \times \boldsymbol{\kappa}]\} \,, \tag{11}$$

in which we recognize the magnetic moment operator. For a lanthanide ion the total spin and angular momenta are added to give a total angular momentum **J**. The relation,

$$\boldsymbol{L} + 2\boldsymbol{S} = g_J \boldsymbol{J} \,, \tag{12}$$

is correct within a J-multiplet, where g_J is the Landé splitting factor. Hence, for elastic scattering and small $\boldsymbol{\kappa}$, found in a near-forward scattering geometry,

$$V_{\mathrm{M}}(\boldsymbol{\kappa}) = g_J r_0 \boldsymbol{\sigma} \cdot \frac{1}{2\kappa^2} [\boldsymbol{\kappa} \times (\boldsymbol{J} \times \boldsymbol{\kappa})] \,. \tag{13}$$

The corresponding neutron cross-section is readily obtained. Assuming that the neutron beam is unpolarised, the average of $|V_{\mathrm{M}}|^2$ over neutron spin states is trivial, and the cross-section is

$$\mathrm{d}\sigma/\mathrm{d}\Omega = (g_J r_0/2\kappa^2)^2 \langle \mu | \boldsymbol{\kappa} \times (\boldsymbol{J} \times \boldsymbol{\kappa}) | \mu \rangle \cdot \langle \mu | \boldsymbol{\kappa} \times (\boldsymbol{J} \times \boldsymbol{\kappa}) | \mu \rangle \,. \tag{14}$$

Here the particular atomic state is characterised by the quantum label $\mu \equiv JM$, where

$$\langle J, M | J^z | J, M \rangle = M \,. \tag{15}$$

Given that there is no magnetic field on the target sample, all values of M contribute equally to the observed cross-section. Hence, we must average M^2 which appears in the cross-section,

$$(2J+1)^{-1} \sum M^2 = \tfrac{1}{3} J(J+1) \,. \tag{16}$$

Finally, the total cross-section is obtained by adding together x, y and z-components which gives the result

$$\mathrm{d}\sigma/\mathrm{d}\Omega = (g_J r_0/2)^2 2J(J+1)/3 \tag{17}$$

for the total elastic scattering in the forward direction.

Let us turn now to the corresponding inelastic cross-section. The matrix elements $\langle J', M' | \boldsymbol{L} + 2\boldsymbol{S} | J, M \rangle$ vanish except for $|J - J'| = 1$. Hence, near the forward direction we observe only the dipole-allowed transitions, i.e., the $J \rightarrow J \pm 1$ transitions out of the Hund's rule ground state. Beyond the limit of small $\boldsymbol{\kappa}$, higher-order transitions contribute to the cross-section, and these are the main subject of the subsequent theory valid for arbitrary values of $\boldsymbol{\kappa}$. The small-$\boldsymbol{\kappa}$ result we present for inelastic events, $J' = J \pm 1$, is of limited practical value since the minimum value of $\boldsymbol{\kappa}$ is usually quite large owing to the kinematic constraints on the scattering process. Even so, the result is a useful guide to the size of the cross-section, and a welcome check on a complete calculation.

The matrix elements required to complete the present calculation are

$$\langle J+1, M | L^z + 2S^z | J, M \rangle^2 = (J+1 \| \Lambda \| J)^2 [(J+1)^2 - M^2] \tag{18}$$

and

$$\langle J+1, M \pm 1 | L^z + 2S^z | J, M \rangle^2 = \tfrac{1}{4} (J+1 \| \Lambda \| J)^2 (J \pm M + 1)(J \pm M + 2) \,, \tag{19}$$

where the square of the reduced matrix element is

$$(J+1\|A\|J)^2 = \frac{(J+L+S+2)(L+S-J)[(J+1)^2-(L-S)^2]}{4(J+1)^2(2J+1)(2J+3)} . \quad (20)$$

We assume that the energy resolution available in the experiment does not allow us to discriminate between states with different M-values. In this instance, the matrix elements quoted are averaged over M, just as in the calculation of the elastic cross-section. Assembling the results, the cross-section for a near-forward scattering geometry in which an ion is excited between states J and $J' = J+1$ separated by an energy Δ is

$$\frac{d^2\sigma}{d\Omega\, dE_f} = \left(\frac{E_f}{E_i}\right)^{1/2} (\tfrac{1}{2}r_0)^2 (J+1\|A\|J)^2 [\tfrac{2}{3}(J+1)(2J+3)]\, \delta(\hbar\omega - \Delta) . \quad (21)$$

The delta function expresses conservation of energy, $\hbar\omega = E_i - E_f = \Delta$, where E_i and E_f are the initial and final neutron energies.

For lanthanide ions, the result is appropriate for transitions from the ground states in the first half of the series where $J = |L-S|$. In the second half of the series, where $J = L+S$, the dipole transitions from the ground state correspond to $J' = J-1$. The appropriate cross-section is obtained by making the replacement $J \to J-1$. The forward scattering cross-sections for all the trivalent lanthanides are given in table 1.

Perhaps it is useful to note that the atomic quantities in the cross-section also occur in the single-ion susceptibility χ. This is expected on general grounds, for the susceptibility and the cross-section are magnetic response functions. When multiplet intervals Δ are large compared to the temperature T the susceptibility (in units of μ_B^2/atom) is

$$\chi = g_J^2 \frac{J(J+1)}{3k_B T} + \frac{1}{6(2J+1)} \left(\frac{h(J+1)}{\Delta} + \frac{h(J)}{\Delta}\right) \quad (22)$$

TABLE 1
Forward scattering cross-sections for dipole transitions from the ground state multiplet of all trivalent lanthanide ions.

Configuration			J	$G(\kappa=0;J,J)$	J'	$G(\kappa=0;J,J')$
Ce^{3+}	f^1	$^2F_{5/2}$	2.5	1.07143	3.5	0.09524
Pr^{3+}	f^2	$^3H_4$	4.0	2.13333	5.0	0.20000
Nd^{3+}	f^3	$^4I_{9/2}$	4.5	2.18182	5.5	0.31818
Sm^{3+}	f^5	$^6H_{5/2}$	2.5	0.11905	3.5	0.71429
Eu^{3+}	f^6	$^7F_0$	0.0	0.0	1.0	2.00000
Tb^{3+}	f^8	$^7F_6$	6.0	15.75	5.0	0.25000
Dy^{3+}	f^9	$^6H_{15/2}$	7.5	18.88889	6.5	0.27778
Ho^{3+}	f^{10}	$^5I_8$	8.0	18.75	7.0	0.25000
Er^{3+}	f^{11}	$^4I_{15/2}$	7.5	15.3	6.5	0.20000
Tm^{3+}	f^{12}	$^3H_6$	6.0	9.52778	5.0	0.13889
Yb^{3+}	f^{13}	$^2F_{7/2}$	3.5	3.42857	2.5	0.07143

in which the function

$$h(J) = 4J(4J^2 - 1)(J\|\Lambda\|J - 1)^2 \tag{23}$$

is supplemented by the rule that $h(J)$ $[h(J+1)]$ is zero for $J = L - S$ $(J = L + S)$ which is appropriate for an ion in the first (second) half of the series. The temperature-independent Van Vleck susceptibility, a correction to the Curie term, is therefore determined by the spin–orbit splittings that can be derived from neutron spectroscopy (e.g., see Williams et al. 1987).

2.2.3. *The dipole approximation*

We have mentioned that the small-$\boldsymbol{\kappa}$ limit is unrealistic when discussing inelastic events because the minimum value of κ is always finite in such experiments. A useful guide to the $\boldsymbol{\kappa}$-dependence of the cross-section is obtained from the so-called dipole approximation to the magnetic interaction operator. Experience shows that this approximation is the next best thing to use beyond the small-$\boldsymbol{\kappa}$ limit when building up a picture of a class of scattering events. To implement this approximation for lanthanide ions, there is next to no extra work involved beyond what we have discussed already.

In the dipole approximation, the magnetic moment operator is replaced by a weighted sum of $\boldsymbol{L}$ and $\boldsymbol{S}$, and the weighting factors depend also on the magnitude, κ, of $\boldsymbol{\kappa}$. The dependence is expressed in terms of spherical Bessel functions averaged over the electron radial density $R_{4f}^2(r)$. It is convenient to define the quantities

$$\langle j_K(\kappa)\rangle = \int_0^\infty \mathrm{d}r\, j_K(\kappa r) R_{4f}^2(r)\,, \tag{24}$$

where $j_K(x)$ is a spherical Bessel function of order K. The dipole approximation is then obtained from the results stated for the small-$\boldsymbol{\kappa}$ limit by replacing the magnetic moment operator by

$$2\langle j_0\rangle \boldsymbol{S} + (\langle j_0\rangle + \langle j_2\rangle)\boldsymbol{L}\,, \tag{25}$$

which reduces to the magnetic moment operator in the limit $\kappa \to 0$.

The modification to the cross-section, brought about by employing the dipole approximation, is more or less obvious. For an inelastic event in which a transition occurs between states $J' \neq J$ the matrix element of $\boldsymbol{J}$ is zero, i.e.,

$$\langle J', M'|\boldsymbol{J}|J, M\rangle = \langle J', M'|\boldsymbol{L} + \boldsymbol{S}|J, M\rangle = 0 \tag{26}$$

and hence

$$\langle J', M'|2\langle j_0\rangle \boldsymbol{S} + (\langle j_0\rangle + \langle j_2\rangle)\boldsymbol{L}|J, M\rangle = (\langle j_0\rangle - \langle j_2\rangle)\langle J', M'|\boldsymbol{S}|J, M\rangle\,. \tag{27}$$

We conclude that the dipole approximation to the cross-section is obtained from our first approximation by multiplying the corresponding expression for the cross-section (21) by $(\langle j_0\rangle - \langle j_2\rangle)^2$.

This new factor can be regarded as an inelastic structure factor for the

transitions $J \to J' = J \pm 1$. For such inelastic events it can be measured as a continuous function of κ. Expanding $\langle j_0 \rangle - \langle j_2 \rangle$ in a power series in κ^2 we find that the coefficients are the radial integrals,

$$\langle r^n \rangle = \int_0^\infty \mathrm{d}r\, R_{4\mathrm{f}}^2(r) r^n \,, \tag{28}$$

which also occur in crystal-field calculations. The dipole approximation therefore predicts a cross-section which falls rapidly with $\boldsymbol{\kappa}$ because of the simultaneous fall of $\langle j_0 \rangle$ and rise of $\langle j_2 \rangle$. Coupled to the fact that the forward scattering cross-section is an order of magnitude weaker than the elastic cross-section, it can be seen that spin–orbit transitions provide a stringent test of neutron scattering techniques.

2.2.4. *General theory of scattering*

We turn now to a first consideration of expressions for the orbital and spin matrix elements which arise when there is no restriction placed on the magnitude of the scattering vector. The matrix elements can be expressed in terms of Racah tensors, as mentioned before.

Let us begin with the orbital, or current, matrix element. Write $\boldsymbol{p} = -\mathrm{i}\hbar\boldsymbol{\nabla}$ and work with spherical vector components labelled by $q = 0, \pm 1$. Atomic states are labelled by θ, J, M, where θ contains all the quantum numbers required to define a state other than J, M. The magnetic neutron operator contains the quantity $\boldsymbol{\kappa} \times \boldsymbol{\nabla}$, and the many-electron matrix element is found to be

$$\begin{aligned} &\left\langle \theta, J, M \left| \sum_\nu \exp(\mathrm{i}\boldsymbol{\kappa} \cdot \boldsymbol{r}_\nu)(\boldsymbol{\kappa} \times \nabla_\nu)_q \right| \theta', J', M' \right\rangle \\ &\quad = -(4\pi)^{1/2} \kappa^2 \sum_{\substack{K,Q \\ K',Q'}} Y_Q^K(\tilde{\boldsymbol{\kappa}}) A(K, K') \langle K, Q, K', Q' | 1, q \rangle \\ &\qquad \times \langle K', Q', J', M' | J, M \rangle \,. \end{aligned} \tag{29}$$

Our definition of spherical harmonics $Y_Q^K(\tilde{\boldsymbol{\kappa}})$ and Clebsch–Gordan coefficients are in accord with the standard references. The quantity $A(K, K')$ is the product of radial integrals, and various factors which arise from the vector coupling coefficients of n equivalent electrons. The latter component of $A(K, K')$ is essentially embodied in the Racah tensor. Let

$$A(K, K') = (\langle j_{K'-1} \rangle + \langle j_{K'+1} \rangle) a(K, K') \,, \tag{30}$$

in which $a(K, K')$ is proportional to $W^{(0,K')}$ and an explicit formula is given in sect. 6. The restrictions on K, K' are $K = K' \pm 1$ only, K' is an odd integer, and its maximum value is $2l + 1$.

The spin matrix element has a similar structure, with $W^{(0,K')}$ replaced by $W^{(1,K)}$. It can be shown that

$$\left\langle \theta, J, M \left| \sum_{\nu} \exp(\mathrm{i}\boldsymbol{\kappa}\cdot\boldsymbol{r}_{\nu})(s_{\nu})_{q} \right| \theta', J', M' \right\rangle$$
$$= (4\pi)^{1/2} \sum_{\substack{K,Q \\ K',Q'}} Y_{Q}^{K}(\tilde{\boldsymbol{\kappa}}) C(K, K') \langle K, Q, K', Q' | 1, q \rangle$$
$$\times \langle K', Q', J', M' | J, M \rangle \,, \tag{31}$$

where K is an even integer and its maximum value is $2l$. The function $C(K, K')$ is

$$C(K, K') = \langle j_{K} \rangle c(K, K') \tag{32}$$

with $c(K, K')$ proportional to $W^{(1,K)}$; an explicit form is provided in sect. 6.

We can take the algebra for scattering of unpolarised neutrons from an isolated magnetic ion one stage further. First, we note that in the general case the matrix element of the magnetic interaction operator, built up from (29) and (31), is

$$\left\langle \theta, J, M \left| \sum_{\nu} (T_{\nu})_{q} \right| \theta', J', M' \right\rangle$$
$$= (4\pi)^{1/2} \sum_{\substack{K,Q \\ K',Q'}} Y_{Q}^{K}(\tilde{\boldsymbol{\kappa}}) [A(K, K') + B(K, K')]$$
$$\times \langle K, Q, K', Q' | 1, q \rangle \langle K', Q', J', M' | J, M \rangle \,, \tag{33}$$

in which the function $B(K, K')$ is obtained directly from $C(K, K')$ using a relation given in sect. 6.

The cross-section for scattering of unpolarised neutrons, accompanied by a transition between states J, J' separated by an energy Δ, is found to be (Balcar and Lovesey 1986)

$$\frac{\mathrm{d}^2\sigma}{\mathrm{d}\Omega\, \mathrm{d}E_{\mathrm{f}}} = \left(\frac{E_{\mathrm{f}}}{E_{\mathrm{i}}}\right)^{1/2} r_0^2 \mathcal{G}(\boldsymbol{\kappa}, J, J')\, \delta(\hbar\omega - \Delta) \,, \tag{34}$$

in which the inelastic structure factor is

$$\mathcal{G}(\boldsymbol{\kappa}, J, J') = \sum_{K'} \left(\frac{3}{K'+1}\right) [A(K'-1, K') + B(K'-1, K')]^2$$
$$+ \sum_{K} \left(\frac{3}{2K+1}\right) [B(K, K)]^2 \,. \tag{35}$$

The first sum covers $K' = 1, 3, \ldots, 2l+1$ and the sum over K includes the values $K = 2, 4, \ldots, 2l$.

The parity of the various contributions to the cross-section merit attention; $K' = 1, 2, \ldots, 2l+1$ for the magnetic multipole transition and $K = 2, 4, \ldots, 2l$ for electric multipole transitions. The latter involves only $B(K, K)$, i.e., the electric multipole is purely spin. An orbital contribution to the electric multipole arises in scattering events which engage electrons in different l-states that are non-degenerate and possess different radial wavefunctions. The quantity $B(K, K)$

vanishes for $J = J'$, so it does not occur in elastic scattering or inelastic transitions between crystal-field levels within a J-multiplet.

In the limit $\kappa \to 0$ the general result (33) reduces to (11), as should be expected. The reduction arises because the radial integrals $\langle j_K \rangle$ vanish in the limit $\kappa \to 0$ except for $K = 0$, where this particular integral is unity.

The dipole approximation, presented in sect. 2.2.3 as the next best thing to the $\kappa \to 0$ limit, has been tested against the complete expression (33) evaluated for rare-earth ions. It is found to be a fair approximation for all cases except the f^1 and f^{13} configurations where it fails quite badly at intermediate κ (Balcar and Lovesey 1986).

3. Experimental aspects of neutron scattering

Inelastic neutron scattering has had a major impact on many aspects of solid state physics in the past 30 years. Its potential to investigate magnetism through interactions with the neutron's magnetic dipole moment was recognised by the pioneers of the technique. Since then, its contribution to our understanding of magnetic phenomena has been significant (Sinha 1978, Fulde and Loewenhaupt 1985, Stirling and McEwen 1987), but it has always been limited by the intensity and spectral range of the beams available. Until recently, the field of inter-multiplet spectroscopy has been confined to the study of the $^7F_0 \to {}^7F_1$ transition in Sm^{2+} and Eu^{3+} systems by the energy range available on conventional steady-state reactor sources where the neutrons have a Maxwell–Boltzmann energy distribution characterised by the physical temperature of the moderator, typically 25 meV. (The energy distribution may be shifted somewhat to higher energies by using a "hot" source such as the 2000 K graphite moderator at the Institut Laue–Langevin's high-flux reactor, but to date studies of intermultiplet transitions have not been made on this source.)

Pulsed neutron sources were originally developed in an attempt to increase the brightness of neutron sources by circumventing the problem of heat removal from the core of a steady-state fission reactor. Accelerator-driven pulsed spallation sources produce neutrons more efficiently by the impact of short bursts of high-energy protons on a target of heavy nuclei (e.g., W or ^{238}U). These bursts occur for a only a small fraction of a given time period, typically $<1\%$. Thus, without compromising the brightness of the source, the time-averaged power densities can be kept at modest levels compatible with ease of heat extraction. In addition to high brightness, the pulsed nature of the source naturally leads to a high intrinisic resolution, an excellent signal-to-background ratio and a strong epithermal component to the spectrum, all of which have been essential to the exploration of intermultiplet excitations. The high resolution is a natural consequence of the sharp – less than 1 μs – proton burst from the accelerator; the signal-to-noise ratio achieved by instruments on a pulsed source is high because the data are collected when the source is effectively off; but the aspect of pulsed sources which has had the most impact in the present study is the rich epithermal spectrum which dominates these undermoderated sources. (This undermodera-

tion is a consequence of the need to use physically small moderators – typically $10 \times 10 \times 5\ \mathrm{cm}^3$ – to preserve the temporal sharpness of the neutron pulse and this results in an intense $1/E$ spectrum available for the first time for inelastic neutron spectroscopy.)

Inelastic spectroscopy requires that the energy of the neutron is determined both before and after the scattering event. At a steady-state source, even where the Maxwellian has been shifted to higher energies by a hot source, the monochromatic flux is severely limited by the poor reflectivity of crystals at high energies. On a pulsed source, however, monochromatisation may be achieved efficiently by phasing the opening of a high-speed chopper with the fast neutron burst. Energy analysis is then naturally performed by the time-of-flight method between the sample and the detector array. This is the principle of the direct geometry time-of-flight chopper spectrometers which have been used at pulsed sources to extend magnetic inelastic neutron spectroscopy to an electron volt and above. The majority of the work described in this review has been performed on the HET spectrometer at the UK pulsed neutron facility, ISIS. A summary of other such sources and their equivalent spectrometers are given in table 2.

On HET, a high resolution (in neutron terms) of 1–2% is achieved by using a fast 600 Hz Fermi chopper located 10 m from the source. Scattered neutrons are detected in two azimuthal arrays of ^{3}He detectors, the first at 4 m from the sample covering 3° to 7° and the second at 2.5 m covering 9° to 29°. A third detector array at 136° has proved to be invaluable in determining (multi) phonon and multiple scattering contributions to the signal.

The traditional kinematic constraints on high-energy magnetic neutron scattering are severe. A large scalar difference between the incident and scattered neutron wavevectors, $\boldsymbol{k}_\mathrm{i}$ and $\boldsymbol{k}_\mathrm{f}$, respectively, is required,

$$\hbar\omega = 2.07(k_\mathrm{i}^2 - k_\mathrm{f}^2)\,, \tag{36}$$

where $\hbar\omega$ is the energy transfer in meV and $\boldsymbol{k}_\mathrm{i}$ and $\boldsymbol{k}_\mathrm{f}$ are in $\mathrm{Å}^{-1}$, whereas the vector difference,

$$\boldsymbol{\kappa} = \boldsymbol{k}_\mathrm{i} - \boldsymbol{k}_\mathrm{f}\,, \tag{37}$$

must be kept small (typically $< 4\ \mathrm{Å}^{-1}$) because of the atomic form factor of the 4f

TABLE 2
Characteristic parameters of pulsed neutron source time-of-flight chopper spectrometers.

Source	Proton energy (MeV)	Target	Proton current (μA)	Frequency (Hz)	Spectrometer	(Operational)	$L_\mathrm{i}/L_\mathrm{f}$ (m)	Resolution (%)
ISIS (UK)	800	^{238}U	200	50	HET	1985	12/4	1–2
IPNS (USA)	500	^{235}U	15	30	HRMECS	1980	13/4	2–4
KENS (Japan)	500	^{238}U	10	30	INC	1988	7/2.5	4–8
LANSCE (USA)	800	W	100	20	PHAROS	1990	20/4	1

and 5f electrons. These conditions may only be achieved with large incident wavevectors and small scattering angles: the design specification of HET. The existence of non-dipolar terms in the intermultiplet cross-section relaxes the constraint on κ somewhat, but the small absolute value of the cross-sections (typically a few hundred $\mu b\,sr^{-1}$), imposes a further constraint on the signal-to-noise ratio which has to be achieved. At energies of an electron volt and above it is necessary to reduce even further the intrinsically low pulsed-source background by the inclusion in the beam line of a chopper which suppresses fast neutrons and which is closed when the protons strike the target.

A significant source of background is multiphonon and multiple scattering processes in the sample itself. Fortunately these generally contribute a featureless decaying tail which extends to high energies. It may be minimised by keeping the sample small (typically still several tens of grams) and by using the lowest possible incident energy consistent with the kinematic constraints. The purity of the material is extremely important since these weak magnetic excitations are easily obscured by the vibrational modes of light interstitials, especially hydrogen.

4. Spin–orbit transitions

4.1. *Overview*

In the context of this chapter, we define spin–orbit transitions to be those in which the absolute values of L and S remain at fixed values but their relative orientation is changed, i.e., $\Delta L = \Delta S = 0$, $\Delta J = \pm 1$, 2 etc. The so-called dipole $J \rightarrow J \pm 1$ transitions have been the most extensively investigated of all the intermultiplet transitions up to the present time. This is because, in general, they have the largest cross-sections and occur at the lowest energies. Lowest of all are the $^7F_0 \rightarrow {}^7F_1$ transitions in Sm^{2+} and Eu^{3+}, at 36 and 46 meV, respectively (Martin et al. 1978), energies that are readily accessible on reactor sources. The remaining transitions are all at energies greater than 100 meV and have only been observed on pulsed neutron sources. The largest spin–orbit splitting so far measured by neutron scattering is the $^3H_6 \rightarrow {}^3H_4$ transition in the metal thulium at an energy of 1560 meV (Osborn et al. 1990).

The supposition that the spin–orbit coupling is relatively insensitive to the local ionic environment (see sect. 2.1.2) is amply confirmed by neutron measurements on metallic systems. The observed spin–orbit splittings are all very close in energy to those previously measured in optically transparent compounds. The only exceptions to this rule so far are in the intermediate valent compounds $EuPd_2Si_2$ (Holland-Moritz et al. 1987) and $Sm_{0.75}Y_{0.25}S$ (Holland-Moritz et al. 1988), in which the transition energies are nearly 20% lower than in the free ion (Martin et al. 1978).

This section is divided into two parts. In sect. 4.2 experiments on "normal" lanthanides, i.e. those in which the $4f^n$ configuration is believed to be stable, are reviewed. Except in the case of neodymium and thulium, the transitions so far observed are $J \rightarrow J \pm 1$. This is because the $J \rightarrow J \pm 2$ transitions, which are not

TABLE 3
Energies (in meV) of lanthanide $J \rightarrow J \pm 1$ transitions in free ions, ions doped into LaF_3 and metals.

Lathanide		J	J'	Free ion[a]	LaF_3[b]	Metallic compound
Ce^{3+}	$^2F_{5/2}$	2.5	3.5	279.4	288.3	274; $CeAl_3$[c]
Pr^{3+}	$^3H_4$	4.0	5.0	266.8	260.0	261; Pr[d]
Nd^{3+}	$^4I_{9/2}$	4.5	5.5		234.4	237; Nd[e]
Sm^{3+}	$^6H_{5/2}$	2.5	3.5		131.5	129; $SmPd_3$[f]
Sm^{2+}	$^7F_0$	0.0	1.0	36.4		36; SmS[g]
						32; $Sm_{0.75}Y_{0.25}S$[h]
Eu^{3+}	$^7F_0$	0.0	1.0		45.5	38; $EuPd_2Si_2$[i]
Tb^{3+}	$^7F_6$	6.0	5.0	254.4	254.7	~256; Tb[j]
Dy^{3+}	$^6H_{15/2}$	7.5	6.5		428.8	
Ho^{3+}	$^5I_8$	8.0	7.0		625.8	
Er^{3+}	$^4I_{15/2}$	7.5	6.5		808.9	
Tm^{3+}	$^3H_6$	6.0	5.0		1017.0	1018; Tm[e]
Yb^{3+}	$^2F_{7/2}$	3.5	2.5	1266.4	1271.4	

[a] Martin et al. (1978).
[b] Carnall et al. (1989).
[c] Osborn et al. (1990).
[d] Taylor et al. (1988).
[e] McEwen (1988).
[f] Williams et al. (1987).
[g] Shapiro et al. (1975).
[h] Holland-Moritz et al. (1988).
[i] Holland-Moritz et al. (1987).
[j] Stirling et al. (1986).

dipole allowed, have cross-sections an order of magnitude weaker, and so are more difficult to observe. The results are compared to the calculated cross-sections and shown to be generally in excellent agreement with theory. Comparisons are also made with the transition energies observed in free-rare earth ions and trivalent lanthanide ions doped in LaF_3 (Carnall et al. 1989); see table 3. Section 4.3 deals with measurements on anomalous lanthanide systems, where significant departures from the normal systems are encountered.

4.2. *Normal lanthanides*

4.2.1. *Praseodymium*

The Hund's rule ground state of the $4f^2$ configuration of the Pr^{3+} ion is $^3H_4$. It is one of the few ions in which free-ion spectra are available for comparison; the others are Ce^{3+}, Pr^{4+}, Sm^{2+}, Tb^{3+} and Yb^{3+} (Martin et al. 1978). These give a spin–orbit splitting of 266.8 meV for the $^3H_4 \rightarrow {}^3H_5$ transition, a value which falls to 260.0 meV in Pr^{3+}:LaF_3 (Carnall et al. 1989). The first observation of this transition in a metal was in $PrAl_2$ at an energy of 260 meV (Loewenhaupt 1985b). This was followed by measurements on praseodymium metal by Stirling et al. (1986) whose signal was severely contaminated by hydrogen impurities. Nevertheless, the spin–orbit peak was identified at about 260 meV from its κ-dependence, which was assumed (erroneously as we now know) to follow the square of the atomic form factor.

The most detailed investigation of the spin–orbit splitting in a metallic system is that of Taylor et al. (1988) on a 100 g sample of high-purity praseodymium metal, containing less than 139 at. ppm of hydrogen. The experiment was performed on

HET using a range of incident energies from 370 to 1600 meV. A clearly resolved peak centred at 261 meV was seen in all the scans, though the multiple scattering produces an appreciable background at incident energies above 1 eV. The κ-dependence of the integrated peak intensity is shown in fig. 2 and compared with the calculation of Balcar and Lovesey. The data are normalised to the integrated paramagnetic scattering of the ground state $^3H_4$ multiplet, measured in the same experiment. This provides an extremely stringent test of the predicted intensity. As expected, the structure factor falls more sharply than the atomic form factor at low κ, but flattens off at intermediate κ where the contribution from the $\langle j_2(\kappa) \rangle^2$

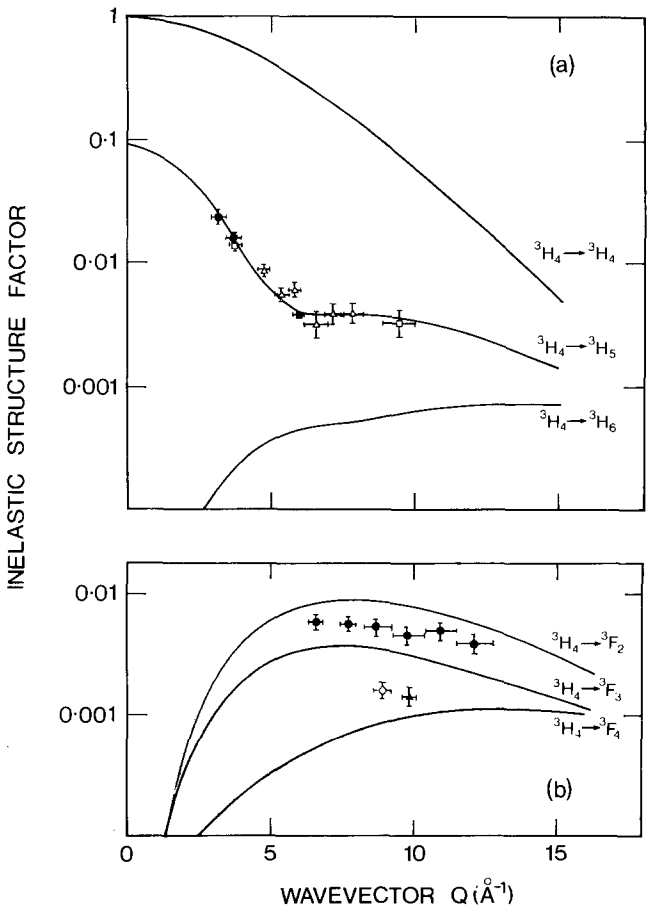

Fig. 2. Neutron inelastic structure factors for intermultiplet transitions in praseodymium. The lines represent the calculated intensities of the $^3H_4 \rightarrow {}^3H_4$, $^3H_5$, $^3H_6$, $^3F_2$, $^3F_3$ and $^3F_4$ transitions. The structure factors are normalised to the $^3H_4 \rightarrow {}^3H_4$ intensity at $\kappa = 0$, which has a cross-section of 620 mb sr^{-1}. (a) The intensity of the 260 meV transition measured with incident energies of 370 meV (filled square); 515 meV (open triangles); 830 meV (open squares); and 1300 meV (filled circles). (b) The intensity of the transitions at 578 meV, $^3H_4 \rightarrow {}^3F_2$ (filled circles); 747 meV, $^3H_4 \rightarrow {}^3F_3$ (open diamond); and 809 meV, $^3H_4 \rightarrow {}^3F_2$ (filled triangle) measured with an incident energy of 1300 meV.

term is more significant. Over the measured κ-range, the cross-section is more than an order of magnitude weaker than the integrated scattering within the $^3H_4$ ground state. It ranges from 60 mb sr^{-1} at $|\kappa| = 0$ to 300 μb sr^{-1} at $|\kappa| = 10$ Å^{-1}.

The non-dipolar $^3H_4 \rightarrow {}^3H_6$ transition is predicted to be at about 530 meV, but is submerged in the much stronger $^3H_4 \rightarrow {}^3F_2$ peak, as discussed in sect. 5.

4.2.2. *Neodymium*

Stirling et al. (1986) report seeing a peak at 240 meV which decreases smoothly with κ. A more detailed investigation has confirmed that the transition at 237 meV is the $^4I_{9/2} \rightarrow {}^4I_{11/2}$ transition, since the κ-variation of the intensity is in good agreement with a free-ion calculation (McEwen 1988). The corresponding value in Nd^{3+}:LaF_3 is about 234.4 meV (Carnall et al. 1989). The $^4I_{9/2} \rightarrow {}^4I_{13/2}$ transition is at about 479 meV. At that energy, a weak feature is seen in the neutron spectra with an integrated intensity consistent with the calculated estimate (fig. 3). However, it is on the limits of the observable.

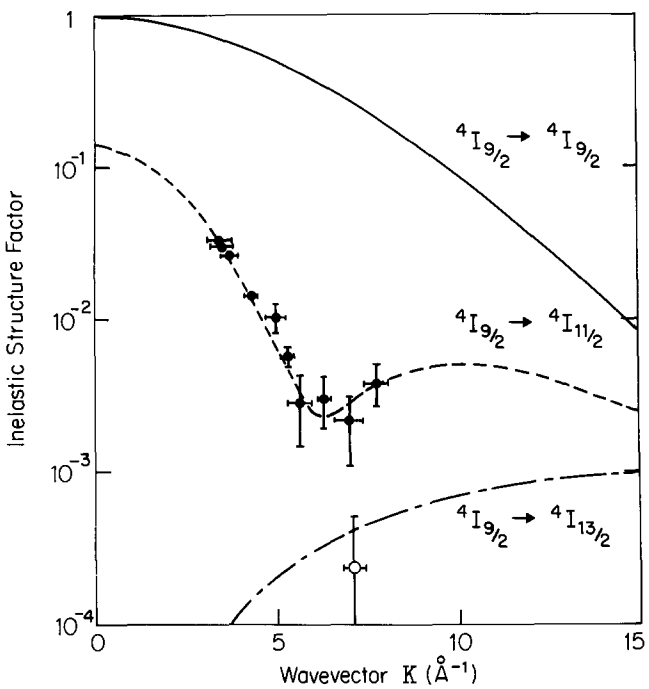

Fig. 3. Neutron inelastic structure factors for intermultiplet transitions in neodymium. The lines represent the calculated intensities of the $^4I_{9/2} \rightarrow {}^4I_{9/2}$ (smooth line), $^4I_{11/2}$ (dashed line) and $^4I_{13/2}$ (chain line) transitions. The structure factors are normalised to the $^4I_{9/2} \rightarrow {}^4I_{9/2}$ intensity at $\kappa = 0$, which has a cross-section of 634 mb sr^{-1}. The filled circles are measured intensities of the 237 meV transition using incident energies of 515 and 828 meV. The open circle is the measured intensity of a small peak observed at 479 meV.

4.2.3. *Samarium*

The atomic form factor of Sm^{3+} ions has a maximum at non-zero κ as a consequence of the antiparallel alignment of L and S. The orbital contribution to the form factor is more extended in κ-space than the spin contribution, and the partial cancellation of the two components produces a minimum at $\kappa = 0$. By contrast, the structure factor of the $^6F_{5/2} \rightarrow {}^6F_{7/2}$ spin–orbit transition is calculated to fall monotonically with increasing κ. This has been verified in measurements on polycrystalline samples of the trivalent samarium compound, $SmPd_3$, and samarium metal, both performed on HET (Williams et al. 1987, Needham 1989). A major problem with neutron experiments on samarium systems are the resonant absorption peaks at 100 and 870 meV in ^{149}Sm. Unless sufficient quantities of the expensive ^{154}Sm isotope are available, the only option is to make use of a transmission window between 400 and 700 meV, within which the absorption is less than 100 b. Using an incident energy of 611 meV, Williams et al. (1987) successfully observed the spin–orbit peak at an energy transfer of 129 meV, about 2.5 meV less than the value in Sm^{3+}:LaF_3 (Carnall et al. 1989). The κ-variation of the measured intensity is once again in good agreement with the calculation, although this time there is no independent normalisation of the intensity. The results of measurements on samarium metal, made under identical experimental conditions, are similar, though the spin–orbit peak is much broader. The full widths at half maximums (FWHMs) are 17 and 30 meV for $SmPd_3$ and Sm, respectively. The instrumental resolution is estimated to be about 12 meV. This is clear evidence for intrinsic broadening of the transitions, probably because of the crystal-field splitting of the excited level.

4.2.4. *Terbium*

There are no unambiguous observations of the $^7F_6 \rightarrow {}^7F_5$ transition in terbium metallic systems. Stirling et al. (1986) measured a sample of terbium metal which was strongly contaminated with hydrogen, producing three strong vibrational peaks at 132, 256 and 370 meV. They interpreted an anomalous κ-dependence of the central peak as evidence of magnetic scattering, which is consistent with the value of 254 meV for the transition energy in free Tb^{3+} ions (Martin et al. 1978).

4.2.5. *Thulium*

Trivalent thulium (f^{12}) is the "hole" analogue of the $Pr^{3+}f^2$ configuration. The splitting of the ^3H term is therefore the inverse of praseodymium with $^3H_6$ as the ground state and $^3H_5$ as the first spin–orbit-split level at 1017 meV in Tm^{3+}:LaF_3 (Carnall et al. 1989). An indication of the strength of ζ_{4f} in the heavy rare-earths is that this is not the lowest transition energy, as spin–orbit-split levels from the ^3H and ^3F terms have crossed with the $^3H_6 \rightarrow {}^3F_4$ transition occurring at only 690 meV. The only metallic system so far investigated is thulium metal. The spin–orbit transition is at too high an energy for a wide κ-range to be measured, but the relative intensities of all the observed transitions (including the Coulomb transitions, see sect. 5) are in good agreement with calculation. Another consequence of the strength of ζ_{4f} is that the $J = 4$ levels are strongly mixed. This has

the effect of increasing the intensity of the $J \rightarrow J-2$ (i.e., $^3H_6 \rightarrow {}^3H_4$) transition, making it readily observable at 1560 meV.

4.3. *Anomalous lanthanides*

4.3.1. *Samarium and europium intermediate valence compounds*

In sect. 4.2.3, $SmPd_3$ and samarium metal were treated as normal lanthanides since their magnetic properties are consistent with those of stable trivalent ions. However, samarium ions are never far from a valence instability, and compounds such as SmB_6 and $Sm_{1-x}Y_xS$ are amongst the most extensively studied of intermediate valence systems (Lawrence et al. 1981). Nevertheless, there have been only a few neutron scattering studies, mainly because of the need for ^{154}Sm-enriched samples. To date, neutron scattering investigations have been confined to SmS (Shapiro et al. 1975, McWhan et al. 1978), $Sm_{1-x}Y_xS$ (Mook et al. 1978, Holland-Moritz et al. 1988, Weber et al. 1989) and a rather inconclusive investigation on SmB_6 (Holland-Moritz and Kasaya 1986). Unfortunately, a similar absorption problem has also restricted neutron investigations of europium intermediate valence systems to a single study of $EuPd_2Si_2$ (Holland-Moritz et al. 1987). This is a pity because in principle, neutron studies of spin–orbit transitions can provide fundamental information on the hybridisation between the two nearly degenerate configurations since they are usually at a high enough energy not to be washed out by the mixing interaction but not so high that the lifetime broadening from the spontaneous charge fluctuations cannot be resolved.

The spin–orbit splitting of the Sm^{2+} ion is the smallest of all the lanthanide ground state configurations. The $^7F_0 \rightarrow {}^7F_1$ transition of the $4f^6$ configuration is at only 36 meV and so gives rise to a significant Van Vleck contribution to the magnetic susceptibility at room temperature. Shapiro et al. (1975) measured the dispersion of the $^7F_1$ level in a single crystal of SmS and showed that the system was an ideal example of the paramagnetic singlet–triplet model. The observed peaks are not intrinsically broadened and, using a mean-field random-phase approximation (RPA) model, the derived energy of the single-ion spin–orbit splitting is identical to the free-ion value, within the experimental error (Martin et al. 1978). The temperature dependence of the cross-section is also consistent with the RPA model (Mook et al. 1978). There is therefore nothing to suggest the proximity of a valence instability, even though SmS undergoes a first-order phase transition from a divalent semiconductor to a mixed valent metal at a pressure of only 6.5 kbar.

Hirst (1970, 1975) has discussed the conditions under which the intra-ionic excitations remain sharp even though the compound is close to a configuration instability, or crossover, the condition being that

$$E_{f^n} + \Delta < E_{f^{n-1}} + \epsilon_c \,, \tag{38}$$

where E_{f^n} is the energy of the lowest level, i.e., the Hund's rule ground state in the f^n configuration, Δ are the energies of the excited intra-configuration excitations for the f^n configuration and ϵ_c is the energy of the bottom of the empty conduction band. In SmS, $n = 6$ and Δ corresponds to the energies of the

$^7F_0 \rightarrow {}^7F_1$, $^7F_2$ etc. transitions. Equation (38) simply states that a particular ionic level of the f^6 configuration will only show broadening provided that the decay into a level of the f^5 configuration, with the emission of a conduction electron, is energetically allowed. Configuration crossover occurs when the inequality is no longer satisifed even for the ground state of the f^6 configuration, ie., with $\Delta = 0$, or rather when the difference in the energies of the two configurations is less than

$$\Delta_{kf} = \pi |V_{kf}|^2 \rho \,, \tag{39}$$

where $|V_{kf}|$ is the hybridisation matrix element between the f electrons and the conduction band, and ρ is the density of states of the conduction band.

In SmS, configuration crossover is induced by applying pressure which has the effect of lowering the conduction band, the transition being first order because of coupling to the lattice. In a second neutron scattering investigation under pressures of up to 10 kbar, the spin–orbit peak disappeared in the collapsed high-pressure phase, with no evidence of additional magnetic scattering, such as crystal-field splittings, from the $4f^5$ configuration (McWhan et al. 1978). It cannot be ruled out that the spin–orit transition is still present but is considerably broadened. There was no evidence of the approach of the instability, the spin–orbit peak remaining resolution limited right up to the transition. It seems therefore that the $^7F_0 \rightarrow {}^7F_1$ transition is at too low an energy to ever satisfy eq. (38). However, higher energy transitions, $J = 0 \rightarrow J = 2$, 3, 4, 5, 6, may show precursor effects below 6.5 kbar (Hirst 1975). The latter are all non-dipolar, with the $^7F_0 \rightarrow {}^7F_2$ transition being particularly weak, but the $^7F_0 \rightarrow {}^7F_3$ transition at 185 meV is reasonably strong at intermediate values of κ (table 4) so this experiment may be practicable.

Whilst no magnetic scattering has been identified in the mixed valence phase of SmS, it has been seen in $Sm_{0.75}Y_{0.25}S$ by Mook et al. (1978) who observed a very broad peak with a FWHM of 15 meV at 30 meV. The addition of yttrium has a similar effect to that of pressure in contracting the lattice. At this composition, the valence changes with temperature from 2.3 to 2.45 at about 200 K (Weber et al. 1989). This means that the compound is at a configuration crossover with the f level effectively pinned at the Fermi level ($E_{f^n} - E_{f^{n-1}} = \epsilon_F$) such that the ground state consists of a hybridised mixture of the two configurations. The valence is then determined by thermodynamic considerations in which the ionic excitation

TABLE 4

Coefficients of radial integrals in the neutron scattering cross-sections of Sm^{2+}, $J = 0 \rightarrow J' = 1, 2, \ldots, 6$ transitions.

J'	$\langle j_0 \rangle^2$	$\langle j_0 \rangle \langle j_2 \rangle$	$\langle j_2 \rangle^2$	$\langle j_2 \rangle \langle j_4 \rangle$	$\langle j_4 \rangle^2$	$\langle j_4 \rangle \langle j_6 \rangle$	$\langle j_6 \rangle^2$
1	2.00000	−3.33333	1.38889	0.00000	0.00000	0.00000	0.00000
2	0.00000	0.00000	0.05556	0.00000	0.00000	0.00000	0.00000
3	0.00000	0.00000	0.79365	0.47619	0.07143	0.00000	0.00000
4	0.00000	0.00000	0.00000	0.00000	0.22727	0.00000	0.00000
5	0.00000	0.00000	0.00000	0.00000	0.33058	0.05510	0.00230
6	0.00000	0.00000	0.00000	0.00000	0.00000	0.00000	0.88384

structure of each configuration plays an important role (Wohlleben 1984). For instance, at high temperatures ($k_B T \gg \Delta_{kf}$) the valence adjusts to maximise the entropy from the two configurations, which are determined by the excitation energies and their degeneracies. The intensity of the peak seen by Mook et al. falls faster with temperature than the RPA model used for SmS predicts, in particular at the valence transition. This is mostly accounted for by the reduction is Sm^{2+}, though not entirely. Nevertheless, this seems to be the first neutron scattering evidence for the persistence of intra-ionic correlations in a strongly mixed valent phase.

The observation of large widths of intraconfigurational peaks is not surprising since they are expected to be broadened by some function of Δ_{kf}. The widths also depend on the precise valence of the compound, the degeneracy of the levels (Wohlleben and Wittershagen 1985) and the effects of projecting the interconfigurational mixing matrix elements on to the ionic $|L, S, J\rangle$ basis (Hirst 1975). This can lead to different widths for different ionic transitions. More surprising is that the peak is shifted to lower energies than in SmS and the free ion, even after allowing for dispersion. From table 3 it can be seen that the intermediate valence compounds $Sm_{0.75}Y_{0.25}S$ and $EuPd_2Si_2$ are the only systems to show a significant renormalisation of the spin–orbit splitting. Indeed this may be a signature of intermediate valence, because the 4f wavefunction close to the ionic core is only affected by substantial mixing of two different electronic configurations (see sect. 2.1.2). It is interesting to note that the spin–orbit coupling in Sm^{3+} ions is lower than in Sm^{2+}: $\zeta_{4f} = 191$ meV and 216 meV, respectively. Using the lower value, the $J = 0 \rightarrow J = 1$ transition would occur at 32 meV which is where it is centred in more recent measurements (Holland-Moritz et al. 1988). This agreement is, of course, fortuitous but it does give some insight into the nature of the hybridised ground state wavefunction.

There appears to be a strong coupling to optic phonons in $Sm_{0.75}Y_{0.25}S$ (Holland-Moritz et al. 1988) which could also lead to an effective energy shift but single-crystal experiments are required to clarify the issue. Incidentally, Weber et al. (1989) plot the κ-dependence of the transition intensity and compare it to the Eu^{2+} atomic form factor. The correct comparison is with the $^7F_0 \rightarrow {}^7F_1$ inelastic structure factor and gives an equally good agreement. However, the κ-range is not sufficiently extended to be sensitive to any differences between the two. Whilst Weber et al. have succeeded in identifying quasielastic scattering from the Sm^{3+} configuration with a linewidth of about 7 meV, there has been no study of the Sm^{3+} spin–orbit peak at 130 meV. Since the transition is well above any phonon energies, its observation would be useful in determining to what extent the resonant phonon coupling is responsible for the renormalisation of the Sm^{2+} spin–orbit level.

$EuPd_2Si_2$ is an intermediate valence compound in which Eu undergoes a shift in valence from 2.33 at 170 K to 2.76 at 130 K (Kemly et al. 1985). Eu^{2+} is isoelectronic to Gd^{3+} which has an $^8S_{7/2}$ ground state, i.e., $L = 0$. There are therefore no spin–orbit transitions, and the first excited level is at nearly 3.5 eV (Martin et al. 1978). Eu^{3+} has a $^7F_0$ ground state separated by only 46 meV from the $^7F_1$ level in $Eu:LaCl_3$ (Martin et al. 1978). At low temperature, Holland-

Moritz et al. (1987) observe an excitation at 38 meV in $EuPd_2Si_2$, but this disappears at the valence transition consistent with the reduction in Eu^{3+} character in the high-temperature region. This drop in intensity with temperature is correlated with a large increase in quasielastic scattering arising from fluctuations within the Eu^{2+}, $^8S_{7/2}$ ground state. In this instance, it is unlikely that the reduction in the peak position from the stable trivalent value is due to phonon coupling since the peak is quite sharp and shows no extra structure. The scale of the shift is similar to $Sm_{0.75}Y_{0.25}S$ and could therefore also be due to a renormalisation of ζ_{4f}, but is unusual since its value (8 meV) is much larger than the intrinsic linewidth (2 meV). It does not appear reasonable to ascribe the shift to an interconfigurational energy difference since this would require the neutron spectra to be dominated by transitions *between* the f^7 and f^6 configurations rather than *within* them.

4.3.2. *Cerium heavy-fermion compounds*

The underlying physics of heavy-fermion and intermediate valence phenomena is believed to be similar, both involving hybridisation between the localised 4f electron wavefunctions and the conduction band whilst preserving the strong intra-atomic correlations of the 4f electrons. In spite of this, charge fluctuations are not significant in the cerium heavy-fermion compounds, all of which are close to being integral valent (Röhler 1987). Instead, the hybridisation produces an effective antiferromagnetic exchange coupling between the localised and itinerant electrons (Schrieffer and Wolf 1966) which can either suppress the magnetism altogether, through spin fluctuations, as in the Kondo effect, producing a Fermi liquid of extremely heavy quasiparticles, or lead to magnetic order through an RKKY-like mechanism. Since the characteristic energy scale of the spin fluctuations, usually called the Kondo temperature, T_K, is only of the order of 10 K, the spin–orbit transition at 279 meV is not of thermodynamic significance. In that case, the hybridisation is confined within the sixfold-degenerate $^2F_{5/2}$ ground state, or even a subset of that manifold if the crystal-field splittings are larger than T_K. On the other hand, this does not apply to cerium intermediate valence systems, such as α-Ce and $CeRu_2$, in which the spin fluctuation temperature may be several thousand Kelvins and the number of f levels available for hybridisation is closer to 14.

Whilst there have been several theoretical investigations of the effect of hybridisation on the crystal-field excitations within the ground multiplet (Maekawa et al. 1985, Lopes and Coqblin 1986), there have been relatively few in which the spin–orbit level is explicitly included. Cox et al. (1986) have shown, in the context of the Anderson impurity model, that when T_K is comparable to the spin–orbit splitting, the inelastic peak is broadened and shifted to lower energies. Given that the cross-section is weak, at about half the intensity of the praseodymium spin–orbit cross-section, they concluded that the transition was unlikely to be seen except in heavy-fermion compounds with low values of T_K. This appears to be confirmed by the failure to observe such a transition in $CePd_3$ in recent measurements on HET (Osborn, unpublished). On the other hand, the

spin–orbit transitions in low-T_K materials should not be dramatically shifted from their free-ion values.

Osborn et al. (1990) have observed the $^2F_{5/2} \rightarrow {}^2F_{7/2}$ spin–orbit transition in $CeAl_3$ (fig. 4), one of the canonical heavy-fermion materials characterised by an especially large electronic specific heat coefficient at 1620 mJ mol^{-1} K^{-2} (Andres et al. 1975). T_K is estimated to be about 5 K (Murani et al. 1980) so a well defined spin–orbit peak was anticipated, especially since the compound has a low nuclear scattering cross-section and therefore low multiple scattering backgrounds. The spin–orbit peak is split into two peaks at low κ at 260 and 291 meV with identical intensities and FWHMs of 49 meV, compared to an estimated resolution width of 12 meV. This is a surprising result because there are no other instances of a splitting of a spin–orbit peak in neutron spectra so far. In general, the instrumental resolution is not good enough to reveal crystal-field splittings of excited multiplets, particularly in metals where the crystal-field potential is well screened and hence rather weak. Overall splittings of the ground state multiplet are commonly in the range 10–20 meV with similar values expected for the spin–orbit levels. In $CeAl_3$, the ground state multiplet is split by just over 7 meV and, although the crystal-field potential has not been solved (in particular, the sixth-degree crystal-field parameters cannot be estimated from the ground multiplet splitting) it is unlikely to produce such a large splitting of the $^2F_{7/2}$ multiplet.

The splitting of the spin–orbit level may be even greater than 30 meV since there is some evidence of inelastic scattering at higher energies (up to 360 meV) emerging at higher κ. Whereas the peaks at 260 and 291 meV are of dipolar character, the higher energy scattering is clearly non-dipolar. This could arise

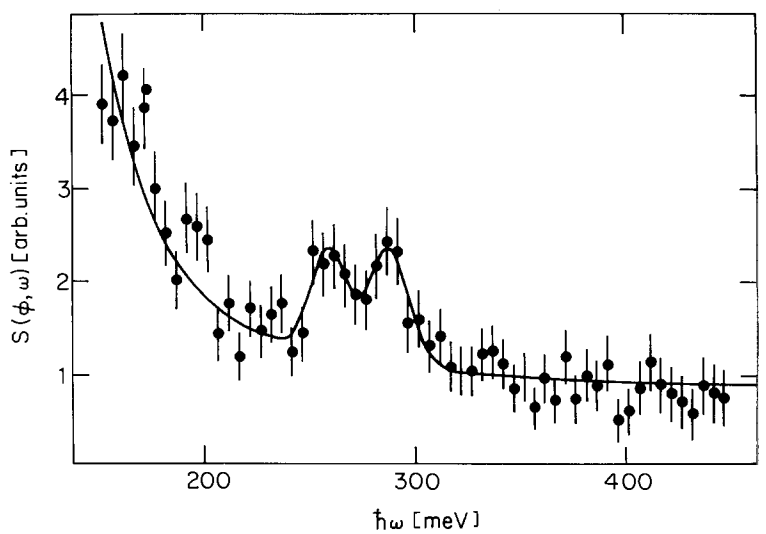

Fig. 4. Neutron inelastic scattering from $CeAl_3$ at 20 K, measured at an angle of 5° with an incident neutron energy of 600 meV on HET. The data have been fitted by two Gaussians and a tail of low-energy scattering.

from scattering from hydrogen impurities, but there does not appear to be any evidence of other vibrational overtones. Non-dipolar transitions are possible between the two multiplets, even though the total cross-section is dipolar. They arise from transitions between crystal-field levels in the two multiplets in which $\Delta M > 1$, e.g., $^2F_{5/2}$, $M = \frac{1}{2} \rightarrow {}^2F_{7/2}$, $M = \frac{7}{2}$.

Goremychkin and Osborn conclude that the crystal-field potential acting on the spin–orbit level is larger than the potential acting on the ground state level. Since extensive optical studies of the crystal-field splittings in ionic systems have shown that a unique potential can be used to analyse the splittings in a large number of different multiplets with only minor discrepancies (Carnall et al. 1989), this observation suggests that a radically different mechanism for the crystal field is in operation, one that can vary from multiplet to multiplet. One possibility is that the crystal-field potential is due to the same hybridisation mechanism that produces the low-temperature Fermi liquid behaviour. It is already known that the hybridisation-mediated exchange between the f electrons and the conduction electrons, which will reflect the point group symmetry of the cerium ion, can give rise to a large contribution to the crystal field (Wills and Cooper 1987, Levy and Zhang 1989). The magnitude of the exchange coupling is given by (Schrieffer and Wolf 1966)

$$\mathcal{J}_{kf} = 2|V_{kf}|^2 \frac{U}{E_{f^n}(E_{f^n} + U)}, \tag{40}$$

where V_{kf} is the hybridisation matrix element, E_{f^n} is the energy of the f level and U is the intra-4f Coulomb repulsion. The energies are with respect to the Fermi energy, so with E_{f^n} negative and $E_{f^n} + U$ positive, $\mathcal{J}_{kf}$ represents an antiferromagnetic exchange coupling. Equation (40) helps to explains why hybridisation exchange is so important in cerium systems, Firstly, $|V_{kf}|$ is large because of the relatively expanded character of the cerium 4f wavefunction, and secondly E_{f^n} is small, though not so small that the Schrieffer–Wolf transformation is invalidated.

The other interesting feature of eq. (40) is that the absolute value of E_{f^n} will be lower for the $^2F_{7/2}$ multiplet than for the $^2F_{5/2}$ level so that $\mathcal{J}_{kf}$ is enhanced. The widths of the excited level will also be increased by any increase in $\mathcal{J}_{kf}$ as is observed. One corollary of this suggestion is that $\mathcal{J}_{kf}$ is probably the dominant component in the crystal-field splitting of the ground state manifold as well, in agreement with the suggestion of Levy and Zhang (1989).

5. Coulomb transitions

5.1. *Introduction*

We have designated as Coulomb transitions those intermultiplet transitions in which $\Delta L \neq 0$, i.e., transitions between levels derived from different Russell–Saunders $^{2S+1}L_J$ terms. As shown in sect. 2.1.1, their energies depend on the

Coulomb repulsion between the electrons in the f shell and are much more sensitive to changes in the local environment than the spin–orbit transitions. They are therefore a useful probe of the way intra-atomic correlations are affected by the metallic state, particularly in the actinides. Nevertheless, there are relatively few investigations of Coulomb transitions in metals since their energies all exceed 500 meV and most exceed 1 eV, as can be seen in fig. 1. The lowest energies are found in Pr^{3+}, Sm^{3+} and Tm^{3+}, all of which have now been studied by neutrons (Taylor et al. 1988, Needham 1989, Osborn et al. 1990). Although Coulomb transitions are non-dipolar, they can have appreciable cross-sections at intermediate values of momentum transfer, and are, in many cases, stronger than the dipolar (i.e., $J \rightarrow J \pm 1$) cross-sections at the same κ.

The recent observations of Coulomb transitions in actinide intermetallic compounds (McEwen et al. 1990, Osborn et al. 1990) are of particular interest because the 5f electrons are on the boundary between localised and itinerant behaviour. The neutron results give direct evidence of the persistence of strong intra-atomic correlations in, e.g., the heavy-fermion compound UPt_3. The theoretical challenge is to reconcile this with the substantial evidence that the f electrons also form a coherent Fermi liquid (Fulde et al. 1988, Zwicknagl 1988).

5.2. *Normal lanthanides*

5.2.1. *Praseodymium*

The Coulomb transitions with the lowest energies are found in the f^2 configuration of the Pr^{3+} ion. In the free ion, the three $^3H_4 \rightarrow {}^3F_{2,3,4}$ transitions are observed between 600 and 850 meV with the $^3H_4 \rightarrow {}^1G_4$ transition at 1230 meV (table 5). Accordingly, praseodymium metal was the first material in which Coulomb transitions were studied by neutron scattering (Taylor et al. 1988). Figure 5 shows the neutron inelastic scattering from the sample described in sect. 4.2.1 using an incident energy of 1300 meV. In addition to the spin–orbit transition at 261 meV, there are three peaks at 578, 747 and 809 meV. These are at similar energies to those of the $^3H \rightarrow {}^3F$ transitions in the free ion, though uniformly shifted down by about 40 meV.

TABLE 5

The experimental and calculated energies (in meV) of intermultiplet transitions from the $^3H_4$ ground state multiplet of the Pr^{3+} ion: free ion (Martin et al. 1978); Pr doped in LaF_3 (Carnall et al. 1989); Pr doped in anhydrous $LaCl_3$ (Dieke 1968); Pr metal (Taylor et al. 1988); calculation using the following parameters, $F_2 = 36.0$ meV, $F_4 = 5.69$ meV, $F_6 = 0.55$ meV and $\zeta_{4f} = 92.2$ meV.

	Free ion	Pr:LaF_3	Pr:$LaCl_3$	Pr metal	Calculation
$^3H_5$	266.8	260.0	262.5	261	259.3
$^3H_6$	544.1	527.5	533.9	—	529.3
$^3F_2$	619.5	619.3	600.9	578	577.3
$^3F_3$	795.4	787.9	772.7	747	751.4
$^3F_4$	849.9	840.7	828.4	809	808.7
$^1G_4$	1230.0	1211.9	1202.3	—	1173.5

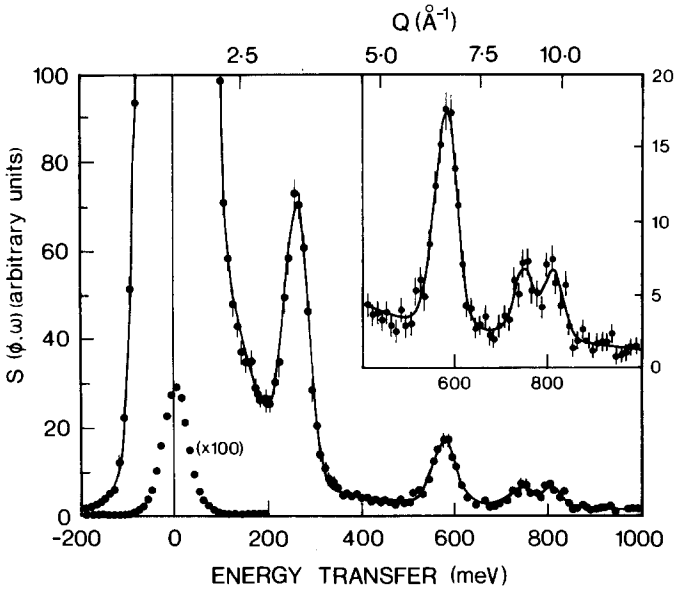

Fig. 5. Neutron scattering cross-section of praseodymium metal at 17 K, measured at an angle of 5° with an incident neutron energy of 1300 meV on HET. The change in scattering vector across the spectrum is shown at the top of the diagram. The instrumental resolution varies from 60 to 25 meV as the energy transfer increases from 0 to 1000 meV. The data have been fitted by four Gaussians and a tail of low-energy scattering. Inset: the results above 400 meV on an expanded scale.

The κ-dependences of the peak intensities are plotted in fig. 2 where they are compared to the calculated cross-sections of the pure $^{2S+1}L_J$ transitions. Taylor et al. argue that the peak at 578 meV must be the $^3H_4 \rightarrow {}^3F_2$ transition since the $^3H_4 \rightarrow {}^3H_6$ transition, predicted to be in the same energy range, is weaker by an order of magnitude. They also point out the need to calculate the intensities in intermediate coupling. In particular, the nominal $^3F_4$ level has the composition

$$^3F_4 \Rightarrow 0.805\,{}^3F_4 - 0.580\,{}^1G_4 - 0.125\,{}^3H_4\,. \tag{41}$$

The substantial admixture of both the $^1G_4$ and $^3H_4$ levels by the spin–orbit coupling increases the intensity of the 809 meV peak to roughly equal that of the 747 meV peak, as observed experimentally. When this is taken into account, the measured intensities of all the Coulomb transitions are approximately a factor two lower than the calculation, in contrast to the good agreement for the spin–orbit transition intensity. Taylor et al. were also unable to see the $^1G_4$ peak, predicted to be just under 1200 meV in energy, using an incident energy of 1600 meV even though its cross-section is calculated to be relatively strong.

The discrepancies between the predictions (i.e., free-ion energies and atomic model intensities) and the neutron scattering measurements are the most significant results of the experiment. The energy shifts are well reproduced by reducing the F_2 Slater integral by 10% from its value in the free ion, keeping the remaining Slater integrals and the spin–orbit coupling fixed (table 5). This represents an

appreciable reduction in the Coulomb repulsion between the two f electrons from that pertaining in the free ion, and is direct evidence of an enhanced screening in the lanthanide metal. As discussed in sect. 2.1.2, smaller shifts are also seen in ionic systems. The reduction in F_2 is 4.4% in Pr:$LaCl_3$ but less in Pr:LaF_3, correlating with the larger polarisibility of the Cl^- ions (Newman 1977). Since these are the only measurements on the Pr^{3+} ion in a metal to date, it has not been established whether, in metallic compounds, there are equivalent correlations with, e.g., the density of states of the conduction band.

The reason for the discrepancy in the intensities is currently a matter for speculation. There are a number of possibilities. Firstly, it may be a consequence of performing the calculations semi-relativistically. The ^3H and ^3F terms are composed of differing amounts of $j = \frac{5}{2}$ and $j = \frac{7}{2}$ character, which in a fully relativistic treatment have different radial wavefunctions. This prevents a complete factorisation of the radial and angular parts of the cross-section, and requires considerable numerical computation. It seems unlikely that this should produce a major drop in intensity, especially since the discrepancies between calculation and experiment are smaller in thulium (see sect. 5.2.3) where relativistic effects are stronger.

A more likely explanation is that the intensities are reduced for the same reason that the Slater parameters are reduced (Osborn 1989), i.e., because the 4f wavefunctions are hybridised with other configurations of higher energy. The f electrons partially occupy more delocalised levels so reducing their mutual electrostatic repulsion from the Hartree–Fock estimates (see sect. 2.1.2). In a metallic environment, there may be additional hybridisation with the band states, implying a correlation between the Slater parameter shifts and the intensity reductions.

5.2.2. *Samarium*

Because of the high multiplicity of the two lowest terms in the Sm^{3+} ion, ^6H and ^6F, the multiplet structure below 1.5 eV is relatively complicated. Above the $J \rightarrow J+1$ transition, the neutron cross-sections are dominated by the $^6H_{5/2} \rightarrow {}^6F_{3/2,5/2}$ transitions which occur at 827 and 889 meV in Sm:LaF_3 (Carnall et al. 1989), along with weaker transitions to the $^6F_{1/2,7/2}$ levels at 797 and 991 meV, respectively. Free-ion spectra are not available, but are not expected to be much different from the fluoride. Needham (1989) reports, in $SmPd_3$, the observation of two peaks at 781 and 842 meV with some evidence of a third at 934 meV. The spectra were taken with an incident energy of 1250 meV, above the absorption resonance at 870 meV, with scattered energies lying in the transmission "window" below the resonance. A detailed comparison with the calculated cross-sections has not been attempted because of the consequent energy dependence of the neutron absorption. Nevertheless, the data are consistent with a uniform reduction of the energies of all the Coulomb transitions by about 50 meV from the values in Sm:LaF_3, in qualitative agreement with the praseodymium results. Once again, the values in Sm:$LaCl_3$ lie between the metal and the fluoride (Martin et al. 1978).

5.2.3. *Thulium*

The energy of the lowest Coulomb transition in trivalent thulium, the $^3H_6 \rightarrow {}^3F_4$ transition, is at just under 700 meV with transitions to the $^3F_3$ and $^3F_2$ levels at just under 2 eV. There are strong deviations from the Landé interval rule [equation (6)] because of intermediate coupling. Moreover, the mixture of the $^3H_4$, $^3F_4$ and $^1G_4$ levels by the spin–orbit interaction substantially alters the transition intensities. Figure 6 shows the inelastic neutron scattering from a 100 g sample of thulium metal, measured at HET by Osborn et al (1990) with an incident energy of 2.14 eV. Four well defined transitions are observed at 684, 1018, 1560 and 1760 meV. Comparison with the transitions in Tm:LaF_3 (Carnall et al. 1989; see table 6) show that these peaks correspond closely in energy with the

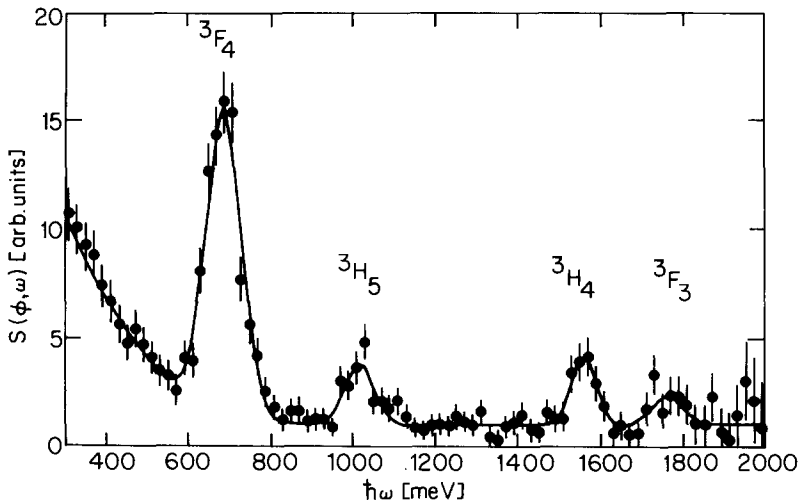

Fig. 6. Neutron scattering cross-section of intermulitplet transitions from the $^3H_6$ ground level in thulium metal at 20 K, measured at an angle of 5° with an incident neutron energy of 2140 meV on HET. The instrumental resolution varies from 56 to 27 meV as the energy transfer increases from 500 to 1800 meV. The data have been fitted by four Gaussians and a tail of low-energy scattering. The peaks are labelled by the final state of the transition.

TABLE 6

The experimental and calculated energies (in meV) of inter-multiplet transitions from the $^3H_6$ ground state multiplet of the Tm^{3+} ion: Tm doped in LaF_3 (Carnall et al. 1989); Tm metal (Osborn et al. 1990); calculation using the following parameters, $F_2 = 59.3$ meV, $F_4 = 8.19$ meV, $F_6 = 0.896$ meV and $\zeta_{4f} = 326.8$ meV.

	Tm:LaF_3	Tm metal	Calculation
$^3F_4$	689.7	694	693.5
$^3H_5$	1017.0	1018	1017.8
$^3H_4$	1550.4	1560	1556.0
$^3F_3$	1774.3	1760	1810.7

$^3H_6 \rightarrow {}^3F_4$, $^3H_5$, $^3H_4$ and $^3F_3$ transitions, respectively. Furthermore, the relative intensities of the $^3H \rightarrow {}^3H$ and the $^3H \rightarrow {}^3F$ transitions are in good agreement with a full intermediate coupling calculation, in contrast to the praseodymium results (fig. 7).

The energies of all the transitions are well reproduced with $F_2 = 59.3$ meV and $\zeta_{4f} = 326.8$ meV. The remaining Slater integral parameters were kept fixed to their hydrogenic ratios (see sect. 2.1.1). The value of ζ_{4f} is identical to that determined by Carnall et al., although the Slater integrals are slightly different because of our neglect of the other weaker free-ion parameters.

Since the transition energies of Pr:LaF_3 are close to those of the free Pr^{3+} ion, it is especially significant that there is no appreciable difference between thulium metal and the fluoride. This suggests that, in the heavy lanthanides, there is no additional screening of the Coulomb interaction to that occurring in the free ion. Osborn et al. (1990) propose that this is a consequence of the lanthanide contraction making the f shell in the heavy lanthanides much less susceptible to perturbation by the external environment. The fact that there are no anomalies in the measured intensities confirms the existence of a correlation between the Slater parameter shifts and the intensity reductions inferred from the praseodymium results (Osborn 1989). Both are a consequence of increased hybridisation of the f states in the lighter lanthanides.

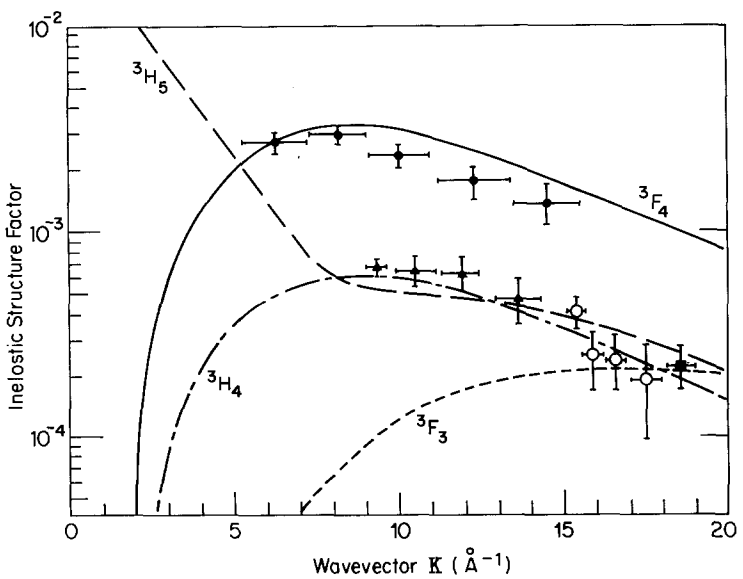

Fig. 7. Neutron inelastic structure factors for intermultiplet transitions in thulium. The lines represent the calculated intensites, taking intermediate coupling into account, of the $^3H_6 \rightarrow {}^3F_4$ (smooth line), $^3H_6 \rightarrow {}^3H_5$ (long-dashed line), $^3H_6 \rightarrow {}^3H_4$ (chain line) and $^3H_6 \rightarrow {}^3F_3$ (short-dashed line) transitions. The calculated structure factors are normalised to the $^3H_6 \rightarrow {}^3H_6$ intensity at $\kappa = 0$, which has a cross-section of 2769 mb sr^{-1}. The measured intensities of transitions to the $^3F_4$ (filled circles), $^3H_5$ (filled triangles), $^3H_4$ (open circles) and $^3F_3$ level (filled square) levels are normalised to the calculated structure factor of the $^3H_6 \rightarrow {}^3F_4$ transition at $\kappa = 6.2$ Å^{-1}.

Investigations of Coulomb transitions in intermediate valent thulium (and samarium) compounds are an obvious development in this field.

5.3. *Uranium alloys*

The study of Coulomb transitions is especially valuable in actinide metals and intermetallic compounds (McEwen et al. 1990, Osborn et al. 1990). Because of the greater radial extent of the 5f charge distribution, the actinide f electrons tend to hybridise more strongly with band electron states than their lanthanide counterparts. In a number of actinide metals, it is evident that the f electrons contribute to the cohesive energy through the formation of 5f bands, either by direct f–f overlap, as in α-uranium, or by hybridisation with conduction bands, as in URu_3 or URh_3 (Oguchi and Freeman 1986, Johansson et al. 1987). In these cases, relativistic band theory is successful in predicting lattice constants, photo-emission and Fermi surfaces (Arko et al. 1985) provided the f states are included as itinerant.

On the other hand, good agreement with the de Haas–van Alphen measurements on UPd_3 (Ubachs et al. 1986) is only obtained by treating the f electrons as core states (Norman et al. 1987), whilst photo-emission results show that there is no f-electron density at the Fermi level in this compound (Baer et al. 1980). It is significant that UPd_3 is the only actinide metal in which well defined crystal-field excitations have been observed by neutron spectroscopy (Shamir et al. 1978, Murray and Buyers 1980, Buyers and Holden 1985). All these results indicate that the uranium ions in UPd_3 have a localised f^2 configuration and behave more like stable lanthanide ions.

Although band theory cannot describe the f electrons in UPd_3 adequately, it can help to explain why they behave differently from the f electrons in other apparently similar compounds. Johansson et al. (1987) have shown that in UX_3 compounds, where X is a 4d transition metal, the d electrons hybridise to form two separate bands; a bonding band, largely composed of X-derived 4d states, and an anti-bonding band, composed of the U-derived 6d states. In most of the compounds, the 5f states hybridise with the 4d states spreading the f contribution to the electronic density of states over several electron volts. In UPd_3, however, the f states lie in the gap between the two d bands and scarcely hybridise at all. In these circumstances, the f electrons gain correlation energy through the localisation process. In a further study of the band structure of $U(Pd_{1-x}Rh_x)_3$ alloys, Eriksson et al. (1988) have studied the Mott transition in which the f-electron character changes from localised to itinerant with increasing x as a consequence of the 4d band moving up in energy.

McEwen et al. (1988) have suggested that similar mechanisms are responsible for the change in magnetic behaviour in $U(Pd_{1-x}Pt_x)_3$ alloys from localised magnetism for $x = 0$ to heavy-fermion superconductivity for $x = 1$. Franse et al. (1985) have shown that the large electronic specific-heat enhancement in UPt_3 is not present until $x > 0.7$. The effect of increasing hybridisation is also evident in the crystal-field spectra (McEwen et al. 1988, 1990b), with the peak at 14 meV

shifting to lower energy and broadening as x increases, becoming quasielastic at $x = 1$. There is always the possibility that some of this broadening is due to lattice disorder, but the absence of well defined crystal-field transitions in UPt_3 confirms that much of the damping is due to the hybridisation.

These results encouraged the first investigation of intermultiplet excitations in a uranium compound (McEwen et al. 1990, Osborn et al. 1990). Whilst crystal-field studies can trace the development of hybridisation, they cannot show what happens to the 5f-electron ground state as it grows. The observation of intermultiplet transitions, however, can establish whether intra-atomic correlations are maintained as the hybridisation is turned on, and gives information on the composition of the hybridised ground state. An estimate of the positions of the intermultiplet transitions in U^{4+} ions can be obtained by using the free-ion parameters of UO_2 (Rahman and Runciman 1966). The lowest transitions are the $^3H_4 \rightarrow {}^3F_2$ and $^3H_5$ transitions at 448 and 692 meV, respectively. The former is a Coulomb transition and so would be significantly reduced in energy by hybridisation. The observation of the $^4I_{9/2} \rightarrow {}^4I_{11/2}$ transition, which occurs at 530 meV in U^{3+}:$LaCl_3$ (Carnall and Crosswhite 1985), would imply the development of intermediate valency.

Figure 8a shows the neutron inelastic scattering from UPd_3. There is a peak at 385 meV with a width of about 60 meV sitting on a multiple scattering background. McEwen et al. (1990a) ascribe the peak to the $^3H_4 \rightarrow {}^3F_2$ transition, which requires $F_2 = 19.7$ meV, a 20% reduction from its value of 23.73 meV in UO_2. To reduce the number of free parameters to one, the ratios of F_4 and F_6 to F_2, and the value of ζ_{5f} are kept fixed to their ionic values. This Slater parameter

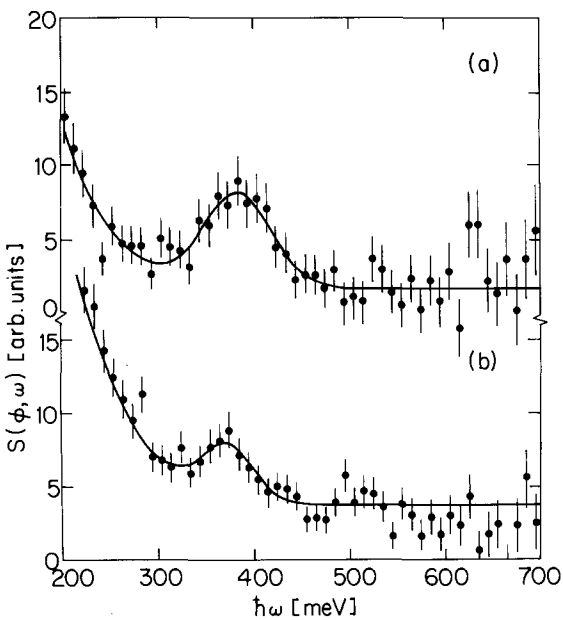

Fig. 8. Neutron inelastic scattering from (a) UPd_3 and (b) UPt_3 at 20 K, measured at an angle of 5° with an incident energy of 800 meV on HET. The data have been fitted to a Gaussian and a tail of low-energy scattering.

shift is much larger than that found in the lanthanides but appears reasonable, given the greater spatial extent of the 5f wavefunctions. This result then confirms the earlier conclusions concerning the localised nature of the 5f shell in UPd_3.

McEwen et al. (1990a) performed equivalent scans for $x = 0.37$, 0.5, 0.75 and 1.0 in the alloy series $U(Pd_{1-x}Pt_x)_3$. A similar peak is seen in every sample although its energy falls to 375 meV at $x = 0.5$. In UPt_3, it is at 373 meV and is both broader and weaker (fig. 8b). The extra reduction of F_2 at $x = 0.5$ occurs in the same composition range as a change in the crystal structure from the dhcp phase of UPd_3 to a 10-layer structure (McEwen et al. 1990b). Nevertheless, apart from this small energy shift, the intermultiplet transition persists across the series, showing that the ground state of the heavy-fermion compound UPt_3 is, like UPd_3, composed of highly correlated 5f states, with a major component formed from the $5f^2\ ^3H_4$ ground level. The measurements do not rule out the presence of a $5f^3$ component, as well, i.e., that UPt_3 is an intermediate valence compound with a hybridised ground state composed of two configurations. However, the failure to observe any $5f^3$-derived peaks implies that the uranium ion is close to tetravalent.

The suggestion that UPt_3 has a fairly localised $5f^2$ configuration is not entirely new. It was proposed by Johansson et al. (1986) after consideration of the molar volumes and crystal structures of similar tetravalent compounds. On the other hand, there is considerable evidence that the f electrons form itinerant bands, even if their contribution to the bonding is small. Most strikingly, de Haas–van Alphen studies (Taillefer and Lonzarich 1988) provide detailed measurements of the Fermi surface topology which are in excellent agreement with relativistic local-density functional band structures (Norman et al. 1988, Christensen et al. 1988) which treat the f electrons as itinerant. Therefore, in spite of the neglect of orbital correlations, which the neutron scattering results show are very strong, one-electron band theory predicts the correct Fermi surface. The resolution of this paradox, that the f electrons are both highly correlated and yet itinerant, is, of course, central to the understanding of heavy-fermion phenomena.

For UPt_3, the resolution of this conflict appears to be rather subtle. Density functional band theory predicts the correct Fermi surface but not the correct quasiparticle masses. To do that requires a reduction of the band widths in a semi-empirical manner (Fulde et al. 1988, Zwicknagl 1988); in the case of UPt_3 the renormalised band widths are about 50 meV (Christensen et al. 1988). This is much less than the intermultiplet splitting so, whilst the f electrons may form bands through hybridisation with the ligand d orbitals, the resulting Fermi liquid must be derived from the f states comprising the $^3H_4$ ground level. It seems that the reason for the success of band theory may be fortuitous. Because of the strength of the spin–orbit interaction and relative weakness of the Coulomb interaction in the actinides compared to the lanthanides, the 5f electrons are closer to being in the *jj*-coupling states than their lanthanide counterparts, for which *LS* coupling is a much better approximation. In the limit of strong spin–orbit coupling, relativistic band theory will predict the correct *jj*-coupling ground state, which has both f electrons in the $j = \frac{5}{2}$ state, and indeed Zwicknagl (1988) has shown that the Fermi surface of UPt_3 consists almost wholly of $j = \frac{5}{2}$

character. She concludes that the Fermi surface topology is given correctly by band theory provided the spin–orbit coupling is strong. To this should be added the condition that the Coulomb repulsion between the f electrons must be comparatively weak, so that it is reasonable to neglect the orbital correlations implied by Hund's rules.

Investigations of the intermultiplet transitions have only just begun, but it is already evident that they can help to clarify the nature of the 5f-electron ground states in actinide metals. The experience gained from measuring Coulomb transitions in the relatively stable configurations of lanthanide compounds has been essential in interpreting the scattering from more strongly hybridised configurations. So far, the similarities between actinide systems and their lanthanide counterparts are more remarkable than their differences. As more actinide compounds are explored, it should be possible to determine the degree of correlation necessary for the development of a particular ground state, whether localised, heavy fermion or itinerant.

6. Theory

6.1. *Tensor operators*

The use of a spherical basis for the representation of tensor components facilitates the application of (tensor) operator techniques to the calculation of matrix elements in atomic spectroscopy.

We select a sufficiently general form of a spherical tensor product which allows the combination of two tensors U^κ_γ, V^k_q while preserving the fundamental properties of a spherical tensor of rank K,

$$X^K_Q = \{U^\kappa_\gamma \otimes V^k_q\}^K_Q , \tag{42}$$

where

$$\{U^\kappa_\gamma \otimes V^k_q\}^K_Q \equiv \sum_{q,q'} U^\kappa_\gamma V^k_q \langle \kappa\gamma kq | KQ \rangle . \tag{43}$$

For convenience, we employ an abbreviation

$$[K, J, \ldots]^{1/2} \equiv \sqrt{[(2K+1)(2J+1)\ldots]} , \tag{44}$$

because (44) or a similar combination of factors appears frequently in our formulae. With this notation, and using a $3j$ symbol, we have

$$X^K_Q = \sum_{q,q'} U^\kappa_\gamma V^k_q [K]^{1/2} (-1)^{-k+k'-Q} \begin{pmatrix} \kappa & k & K \\ \gamma & q & -Q \end{pmatrix} . \tag{45}$$

A tensor operator is thus created from U and V, and the analogy to the coupling of angular momentum eigenfunctions is underlined by the presence of the Clebsch–Gordan coefficient in (43) or, equivalently, the $3j$ symbol in (45). If, on the other hand, we are given a double tensor, this may be represented as a sum of tensor products by

$$U^{\kappa}_{\gamma} V^{k}_{q} = \sum_{K,Q} \langle \kappa\gamma kq | KQ \rangle X^{K}_{Q} \,. \tag{46}$$

The special significance of this equation derives from the fact that some of the interaction operators considered here contain double tensors, while the general formulae used in the following refer to tensor products of the form X^{K}_{Q}.

The above formulation includes the possibility of obtaining the final rank $K = 0$ from two tensors of the same rank:

$$X^{0}_{0} = \sum_{q} U^{k}_{q} V^{k}_{-q} \begin{pmatrix} k & k & 0 \\ q & -q & 0 \end{pmatrix} = (-1)^{k} \frac{1}{[k]^{1/2}} \sum_{q} (-1)^{q} U^{k}_{q} V^{k}_{-q} \,. \tag{47}$$

Here, the right-hand side is, except for the prefactor, the scalar product of two tensor operators and, in the case of $k = 1$, this reduces to the dot product of two vectors, albeit expressed in spherical components. For the $3j$ symbol in (47)

$$\begin{pmatrix} k & k & 0 \\ q & -q & 0 \end{pmatrix} = \begin{pmatrix} 0 & k & k \\ 0 & q & -q \end{pmatrix} = \frac{(-1)^{k-q}}{[k]^{1/2}} \,.$$

We use this value of the $3j$ symbol for the case where one of the two operators is reduced to a (unit) scalar

$$\begin{aligned} \{C^{0}_{0} \otimes V^{K}_{Q}\}^{K}_{Q} &= \sum_{Q} [K]^{1/2} (-1)^{K-Q} \begin{pmatrix} 0 & K & K \\ 0 & Q & -Q \end{pmatrix} \\ &= C^{0}_{0} V^{K}_{Q} \equiv V^{K}_{Q} \,. \end{aligned} \tag{48}$$

The last expression allows us also to apply general results derived for coupled tensors to single tensor operators.

The spherical formalism hides at first glance the customary Cartesian expressions, and this is particularly noticeable for the vector product:

$$\begin{aligned} (\boldsymbol{u} \times \boldsymbol{v})^{1}_{-q} &= \mathrm{i}(-1)^{1-q} \sqrt{6} \sum_{q',q''} u^{1}_{q'} v^{1}_{q''} \begin{pmatrix} 1 & 1 & 1 \\ q' & q'' & -q \end{pmatrix} \\ &= (-\mathrm{i}) \sqrt{2} \{u^{1}_{q'} \otimes v^{1}_{q''}\}^{1}_{q} . \end{aligned} \tag{49}$$

In the context of atomic spectroscopy, with special emphasis on the lanthanide atoms and ions, most configurations will consist of more than one electron and the corresponding operators of interest will contain a sum of single-particle operators, e.g.,

$$\boldsymbol{S} = \sum_{\nu} (\boldsymbol{s}_{\nu}) \,, \qquad \boldsymbol{L} = \sum_{\nu} (\boldsymbol{l}_{\nu}) , \tag{50}$$

and if we refer to a general operator

$$X^{K}_{Q} = \sum_{\nu} (x_{\nu})^{K}_{Q} . \tag{51}$$

Here, ν labels the n equivalent electrons in an atomic shell of angular momentum l.

6.2. *Wigner-Eckart theorem*

After arranging our notation to accommodate spherical tensors we turn to a powerful tool for the calculation of matrix elements. The Wigner–Eckart theorem allows the factorisation of a matrix element into a part containing the dependence of the "magnetic" quantum numbers, essentially a $3j$ symbol, and a part independent of these, called the reduced matrix element and already employed in sect. 2;

$$\langle v, S, L, J, M|X_Q^K|v', S', L', J', M'\rangle$$
$$= (-1)^{J-M}\begin{pmatrix} J & K & J' \\ -M & Q & M' \end{pmatrix}\left(v, S, L, J\left\|\sum_\nu (x_\nu)^K\right\|v', S', L', J'\right). \tag{52}$$

In order to achieve a more compact notation we make the abbreviations $\theta = v, S, L,\ \theta' = v', S', L'$ etc. as in sect. 2. Again, with out main interest centered on the lanthanide series, we have used in (52) eigenstates of the total angular momentum operators $\boldsymbol{J}^2$, J^z in the matrix element.

The coupling of Russell–Saunders states $|\theta, M_S, M_L\rangle$ by means of Clebsch–Gordan coefficients,

$$|\theta, J, M\rangle = \sum_{M_S, M_L} \langle S, M_S, L, M_L|J, M\rangle|\theta, M_S, M_L\rangle \tag{53}$$

has a consequence for the reduced matrix element in (52)

$$\left(v, S, L, J\left\|\sum_\nu (x_\nu)^K\right\|v', S', L', J'\right)$$
$$= [J, K, J']^{1/2}\begin{Bmatrix} S & L & J \\ S' & L' & J' \\ \kappa & k & K \end{Bmatrix}\left(\theta\left\|\sum_\nu (u_\nu)^\kappa (v_\nu)^k\right\|\theta'\right). \tag{54}$$

We note for later applications of this formula that, κ in (54) will be restricted to the values 1 and 0. Also, the operators u_γ^κ, v_q^k operate in different spaces, e.g., the orbital or the spin part of a wavefunction. Note, furthermore, that the reduced matrix element on the right-hand side of (54) contains only a product of tensor components and not a tensor product.

6.3. *Many-electron matrix elements*

If a reduced matrix element between many-electron states is to be expressed in terms of those of single-electron states, we have to introduce the concept of fractional parentage coefficients pioneered by Racah. Collecting the general parts of a reduced matrix element between states with n equivalent electrons, we are led to the definition of a Racah tensor and, in this case, the fractional parentage coefficients will appear explicitly only in this definition:

$$(\theta\|W^{(\kappa,k)}\|\theta') = n[S, \kappa, S', L, k, L']^{1/2}(-1)^{s+\kappa+L+S+l+k}$$
$$\times \sum_{\bar\theta} (\theta|\}\bar\theta)(\bar\theta\{|\theta')(-1)^{\bar S+\bar L}\begin{Bmatrix} S & \kappa & S' \\ s & \bar S & s \end{Bmatrix}\begin{Bmatrix} L & k & L' \\ l & \bar L & l \end{Bmatrix}. \tag{55}$$

The reduced matrix element on the right-hand side of (54) consists of single-electron reduced matrix elements belonging to the specific operators, and the reduced matrix element of the corresponding Racah tensor. The latter, clearly, is independent of the nature of u_γ^κ and v_q^k,

$$\left(\theta \left\| \sum_\nu (u_\nu)^\kappa (v_\nu)^k \right\| \theta'\right)$$
$$= (s\|u^\kappa\|s)(l\|v^k\|l)\,\frac{1}{[\kappa, k]^{1/2}}\,(\theta\|W^{(\kappa,k)}\|\theta'). \tag{56}$$

We may proceed even further, including the $9j$ symbol and any factors of (54) in the definition of yet another Racah tensor, and arriving at a compact expression for the reduced matrix element of a tensor product,

$$\left(v, S, L, J \left\| \sum_\nu (x_\nu)^K \right\| v', S', L', J'\right)$$
$$= (s\|u^\kappa\|s)(l\|v^k\|l)(\theta, J\|W^{(\kappa,k)K}\|\theta', J'). \tag{57}$$

The main effort of calculating a many-electron matrix element is obtaining a value for the reduced matrix elements of the Racah tensors $W^{(\kappa,k)}$ and $W^{(\kappa,k)K}$. Once a list of these quantities is available, calculation of the full matrix element represents a relatively simple task, since it requires the specific reduced single-electron matrix elements of u^κ nd v^k, for instance.

An example will provide us with an opportunity to apply our formalism. Use of a general tensor product includes the option to consider also the matrix elements of a single vector operator. There is, however, a price to pay, since the Wigner–Eckart theorem (52) requires even a unit scalar c^0 to have a non trivial reduced matrix element

$$(s\|c^0\|s) = \sqrt{(2s+1)}\,, \qquad (l\|c^0\|l) = \sqrt{(2l+1)}\,, \tag{58}$$

and these values have to be taken into account in (56) and (57). As a consequence we find, for $l = 3$,

$$(\theta, J\|\boldsymbol{L}\|\theta', J') = (l\|\boldsymbol{l}\|l)\sqrt{2}(\theta, J\|W^{(0,1)1}\|\theta', J')\,, \tag{59}$$

$$(\theta, J\|\boldsymbol{S}\|\theta', J') = \sqrt{7}(s\|\boldsymbol{s}\|s)(\theta, J\|W^{(1,0)1}\|\theta', J')\,. \tag{60}$$

The reduced matrix elements for the single-electron operators are

$$(l\|\boldsymbol{l}\|l) = \sqrt{[l(l+1)(2l+1)]} = 2\sqrt{21}\,, \tag{61}$$

$$(s\|\boldsymbol{s}\|s) = \sqrt{[s(s+1)(2s+1)]} = \sqrt{\tfrac{3}{2}}\,. \tag{62}$$

We shall now consider the case $J = J' = 4$ for praseodymium, Pr^{3+}. The reduced matrix elements of the Racah tensors are

$$({}^3\mathrm{H}_4\|W^{(0,1)1}\|{}^3\mathrm{H}_4) = 3\sqrt{\tfrac{6}{35}}\,,$$
$$({}^3\mathrm{H}_4\|W^{(1,0)1}\|{}^3\mathrm{H}_4) = -2\sqrt{\tfrac{6}{35}}\,, \tag{63}$$

and the final result from (59) and (60) is

$$({}^3\mathrm{H}_4\|\boldsymbol{L}\|{}^3\mathrm{H}_4) = 36\sqrt{\tfrac{1}{5}}\,,$$

$$({}^3\mathrm{H}_4\|\boldsymbol{S}\|{}^3\mathrm{H}_4) = -6\sqrt{\tfrac{1}{5}}\,. \tag{64}$$

Because we have restricted attention to a J-multiplet, operator equivalences exist, i.e., $\boldsymbol{S} = g_S\boldsymbol{J}$ and $\boldsymbol{L} = g_L\boldsymbol{J}$ together with the result

$$(\theta, J\|\boldsymbol{J}\|\theta, J) = \sqrt{[J(J+1)(2J+1)]}\,. \tag{65}$$

With the well known expressions

$$g_S = \frac{J(J+1) + S(S+1) - L(L+1)}{2J(J+1)}\,, \tag{66}$$

$$g_L = \frac{J(J+1) + L(L+1) - S(S+1)}{2J(J+1)}\,. \tag{67}$$

the results given in (64) are easily reproduced for Pr^{3+} with $L = 5$, $S = 1$ and $J = 4$.

If we apply our formulae to an intermultiplet case $J \neq J'$, e.g., $J = 4$ and $J' = 5$ for Pr^{3+}, the reduced matrix elements are

$$({}^3\mathrm{H}_4\|W^{(0,1)1}\|{}^3\mathrm{H}_5) = -\tfrac{3}{2}\sqrt{\tfrac{1}{35}} \tag{68}$$

$$({}^3\mathrm{H}_4\|W^{(1,0)1}\|{}^3\mathrm{H}_5) = 6\sqrt{\tfrac{1}{35}} \tag{69}$$

and we find from (59) and (60)

$$({}^3\mathrm{H}_4\|\boldsymbol{S}\|{}^3\mathrm{H}_5) = -({}^3\mathrm{H}_4\|\boldsymbol{L}\|{}^3\mathrm{H}_5) = 3\sqrt{\tfrac{6}{5}}\,. \tag{70}$$

This is not unexpected because the operator $\boldsymbol{J} = \boldsymbol{L} + \boldsymbol{S}$ has no matrix elements between states with differing J-values and, thus, the reduced matrix elements for $\boldsymbol{L}$ and $\boldsymbol{S}$ must be of opposite sign and of the same size.

To round off our experience, in handling the formalism developed above, we consider the angular part of the spin–orbit interaction (without an r-dependent part)

$$\mathscr{H}_{sl} = \sum_\nu \boldsymbol{s}_\nu \cdot \boldsymbol{l}_\nu = \sum_\nu \sum_q (-1)^q (s_\nu)_q (l_\nu)_{-q}\,. \tag{71}$$

Here, the second term on the right-hand side is already written in spherical components. From eq. (47) we see that the scalar product of $\boldsymbol{s}_\nu$ and $\boldsymbol{l}_\nu$ is proportional to a tensor product of rank $K = 0$,

$$\sum_\nu \boldsymbol{s}_\nu \cdot \boldsymbol{l}_\nu = (-1)\sqrt{3}\{s_q^1 \otimes l_q^1\}_0^0\,. \tag{72}$$

We choose again Pr^{3+} with $J = J' = 4$. The reduced matrix element of the Racah tensor is, in the ground state,

$$({}^3\mathrm{H}_4\|W^{(1,1)0}\|{}^3\mathrm{H}_4) = \sqrt{\tfrac{3}{14}}\,, \tag{73}$$

and together with (72) and (57) we find

$$\left({}^3\mathrm{H}_4 \left\| \sum_\nu \boldsymbol{s}_\nu \cdot \boldsymbol{l}_\nu \right\| {}^3\mathrm{H}_4\right) = -9\,. \tag{74}$$

The full matrix element including the corresponding $3j$ symbol is, for $M = J$,

$$\left\langle \theta, J, J \left| \sum_\nu \boldsymbol{s}_\nu \cdot \boldsymbol{l}_\nu \right| \theta, J, J \right\rangle = -3\,. \tag{75}$$

This result may be checked against the well known equivalent operator, for a J-multiplet,

$$2\lambda \boldsymbol{S} \cdot \boldsymbol{L} = \lambda(\boldsymbol{J}^2 - \boldsymbol{L}^2 - \boldsymbol{S}^2)\,, \tag{76}$$

where $\lambda = \pm 1/2S$ in the first and second half of the lanthanide series, respectively. Although the spin–orbit interaction is diagonal within the multiplet of J-states belonging to an LS term, there may be non-zero matrix elements between states belonging to different terms. The spin–orbit interaction can thus lead to a mixing of states with the same J from different terms. For our example, Pr^{3+}, we find the following reduced matrix elements of the corresponding Racah tensors:

$$({}^3\mathrm{H}_4 \| W^{(1,1)0} \| {}^3\mathrm{H}_4) = \sqrt{\tfrac{3}{14}}\,,$$

$$({}^3\mathrm{H}_4 \| W^{(1,1)0} \| {}^3\mathrm{F}_4) = 0\,,$$

$$({}^3\mathrm{H}_4 \| W^{(1,1)0} \| {}^1\mathrm{G}_4) = \tfrac{1}{3}\sqrt{\tfrac{5}{7}}\,,$$

$$({}^3\mathrm{F}_4 \| W^{(1,1)0} \| {}^3\mathrm{F}_4) = -\tfrac{1}{2}\sqrt{\tfrac{3}{14}}\,,$$

$$({}^3\mathrm{F}_4 \| W^{(1,1)0} \| {}^1\mathrm{G}_4) = -\tfrac{1}{3}\sqrt{\tfrac{11}{14}}\,,$$

$$({}^1\mathrm{G}_4 \| W^{(1,1)0} \| {}^1\mathrm{G}_4) = 0\,.$$

In order to quantify the energies of the spin–orbit interaction, we have to include the atomic average of the radial functions $\zeta_{nl} = \langle \zeta(r) \rangle_l$ which measures the strength of the interaction within a shell of equivalent electrons. To obtain the influence of spin–orbit coupling on the atomic energy levels, a simultaneous diagonalisation of the spin–orbit and the Coulomb interactions is required.

6.4. *Orbital interactions*

In this and the subsequent section we provide explicit expressions for the orbital and spin matrix elements, respectively, which describe the scattering of neutrons by equivalent, non-relativistic electrons in a single atomic shell. Derivations of the expressions are reported in several references.

First, we provide some general features of the expressions not covered in the introductory material of sect. 2 because they are slightly too technical. A proof that the orbital matrix element is proportional to an odd-rank Racah tensor is not a back-of-an-envelope exercise. The available proofs start with the comparison of one-electron matrix elements evaluated for two equivalent forms of the orbital interaction. For the reader who sets about finding a simpler proof, we inject the

observation that the important papers by Trammell (1953) and Stassis and Deckman (1976) contain errors which directly relate to the question in hand. Both papers contain an expression, for the n-electron orbital matrix element, that shows a term proportional to the difference between initial and final electron energies. Such a term carries with it an even-rank Racah tensor. However, it appears because their reasoning is wrong; in truth it is not present for non-relativistic electrons in a single shell, for it is correctly derived from the commutator of the kinetic energy with a spatial quantity, and the nl-diagonal matrix element of such a function vanishes. A proof that the spin matrix element is proportional to an odd-rank tensor is relatively simple. Note, in passing, that reduced matrix elements of many electron operators, such as the spin–orbit interaction, are proportional to even-rank tensors which do not have the remarkable property of odd-rank tensors mentioned in sect. 2.

An odd-rank tensor can be associated with even- or odd-parity contributions to a matrix element, and these are conventionally described as electric and magnetic multipole contributions, respectively (Stassis and Deckman 1976). The orbital matrix element contains magnetic multipole terms, whereas the spin matrix element contains both magnetic and electric multipole terms. In terms of the notation introduced in sect. 2, $A(K, K \pm 1)$ and $B(K, K \pm 1)$ are magnetic multipole terms, and $B(K, K)$ is an electric multipole term. The latter term vanishes for $S = S'$, $L = L'$ and $J = J'$, that is it does not contribute to the elastic form factor of an isolated magnetic ion.

We now turn to the main purpose of the section, namely, the provision of a formula for the orbital matrix element. The result given in eq. (29) for the matrix element of the orbital contribution may be rewritten with the use of a $3j$ symbol

$$\begin{aligned}
&\left\langle \theta, J, M \left| \sum_{\nu} \exp(\mathrm{i}\boldsymbol{\kappa}\cdot\boldsymbol{r}_{\nu})(\boldsymbol{\kappa}\times\boldsymbol{\nabla}_{\nu})_{q} \right| \theta', J', M' \right\rangle \\
&\quad = (-1)^{J-M}\begin{pmatrix} J & K' & J' \\ -M & Q' & M' \end{pmatrix}\left(\theta, J \left\| \sum_{\nu} \exp(\mathrm{i}\boldsymbol{\kappa}\cdot\boldsymbol{r}_{\nu})(\boldsymbol{\kappa}\times\boldsymbol{\nabla}_{\nu}) \right\| \theta', J'\right) \\
&\quad = (-1)^{J-M}\begin{pmatrix} J & K' & J' \\ -M & Q' & M' \end{pmatrix}\left[-(4\pi)^{1/2}\kappa \sum_{\substack{K,Q \\ K',Q'}} Y^{K}_{Q}(\tilde{\boldsymbol{\kappa}})\right. \\
&\qquad \left. \times [J]^{1/2}(-1)^{J'-K'-J}A(K, K')\langle K, Q, K', Q'|1, q\rangle\right]. \qquad (77)
\end{aligned}$$

The contents of the large square brackets must thus represent the reduced matrix element in accordance with (52). Since the operator does not contain a spin part, we may use (48) and interpret the interaction as a tensor product with a unit scalar operating in spin space. The real space operator is, however, not yet in the form of a spherical tensor operator, but using (46) we arrive at

$$\begin{aligned}
&\left(\theta, J \left\| \sum_{\nu} \exp(\mathrm{i}\boldsymbol{\kappa}\cdot\boldsymbol{r}_{\nu})(\boldsymbol{\kappa}\times\boldsymbol{\nabla}_{\nu}) \right\| \theta', J'\right) \\
&\quad = (s\|c^{0}\|s)(l\|\exp(\mathrm{i}\boldsymbol{\kappa}\cdot\boldsymbol{r})(\boldsymbol{k}\times\boldsymbol{\nabla})\|l)(\theta, J\|W^{(0,K')K'}\|\theta', J'). \qquad (78)
\end{aligned}$$

With the first factor equal to $\sqrt{2}$, only the single-electron reduced matrix element for the orbital operators remains to be calculated. With some effort the following expression may be derived:

$$(l\|\exp(\mathrm{i}\boldsymbol{\kappa}\cdot\boldsymbol{r})(\boldsymbol{\kappa}\times\boldsymbol{\nabla})\|l)$$
$$= -\kappa^2(4\pi)^{1/2}\sum_{\substack{K,Q\\K',Q'}} Y_Q^K(\tilde{\boldsymbol{\kappa}})\langle K, Q, K', Q'|1, q\rangle\,\mathrm{i}^{K'-1}$$
$$\times\frac{(2l+1)^2}{\sqrt{3}}A(K', K', l)(\langle j_{K'-1}\rangle + \langle j_{K'+1}\rangle)G(K')\,, \tag{79}$$

where

$$G(K') = \begin{cases}\sqrt{K'}\,, & K = K'+1\,,\\ \sqrt{(K'+1)}\,, & K = K'-1\,,\end{cases} \tag{80}$$

and the factor $A(K', K', l)$ is

$$A(K', K', l) = (-1)^{l+1}\left(\frac{(2l+3)(l+1)}{(2l+1)}\right)^{1/2}\begin{pmatrix} l & K' & l+1\\ 0 & 0 & 0\end{pmatrix}\begin{Bmatrix}1 & K' & K'\\ l & l+1 & l\end{Bmatrix}. \tag{81}$$

Collecting all the results we are now in a position to present the quantities $A(K, K')$ used in (77), and also $a(K, K')$ as defined in (30)

$$a(K, K') = (-1)^{J'-K'-J}\,\mathrm{i}^{K'-1}\sqrt{\tfrac{2}{3}}\,\frac{(2l+1)^2}{[J]^{1/2}}$$
$$\times G(K')A(K', K', l)(\theta, J\|W^{(0,K')K'}\|\theta', J')\,. \tag{82}$$

The restrictions on K, K' are $K = K' \pm 1$, only, K' is an odd integer, and its maximum value is $2l+1$. The following equation

$$A(K'+1, K') = \sqrt{\left(\frac{K'}{K'+1}\right)}\,A(K'-1, K')\,, \tag{83}$$

describes the relationship between the two $A(K, K')$.

It is, perhaps, worthwhile to note the relation with the Racah tensor $W^{(0,K')}$

$$(\theta, J\|W^{(0,K')K'}\|\theta', J')$$
$$= (-1)^{K'+J+S+L'}\,\frac{[J, J']^{1/2}}{[S, K']^{1/2}}\begin{Bmatrix}J' & K' & J\\ L & S & L'\end{Bmatrix}(\theta\|W^{(0,K')}\|\theta')\,. \tag{84}$$

The reduced matrix element $(\theta\|W^{(0,K')}\|\theta')$ is often expressed in terms of the reduced matrix elements of a quantity V according to the relation

$$(\theta\|W^{(0,K')}\|\theta') = \left(\frac{2S+1}{2}\right)^{1/2}(\theta\|V^{(K')}\|\theta')\,. \tag{85}$$

Values of $(\theta\|V^{(K')}\|\theta')$ are provided by Nielson and Koster (1963) and Condon and Odabaşi (1980) for example.

6.5. *Spin interactions*

An important step in the calculation of the spin contribution to the magnetic interaction, eq. (33), is the result given in (31) which may be rewritten as

$$\begin{aligned}
&\left\langle \theta, J, M \left| \sum_{\nu} \exp(\mathrm{i}\boldsymbol{\kappa}\cdot\boldsymbol{r}_{\nu})(s_{\nu})_{q} \right| \theta', J', M' \right\rangle \\
&\quad = (-1)^{J-M} \begin{pmatrix} J & K' & J' \\ -M & Q' & M' \end{pmatrix} \left(\theta, J \left\| \sum_{\nu} \exp(\mathrm{i}\boldsymbol{\kappa}\cdot\boldsymbol{r}_{\nu}) s_{\nu} \right\| \theta', J' \right) \\
&\quad = (-1)^{J-M} \begin{pmatrix} J & K' & J' \\ -M & Q' & M' \end{pmatrix} \Bigg((4\pi)^{1/2} \sum_{\substack{K,Q \\ K',Q'}} Y_{Q}^{K}(\tilde{\boldsymbol{\kappa}}) C(K, K') \\
&\qquad \times \langle K, Q, K', Q' | 1, q \rangle [J]^{1/2} (-1)^{J'-K'-J} \Bigg) . \qquad (86)
\end{aligned}$$

The second equality emphasizes the relationship between the quantities $C(K, K')$ and the reduced matrix element. In contrast to the previous section, the interaction operator operates in both spin and real space, where the real space tensors emerge as $Y_{Q}^{K}(\tilde{\boldsymbol{r}})$ from a plane-wave expansion of the exponential. The application of eq. (46) allows us to make use of eq. (57) and we obtain

$$\begin{aligned}
&\left(\theta, J \left\| \sum_{\nu} \exp(\mathrm{i}\boldsymbol{\kappa}\cdot\boldsymbol{r}_{\nu}) s_{\nu} \right\| \theta', J' \right) \\
&\quad = (s\|s\|s)(l\|\exp(\mathrm{i}\boldsymbol{\kappa}\cdot\boldsymbol{r})\|l)(\theta, J\|W^{(1,K)K'}\|\theta', J') . \qquad (87)
\end{aligned}$$

The reduced matrix element for the single-electron spin operator is given in (62) and has the value $\sqrt{\frac{3}{2}}$. The second reduced matrix element may be taken from Judd (1963) and the complete reduced matrix element is found to be

$$\begin{aligned}
&\left(\theta, J \left\| \sum_{\nu} \exp(\mathrm{i}\,\boldsymbol{\kappa}\cdot\boldsymbol{r}_{\nu}) s_{\nu} \right\| \theta', J' \right) \\
&\quad = (4\pi)^{1/2} \sum_{\substack{K,Q \\ K',Q'}} \mathrm{i}^{K} Y_{Q}^{K*}(\tilde{\boldsymbol{\kappa}}) \langle 1, qK, Q | K', Q' \rangle (-1)^{l} [l, l, K]^{1/2} \\
&\qquad \times \sqrt{\frac{3}{2}} \begin{pmatrix} l & K & l \\ 0 & 0 & 0 \end{pmatrix} \langle j_{K} \rangle (\theta, J\|W^{(1,K)K'}\|\theta', J') . \qquad (88)
\end{aligned}$$

Effecting some minor arrangements in the Clebsch–Gordan coefficient, in preparation for a comparison with (86), we arive at the following result for $c(K, K')$, defined in accordance with eq. (32):

$$\begin{aligned}
c(K, K') = \mathrm{i}^{K} \sqrt{\frac{1}{2}} \frac{[l, l, K, K']^{1/2}}{[J]^{1/2}} (-1)^{l+J+K'-J'} \\
\times \begin{pmatrix} l & K & l \\ 0 & 0 & 0 \end{pmatrix} (\theta, J\|W^{(1,K)K'}\|\theta', J') . \qquad (89)
\end{aligned}$$

The $3j$ symbol requires K to be even and $K \leqslant 2l$. The reduced matrix element is related to the Racah tensor $W^{(1,K)}$ by an expression analogous to eq. (84),

$$(\theta, J\|W^{(1,K)K'}\|\theta', J') = \frac{[J, K', J']^{1/2}}{[1, K]^{1/2}} \begin{Bmatrix} S & L & J \\ S' & L' & J' \\ 1 & K & K' \end{Bmatrix} (\theta\|W^{(1,K)}\|\theta') . \quad (90)$$

There is only one task left before we reach the final result embodied in eq. (33). The magnetic interaction requires a double vector product with the unit vector $\tilde{\boldsymbol{\kappa}}$ as shown in eq. (8). If the component of (86) parallel to $\tilde{\boldsymbol{\kappa}}$ is subtracted to leave only those parts which are orthogonal to $\tilde{\boldsymbol{\kappa}}$, we arrive at the quantities $B(K, K')$, where

$$B(K, K') = C(K, K') - \sum_{K''} C(K'', K)[K'', K]^{1/2}(-1)^{K+K'} \times \sum_{\bar{K}} (2\bar{K} - 1) \begin{bmatrix} \begin{pmatrix} 1 & 1 & \bar{K} \\ 0 & 0 & 0 \end{pmatrix} \begin{pmatrix} \bar{K} & K'' & K \\ 0 & 0 & 0 \end{pmatrix} \begin{Bmatrix} K' & K & 1 \\ \bar{K} & 1 & K'' \end{Bmatrix} \end{bmatrix} . \quad (91)$$

This formidable looking expression allows only two terms in the sum over $\bar{K}$, namely $\bar{K} = 0, 2$. In the case $K = K'$ we obtain a very simple result, $B(K, K) = C(K, K)$. For $K' = K \pm 1$ each $B(K, K')$ is given as a linear combination of $C(K, K')$ and $C(K \pm 2, K')$, respectively. The following equation:

$$B(K' + 1, K') = \sqrt{\left(\frac{K'}{K' + 1}\right)} B(K' - 1, K') , \quad (92)$$

describes the same relation between the $B(K, K')$ for $K = K' \pm 1$ as given in the previous section for the orbital part.

Acknowledgements

The rapid development of this subject has been due to the work of a number of people. Particular mention should be made of Professor K.A. McEwen, with whom two of us (R.O and A.D.T.) have enjoyed a fruitful collaboration, and Dr W.G. Williams who stimulated the first measurements of spin–orbit splittings at the ISIS Facility.

Appendix: evaluation of neutron cross-sections

In this appendix, we summarise the formulae required in the calculation of neutron scattering cross-sections, give an example of such a calculation and conclude with tables of the necessary coefficients. Firstly, we remind you of the definition of the cross-section obtained in sect. 2.2.4.

$$\frac{d^2\sigma}{d\Omega\, dE_f} = \left(\frac{E_f}{E_i}\right)^{1/2} r_0^2 \mathcal{G}(\boldsymbol{\kappa}, J, J')\, \delta(\hbar\omega - \Delta) \quad (A1)$$

with $\mathcal{G}(\kappa, J, J')$ given by

$$\mathcal{G}(\kappa, J, J') = \sum_{K'} \left(\frac{3}{K'+1}\right) [A(K'-1, K') + B(K'-1, K')]^2 + \sum_{K} \left(\frac{3}{2K+1}\right) [B(K, K)]^2 ,$$

with $K' = 1, 3, 5, 7$ and $K = 2, 4, 6$.

The major effort entering a calculation of matrix elements for magnetic neutron scattering is concentrated in the quantities denoted $A(K, K')$ and $B(K, K')$. From the discussion in sections 2.2.4 and 6.4 we have found the factor $A(K, K')$ to be associated with both the radial averages $\langle j_{K'-1} \rangle$ and $\langle j_{K'+1} \rangle$. To emphasise this fact in the tables, the corresponding numbers $K'-1$, $K'+1$ are given as subscripts in the form $A(K, K')_{K'-1,K'+1}$. The values of $B(K, K')$ associated with $\langle j_{K'-1} \rangle$ and $\langle j_{K'+1} \rangle$ are different and, therefore, enter separately in the tables as $B(K, K')_{K'-1}$ and $B(K, K')_{K'+1}$. For both quantities $A(K, K')$ and $B(K, K')$ the values for $K = K'-1$ and $K = K'+1$ are related as indicated in eqs. (83) and (92). To summarise,

$$A(K, K') = A(K, K')_{K'-1,K'+1}(\langle j_{K'-1} \rangle + \langle j_{K'+1} \rangle) ,$$

$$B(K'-1, K') = B(K'-1, K')_{K'-1} \langle j_{K'-1} \rangle + B(K'-1, K')_{K'+1} \langle j_{K'+1} \rangle ,$$

$$B(K, K) = B(K, K)_K \langle j_K \rangle .$$

The top line in each table lists the lanthanide ion, the electronic configuration, and the L, S- and L', S'-values for selected terms. The second line contains the J-value of the ground state and each following column is characterised by the J'-values available in the L', S'-multiplet. If an element is forbidden by the conditions imposed through $6j$ or $9j$ symbols the entry is left blank. A single 0 indicates a zero value for the corresponding quantity. Each non-zero entry lists the square of the value in prime factored notation, i.e., the numbers given represent the powers of consecutive prime numbers arising from a factorisation. A negative sign is indicated by an asterisk in front of the first digit. A negative power is underlined and, to increase readability, a comma is inserted after each group of four exponents.

The first entry in the table for Ce^{3+}, f^1, ^2F–^2F in the column $J' = \frac{5}{2}$ is

$$[A(0, 1)_{0,2}]^2 = *4\underline{2}1\underline{1} ,$$

$$A(0, 1)_{0,2} = -\frac{2^2}{3}\sqrt{\frac{5}{7}} .$$

If a prime number exponent has two digits some blank space separates these from the following digits. In the last row for Pr^{3+}, f^2, ^3H–^3H, we find for $J' = 5$,

$$[B(6, 7)_6]^2 = 12\ \underline{5}00, \underline{2}11 ,$$

$$B(6, 7)_6 = \frac{2^6}{(3^2 \times 11)}\sqrt{\left(\frac{17}{3 \times 13}\right)} .$$

In some cases a prime number is given explicitly to simplify the notation. As an

example we use Sm^{3+}, f^5, ^6H–^6H for $J' = \frac{9}{2}$:

$$[B(2,3)_2]^2 = *3\underline{8}11, \underline{1}1\,(31)^2\,,$$

$$B(2,3)_2 = -\frac{2\times 31}{3^4}\sqrt{\left(\frac{2\times 13}{5\times 7\times 11}\right)}\,.$$

Let us now consider the calculation of the inelastic structure factor (A1). As an example, we choose the dipole-allowed transition $J=4$, $J'=5$ of Pr^{3+}, f^2, $^3H \rightarrow {}^3H$, and work through the first three terms up to $\langle j_2\rangle^2$. For this we need five As and Bs, namely $A(0,1)$, $B(0,1)$, $A(2,3)$, $B(2,3)$ and $B(2,2)$. Inspection of the appropriate table shows that $A(2,3)=0$ and

$$A(0,1) = \sqrt{\tfrac{2}{15}}\,(\langle j_0\rangle + \langle j_2\rangle)\,,$$

$$B(0,1) = -2\sqrt{\tfrac{2}{15}}\,\langle j_0\rangle - \tfrac{13}{45}\sqrt{\tfrac{1}{30}}\,\langle j_2\rangle\,,$$

$$B(2,3) = -\tfrac{32}{135}\sqrt{\tfrac{26}{15}}\,\langle j_2\rangle + \cdots\,, \tag{A2}$$

$$B(2,2) = -\tfrac{13}{27}\sqrt{\tfrac{5}{6}}\,\langle j_2\rangle\,, \tag{A3}$$

where we have omitted the $\langle j_4\rangle$ term in $B(2,3)$. From (35) we find

$$\mathcal{G}(\kappa, J, J') = \tfrac{3}{2}[A(0,1)+B(0,1)]^2 + \tfrac{3}{4}[A(2,3)+B(2,3)]^2 + \tfrac{3}{5}[B(2,2)]^2 \tag{A4}$$

$$= 0.200\langle j_0\rangle^2 - 0.342\langle j_0\rangle\langle j_2\rangle + 0.335\langle j_2\rangle^2 + \cdots\,. \tag{A5}$$

(A6)

It is instructive to compare this with the dipole approximation obtained from eqs. (21) and (27), namely,

$$\tfrac{1}{5}[\langle j_0\rangle - \langle j_2\rangle]^2\,, \tag{A7}$$

which is in tolerable agreement with the exact expression evaluated to order $\langle j_2\rangle^2$.

Ce^{3+} (f^1) ^2F–^2F		
$J=\frac{5}{2}$	$J'=\frac{5}{2}$	$J'=\frac{7}{2}$
$A(0,1)_{0,2}$	$*4\underline{2}1\underline{1}$	$2\underline{2}0\underline{1}$
$A(2,3)_{2,4}$	$*3\underline{1}1\underline{2}$	$4\underline{1}0\underline{2}$
$A(4,5)_{4,6}$	$*30\underline{1}1, \underline{2}$	$20\underline{2}1, \underline{2}$
$B(0,1)_0$	$0\underline{2}1\underline{1}$	$*4\underline{2}0\underline{1}$
$B(0,1)_2$	$*4\underline{2}1\underline{1}$	$*0\underline{2}0\underline{1}$
$B(2,2)_2$	0	$*\underline{1}3\underline{1}1$
$B(2,3)_2$	$5\underline{1}1\underline{2}$	$*8\underline{3}0\underline{2}$
$B(2,3)_4$	$*3\underline{1}1\underline{2}$	$*0\underline{1}0\underline{2}$
$B(4,4)_4$	0	$*\underline{2}2\underline{0}1, \underline{1}$
$B(4,5)_4$	$10\underline{1}1, \underline{2}$	$*4\underline{2}0\underline{1}, \underline{2}$
$B(4,5)_6$	$*30\underline{3}1, \underline{2}$	$*0\underline{2}4\underline{1}, \underline{2}$
$B(6,6)_6$		$*\underline{1}3\underline{2}1, \underline{1}1$
$B(6,7)_6$		

Pr^{3+} (f^2) ^3H–^3H			
$J = 4$	$J' = 4$	$J' = 5$	$J' = 6$
$A(0, 1)_{0,2}$	*401	111	
$A(2, 3)_{2,4}$	0	0	0
$A(4, 5)_{4,6}$	6110, 41	*4210, 31	2211, 41
$B(0, 1)_0$	421	*311	
$B(0, 1)_2$	*4630, 02	*1530, 02	
$B(2, 2)_2$	0	*1710, 02	2700, 11
$B(2, 3)_2$	5430, 12	*11 730, 01	7710, 11
$B(2, 3)_4$	5210, 32	1310, 21	*1310, 31
$B(4, 4)_4$	0	1010, 21	*1010, 11
$B(4, 5)_4$	*4110, 41	4210, 31	*8211, 41
$B(4, 5)_6$	6330, 412	*2630, 312	*0651, 412
$B(6, 6)_6$	0	1730, 212	*0730, 111
$B(6, 7)_6$	*7601, 312	12 500, 211	*10 310, 311

Pr^{3+} (f^2) ^3H–^3F			
$J = 4$	$J' = 2$	$J' = 3$	$J' = 4$
$A(0, 1)_{0,2}$			
$A(2, 3)_{2,4}$	*5302, 1	2311	*2202
$A(4, 5)_{4,6}$	0	0	0
$B(0, 1)_0$		0	0
$B(0, 1)_2$		*1510, 1	1620, 1
$B(2, 2)_2$	3721, 1	*0720, 1	0201
$B(2, 3)_2$	7702, 1	*10 711	8422
$B(2, 3)_4$	*3302, 12	*2311, 22	2222, 22
$B(4, 4)_4$	1011, 22	*4010, 22	4501, 21
$B(4, 5)_4$	2210, 32	*3210, 31	3100, 31
$B(4, 5)_6$	6632, 3	*1634, 31	*1342, 31
$B(6, 6)_6$	*2721, 21	*0751, 21	*0221, 21
$B(6, 7)_6$		9511, 21	*12 611, 21

Pr^{3+} (f^2) ^3H–^1G	
$J = 4$	$J' = 4$
$A(0, 1)_{0,2}$	
$A(2, 3)_{2,4}$	
$A(4, 5)_{4,6}$	
$B(0, 1)_0$	0
$B(0, 1)_2$	*532
$B(2, 2)_2$	*4301, 1
$B(2, 3)_2$	*8320, 1
$B(2, 3)_4$	*0300, 32
$B(4, 4)_4$	*2001, 31
$B(4, 5)_4$	*3200, 41
$B(4, 5)_6$	5242, 41
$B(6, 6)_6$	4321, 31
$B(6, 7)_6$	8311, 31

Pr^{3+} (f^2) ^3F–^3F			
$J=4$	$J'=4$	$J'=3$	$J'=2$
$A(0,1)_{0,2}$	*201	*21	
$A(2,3)_{2,4}$	1212, 1	1301, 1	2312
$A(4,5)_{4,6}$	*2110, 21	*2220, 21	*1220, 2
$B(0,1)_0$	*021	01	
$B(0,1)_2$	*261	*25	
$B(2,2)_2$	0	173	2711
$B(2,3)_2$	1412, 1	*1701, 1	*6712
$B(2,3)_4$	*1212, 1	*3301, 1	*2312
$B(4,4)_4$	0	1000, 1	4001, 1
$B(4,5)_4$	2110, 21	2200, 21	*3200, 2
$B(4,5)_6$	*2330, 21	*2660, 21	*1640, 2
$B(6,6)_6$	0	1721, 11	1731, 11
$B(6,7)_6$	5621, 11	4521, 11	

Pr^{3+} (f^2) ^3F–^1G	
$J=4$	$J'=4$
$A(0,1)_{0,2}$	
$A(2,3)_{2,4}$	
$A(4,5)_{4,6}$	
$B(0,1)_0$	0
$B(0,1)_2$	2310, 1
$B(2,2)_2$	*3311, 2
$B(2,3)_2$	3312, 2
$B(2,3)_4$	*1352, 2
$B(4,4)_4$	3031, 21
$B(4,5)_4$	*0230, 31
$B(4,5)_6$	2232, 31
$B(6,6)_6$	*3331, 21
$B(6,7)_6$	7321, 21

Pr^{3+} (f^2) ^1G–^1G	
$J=4$	$J'=4$
$A(0,1)_{0,2}$	*221
$A(2,3)_{2,4}$	3232, 1
$A(4,5)_{4,6}$	2110, 41
$B(0,1)_0$	
$B(0,1)_2$	
$B(2,2)_2$	
$B(2,3)_2$	
$B(2,3)_4$	
$B(4,4)_4$	
$B(4,5)_4$	
$B(4,5)_6$	
$B(6,6)_6$	
$B(6,7)_6$	

Nd^{3+} (f^3) ^4I–^4I				
$J=\frac{9}{2}$	$J'=\frac{9}{2}$	$J'=\frac{11}{2}$	$J'=\frac{13}{2}$	$J'=\frac{15}{2}$
$A(0,1)_{0,2}$	*0002, 1	0101, 1		
$A(2,3)_{2,4}$	7102, 31	*9201, 31	6110, 21	*4211, 21
$A(4,5)_{4,6}$	*3012, 612	1311, 612	*1003, 511	4101, 511
$B(0,1)_0$	0200, 1	*2101, 1		
$B(0,1)_2$	*0202, 3	*2521, 3		
$B(2,2)_2$	0	*3221, 11	3411, 21	
$B(2,3)_2$	3102, 31	*9221, 31	2310, 01	*8411, 21
$B(2,3)_4$	7302, 512	*5201, 512	*6310, 412	0011, 412
$B(4,4)_4$	0	3111, 312	*5121, 412	2121, 411
$B(4,5)_4$	*5212, 612	5111, 612	*3223, 511	8121, 511
$B(4,5)_6$	*3050, 6322	1151, 6322	1241, 5312	*2341, 5312
$B(6,6)_6$	0	*2241, 3112	5430, 4112	*1331, 4111
$B(6,7)_6$	5231, 5312	*18 531, 5312	6040, 4311	*10 241, 4311

Nd^{3+} (f^3) ^4I–^4F				
$J = \frac{9}{2}$	$J' = \frac{3}{2}$	$J' = \frac{5}{2}$	$J' = \frac{7}{2}$	$J' = \frac{9}{2}$
$A(0,1)_{0,2}$				
$A(2,3)_{2,4}$	*2012, 01	1312, 11	*0102, 11	1102, 1
$A(4,5)_{4,6}$	0	0	0	0
$B(0,1)_0$				
$B(0,1)_2$				
$B(2,2)_2$				
$B(2,3)_2$	0	0	0	0
$B(2,3)_4$	*2212, 21	*3112, 31	4102, 31	*3102, 3
$B(4,4)_4$	4422, 31	*5025, 31	6115, 3	*5112, 3
$B(4,5)_4$	3122, 41	*3022, 4 $(29)^2$	4012, 4	*3012, 4
$B(4,5)_6$	*3122, 41	7022, 42	6232, 42	*7232, 42
$B(6,6)_6$	2111, 3	*3112, 3	5322, 3	*2341, 3
$B(6,7)_6$		*8422, 32	9212, 32	*7211, 321

Pm^{3+} (f^4) ^5I–^5I					
$J = 4$	$J' = 4$	$J' = 5$	$J' = 6$	$J' = 7$	$J' = 8$
$A(0,1)_{0,2}$	*2212	1211			
$A(2,3)_{2,4}$	7212, 3	*9211, 21	9201, 3	*4201, 21	
$A(4,5)_{4,6}$	*4112, 612	4111, 512	*2102, 602	1112, 511	*1101, 511
$B(0,1)_0$	621	*3211			
$B(0,1)_2$	2412, 2	3411, 2			
$B(2,2)_2$	0	3431, 2	*4411, 1		
$B(2,3)_2$	*3212, 3	3411, 01	*3401, 302	4201, 21	
$B(2,3)_4$	*7412, 502	3211, 412	3201, 502	*0421, 412	
$B(4,4)_4$	0	*1111, 412	1121, 302	*3311, 412	3121, 411
$B(4,5)_4$	6312, 612	*4111, 512	2124, 602	*5314, 511	5121, 511
$B(4,5)_6$	4150, 6322	*0351, 5322	2340, 6222	1150, 5312	*1341, 5312
$B(6,6)_6$	0	3451, 4122	*2441, 3012	2041, 4112	*2441, 4111
$B(6,7)_6$	*5421, 5322	6421, 4314	*6461, 5212	12 451, 4311	*8441, 3311

Sm^{3+} (f^5) ^6H–^6H

$J = \frac{5}{2}$	$J' = \frac{5}{2}$	$J' = \frac{7}{2}$	$J' = \frac{9}{2}$	$J' = \frac{11}{2}$	$J' = \frac{13}{2}$	$J' = \frac{15}{2}$
$A(0,1)_{0,2}$	*2011	1111				
$A(2,3)_{2,4}$	0	0	0	0		
$A(4,5)_{4,6}$	3211, 42	*3331, 42	3341, 4	*8231, 4	5110, 4	*2111, 4
$B(0,1)_0$	0231	*3111				
$B(0,1)_2$	2611, 02	*1531, 02				
$B(2,2)_2$	0	2801, 02	*6810, 01			
$B(2,3)_2$	*3512, 02	7832, 22	*3811, 11 (31)^2	7530, 11		
$B(2,3)_4$	*3312, 22	1412, 24	*3411, 31	*1310, 31		
$B(4,4)_4$	0	*1111, 32	5100, 31	*1610, 3	5010, 3	
$B(4,5)_4$	1211, 42	*11 311, 42	1301, 4 (41)^2	*10 211, 42	3110, 42	*8111, 4
$B(4,5)_6$	*3431, 402	1731, 4020, 2	*3743, 422	6431, 422	5530, 422	*0551, 422
$B(6,6)_6$		*0811, 312	9831, 302	*5012, 302	6631, 302	*1632, 001
$B(6,7)_6$			8501, 324	*10 612, 322 (31)^2	7441, 221	*10 322, 221

Sm^{3+} (f^5) ^6H–^6F

$J = \frac{5}{2}$	$J' = \frac{1}{2}$	$J' = \frac{3}{2}$	$J' = \frac{5}{2}$	$J' = \frac{7}{2}$	$J' = \frac{9}{2}$	$J' = \frac{11}{2}$
$A(0,1)_{0,2}$						
$A(2,3)_{2,4}$	*4203, 1	1223, 1	*2323, 1	6403, 1	*2433, 1	1303, 1
$A(4,5)_{4,6}$			0	0	0	0
$B(0,1)_0$		0	0	0		
$B(0.1)_2$		2421, 1	*7622, 1	2522, 1		
$B(2,2)_2$	*3611, 1	1602, 12	*1202, 1	1832, 1	*1812, 002	
$B(2,3)_2$	*6603, 1	7621, 1	*4523, 3	14 823, 1	*4811, 1	7523, 1
$B(2,3)_4$	2203, 12	*3201, 12	0303, 12	2403, 12	*0411, 32	3323, 32
$B(4,4)_4$		5022, 14	*2422, 12	0122, 22	*2102, 322	5401, 31
$B(4,5)_4$			*0222, 32 (43)^2	4322, 32	*0301, 41 (59)^2	4200, 41
$B(4,5)_6$			*4422, 3	2742, 3	4743, 41	*2442, 41
$B(6,6)_6$				*1842, 21	2831, 312	*1221, 31
$B(6,7)_6$					7501, 3100, 2	*12 621, 31

Eu^{3+} (f^6) ^7F–^7F							
$J = 0$	$J' = 0$	$J' = 1$	$J' = 2$	$J' = 3$	$J' = 4$	$J' = 5$	$J' = 6$
$A(0, 1)_{0,2}$		21					
$A(2, 3)_{2,4}$				3101			
$A(4, 5)_{4,6}$						2010, 2	
$B(0, 1)_0$		*41					
$B(0, 1)_2$		*03					
$B(2, 2)_2$			*131				
$B(2, 3)_2$				5301			
$B(2, 3)_4$				*1101			
$B(4, 4)_4$					*1110, 1		
$B(4, 5)_4$						2010, 2	
$B(4, 5)_6$						*0230, 2	
$B(6, 6)_6$							*1321, 11
$B(6, 7)_6$							

Gd^{3+} (f^7) ^8S–^8S		
$J = \frac{7}{2}$		$J' = \frac{7}{2}$
$A(0, 1)_{0,2}$		
$A(2, 3)_{2,4}$		
$A(4, 5)_{4,6}$		
$B(0, 1)_0$		*0001
$B(0, 1)_2$		
$B(2, 2)_2$		
$B(2, 3)_2$		
$B(2, 3)_4$		
$B(4, 4)_4$		
$B(4, 5)_4$		
$B(4, 5)_6$		
$B(6, 6)_6$		
$B(6, 7)_6$		

Tb^{3+} (f^8) ^7F–^7F							
$J=6$	$J'=6$	$J'=5$	$J'=4$	$J'=3$	$J'=2$	$J'=1$	$J'=0$
$A(0,1)_{0,2}$	*1101	*11					
$A(2,3)_{2,4}$	*4200, 1	*23	*1100, 1	*1301			
$A(4,5)_{4,6}$	*0111, 401	*0220, 301	*2021, 4	*1212, 3	*1121, 3	*1110, 3	
$B(0,1)_0$	*1101	11					
$B(0,1)_2$	*1501	*15					
$B(2,2)_2$	0	2411	2510, 1				
$B(2,3)_2$	4200, 1	25	*3500, 1	*3501			
$B(2,3)_4$	*4000, 3	*0100, 2	*3100, 3 $(23)^2$	*3301, 2			
$B(4,4)_4$	0	1101, 2	5400, 1	5112, 2	2300, 2		
$B(4,5)_4$	0111, 401	0200, 301	6001, 4	0	*1101, 3	*1110, 3	
$B(4,5)_6$	*0131, 421	*4440, 321	*0441, 42 $(29)^2$	*1432, 12	*1141, 32	*1330, 3202	
$B(6,6)_6$	0	1420, 201	0520, 101	0441, 2	2250, 2	0440, 1	1321, 1
$B(6,7)_6$	5521, 3211	6520, 2211	8120, 321	8521, 221	6540, 12	4220, 12	

Dy^{3+} (f^9) ^6H–^6H						
$J=\frac{15}{2}$	$J'=\frac{15}{2}$	$J'=\frac{13}{2}$	$J'=\frac{11}{2}$	$J'=\frac{9}{2}$	$J'=\frac{7}{2}$	$J'=\frac{5}{2}$
$A(0,1)_{0,2}$	*0310, 001	*031				
$A(2,3)_{2,4}$	0	0	0	0		
$A(4,5)_{4,6}$	0210, 4111	0210, 4111	2010, 4111	1021, 411	0011, 401	1011, 4
$B(0,1)_0$	*0310, 001	231				
$B(0,1)_2$	*0510, 001	*251				
$B(2,2)_2$	0	3210, 011	3501, 01			
$B(2,3)_2$	2112, 0111	0	*4512, 111	*7311, 11		
$B(2,3)_4$	6112, 2111	2111, 211	12 112, 311	1311, 31 $(59)^2$		
$B(4,4)_4$	0	*0310, 3111	*6331, 311	*1021, 311	*8030, 3	
$B(4,5)_4$	*4010, 4111	*6010, 4111	6030, 4111	5223, 411	4231, 4010, 2	5011, 4
$B(4,5)_6$	0050, 4311	2250, 4311	2430, 4311, 02	3241, 4310, 2	0231, 401	3451, 422
$B(6,6)_6$	0	*3231, 3111	*3531, 3111	*4231, 3111	*5232, 301	*4532, 001
$B(6,7)_6$	*4521, 2311, 1	*8521, 2311	*6211, 3311	7541, 3311	4512, 2011	7222, 221

Dy^{3+} (f^9) ^6H–^6F						
$J = \frac{15}{2}$	$J' = \frac{11}{2}$	$J' = \frac{9}{2}$	$J' = \frac{7}{2}$	$J' = \frac{5}{2}$	$J' = \frac{3}{2}$	$J' = \frac{1}{2}$
$A(0,1)_{0,2}$						
$A(2,3)_{2,4}$	*2101, 101	*2111, 1				
$A(4,5)_{4,6}$	0	0	0	0		
$B(0,1)_0$						
$B(0,1)_2$						
$B(2,2)_2$	351					
$B(2,3)_2$	6501, 101	*8311, 1				
$B(2,3)_4$	*0121, 301	*2311, 3 $(41)^2$				
$B(4,4)_4$	2300, 301	4003, 301	1001, 2			
$B(4,5)_4$	0001, 4011	4201, 401	*3200, 301	*4000, 3		
$B(4,5)_6$	6421, 4211	0221, 423	7220, 321	0420, 32 $(67)^2$		
$B(6,6)_6$	*1520, 3011	*1211, 3011	*4221, 201	*1501, 101 $(37)^2$	*1201, 1	
$B(6,7)_6$	*6220, 3211	*8521, 3211	*9501, 1211	8211, 121	6511, 111	9500, 11

Ho^{3+} (f^{10}) ^5I–^5I					
$J = 8$	$J' = 8$	$J' = 7$	$J' = 6$	$J' = 5$	$J' = 4$
$A(0,1)_{0,2}$	*12	*11			
$A(2,3)_{2,4}$	0102, 0001	0002, 0101	2102, 1	2202, 11	
$A(4,5)_{4,6}$	*1010, 2101	*1130, 4101	*3010, 5001	*4100, 4101	*1101, 51
$B(0,1)_0$	*1	11			
$B(0,1)_2$	*122	*132			
$B(2,2)_2$	0	0201	2211, 1		
$B(2,3)_2$	2122, 0001	*2222, 0101	*2122, 1	*2202, 11	
$B(2,3)_4$	0102, 2001	2202, 2101	4102, 3 $(23)^2$	4002, 31 $(29)^2$	
$B(4,4)_4$	0	*2311, 2101	*6711, 4001	*6722, 31	*3121, 41
$B(4,5)_4$	*3210, 2101	*3310, 4101	1210, 5001	0120, 2101	5321, 51
$B(4,5)_6$	*1050, 2301	*1190, 4301	*1450, 5201	*0140, 2301	*1141, 5302
$B(6,6)_6$	0	0240, 2101	1260, 4001	2141, 3101	2241, 4101
$B(6,7)_6$	5221, 2301, 1	5330, 2301, 1	*4220, 3201	*4241, 3301	*8241, 3301

Er^{3+} (f^{11}) ^4I–^4I				
$J = \frac{15}{2}$	$J' = \frac{15}{2}$	$J' = \frac{13}{2}$	$J' = \frac{11}{2}$	$J' = \frac{9}{2}$
$A(0,1)_{0,2}$	*2110, 001	*111		
$A(2,3)_{2,4}$	2112, 0111	1111, 011	2112, 211	1201, 21
$A(4,5)_{4,6}$	*2010, 4111	*1010, 4111	*2010, 5111	*1111, 511
$B(0,1)_0$	*0110, 001	311		
$B(0,1)_2$	2530, 001	1532		
$B(2,2)_2$	0	*2410, 011	*3501, 11	
$B(2,3)_2$	*4132, 0111	5331, 011	4512, 2112	5401, 21
$B(2,3)_4$	*2112, 2111	*3511, 211	*4132, 411	*3001, 412
$B(4,4)_4$	0	5310, 3111	0511, 411	5111, 411
$B(4,5)_4$	0210, 4111	0	*0010, 5111	*5111, 511
$B(4,5)_6$	2050, 4311	1250, 2311	2450, 5311, 2	1351, 5312
$B(6,6)_6$	0	*2451, 3111	*3551, 4111	*2341, 4111
$B(6,7)_6$	*6521, 2311, 1	*7521, 2311	6231, 4311	7251, 4311

Tm^{3+} (f^{12}) ^3H–^3H			
$J = 6$	$J' = 6$	$J' = 5$	$J' = 4$
$A(0,1)_{0,2}$	*1321	*131	
$A(2,3)_{2,4}$	0	0	0
$A(4,5)_{4,6}$	0111, 401	0010, 301	2011, 4
$B(0,1)_0$	*1301	131	
$B(0,1)_2$	1501	351	
$B(2,2)_2$	0	*2201	*2500, 1
$B(2,3)_2$	*4200, 1	231	7510, 1
$B(2,3)_4$	*8200, 3	*4310, 2	*1110, 3
$B(4,4)_4$	0	3111, 2	1210, 1
$B(4,5)_4$	4111, 401	*4210, 301	*8011, 4
$B(4,5)_6$	*0151, 421	*2250, 321	*0451, 422
$B(6,6)_6$	0	1230, 201	0530, 101
$B(6,7)_6$	5541, 3211	6510, 2211	*10 110, 321

Tm^{3+} (f^{12}) ^3H–^3F			
$J = 6$	$J' = 4$	$J' = 3$	$J' = 2$
$A(0,1)_{0,2}$			
$A(2,3)_{2,4}$	*01	*0101	
$A(4,5)_{4,6}$	0	0	0
$B^*0,1)_0$			
$B(0,1)_2$			
$B(2,2)_2$	*351		
$B(2,3)_2$	*45	4301	
$B(2,3)_4$	2120, 2	2341, 2	
$B(4,4)_4$	*4220, 2	*4112, 2	*2300, 2
$B(4,5)_4$	*1021, 3	0212, 3	5101, 3
$B(4,5)_6$	*7441, 32	*4232, 32	*1141, 32
$B(6,6)_6$	3520, 201	3221, 2	0030, 2
$B(6,7)_6$	7120, 221	7521, 221	*12 520, 12

Yb^{3+} (f^{13}) ^2F–^2F		
$J = \frac{7}{2}$	$J' = \frac{7}{2}$	$J' = \frac{5}{2}$
$A(0,1)_{0,2}$	*0201	*0101
$A(2,3)_{2,4}$	*2102, 1	*2002
$A(4,5)_{4,6}$	*0011, 21	*0121, 2
$B(0,1)_0$	*0001	2101
$B(0,1)_2$	0201	2101
$B(2,2)_2$	0	*3211
$B(2,3)_2$	*2102, 1	6202
$B(2,3)_4$	2102, 1	2202
$B(4,4)_4$	0	*4301, 1
$B(4,5)_4$	*0211, 21	2301, 2
$B(4,5)_6$	0031, 21	2141, 2
$B(6,6)_6$	0	*3221, 11
$B(6,7)_6$	*4221, 11	

References

Andres, K., J.E. Graebner and H.R. Ott, 1975, Phys. Rev. Lett. **35**, 1779.

Arko, A.J., D.D. Koelling and J.E. Schirber, 1985, Energy band structure and Fermi surface of actinide materials, in: Handbook on the Physics and Chemistry of the Actinides, Vol. 2, eds A.J. Freeman and G.H. Lander (North-Holland, Amsterdam) ch. 3, p. 175.

Baer, Y., and W.-D. Schneider, 1987, High energy spectroscopy of lanthanide materials - an overview, in: Handbook on the Physics and Chemistry of Rare Earths, Vol. 10, eds K.A. Gschneidner Jr, L. Eyring and S. Hüfner (North-Holland, Amsterdam) ch. 62, p. 1.

Baer, Y., H.R. Ott and K. Andres, 1980, Solid State Commun. **36**, 387.

Balcar, E., and S.W. Lovesey, 1986, J. Phys. C **19**, 4605.

Balcar, E., and S.W. Lovesey, 1989, Theory of Magnetic Neutron and Photon Scattering (Oxford University Press, Oxford).

Barnes, R.G., 1979, NMR, EPR and Mössbauer effect: metals, alloys and compounds, in: Handbook on the Physics and Chemistry of Rare Earths, Vol. 2, eds K.A. Gschneidner Jr and L. Eyring (North-Holland, Amsterdam) ch. 18, p. 387.

Brandt, N.B., and V.V. Moshchalkov, 1984, Adv. Phys. **33**, 373.

Buyers, W.J.L., and T.M. Holden, 1985, Neutron scattering from spins and phonons in actinide systems, in: Handbook on the Physics and Chemistry of the Actinides, Vol. 2, eds A.J. Freeman and G.H. Lander (North-Holland, Amsterdam) ch. 4, p. 239.

Campagna, M., and F.U. Hillebrecht, 1987, f-Electron hybridization and dynamical screening of core holes in intermetallic compounds, in: Handbook on the Physics and Chemistry of Rare Earths, Vol. 10, eds K.A. Gschneidner Jr, L. Eyring and S. Hüfner (North-Holland, Amsterdam) ch. 63, p. 75.

Carnall, W.T., and H.M. Crosswhite, 1984, Argonne National Laboratory Report, ANL-84-90.

Carnall, W.T., G.L. Goodman, K. Rajnak and R.S. Rana, 1989, J. Chem. Phys. **90**, 3443.

Christensen, N.E., O.K. Andersen, O. Gunnarsson and O. Jepsen, 1988, J. Magn. & Magn. Mater. **76 & 77**, 23.

Condon, E.U., and H. Odabaşi, 1980, Atomic Structure (Cambridge University Press, Cambridge).

Cooper, B.R., R. Siemann, D. Yang, P. Thayamballi and A. Banerjea, 1985, Hybridization-induced anisotropy in cerium and actinide systems, in: Handbook on the Physics and Chemistry of the Actinides, Vol. 2, eds A.J. Freeman and G.H. Lander (North-Holland, Amsterdam) ch. 6, p. 435.

Cox, D.L., N.E. Bickers and J.W. Wilkins, 1986, J. Magn. & Magn. Mater. **54–57**, 333.

Dieke, G.H., 1968, Spectra and Energy Levels of Rare Earths Ions in Crystals (Interscience, New York).

Eriksson, O., B. Johansson, M.S.S. Brooks and H.L. Skriver, 1988, Phys. Rev. B **38**, 12858.

Franse, J.J.M., A. de Visser, A. Menovsky and P.H. Frings, 1985, J. Magn. & Magn. Mater. **52**, 61.

Freeman, A.J., and J.P. Desclaux, 1972, Int. J. Magn. **3**, 311.

Freeman, A.J., and J.P. Desclaux, 1979, J. Magn. & Magn. Mater. **12**, 11.

Freeman, A.J., and R.E. Watson, 1962, Phys. Rev. **127**, 2058.

Freeman, A.J., B.I. Min and M.R. Norman, 1987, Local density supercell theory of photoemission and inverse photoemission spectra, in: Handbook on the Physics and Chemistry of Rare Earths, Vol. 10, eds K.A. Gschneidner Jr, L. Eyring and S. Hüfner (North-Holland, Amsterdam) ch. 65, p. 165.

Fulde, P., and M. Loewenhaupt, 1985, Adv. Phys. **34**, 589.

Fulde, P., J. Keller and G. Zwicknagl, 1988, Solid State Phys. **41**, 1.

Goldschmidt, Z.B., 1978, Atomic properties (free atom), in: Handbook on the Physics and Chemistry of Rare Earths, Vol. 10, eds K.A. Gschneidner Jr and L. Eyring (North-Holland, Amsterdam) ch. 1, p. 1.

Güntherodt, G., A. Jayaraman, E. Anastassakis, E. Bucher and H. Bach, 1981, Phys. Rev. Lett. **46**, 855.

Herbst, J.F., and J.W. Wilkins, 1987, Calculation of 4f excitation energies in the metals and relevance to mixed valence systems, in: Handbook on the Physics and Chemistry of Rare Earths, Vol. 10, eds K.A. Gschneidner Jr, L. Eyring and S. Hüfner (North-Holland, Amsterdam) ch. 68, p. 321.

Hirst, L.L., 1970, Phys. Kondens. Materie **11**, 255.

Hirst, L.L., 1975, Phys. Rev. Lett. **35**, 1394.

Holland-Moritz, E., and M. Kasaya, 1986, Phys. B **136**, 424.

Holland-Moritz, E., E. Braun, B. Roden, B. Perscheid, E.V. Sampathkumaran and W. Langel, 1987, Phys. Rev. B **35**, 3122.

Holland-Moritz, E., E. Zirngiebl and S. Blumenröder, 1988, Z. Phys. B **70**, 395.

Johansson, B., O. Eriksson, M.S.S. Brooks and H.L. Skriver, 1986, Phys. Scripta T **13**, 65.

Johansson, B., O. Eriksson, M.S.S. Brooks and H.L. Skriver, 1987, J. Less Common Metal **133**, 25.

Judd, B.R., 1955, Proc. Roy. Soc. (London) A **228**, 120.

Judd, B.R., 1963, Operator Techniques in Atomic Spectroscopy (McGraw-Hill, New York).

Kemly, E., M. Croft, V. Murgai, L.C. Gupta, C. Godart, R.D. Parks and C.V. Segre, 1985, J. Magn. & Magn. Mater. **47&48**, 403.

Lang, J.K., Y. Baer and P.A. Cox, 1981, J. Phys. F **11**, 121.

Lawrence, J.M., P.S. Riseborough and R.D. Parks, 1981, Rep. Prog. Phys. **44**, 1.

Levy, P.M., and S. Zhang, 1989, Phys. Rev. Lett. **62**, 78.

Loewenhaupt, M., 1985a, in: Proc. Conf. on Neutron Scattering in the Nineties (IAEA, Vienna) p. 435.

Loewenhaupt, M., 1985b, Phys. B **130**, 347.

Lopes, L.C., and B. Coqblin, 1986, Phys. Rev. B **33**, 1804.

Lovesey, S.W., 1978, J. Phys. C **11**, 3971.

Maekawa, S., S. Takahashi, S. Kashiba and M. Tachiki, 1985, J. Appl. Phys. **57**, 3169.

Martin, W.C., R. Zalubas and L. Hagan, 1978, Atomic Energy Levels - The Rare-earth Elements, National Bureau of Standards Report NSRDS-NBS 60 (U.S. Department of Commerce, Washington, DC).

McEwen, K.A., 1978, Magnetic and transport properties of the rare earths, in: Handbook on the Physics and Chemistry of Rare Earths, Vol. 1, eds K.A. Gschneidner Jr and L. Eyring (North-Holland, Amsterdam) ch. 6, p. 411.

McEwen, K.A., 1988, J. Magn. & Magn. Mater. **76 & 77**, 391.

McEwen, K.A., W.G. Stirling, C.-K. Loong and G.H. Lander, 1988, J. Magn. & Magn. Mater. **76 & 77**, 426.

McEwen, K.A., R. Osborn and A.D. Taylor, 1990a, to be published.

McEwen, K.A., U. Steigenberger, J.L. Martinez and J.S. Abell, 1990b, Phys. B **163**, 371.

McWhan, D.B., S.M. Shapiro, J. Eckert, H.A. Mook and R.J. Birgeneau, 1978, Phys. Rev. B **18**, 3623.

Mook, H.A., T. Penney, F. Holtzberg and M.W. Schafer, 1978, J. Phys. **39**, C6-837.

Morrison, C.A., and R.P. Leavitt, 1982, Spectroscopic properties of triply ionized lanthanides in transparent host crystals, in: Handbook on the Physics and Chemistry of Rare Earths, Vol. 5, eds K.A. Gschneidner Jr and L. Eyring (North-Holland, Amsterdam) ch. 46, p. 461.

Morrison, J.C., and K. Rajnak, 1971, Phys. Rev. A **4**, 536.

Murani, A.P., K. Knorr, K.H.J. Buschow, A. Benoit and J. Flouquet, 1980, Solid State Commun. **36**, 523.

Murray, A.F., and W.J.L. Buyers, 1980, in: Crystalline Electric Fields and Structural Effects in f-electron Systems, eds J.E. Crow, R.P. Guertin and T.W. Mihalisin (Plenum Press, New York) p. 257.

Needham, L.M., 1989, Ph.D. thesis (University of Oxford, Oxford).

Newman, D.J., 1977, Austr. J. Phys. **30**, 315.

Nielson, C.W., and G.F. Koster, 1963, Spectroscopic Coefficients for the p^n, d^n and f^n Configurations (MIT Press, Cambridge, MA).

Norman, M.R., T. Oguchi and A.J. Freeman, 1987, J. Magn. & Magn. Mater. **69**, 27.

Norman, M.R., R.C. Albers, A.M. Boring and N.E. Christensen, 1988, Solid State Commun. **68**, 245.

Oguchi, T., and A.J. Freeman, 1986, **61**, 233.

Osborn, R., 1989, Phys. B **159**, 151.

Osborn, R., K.A. McEwen, E.A. Goremychkin and A.D. Taylor, 1990, Phys. B **163**, 37.

Racah, G., 1943, Phys. Rev. **63**, 171.

Rahman, H.U., and W.A. Runciman, 1966, J. Phys. Chem. Solids **27**, 1833.

Rajnak, K., and B.G. Wybourne, 1963, Phys. Rev. **132**, 280.

Rhyne, J.J., 1972, Bulk magnetic properties, in: Magnetic Properties of Rare Earth Metals, ed. R.J. Elliott (Plenum Press, London and New York) ch. 4, p. 128.

Röhler, J., 1987, X-ray absorption and emission spectra, in: Handbook on the Physics and Chemistry of Rare Earths, Vol. 10, eds K.A. Gschneidner Jr, L. Eyring and S. Hüfner (North-Holland, Amsterdam) ch. 71, p. 453.

Schrieffer, J.R., and P.A. Wolff, 1966, Phys. Rev. **149**, 491.

Shamir, N., M. Melamud, H. Shaked and M. Weger, 1978, Phys. B **94**, 225.

Shapiro, S., R.J. Birgeneau and E. Bucher, 1975, Phys. Rev. Lett. **34**, 470.

Sinha, S.K., 1978, Magnetic structures and inelastic neutron scattering: metals, alloys and compounds, in: Handbook on the Physics and Chemistry of Rare Earths, Vol. 1, eds K.A. Gschneidner Jr and L. Eyring (North-Holland, Amsterdam) ch. 7, p. 489.

Stassis, C., and H.W. Deckman, 1976, J. Phys. C **9**, 2241.

Stewart, G.R., 1984, Rev. Mod. Phys. **56**, 755.

Stirling, W.G., and K.A. McEwen, 1987, Magnetic excitations, in: Methods of Experimental Physics, Vol. 23, Part C, eds K. Sköld and D.L. Price (Academic Press, Orlando, FL) ch. 20, p. 159.

Stirling, W.G., K.A. McEwen and C.-K. Loong, 1986, Phys. B **136**, 420.

Taillefer, L., and G.G. Lonzarich, 1988, Phys. Rev. Lett. **60**, 1570.

Taylor, A.D., R. Osborn, K.A. McEwen, W.G. Stirling, Z.A. Bowden, W.G. Williams, E. Balcar and S.W. Lovesey, 1988, Phys. Rev. Lett. **61**, 1309.

Trammell, G.T., 1953, Phys. Rev. **92**, 1387.

Ubachs, W., A.P.J. van Deursen, A.F. de Vroomen and A.J. Arko, 1986, Solid State Commun. **60**, 7.

Weber, W., E. Holland-Moritz and K. Fischer, 1989, Europhys. Lett. **8**, 257.

Williams, W.G., B.C. Boland, Z.A. Bowden, A.D. Taylor, S. Culverhouse and B.D. Rainford, 1987, J. Phys. F **17**, L151.

Wills, J.M., and B.R. Cooper, 1987, Phys. Rev. B **36**, 3809.

Wohlleben, D., 1984, in: Physics and Chemistry of Electrons and Ions in Condensed Matter, eds J.V. Acrivos, N.F. Mott and A.D. Yoffe, NATO ASI Series C **130** (Reidel, Dordrecht) p. 85.

Wohlleben, D., and B. Wittershagen, 1985, J. Magn. &. Magn. Mater. **52**, 32.

Zirngiebl, E., S. Blumenröder, G. Güntherodt, A. Jarayaman, B. Batlogg and M. Croft, 1985, Phys. Rev. Lett. **54**, 213.

Zwicknagl, G., 1988, J. Magn. & Magn. Mater. **76 & 77**, 16.

Handbook on the Physics and Chemistry of Rare Earths, Vol. 14
edited by K.A. Gschneidner, Jr. and L. Eyring

Chapter 94

NMR IN INTERMETALLIC COMPOUNDS

ELMAR DORMANN
Physikalisches Institut, Universität Bayreuth, P.O.B. 10 12 51,
D-8580 Bayreuth, Fed. Rep. Germany

Contents

List of symbols

$A(T)$	hyperfine coupling constant at temperature T	$a(0)$	$q = 0$ component of hyperfine coupling constant
a	magnetic hyperfine splitting frequency/lattice constant	a_s, a_d	individual conduction electron hyperfine coupling constants

AF	antiferromagnet
$C_{3/2}$; $C'_{3/2}$; $C''_{5/2}$	coefficients for powers of temperature in spin-wave approximation for: hyperfine field; magnetization; hyperfine coupling constant
CDW	charge density wave
CEF	crystal electric field
d	diameter of single crystalline (SC) sphere
Δd	deviation from sphericity of SC sphere
E_F	Fermi energy
eq, $V_{\zeta\zeta}$, EFG	electric field gradient
eQ	nuclear electric quadrupole moment
FM	ferromagnet
FIM	ferrimagnet
g_s; g_f	g-factor of conduction electrons; Landé g-factor of 4f shell electrons
h	Planck's constant
$h(T)$	normalized hyperfine field
H_{an}	anisotropy field
H_{cp}	core polarization contribution to hyperfine field
H_{c1}, H_{c2}	critical fields of type-II superconductor
H_D	demagnetizing field
ΔH_D, $\Delta H'_D$	width of distribution of demagnetizing fields
H_{dip}	dipolar field at nucleus
H_{hf}; $H_{hf}(T)$	hyperfine field; at temperature T
H_L	Lorentz field
H_N	contribution of all (nearest and remote) magnetic neighbours to the hyperfine field
H_{nn^0} (ΔH_{nn})	contribution of a nearest-neighbour magnetic moment to hyperfine (resonance) field
H_0	applied external magnetic field
H_{own}; H_{4s}; H_{orb}	total contribution of 3d electronic moment to hyperfine field at own nucleus; contribution via conduction electrons; orbital contribution
H_{res}	resonance field
ΔH_{res}	shift of resonance field
H_{rn}	contribution to remote neighbours to H_N
H_s	self-polarization contribution to the hyperfine field (via conduction electrons, induced by the magnetic moment at the same site)
H_1; $H_{1,0}$; $H_{1,eff}$	amplitude of RF field; external; enhanced
H_{4f}	contribution of 4f shell to hyperfine field
$\mathcal{H}_{CEF}(W, x)$	crystal-field Hamiltonian (cubic crystalline electric field parameters W, x)
$\mathcal{H}_{MF}(\lambda)$	molecular field Hamilton operator
$\mathcal{H}_Q$	nuclear quadrupole Hamilton operator
$\mathcal{H}_{Ze}$	Zeeman part of Hamiltonian
I; I_ζ	nuclear spin; ζ-component of nuclear spin
J	electronic total angular momentum
$J(q)$, $J(o)$	q, $q=0$ component of exchange integral
J_{sf}	s–f exchange coupling constant derived from correlation of $K(T)$ and $\chi(T)$
J_{4f-s}, J_{4f-d}	4f-conduction electron exchange interaction coupling parameters
$K(T)$	Knight shift at temperature T
$K(\chi)$	correlation of $K(T)$ with $\chi(T)$ with T as an implicit parameter
K_0	bare Knight shift in intermetallic compound without 4f contribution
K_{sp}, K_d, K_{orb}	s + p, d and orbital parts of Knight shift
$K_\parallel$, $K_\perp$, K_{iso}, K_{ani}	various components or parts of K
k_F	Fermi wavevector
L; L_z	electronic total orbital angular momentum; z component
l_z	z-component of conduction electron orbital angular momentum

M; $M(H)$; $M(T)$	macroscopic magnetization; at field H; at T
M_s; $M_s(T)$	spontaneous magnetization (of domain); at T
$m(T)$	normalized magnetization
m_I	z-component of nuclear spin
MF	molecular field
N	demagnetization factor (tensor)
N_A	Avogadro's number
N_i, (n_i)	number of (occupied) sites per shell
$n(\Phi)$; $n(\nu, \eta)$	number of nuclei per orientation interval Φ, $\Phi + d\Phi$; resonating at ν with enhancement η
p	pressure
P; P_0	nuclear quadrupole frequency parameter; free-ion value
$P^{(1)}$, $P^{(2)}$	first- and second-order contribution to P
PM	paramagnet
q	wavevector
r; r_{nm}; r_i	radius; distance between n and m or between '0' and site i
rf	radiofrequency
S	electronic total spin angular momentum
S_z	z-component of S
s_z	z-component of conduction electron spin polarization
SC	single crystal
sc	superconductor
ΔS	surface roughness
T	absolute temperature
T_c	ferromagnetic ordering temperature/superconducting transition temperature
T_{FM}	ferromagnetic Curie temperature
T_K	Kondo temperature
T_N	Néel temperature
T^*	limiting temperature of Fermi-liquid state (for $T < T^*$)
T_1	spin–lattice relaxation time
T_2	transversal relaxation time
w	parameter of octupolar contribution to hyperfine splitting
X	partner element in intermetallic compound
x	concentration in pseudobinary (pseudoternary) compounds
Z	average number of conduction electrons per atom
z_i	ionic charge
α, α_i	hyperfine coupling constant, correlating K and χ, or individual contribution
γ; γ_0	gyromagnetic ratio; bare nuclear gyromagnetic ratio
γ_∞	Sternheimer antishielding factor
δ	skin depth
η; $\eta(\Phi)$; $\eta(H_0)$	enhancement factor; at orientation Φ in Bloch wall; for domain in external field H_0
η_{rf}; η_s	enhancement factor of rf field; of signal
θ	angle between direction of magnetic hyperfine field and EFG axis/angle between spin direction and radius vector between the spins
θ_p	paramagnetic Curie temperature
μ	magnetic permeability
μ_B	Bohr magneton
μ_i	magnetic moment per atom
ν_Q	nuclear quadrupole splitting (in frequency units)
ν_{rf}	frequency of radiofrequency field
ν_{res}; $\nu_{res}(T)$	resonance frequency; at temperature T
σ	electrical conductivity
τ	pulse separation
τ_{eff}	effective value of relaxation time of 4f moments
Φ	orientation angle of mag-

	netization in wall with respect to neighbouring domain	χ_{VV}	row d band, 4f electrons van Vleck type induced orbital paramagnetism
$\chi(T)$	magnetic susceptibility at temperature T	χ_{dia}, χ_L	contribution to susceptibility by core or conduction electron Landau diamagnetism
χ_{sp}, χ_d, χ_f	paramagnetic susceptibility from s + p−, nar-		

1. Introduction

The application of NMR to rare-earth intermetallic compounds has already been treated by Barnes (1979) in chapter 18 of this Handbook in a more general context, together with EPR and the Mössbauer effect in metals, alloys and compounds. The present more specialized chapter deals with the more recent developments in this field which have been published after 1977, especially for magnetically ordered compounds. Earlier results are included in tabular form in the appendix, however. The progress in experimental techniques and our understanding of NMR in intermetallic compounds has been remarkable during the last decade. Since the pioneering NMR measurements of a wall-free, carefully polished, single-crystal $GdAl_2$ sphere by Fekete et al. (1975), more precise NMR experiments of intermetallic ferromagnets became possible. The measurement of the high-field Knight shift in ferromagnets and the detailed study of anisotropic interactions are typical examples. These more precise NMR techniques also revealed a number of – at least eventual – pitfalls of the earlier analyses with help of zero-field wall signals. Therefore, in sect. 1 of this chapter we discuss some details of the NMR techniques to orient a non-specialist and to make him aware of these typical problems of the application of NMR. In contrast, we refer the reader to the standard textbooks by Abragam (1961), Slichter (1978), and Fukushima and Roeder (1981) or ch. 18 of this Handbook for a general introduction to NMR and to the influence of the magnetic dipole interaction and the electric quadrupole interaction on the NMR spectrum and the nuclear-spin relaxation processes.

In sections 2–5, special applications are selected to demonstrate the potentialities of NMR in intermetallic compounds. Following the concluding remarks in sect. 6, tabular data of NMR with different nuclei in rare-earth intermetallic compounds are included in an appendix.

1.1. *Powder samples or single crystals?*

Since NMR is a radiofrequency technique using frequencies ν_{rf} up to several hundreds of MHz, the NMR spectroscopist has to tackle the problem of the skin depth for electromagnetic radiation in metals. The skin depth δ,

$$\delta = (\pi\mu\sigma\nu_{rf})^{-1/2} \tag{1}$$

(with the magnetic permeability μ and the electrical conductivity σ) amounts typically to about 10 μm or below. The most frequently adopted procedure of solving the sensitivity problem is, therefore, to use powder samples for the NMR of intermetallic compounds with grain sizes smaller than the skin depth. An annealing treatment after powdering is generally recommended in order to heal spurious strains so as to reduce line broadening, at least if nuclei susceptible to quadrupolar broadening are studied.

Most investigations nowadays use pulsed NMR spectrometers. Appropriate instruments for the lower radiofrequency range (3–200 MHz) are commercially available. They have to be equipped with a reliable system for the control of tuning, sensitivity and rf field amplitude and pulse shape in order to allow the analysis of broad line profiles or relative intensities. An automatic broad-band frequency variable spectrometer for the study of hyperfine fields in ferromagnetic materials has been introduced recently, working in a frequency range from 10 to 1000 MHz (Webber and Riedi 1981, Dumelow and Riedi 1987). Dedicated high-frequency instruments have been developed, as well (see, e.g., McCausland and Mackenzie 1980). Transients, such as spurious ringing signals which follow the rf pulses are a well known problem in pulsed NMR experiments (see, e.g., Clark 1964), especially for magnetically ordered materials and/or applied external magnetic fields. They may be caused by excitation of acoustic modes in the coil or the sample. Different techniques have been suggested for the prevention of this phenomenon, which plagues low-frequency studies in particular – see, e.g., Speight et al. (1974). Generally the storage of powder samples under silicon oil or paraffin is favourable in order to damp magnetoacoustic oscillations and to reduce sample oxidation as well.

Evidently, powder samples are not acceptable, if the orientation dependence of the NMR spectrum has to be explored. Furthermore, for powder samples of paramagnetic or ferromagnetic materials, severe line broadening due to varying demagnetizing fields is observed in external fields. Thus, NMR of a single crystal is essential, if more than the discrimination between signals originating from nuclei in domains or Bloch walls and more than the qualitative decision between a positive or negative sign of the hyperfine field is required. Stakelon and Follstaedt (1978) analysed the factors determining the sensitivity of NMR measurements using bulk metal single-crystal samples. They showed that the absolute signal intensity from a metallic single crystal with a near-optimum coil can be at least 10% of that from a powdered sample with particle radii approximately equal to the rf skin depth. The main requirement is that the NMR coil has to be wrapped around the crystal relatively tightly (see fig. 1) and usually separated by a thin layer (20 μm) of mylar.

The technique using non-magnetic metallic single crystals in NMR was long ago introduced by Jones and Williams (1962), when they analysed the anisotropy of the nuclear magnetic resonance in white tin. It is only 14 years ago, however, since the techniques appropriate for the NMR of ferromagnetically ordered metallic single crystals were introduced by Fekete et al. (1975). However, the requirements for the sample preparation are relatively severe. Otherwise the full

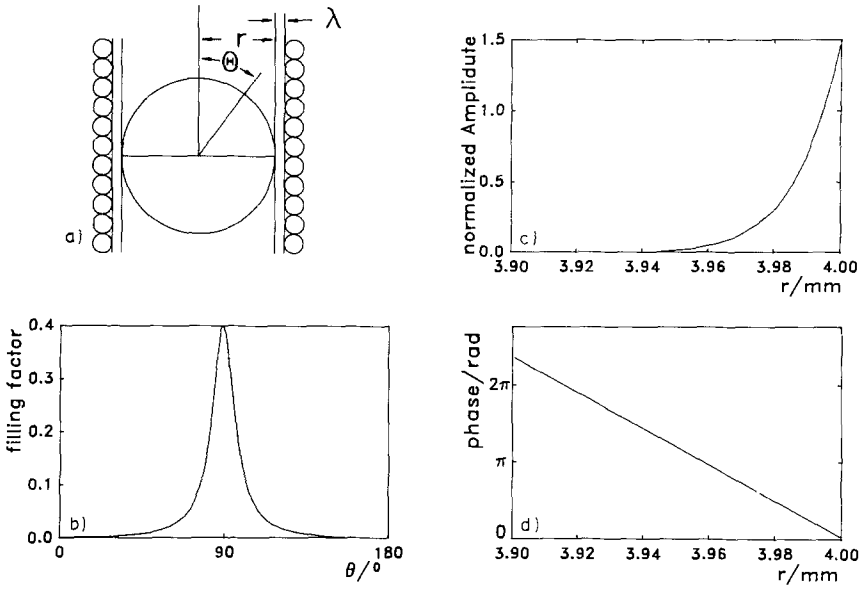

Fig. 1. NMR in a metallic single crystal. Geometry for the calculation (a) and angular variation (b) of the filling factor for a metallic sphere inside a cylindrical coil, separated by a thin layer of Mylar. Data: $r = 4$ mm, $\lambda = 20$ μm, $\delta = 13.5$ μm ($1/\sigma = 1.8$ μΩ cm, $\nu_{rf} = 25.1$ MHz). Amplitude (c) and phase (d) of the radiofrequency magnetic field inside the metallic sphere. The amplitude is normalized to the value far outside the sphere (after Kropp 1983).

information and resolution accessible by NMR is not exploited, which is due to the well defined crystal structure and comparatively narrow NMR lines of intermetallic compounds.

Let us discuss this important aspect in more detail. In Pauli paramagnetic intermetallic compounds, the shape of the single crystal is of minor importance, but not so in ferromagnetics. This can be seen from eq. (3): the resonance field H_{res} at the nucleus,

$$\nu_{res} = (\gamma/2\pi)|\boldsymbol{H}_{res}|\,, \tag{2}$$

(with the gyromagnetic ratio γ of the respective nucleus) in the ferromagnetic material in an applied external field H_0 is equal to the vectorial sum

$$\boldsymbol{H}_{res} = \boldsymbol{H}_0 + \boldsymbol{H}_D + \boldsymbol{H}_L + \boldsymbol{H}_{hf}\,. \tag{3a}$$

The hyperfine field H_{hf} may be anisotropic and is frequently decomposed into its isotropic and anisotropic contributions, the latter being caused, e.g., by the classical dipolar field of the magnetic neighbours. The demagnetizing field

$$\boldsymbol{H}_D = -\boldsymbol{N}\boldsymbol{M}(\boldsymbol{H}) \tag{3b}$$

depends on the sample shape via the demagnetization factor (tensor) N and on the macroscopic sample magnetization $M(H)$, while the Lorentz field amounts to

$$\boldsymbol{H}_L = +\tfrac{4}{3}\pi\boldsymbol{M}_s \tag{3c}$$

with spontaneous magnetization M_s. Thus

$$\boldsymbol{H}_{res} = \boldsymbol{H}_0 - \boldsymbol{N}\boldsymbol{M}(\boldsymbol{H}) + \tfrac{4}{3}\pi \boldsymbol{M}_s + \boldsymbol{H}_{hf} . \tag{3d}$$

For a multidomain ferromagnetic sample in zero external field, the magnetization is homogeneous within a domain, but the directions of magnetizations differ for different domains. Thus the macroscopic magnetization $M(H_0 = 0)$ and the average demagnetizing field vanish, and

$$\boldsymbol{H}_{res} = \boldsymbol{H}_{hf} + \tfrac{4}{3}\pi \boldsymbol{M}_s . \tag{3e}$$

If an external field is applied, $M(H)$ and H_D deviate from zero. Their magnitude and direction vary within the sample, if an ellipsoidal sample shape is not adopted. The most favourable geometry is a sphere, because then the demagnetization field will be homogenous and, for samples with negligible magnetic anisotropy, collinear with the external field. As long as the external field strength H_0 is below $\frac{4}{3}\pi M_s$, H_0 and $\boldsymbol{N}\boldsymbol{M}(\boldsymbol{H})$ compensate each other and no NMR line shift is observed, as shown in fig. 2. For an external field above technical saturation ($\boldsymbol{H}_0 > \boldsymbol{N}\boldsymbol{M}_s$), the NMR line will shift in proportion to the gyromagnetic ratio, as indicated in fig. 2, with the sign of the slope depending on the sign of the hyperfine field.

Any deviation from an ideal spherical shape will lead to a non-vanishing value of $\frac{4}{3}\pi \boldsymbol{M}_s - \boldsymbol{N}\boldsymbol{M}(\boldsymbol{H})$ and, in general, to a distribution of H_D and resonance frequencies and thus to line broadening. Two types of deviations have to be distinguished, as was first discussed and experimentally proven by Fekete et al. (1975). One contribution is already troublesome for NMR in an insulating ferromagnetic sphere of diameter d; if there is a small deviation Δd from

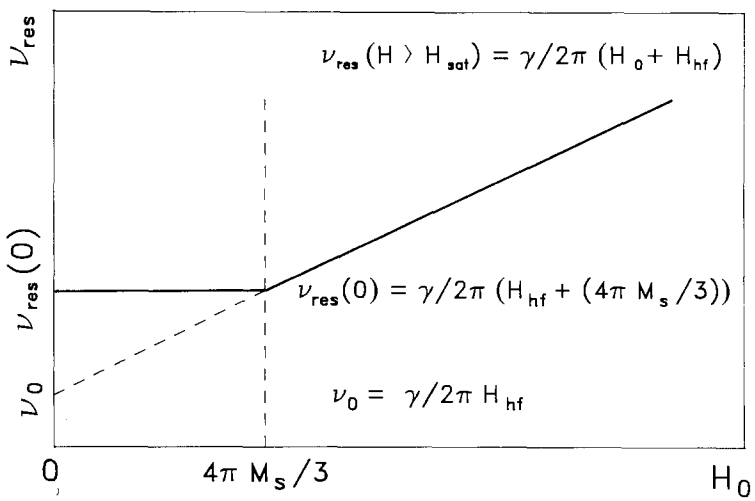

Fig. 2. Qualitative variation of the nuclear magnetic resonance frequency with the strength of an applied external field for a spherical ferromagnetic sample with negligible magnetic anisotropy and isotropic, positive hyperfine field at low temperature (saturated magnetization).

sphericity, which extends over a long range (of the order of d), then there will be a distribution of demagnetization fields with a width

$$\Delta H_D \approx \frac{\Delta d}{d} (\tfrac{4}{3}\pi M_s) \tag{4a}$$

leading to line broadening. The second problem, more difficult to overcome, plagues preferentially metallic ferromagnets, where the NMR signal originates only from nuclei in the skin depth δ. In addition, scratches and holes in the surface, which means small deviations Δs from the ideal sphere geometry, which fluctuate over short distances of the same order as Δs, will give a broadening of the NMR line of about (Fekete et al. 1975)

$$\Delta H'_D \approx \frac{\Delta s}{\delta} (\tfrac{4}{3}\pi M_s) . \tag{4b}$$

This contribution can only be overcome by a careful polishing of the sphere. Techniques that can generally be applied for grinding single crystals of cubic or even anisotropic materials into spheres of sufficient quality for condition (4a) with the help of variants of the lapidaries' method were long ago reported by Bond (1954) and Durand (1959). Also spark machining of cubic Laves-phase compounds, which contain gadolinium, was discussed (Ayling and Creagh 1977). Usually, in a second, more time consuming step the surface is polished by blowing the sphere inside a circular channel whose walls are coated with abrasive diamond paste using pressed nitrogen for driving. The final emery paste must have a mesh of 0.25 μm or below. Occasionally electropolishing can be applied as well. Vacuum annealing for several days heals the surface defects produced during the polishing procedure. With this treatment, line broadening according to eq. (4b) can be reduced sufficiently so that even Knight shift measurements in ferromagnetically ordered compounds have become feasible.

1.2. *NMR signals from domains and domain walls*

Whilst the interpretation of NMR spectra obtained from Pauli paramagnetic intermetallic compounds is relatively straightforward, a superficial analysis of zero-field NMR spectra of ferromagnetically ordered compounds can be very misleading. In the past, a number of problems originated because the peculiarities of NMR in ferromagnetic materials were not taken into account. An NMR property of ferromagnets, gratifying at least in principle, is the enhancement of the radiofrequency field amplitude H_1 and of the NMR signal strength. The electronic magnetization in the domain or the Bloch wall, being driven non-resonantly by the rf field, is at the origin of the rf field enhancement via the hyperfine interaction

$$H_{1,\mathrm{eff}} = H_{1,0}(1 + \eta) . \tag{5}$$

Since enhancement factors η for nuclei situated in Bloch walls ranging between 100 and 10 000 (or between 10 and 1000 for nuclei in domains) were observed, the

advantage for the detectability of NMR signals is obvious. We refer the reader to the reviews by Narath (1967) and McCausland and Mackenzie (1980) for a discussion of the enhancement mechanisms in domains and walls. The main disadvantage of the enhancement mechanism is that the NMR signal strengths of different NMR lines of the same NMR isotope in the same sample can be enhanced by different factors, such that the relative intensities do not give a direct picture of the *number* of nuclei resonating at a certain frequency. This problem is especially severe in the zero-field NMR of multidomain particles. Frequently, at least for short rf pulses of weak amplitude H_1, only the NMR signals originating from the nuclei in the domain walls are observed, because wall motion shields the domains against the rf field. Thus, evidently, all information accessible by such NMR refers to the Bloch walls only – an aspect that was frequently forgotten, when conclusions about the temperature dependence or the easy direction of the magnetization were drawn from such signals or spectra. If the hyperfine interaction is anisotropic, the situation may be even more complicated: then two different resonances, enhanced by the wall motion, may be observed – one from nuclei situated at the wall center and one from those at the wall edge. This has its origin in the variation of the enhancement factor $\eta(\Phi)$ and the number of nuclei per orientation interval, $n(\Phi)$ in the Bloch wall ($0 \leq \Phi \leq 180°$): the signal of the small number of wall-center nuclei, $\eta(\Phi \approx 90°)^2 n(\Phi \approx 90°)$ may be comparable to that of the large number of wall-edge nuclei $\eta(\Phi \approx 0°/180°)^2 n(\Phi \approx 0°/180°)$, because the enhancement factor is largest in the wall center. Butler (1973) [using a simplified approach compared with the original treatment of NMR in multidomain ferromagnets by Turov and Kurkin (1969)] showed several examples where the complicated NMR spectra could be reproduced along these lines. For further examples, see also Kunkel and Searle (1981) or Al-Assadi et al. (1984).

Bringing this discussion to an end, we can summarize our conclusions by stating that again the most clearcut conditions can be obtained for NMR in a magnetized sphere, because then there are no more wall signals and the variation of the enhancement factor with the external field strength for the domain nuclei can be estimated using

$$\eta(H_0 > H_{sat}) = \frac{H_{hf}}{H_0 + H_{an}} \tag{6}$$

(with the anisotropy field H_{an}).

1.3. *NMR spectra*

Some remarks are finally in place as to what is generally plotted as 'the NMR spectrum'. Considerable differences between relative signal intensities and linewidths can commonly be observed between the NMR spectra of different authors. In part they can be linked with the conditions of sample preparation and sample treatment. For example, accidental quadrupolar broadening can occur due to the grinding procedure or external strains caused by the squeezing influence of frozen oil or vacuum grease on the powder sample or the single crystal. Occasionally,

differences originiate also from the different weighting of orientation-dependent spectra, as can be judged from the different spectra of ^{157}Gd in ferromagnetically ordered $GdAl_2$ shown as an example in fig. 3. In such a case, the measuring technique as well as the sample preparation is of importance.

The NMR spectrum can be measured in two different modes, either by varying the frequency or the magnetic field strength. The latter is generally much easier to perform. In ferromagnetic substances the amplitudes of the spectra are usually distorted because the rf-field enhancement factor η_{rf} and the NMR signal enhancement factor η_s for nuclei in domains decrease with increasing field strength according to eq. (6). Whereas the η_{rf} variation can easily be taken care of by an increase of the rf amplitude with increasing H_0, the $\eta_s(H_0)$ variation usually remains if not explicitly corrected for. (This can be visualized from the lowest trace of fig. 3: the high-field quadrupolar satellite is smaller in amplitude than the low-field one.)

Zero-field spectra of ferromagnetic materials evidently have to be measured as a function of the rf frequency, in favourable cases by Fourier-transform techniques or else 'point by point', adopting a reliable procedure of controlling the

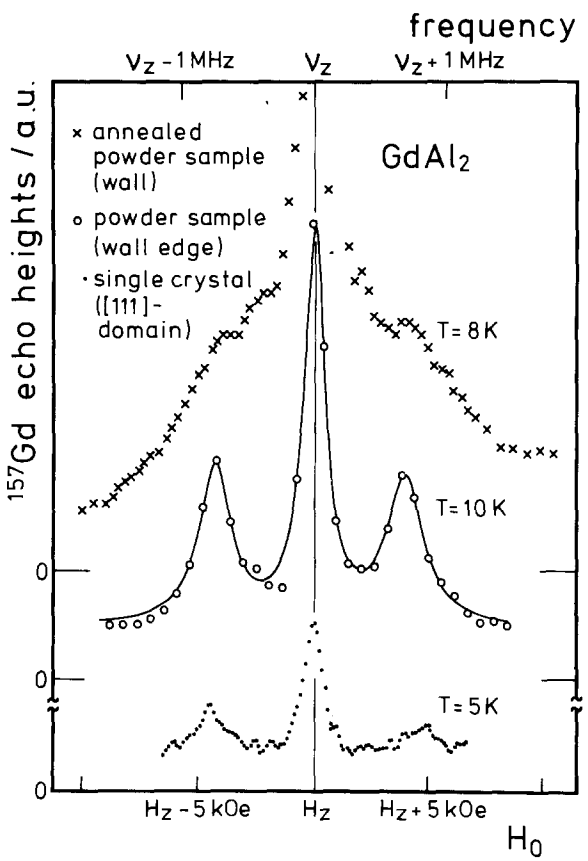

Fig. 3. Examples for the differences between the line profiles of ^{157}Gd NMR spectra of ferromagnetically ordered $GdAl_2$. Zero-field spectra of an annealed powder sample (x) and of a powder sample prepared for optimum resolution of the quadrupolar splitting (○) plotted against frequency, and NMR spectrum of a single-crystalline high-quality sphere plotted against external field strength in the [111] easy direction (●) on corresponding horizontal scales (Dormann and Dressel 1989).

tuning, sensitivity and rf-field amplitude. Depending on the kind of adjustment of the rf amplitude, the uncorrected NMR spectrum varies like $\eta_s \eta_{rf} n(\nu, \eta)$ (if the rf amplitude is not varied over the spectrum) or like $\eta_s n(\nu, \eta)$ (if the NMR signal strength is optimized at each frequency with respect to the rf-field amplitude H_1). If such an NMR spectrum has to be converted into a plot of the *number* of resonating spins against frequency, $n(\nu)$, it has to be corrected for the frequency dependence of the enhancement factor η. A rough determination of the rf-field amplitude acting on the sample and thus the enhancement η_{rf} can be achieved, if the rf field is monitored with the help of a coupling loop and an oscilloscope, which are calibrated by using 90° pulses for a sample of protons in an external magnetic field instead of the sample in question. More ingenious versions have been suggested as well, see, e.g., Pieper et al. (1984).

What (for magnetic or non-magnetic compounds) is actually plotted 'point by point' as NMR signal against frequency? A careful solution would be to calculate the Fourier-transform amplitudes at the respective frequency from the spin echo for different pulse separations and to extrapolate the $\exp(-2\tau/T_2)$ dependence to zero pulse separation in order to eliminate the influence of an eventual frequency dependence of the spin–spin relaxation time T_2. This is quite tedious. Occasionally the *area* under the echo, after phase-sensitive detection at the frequency ν_{rf} is plotted; this corresponds to the Fourier-transform amplitude at ν_{rf} but it is more easily perturbed by problems with the baseline correction. Frequently, also, only the *amplitude* of the phase-sensitively detected echo is plotted against frequency. This is the quantity most easily accessible, but it is proportional to the echo area only if the echo shape does not vary within the frequency range of interest. This technique gives broadened and distorted spectra for narrow-line NMR spectra if the excitation band width (via the rf-pulse length) and the detection band width (via the filter width of preamplifier or phase-sensitive detection) are not selected carefully (i.e., narrow enough). Unfortunately, NMR researchers frequently tend to forget to indicate the special conditions under which 'their spectrum' was taken and thus generate unnecessary confusion!

2. Microscopic information about the macroscopic properties of magnetically ordered intermetallic compounds

NMR can be used to obtain information about different macroscopic properties of magnetic intermetallic compounds, such as the temperature dependence of the magnetic susceptibility of the main phase and of impurities (or impurity phases), ordering temperatures (θ_p, T_c), magnetic phase transitions with and without an external field, type of magnetic order, influence of deviations from stoichiometry and annealing treatments and others. As examples, we select here information arbitrarily about the temperature dependence of the spontaneous magnetization (sect. 2.1) and on the direction of easy magnetization ('easy direction') (sect. 2.2) of magnetically ordered compounds.

2.1. *Temperature dependence of the spontaneous magnetization*

NMR presents a convenient local probe for the temperature dependence of the spontaneous magnetization. Evidently, the measurement of the temperature dependence of the zero-field resonance frequency is much easier than the careful analysis of the variation of the resonance frequency with orientation and strength of an external field and with temperature in a single crystal. It has, however, always to be kept in mind that the zero-field NMR analysis of a multidomain powder sample can only yield information about the phenomena in the Bloch wall if the zero-field signal originates from nuclei in the Bloch wall. This variation should *not* be compared with the temperature dependence of the magnetization in the domain. Only a careful NMR analysis is thus worthwhile for a discussion of the eventual differences in the variations of $\nu_{res}(T)/\nu_{res}(0\,\mathrm{K})$, $h(T) = H_{hf}(T)/H_{hf}(0\,\mathrm{K})$ and $m(T) = M_s(T)/M_s(0\,\mathrm{K})$, that could prove the temperature dependence of the hyperfine coupling constant (after correction for the volume variation!). Narath (1967) has already given different examples proving that the temperature dependences of the zero-field resonance frequencies for domain and domain wall signals may be different (e.g., ^{53}Cr in CrX_3 with X = Br, Cl, I).

Generally it is easy to follow the temperature dependence of zero-field NMR spectra in the ferromagnetically ordered state up to about $(0.5\text{–}0.7)T_c$. This was done, e.g., for ^{67}Zn and ^{155,157}Gd in GdZn ($T_c = 267$ K), and ^{27}Al and ^{155,157}Gd in $GdAl_2$ ($T_c = 172$ K), by Herbst et al. (1974), and for ^{153}Eu in $EuPt_2$ ($T_c = 105$ K) by Dressel et al. (1988). Short relaxation times T_1 and T_2 and the strong influence of temperature instabilities – via large $\partial\nu_{res}/\partial T$ for T approaching T_c – are obstacles to an extension of the temperature range, which can be, however, overcome. For example, Barash and Barak (1984) measured the NMR of ^{27}Al, ^{155}Gd and ^{157}Gd in ferromagnetic $GdAl_2$ and of ^{27}Al in ferromagnetic $DyAl_2$ over a wide temperature range in zero external field. [The temperature dependence of the NMR frequencies for $GdAl_2$ agreed with Bloch's $T^{3/2}$ law up to $0.5T_c$, while that for $DyAl_2$ was explained in terms of molecular fields (MF) and crystal electric fields (CEF).] They were able to follow the temperature dependence up to $T = 0.94T_c$, using the temperature variation instead of the frequency variation to record the NMR lines.

If spin-wave excitations are dominant, the magnitude of the hyperfine field decreases as the temperature is raised like

$$h(T) = \frac{H_{hf}(T)}{H_{hf}(0\,\mathrm{K})} = 1 - C_{3/2}T^{3/2} - C_{5/2}T^{5/2}. \tag{7a}$$

Edwards (1976) showed that – at constant volume – the coefficient $C_{3/2}$ in eq. (7a) is identical to that of the reduced magnetization

$$m(T) = \frac{M_s(T)}{M_s(0\,\mathrm{K})} = 1 - C'_{3/2}T^{3/2} - C'_{5/2}T^{5/2}, \tag{7b}$$

i.e., $C_{3/2} = C'_{3/2}$ (if spin-wave excitations are dominant). The explicit temperature

dependence of the normalized hyperfine coupling constant contains a $T^{5/2}$ term in the lowest order:

$$\frac{A(T)}{A(0\,\mathrm{K})} = 1 - C''_{5/2}T^{5/2} + C''_{7/2}T^{7/2}\,. \tag{7c}$$

Thus the values of the coefficient $C_{3/2}$ for different sites in the same crystal should also be the same. Nagai et al. (1976) found different coefficients $C_{3/2}$, ranging from $(5\text{–}8.5)\times 10^{-6}\,\mathrm{K}^{-3/2}$ for different Co sites from a constant-pressure NMR analysis of Gd_2Co_{17} [omitting, however, the $C_{5/2}$ term in eq. (7a)]. Oppelt et al. (1976) observed different temperature dependences of $h(T)$ for the two non-equivalent Y sites (with 18 and 12 nearest Fe neighbours) in YFe_3, as well. Riedi and Webber (1983) reinvestigated the normalized hyperfine fields at the two Y sites in YFe_3. No difference was observed up to $T = 35$ K, the limit of the $T^{3/2}$ law. Differences evident at temperatures above 100 K were shown to arise from higher-order spin-wave terms. Riedi and Webber (1983) also analysed the pressure dependence of H_{hf} up to $p = 15$ kbar, as is necessary for a more precise comparison of the temperature dependences in eqs. (7a) and (7b). The pressure dependence was in agreement with the picture that the yttrium hyperfine field results predominantly from polarization of s-like conduction electrons, with only a small d-band contribution.

2.2. *Easy direction of the magnetization*

The characteristic line profile caused by the contribution of the dipolar field H_{dip}, which depends on the orientation of the magnetization, to the resonance field at a non-cubic lattice site can be used to dismantle the easy direction of magnetization. An early NMR example was the ^{27}Al line shape analysis in ferromagnetically ordered RAl_2 (R = rare earth) by Kaplan et al. (1973).

This is an area of NMR applications where the probability of pitfalls is especially high: frequently, the experiments are performed with powder samples containing walls *and* magnetic domains. Then the zero-field NMR spectrum may reflect the direction of magnetization in the center of the Bloch wall, where only a small number of nuclei are situated, which encounter, however, the largest rf field and signal enhancement factor. In the way, an interesting piece of information for the understanding of the wall type may be obtained, but evidently it does not reveal the *easy* direction of the magnetization. Only if the necessary experimental tests (e.g., variation of the NMR spectrum with the strength of the rf field or the external field, determination of the enhancement factor, dependence on sample preparation) are performed, proving that the signal originates from wall edges or domains, can the easy direction be derived reliably. For a discussion of related problems also see Bowden et al. (1983).

With the help of NMR, spin reorientations – with temperature in $HoCo_2$ (Guimarães et al. 1987) or with concentration x in pseudobinary compounds like $Gd_{1-x}Dy_xAl_2$ (Ichinose et al. 1984a) or $Tb_{1-x}Dy_xCo_2$ (Hirosawa and Nakamura 1982b) – were also analysed. We have compiled many other examples for this type

of application in tables B6 (^{27}Al), B10 (^{55}Mn) and B12 (^{59}Co) in the appendix.

The anisotropy of the quadrupolar interaction and especially the interplay between the magnetic dipole and electric quadrupole interactions may be used for the derivation of the easy direction of the magnetization, as well. Both extremes – electric quadrupolar interactions that are weak or strong compared with the magnetic hyperfine interaction – are useful. The [100] direction was derived, using NMR on Ir in $GdIr_2$ for the portion of the sample from which the NMR signal stems from, by Dormann and Buschow (1973) and Dormann et al. (1976) – this is an example, where the electric quadrupolar contribution is much larger than the magnetic dipolar one. There are many examples, where the $3\cos^2\theta - 1$ dependence of the quadrupolar splitting (McCausland and Mackenzie 1980) or of the quadrupolar echo modulation (Abe et al. 1966) could be used for the derivation of the direction of the magnetization in the case of a 'weak' quadrupolar interaction. We mention $Gd_{1-x}Dy_xAl_2$ by Miles et al. (1977), $DyAl_2$ by Bowden et al. (1982) and $GdAl_2$ by Dumelow et al. (1988) as examples.

In some intermetallic compounds, such as RZn with the simple cubic CsCl structure, no lattice sites with a low enough symmetry are available in order to use the techniques discussed above for the derivation of the easy direction. Eckrich et al. (1976) showed that, nevertheless, NMR can be applied in this case: a small concentration of non-magnetic atoms – such as Sc, Y or La – was introduced. The ^{67}Zn NMR line profile for Zn atoms with seven Gd and one Sc, Y or La nearest neighbours in pseudobinary compounds of the general form $Gd_{1-x}(Sc/Y/La)_xZn$ was analysed. It indicated the orientation of the magnetization in this portion of the sample via the $3\cos^2\theta - 1$ dependence of the dipolar field contribution of the 'magnetic hole' to the resonance field. By the use of different non-magnetic ions and extrapolation to vanishing concentration ($x \to 0$) one can determine the easy direction, but one has to make sure, however, that the easy direction of the system under study is not influenced by the non-magnetic dilution.

3. NMR information about the electronic structure of intermetallic compounds with non-magnetic partners

The analysis of the electronic structure of intermetallic compounds of the lanthanides with non-magnetic partners is an area of especially successful application of NMR. The nuclei of all rare earth ions except cerium and promethium are accessible. For five lanthanides, two different stable NMR isotopes are available with sufficient natural abundances – see tables A3–A15 in the appendix. They have different magnetic dipole and electric quadrupole moments, allowing a clearcut distinction between both types of hyperfine interactions in the NMR spectra. In many cases, the nuclei of the non-magnetic partners can also be investigated by NMR. Generally, highly resolved spectra are obtained with no problems in the assignment of the NMR lines to the respective isotopes.

For a comprehensive earlier review of the physical properties, compositions and crystal structures of intermetallic compounds formed between rare-earth elements and non-magnetic metals, including NMR applications, see Buschow (1979).

3.1. *Band structure information*: *Knight shift in non-magnetic compounds*

The use of NMR as a local probe for conduction electron wavefunctions and orbital character already has a long and fruitful tradition. Thus we refer to the extensive review on *Metallic Shifts in NMR* by Carter et al. (1977) for an introduction to the field, the relevant relations and further references. The introduction of the 'Jaccarino–Clogston–plot' type of correlation between the temperature-dependent Knight shifts and magnetic susceptibilities gave an important source of qualitative information. Usually the set of eqs. (8a–c), correlating the Knight shift $K(T)$, the nuclear spin–lattice relaxation time T_1 and the total magnetic susceptibility per mole $\chi(T)$, was applied (Narath 1967):

$$K(T) = K_{sp} + K_d(T) + K_{orb}\,, \tag{8a}$$

$$(T_1T)^{-1} = (T_1T)^{-1}_{sp} + (T_1T)^{-1}_{d} + (T_1T)^{-1}_{orb} + (T_1T)^{-1}_{dip} + (T_1T)^{-1}_{Q}, \tag{8b}$$

$$\chi(T) = \chi_{sp} + \chi_d(T) + \chi_{VV} + \chi_L + \chi_{dia}\,. \tag{8c}$$

Conduction electrons in broad bands of s- and p-like character contribute to all three quantities (sp). The Landau orbital diamagnetism (L) of these electrons is frequently considered only in the free-electron approximation, and taken care of by introducing a factor of two thirds in front of χ_{sp}, whilst χ_{dia} represents only the core diamagnetism. More localized non-s-like electrons in narrow bands give temperature-dependent contributions. In addition to the spin part (d) of the susceptibility, which is noticeable at the nucleus via core polarization (and finally Fermi-contact interaction) or via dipolar interaction (dip), van Vleck type induced orbital contributions of the magnetic susceptibility lead to orbital (orb) contributions of K and $1/T_1$, and eventually also to quadrupolar contributions (Q) of $1/T_1$. In this chapter we will use the symbol 'α_i' (instead of H^i_{hf}) for the hyperfine coupling constant(s) (with units of Oe μ_B^{-1} or Oe/electron) in the equation

$$K_i = \alpha_i \chi_i / N_A \mu_B\,, \tag{9}$$

relating the respective Knight shift and molar susceptibility contributions, in order to reserve the symbol 'H_{hf}' for the total hyperfine field (with units of Oe) of magnetically ordered compounds (N_A is Avogadro's number). Carter et al. (1977) can serve as a reference for a compilation of the absolute values of the respective coupling constants α_i.

Band structure calculations have improved considerably in the past 20 years and give a more detailed picture of the character of the conduction electrons at different sites in intermetallic compounds to be compared with the NMR results; see, e.g., examples for CsCl-type intermetallic compounds by Belakhovsky et al. (1972, 1973) and Seipler et al. (1977).

3.1.1. *High-field Knight shift in magnetically ordered compounds*

The measurement of the Knight shift for ferromagnetically ordered states also seemed interesting, because there were several indications of a change of the band structure due to magnetic ordering. For example, Devine and Berthier (1979) compared the data on hyperfine fields in magnetically ordered $ErAl_2$ and $DyAl_2$ with ESR results for Er and Dy in $ScAl_2$, $LuAl_2$ and $YbAl_2$, and concluded that the self-polarization effects might be different in the ferromagnetic and paramagnetic phases. The modification of the conduction electron band structure due to exchange splitting effects might thus play an important role in RAl_2 compounds. In fact, Knight shift analysis of ferromagnetic intermetallic compounds turned out to be possible along the lines presented in sect. 1.1. and indicated such changes for the Al site of $GdAl_2$ (Kropp et al. 1983).

'High-field' Knight shift data for ^{27}Al and ^{157}Gd in ferromagnetically ordered $GdAl_2$ (cubic Laves phase, $T_c = 171\,K$) have been reported by Kropp et al. (1983) and for ^{67}Zn, ^{157}Gd and ^{157}Gd in ferromagnetically ordered GdZn (CsCl-type structure, $T_c = 269\,K$) by Kropp et al. (1984). These measurements required not only a high-quality polished single-crystalline sphere, but also

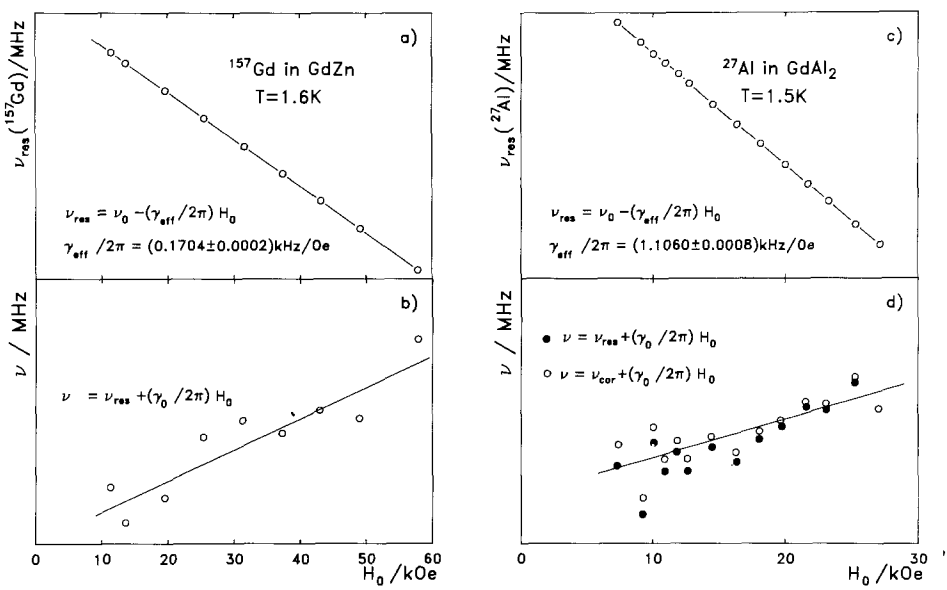

Fig. 4. High-field Knight shift measurements of single-crystalline spheres of ferromagnetically ordered intermetallic compounds. Parts (a, c) show the shift of the center of the NMR lines for magnetic field applied along the [111] (easy) direction for the ^{157}Gd resonance line in GdZn (a) and for the center of the ^{27}Al 'a'-site ($m_I = +\frac{1}{2} \leftrightarrow -\frac{1}{2}$) transition in $GdAl_2$ (c). The hyperfine field is negative in both cases. Parts (b, d) show these data on a 'magnified' scale: the resonance frequency shift corresponding to the bare nuclear gyromagnetic ratio γ_0 ($^{157}\gamma_0/2\pi = 0.1713\,kHz\,Oe^{-1}$ (b) and $^{27}\gamma_0/2\pi = 1.10936\,kHz\,Oe^{-1}$ (d)) is eliminated. The slope of the full line if proportional to $-K$ and reveals that the Knight shifts of ^{157}Gd in GdZn [$^{157}K = -(5.0 \pm 1.9) \times 10^{-3}$] and of ^{27}Al in $GdAl_2$ [$^{27}K = -(2.5 \pm 0.9) \times 10^{-3}$] are negative. The influence of the external magnetic field on the spin-wave excitations had to be considered (ν_{cor}) even for $T = 1.5\,K \ll T_c$ in $GdAl_2$. (Adapted from Kropp 1983).

magnetic fields, which are sufficiently far above technical saturation, and a low temperature $T \ll T_c$, see fig. 4. If the measuring temperature would not be reduced sufficiently to approach the ferromagnetic ground state of the compound, the influence of the magnetic field on the spin-wave excitations and the accompanying variation of the magnetic hyperfine field would be much larger than the Knight shift. This would increase the error bar of the appropriately corrected resonance frequency data to a size that would make the shift information meaningless (Kropp et al. 1983). The NMR investigation proved the predominance of non-s conduction electrons in the density of states at the Fermi level of ferromagnetic $GdAl_2$ and GdZn, for the gadolinium as well as for the non-magnetic sites.

3.2. *Analysis of the conduction electron spin polarization*

3.2.1. *Uniform polarization model*

NMR investigations can give detailed information about the indirect magnetic interactions in intermetallic rare-earth compounds. Different degrees of sophistication were applied, when the conduction electron polarization was analysed – depending on whether the type of conduction electrons contributing to the indirect interactions, the distance dependence of the polarization or their anisotropy were of interest (Dormann et al. 1980). The simplest, qualitative version introduced by Jaccarino et al. (1960) is the so-called 'uniform polarization model'. The observed Knight shift in the paramagnetic intermetallic compound, depending on temperature, is correlated with the paramagnetic part of the total susceptibility:

$$K = K_0 \left(1 + J_{sf} \frac{\langle \boldsymbol{S} \cdot \boldsymbol{J} \rangle}{g_s g_f \mu_B^2 J(J+1)} \chi_f\right), \tag{10a}$$

$$K = K_0 \left(1 + J_{sf} \frac{(g_f - 1)}{2 g_f \mu_B^2} \chi_f\right). \tag{10b}$$

Here χ_f is the 4f electron susceptibility *per 4f ion* and K_0 is the Knight shift of the same nucleus for the same intermetallic compound without 4f moments. It is taken from the analysis with eq. (10b) or from an isostructural Pauli paramagnet, e.g., one of the corresponding Y, La or Lu compounds. The exchange coupling constant J_{sf} contains the conduction electron polarization in an integral form. The name 'uniform polarization model' is misleading, because the model never required the conduction electron polarization to be uniform, even if its spatial variation was not taken into account explicitly. Following the first ^{27}Al NMR discussion for RAl_2 by Jaccarino et al. (1960) there have been many NMR analyses with the help of this model, as is evident from the number of J_{sf} values collected in the tables of the appendix. Jena and Lam (1978) analysed the systematics of the $K(\chi)$ correlation for the rare-earth monopnictides RX (with R = Y and Ce–Yb and X = N, P, As, Sb and Bi) and found that K_0 (being relatively independent of the element R) depends sensitively (roughly like the $\frac{5}{4}$

power) on the atomic number of the group VA element. Occasionally instead of eq. (10b) an equivalent relation corresponding to eq. (9) was also used:

$$K(T) = K_0 + \frac{\alpha}{N_A \mu_B} \chi(T) . \tag{10c}$$

For example, Lysak and MacLaughlin (1985) used this form for ^{27}Al NMR analysis in $CeAl_3$, yielding $K_{iso,0} = +0.064\%$ and $\alpha = +3.32\,\text{kOe}\,\mu_B^{-1}$. A $K \leftrightarrow \chi$ analysis for ^{27}Al was used by Hågan and Pop (1986) for $Tb_2Ni_{17-x}Al_x$ ($17 \geq x \geq 15.75$) in order to derive the different mechanisms of coupling between Ni 3d moments and the ^{27}Al nucleus. The uniform polarization model was also used in order to decompose the macroscopic magnetic susceptibility of samples that were suspected of containing magnetic impurities (or impurity phases) with the help of the $K \leftrightarrow \chi$ correlation (Goebel et al. 1975).

3.2.2. *RKKY-type analysis of the conduction electron polarization*

Each time when the hyperfine fields at different sites in the same intermetallic compound were available – as for the ^{27}Al sites in R_3Al_{11} in an NMR analysis by van Diepen et al. (1969) – or when the hyperfine fields and asymptotic paramagnetic Curie temperatures θ_p could be correlated, or when the conduction electron concentration could be varied in pseudobinary intermetallic compounds, the RKKY model [as introduced by Jaccarino (1961) for the discussion of ^{27}Al NMR in RAl_2] was the favourite framework for the NMR spectroscopists. For eq. (10b), J_{sf} is calculated as

$$J_{sf} = -12\pi Z J(0) \sum_n^{\text{I}} F(2k_F r_{nm}) , \tag{11a}$$

with the oscillating RKKY function

$$F(2k_F r) = [(2k_F r)\cos(2k_F r) - \sin(2k_F r)]/(2k_F r)^4 . \tag{11b}$$

The summation, Σ^{I}, is over all magnetic sites n at the distances r_{nm} from the nuclear site (m) considered as the origin. Z is the average number of conduction electrons per atom, and k_F and E_F are the Fermi wavevector and Fermi energy, respectively. The q-dependence of the exchange integral was generally neglected, i.e.,

$$J(q = 0) = J(q = 2k_F) = J(0) , \tag{11c}$$

corresponding to a δ-like exchange interaction. The paramagnetic Curie temperature is calculated along the same lines (de Gennes 1962) as

$$\theta_p = -\frac{3\pi Z^2 J(0)^2}{4k_B E_F} (g_f - 1)^2 J(J+1) \sum_{n \neq m}^{\text{R}} F(2k_F r_{nm}) . \tag{11d}$$

Here the RKKY summation Σ^{R} has to be taken over all other magnetic (R) sites with a magnetic ion at the origin (m). In the ferromagnetically ordered state, the

contribution of all magnetic neighbours to the hyperfine field is calculated as

$$H_N = \frac{9\pi Z^2}{2E_F} J(0)a(0)\langle S_z\rangle \sum_{n\neq m}^{I,R} F(2k_F r_{nm}), \tag{11e}$$

with $a(0)$ the Fourier component of the hyperfine coupling constant for wavevector $q=0$ (and, e.g., $\langle S_z\rangle = -\frac{7}{2}$ for Gd^{3+} as $T\to 0$). We refer the reader to the original RKKY work by Ruderman and Kittel (1954), Kasuya (1956) and Yosida (1957) and to the different applications of the model by de Wijn et al. (1968) and Buschow et al. (1970) for further details and references. In general – especially for pseudobinary compounds with variable conduction electron concentration – the Fermi wavevector was used as an adjustable parameter, with k_F' deviating by up to 30% from k_F. For example, for GdCuAl – using also the series $Gd_{1-x}Th_xCuAl$ for comparison – Buschow et al. (1971) derived $k_F'/k_F = 0.72$ ($k_F = 1.13$ Å^{-1}) and $2J(0) = +0.50$ eV. Similar investigations for the magnetically ordered state were reported for pseudobinary compounds with the CsCl-type structure such as $GdAg_{1-x}In_x$ or $GdZn_{1-x}Ag_x$ by Oppelt et al. (1972a). Modifications of the simple RKKY model were used as well, see, e.g., Oppelt et al. (1972b).

Whereas the paramagnetic shift of the nuclear magnetic resonance frequency for a given applied field is related to the *strength* of the local hyperfine *field* at the nuclear site, induced by the electronic moments, the nuclear spin–lattice relaxation rate yields information about the low-frequency *spectrum* of thermally induced spin *fluctuations*. The influence of pair-correlation effects on the NMR relaxation in paramagnets was analysed experimentally and theoretically by Silbernagel et al. (1968) for ^{27}Al NMR in RAl_2 compounds or for $La_{1-x}Gd_xAl_2$ by Ebner and Sung (1973). More sophisticated versions of the RKKY model are necessary for such investigations (Fradin 1970), because different ranges of the q-dependence of the exchange integral are sensed by different experiments. Whereas the Knight shift indicates the uniform term of the Fourier decomposition, $J(q=0)$, $1/T_1$ traces $|J(q_c)|^2$ for the critical wavevector spanning the (nesting) Fermi surface and leading to magnetic order at low temperature. Since exchange ($J>0$) and interband mixing ($J<0$) enter for $K(T)$ and $1/T_1$ with different weights, large differences between $J(q=0)$ and $J(q_c)$ can result (Fradin 1970).

3.2.3. *Correlation of magnetic ordering temperatures and transferred hyperfine fields*

As is evident from a comparison of eqs. (11d) and (11e), there is also a direct empirical access to the conduction electron spin polarization, if magnetic ordering temperatures and transferred hyperfine fields at the R site are compared. Both quantities contain the spin polarization at the R site, induced by all the other R electronic spins

$$\langle s_z\rangle_{ce} = -\frac{9\pi Z^2}{4E_F} J(0)\langle S_z\rangle_R \sum_{n\neq m}^{R} F(2k_F r_{nm}). \tag{11f}$$

The eqs. (11d) and (11e) can thus be generalized, not implying anymore the special distance dependence of the RKKY model [eq. (11f)] and allowing the experimental distinction between the influence of 6s-(6p-) and 5d-like conduction electrons to be made:

$$T_c \approx \theta_p = \frac{S_R(S_R+1)}{3k_B\langle S_z\rangle_R}\left(J_{4f-s}\langle s_z\rangle_s + J_{4f-d}\langle s_z\rangle_d\right) \tag{12a}$$

and

$$H_N(R) = -2(a_s\langle s_z\rangle_s + a_d\langle s_z\rangle_d)\,. \tag{12b}$$

Whereas both exchange coupling constants are assumed to have the same sign and comparable magnitude, opposite signs and different strengths for the hyperfine coupling constants for conduction electrons with 6s or 5d character at the lanthanide site are considered ($a_d \approx -0.1a_s$). For more details and references for the coupling constants see Dormann (1977) and Kropp et al. (1979b).

The ordering temperature is directly accessible; the contribution of the neighbours H_N to the hyperfine field at the magnetic rare-earth ion's site is, however, only *one* of the three components of the hyperfine field H_{hf}, which itself is conveniently accessible to NMR measurements:

$$H_{hf} = H_{4f} + H_S + H_N, \tag{13a}$$

for a lanthanide ion in general, and

$$H_{hf} = H_{cp} + H_S + H_N, \tag{13b}$$

for Eu^{2+} or Gd^{3+} ions with half-filled 4f shells and thus a $^8S_{7/2}$ ground state. Due to the large orbital contributions to H_{4f} for non-S state ions, only in favourable cases – see sections 3.3.4 and 3.3.5 – is it possible to separate H_N from the influence of the lanthanide ion's own conduction electron spin polarization H_S – the so-called self-polarization field – and the 4f-shell contribution, H_{4f}, in eq. (13a). The situation is more agreeable for the S-state ions, eq. (13b), because in the absence of a 4f-shell orbital moment, the remaining core polarization contribution H_{cp} is small, assumed to be constant and known experimentally – e.g., $H_{cp}(Gd) = -(332 \pm 6)$ kOe (Koi 1969). Nevertheless it was a precondition for the usefulness of eqs. (12a) and (12b), that it could be proved that *non-magnetic* rare-earth ions such as Sc, Y, La or Lu, introduced in small concentrations in pseudobinary intermetallic compounds, could serve as excellent direct NMR probes for H_N. For example, the ^{139}La NMR spectrum in $Gd_{1-x}La_xRh_2$ has been measured for $0.5 \geq x \geq 0.01$ (Dormann et al. 1977a), H_{hf}(La) for a vanishing La concentration has been determined by extrapolation (see, e.g., fig. 5) and H_{hf}(La) could be converted to H_N(Gd) by use of the known hyperfine coupling constants. [The required outer-electron coupling constants for the various elements were interpolated between the values given by Campbell (1969)].

Such an NMR analysis for ferromagnetic Gd intermetallics revealed that the s-like conduction electrons predominate only in those compounds investigated that have a weak coupling – or low ordering temperature –, i.e., GdRh, $GdRh_2$,

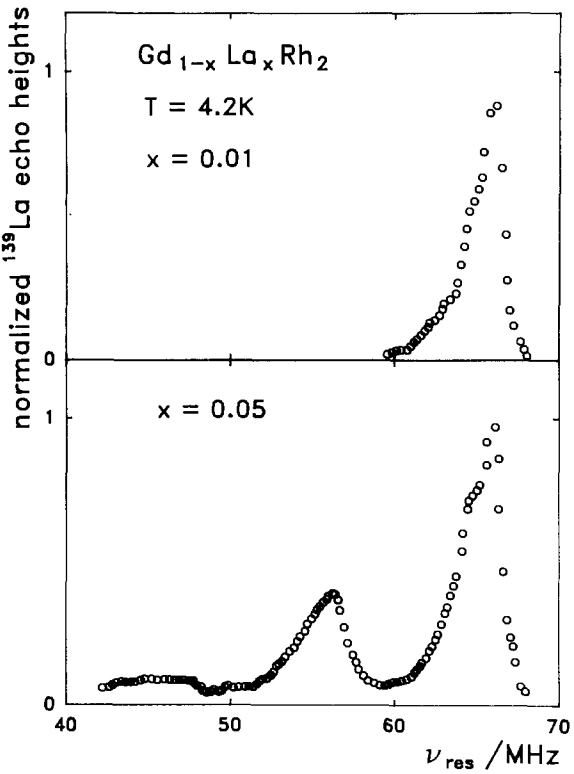

Fig. 5. Zero-field ^{139}La NMR spectra from $Gd_{1-x}La_xRh_2$ with a small non-magnetic dilution x at $T = 4.2$ K (adapted from Dormann et al. 1977a). The main line originates from La with four Gd nearest neighbours, the satellites from La with three Gd/one La or two Gd/two La nearest neighbours. The shoulder of the main line indicates the influence of second and third nearest neighbours ($N_2 = N_3 = 12$).

$GdPt_2$, GdNi, $GdNi_2$ and $GdIr_2$ (Dormann 1977). In the compounds that have high ordering temperatures ($GdAl_2$, GdZn), the 5d-like conduction electrons are clearly essential. A corresponding analysis for the antiferromagnetic GdAg by Goebel and Dormann (1979) proved that if the contribution of d-like conduction electrons predominates then this can also lead to antiferromagnetic coupling. In Eu intermetallics (Eu^{2+}) Kropp et al. (1979b) found that coupling via non-s conduction electrons is important in many compounds even including those with low magnetic ordering temperatures.

In the above analysis, only the *spin* polarization of the conduction electrons was considered. This seems permissible: Berthier et al. (1978b) analysed the mechanism of magnetic coupling in RAl_2 and RZn (T_c and H_N for the whole lanthanide series). They concluded that, although strong orbital polarization of the conduction band is present in the vicinity of the 4f electrons, it does not propagate between them.

3.2.4. *Distance dependence of the transferred hyperfine interaction*

NMR investigation of non-magnetically diluted, ferromagnetically ordered intermetallic compounds like $Gd_{1-x}La_xZn$ allows one to analyse the distance dependence of the transferred hyperfine interaction at the sites of the lanthanide and the non-magnetic partner. Usually, a statistical occupation of the different

neighbour shells is assumed. In this case, for a La concentration x and a neighbour shell i with N_i sites (e.g., $N_1 = 8$ for the Zn site in GdZn, of CsCl-type structure), the probability for the occurrence of n_i La ions in the ith shell is

$$W(n_i, N_i, x) = \frac{N_i!}{n_i!(N_i - n_i)!} x^{n_i}(1-x)^{N_i - n_i} . \tag{14}$$

With these probabilities and a RKKY-like distance dependence (adjusting k_F' and $a(0)$), the ^{27}Al NMR line profiles in $Gd_{1-x}La_xAl_2$ or $Gd_{1-x}Y_xAl_2$ could be explained qualitatively (Dormann et al. 1973). Such experiments can be in keeping with an RKKY-like oscillatory distance dependence; however, they cannot prove or disprove it in detail. In more favourable situations the contribution of *distinct* magnetic neighbours to the transferred hyperfine field can be derived by zero-field NMR of pseudobinary compounds with powder samples. The contribution of one nearest magnetic Ln (Ln = lanthanide) neighbour to the hyperfine field at the eightfold-coordinates Zn in the CsCl-type structure was easily derived by ^{67}Zn zero-field NMR measurements in $Gd_{1-x}R_xZn$ (R = Sc, Y, La, Ln) by Eckrich et al. (1972, 1976) because the eight nearest-neighbour Gd ions contribute 82.5% of the total Zn hyperfine field. Despite the occurrence of a large broadening of the zero-field ^{139}La NMR lines, the appearance of satellites to the main ^{139}La resonance line could also be observed in $Gd_{1-x}La_xIr_2$ by Dormann et al. (1976) and in $Gd_{1-x}La_xRh_2$ by Dormann et al. (1977a), see fig. 5 for an example. This means that the predominant neighbour contribution could be read directly from the NMR spectrum.

The predominating contributions of the nearest neighbours (nn) to H_N were observed in many intermetallic compounds: the six nn Gd atoms contribute to the hyperfine field at the non-magnetic sites $(78 \pm 5)\%$ in GdP (Myers and Narath 1973a) or up to 100% in $GdIr_2$, 92% in $GdPt_2$ and 85% in $GdAl_2$, whereas the four nn Gd atoms already contribute to H_N for the magnetic site 60% in $GdRh_2$, 56% in $GdIr_2$ and 80% in $GdPt_2$ (Dormann 1977).

The decision, as to which lanthanide neighbours are responsible for the dominant hyperfine field contributions observed, is not always unequivocal – at least if it is based on the concentration dependence of the line intensities in the zero-field spectra of powder samples, relying on statistical site occupation, and suffering from the errors in the determination of the relative intensities. A clear-cut assignment can be obtained through an analysis of the angular dependence of the NMR spectrum in an external magnetic field, performed with a single crystal. For example, from such investigations on paramagnetic $La_{1-x}Gd_xAg$ with a small Gd concentration ($x = 0.005$), it could be determined that the *third*-nearest Gd neighbour gives the *largest* contribution to the ^{139}La hyperfine field (Goebel and Dormann 1979). This neighbour was identified via the dipole part of the anisotropy of the hyperfine interaction – see fig. 6. (It is the neighbour along the [111] diagonal of the CsCl unit cell, along a La–Ag–Gd 'bond' direction.)

In general it is difficult to derive more than three distinct neighbour contributions by NMR line shape analysis in magnetically ordered compounds, without

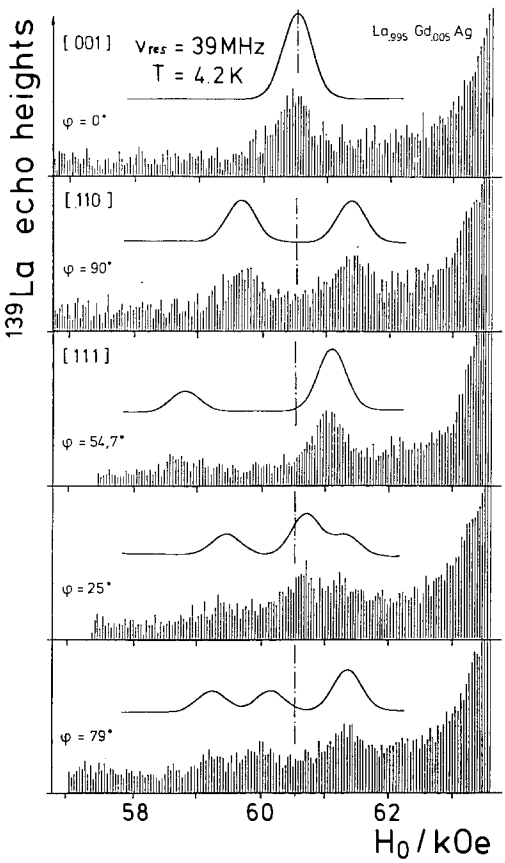

Fig. 6. ^{139}La echo heights plotted against external magnetic field for a single crystal of $La_{0.995}Gd_{0.005}Ag$ for different orientations (φ is the angle between H_0 and the [001] direction in the (110) rotation plane). For $\nu_{res} = 39$ MHz, $T = 4.2$ K the main ^{139}La line is at $H_0 = 64.4$ kOe; only that part of the spectrum is shown, where satellite 'A' is located. The solid lines show the calculated satellite splitting due to a Gd moment in the third nearest R shell. (Adapted from Goebel and Dormann 1979).

special 'a priori' assumptions for the distance dependence. The conditions are somewhat more favourable in paramagnetic compounds with a small concentration of magnetic moments. Three to four distinct neighbour contributions were derived for the Rh site in GdRh, the Zn site in GdZn and for the lanthanide sites of GdZn, LaAg, $GdIr_2$ and $GdRh_2$ by Dormann and Buschow (1976), Eckrich et al. (1976), Goebel et al. (1977) and Dormann et al. (1976, 1977a).

3.2.5. *Anisotropy of the transferred magnetic hyperfine interaction*

We mentioned in sect. 2.2 that the easy direction of the magnetization was derived for RAl_2 compounds by several authors with help of the ^{27}Al NMR line splittings, which are caused by the dipolar contribution H_{dip} to the hyperfine field at the crystallographically equivalent but magnetically inequivalent Al sites in the cubic Laves phase structure. The line splittings observed in the NMR powder spectra of the ferromagnetically ordered compounds were *larger*, however, than could be explained by the classical dipole field of the lanthanide magnetic moments – by about 13% in $GdAl_2$, but up to 40% in other RAl_2 compounds (Kaplan et al. 1973). This indicates the existence of anisotropic contributions to

the transferred hyperfine field H_N(Al). Such 'pseudodipolar' contributions have to be explained by the influence of polarized non-s-like electrons, e.g., p electrons at the aluminum site. Similar indications of pseudodipolar contributions were obtained from the analysis of the line splitting in Y- or La-diluted GdZn, for the ^{67}Zn NMR line that originates from Zn atoms surrounded by seven Gd and one La or Y ion, instead of, as originally, eight Gd nearest neighbours in the cubic CsCl structure. Here, as well, a 30% larger splitting than that corresponding to the classical dipole field was observed (Eckrich et al. 1976). These experiments give the additional information that the respective pseudodipolar contribution originates from the nearest neighbours.

A more clear-cut proof of anisotropic contributions to the transferred hyperfine fields was the detailed analysis of the angular dependence of the ^{27}Al NMR in a single-crystal sphere of $GdAl_2$ by Fekete et al. (1975). This investigation gave the unequivocal proof that the anisotropic contribution to the hyperfine field has the same anisotropy as the classical dipolar field, but that outside the error bar it is clearly larger than the classical point-dipole contribution. Barash et al. (1983) measured the NMR of ^{27}Al in a spherical single crystal of $DyAl_2$ in the *paramagnetic* state. The well split spectrum yielded a quadrupole frequency $\nu_Q = 561$ kHz and an isotropic hyperfine coupling constant $\alpha = -3.17$ kOe μ_B^{-1} – in agreement with the data in the ferromagnetic state. In this case, the anisotropy of the spectrum was 10% stronger than is predicted by the classical dipole contribution.

We have mentioned already, that – via the dipolar part of the anisotropy of the hyperfine interaction – with ^{139}La NMR in a paramagnetic single crystal of $La_{0.995}Gd_{0.005}Ag$ a third nearest Gd neighbour was identified as the one with the largest contribution to the hyperfine field (Goebel and Dormann 1979). Figure 6 shows the interesting part of the ^{139}La NMR spectra in comparison with the line profiles calculated by considering a dipolar form of the anisotropy:

$$\Delta H_{res} = \Delta H_{iso} + \Delta H_{ani}(3\cos^2\theta - 1)\,. \tag{15}$$

It is important to note that in this case of an unequivocal site assignment the line splitting (ΔH_{ani}) was *four* times larger than could be explained by a classical dipole interaction with the Gd moment of 7 μ_B. This is an especially clear proof for the presence of pseudodipolar or orbital contributions to the indirect interaction, even in intermetallic compounds containing only S-state lanthanide ions.

3.2.6. *Evidence for magnetically induced nuclear quadrupole interaction*

Further evidence for non-s, especially orbital contributions to the hyperfine interaction in magnetically ordered intermetallic compounds is obtained from a closer inspection of nuclear quadrupole interactions. For an electric field gradient (EFG) of axial symmetry $eq = V_{\zeta\zeta}$ caused, e.g., by the low-symmetry arrangement of ionic charges in the crystal lattice, the quadrupole interaction of the nuclear spin I with the quadrupole moment eQ (Barnes 1979, McCausland and Mackenzie

1980) is

$$\mathcal{H}_Q = \frac{3e^2qQ}{4I(2I-1)}\left[I_\zeta^2 - \tfrac{1}{3}I(I+1)\right] \tag{16a}$$

or

$$\mathcal{H}_Q = hP\left[I_\zeta^2 - \tfrac{1}{3}I(I+1)\right]. \tag{16b}$$

For the predominating magnetic dipole term in the hyperfine interaction and for half-integer spin $I > 1$, as usually encountered in magnetically ordered rare-earth intermetallic compounds, $2I-1$ quadrupole satellites of the main (Zeeman) resonance ($m_I = +\frac{1}{2} \leftrightarrow -\frac{1}{2}$) are observed with frequency separations of

$$\nu_Q = P(3\cos^2\theta - 1). \tag{16c}$$

Here θ is the angle between the axis of the EFG, ζ, and the direction z of the magnetic resonance field H_{res}, eq. (3d). In addition to the direct resolution of quadrupolar splitting or the resolution by double-resonance techniques introduced recently (Pieper et al. 1986), the technique of analysing the spin-echo modulation caused by the quadrupole interaction (in addition to multiple echoes), as introduced by Abe et al. (1966), was applied in particular. It allows one to derive the weak unresolved quadrupolar interaction in the presence of the larger magnetic hyperfine interaction. Shamir et al. (1971), Degani and Kaplan (1973) and later on many other groups applied this technique for the study of the ^{27}Al quadrupolar interaction in RAl_2. In addition to the well known lattice EFG at the axially symmetric site, Degani and Kaplan (1973) observed a contribution to the EFG that was linearly proportional to the magnetization. The strength of a possible magnon-induced pseudoquadrupole interaction in ordered systems was analyzed by Zevin and Kaplan (1975). Within the framework of the long-wavelength magnon approximation, they showed that this contribution is indeed linear in the magnetization and that it could account for the ^{27}Al results for $GdAl_2$. However, the explanation with the pseudoquadrupole effect is not yet without controversy. Gehring and Walker (1981) showed that this effect can be related to the difference between the transverse and longitudinal magnetic susceptibilities. They concluded – while agreeing for the linear magnetization dependence – from the model calculations that they performed for $GdAl_2$, that the pseudoquadrupole effect appears to be too small to be observed. Recently, Dumelow et al. (1988) reinvestigated the ^{27}Al quadrupolar interaction for $GdAl_2$ with the help of powder samples. They analysed signals from domains and walls and also used holmium substitution and external fields. They found that their results were incompatible with a significant magnetic contribution to the EFG at the Al sites *unless* such a contribution had its principal axis along the $\langle 111 \rangle$ axis of the lattice EFG at the Al site in both the domains and the domain walls, i.e., *independent* of the *direction* of the magnetization. Thus an orbital polarization of p-like conduction electrons at the Al site of the magnetically ordered compound might be at the origin of this puzzle.

The magnetically induced electric quadrupolar interaction was recently observed in several cubic, ferromagnetically ordered intermetallic compounds at the nucleus of the rare-earth S-state ions Gd^{3+} and Eu^{2+}, despite the fact that the nuclei are residing on nominally cubic lattice sites: e.g., nuclear quadrupole splittings ν_Q of 0.6–0.8 MHz were derived for ^{155}Gd and ^{157}Gd in $GdAl_2$, $GdIr_2$ and $GdRh_2$ or of 0.7 and 1.5 MHz for ^{153}Eu in $EuPd_2$ and $EuPt_2$, respectively, all at 4.2 K. Figure 3 showed an example ($I = \frac{3}{2}$); see Kropp et al. (1979a, 1983), Barash and Barak (1984), Dormann et al. (1984, 1986), Dormann and Dressel (1989), Dressel et al. (1988), and Dressel and Dormann (1988) for further details. For $GdAl_2$ and $EuPt_2$ the temperature dependence of ν_Q was measured and found to vary roughly as $[M_s(T)/M_s(0\,K)]^2$, as is expected for a magnetically induced EFG at a cubic site. In addition to the relativistic single-ion quadrupolar interaction that should always be observed in magnetically ordered Gd and Eu intermetallic compounds, the lattice contribution caused by the magnetostriction and an eventual contribution of orbitally polarized conduction electrons at the lanthanide site have been identified as the most important contributions to the EFG.

3.3. *Crystal-field effects and orbital contributions to the hyperfine interactions*

3.3.1. *Extensions of the RKKY framework*

In addition to the evidence from the analysis of the angular dependence of the transferred hyperfine interaction, which indicated that orbital contributions to the hyperfine interactions should be taken into account, further hints were obtained. If the contributions of the conduction electrons to the magnetic order and hyperfine field at the rare-earth site, as discussed in sect. 3.2.3, were considered for the whole lanthanide series, analyses based on the isotropic bilinear exchange interactions between 4f and conduction electrons have generally not been able to explain the systematic variation of these contributions across the lanthanide series satisfactorily. Therefore, several theoretical papers have studied the indirect exchange and hyperfine interactions in more detail. Indirect exchange via spin–orbit-coupled states was considered by Levy (1969), who found the resulting new terms in the interaction Hamiltonian necessary in order to fit the Curie point data on several series of intermetallic rare-earth compounds. Numerical results by Ray (1974) indicated that d electrons contribute predominantly to both the isotropic and anisotropic exchange. Belorizky et al. (1981) developed the model framework necessary to explain the variations within the lanthanide series by taking the full 4f-conduction electron exchange interaction (higher-rank coupling) and the crystallographic symmetry of the rare-earth site into account. They also included spin–orbit coupling of the conduction electrons. (As discussed before, the conduction electrons in the lanthanide intermetallic compounds of principle interest are primarily of 5d and 6s character.) They derived the expressions for the orbital and spin polarizations of these conduction electrons and for their contribution to the hyperfine field and the magnetization. The 'ab initio' calculations of indirect multipole interactions for DyZn by Schmitt and Levy (1984) are another example

of such improvements. These results underscored again the predominant effect of the d electrons in the conduction band: their orbital character is the origin of the strong tetragonal quadrupolar interactions observed in the rare-earth CsCl-type intermetallic compounds.

Recently, Orlov (1985, 1986) suggested a 'crystal potential model' for the interpretation of crystalline electric field effects in intermetallics and used it for a discussion of these effects in $PrAl_3$ or of the sign and magnitude of the magnetic crystal anisotropy for RX_5 and R_2X_{15} compounds. This effective crystal potential $V(r)$ has the crystal symmetry and is constructed from experimental data or calculated from first principles; it oscillates and decreases rapidly with distance.

Generally the agreement between experiment and calculation for each series of intermetallic compounds is improved decisively with the improved theoretical models at the cost, however, of an increased number of free parameters or a less convenient form of the relations.

3.3.2. *Crystal-field effects for lanthanides in paramagnetic compounds*

Pronounced crystal-field effects were observed in the paramagnetic phase NMR for intermetallic compounds of Ce, Pr, Sm or Tm. Crystal-field effects for Tm^{3+} in $TmAl_3$ have been analysed by de Wijn et al. (1970) by a combination of the temperature dependences of the ^{27}Al Knight shift and of the magnetic susceptibility. These authors also analysed the quadrupole interaction for the Al site in the cubic Cu_3Au structure. Comparing the experimental value $|e^2qQ/h| = 7.6$ MHz with the point-charge model value (Abragam 1961)

$$q = (1 - \gamma_\infty) \sum_i Z_i(3\cos^2\theta_i - 1)/r_i^3$$

(where the quantities have their usual meanings) they estimated charges of $+3e$ and $-e$ for the Tm and Al sites, respectively. Malik and Vijayaraghavan (1971b) considered the influence of the crystalline field on the Knight shift anomalies (crossover point) of ^{27}Al in $SmAl_2$ and ^{119}Sn in $SmSn_3$. These shift anomalies caused by the strong J-mixing for samarium, as well as other anomalies such as the axis of easy magnetization in $SmFe_2$, were reviewed by de Wijn et al. (1976). In several intermetallic compounds of rare-earth and pnictide nuclei, pressure effects on the Knight shifts have been measured up to 4 kbar as a function of temperature (4–300 K) by Weaver and Schirber (1976b). An attempt to separate the effects of crystal field and exchange was made. Even with the inclusion of exchange, the point-charge model was unable to account for the results in a straightforward manner, which was attributed to conduction electron effects. Follstaedt et al. (1977) showed that the nearest-neighbour satellite resonance shifts in LaP:Ce are not proportional to the Ce^{3+} susceptibility above $T = 26$ K (requiring an anisotropic exchange interaction for their interpretation).

3.3.3. *Crystal-field splitting, magnetic order and the hyperfine interaction*

In a pioneering investigation, the ^{27}Al NMR in ferromagnetic RAl_2 (R = Pr–Ho) has been studied by Kaplan et al. (1973) using powder samples. The easy

direction of magnetization has been observed as mentioned before and a calculation, in agreement with the observations, has been developed. The isotropic exchange parameters J_{4f-s} were determined and were observed to decrease in the lanthanide series by almost a factor of three.

For a general introduction to the field of NMR in magnetically ordered compounds with non-S state lanthanide ions, we refer the reader to Taylor (1971) or McCausland and Mackenzie (1980), where the interplay of the exchange and crystal-field interactions has been analysed. Generally, for cubic systems like RAl_2 at least a three-parameter mean-field model is adopted, based on a single-ion Hamiltonian comprising a crystal field of cubic symmetry [CEF parameters W, x; Barnes (1979)] and an isotropic molecular field constant (λ):

$$\mathcal{H} = \mathcal{H}_{\mathrm{CEF}}(W, x) + \mathcal{H}_{\mathrm{MF}}(\lambda) + \mathcal{H}_{Ze}(H_0)\,. \tag{17}$$

In addition to the magnetic dipole and electric quadrupole an octupolar contribution (w) of the hyperfine interaction at the lanthanide site has also to be considered. The transition freqeuncy is described by (McCausland and Mackenzie 1980)

$$\nu_{m_I, m_I-1} = a + (2m_I - 1)P + (3m_I^2 - 3m_I + 1)w\,. \tag{18a}$$

The nuclear quadrupole frequency parameter P contains second-order corrections $P^{(2)}$ to the first-order part,

$$P^{(1)} = \frac{\langle 3J_z^2 - J(J+1)\rangle}{J(2J-1)}\, P_0, \tag{18b}$$

(with the free-ion value P_0) that generally can not be neglected (Waind et al. 1983). Along these lines McMorrow et al. (1986) performed recently for the first time a complete analysis of the hyperfine interactions for ^{165}Ho in a *single crystal* of $H_{0.01}Gd_{0.99}Al_2$ with an applied external field ($H_0 \leqslant 80$ kOe).

In the past, there were several reports of lanthanide-site NMR for ferromagnetically ordered RAl_2, based on powder samples. Berthier et al. (1977) analysed the variation of the ^{163}Dy NMR with x in $Dy_{1-x}Y_xAl_2$. They observed satellite lines, which showed the modification of H_{4f} (after separation of the various contributions in eq. (13a)). This modification is caused by the variation of the molecular field, which influences the angular momentum ($\langle J_z \rangle$) of the ground state wavefunction, and hence the 4f moment. Berthier et al. (1978b) also analysed the conduction electron spin and orbital polarization effects in RAl_2 compounds with R = Nd, Dy, Tb and Er. The hyperfine fields were separated into their various components [eq. (13a)]. They deduced the variation of the self-polarization field H_S with the lanthanide element. The observed behaviour indicated a strong dependence on the lanthanide *orbital* moment and was accounted for by including both the spin and the orbital polarizations of the conduction bands. From a comparison with the transferred hyperfine field at the Al nuclei, they concluded that the large orbital polarization did not extend to these sites. Magnetic hyperfine and electric quadrupole interactions were analysed

for ^{159}Tb and ^{167}Er in $R_{1-x}Gd_xAl_2$ by Berthier and Devine (1980b). They found that the effective molecular field, seen by the lanthanide ions, varies in these compounds less than predicted from a simple scaling according to the Curie temperatures. The required change of the orbital polarization of the conduction band was correlated with a modification of the band structure. The hyperfine parameters of holmium in RAl_2 (at 1.4 K) have shown to be strongly anisotropic; Waind et al. (1983) in their analysis of ^{165}Ho NMR in pseudobinary compounds, could also reproduce the observed directions of the spontaneous magnetization. An extensive analysis of ^{165}Ho NMR in $HoAl_2$, in which the exchange and crystal-field parameters were optimized together, was performed by Prakash et al. (1984), giving detailed information about the crystal-field ground state.

Summarizing the development of the different NMR investigations, it seems that orbital contributions of the conduction electrons are existing, but were probably overestimated in earlier work. A reasonable derivation of the exchange and crystal-field parameters can only be achieved if the magnetic dipole hyperfine interaction at the lanthanide site – giving access to $\langle J_z \rangle$ – *and* the electric quadrupolar contributions – indicating $\langle J_z^2 \rangle$ – are analysed together (as well as the conduction electron and neighbour ion contributions to H_{hf} and P).

3.3.4. *The quadrupolar interactions for lanthanide nuclei*

Devine and Berthier (1981) used NMR measurements of the quadrupolar splitting at the lanthanide sites in RAl_2-, RFe_2- and RZn-ordered compounds and determined the value of $\langle J_z \rangle$ for the 4f electrons. Extended discussions of this technique were presented by Berthier and Belorizky (1984), Belorizky et al. (1984), and Belorizky and Berthier (1985). They considered both the possibilities and the difficulties (e.g., possible errors in $P^{(2)}$) in the determination of the 4f-shell magnetic moments in cubic lanthanide intermetallic compounds by performing a zero-field NMR quadrupolar hyperfine splitting analysis and compared these with the other, more standard techniques like magnetization measurements, polarized neutron diffraction, elastic and inelastic neutron spectroscopy. Since the 4f electronic moment can be obtained directly via zero-field NMR, with good accuracy, this procedure allows a much easier separation of the magnetic effects arising from localized 4f electrons of the lanthanide ion from those arising from the conduction electrons or other atoms.

3.3.5. *Analysis of the self-polarization field*

Earlier, Belorizky et al. (1979) analysed the contributions to the self-polarization field H_S from orbital, magnetic dipole-dipole, contact or core polarization with group symmetry arguments in order to determine the independent parameters of the problem for cubic compounds. The recent progress in the accuracy of the determination of the 4f part of the hyperfine field in cubic intermetallic compounds, H_{4f} [eq. (13a)], by using NMR quadrupolar splitting results, has enabled a more accurate determination of the self-polarization field H_S (Berthier and Belorizky 1986, Belorizky and Berthier 1986). It was shown by these two authors that, for the cubic ferromagnetic RAl_2 and RZn series, H_S increases

roughly proportional to $\langle S_z \rangle$, the total 4f *spin* of the lanthanide ion

$$H_S = \alpha_s \langle S_z \rangle + \alpha_L \langle L_z \rangle, \tag{19}$$

with $\alpha_s = 51.7$ kOe and 15.7 kOe for RAl_2 and RZn, respectively, and $\alpha_L = 4 \pm 8$ kOe or 12 ± 19 kOe for RAl_2 or RZn, respectively. The orbital effects in the RAl_2 series are present, but relatively weak – at most 30% of the spin-polarization field. Orbital effects are more important in the RZn series (for ErZn they are three times larger than the spin-polarization part). For the RAl_2 series Berthier and Belorizky (1986) obtained estimates for the local orbital, spin and quadrupolar polarization of 5d-like conduction electrons: $\langle l_z \rangle_d \leq 0.06$, $\langle s_z \rangle_d \leq 0.09$ and $\langle l_z^2 - 2 \rangle_d \leq 0.05$.

4. Intermetallic compounds with 3d transition metals

An enormous number of NMR investigations were devoted to the different intermetallic compounds between rare-earth elements and 3d transition metals. This can be judged by the length of the tables B10–B12 in the appendix, collecting NMR work done with ^{55}Mn, ^{57}Fe and ^{59}Co as nuclear probes. The study of the local field at the non-magnetic rare-earth ions Sc, Y or La in such intermetallic compounds was a widely used method for examining the electronic structure. In addition, many of these compounds are of great technological importance. Others are useful model systems, showing a variety of magnetic behaviours for a relatively simple crystal structure. Thus cubic Laves phase compounds RX_2 have received considerable attention in recent years. Here, weak unenhanced paramagnetism for YNi_2, exchange-enhanced Pauli paramagnetism for YCo_2, ferromagnetism for $GdNi_2$, collinear ferrimagnetism for $GdCo_2$ or $GdFe_2$ as well as complicated magnetic behaviour in RMn_2 can be observed. Several authors used NMR for the study of the electronic structure of these compounds. Also, examples are found in the R-3d series, where the formation of a local moment on a transition metal depends critically on the number and kind of nearest neighbours, as considered in the earlier model of Jaccarino and Walker (1965).

However, this is also an area of NMR applications that was rather controversial in the past, with a number of mistakes and changes in interpretation. Indeed, frequently there are several inequivalent lattice sites in such compounds and the assignment of NMR lines to these sites is non-trivial. Future single-crystal NMR work still has a wide field for application! Sometimes, a calculation of the line shifts or line splittings due to the contribution of the classical dipole field was combined with previous knowledge of the easy direction of the magnetization to achieve the site assignment; or the crystal field at the respective Co sites was calculated with the point-charge model in order to exploit the influence of the Co site anisotropy for the assignment. Other standard techniques to help with the assignments, such as the investigation of pseudobinaries, turned out to be unreliable, because changes in the easy direction or non-statistical site occupation

were occasionally found. Such phenomena can be very helpful, if they are understood once, but they require very careful investigations, which were not always performed. Large anisotropies for the hyperfine interaction, especially for Co, and partially different moments of the same 3d element at different sites are well known complications. On the whole, it is an important, fascinating, but a difficult area for NMR applications.

4.1. *Intermetallic R–Fe compounds*

Rare-earth intermetallic compounds with iron are analysed more easily by NMR than those with cobalt or manganese, because the Fe moment is less sensitive to the environment. Thus many NMR studies were reported despite the disadvantageous NMR properties of the favourite Mössbauer nucleus ^{57}Fe (small natural abundance, small nuclear magnetic moment). ^{89}Y was the favourite 'non-magnetic' rare-earth NMR probe.

A large positive hyperfine field is transferred from the iron sublattice to the lanthanide site for heavy lanthanide ions, as can be seen from the comparison of the lanthanide hyperfine fields in RFe_2 and RAl_2: $H_{N,Fe} \approx +620$ kOe for R = Gd (Budnick and Skalski 1967). A much weaker difference is observed between $GdFe_2$ and YFe_2. Al-Assadi et al. (1984) estimated that at most one third of the difference in the hyperfine fields of about 124–138 kOe is due to a direct transferred hyperfine field from the Gd ions. They investigated the ^{165}Ho NMR in $Gd_xY_{0.97-x}Ho_{0.03}Fe_2$ and analysed their results in terms of a model involving a *non-linear* dependence of the transferred hyperfine field from iron atoms on the number of Gd neighbours. Nikitin et al. (1976) showed via the NMR of $Gd_{1-x}Y_xFe_3$ that the contribution of the Gd sublattice to the hyperfine fields at the Y_{II} and Gd_{II} nuclei is 26 and 75 kOe, respectively. They observed resolved satellites for Y and Gd, and derived that the hyperfine interaction of the Gd nuclei with the nearest neighbours in the Gd sublattice is anisotropic. Vasil'kovskii et al. (1983) introduced a model for Y–Fe compounds based on NMR analysis of Y hyperfine fields, where the superposition of a 'collectivized' and a 'localized' component of the moment is assumed in order to explain the observed distribution of local fields at the Y nuclei. Later on, they extended their analysis; Vasil'kovskii et al. (1988) compared the hyperfine fields for Y in a large number of Y–Fe and Y–Co intermetallic compounds. They concluded that the local fields, induced by 3d sublattice atoms, depend on the type of the 3d atom, but are almost independent of its magnetic moment and the stoichiometry of the compound. Their results were again explained with the assumption that there is a system of spin-polarized, 'collectivized' electrons, whose spin polarization (which is alligned *anti*parallel to the 3d sublattice magnetization) determines the field at the rare-earth nuclei and contributes to the moment of the 3d atoms, but that there is also another localized contribution of the spin density that does not act at the Y nucleus. Instead, Dumelow et al. (1986) concluded from their NMR pressure analysis of YFe_2 that a *moment*, antiparallel to the Fe moment (of about $-0.45\ \mu_B$) exists in YFe_2 at the Y site.

The influence of the lanthanide moments on the iron sublattice is in general relatively weak. The Fe moment increases from YFe_2 to $GdFe_2$ only by a small amount. It is generally agreed that the Gd and Fe moments in the magnetically ordered phase of $GdFe_2$ or $Gd_{1-x}Y_xFe_2$ compounds are antiparallel to one another. Nitikin et al. (1975a) explained the existence of three lines for ^{57}Fe in $GdFe_3$ by the difference between the magnetic moments of the Fe atoms in different crystallographic positions. For $Gd_{1-x}Y_xFe_3$, Nikitin et al. (1976) considered that the magnetic moments of the iron atoms, varying with the crystallographic site, depend on the exchange interaction between the rare-earth and iron sublattices.

In a detailed and comprehensive analysis, Meyer et al. (1981) concluded from a number of different investigations in $PrFe_2$, $NdFe_2$ and $YbFe_2$ that the crystalline electric field at the lanthanides is not constant throughout the RFe_2 series. For the isotropic as well as the anisotropic parts of the Fe hyperfine field, in addition to intrinsic d contributions, contributions originating from the lanthanides could also be derived. Due to the self-polarization field and the field transferred from Fe, the hyperfine field for the lanthanide nucleus is larger than the free-ion value for the second half, but smaller for the first half of the series. Belorizky et al. (1988) analysed the dependence of the R–R exchange interactions on the nature of the R atom in many intermetallics, including R-3d compounds such as $R_2Fe_{14}B$ or RCo_2. They concluded that the molecular field coefficient describing the exchange interactions between lanthanide spin moments decreases in a given series by almost an order of magnitude from compounds with a light lanthanide to those with heavy lanthanide elements. Simultaneously a decrease is observed in the transferred hyperfine field at the non-magnetic sites. They showed that this behaviour can be coherently understood by considering that both the R–R and R–X indirect exchange interactions in lanthanide intermetallics occur via 5d conduction electrons and that the dominant 4f–5d exchange at lanthanide sites decreases from Pr to Tm by a factor of three.

Resolved *satellites* of the NMR lines originating from the rare-earth nuclei could generally be observed for intermetallic compounds if iron was replaced partially by other 3d or non-magnetic elements. Very well resolved satellite structures of the ^{89}Y resonance have been reported by Oppelt and Buschow (1976) for $Y(Fe_{1-x}X_x)_2$ with X = Al, Co, Pt. They concluded that the Y hyperfine field is mainly determined by the interactions with the nearest magnetic neighbour atoms. They analysed the transferred hyperfine fields obtained for various values of x and determined the change of the magnetic moments of the 3d atoms with composition in $Y(Fe_{1-x}Co_x)_2$. They obtained indications of partial delocalization of the magnetic moments with increasing x. Later on, Oppelt et al. (1977) extended their analysis also to intermetallic compounds with other non-magnetic rare-earth atoms. Yamada and Ohmae (1980) investigated ^{59}Co and ^{89}Y NMR of $Y(Fe_{1-x}Co_x)_2$ over the whole concentration range x. They concluded that on the Fe-rich side, the Co moment first decreases slightly ($x \leqslant 0.3$) and then rapidly with increasing Co content. Furthermore, Ichinose et al. (1985) observed well resolved Y satellites, when they followed the ^{89}Y and ^{27}Al hyperfine fields in

$Y(Fe_{1-x}Al_x)_2$ in zero-field spectra with the composition x. They showed that the concentration dependences of both hyperfine fields resemble those of the mean magnetic moment of the Fe atoms, in accordance with the behaviour of fairly well localized moments of the Fe atoms. Satellites of the Y and Gd NMR lines were observed also by Vasil'kovskii et al. (1988) for $Y(Fe_{1-x}X_x)_2$ and $Gd(Fe_{1-x}X_x)_2$ with X = Al and Co. They could be extrapolated to give the hyperfine contributions from Fe and Co atoms to the local fields at the Y and Gd nuclei for various compositions. However, they concluded from the pressure dependence of the ^{89}Y hyperfine field in $Y(Fe_{0.95}Co_{0.05})_2$ that the variation of the Y hyperfine field with Co content, extrapolated from such a variation, might actually be caused by the variation of the interatomic distance.

In conclusion, even for the relatively 'simple' case of the R–Fe intermetallic compounds, a final conclusive picture of the electronic structures and hyperfine interactions for these compounds is in general not yet established. However, NMR has given many clear pieces of evidence for a better understanding.

4.2. *Intermetallic R–Co compounds*

The results in this area of NMR applications do not always agree very well – experimentally as well as with respect to the interpretation. Generally the cobalt hyperfine field in R–Co intermetallic compounds is anisotropic, and on some occasions even positive, both of which are indications of the presence of an orbital moment of Co. Due to its simplicity, the Laves phase structure is most appropriate for an analysis: there is only one R site; the Co sites – up to four magnetically inequivalent, but crystallographically equivalent sites – can be distinguished, because there is an electric quadrupolar interaction in addition to the magnetic hyperfine interaction, with the EFG axis lying along the local $\langle 111 \rangle$ axes (Figiel and Jaszczewski 1980). Many results of NMR investigations of the R–Co series of intermetallic compounds were discussed by Figiel (1983) (in Polish). If R is a lanthanide element with a 4f moment, the 3d moment of Co is polarized below a certain temperature by a molecular field through (indirect) 4f–3d exchange interactions. The direction of the polarization is always antiparallel to that of the 4f spin. This leads to parallel coupling between 4f and 3d moments in RCo_2 for light lanthanides and an antiparallel coupling for the heavy lanthanides.

Taylor and Christopher (1969) investigated for the first time the Co hyperfine fields in ferrimagnetically ordered $GdCo_2$ and related compounds. They analysed the Co hyperfine field as a superposition of a contribution of the Co ion's 'own' moment and the Co- and R-neighbour contributions,

$$H_{\mathrm{hf,Co}} = H_{\mathrm{own,Co}} + H_{\mathrm{N,Co}} + H_{\mathrm{N,R}}. \tag{20a}$$

For more detailed investigations $H_{\mathrm{own,Co}}$ was later generally decomposed into

$$H_{\mathrm{own,Co}} = H_{\mathrm{cp}} + H_{\mathrm{4s,Co}} + H_{\mathrm{orb}}. \tag{20b}$$

The classical dipole field and the Lorentz field also have to be included. Hirosawa and Nakamura (1982a) performed a careful and detailed analysis of the Co

hyperfine interaction in RCo_2. They observed that the quadrupolar interaction frequency ν_Q in the magnetically ordered state is always larger than in the respective paramagnetic compounds (e.g., Barnes and Lecander 1967). Hirosawa and Nakamura (1982a) used also $Tb_{1-x}Y_xCo_2$ for the derivation of the R contribution to the Co hyperfine field and observed well resolved satellites. They indicate the primary importance of the nearest-neighbour interaction between Tb and Co. It is especially gratifying that in this investigation for *both* magnetically inequivalent sites (magnetization direction $\langle 111 \rangle$: $\theta = 0°$ and 70.5° sites) the NMR lines corresponding to Co with six Tb, and with five Tb one Y are resolved. The hyperfine coupling constant for the total spin part of the Co hyperfine field was determined to be $\alpha_s \approx -130\,\text{kOe}\,\mu_B^{-1}$ (spin), whereas $\alpha_L = +650\,\text{kOe}\,\mu_B^{-1}$ (orb) was obtained for the orbital part coupling constant. The isotropic orbital part of the Co moment varies between 3% of the total Co moment in $GdCo_2$ and 26% in $PrCo_2$. The anisotropic contribution is large and reaches up to 26% for $SmCo_2$. Since different signs of the ^{59}Co NMR line shifts for the magnetically inequivalent sites were observed in external fields in magnetically ordered RCo_2 by Hirosawa and Nakamura (1982a), they had clear evidence that the resonance field at Co should be extremely anisotropic. Yoshie (1978) studied the variation of the ^{59}Co NMR in $Y_{1-x}Gd_xCo_2$ for $0.1 \leqslant x \leqslant 1$. The shift by 16.8 ± 4.0 kOe observed in this range was interpreted as the contribution of 4f electrons to the cobalt hyperfine field in $GdCo_2$. Yoshimura et al. (1984a) investigated the local-environment effects in the $R_{1-x}Y_xCo_2$ system. In $Dy_{1-x}Y_xCo_2$, the magnetic moment of Co and the hyperfine field distribution of the Co nuclei have been synthesized by superposition of the contributions from the Co atoms with the various R nearest-neighbour configurations. The dipole field due to the lanthanide ions in the nearest-neighbour shell turned out to play an important role in analysing the Co NMR spectra. They concluded that the nearest-neighbour interaction between R and Co is of prime importance in the RCo_2 series. The most pronounced dependence of the Co moment on the number of R nearest-neighbour ions has been observed for large Y concentrations.

Cannon et al. (1975) used the Jaccarino–Walker model for the transition–metal moment in some cubic Laves phase compounds. Specifically, they showed that in the $Gd(Co_{1-x}Ni_x)_2$ system the Co moment appears to be critically dependent on the number and type of its nearest neighbours. Ichinose (1987) measured the NMR of ^{27}Al, ^{55}Mn, ^{59}Co and $^{155/157}$Gd in $Gd(X_{1-x}Co_x)_2$ for X = Al, Mn, Fe and Ni. He found from the analysis of the NMR spectra that the concentration dependence of the ^{59}Co hyperfine field is proportional to the sum of the conduction electron polarization arising from nearest-neighbour transition atoms and that the Co atoms carry a magnetic moment induced by the neighbouring X atoms.

For ^{59}Co in $(Gd_{1-x}Y_x)Co_2$, Hirosawa et al. (1979) observed the coexistence of two types of Co atoms in the concentration range close to the critical concentration ($x \approx 0.10$): one has a magnetic moment that couples antiparallel with the Gd moment, and the other has no moment. Yamada and Ohmae (1980) also showed by NMR analysis of $Y(Fe_{1-x}Co_x)_2$ the coexistence of magnetic and

non-magnetic Co, by observation of ^{59}Co NMR both in zero and external fields at the critical concentration for the destruction of ferromagnetism. The Co moment was assumed to be induced by magnetic Fe among its near neighbours. YCo_2 and $LuCo_2$ are exchange-enhanced Pauli paramagnets. The Knight shift of ^{59}Co in YCo_2 is temperature dependent (Hirosawa et al. 1979), as is the magnetic susceptibility. The correlation of both quantities gave the hyperfine coupling constant $\alpha = -89\,\text{kOe}\,\mu_B^{-1}$ associated with the Co magnetization. Its size indicated an important role of the orbital moment on the magnetism of YCo_2 (Hirosawa and Nakamura 1982a). The orbital magnetism in the paramagnetic phase was further analysed with the help of ^{59}Co Knight shift measurements: the anisotropy of the ^{59}Co Knight shift in YCo_2 at 4.2 K was measured by Hirosawa and Nakamura (1982c); $K_{\parallel} = 2.1 \pm 0.2\%$ and $K_{\perp} = 1.36 \pm 0.015\%$. Their analysis of the temperature dependence of the ^{59}Co Knight shift required the consideration of many, partially compensating contributions, as the analysis of the hyperfine field in the ordered state does. By analysis of the temperature dependence of T_1 for YCo_2, Yoshimura et al. (1984b) showed that the spin fluctuations with small wave number q play an important role in determining the magnetic properties of the 'nearly ferromagnetic' compound YCo_2. The necessary condition $T_1^{-1} \sim T\chi_d$ was fulfilled with reasonable accuracy. They concluded that $\chi(q)$ is enhanced only in the small-q region. Nagai et al. (1988b) analysed the Knight shift and the spin–lattice relaxation time of ^{59}Co in $Y(Ni_{1-x}Co_x)_2$; they observed x-dependent changes that could be explained by the change in the density of states, which is dominated by Y contributions for low Co content and by the unenhanced and exchange-enhanced Pauli paramagnetism for higher Co concentration. Yoshie et al. (1985a) also observed ^{59}Co in $YCo_{3-x}Ni_x$, for $x \geq 0.65$, whose field dependence indicated a nearly paramagnetic state of Co.

Streever (1979) used NMR results (i.e., the large anisotropy $H_{\parallel} - H_{\perp}$ for ^{59}Co) to evaluate the spin–orbit contribution to the magnetic anisotropy of Co atoms at *individual* Co sites in RCo_5 compounds. The easy c-axis Co anisotropy of RCo_5 compounds has been found to arise from the 2c sites, while the 3g sites make a smaller opposing contribution. The anisotropy parameters of the individual sites have been used to calculate the variation of the anisotropy with composition in mixed $R(Co_{1-x}Fe_x)_5$ compounds (and also in some related structures, e.g., R_2Co_{17}). Yoshie et al. (1988a, b) analysed the ^{59}Co NMR of RCo_5 in the presence of an applied external field. They used the fact that Ni enters preferentially on 2c sites in $R(Co_{1-x}Ni_x)_5$ for the site assignment (Yoshie et al. 1987). From the NMR study of YCo_5 they found that the Co hyperfine field at the Co 2c site has a *positive* sign (+15 kOe) on contrast to the negative sign (−92 kOe) at the 3g site. This result suggested that the cobalt atoms at the 2c site in YCo_5 have large orbital moments.

Streever (1975a) was the first to analyse NMR of R_2Co_{17} compounds. By considering the number of local Co and Nd atoms around a Co site in Nd_2Co_{17}, he showed which ^{59}Co NMR lines corresponded to the four different Co sites. Inomata (1976a) redetermined the effective Co hyperfine coupling constants for own and neighbouring moments. Inomata (1981) found that in $Y_2(Co_{1-x}X_x)_{17}$ Cu

substitution for Co was at random, while Al mainly prefers 6c dumbbell sites – which explains changes in the anisotropy. Calculating the crystal field in YCo_5 and Y_2Co_{17} with the point charge model, he estimated the contribution of Y or Co on the Co-site magnetic anisotropy. Kawakami (1981) derived the anisotropy of the ^{59}Co hyperfine field for $Gd_2(Co_{1-x}Fe_x)_{17}$: $H_{\parallel} - H_{\perp} = +31$ kOe for 18h sites, +30 kOe for 9d sites and −20 kOe for 18f sites. Since a preferential substitution of Co by Fe was observed, these results had to be correlated with the composition dependence of the magnetic anisotropy. Figiel (1982a) analysed the anisotropy of $R_2(CO_{1-x}Mn_x)_{17}$ compounds. The corresponding changes of the local anisotropy energy and the orbital part of the Co magnetic moment for each of the Co structural sites were calculated and discussed. He concluded that only two of the four Co sites in the R_2Co_{17} structure play a dominant role in determining the anisotropy energy of the compound. Kakol and Figiel (1986) used the single-ion anisotropy model (point-charge- crystal-field calculations with shielding effects of band electrons) also to interpret their data of $Y_2(Co_{1-x}Mn_x)_{17}$ and $Gd_2(Co_{1-x}Mn_x)_{17}$ pseudobinaries.

4.3. *Intermetallic R–Mn compounds*

Intermetallic R–Mn compounds were recently rather actively studied with the help of NMR. They show interesting, occasionally puzzling, magnetic behaviour. NMR turned out to be a useful probe for these investigations. A large part of the activities was devoted to YMn_2 and related pseudobinary compounds. YMn_2 has a first-order phase transition at about $T_N = 110$ K from a high-temperature paramagnetic state with small susceptibility (χ increases with T for $T > T_N$ indicative of itinerant electron character) to a low-temperature antiferromagnetic state with an Mn moment of about 2.7 μ_B.

Different Y–Mn intermetallic compounds were analysed with ^{55}Mn NMR by Yoshimura and Nakamura (1983). They concluded that YMn_2 is an antiferromagnet with a [111] easy direction of magnetization and $T_N \approx 100$ K. A hyperfine coupling constant of $|\alpha| \approx 42.7$ kOe μ_B^{-1} was derived from YMn_2, the same as for YMn_{12}, a compound that also behaved as an itinerant electron antiferromagnet ($T_N = 120$ K). Complex ferrimagnetic behaviour was observed for Y_6Mn_{23}. Nagai et al. (1983) analysed the complicated ^{89}Y satellite structures in $Y(Fe_{1-x}Mn_x)_2$ by spin-echo NMR and concluded that two kinds of Mn should occur at low x, one with a moment of 0.5 μ_B antiparallel to the Fe moment and one with a moment of 2.7 μ_B parallel to the Fe moment. Yoshimura et al. (1986b) reported that the NMR results for $Y(Mn_{1-x}X_x)_2$ can be described by the localized-moment model for X = Al, both in the paramagnetic and the ordered states. For X = Fe and Co, the Mn moment becomes much smaller as x increases and the results of NMR suggest that these alloys are weakly itinerant antiferromagnets. The different behaviour of the Mn moment could be related to the atomic spacing of Mn in these systems. Nakamura et al. (1988f) studied the influence of chemical pressure on the magnetism of YMn_2 via substitution of R = Sc or La in $Y_{1-x}R_xMn_2$. Substitution of Sc for Y leads to a shrinkage of the lattice, makes the Mn moment

unstable and stabilizes the paramagnetic state down to the lowest temperature; instead, La with the larger atomic volume stabilizes the Mn magnetic moment.

The ^{55}Mn NMR spectra of the light RMn_2 compounds $PrMn_2$, $NdMn_2$ and $SmMn_2$ show quadrupole splitting (Yoshimura and Nakamura 1984) and their field dependence indicates the antiferromagnetism of these compounds. Several NMR investigations have shown the crucial role of the interatomic distances for the Mn magnetism in RMn_2 compounds. For example, the Mn hyperfine field obtained by NMR measurements on RMn_2 and $R_{1-x}R'_xMn_2$ by Shimizu (1985a) increases rapidly as the lattice constant increases from 7.62 Å to 7.64Å, indicating a strong influence of the lattice constant on Mn ordering. Shimizu (1985b) also analysed the Tb hyperfine field in $Tb_{1-x}R_xMn_2$ for R = Gd or Lu and in comparison with $GdMn_2$, using the decomposition

$$H_{hf}(Tb) = H_{4f} + H_S + H_{N,R} + H_{N,Mn} .$$

For $GdMn_2$, he derived a negative value for H_S, whereas a positive value was obtained for $TbMn_2$. This was taken as evidence for the contribution of the parent orbital moment to H_S. From the analysis of ^{55}Mn NMR in RMn_2 Yoshimura et al. (1986a) concluded that one of the most important factors for the onset of the Mn moment in YMn_2 would be interatomic spacing of Mn in the C14 and C15 structures. After decomposition of the total Mn resonance field into its different contributions, they analysed the contribution of the Mn atom to the hyperfine field, which is proportional to the Mn moment, versus the lattice constant. A large lattice constant ($a \geq 7.5$ Å) – which is the case for R = Y, Pr, Nd, Sm, Gd, Tb – stabilizes the Mn moment, whereas a small atomic spacing (R = Dy, Ho, Er and Tm) makes the Mn moment unstable (R = Dy is a borderline case). Wada et al. (1987) discussed the stability of Mn moments and spin fluctuations in RMn_2 on the basis of the results of thermal expansion and NMR measurements. Again it has been shown that the interatomic distance plays a crucial role in determining the Mn magnetism in RMn_2.

5. Intermetallic compounds with special properties

5.1. *Van Vleck paramagnets*

As was discussed by Andres and Bucher (1968), the intermetallic compounds with rare-earth ions in the singlet ground state, such as praseodymium (^{141}Pr), turned out to be rather suitable for the production of very low temperatures by means of nuclear adiabatic demagnetization. Since the pioneering studies of Jones (1967, 1969) on the Pr and Tm intermetallic compounds, it has been known that the (effective) resonance field at the nucleus of these van Vleck paramagnets may be several times the applied magnetic field H_0. All the main points of interest for cooling applications, i.e., the interaction of the lanthanide nuclei with the magnetizing field, the static nucleus–nucleus interactions and the static and

dynamic nucleus–electron interactions can be studied with the help of NMR (Kaplan et al. 1980).

Mostly, the low-temperature lanthanide 'Knight' shifts could only be measured. Weaver and Schirber (1976a) (see Schirber and Weaver 1979) analysed the pressure dependences $\partial(\ln K)/\partial p$ and the temperature dependences of the NMR shifts in compounds such as PrP, PrAs or TmP (and others) with the NMR of ^{141}Pr, ^{169}Tm and the nuclei of the non-magnetic partners! From the temperature dependence, one can – at least in principle – distinguish between crystal-field and exchange effects. The ^{141}Pr NMR study of Kaplan et al. (1980) on a $PrNi_5$ single crystal gave an upper limit of the zero-field quadrupolar-like nucleus–electron interaction and provided accurate values of the magnetic field enhancement factors as a function of the crystal orientation and of the temperature. Satoh et al. (1981) measured the ^{141}Pr NMR in the singlet ground state system $Pr_{1-x}La_xIn_3$ and analysed the field dependence of the resonance frequency and the composition dependences of the nuclear spin–spin and spin–lattice relaxations. The nuclear relaxation rate $1/T_1$ has been studied theoretically in substances with a singlet ground state such as $PrNi_5$ by Ishii (1988). He showed that $1/T_1$ deviates from the Korringa law with decreasing temperature and vanishes at the nuclear ordering temperature.

5.2. *Itinerant-electron ferromagnets*

Already two decades ago, the effect of localized lanthanide magnetic moments on the conduction electron ferromagnet $ZrZn_2$ was analysed by Asanuma and Yamadaya (1968) with ^{91}Zr NMR in $Zr_{1-x}Gd_xZn_2$ ($x \leq 0.015$), using a $K \leftrightarrow \chi$ analysis. The value obtained for α, i.e., $\alpha \approx -38\,\text{kOe}\,\mu_B^{-1}$, was small and essentially independent of the Gd concentration. Moriya (1977) explained how the spin fluctuations of itinerant-electron magnets can be studied with the help of NMR spin relaxation. Sc_3In is a weak band-magnet that orders ferromagnetically with $T_c \approx 6\,\text{K}$ and $\mu_{Sc} \approx 0.07\,\mu_B$. NMR and T_1 for ^{45}Sc in the itinerant-electron ferromagnet Sc_3In was studied in both the ferromagnetic and paramagnetic states by Hioki and Masuda (1977). The correlation of $K(T)$ and $\chi(T)$ gave a hyperfine coupling constant of $\alpha = +58.4\,\text{kOe}\,\mu_B^{-1}$ per Sc atom. This was interpreted as an indication of strong 3d admixture in the wavefunction at the Fermi surface and of the d-spin contribution to the susceptibility. Yoshimura et al. (1988) analysed the nuclear spin–lattice relaxation rates, $1/T_1$, of various kinds of metallic magnets, and $1/T_1$ was found to be independent of temperature. They ascertained that the values of $1/T_1$ in the weak itinerant ferromagnets like $Y(Co–Al)_2$ were explained by the self-consistent renormalization theory taking into account spin fluctuations only around $q = 0$.

5.3. *Hydrogen in intermetallic compounds*

Hydrogen in rare-earth intermetallics has been an area of minor NMR activity in the last decade, compared with the period covered by Barnes (1979) in chapter

18 of this Handbook. However, several interesting recent investigations are mentioned in the tables of the appendix, e.g., for the NMR probes ^{139}La (A3), ^{159}Tb (A9), ^{167}Er (A12), ^{1}H, ^{2}H (B1) and ^{59}Co (B12), where the letters and numbers in parentheses refer to the table numbers.

5.4. *'Conventional' superconductors*

Frequently, NMR has been applied for the study of 'simple' superconducting intermetallic compounds. We refer to the review of MacLaughlin (1976) for a general introduction. Occasionally, NMR has also been applied to tackle more complicated systems, like heavy-fermion superconductors (sect. 5.5.1) or systems, where the eventual coexistence between magnetism and superconductivity was of interest (sect. 5.4.1). NMR has made important contributions to a better understanding of the high-T_c oxide compounds, as well. The latter, growing, field of activity has to be covered in a future volume of this Handbook.

Nuclear spin–lattice relaxation ($1/T_1$) has frequently been used to study the nature of the superconducting state, because it gives information about low-energy excitations (and the so-called coherence factor). Zero-field NQR is generally more reliable for investigations of superconductors, since only the rf field, and not the static magnetic field as well, must penetrate the sample. If due care is taken in the analysis, the rf penetration need not even be homogeneous. T_1, T_2 (T_2^*) and the spectrum can be used as information sources. The necessary requirement is, however, that a nucleus with $I > \frac{1}{2}$ and a reasonable quadrupole moment resides in the intermetallic compound on a site with a symmetry lower than cubic, resulting in a large enough NQR frequency ν_Q. ^{27}Al, ^{63}Cu and ^{139}La turned out to be useful NQR probes. If spin–lattice relaxation times are long enough, field-cycling NMR experiments are also appropriate for the analysis of superconductors. Relaxation experiments are less susceptible to experimental problems than Knight shift measurements, which require the application of an external magnetic field, which is in conflict with superconductivity. At least the accuracy suffers severely under the influence of the internal-field distribution in the field range $H_{c1} \ll H_0 < H_{c2}$ in type-II superconductors.

Several authors have analysed the influence of paramagnetic impurities on the relaxational behaviour of conventional superconductors. MacLaughlin et al. (1973) analysed zero-field nuclear spin–lattice relaxation rates in superconducting magnetic pseudobinary compounds $(LaGd)Al_2$ in terms of direct impurity and conduction electron contributions. The temperature dependence of the Korringa rate exhibited the effect of impurity pair breaking near the superconducting transition. MacLaughlin et al. (1976) found that the ^{139}La spin–lattice relaxation times in $La_{1-x}Ce_xAl_2$ agree with the theory based on weak exchange coupling between conduction electrons and paramagnetic impurities. Matsui and Masuda (1977) studied the ^{27}Al relaxation in $(La(Gd, Ce))_3Al$, both in the normal and the superconducting states. Here too, the impurity-induced relaxation rates were found to play an important role.

5.4.1. *Superconductivity and magnetic order?*

The coexistence of superconductivity and magnetic order is an exciting problem for many researchers. We refer to the review of Roth (1978) for an introduction. Experiments on magnetically ordered superconductors were also reviewed by Maple (1983). There are several rare-earth intermetallic compounds in which NMR has been applied to investigate the details of an eventual coexistence between magnetism and superconductivity. Unfortunately, in this area the chances are high that one may jump into a pitfall with the NMR analysis, because many of the interesting intermetallic compounds are not easy to prepare in single-phase form; the risk is thus imminent, that NMR is observed in a magnetic phase, but superconductivity occurs in the other phase of a two-phase sample.

The RRh_4B_4 structure allows sufficient separation between the magnetic lanthanide ion and the superconducting electron. Ferromagnetism is observed for R = Gd, Tb, Dy, Ho or Er; for R = Er, the long-range ferromagnetic order destroys the superconductivity. For R = Nd, Sm and Tm long-range antiferromagnetic order and superconductivity coexist. Superconductivity is also found for R = Lu (Kohara et al. 1983). After the discovery of 're-entrant' superconductivity in the ternary compound $ErRh_4B_4$ by Fertig et al. (1977), where long-range ferromagnetic order quenches superconductivity below $T_{FM} < T_c$, there have been a number of NMR investigations dealing with the question of superconductivity and magnetic order in rhodium–boride compounds containing a lanthanide ion with a localized magnetic moment.

^{11}B NMR of Tse et al. (1979) in $Y_{1-x}Er_xRh_4B_4$ ($x \leqslant 0.1$) indicated that the conduction electrons in this system couple strongly to the local moments, despite the extremely weak influence of x on the superconducting transition temperature T_c. The presence of large hyperfine fields was claimed for the boron sites in the superconducting state (for $H_{c1} \ll H_0 < H_{c2}$) from the pronounced loss of the ^{11}B signal below the transition temperature $T_c(H_0)$. In contrast, Kumagai et al. (1979) found only a small polarization of the conduction electrons at the B site in the magnetically ordered compounds RRh_4B_4 (R = Tb, Dy, Ho and Er) via ^{11}B NMR. The hyperfine field at the Gd nuclei in $GdRh_4B_4$ was observed to be largely anisotropic (forming a powder pattern in the NMR wall spectrum). Kumagai et al. (1980) observed T_1 anomalies for $ErRh_4B_4$ ($T_c = 8.15$ K) in low magnetic fields (2.2 kOe). Johnston and Silbernagel (1980) found by ^{11}B NMR in $GdRh_4B_4$ and $LuRh_4B_4$ that in both examples the anisotropic part of the Knight shift was larger than the isotropic one. The absence of any detectable temperature dependence for K_{iso} and K_{ani} in $LuRh_4B_4$ between 90 and 300 K, in spite of a large variation of the static susceptibility of the material, indicated a weak interaction of the ^{11}B with the Rh d-like electrons responsible for the T-dependence of the susceptibility. The authors suggested that the decoupling between certain classes of conduction electrons might be important for the unusual superconducting and magnetic properties. ^{11}B NMR was also measured in the paramagnetic and ordered state of $GdRh_4B_4$ ($T_{FM} = 5.6$ K) by Kohori et al. (1983a, 1984). Kumagai and Fradin (1983b) studied the ^{11}B spin dynamics in $(Y_{1-x}R_x)Rh_4B_4$ for R = Gd and Er with the adiabatic demagnetization–remag-

netization field cycle method. ^{11}B NMR was measured for $SmRh_4B_4$ in the paramagnetic, antiferromagnetically ordered and superconducting state ($T_c \approx 2.5$ K, $T_N = 0.87$ K) by Kohori et al. (1983a, b). Kohori et al. (1985) also analysed ^{11}B NMR in $R(Rh_{1-x}Ir_x)_4B_4$ for R = Tb, Dy and Ho. They observed the decrease of T_{FM} with increasing Ir concentration x and the appearance of antiferromagnetic long-range order coexisting with superconductivity for larger values of x, with $T_c > T_N$ at the Ir-rich side.

$(Ce_{1-x}Gd_x)Ru_2$ is another rare-earth intermetallic compound suspected of showing coexistence between superconductivity and magnetic order for pseudo-binaries with $x \approx 0.1$. Speculatively, Kumagai and Asayama (1975) concluded from Gd NMR on a coexistence between superconductivity and ferromagnetism. Kumagi et al. (1978) measured Gd NMR at $T = 60$ mK in zero field down to $x = 0.105$ and with field down to $x = 0.095$ (even at 1.2 K). From the variation of the hyperfine field and T_c with composition, they concluded that the NMR signal should *not* originate from a precipitated ferromagnet. They discussed the possibilities of spin-glass type and short-range order. A sharp superconducting transition was observed for $x \leqslant 0.110$. The temperature dependences of T_1 for $x = 0.105$ and 0.110 were considered suggestive of a small energy gap associated with a superconducting state *at* the ferromagnetic sites. Matsumura et al. (1982) measured the temperature dependence of T_1 for the zero-field NMR signal as a test for the coexistence between superconductivity and ferromagnetism. They reported that T_1 increases exponentially with lowering of the temperature due to the energy gap. In addition, Kohori et al. (1983b) inferred the coexistence from the zero-field NMR and T_1 reflecting the superconducting energy gap in $(Ce_{1-x}Gd_x)Ru_2$ for $x \approx 0.12$, where superconducting and magnetic ordering temperatures roughly coincide.

Y_4Co_3 was regarded as a new type of magnetic superconductor, because experiments indicated the interplay between itinerant electron ferromagnetism and superconductivity. This is different from the rare-earth rhodium borides or the Chevrel phases, where magnetism is associated with localized lanthanide moments (Takigawa et al. 1983c). NMR results dealing with this question for Y_4Co_3 were reported by three different groups in 1983: Lewicki et al. (1983), Takigawa et al. (1983c) and Wada et al. (1983). Y_4Co_3 is a compound that is difficult to prepare at least 'close to single phase' and was sometimes considered to be Y_9Co_7. Its magnetic ordering temperature $T_M \approx 4.5$–5 K is larger than the superconducting transition temperature $T_c \approx 2.5$ K. The saturation magnetization is small, corresponding to an average moment of 0.01–0.037 μ_B per Co atom. Pulsed ^{59}Co NMR and NQR have been performed by Wada et al. (1983) in the paramagnetic and ferromagnetic states. They analyzed two sites with small positive Knight shift, corresponding to nearly non-magnetic Co sites. The effect of spin fluctuations was seen in an enhancement of the ^{59}Co relaxation rate around the ferromagnetic ordering temperature. They suggested that the magnetic moment of the compound should mainly be carried by the d electrons of the Co atoms at the remaining (linear-chain) site. Takigawa et al. (1983c) observed three kinds of ^{59}Co resonance signals, corresponding to the three (6h, 2d and 2b) sites

of the hexagonal structure (the 2b sites being occupied once per unit cell in Y_4Co_3, but four thirds per unit cell in Y_9Co_7). They did not find the resonance line with large positive shift that Figiel et al. (1981) and Lewicki et al. (1983) attributed to 2d sites. A zero-field Co line observed at 18 MHz indicated a Co moment of 0.23 μ_B, corresponding to an average moment of 0.11 μ_B for the Co 2b sites.

5.5. *Intermediate-valence, Kondo-lattice and heavy-fermion systems*

This is an area of solid state physics that has been intensely studied in recent years. Other chapters of this Handbook are devoted to this subject: chapter 11, volume 1, chapters 62–66, 68 and 71, volume 10; chapters 76 and 78, volume 11; chapter 83, volume 12; and chapters 95, 96 and 97 in this volume. There have also been several recent reviews for this field – as far as NMR applications to intermediate-valence compounds are concerned, one might get the impression that there are more reviews than original work! For a review of unstable-moment phenomena in rare-earth compounds, including key thermodynamic experiments, such as susceptibility and lattice constant, spectroscopic experiments and theoretical work, we refer the reader to Lawrence et al. (1981). A general overview was also given by Parks (1985). NMR and relaxation experiments in rare-earth compounds, which exhibit unstable 4f magnetism and related effects, were reviewed by MacLaughlin (1985). He concluded that in several systems paramagnetic NMR shifts indicate a modification of the electronic band structure below the characteristic temperatures, found from the classical experiments like susceptibility and specific heat (i.e., shift anomalies as compared to eqs. (9) and (10c) are observed). Shift anomalies are small or absent in compounds with low characteristic temperature and integral or nearly integral valence, like $CeCu_2Si_2$ and $CeRu_2Si_2$. Nuclear spin–lattice relaxation rates yield estimates of spin fluctuation rates and are sensitive to the onset of correlated near-neighbour fluctuations. Crisan (1986) reported a formula for the NMR relaxation rate of heavy fermion systems. In their recent review, Asayama et al. (1988a) pointed to the fact that in several heavy-fermion materials an antiferromagnetic type of ordering is observed to appear in the ground state. The anisotropic superconductivity coexists or competes with the magnetic ordering. Recently, MacLaughlin (1989) has reviewed the use of NMR and related techniques in the study of the magnetism of 'unstable magnets', i.e., intermediate-valence and heavy-fermion materials. He mentioned that for temperatures below the characteristic or 'Kondo' temperature T_0 the experiments give evidence for:

(i) modification of the transferred hyperfine field (non-linear $K(\chi)$);

(ii) onset of spatial correlations between f spin fluctuations:

(iii) strong energy-gap anisotropy, with zeros of the gap along lines on the Fermi surface in heavy-fermion superconductors;

(iv) very weak static magnetism, with average moments of about 10^{-1}–10^{-3} μ_B per 4f atom in $CeAl_3$ or $CeCu_2Si_2$. In addition, Panissod et al. (1988) reviewed the NMR study of electron spin fluctuations in intermediate-valence, Kondo and

heavy-fermion compounds. They pointed to the fact that a universal thermal dependence of the f-electron fluctuation rate $1/\tau_{\text{eff}}$ is observed. $1/\tau_{\text{eff}}$ is constant for $T \ll T_0$ in the Fermi-liquid regime and $1/\tau_{\text{eff}} \sim T^{1/2}$ for $T \gg T_0$.

The dense Kondo system CeB_6 was studied by Kawakami et al. (1981, 1982, 1983) and Takigawa et al. (1983a, b). It seems to have three magnetic phases. In the highest temperature phase I ($T > 3.1$ K), a pronounced Kondo effect is observed, with a log T dependence of the resistivity and negative magnetoresistance. Here the NMR spectrum was characteristic of the paramagnetic phase, and quadrupolar splitting was observed at 77 K (Kawakami et al. 1981). In an intermediate phase II, an antiferromagnetic component seems to be induced by the external field, increasing with field and being zero in zero field. NMR line splitting into two lines for the magnetic field in the [111] direction (and more for the other directions) is observed. Whereas the ^{11}B splitting behaves like that observed in antiferromagnetic ordered compounds (Kawakami et al. 1981, Takigawa et al. 1983a), no long-range order is detected by neutron scattering in phase II. From an analysis of the orientation, field and temperature dependence of the ^{11}B NMR line splitting in a single crystal for phase II, possible antiferromagnetic structures could be inferred. The change in the NMR spectrum from phase II to III ($T \leq 2.3$ K) seems more drastic with decreasing temperature (or increasing field). In this phase, long-range order with multiple q-structures is detected by neutron scattering.

Shimizu et al. (1985a) analysed the spin–lattice relaxation time, T_1, of Cu nuclei for a $CeCu_6$ single crystal. The NMR spectrum is complicated due to the presence of four formula units per unit cell and five groups of inequivalent Cu sites. However, from the temperature dependence of T_1 an effective value for the relaxation rate of the Ce moments, $1/\tau_{\text{eff}}$, could be estimated, which would be the largest in the series $CeCu_6$ ($\hbar/\tau = 9$ meV, $T_K = 2$–3 K), $CeCu_2Si_2$ ($\hbar/\tau = 0.8$ meV, $T_K = 11$–14 K) and $CeAl_3$($\hbar/\tau = 0.5$ meV, $T_K = 5$ K). The transition from the magnetic regime to the non-magnetic Fermi-liquid regime of the typical Kondo-lattice compound $CeCu_6$ was explored by Kitaoka et al. (1985b) with the help of the ^{63}Cu NQR from a microscopic point of view. They had a large single crystal available, giving narrow NQR lines. They concluded that $CeCu_6$ shows heavy-fermion properties at low temperatures, $T \leq T^* \approx 0.2$ K. In the Fermi-liquid state below T^* the Korringa law $T_1T \approx 0.011$ s K = const. was obeyed, whereas for $T \geq 6$ K, $1/T_1 \approx$ const. $\approx 150\ \text{s}^{-1}$.

Kitaoka et al. (1985a) showed with ^{29}Si NMR ($K(T)$, $1/T_1$) that $CeRu_2Si_2$ is a non-magnetic Kondo-lattice compound below $T_K = 12$ K. They found that $K_{\parallel}$ depended on temperature, while $K_{\perp}$ did not. $K_{\parallel}/K_{\perp}$ was about 30 at 4.2 K, and the anisotropy about one order of magnitude larger than the dipolar contribution. $1/T_{1\perp}$ was independent of temperature for $12\ \text{K} < T < 70$ K, whereas for $T < T^* = 8$ K as a Korringa relaxation $T_{1\perp}T = 1.0$ s K was observed indicating a Fermi-liquid state, T_1T of ^{63}Cu was analysed by NMR or NQR in $CeCu_2Si_2$ ($T_K = 10$ K) in the temperature range above T_c (in the normal coherent state of the Kondo-lattice system), as well as in the Kondo-lattice compounds $CeRu_2Si_2$ ($T_K = 12$ K) and $CeCu_6$ ($T_K = 6$ K) by Kitaoka et al. (1986). T_1T was considered

to be almost constant below $T^* = 2.5$ K for $CeCu_2Si_2$, $T^* \approx 6$ K for $CeRu_2Si_2$ and $T^* = 0.2$ K for $CeCu_6$.

The magnetism of $CeAl_3$ was probed with NMR by Lysak and MacLaughlin (1985) at temperatures $T > T^* \approx 0.5$ K, below which the system can be described as a degenerate Fermi fluid. Magnetism and NMR at high temperatures could be described well by a model of independent Ce^{3+} ions. A change of slope in the relation between the ^{27}Al isotropic frequency shift K_{iso} and the bulk susceptibility χ has been found below about 10 K and was attributed to a temperature-dependent transferred hyperfine field in this temperature range. This hyperfine field anomaly was believed to be probably not the same as that previously noted at $T \approx T^*$ in other lanthanide compounds, where the moment instability is associated with intermediate valence. The temperature range was rather characteristic of crystalline electric field splittings. In $CeAl_2$ an anisotropic hyperfine interaction in the presence of CEF splitting has been invoked to explain a similar shift anomaly. The temperature dependence of the effective Ce spin fluctuation rate, obtained from measured spin–lattice relaxation rates $1/T_1$, indicated the onset of near-neighbour spatial correlations between dynamic Ce spin fluctuations at low temperature.

Nakamura et al. (1988c) pointed to the fact that conventionally, the heavy-fermion systems have been classified into three types of ground states: paramagnetic, antiferromagnetic and superconducting. More recently, several of the compounds – e.g., $CeAl_3$, $T_N = 1.2$ K, Nakamura et al. (1988a) – were found to be ordered antiferromagnetically at low temperature, suggesting a close correlation between superconductivity and antiferromagnetism. They questioned whether the normal Fermi liquid was stable at low temperatures or whether long-range ordering might set in eventually at low temperatures. Also the heavy fermion system $CeInCu_2$ was reported to show antiferromagnetic-like ordering behaviour at 1.1 K.

Sampathkumaran et al. (1979c) showed that the quadrupole coupling constant e^2qQ for ^{63}Cu in $EuCu_2Si_2$ has a strong temperature dependence, in contrast to $YbCu_2Si_2$ or $SmCu_2Si_2$. Sampathkumaran et al. (1985) observed a strong anomaly in the expected linear relationship between the ^{31}P NMR Knight shift and the bulk magnetic susceptibility at low temperatures for the intermediate-valence compound $EuNi_2P_2$. They showed that this anomaly should not be caused by the CEF or lattice volume effects. Instead, they believed that it results from the formation of the hybridized 4f conduction electron ground state.

For the intermediate-valence compound YbCuAl, MacLaughlin et al. (1979) observed a linear relationship between ^{27}K and χ only for temperatures above the maximum of the bulk susceptibility. For $T < T_{max} \approx 27$ K, this relation was no longer obeyed. This was tentatively attributed to a temperature-dependent effect of intermediate valence on the transferred hyperfine coupling between the Yb moments and the ^{27}Al nuclei. The T_1 relaxation data yielded a 4f spin fluctuation rate via

$$(K^2 T_1 T)^{-1} \chi = 2\gamma_I^2 k_B \tau_{eff}, \tag{21}$$

which decreases by about a factor of two between T_{max} and 100 K. B NMR was analysed in the intermediate-valence compound YbB_{12} (2.9+) by Kasaya et al. (1985). Whereas the isotropic part of the Knight shift was essentially independent of the temperature, K_{ani} depended on T. $1/T_1$ has been derived as a function of the temperature and seemed to be activated at low T.

Shimizu et al. (1987) analysed the correlation between CEF splitting, Kondo temperature T_K and the temperature for the onset of non-linearity in the $K(T) \leftrightarrow \chi(T)$ relation for many dense Kondo systems. (The coherence length in the single-site Kondo effect, which presents the spatial extent of the spin correlations between the localized moment and the conduction electrons, is inversely proportional to the Kondo temperature T_K.) ^{63}Cu NMR was considered to be appropriate for measuring the conduction electron spin polarization. They showed for a $YbCu_2Si_2$ single crystal via ^{63}Cu NMR that the dipolar contribution to the hyperfine field at Cu is not responsible for the $K \leftrightarrow \chi$ anomaly. Instead they analysed the transferred hyperfine coupling between Yb 4f electrons and the Cu nuclear spin and interpreted the anomaly as a CEF effect in the framework of the single-site model. They concluded that the orbitally dependent exchange interaction between the 4f and the conduction electrons is responsible for the anomaly in the hyperfine coupling.

We refer the reader to the tables in the appendix for further references.

5.5.1. *Heavy-fermion superconductors*

The rare-earth intermetallic compound $CeCu_2Si_2$ has, like UBe_{13} and UPt_3, the special property of a transition to a superconducting state at low temperatures ($T_c \approx 0.6$ K). For the cerium compound, experimental conditions are less favourable for NMR, because $H_{c2} \approx 2$ kOe is relatively small.

In a Knight shift study of $CeCu_2Si_2$, Ueda et al. (1987) observed a drastic decrease of the Knight shift of ^{29}Si ($K_\perp(T)$) and ^{63}Cu ($K_\parallel$, $K_\perp$) below T_c, independent of the crystallographic axis. This was taken as support for an even-parity pairing description.

MacLaughlin et al. (1984) observed a maximum of $1/T_1$ at about $T_c \approx 0.6$ K and a rapid decrease of $1/T_1$ below 0.55 K by ^{63}Cu NQR, in agreement with the opening of a gap in a superconducting sample of $CeCu_2Si_2$. Kitaoka et al. (1984, 1985c, 1986) analysed T_1T for ^{63}Cu in the superconducting and normal states by NMR and NQR and for sampes of different stoichiometry ($CeCu_{2.02}Si_2$, $T_c = 0.72$ K, and $CeCu_{1.99}Si_2$ with $T_c = 0.6$ K). They decided that NQR measurements of $1/T_1$ at zero external field give the correct spin–lattice relaxation behaviour of the superconductor. They reported that the nuclear spin–lattice relaxation rate $1/T_1$ of ^{63}Cu shows a rapid decrease below T_c, rather than the enhancement just below T_c, which is a characteristic of BCS superconductors. $1/T_1$ decreases below T_c proportional to T^3 with decreasing temperature. This behaviour was considered to point to an anisotropic s-wave model for singlet pairing, with zeros of the gap along lines at the Fermi surface. The temperature dependence of the nuclear spin–lattice relaxation in the heavy-fermion superconducting state, for the case that the energy gap has nodes, was considered by Bahlouli (1986). Asayama et al.

(1988b) concluded that, *generally*, $1/T_1$ in superconducting heavy-fermion systems does not show an enhancement just below T_c and decreases in proportion to T^3 at low temperature in contrast to the BCS behaviour, indicating the anisotropic nature of the superconductivity with zero gaps on lines at the Fermi surface.

6. Concluding remarks

We have reviewed a number of examples, where NMR was used for the study of intermetallic rare-earth compounds. For space reasons, the known complimentary techniques such as muon spin rotation or 'nuclear' NMR-related methods were not included. The derivation of the temperature dependence of the spontaneous magnetization and the direction of easy magnetization were only two examples out of a large choice, where NMR has given microscopic information on macroscopic properties. The application of NMR in the investigation of the electronic structure of intermetallic compounds with non-magnetic partners has been an area of special success, in which accurate information about the atomic levels has been obtained. We have shown that the use of single crystals and the measurement of magnetically ordered compounds with an applied external field in order to eliminate the wall signals gives more clearcut NMR results in such intermetallic compounds than can be obtained by zero-field NMR. The application of NMR to intermetallic compounds of rare-earth elements with 3d transition metals gives information on questions of large technological importance; this area of considerable current activity was only briefly summarized. Similarly, the NMR analysis of many intermetallic compounds with 'unconventional' properties has only been considered in a rather brief form. However, the tables compiled in the appendix of this chapter allow easy access to additional references. Despite the fact that many potential applications had to be left out of this review, many areas requiring future activities became evident. In addition, new experimental routes like the application of NMR tomographic techniques to solids will have to be considered. Many NMR spectroscopists are presently struggling for a better understanding of high-T_c oxide compounds; this review might show them like others interested in the field, that there are still many potential areas of the NMR application to rare-earth intermetallic compounds worthy of a better analysis.

Acknowledgements

I thank my 'teachers' B. Elschner, V. Jaccarino and N. Kaplan for many enlightening discussions and I use this opportunity to congratulate the first two of them on their respective sixty fifth birthdays. It is a pleasure for me to thank also Y. Berthier, J. Budnick, K.H.J. Buschow, W.G. Clark, H. Figiel, A.P. Guimarães, H. Lütgemeier, D.E. MacLaughlin, M.A.H. McCausland, P.C. Riedi, H. Yasuoka, V. Zevin and W. Zinn for discussions.

Appendix: Tabular data of NMR in rare-earth intermetallic compounds

The reader is referred to the original papers for the error limits which were omitted in the tables in order to save space. The nuclear data are taken from Bruker's tables (Bruker 1989), Carter et al. (1977), Barnes (1979) or the references given in the tables.

TABLE A1

Nuclear magnetic resonance of the nucleus ^{45}Sc in intermetallic compounds. Nuclear data: ^{45}Sc, $I = \frac{7}{2}$, natural abundance 100%, $\gamma/2\pi = 1.0344\,\text{MHz kOe}^{-1}$, $Q = -0.22 \times 10^{-24}\,\text{cm}^2$.

Compound	Temperature (K)	Remarks	Reference
(a) Paramagnetic states			
Sc_3In	6–270	$K(T)$, T_1T (itinerant electron FM)	Hioki and Masuda (1977)
ScN	1.2, 4.2, 20	$K \approx 0$, ($T_1T > 600$ s K)	Kume and Yamagishi (1964)
ScX	2–600	X = P, As, Sb: $K = 0.04 \ldots 0.05\%$	Jones (1969)
ScNi	300	$K = 0.237\%$	Schmidt (1973)
ScX	77, 300	X = Cu, Ru, Rh, Pd, Ag, Ir: $K(T)$	Seipler et al. (1977)
ScH_2	77, 300	$K = 0.07\%$, $T_1T = 25.0$ s K	Schreiber (1965)
ScB_2	77, 300	$K_{iso} = +0.06\%$, $\nu_Q = 0.472$ MHz	Barnes et al. (1970)
ScB_2	4–300	$K = +0.07\%$, $e^2qQ/h = 6.1$ MHz	Carter and Swartz (1971)
$ScAl_2$	10–80	$K = 0.18\%$, $T_1T = 3.7$ s K	Chock et al. (1977)
$ScMn_2$	4.2, 77, 300	K, ν_Q	Barnes and Lunde (1970)
$Y_{0.97}Sc_{0.03}Mn_2$	4.2–300	$1/T_1 \sim T^{1/2}$	Yoshimura et al. (1987)
$Y_{0.98}Sc_{0.02}Mn_2$	4.2	$K \approx 0$	Nakamura et al. (1988f)
$Y_{1-x}Sc_xMn_2$	0.3–300	$x = 0.03/0.08$: $1/T_1T = \alpha(T + \theta)^{-1/2} + \beta$	Nakamura et al. (1988e)
$Sc(Co_{1-x}Ni_x)_2$	300	$0 \leq x \leq 1$: $-0.43\% \leq K \leq +0.39\%$	Barnes et al. (1966)
ScX_2	–	X = Ru, Os: $K \leftrightarrow \chi_d$ (orbital paramagnetism)	Martynova et al. (1976)
$Sc_5Ir_4Si_{20}$	70–300	$\nu_{res}(T)$	Cu et al. (1988)
ScB_6	4.2, 20, 77, 300	$K = -0.04\%$	Gossard and Jaccarino (1962)
(b) Magnetically ordered states			
Sc_3In	1.5–6	$H_{res}(H_0/T)$, T_1T	Hioki and Masuda (1977)
$Gd_{0.9}Sc_{0.1}Zn$	4.2	$H_{hf} = -43.6$ kOe	Eckrich et al. (1976)
GdX:Sc	4.2	1 at%; X = Zn, Cd: $H_{res} = 38.7, 40.2$ kOe	Kasamatsu et al. (1988)
$ScFe_2$	4.2, 77, 293	($MgCu_2$): $H_{res}(4.2\text{ K}) = -100.8$ kOe, ΔH(12Fe–11Fe1Sc) = 6.2 kOe	
		($MgNi_2$): $H_{res}(4.2\text{ K}) = -95.0/-98.1$ kOe,	
$Sc_{1-x}Zn_xFe_2$	4.2	$0 \leq x \leq 1$; -103.4 kOe $\leq H_{inf} \leq -63.8$ kOe	Pokatilov et al. (1989)
$Sc(Fe_{1-x}Co_x)_2$	4.2	$0 \leq x \leq 0.1$; $\nu_{res}(0) = 76$ MHz	Oppelt et al. (1977)

TABLE A2

Nuclear magnetic resonance of the nucleus ^{89}Y in intermetallic compounds. Nuclear data: ^{89}Y, $I = \frac{1}{2}$, natural abundance 100%, $\gamma/2\pi = 0.20859$ MHz kOe^{-1}.

Compound	Temperature (K)	Remarks	Reference
(a) Paramagnetic states			
YX	2–600	X = P, As, Sb, Bi: $K = 0.11\%$	Jones (1969)
YCu	1.5–300	$K = 0.30\%$	Von Meerwall et al. (1975)
YRh	77, 300	$K = 0.235, 0.236\%$	Seipler et al. (1977)
YAg	77, 300	$K = +0.27\%, +0.32\%$	Schmidt (1973)
YH_2	77, 300	$K = 0.11\%$	Schreiber (1965)
YH_2	1–4	$T_1T = 550$ s K	Narath and Fromhold (1967)
YB_2	77, 300	$K_{iso} = +0.16\%$	Barnes et al. (1970)
YB_2	300	$K = 0.20\%$	Carter and Swartz (1971)
YRh_4B_4	2–4.2	$T_1T = 92$ s K	Kohori et al. (1984)
(b) Magnetically ordered states			
YFe_2	4.2	$H_{res} = -220$ kOe	Oppelt and Buschow (1973)
YFe_2	4.2	$\nu(0/10$ kbar$) = 45.90/46.37$ MHz	Belov et al. (1981)
YFe_2	4.2	$\nu_0 = 45.9$ MHz, $\partial\nu/\partial p = +50.5$ kHz kbar^{-1}	Vasil'kovskii et al. (1981a)
YFe_2	4.2	$H_{res} = -219.6$ kOe	Vasil'kovskii et al. (1983)
YFe_2	4.2, 77, 300	$(\partial(\ln H_{hf})/\partial p)_T$	Riedi and Webber (1983)
YFe_2	4.2	$\nu_0 = 45.94$ MHz; $\partial(\ln H_{hf})/\partial p = 6.7 \times 10^4$ kbar^{-1}	Riedi et al. (1985), Dumelow et al. (1986)
$Gd_{1-x}Y_xFe_2$	77–270	$\nu(x)$; $\nu(x=1) = 45.3$ MHz; 5 satellites $\Delta\nu \approx 2.2$ MHz; $\nu(x=1, T)$	Vasil'kovskii et al. (1974)
$Y_{1-x}R_xFe_2$	4.2	R = Tb, Dy, Ho; $0 \leq x \leq 0.2$: line profile	Alves et al. (1986)
$(Dy_xY_{1-x})Fe_2$	4.2	$0.005 \leq x \leq 0.02$; domain wall mobility	Alves et al. (1990)
$Y(Fe_{1-x}X_x)_2$	4.2	X = Al, Co, Pt; (resolved nn contrib.)	Oppelt and Buschow (1976)
$Y(Fe_{1-x}X_x)_2$	4.2	X = Al, V, Mn, Co, Ni: $0 \leq x \leq 0.05$: well resolved satellites	Ichinose et al. (1983)
$Y(Fe_{1-x}Al_x)_2$	4.2	$0 \leq x \leq 0.2$: well resolved satellites	Ichinose et al. (1985)
$Y(Fe_{1-x}X_x)_2$	4.2	X = Al/Co: satellites $\Delta\nu = 3.5/1.4$ MHz	Vasil'kovskii et al. (1988)
$Y(Fe_{1-x}Co_x)_2$	77	$0 \leq x \leq 1$: satellites	Yamada and Ohmae (1980)
$Y(Fe_{1-x}Mn_x)_2$	4.2	$0 \leq x \leq 0.2$: satellites of lower intens., $\Delta\nu = 5.7$ MHz	Besnus et al. (1982)
$Y(Fe_{1-x}Mn_x)_2$	4.2	$0 \leq x \leq 0.3$: $\rightarrow 0.5/2.7$ μ_B per Mn	Nagai et al. (1983)

TABLE A2 (cont'd)

Compound	Temperature (K)	Remarks	Reference
$Y(Fe_{1-x}Mn_x)_2$	4.2	$x \leq 0.5$; 0.5/2.7 μ_B per Mn	Nagai (1989)
$Y(Fe_{0.95}Co_{0.05})_2$	4.2	$p \leq 8$ kbar	Vasil'kovskii et al. (1988)
YFe_3	4.2	$H_{res} = -231/185$ kOe	Oppelt and Buschow (1973)
YFe_3	4.2	$\nu = 48.1$ MHz	Nikitin et al. (1975a)
YFe_3	4.2–380	$H_{res}^{I,II}(T)$	Oppelt et al. (1976)
YFe_3	4.2	$H_{res}(3a/6c) = -183.7/-230$ kOe	Vasil'kovskii et al. (1983)
YFe_3	4.2, 77, 330	$(\partial(\ln H_{hf})/\partial p)_T$	Riedi and Webber (1983), Riedi et al. (1985)
$Gd_{1-x}Y_xFe_3$	4.2–300	$H_{hf}^{I,II}(x = 0/1, T)$; $H_{hf}^{I,II}(x)$, $\nu^{I/II}(x = 1) = 38.4/48.2$ MHz, 4 satellites	
		$\Delta\nu^{II} \approx 1.6$ MHz	Nikitin et al. (1976)
YCo_3	4.2	$H_{res} \leftrightarrow$ sites	Figiel et al. (1976)
Y_2Co_7	4.2	$H_{res} \leftrightarrow$ sites	Figiel et al. (1976)
Y_6Mn_{23}	4.2	$\nu_{res} = 44$ MHz (209 kOe)	Nagai et al. (1981)
Y_6Mn_{23}	4.2	spectrum 40–50 MHz	Yoshimura and Nakamura (1983)
YCo_5	4.2	$H_{res} = -101.7$ kOe	Figiel et al. (1976)
$Y_2Fe_{14}B$	1.4	$H_{hf} = 230$ kOe	Berthier et al. (1986a)
$Y_2Fe_{14}B$	4.2	$\nu_{res} = 36.7/48.4$ MHz	Erdmann et al. (1987)
$Y_2Co_{14}B$	4.2	24.3/22.8 MHz	Figiel et al. (1987b)
$Y_2Co_{14}B$	4.2	$\nu_{res} = 14.6/21.2$ MHz	Erdmann et al. (1987)
Y_2Fe_{17}	4.2	$H_{res} = -204$ kOe	Oppelt and Buschow (1973)
Y_2Fe_{17}	4.2	$H_{res} = -204$ kOe	Vasil'kovskii et al. (1983)
Y_2Fe_{17}	4.2	$\partial(\ln H_{res})/\partial p$, $p \leq 6$ kbar	Riedi et al. (1985)
Y_2Co_{17}	4.2	rhomb./hexag., $H_{res} \leftrightarrow$ sites	Figiel et al. (1976)
Y_2Co_{17}	4.2	Th_2Zn_{17}, Th_2Ni_{17}, stacking faults	Figiel et al. (1977)
$Y_2X_{14}B$	4.2	X = Fe/Co: $H_{inf}(Y) = 17.6/23.2$ (7/10T)	Erdmann and Rosenberg (1989)
Y_2Fe_{17}, Y_6Fe_{23}, YFe_2	4.2	$\mu_y = -0.4\mu_{13}$; pressure dependence of $H_{inf}(Y)$	Riuitage et al. (1990)
$(Y_{1-x}Gd_x)_2Co_{17}$	4.2	rhomb./hexag., $0 \leq x \leq 0.9$	Figiel (1982b)

TABLE A3

Nuclear magnetic resonance of the nucleus ^{139}La in intermetallic compounds. Nuclear data: ^{139}La, $I = \frac{7}{2}$, natural abundance 99.9%, $\gamma/2\pi = 0.60146$ MHz kOe^{-1}, $Q = +0.22 \times 10^{-24}$ cm^2.

Compound	Temperature (K)	Remarks	Reference
(a) Paramagnetic states			
LaX	2–600	X = P, As, Sb: $K = 0.16\%$–0.17%	Jones (1969)
LaX	77, 300	X = Mg, Zn, Ag, $Ag_{0.5}Zn_{0.5}$, $Ag_{0.75}In_{0.25}$: $K(T)$	Schmidt (1973)
LaX	10–280	X = Zn, Ag: $K(T) \leftrightarrow \chi(T)$	Goebel et al. (1975)
LaAg	1.5–300	$K = 0.70\%$, $T_1T = 0.536$ s K	von Meerwall et al. (1975)
$La_{1-x}Gd_xX$	4.2–300	X = Zn, Ag; $0.0025 \leq x \leq 0.1$: neighbour contributions	Goebel et al. (1977)
$La_{0.995}Gd_{0.005}Ag$	4.2	SC; $\Delta H^{3\,nn}_{iso/ani} = 4.1/0.92$ kOe	Goebel and Dormann (1979)
LaH_2	76–670	K, $T_1T = 11.3$ s K	Schreiber and Cotts (1963)
$LaAl_2$	4.2–295	K	Jaccarino et al. (1960)
$LaAl_2$	90–300	$K(T)$, T_1T	Silbernagel and Wernick (1973)
$La_{1-x}Ce_xAl_2$	1.4–4.2	$0 \leq x \leq 0.003$: T_1 (field cycling); $(T_1T)_{non\text{-}sc,x=0} = 0.21$ s K; sc gap, $x \leq 0.5\%$	MacLaughlin et al. (1976) MacLaughlin (1977)
$La_{1-x}Gd_xAl_2$	1.2–300	$0.0013 \leq x \leq 0.10$; $T_1T(x \rightarrow 0) = 0.752$ s K	McHenry et al. (1972)
$La_{1-x}Gd_xAl_2$	1.6–4.2	$x \leq 0.3\%$: $T_1(T, H_0)$ (field cycling)	MacLaughlin (1977)
$La_{1-x}Th_xRu_2$	1.4–300	$0 \leq x \leq 1$: $K(x, T)$	Shaltiel et al. (1965)
$LaH_{2.69}$	233–298	$K = +0.095\%$–$+0.13\%$	Zogał (1979)
LaH_x, LaD_x	4.2–350	$2.89 \leq x \leq 3.00$: $K(T)$, $K(T \geq 210$ K$) = +0.10\%$; line shape, $T < 210$ K: Eg = 0.10 eV	Barnes et al. (1980)
$LaIn_3$	1.6–300	K, ΔH, T_2, T_1T	Welsh et al. (1971a)
$La(In_xSn_{1-x})_3$	1.6–300	$K(x)$, $T_1T(x)$	Toxen et al. (1973)
$LaSn_3$	77, 174, 300	$K = 0.207\%$–0.234%	Borsa et al. (1967)
$LaSn_3$	1.6–300	$K(T)$, T_2, T_1T	Welsh et al. (1971b)
$La(R)X_3$	1.5–4.2	R = Ce, Gd; X = In, Sn, Pb: ΔH, $T_{1,impurity}$	Welsh et al. (1975)
$LaNi_5H_x$	4.2	$x = 0$: $\nu_Q = 2.1$ MHz, $K_\parallel \approx 0.08\%$	Rubinstein et al. (1979)
LaB_6	4.2, 20, 77, 300	$K = -0.04\%$	Gossard and Jaccarino (1962)

TABLE A3 (cont'd)

Compound	Temperature (K)	Remarks	Reference
(b) Magnetically ordered states			
$Gd_{0.9}La_{0.1}Ni$	4.2	$H_N = +90$ kOe	Dormann and Buschow (1977)
$Gd_{0.9}La_{0.1}Zn$	4.2	$\nu_{res} = (57 \pm 2)$ MHz	Eckrich et al. (1972)
$R_{0.9}La_{0.1}Zn$	4.2	R = Gd, Tb, Ho	Eckrich et al. (1976)
$Gd_{1-x}La_xRh$	4.2	$x = 0.05, 0.1$: $H_{hf} = 55.9$ kOe	Dormann and Buschow (1976)
$Gd_{1-x}La_xAg$	4.2	$0.01 \leq x \leq 0.2$; AF; $\lvert H_N \rvert = 97.3$ kOe	Goebel and Dormann (1979)
$Gd_{0.9}La_{0.1}Al_2$	1.4	$H_{res} = 19.7$ kOe; T_1, T_2	Berthier and Devine (1978)
$Gd_{1-x}La_xNi_2$	4.2	$0 \leq x \leq 0.4$: $H_N = +60.8$ kOe, $H_N(x)$	Dormann and Buschow (1977)
$Gd_{1-x}La_xRh_2$	4.2	$x \leq 0.5$: $H_N \leftrightarrow T_c$, $H_{nn} \leftrightarrow d$	Dormann et al. (1977a)
$Gd_{1-x}La_xIr_2$	4.2	$0 \leq x \leq 0.2$: $H_{hf}(x \rightarrow 0) = +87.4$ kOe, H_{nn}	Dormann et al. (1976)
$Gd_{0.9}La_{0.1}Ni_3$	4.2	H_N, H_{nn}	Dormann and Buschow (1977)
$LaMn_2Si_2$	4.2/77	$\nu_{res} = 53.0/51.6$ MHz	Sampathkumaran et al. (1982b)
$LaMn_2Ge_2$	77	$\nu_{res} = 51.0$ MHz	Sampathkumaran et al. (1982b)
$Y_{1-x}La_xMn_2X_2$	4.2	X = Si/Ge; $0.3 \leq x \leq 1$; $\nu_{res}(x = 1) = 50$ MHz, ν_Q	Ichinose et al. (1988b)
$Eu_{1-x}La_xCu_5$	≤ 4.2	$x = 0.025, 0.05$: $\nu_{res} = 28$ MHz	Kropp et al. (1979b)
$La_2Fe_{14}B$	4.2	spectrum	Rosenberg et al. (1986)

TABLE A4

Nuclear magnetic resonance of the nucleus ^{141}Pr in intermetallic compounds. Nuclear data: ^{141}Pr, $I = \frac{5}{2}$, natural abundance 100%, $\gamma/2\pi = 1.295$ MHz kOe^{-1}, $Q = -5.8 \times 10^{-26}$ cm^2.

Compound	Temperature (K)	Remarks	Reference
(a) Paramagnetic states			
PrX	1.5–77	X = P, As: $\Delta H_{res}(T)/H_0$; ΔH_{res}(4.2 K, PrAs)/$H_0 = 6.5$, $J_{sf} \approx -0.7$ eV	Jones (1967)
PrX	4.2	X = S, Se, Te: $H_{hf}/H_0 = 5.84, 5.52, 7.78$	Bucher et al. (1975)
PrP	4.2	$K(p)$, $p \lesssim 6$ kbar	Weaver and Schirber (1976a)
PrAs	4.2	d(ln K)/dp	Weaver and Schirber (1976a)
PrX	4	X = N, P, As, Sb: K; K(X = Sb, 4 K) = 930% d(ln K)/dp	Weaver et al. (1977)
PrX	(4)	X = N, P, S, As, Se, Sb: K, d(ln K)/dp	Schirber and Weaver (1979)
$Pr_{1-x}La_xIn_3$	1.2–4.2	$T_1(x, T)$, $T_2(x, T)$: $T_1T = 270$ μs K $\neq f(x)$ $K(x = 0) = 5.7$	Satoh et al. (1981)
$PrNi_5$	1.2–10	$\Delta H(T) \rightarrow$ Pr–Pr exchange coupling	Levin et al. (1979)
$PrNi_5$	1.2–8	$H_{res}/H_0 = f(\theta)$, $P \approx 0.6$ MHz, χ_{ion}, J_{Pr-Pr}	Kaplan et al. (1980)
(b) Magnetically ordered states			
$Pr_{0.02}Nd_{0.98}Al_2$	1.4	$a = 4015$ MHz, $P = 1.57$ MHz	Ross et al. (1983)
$Pr_{0.01}Gd_{0.99}Al_2$	1.4	$a = 3875$ MHz, $P = 1.66$ MHz	Ross et al. (1983)

TABLE A5

Nuclear magnetic resonance of the nuclei ^{143}Nd and ^{145}Nd in intermetallic compounds with magnetically ordered states. Nuclear data: ^{143}Nd, $I = \frac{7}{2}$, natural abundance 12.2%, $\gamma/2\pi = 0.2315$ MHz kOe^{-1}, $Q = -0.48 \times 10^{-24}$ cm^2; ^{145}Nd, $I = \frac{7}{2}$, natural abundance 8.3%, $\gamma/2\pi = 0.144$ MHz kOe^{-1}, $Q = -0.30 \times 10^{-24}$ cm^2.

Compounds	Temperature (K)	Remarks	Reference
$NdAl_2$	1.4	$^{143}\nu_{res} = -786$ MHz	Berthier et al. (1978b)
$NdAl_2$	1.4	$\|a\| = 786$ MHz, $\|P\| = 3.25$ MHz	Berthier and Belorizky (1984)
$NdFe_2$	1.4	$^{143}\nu_{res} = 790$ MHz, $^{143}\|P\| = 2.3$ MHz	Meyer et al. (1981)
$NdCo_3$	4.2	$\nu_{res} = 818$ MHz/507 MHz; $^{143}P = \pm 5$ MHz	Streever (1975a)
$NdMn_2Ge_2$	4.2	$\nu_{res} = 692/428$ MHz	Sampathkumaran et al. (1982b)
$NdCo_5$	4.2	$\nu_{res} = 795$ MHz/494 MHz	Streever (1975a)
$Nd_2Fe_{14}B$	4.2	$^{143/145}\nu_{res}^{I,(II)} = 801/498.6(820/510.5)$ MHz	Potenziani (1985)
$Nd_2Fe_{14}B$	1.4	$H_{hf}^{1(2)} = 3600(3450)$ kOe	Berthier et al. (1986a)
$Nd_2Co_{14}B$	4.2	$^{145}\nu_{res} = 565.8$ MHz, $\nu_Q = 0.36$ MHz	Figiel et al. (1987b)
$Nd_2(Co, Fe)_{14}B$	4.2	$^{145}\nu_{res} = 544$ MHz, $\nu_Q = 2.58$ MHz; $\nu_{res} = 566$ MHz, $\nu_Q = 0.3$ MHz; double resonance, additional ν_Q	Nadolski et al. (1989)
Nd_2Co_{17}	4.2	$\nu_{res} = 905$ MHz/563 MHz; $^{143}P = \pm 3.5$ MHz	Streever (1975a)

TABLE A6

Nuclear magnetic resonance of the nuclei ^{147}Sm and ^{149}Sm in intermetallic compounds with magnetically ordered states. Nuclear data: ^{147}Sm, $I = \frac{7}{2}$, natural abundance 15.1%, $\gamma/2\pi = 0.176\,\text{MHz kOe}^{-1}$, $Q = -0.20 \times 10^{-24}\,\text{cm}^2$; ^{149}Sm, $I = \frac{7}{2}$, natural abundance 13.8%, $\gamma/2\pi = 0.145\,\text{MHz kOe}^{-1}$, $Q = +5.2 \times 10^{-26}\,\text{cm}^2$.

Compound	Temperature (K)	Remarks	Reference
$SmAl_2$	1.4	$H_{res} = +3396$ kOe, $^{147}P = 4.8$ MHz	Vijayaraghavan et al. (1977)
$SmFe_2$	1.4	$H_{res} = +3042$ kOe, $^{147}P = 5.3$ MHz	Vijayaraghavan et al. (1977)
$SmCo_2$	1.4	$H_{res} = +3188$ kOe, $^{147}P = 5.1$ MHz	Vijayaraghavan et al. (1977)
$SmCo_5$	4.2	$\nu_{res} = 602/502$MHz ($H_{res} = 3.42$ MOe), $^{147}P = \pm 4.7$ MHz	Streever (1975b)
$SmCo_5$	1.4	$H_{res} = +3440$ kOe, $^{147}P = 4.8$ MHz	Vijayaraghavan et al. (1977)

TABLE A7

Nuclear magnetic resonance of the nuclei ^{151}Eu and ^{153}Eu in intermetallic compounds with magnetically ordered states. Nuclear data: ^{151}Eu, $I = \frac{5}{2}$, natural abundance 47.8%, $\gamma/2\pi = 1.0559\,\text{MHz kOe}^{-1}$, $Q = +1.14 \times 10^{-24}\,\text{cm}^2$; ^{153}Eu, $I = \frac{5}{2}$, natural abundance 52.2%, $\gamma/2\pi = 0.4638\,\text{MHz kOe}^{-1}$, $Q = +2.92 \times 10^{-24}\,\text{cm}^2$.

Compound	Temperature (K)	Remarks	Reference
$EuPd_2$	4.2	$H_{hf} = +20.8$ kOe; $^{153}\nu_Q = 0.7$ MHz	Kropp et al. (1979a)
$Eu_{1-x}X_xPd_2$	4.2	X = Ca, Ba; $x \leq 0.2$; $H_{res}(x)$	Kropp et al. (1979a, b)
$EuPt_2$	4.2	$H_{hf} = -33.3$ kOe; $^{153}\nu_Q = 1.4$ MHz	Kropp et al. (1979a)
$EuPt_2$	2–60	$\nu_{res}(T)$; $^{153}\nu_Q(T)$; $\nu_Q(0\,\text{K}) = 1.46$ MHz	Dressel et al. (1988)
$EuPt_2$	4.2	$^{153}\nu_Q(H_0)$	Dressel and Dormann (1988)
$Eu_{1-x}X_xPt_2$	4.2	X = Ca, Ba; $x \leq 0.2$; $H_{res}(x)$	Kropp et al. (1979a, b)
$Eu_{1-x}La_xCu_5$	≤4.2	$0 \leq x \leq 0.2$: $H_{res}(x)$	Kropp et al. (1979b)
EuB_6	1.7, 4.2	$^{153}\nu_{res} = 148.5$ MHz; pulsed gradient spin echo, self-diffusion	Bajaj (1976)

TABLE A8

Nuclear magnetic resonance of the nucleus ^{155}Gd and ^{157}Gd in intermetallic compounds with magnetically ordered states. Nuclear data: ^{155}Gd, $I = \frac{3}{2}$, natural abundance 14.7%, $\gamma/2\pi = 0.1307$ MHz kOe^{-1}, $Q = +1.59 \times 10^{-24}$ cm^2; ^{157}Gd, $I = \frac{3}{2}$, natural abundance 15.6%. $\gamma/2\pi = 0.1713$ MHz kOe^{-1}, $Q = +1.69 \times 10^{-24}$ cm^2.

Compound	Temperature (K)	Remarks	Reference
GdN	2.2, 4.2	$\nu_{res}(4.2\text{ K}) = 44.090/58.500$ MHz	Boyd and Gambino (1964)
GdZn	4.2	$\nu_{res} = 51.2$ MHz/67.2 MHz	Oppelt et al. (1972a)
GdZn	4.2–180	$\nu_{res}(T) \leftrightarrow M_s(T)$	Herbst et al. (1974)
GdZn	1.6	SC: $K = -0.50\%$	Kropp et al. (1984)
$Gd_{1-x}R_xZn$	4.2	R = Y, La; $0 \leq x \leq 0.2$: $\nu_{res}(x)$	Eckrich et al. (1972)
$Gd_{0.9}R_{0.1}Zn$	4.2	R = Sc, Y, La, Ce, Pr, Nd, Sm, Tb, Dy, Ho, Er	Eckrich et al. (1976)
$GdZn_{1-x}Mg_x$	4.2	$0 \leq x \leq 1$: $\nu_{res}(x)$	Buschow and Oppelt (1974)
$GdZn_{1-x}Ag_x$	4.2	$\nu_{res}(x)$	Oppelt et al. (1972a)
$GdZn_{1-x}Ag_{0.5x}In_{0.5x}$	4.2	$\nu_{res}(x)$	Oppelt et al. (1972a)
$GdZn_{1-x}Cd_x$	4.2	$\nu_{res}(x)$	Oppelt et al. (1972a)
$GdZn_{1-x}In_x$	4.2	$\nu_{res}(x)$	Oppelt et al. (1972a)
$Gd_{1-x}La_xRh$	2, 4.2	$0 \leq x \leq 0.1$; $\nu_{res}(0) = 23.2$ MHz/30.4 MHz	Dormann and Buschow (1976)
$GdAg_{1-x}In_x$	4.2	$\nu_{res}(x)$	Oppelt et al. (1972a)
GdX_2	4.2	X = N, Al, Mn, Fe, Rh, Pt: H_{res}	Gegenwarth et al. (1967)
$GdMg_2$	4.2	$H_{res} = -242.2$ kOe	Dormann et al. (1982)
$GdAl_2$	4.2, 77	$\nu_{res}(4.2\text{ K}) = 20.6/27.0$ MHz	Budnick et al. (1965)
GdX_2	4.2	X = Al, Mn, Fe, Rh, Pt: H_{res}	Budnick and Skalski (1967)
GdX_2	4.2, (2.5)	X = Al, Rh, Ir, Pt: H_{hf}	Dormann and Buschow (1973)
$GdAl_2$	4.2–80	$\nu_{res}(T) \leftrightarrow M_s(T)$	Herbst et al. (1974)
$GdAl_2$	4.2, 77	spin echo decay $f(\tau)$	Bowden et al. (1983)
$GdAl_2$	1.8	SC: $K = +0.52\%$; $^{157}\nu_Q = 0.774$ MHz	Kropp et al. (1983)
$GdAl_2$	4.2, 85–140	$\nu(T) \leftrightarrow M(T)$	Barash and Barak (1984)
$GdAl_2$	2–130	$^{155/157}\nu_Q(T)$	Dormann et al. (1984)
$GdAl_2$	4.2	$T_1(H_1)$, $T_2(H_1)$	Oliveira and Guimarães (1988)
$GdAl_2$	5–10	line profiles	Dormann and Dressel (1989)
$Gd_{1-x}Y_xAl_2$	4.2	$0 \leq x \leq 0.6$: $\nu_{res}(x)$	Dintelmann et al. (1970)
$Gd_{1-x}Y_xAl_2$	4.2	$0 \leq x \leq 0.7$; $H_N = -22$ kOe	Dintelmann and Buschow (1971)
$GdFe_2$	4.2	$H_{res} = 453$ kOe	Gegenwarth et al. (1966)
$Gd_{1-x}Y_xFe_2$	77–270	$x \leq 0.6$: $\nu_{res}(x)$; $\nu(x=0) = 51.1/73.5$ MHz; $\nu(x=0, T)$	Vasil'kovskii et al. (1974)
$Gd(Fe_{1-x}Co_x)_2$	4.2	$\nu(x)$; $x = 0.1$: satellites $\Delta\nu = 3.2$ MHz	Belov et al. (1976)

$Gd(Fe_{1-x}Co_x)_2$	4.2	$0 \leq x \leq 1$	Ichinose (1987)
$Gd(Fe_{1-x}X_x)_2$	4.2	X = Al, Co; $\Delta\nu_{sat}^{Al} = 7.0$ MHz, $\Delta\nu_{sat}^{Co} = 3.0$ MHz	Vasil'kovskii et al. (1988)
$Ce_{1-x}Gd_xRu_2$	0.5–4.2	$x \geq 0.105$: ν_{res}, T_2; FM $\leftrightarrow$ sc	Kumagai and Asayama (1975)
$Ce_{1-x}Gd_xRu_2$	0.06–4.2	$0.105 \leq x \leq 0.26$: $H_{hf} = -206 + 88x$ kOe; T_1, T_2, signal intensity $f(x, T)$	Kumagai et al. (1978)
$Ce_{1-x}Gd_xRu_2$	0.025–1.3	$1/T_2 \rightarrow T_1$; $^{157}\nu(x = 0.100) \approx 30$ MHz; ($x = 0.176$: T_2T = const.)	Matsumura et al. (1982)
$Ce_{1-x}Gd_xRu_2$	0.024–0.3	$0.100 \leq x \leq 0.119$: $T_1(T)$, $T_2(T)$	Kohori et al. (1983b)
$GdRh_2$	4.2	line profile $\rightarrow \nu_Q$	Dressel et al. (1988)
$Gd_{1-x}La_xRh_2$	4.2	$x \leq 0.5$; $H_N \leftrightarrow T_c$	Dormann et al. (1977a)
$GdIr_2$	4.2	line profile $\rightarrow \nu_Q$	Dormann et al. (1986)
$Gd_{1-x}R_xIr_2$	4.2	R = Y, La; $0 \leq x \leq 0.2$: $H_{hf}(x)$, $H_{rn}(x)$	Dormann et al. (1976)
$Gd_{1-x}R_xPt_2$	4.2	R = Sc, La; $0 \leq x \leq 0.3$	Dormann et al. (1977b)
$GdPt_x$	4.2	$2 \leq x \leq 3$; $H_{hf}(x = 2) = -178.1$ kOe	Dormann et al. (1977b)
$GdFe_3$	4.2	$\nu_{res}^{I(II)} = 54.3/70.5\ (65.0/82.0)$ MHz	Nikitin et al. (1975a)
$Gd_{1-x}Y_xFe_3$	4.2–300	$H_{hf}^{I,II}(x)$; satellites $\Delta\nu^{II} = 3.8$ MHz; $H_{hf}^{I,II}(x = 0/1, T)$;	Nikitin et al. (1976)
Gd_2Co_7	77	$H_{res}^{I(II)} = 250(300)$ kOe	Ueno et al. (1971)
Gd_6Mn_{23}	4.2	spectrum	Nagai et al. (1988a)
$Gd_2Fe_{14}B$	1.4	$H_{hf}^{1(2)} = 147(279)$ kOe	Berthier et al. (1986a)
$Gd_2Fe_{14}B$	4.2	spectrum (383 kOe)	Rosenberg et al. (1986)
$GdRh_4B_4$	1.2	$\lvert H_{iso}\rvert = 352$ kOe, $\lvert H_{ani}\rvert = 54$ kOe	Kumagai et al. (1979)
Gd_2Mn_{23}	4.2	$\nu_{res} = 42/55$ MHz, $H_{res} = 322$ kOe	Nagai et al. (1981)

TABLE A9

Nuclear magnetic resonance of the nucleus ^{159}Tb in intermetallic compounds, with magnetically ordered states. Nuclear data: ^{159}Tb, $I = \frac{3}{2}$, natural abundance 100%, $\gamma/2\pi = 1.0133$ MHz kOe^{-1}, $Q = +1.34 \times 10^{-24}$ cm^2.

Compound	Temperature (K)	Remarks	Reference
TbZn	1.2	$\nu_Q = 725$ MHz	Devine and Berthier (1981)
TbAg	1.4	AF; $H_{res} = (+)3230$ kOe	Vijayaraghavan et al. (1977)
$TbAl_2$	1.4	$H_{res} = (+)3205$ kOe	Vijayaraghavan et al. (1977)
$TbAl_2$	1.4	$\nu_{res} = 3248$ MHz	Berthier et al. (1978b)
TbX_2	1.2	X = Al, Fe: $\nu_Q = 710\,674$ MHz	Devine and Berthier (1981)
$Tb_{1-x}Gd_xAl_2$	1.4	$x = 0(0.9)$: $\nu = 3248(3264)$ MHz, $\nu_Q = 710(728)$ MHz	Berthier and Devine (1980b)
$TbMn_2$	1.4	$a = 3116$ MHz, $P = 334$ MHz	Shimizu (1982)
$Tb_{1-x}Gd_xMn_2$	1.4	$0 \leq x \leq 0.8$: $H_{res} = 3336 \rightarrow 3365$ kOe	Shimizu (1985b)
$Tb_{1-x}Lu_xMn_2$	1.4	$0 \leq x \leq 0.25$; $H_N^R/S_R = +20$ kOe/spin	Shimizu (1985b)
$TbFe_2$	1.4	$H_{res} \rightarrow$ cond. electron contribution	Berthier et al. (1981)
$TbFe_2$	2–6	$\nu = 3110$ MHz; $T_1(T)$, $T_2(T)$; $T_1(4.2\text{ K}) = 110\ \mu$s, $T_2 = 22\ \mu$s	Shevchenko et al. (1983)
$TbFe_2$	4.2	$a = 3800$ MHz, $P = 345$ MHz	de Azevedo et al. (1985)
$Tb_{0.8}Y_{0.2}Fe_2$	4.2	satellites $\nu = 3797, 3789, 3779$ MHz; H_{nn}^R	Shimizu and Okeya (1986)
$Tb(Fe_{1-x}Co_x)_2$	1.6, 4.2	$x \leq 0.8$; 3798 kOe($x = 0$) $\cdots$ 3389 kOe($x = 1$), $\nu_Q = 685 \cdots 675$ MHz; $x \leq 0.2$: satellites	Shimizu and Okeya (1986)
$Tb_{1-x}Y_xCo_2$	1.4	$0 \leq x \leq 0.6$: $P(x)$; $P(0) = 381$ MHz; $\rightarrow \mu_{Tb}$	Berthier et al. (1986b)
$Tb_{0.07}Gd_{0.93}Ni_2$	4.2	ν_{res}, T_1: Ni contribution to exchange coupling	Shevchenko et al. (1987)
$TbFe_2H_x$	1.4	$0 \leq x \leq 3.3$; $\langle J_z \rangle$, H_N^{Fe}, H sites	Berthier et al. (1985)
$TbFe_3$	4.2	$a^{1(2)} = 3623(3762)$ MHz, $P^{1(2)} = 320(349.5)$ MHz	de Azevedo et al. (1985)

TABLE A10

Nuclear magnetic resonance of the nuclei ^{161}Dy and ^{163}Dy in intermetallic compounds with magnetically ordered states. Nuclear data: ^{161}Dy, $I = \frac{5}{2}$, natural abundance 18.7%, $\gamma/2\pi = 0.144\,\text{MHz kOe}^{-1}$, $Q = +2.47 \times 10^{-24}\,\text{cm}^2$; ^{163}Dy, $I = \frac{5}{2}$, natural abundance 25.0%. $\gamma/2\pi = 0.203\,\text{MHz kOe}^{-1}$, $Q = +2.51 \times 10^{-24}\,\text{cm}^2$; $^{161}a/^{163}a = -0.71415(2)$, $^{161}P/^{163}P = 0.94684(6)$ (Berthier et al. 1975).

Compound	Temperature (K)	Remarks	Reference
DyZn	1.2	$\nu_Q = 411$ MHz	Devine and Berthier (1981)
$DyAl_2$	≤ 4.2	$^{161}a = -845.2$ MHz, $^{161}P = 210.0$ MHz	Berthier et al. (1975)
$DyAl_2$	1.4	$^{163}\nu_{res} = 1183.5$ MHz	Berthier et al. (1978b)
DyX_2	1.2	X = Al, Fe: $^{163}\nu_Q = 443$, 443 MHz	Devine and Berthier (1981)
$Dy_{1-x}R_xAl_2$	1.4	R = Y, Gd; $0 \leq x \leq 0.35$; $^{163}a(0) = 1183.5$ MHz, $2P(0) = 443.8$ MHz; satellites; $x_{Gd} = 0.025$: $\Delta\nu = 4.0$ MHz	Berthier et al. (1977)
$Dy_{1-x}Y_xAl_2$	1.4	$0 \leq x \leq 0.5$; $\eta^{wall}(x)$; $\nu(0) = 1183.5$ MHz; satellites	Barbara and Berthier (1977)
$Dy_{0.9}R_{0.1}Al_2$	1.4	R = Sc, Y, La, Lu: satellites; →perturbation of MF and CEF	Berthier and Devine (1979c)
$Dy_{1-x}Gd_xAl_2$	1.4	$0 \leq x \leq 0.99$: $\nu_{res}(x)$ for 0, 1, 2, 3, 4 Gd nn, $\nu_Q(x)$	Berthier and Devine (1979a)
$Dy_{1-x}Gd_xAl_2$	1.4	$0 \leq x \leq 0.95$; $x = 0.2$, $^{163}\nu$(4Dy, 3Dy1Gd, 2Dy2Gd, 1Dy3Gd) = 1183.2, 1186.8, 1190. 25, 1193.0 MHz	Berthier and Devine (1980a)
$DyMn_2$	1.4	$^{163}a = 1162$ MHz, $P = 205$ MHz	Shimizu (1982)
$DyFe_2$	1.4	H_{res} → cond. electron contribution	Berthier et al. (1981)
$Dy_2Fe_{14}B$	1.4	$H_{hf}^{1(2)} = 6200(6327)$ kOe	Berthier et al. (1986a)

TABLE A11

Nuclear magnetic resonance of the nucleus ^{165}Ho in intermetallic compounds with magnetically ordered states. Nuclear data: ^{165}Ho, $I = \frac{7}{2}$, natural abundance 100%, $\gamma/2\pi = 0.8901$ MHz kOe^{-1}, $Q = +3.49 \times 10^{-24}$ cm^2 (Shaw et al. 1983).

Compound	Temperature (K)	Remarks	Reference
$HoAl_2$	1.4–1.5	$\langle J_z \rangle$, $\langle J_z^2 \rangle$ analysis; $H_0 \leq 27$ kOe ν_+, $\nu_- = 6512$, 5825 MHz	Prakash et al. (1984)
$Ho_{0.01}R_{0.99}Al_2$	1.4	R = Gd, Tb, Dy, Er; Gd(Pr), Gd(Nd), Gd(Tb), Gd(Dy), Gd(Er), Gd(Tm): a, P, w-analysis	Waind et al. (1983)
$Ho_{0.01}Gd_{0.99}Al_2$	1.3	SC($H_0 \leq 80$ kOe): $a(H_0)$, $P(H_0)$, $w(H_0)$	McMorrow et al. (1986)
$Gd_xY_{0.97-x}Ho_{0.03}Fe_2$	≤4.2	$0 \leq x \leq 0.97$: $a(x)$ non-linear; $P = 59.5$ MHz	Al-Assadi et al. (1984)
$Gd_{0.97-x}Ce_xHo_{0.03}Fe_2$	4.2	$0 \leq x \leq 0.97$; $H_{hf}(x = 0) = 788.4$ kOe, $dH_{hf}/dx \approx -377$ kOe; $P = 60$ MHz	Prakash et al. (1983)
$Gd_xY_{0.97-x}Ho_{0.03}Co_2$	4.2	$0.27 \leq x \leq 0.97$: $a = 6602$ MHz, $P = 60$ MHz, H_{nn}(Gd) = +32 kOe	Arif and McCausland (1975)
$Gd_xY_{0.97-x}Ho_{0.03}Co_2$	4.2	$0.27 \leq x \leq 0.97$: neighbour contribution	Arif et al. (1977)
$Ho_{0.01}Gd_{0.99}(Rh_{1-x}Fe_x)_2$	1.6	$0 \leq x \leq 0.06$: $a(x)$, $P(x)$	Tari (1978)

TABLE A12

Nuclear magnetic resonance of the nucleus ^{167}Er in intermetallic compounds with magnetically ordered states. Nuclear data: ^{167}Er, $I = \frac{7}{2}$, natural abundance 22.8%, $\gamma/2\pi = 0.122$ MHz kOe^{-1}, $Q = +2.8 \times 10^{-24}$ cm^2.

Compound	Temperature (K)	Remarks	Reference
ErZn	1.2	$\nu_Q = 65$ MHz	Devine and Berthier (1981)
$ErAl_2$	1.4	$\nu_{res} = -890$ MHz	Berthier et al. (1978b)
ErX_2	1.2	X = Al, Fe: $\nu_Q = 118$, 130 MHz	Devine and Berthier (1981)
$Er_{1-x}Gd_xAl_2$	1.4	$0 \leq x < 1$; satellites (x), $\nu_Q(x)$	Berthier and Devine (1979b)
$Er_{1-x}Gd_xAl_2$	1.4	$0 \leq x \leq 0.95$; satellites	Berthier and Devine (1980b)
$ErMn_2$	1.4	$a = 910$ MHz, $P = 54$ MHz	Shimizu (1982)
$ErFe_2$	1.4	$H_{res} \rightarrow$ cond. electron contribution	Berthier et al. (1981)
$Er_{1-x}La_xFe_2$	1.2	$x = 0$, 0.1: $\nu_{res} \approx 998$ MHz; T_1	Berthier and Devine (1981)
$ErFe_2H_x$	1.4	$x = (1.45)$, (1.6), 1.84, (2.6), (3.3); $P(x)$, CEF(x), H-location, -diffusion and -filling	Ait-Bahammou et al. (1986)

TABLE A13

Nuclear magnetic resonance of the nucleus ^{169}Tm in intermetallic compounds. Nuclear data: ^{169}Tm, $I = \frac{1}{2}$, natural abundance 100%, $\gamma/2\pi = 0.351$ MHz kOe^{-1}.

Compound	Temperature (K)	Remarks	Reference
(a) Paramagnetic states			
TmX	1.5–27	X = P, As, Sb: $\Delta H_{res}/H_0(T)$, $\Delta H_{res}/H_0(T = 4.2\ K, X = Sb) = +88.7$, $J_{sf} \approx -0.2$ eV	Jones (1967)
TmX	4.2	X = P, As, Sb, Bi: K, $\Delta H(\nu)$	Smith et al. (1971)
TmP	4.2, 27	K(p), $p \leq 4$ kbar	Weaver and Schirber (1976a)
TmH_2	3–37	$H_{res}/H_0(T)$; $T_1(T)$; $T_2(T)$	Winter et al. (1990)
(b) Magnetically ordered states			
$TmFe_2$	1.4	$H_{res} \rightarrow$ cond. electron contribution	Berthier et al. (1981)

TABLE A14

Nuclear magnetic resonance of the nuclei ^{171}Yb(^{173}Yb) in intermetallic compounds with paramagnetic states. Nuclear data: ^{171}Yb, $I = \frac{1}{2}$, natural abundance 14.3%, $\gamma/2\pi = 0.74990$ MHz kOe^{-1}, (^{173}Yb, $I = \frac{5}{2}$, natural abundance 16.1%, $\gamma/2\pi = 0.2066$ MHz kOe^{-1}, $Q = +2.8 \times 10^{-24}$ cm^2).

Compound	Temperature (K)	Remarks	Reference
YbCd	76, 300	$K = 0.334$ %	Schmidt (1973)
YbIn	76, 300	$K = 0.20\%, 0.279\%$	Schmidt (1973)
$YbAl_2$	1.8, 4.2, 20.4	$K = 7.76\%$, $T_1T = 0.12$ s K (1.8 K)	Gossard et al. (1964)
$YbAl_2$	4.2–80	$K = 7.7\%$, $T_1T = 0.035$ s K, $\alpha = 1.1$ MOe μ_B^{-1}	Shimizu et al. (1985b)
$YbAl_3$	1.4–4.2	$K = 100\%$, $T_1T = 1.6 \times 10^{-4}$ s K, $\alpha = 1.2$ MOe μ_B^{-1}	Shimizu et al. (1985b)
$YbAl_2Ga_2$	—	$K(T) \approx 0$	Sampathkumaran et al. (1980b)

TABLE A15

Nuclear magnetic resonance of the nucleus ^{175}Lu in intermetallic compounds. Nuclear data: ^{175}Lu, $I = \frac{7}{2}$, natural abundance 97.4%, $\gamma/2\pi = 0.4857\,\text{MHz kOe}^{-1}$, $Q = +5.6 \times 10^{-24}\,\text{cm}^2$.

Compound	Temperature (K)	Remarks	Reference
(a) Paramagnetic states			
LuCu	76, 300	$K = -0.33\%, -0.34\%$	Schmidt (1973)
LuPd	76, 300	$K = 0.12\%, 0.13\%$	Schmidt (1973)
$Lu_5X_4Si_{10}$	49–310	X = Rh, Ir: ν_Q, $\eta \approx 0.4$, $K(T) \rightarrow$ CDW transition	Chu et al. (1988)
(b) Magnetically ordered states			
$Lu_2Fe_{14}B$	1.4	$H_{hf} = 640$ kOe	Berthier et al. (1986a)

TABLE B1

Nuclear magnetic resonance of the nuclei ^1H and ^2H in intermetallic compounds with paramagnetic states. Nuclear data: ^1H, $I = \frac{1}{2}$, natural abundance 99.98%, $\gamma/2\pi = 4.25759$ MHz kOe^{-1}; ^2H, $I = 1$, natural abundance 0.02%, $\gamma/2\pi = 0.653566$ MHz kOe^{-1}, $Q = +2.87 \times 10^{-27}$ cm^{-2}.

Compound	Temperature (K)	Remarks	Reference
RH_x	77–1000	R = Y, Sc: H diffusion	Weaver (1972)
LaH_x	77–673	$0.4 \leq x \leq 2.85$: H diffusion	Schreiber and Cotts (1963)
LaH_x	4.2–350	$2.89 \leq x \leq 3.00$: line shape, ΔH, T_1; $T > 77$ K: T_1T = constant	Barnes et al. (1980)
$LaH_{2.69}$	225–300	T_{2e}, spectrum	Göring et al. (1980)
CeH_x	6–12	$2 \leq x \leq 3$: $K(x, T)$, $\Delta H(x, T)$	Kopp and Schreiber (1967)
RH_x	77–300	R = Ce, Pr, Nd, Sm; $2 \leq x \leq 2.5$: T_1T	Shen et al. (1969)
RH_2	78–293	R = Pr, Nd, Sm, Gd, Tb: $K = +0.15 - +0.047\%$, $+0.20 - +0.060\%$, $-0.027 - -0.016\%$, $-1.5 - -0.50\%$, $-1.85 - -0.58\%$; $K(T) \leftrightarrow \chi(T)$	Zogał (1983)
TmH_2	3–300	$T_1(T)$, $T_2(T)$; van Vleck state	Winter et al. (1990)
CeD_x	77–573	$2.01 \leq x \leq 2.90$: T_1, $T_2(^2H)$	Raizman et al. (1985)
$Y_{1-x}Ce_xH_y$	370–620	$1.91 \leq y \leq 2.0$, $0 \leq x \leq 0.65$: T_1, T_2; diffusion	Khodosov and Khodos (1971)
$Y_{1-x}Ce_xH_y$	1–400	$1.9 \leq y \leq 2.0$, $0.07 \leq x \leq 0.54$: T_{1e}	Khodosov et al. (1974)
$R_{1-x}Gd_xH_y$	120–1300	R = Y/La; $x \leq 900$ ppm; $1.8 \leq y \leq 2/y \approx 2.2$; $H \leftrightarrow D$; $T_1(^1H, ^2H)$; impurity effects	Phua et al. (1983)
YN_iAlH_x	150–400	$0.12 \leq x \leq 1.17$; two lines; T_1; activation energy 0.24/0.33 eV/atom	Bandyopadhyay et al. (1990)
$LaNi_{5.3}H_6$	118–300	$\Delta H \rightarrow$ H diffusion	Halstead (1974)
$LaNi_5H_x$	4.2–400	H diffusion; ^2H	Barnes et al. (1976)
$LaNi_{5+x}H_6$	150–300	$-0.2 \leq x \leq +0.2$: T_1, $T_{1\rho}$, T_2; H diffusion	Halstead et al. (1976)
$LaNi_5H_{6.1}$	77–298	line width (298 K) = 0.4 Oe	Rubinstein et al. (1979)
$LaNi_{5-y}Al_yH_x$	100–510	$0 \leq y \leq 1.2$, $4 \leq x \leq 6.2$, β-phase: T_1, T_{2d} H diffusion	Bowman et al. (1979)
$LaNi_{4.75}Co_{0.25}H_{6.1}$	77–298	line width = 2.4 Oe	Rubinstein et al. (1979)
$LaNi_{4.75}Pt_{0.25}H_{5.2}$	77–298	line width = 3.0 Oe	Rubinstein et al. (1979)

TABLE B2

Nuclear magnetic resonance of the nucleus ^{9}Be in intermetallic compounds with paramagnetic states. Nuclear data: ^{9}Be, $I = \frac{3}{2}$, natural abundance 100%, $\gamma/2\pi = 0.5983$ MHz kOe^{-1}, $Q = +5.3 \times 10^{-26}$ cm^2.

Compound	Temperature (K)	Remarks	Reference
RBe_{13}		R = La, Ce, Nd, Gd: $T_1(T)$, (K); $(K_{La} \leq 0.005\%)$	Borsa et al. (1973)
RBe_{13}	1.5–700	R = La, Ce, Nd, Gd: K_{iso}; $K_{ani}(\chi)$; $T_1(T)$; $K_0(La) \leq 0.005\%$	Borsa and Olcese (1973)

TABLE B3

Nuclear magnetic resonance of the nucleus ^{11}B (^{10}B) in intermetallic compounds. Nuclear data: ^{11}B, $I = \frac{3}{2}$, natural abundance 81.2%, $\gamma/2\pi = 1.3660$ MHz kOe^{-1}, $Q = +4.0 \times 10^{-26}$ cm^2 (^{10}B, $I = 3$, natural abundance 18.8%, $\gamma/2\pi = 0.45742$ MHz kOe^{-1}, $Q = 8.6 \times 10^{-26}$ cm^2).

Compound	Temperature (K)	Remarks	Reference
(a) Paramagnetic states; or magnetically ordered states with external fields			
RB_2	77, 300	R = Sc, Y: ν_Q, K_{iso}	Barnes et al. (1970)
RB_2	4.2, 77, 300	R = Sc, Y: K, ν_Q	Carter and Swartz (1971)
LaB_4	4–300	ν_Q, K_{iso}, K_z	Creyghton et al. (1973)
NdB_4	77, 296	4e, 8j, 4h sites	Creyghton et al. (1973)
$U_xY_{1-x}B_4$	75–292	$0 \leq x \leq 1$: ΔH, line shape	Fukushima et al. (1975)
RRh_3B_2	77–300	R = La–Gd; R = Pr, Nd: $K \sim \chi$; R = Sm: K = const.; R = Ce, Pr, Nd, Sm (300 K): e^2qQ/h = 332–425 kHz	Malik et al. (1982b)
$SmRh_3B_2$	77–300	$1/T_1 \rightarrow$ itinerant weak AF	Ohno et al. (1989)
RB_6	4.2, 20, 77, 300	R = Sc, Y, La, Ce, Pr, Nd, Sm, Gd, Dy, Ho: $K(T)$, $dK/d\chi$, e^2qQ/h	Gossard and Jaccarino (1962)
RB_6	300	R = Y, La, Ce, Pr, Nd, Eu, Dy, Yb	McNiff and Shapiro (1963)
RB_6	300	R = La, Sm, Eu, Yb: $\|eq\|$	Aono and Kawai (1979)
RB_6	100–480	R = La, Pr, Sm: ν_Q = 0.509, 0.548, 0.568 MHz; K_{iso} = +0.03, −0.04, −0.03%; $K_{\|}$	Bose et al. (1980)
CeB_6	1.4–4.2, 77	10.7 MHz: $K(T)$, line splittings; T = 77 K: e^2qQ/h = 1.06 MHz, K = +0.14%	Kawakami et al. (1981)

CeB_6	1.2–4.2	spin echo: 2.5, 6.5, 13.33, 18.0 MHz	Kawakami et al. (1982)
CeB_6	1.5–7	SC; line splitting (phase II); $f(T, \theta, H) \rightarrow$ possibly AF spin structure	Takigawa et al. (1983a)
CeB_6	1.2–4.2	SC; angular dependence $\rightarrow$ phase II = commensurate AF	Kawakami et al. (1983)
RB_6	2–1050	R = Ce, Sm: $T_1(T)$	Takigawa et al. (1983b)
SmB_6	1.5–300	$T_1(T)$; activated for $T > 15$ K; $K_{iso} = -0.05\%$; $e^2qQ/h = 1.185$ MHz;	Peña et al. (1981a)
SmB_6	2.5–850	$\nu_Q = 0.60$ MHz; 4.2–300 K: $K_{iso} = -0.06\%$, $K_\parallel = -0.04\%$, $\alpha_{iso} = -1.1$ kOe μ_B^{-1}, $\alpha_\parallel = -0.7$ kOe μ_B^{-1}; $T_1(T)$	Takigawa et al. (1981)
SmB_6	2–200	$K_{iso} = -0.07\%$, $K \leftrightarrow \chi$, $\alpha = -0.84$ kOe μ_B^{-1}, $e^2qQ/h = 1.15$ MHz; $T_1(T)$	Peña et al. (1981b)
$Sm_{1-x}La_xB_6$	4–300	$0 \leq x \leq 0.75$: $T_1(T, x)$	Kasuya et al. (1983)
$GdCo_4B_4$	77–300	K_{iso}, $K_{ani} \leftrightarrow \chi$	Ueda et al. (1984)
YRh_4B_4	1.2	$\nu(H)$	Kumagai et al. (1979)
RRh_4B_4	1.2	R = Gd, Tb, Dy, Ho, Er: $\nu(H)$	Kumagai et al. (1979)
RRh_4B_4	90–300	R = Gd, Lu: e^2qQ/h, η, K_{iso}, K_{ani}, $\Delta\nu$	Johnston and Silbernagel (1980)
$ErRh_4B_4$	1.2–4.2	T_1, T_2; $T_1T(H = 3.6$ kOe$) = 58$ s K	Kumagai et al. (1980)
$SmRh_4B_4$	0.04–1.2	$H_0 \neq 0$; ΔH, $T_1(T)$	Kohori et al. (1983b)
RRh_4B_4	0.05–300	R = Sm, Gd: K_{iso}, K_{ani}, T_1, ΔH	Kohori et al. (1983a)
RRh_4B_4	(1.2–10); 300	R = Nd, (Sm), Gd, Tb, Dy, Ho, Er, Tm: K_{iso}, K_{ani}	Kohori et al. (1984)
$DyRh_4B_4$	0.5–300	$T_1(T) \rightarrow JN(E_F)$, CEF	Kohori et al. (1985)
$Y_{1-x}Er_xRh_4B_4$	4.2–77	$x \leq 0.1$: $(T_1T)(x)$, signal intensity $\leftrightarrow T_{sc}(H)$	Tse et al. (1979)
$R_{1-x}R'_xRh_4B_4$	2.4–300	R = Y, Lu; R′ = Gd, Er; $x \leq 0.005$: $T_1(H)T$	Kumagai and Fradin (1983a)
$Y_{1-x}R_xRh_4B_4$	2.4–30	R = Gd, Er; $0.0002 \leq x \leq 0.005$; $T_1(H, T)$, (adiabatic field cycling)	Kumagai and Fradin (1983b)
$Y_{1-x}R_xRh_4B_4$	8–42	R = Tb, Ho: $(1/T_1)_n \sim \exp(-\Delta/kT)$; R = Dy: anomalies of $T_2(T)$, $K(T)$, $\Delta H(T)$	Kumagai et al. (1985)
YbB_{12}	4.2–300	K_{iso} = const.; $K_\parallel(T) \sim \chi$ (30–300 K); $\alpha = 650$ Oe μ_B^{-1} Yb; $T_1(T)$	Kasaya et al. (1985)
(b) Magnetically ordered states (zero-field NMR)			
$R_2Co_{14}B$	4.2	R = Y: $^{11}\nu = 50.25, 53.00, 55.7$ MHz; $^{10}\nu_0 = 17.75, 17.65$ MHz; $^{10}\nu_Q = 0.56, 0.69$ MHz R = Nd: $^{11}\nu = 53.9, 57.4, 61.2$ MHz; $^{10}\nu_0 \approx 20$ MHz; $^{10}\nu_Q \approx 0.5$ MHz	Figiel et al. (1987b)

TABLE B3 (cont'd)

Compound	Temperature (K)	Remarks	Reference
$R_2X_{14}B$	4.2	R = Y, La; X = Co, Fe: $^{10}\nu_{res}$, $^{11}\nu_{res}$; $^{10}\nu_{res}$ = 11.5–20 MHz; $^{11}\nu$(X = Co, R = Y/La) ≅ 19.2/18.4 MHz	Erdmann et al. (1987)
$R_2X_{14}B$	4.2	R = Sm, Gd, Lu; X = Fe, Co	Erdmann et al. (1988b)
$Nd_2(Co_{1-x}X_x)_{14}B$	4.2, 77	X = Mn, Fe, Ni	Ichinose et al. (1988a)
$R_2Fe_{14}B$	4.2	R = La, Ce, Gd: spectrum	Rosenberg et al. (1986)
$R_2Fe_{14}B$	4.2	R = La, Ce, Sm, Er: H_{res} = 28.1/15, 26.8/15, 40.3, 47.5 kOe	Erdmann et al. (1988c)
$R_2Fe_{14}B$	4.2	R = La/Sm; $^{10}B/^{11}B$; wall spectra	Erdmann et al. (1990)
$Nd_2Fe_{14}B$	4.2	H_{hf} = 31.25 kOe; $^{11}\nu(^{10}\nu)$ = 42.5(14.3) MHz	Rosenberg et al. (1985)
$Nd_2Fe_{14}B$	1.3, 4.2	natural/^{10}B-enriched; H_0 = 0/6 kOe, 10–80 MHz	Zhang et al. (1988)
$Nd_2Fe_{14}B$	1.3, 4.2	10–80 MHz; 0/6.0 kOe; $^{10}B/^{11}B$	Zhang et al. (1990)
RCo_4B_4	1.3	R = Gd, Tb, Dy: AF spin structure	Ueda et al. (1984)
RRh_4B_4	1.3	R = Gd, Tb, Dy, Ho; H_{res} = 3.15, —, 4.69, 4.61 kOe	Kohara et al. (1983)
RRh_4B_4	1.3	R = Gd, Tb, Dy, Ho: H_{hf} = 3.15, 3.95, 4.69, 4.61 kOe	Kohori et al. (1983b)
$Dy(Ir_{0.7}Rh_{0.3})_4B_4$	0.5–300	AF structure, zero-field spectra	Kohori et al. (1985)

TABLE B4

Nuclear magnetic resonance of the nucleus ^{13}C in intermetallic compounds with magnetically ordered states. Nuclear data: ^{13}C, $I = \frac{1}{2}$, natural abundance 1.1%, $\gamma/2\pi$ = 1.07054 MHz kOe^{-1}.

Compound	Temperature (K)	Remarks	Reference
$Gd_2Fe_{14}C$	4.2	ν_{res}(4g) = 25.6 MHz	Erdmann et al. (1989)

TABLE B5

Nuclear magnetic resonance of the nucleus ^{25}Mg in intermetallic compounds with paramagnetic states. Nuclear data: ^{25}Mg, $I = \frac{5}{2}$, natural abundance 10.1%, $\gamma/2\pi$ = 0.26054 MHz kOe^{-1}, $Q = +0.22 \times 10^{-24}$ cm^2.

Compound	Temperature (K)	Remarks	Reference
RMg	26–300	R = La, Ce: $K(T)$; K(R = La) = 0.02–0.04%	Schmidt (1973)

TABLE B6

Nuclear magnetic resonance of the nucleus ^{27}Al in intermetallic compounds. Nuclear data: ^{27}Al, $I = \frac{5}{2}$, natural abundance 100%, $\gamma/2\pi = 1.10936\,\text{MHz kOe}^{-1}$, $Q = +0.15 \times 10^{-24}\,\text{cm}^2$.

Compound	Temperature (K)	Remarks	Reference
(a) Paramagnetic states			
$La_{3-x}Gd_xAl$	1.2–4.2	$0 \leqslant x \leqslant 0.02$: $T_1(x, T, H)$	Masuda and Hashimoto (1971)
$(La_{1-x}R_x)_3Al$	1.2–20	R = Ce, Gd: T_1 (normal, supercond.)	Matsui and Masuda (1977)
RAl	150–350	R = La, Gd, Tb, Dy, Ho, Er: $K(T)$; $-0.16\,\text{eV} \leqslant J_{sf} \leqslant -0.14\,\text{eV}$; $2J(0) = -0.39\,\text{eV}$ (RKKY)	van Diepen et al. (1968b)
CeAl	90–475	$K(T)$, ΔH, ν_Q; $K_0 = +0.10\%$; $J_{sf} = -0.25\,\text{eV}$	Niculescu et al. (1972)
$ScAl_2$	295	$K(T)$	Cherchernikov et al. (1969)
RAl_2	295	R = Y, La, Lu: K_0	Barnes and Jones (1967)
RAl_2	4.2–300	R = La, Ce, Pr, Nd, Sm, Eu, Gd, Tb, Dy, Ho, Er, Tm, Yb, Lu: $K(T)$, ν_Q, J_{sf}	Jaccarino et al. (1960); Jaccarino (1961)
RAl_2	77–373	R = La, Ce, Pr, Nd, Sm, Yb, Lu: $1/T_1 = 1/T_{1,s} + 1/T_{1,f}$; $\rightarrow \tau_c$	Silbernagel et al. (1968)
$LaAl_2$	90–300	$K(T)$, ν_Q, T_1T	Silbernagel and Wernick (1973)
$CeAl_2$	140–460	$K(T)$, χ; $K_0 = +0.136\%$; $J_{sf} = -0.23\,\text{eV}$	Niculescu et al. (1971)
$CeAl_2$	90–475	$K(T)$, ΔH, ν_Q; $K_0 = +0.085\%$, $J_{sf} = -0.2\,\text{eV}$	Niculescu et al. (1972)
$CeAl_2$	2–295	$T > 3.8\,\text{K}$ (PM): $K(\chi)$, K_{iso}, K_{ani}, e^2qQ	MacLaughlin and Hewitt (1978)
$CeAl_2$	3.9–295	K_{iso}, K_{ani}, e^2qQ, T_1 (NMR, NQR)	MacLaughlin et al. (1981)
$PrAl_2$	77–300	$K(T)$, ν_Q-powder analysis	Jones et al. (1963)
$SmAl_2$	150–390	$K(T) < 0$	Buschow et al. (1967)
$SmAl_2$	150–400	$K(T)$, ν_Q	de Wijn et al. (1973)
$GdAl_2$	350–575	$K(T)$, ν_Q, $K_0 = +0.13\%$, $J_{sf} = -0.13\,\text{eV}$	Jones and Budnick (1966)
$GdAl_2$	200–350	$K_{iso}(\chi)$, $\alpha = -7.3\,\text{kOe}\,\mu_B^{-1}$, $K_\parallel(\chi)$, $\nu_Q(340\,\text{K}) = 600\,\text{kHz}$	Barash et al. (1982)
$DyAl_2$	96–350	$K_{iso}(\chi)$, $\alpha = -3.24\,\text{kOe}\,\mu_B^{-1}$, $K_\parallel(\chi)$, $\nu_Q(340\,\text{K}) = 557\,\text{kHz}$	Barash et al. (1982)
$DyAl_2$	330	SC: ν_Q, $K_{iso}(T)$, $K_\parallel(T)$	Barash et al. (1983)
RAl_2	—	R = Tm, Yb: $\Delta\nu \rightarrow K_{iso}$, $K_\parallel$, ν_Q	Barnes et al. (1961)
$Y_{1-x}Dy_xAl_2$	1.6–20.4	$3 \times 10^{-3} \leqslant x \leqslant 7 \times 10^{-3}$: $T_1(T)$	Abe (1975)
$La_{1-x}Gd_xAl_2$	1.5–20	$0 \leqslant x \leqslant 0.1$: NQR/NMR; ν_Q, T	MacLaughlin and Daugherty (1972)

TABLE B6 (cont'd)

Compound	Temperature (K)	Remarks	Reference
$La_{1-x}Gd_xAl_2$	1.2–300	$0.0013 \leq x \leq 0.10$: K, T_1	McHenry et al. (1972)
$La(Gd)Al_2$	1.4–4.2	0–3000 ppm; $1/T_1$(NQR); $(T_1T)_n = 18.2$ s K	MacLaughlin et al. (1973)
YCuAl	—	$K_0 = +0.043\%$	Buschow et al. (1971)
YCuAl	4.2–295	$K_0 = 0.045\%$; T_1	MacLaughlin et al. (1979)
GdCuAl	190–300	$K(T) \leftrightarrow \chi(T)$; $J_{sf} = -0.31$ eV	Buschow et al. (1971)
YbCuAl	4.2–295	$K(T) \leftrightarrow \chi(T)$; $T_1(T)$	MacLaughlin et al. (1979)
YbCuAl		$K(\chi)$ non-linear for $T < T_{max} \approx 27$ K; $K_0 = +0.075\%$, $\alpha = +1.12$ kOe μ_B^{-1}	MacLaughlin (1981)
$ScAl_3$	295	$K = +0.16\%$	Cherchernikov et al. (1969)
RAl_3	78–450	R = La, Ce, Pr, Nd, Gd, Tb: $K(T)$, ν_Q, $J_{sf} = -0.2$ eV	van Diepen et al. (1967)
$CeAl_3$	140–460	$K(T)$, ΔH, χ; $K_0 = +0.075\%$; $J_{sf} = -0.439$ eV	Niculescu et al. (1971)
$CeAl_3$	90–475	$K(T)$, ΔH, K_0; $J_{sf} = -0.33$ eV	Niculescu et al. (1972)
$CeAl_3$	1.5–300	$K_{iso}(T) \leftrightarrow \chi(T)$; $T_1(T)$	Lysak and MacLaughlin (1985)
$CeAl_3$	0.3–50	$\Delta H(T)$; $1/T_1(T)$; AF ord., $T_N = 1.2$ K	Nakamura et al. (1988a)
$CeAl_3$	0.4, 1.2	spectrum $f(H_0)$; 3 kOe; ΔH	Nakamura et al. (1988b)
$Ce_xLa_{1-x}Al_3$	3.5–300	$x = 0, 0.3, 0.7, 1.0$; spectra, T_1	Joon et al. (1989)
$Ce_{1-x}Gd_xAl_3$	1.5–300	$0 \leq x \leq 0.02$; $1/T_1$, K_{iso}, K_{ani}	Moore et al. (1990)
$SmAl_3$	78–400	$K(T)$; $\lvert e^2qQ\rvert/h = 0.8$ MHz; van Vleck paramagnetism	de Wijn et al. (1967)
RAl_3	100–420	R = Dy, Ho, Er: $K(T)$; J_{sf}	van Diepen et al. (1968a)
RAl_3	100–300	R = Er, Tm, Yb: $K \leftrightarrow \chi$; J_{sf}; e^2qQ	de Wijn et al. (1970)
$YbAl_3$	4.2–300	$K(T) \leftrightarrow \chi(T)$; ν_Q	Buschow et al. (1979)
$YbAl_3$		$K(\chi)$ non-linear for $T < T_{max} \approx 120$ K; $K_0 = +0.022\%$, $\alpha = 0.78$ kOe μ_B^{-1}	MacLaughlin (1981)
R_3A_{11}	86–300	R = La, Pr, Nd: $K_{I,II}(T)$; $J_{sf}^{I,II}$; $2J(0)$	van Diepen et al. (1969)
RAl_2Ga_2	—	R = La, Ce, Pr, Nd, Eu, Yb: $e^2qQ/h = 4.40$, 4.10, 4.00, 3.95, 5.50, 4.50 MHz	Sampathkumaran et al. (1980b)
$CeAl_4$	140–460	$K(T)$, ΔH, χ; $K_0 = +0.08\%$; $J_{sf} = -0.169$ eV	Niculescu et al. (1971)
$CeAl_4$	90–475	$K(T)$; ΔH; K_0; $J_{sf} = -0.17$ eV	Niculescu et al. (1972)
$EuAl_4$	86–300	$K(T)$; $J_{sf} = -0.14$ eV; $2J(0) = -0.5$ eV	van Diepen et al. (1969)
$Gd_2X_6Al_{11}$	130–450	X = Co, Cu: $K(T) \leftrightarrow \chi(T)$; J_{sf}, J_{sd}	Pop et al. (1978)
$Tb_2Ni_{17-x}Al_x$	160–410	$17 > x > 15.75$: $K(T) \leftrightarrow \chi(T)$	Hågan and Pop (1986)
$Ce_{1-x}R_xAl_{13}$	100–475	R = Y, La: $K(T)$, (satellite)	Niculescu et al. (1973b)

$Ce_{1-x}R_xAl_{13}$	100–475	R = Gd, Tb, Er; $0 \leq x \leq 0.07$: $K(T)$, $K_{satellite}(T)$, $\Delta H(T)$	Niculescu et al. (1973a)
(b) Magnetically ordered states			
$GdAl_2$	4.2, 77	$\nu(4.2\,K) = 49.2\,MHz$; $H_{hf} < 0$	Budnick et al. (1965)
RAl_2	4.2	R = Pr, Nd, Sm, Gd, Tb, Dy, Ho: easy axis, anisotropy, J_{sf}	Kaplan et al. (1973)
$CeAl_2$	1.5–300	AF: T_1(NQR), $\Delta\nu$, N_{rel} ($\nu \approx 1.45\,MHz$)	MacLaughlin (1980)
$CeAl_2$	1.5–3.9	AF: NQR(1.45 MHz): $\Delta\nu$, N_{rel}, T_1	MacLaughlin et al. (1981)
$SmAl_2$	1.4	$H_{res} = +32.5\,kOe$	Vijayaraghavan et al. (1977)
$GdAl_2$	4.2	spectrum spin echo ampl.oscil. (ν_Q)	Shamir et al. (1971)
$GdAl_2$	4.2, 77	line profiles	Dormann (1972)
$GdAl_2$	4.2–112	$\nu_Q(T; M)$; magn. induced quadr. interaction	Degani and Kaplan (1973)
$GdAl_2$	4.2–120	$H_{hf}(T) \leftrightarrow M_s(T)$	Herbst et al. (1974)
$GdAl_2$	4.2	SC; $A_{zz}/\gamma\hbar = -15.313\,kOe$, $A_{\perp}/\gamma\hbar = -14.825\,kOe$	Fekete et al. (1975)
$GdAl_2$	4.2–77	[221]→[111] spin reorientation?	Bowden et al. (1977)
$GdAl_2$	4.2	[111]; spin reorient. improbable	Eidelman et al. (1978)
$GdAl_2$		[111] easy axis confirmed	Bowden (1978)
$GdAl_2$	4.2, 77	origin of signals; a: [111] domain, b: [110] wall; $\nu_Q(\nu, T)$ discussion	Bowden et al. (1983)
$GdAl_2$	1.5	SC; $K = -0.25\%$	Kropp et al. (1983)
$GdAl_2$	4.2, 85–160	$\nu(T) \leftrightarrow M(T)$ ($T \leq 0.94T_c$)	Barash and Barak (1984)
$GdAl_2$	4.2, 77	$\nu_Q(\nu_{res})$; origin of signals; $\partial(\ln P)/\partial(\ln p) = +14\,kbar^{-1}$	Dumelow et al. (1988)
$GdAl_2$		$\partial(\ln P)/\partial(\ln V)) = -1.1$	Riedi et al. (1988)
$GdAl_2$	4.2	$T_1(H_1)$, $T_2(H_1)$	Oliveira and Guimarães (1988)
$GdAl_2$	4.2	SC/powder spectra; simulation of wall spectra	Bauer and Dormann (1990)
$DyAl_2$	4.2	quadrupole oscillation, origin of signals	Bowden et al. (1982)
$DyAl_2$	4.2, 10–26	$\nu(T) \leftrightarrow M(T)$ ($T \leq 0.42T_c$)	Barash and Barak (1984)
$Sm_{1-x}Gd_xAl_2$		$0 \leq x \leq 0.5$: $H_{res}(x)$	Grover et al. (1979)
$Gd_{1-x}Y_xAl_2$	4.2	$0 \leq x \leq 0.6$: $\nu_{res}(x)$	Dintelmann et al. (1970)
$Gd_{1-x}Y_xAl_2$	4.2	$0 \leq x \leq 0.2$: $H_{hf}(x)$	Dintelmann and Buschow (1971)
$Gd_{1-x}R_xAl_2$	4.2	R = Y, La; $0 \leq x \leq 0.3$: line profile ↔ RKKY	Dormann et al. (1973)
$Gd_{1-x}Tb_xAl_2$	4.2	$0 \leq x \leq 1$: $H_{res}(a, b)$ linear $(x) \leftrightarrow$ [111], H_{dip}^{Gd} 14% larger than for point dipoles	Ichinose et al. (1984b)

TABLE B6 (cont'd)

Compound	Temperature (K)	Remarks	Reference
$Gd_{1-x}Dy_xAl_2$	4.2	$0 \leq x \leq 0.085$: [111]→[100]; $\nu_Q(\nu; 3\cos^2\theta - 1)$	Miles et al. (1977)
$Gd_{1-x}Dy_xAl_2$	4.2	$0 \leq x \leq 0.3$: [111]; $0.4 \leq x \leq 1$: [100]	Ichinose et al. (1984a)
$Y(Mn_{1-x}Al_x)_2$	1.3, 4.2–20	$0 \leq x \leq 0.3$: $(1/T_1)_{\text{Korringa}} = \text{const.}\ (x)$	Yoshimura et al. (1986b)
$Y(Mn_{0.90}X_{0.08}Al_{0.02})_2$		X = Co, Fe: $T_1(T)$	Yoshimura et al. (1986b)
$Gd(Al_{1-x}Co_x)_2$	4.2	$0 \leq x \leq 1$; $0.4 \leq x \leq 0.6$: $\nu_{res}(6h/2a) = 37/27$ MHz	Ichinose (1987)
$Y(Fe_{1-x}Al_x)_2$	4.2	$x = 0.02$: $H_{hf} = -27.9$ kOe	Oppelt and Buschow (1976)
$Y(Fe_{1-x}Al_x)_2$	4.2	$0 \leq x \leq 0.2$; $\nu \leq 29$ MHz	Ichinose et al. (1985)

TABLE B7

Nuclear magnetic resonance of the nucleus ^{29}Si in intermetallic compounds with paramagnetic states. Nuclear data: ^{29}Si, $I = \frac{1}{2}$, natural abundance 4.7%, $\gamma/2\pi = 0.84577$ MHz kOe^{-1}.

Compound	Temperature (K)	Remarks	Reference
$CeSi_x$	1.3–300	$1.70 \leq x \leq 2.00$: $T_1(x, T)$	Kohori et al. (1986)
RX_2Si_2	77–550	R = La, Ce; X = Cu, Ag, Au: $K_{R=La} = +0.1\%$, $K_{R=Ce}(T)$;	Sampathkumaran et al. (1979a)
RCu_2Si_2	(77), 300	R = La, Ce, Pr, Sm, Gd, Er, Tm, Yb: K_{iso}; K_0(R = Y, La; 77–500 K) = 0.08%	Sampathkumaran et al. (1979b)
$LaCu_2Si_2$	4.2–77	$K_{iso} = 0.084$–0.087%; $T_1T = 39.5$–49 s K	Aarts et al. (1983)
$CeCu_2Si_2$	1.5–300	$K_{iso}(\chi)$ linear for $T > 7$ K; $\alpha = 5.1$ kOe μ_B^{-1}; K_{ani} increase at low T; $T_{1,\parallel/\perp}(T)$	Aarts et al. (1983)
$CeCu_2Si_2$	0.2–50	$K_\parallel(T)$; $K_\perp(T)$; $K_\perp(0.2\text{ K}) = 0.4K_\perp(T_c(H))$	Ueda et al. (1987)
$CeRu_2Si_2$	2–300	$0.10\% \leq K \leq 0.38\%$; $K(\chi)$ linear; $\alpha = 1.1$ kOe μ_B^{-1}	Gupta et al. (1983)
$CeRu_2Si_2$	1.5–150	$K(T)$, $T_1(T)$; powder ($K_\parallel$, $K_\perp$)	Kitaoka et al. (1985a)
$CeRu_2Si_2$	1.2–77	T_1T	Kitaoka et al. (1986)
$YbPd_2Si_2$	4.2–200	K, T_1T; $K_\perp \approx -0.15\%$; $K_\parallel = f(T)$; $K_{0,\parallel} \approx 0.13\%$; $K_\parallel \leftrightarrow \chi$: $\alpha = 0.75$ kOe μ_B^{-1}, $K(\chi)$ non-linear for $T < 25$ K	Besnus et al. (1988)

TABLE B8

Nuclear magnetic resonance of the nucleus ^{31}P in intermetallic compounds with paramagnetic states. Nuclear data: ^{31}P, $I = \frac{1}{2}$, natural abundance 100%, $\gamma/2\pi = 1.7236$ MHz kOe^{-1}.

Compound	Temperature (K)	Remarks	Reference
RP	1.5–680	R = Sc, Y, La, Ce, Pr, Nd, Sm, Eu, Gd, Tb, Dy, Ho, Er, Tm, Yb, Lu: $K(T)$	Jones (1969)
RP	76, 300	R = Ce, Pr, Nd, Sm, Eu, Gd, Tb, Dy, Ho, Er, Tm, Yb: $T_1(T)$	Myers and Narath (1974)
CeP	9–200	$K(\chi)$ non-linear	Myers and Narath (1973b)
CeP	37–298	$d(\ln K)/dp$, $p \leq 4$ kbar	Weaver and Schirber (1976a)
PrP	4.2–300	$K(p)$, $d(\ln K)/dp$, $p \leq 4$ kbar	Weaver and Schirber (1976b)
EuP	100–600	$K(T)$; $K_0 = 0.06\%$, $J_{sf} = -0.37$ eV	Jones (1968)
GdP	300	$T_1(H)$	Myers and Narath (1971)
GdP	300	T_1, $T_2(H)$	Myers and Narath (1973a)
GdP	—	$T_1(H)$ analysis	Tucker (1974)
YbP	4–300	$d(\ln K)/dp$	Weaver and Schirber (1976a)
YbP	0.38–600	$1/T_1$; $T_{ord} \approx 0.7$ K; $K(\chi)$ slope change at $T \approx 100$ K	Takagi et al. (1988b)
$Y_{1-x}Tb_xP$	4–300	$x = 0.005, 0.05, 0.10, 0.30$: $K(x, T)$, ΔH	Quinn and Weaver (1976)
La(Ce)P	0.4–300	$\leq 5\%$; $\Delta H_{nn}/\langle J_z \rangle \neq$ const. for $T \geq 26$ K	Follstaedt et al. (1977)
R(Gd)P	2	R = La, Lu: $^{31}H_{nn}$(Gd)	Myers and Narath (1973a)
EuX_2P_2	77–500	X = Co, Ni: $K(T)$	Sampathkumaran et al. (1982a)
$EuNi_2P_2$	5–300	$K(T) \leftrightarrow \chi(T)$	Sampathkumaran et al. (1985)

TABLE B9

Nuclear magnetic resonance of the nucleus ^{51}V in intermetallic compounds, with magnetically ordered states. Nuclear data: ^{51}V, $I = \frac{7}{2}$, natural abundance 99.8%, $\gamma/2\pi = 1.1193$ MHz kOe^{-1}, $Q \approx -5.2 \times 10^{-26}$ cm^2.

Compound	Temperature (K)	Remarks	Reference
$Y(Fe_{0.99}V_{0.01})_2$	4.2	$a = 51.5$ MHz; $2P = 171$ kHz	Dumelow et al. (1987)
$Ho(Fe_{0.96}V_{0.04})_2$	4.2	$a = 60.0$ MHz; $2P = 178$ kHz	Dumelow et al. (1987)
$Y_{0.97}Ho_{0.03}(Fe_{0.99}V_{0.01})_2$	4.2	$a = 52.0$ MHz; $2P = 172$ kHz	Dumelow et al. (1987)

TABLE B10

Nuclear magnetic resonance of the nucleus ^{55}Mn in intermetallic compounds. Nuclear data: ^{55}Mn, $I = \frac{5}{2}$, natural abundance 100%, $\gamma/2\pi = 1.0501$ MHz kOe^{-1}, $Q = +0.4 \times 10^{-24}$ cm^2.

Compound	Temperature (K)	Remarks	Reference
(a) Paramagnetic states			
$ScMn_2$	4.2, 77, 300	K, ν_Q	Barnes and Lunde (1970)
$ScMn_2$	77–230	$T_1T = 0.057$ s K	Yoshimura et al. (1987)
RMn_2	77, 300	R = Er, Tm: $K_{I,II}(T)$, ν_Q	Barnes and Lunde (1975)
$Y_{0.97}Sc_{0.03}Mn_2$	4.2–180	$1/T_1 \sim T^{1/2}$	Yoshimura et al. (1987)
$Y_{0.97}Sc_{0.03}Mn_2$	0.3–20	NQR; $1/T_1(T)$	Nakamura et al. (1988e)
(b) Magnetically ordered states			
GdX: Mn	4.2	X = Zn, Cd; 1 at.%; $H_{res} = +162.8/173.9$ kOe	Kasamatsu et al. (1988)
YMn_2	4.2	$H_{hf} = 120$ kOe; AF; $\mu_{Mn} = 2.7\ \mu_B$	Shiga et al. (1983)
YMn_2	4.2	[111] 3:1 shape: 112.4/123.8 kOe; AF; ± 42.7 kOe μ_B^{-1}	Yoshimura and Nakamura (1983)
RMn_2	1.4	R = Gd, Tb, Dy, Ho, Er, Tm: $H_{hf} = 130, 104, 70, 24, 19, 12.4$ kOe	Shimizu et al. (1981)
RMn_2	4.2	R = Gd, Tb, Ho: $H_{hf} = (96.2 + 4.7(g-1)J)$ kOe	Nagai et al. (1981)
RMn_2		H_{hf}(R) ↔ Mn ion moment	Malik et al. (1982a)
RMn_2	4.2	R = Pr, Nd, Sm; 2 sites; $\nu_{center} \cong 145$, 136, 101 MHz; AF; quadrupole split.	Yoshimura and Nakamura (1984)
RMn_2	1.4, 4.2	R = Gd, Tb, Dy, Ho, Er: $H_{res} = 130.5 \ldots 19$ kOe	Shimizu (1985a)
RMn_2	4.2, 77	$\nu CH_0 \leq 60$ kOe); R = Gd, Tb, (Dy): $\mu_{Mn} \approx 2.5\ \mu_B$; R = (Dy), Ho, Er, Tm: $\mu_{Mn} \approx 0$; R = Dy: 2 lines 73/25 MHz	Yoshimura et al. (1986a)
$R_{1-x}R'_xMn_2$	1.4, 4.2	R = Gd, Tb; R′ = Y, Er, Lu: ν_{res}	Shimizu (1985a)
$Tb_{1-x}Gd_xMn_2$	1.4	$x = 0.6/0.4$: $\nu = 127/125$ MHz	Shimizu (1985b)
$Y_{1-x}R_xMn_2$	(1.4), 4.2	R = La: $0 \leq x \leq 0.25$; R = Sc, $x \leq 0.02$: $\nu_{res} \approx$ 120 MHz (AF); R = Sc, $x = 0.02$: $K \approx 0$; ν_Q	Nakamura et al. (1988f)
$Y_{1-x}Tb_xMn_2$	1.4	$0 \leq x \leq 0.1$: 120 MHz line → symmetric	Berthier et al. (1988a)
$Gd_{1-x}Lu_xMn_2$	4.2	$0 \leq x \leq 0.3$, zero-field spectra	Makihara et al. (1988)
$Y(Mn_{1-x}Al_x)_2$	1.3	$0 \leq x \leq 0.28$: $\nu_{res} \approx 120$ MHz	Shiga et al. (1986)

$Y(Mn_{1-x}X_x)_2$	1.3, 4.2–20	X = Al, Fe, Co; $0 \leq x \leq 0.3$	Yoshimura et al. (1986b)
$Gd(Mn_{1-x}Co_x)_2$	1.7	$H_{res} \approx 119$ kOe $\neq f(x)$ for $x \leq 0.2$	Okamoto et al. (1986)
$Gd(Mn_{1-x}Co_x)_2$	4.2	$0 \leq x \leq 1$; $\nu_{res}(x = 0) = 120$ MHz	Ichinose (1987)
$Y(Fe_{1-x}Mn_x)_2$	4.2	$0 \leq x \leq 0.2$: ν(Mn on Fe sites) ≈ 120 MHz; ν(Mn on Y sites) = 380, 365, 352 MHz	Besnus et al. (1982)
$Y(Fe_{1-x}Mn_x)_2$	4.2	$x \leq 0.5$; $x = 0.05$: 3:1 ratio	Nagai (1989)
Y_6Mn_{23}	4.2	FIM, 42.7 kOe/μ_B; $\nu(32f_1, f_2) \approx 92$ MHz, ν(24d/4b) = 114/128 MHz	Yoshimura and Nakamura (1983)
R_6Mn_{23}	4.2	R = Y, Gd, Ho; 4 sites; H_N^R	Nagai et al. (1988a)
$(Y_{1-x}Gd_x)_6Mn_{23}$	4.2, −300	$0 \leq x \leq 1$: $H_{res}(T)$; $H_N^{Gd} \leq 13$ kOe	Nagai et al. (1981)
$LaMn_2Si_2$	4.2, 77	173.2, 169.5 MHz	Sampathkumaran et al. (1982b)
RMn_2Ge_2	4.2, (77)	R = La; Ce; Pr; Nd; Tb; Dy; Er: ν_{res} = (211.5); (199.5); (194.0); 199.0 (194.0); 188; 194.5; 203.0 MHz	Sampathkumaran et al. (1982b)
RMn_2Ge_2	1.7–390	R = La: ν_{res} = 206–228 MHz; R = Nd, Gd: $\nu_{res}(T)$ anomalous (T_{ord} = 30, 95 K); R = Gd: $e^2qQ/h = 3.2$ MHz, ν_{res}(4.2 K) = 180, 196(−230) MHz	Hiraoka et al. (1987)
$Y_{1-x}La_xMn_2X_2$	4.2	X = Si/Ge; $0.3 \leq x \leq 1$; $\nu_{res}(x = 1)$ = 173/213 MHz	Ichinose et al. (1988b)
YMn_{12}	4.2	FIM; ν(8i, 8j) ≈ 15 MHz, ν(8f) = 3 MHz	Yoshimura and Nakamura (1983)

TABLE B11

Nuclear magnetic resonance of the nucleus ^{57}Fe in intermetallic compounds in magnetically ordered states. Nuclear data: ^{57}Fe, $I = \frac{1}{2}$, natural abundance 2.1%, $\gamma/2\pi = 0.13756$ MHz kOe^{-1}.

Compound	Temperature (K)	Remarks	Reference
$ScFe_2$	4.2, 77, 293	$(MgCu_2)$: $H_{res}(4.2\ K) = -189.7/-200.3$ kOe, $(MgNi_2)$: $\lvert H_{res}\rvert = 175.2/189.0/197.0$ kOe	Pokatilov et al. (1985)
YFe_2	4.2	$H_{res} = 206.5/212$ kOe (1:3)	Oppelt and Buschow (1973)
YFe_2	4.2	$\nu(0/10\ kbar) = 28.80/28.54$ MHz	Belov et al. (1981)
YFe_2	4.2	$\nu_0 = 28.8$ MHz; $d\nu/dp = -24.5$ kHz/kbar ($p \leq 7$ kbar)	Vasil'kovskii et al. (1981a)
YFe_2	4.2	$\nu_{res} = 28.8$ MHz	Vasil'kovskii et al. (1983)
YFe_2	4.2	$\nu_0 = 29.36$ MHz; $\partial(\ln H)/\partial p = -4.2 \times 10^{-4}$ kbar^{-1}	Dumelow et al. (1986)
$SmFe_2$	1.4	$H_{res} = 182/228$ kOe	Vijayaraghavan et al. (1977)
$GdFe_2$	4.2	$\nu_{res} = 31.3/32.4$ MHz	Gegenwarth et al. (1966)
$GdFe_2$	4.2	$\nu_0 = 32.5/31.3$ MHz; $d\nu/dp = 27.5$ kHz kbar^{-1}; ($p \leq 7$ kbar)	Vasil'kovskii et al. (1981b)
RFe_2		R = Y, Gd, Tb, Dy, Ho, Er, Tm: H_{hf} (lattice constant)	Vasil'kovskii et al. (1981b)
$Gd_{1-x}Y_xFe_2$	4.2	$H_{hf}(x)$, discontinuity at $x \approx 0.57$; $x = 0$: 240/255 kOe; $x = 1$: 220/210 kOe	Nikitin et al. (1975b)
$Sc_{1-x}Zr_xFe_2$	4.2	$0 \leq x \leq 1$; $H_{hf}(x)$	Pokatilov et al. (1989)
$Gd(Co_{1-x}Fe_x)_2$	4.2	$x = 0.1 \rightarrow 0.8$: $\lvert H_{res}\rvert = 260 \rightarrow 240$ kOe	Belov et al. (1976b)
YFe_3	4.2	$\nu_{res}^{II} = 31.3$ MHz	Nikitin et al. (1975a)
$GdFe_3$	4.2	$\nu_{res}^{I,II,III} = 38, 31.4\ 35.3$ MHz	Nikitin et al. (1975a)
$Gd_{1-x}Y_xFe_3$	4.2–300	$H_{hf}(x)$, 3 sites; $\nu(x = 0) = 31.5, 35.3, 38.0$ MHz; $\nu(x = 1) = 31.7, 34.7$ MHz	Nikitin et al. (1976)
$Y_2Fe_{14}B$	4.2	Fe spectrum poorly resolved; $\nu)k_1) = 44.2$ MHz	Erdmann et al. (1987)
$R_2Fe_{14}B$	4.2	R = La, Ce, Gd: spectrum	Rosenberg et al. (1986)
$R_2Fe_{14}B$	4.2	R = La, Ce, Sm, Er: site assignment	Erdmann et al. (1988c)
$Nd_2Fe_{14}B$	4.2	$H_{res} = 300 \ldots 375$ kOe	Rosenberg et al. (1985)
$Nd_2Fe_{14}B$	1.3, 4.2	$H_0 = 0/6$ kOe; wall edge/center; Fe precipitate	Zhang et al. (1988)
$Nd_2Fe_{14}B$	1.3, 4.2	^{10}B enriched; Fe: 41.5, 44.0, 44.7, 46.0, 48.5, 52.0, 53.0 MHz	Zhang et al. (1989)
$Lu_2Fe_{14}B$	4.2	$H_{hf}(8j_1.\ 16k_2, 8j_2) = 294, 330, 371$ kOe	Erdmann et al. (1988b)
$Gd_2Fe_{14}C$	4.2	$H_{res}(16k_1, 16k_2, 8j_1, 8j_2) = 323, 349, 314, 390$ kOe; T_2	Erdmann et al. (1989)
$GdFe_{12-x}Mo_x$		$x = 2$; comparison with Mössbauer effect	Sinnemann et al. (1989)
$Fe_{10}Si_2$	4.2	R = Er, Lu; spectra	Sinnemann et al. (1990)

TABLE B12

Nuclear magnetic resonance of the nucleus ^{59}Co in intermetallic compounds. Nuclear data: ^{59}Co, $I = \frac{7}{2}$, natural abundance 100%, $\gamma/2\pi = 1.0054$ MHz kOe^{-1}, $Q = +0.42 \times 10^{-24}$ cm^2.

Compound	Temperature (K)	Remarks	Reference
(a) Paramagnetic states			
Y_4Co_3	1.79–4.2	$-2\%(1.79\text{ K}, 4\text{ MHz}) \leq K \leq +2.5\%(4.2\text{ K}, 9\text{ MHz})$	Lewicki et al. (1983)
Y_4Co_3	1.3–77(–130)	(6h/2d): $K_{iso} = 1.47/2.88\%$, $\nu_Q =$ 0.83/1.25 MHz; (T_1'(6h))	Wada et al. (1983)
Y_4Co_3	1.5–250	3 sites: $K(T)$, ν_Q; only K(2b) large, negative ($\alpha = -78$ kOe μ_B^{-1} Co(2b))	Takigawa et al. (1983c)
Y_9Co_7	1.5–4.2	$T_1(T)$, $T_2(T)$; non-magnetic Co sites	Figiel et al. (1987a)
RCo_2	300	R = Sc, Y, Ce, (Pr), Nd, Er, Tm, Lu: ν_Q	Barnes and Lecander (1967)
YCo_2	4.2–150	$K \leftrightarrow \chi$, $\alpha = -89$ kOe μ_B^{-1}	Hirosawa et al. (1979)
RCo_2	4.2–280	R = Y, $T = 4.2$ K: $K_\parallel$, $K\perp$; R = Pr, Er, Tm: $K(T)$	Hirosawa and Nakamura (1982c, e)
YCo_2	4.2–500	$K(T) \leftrightarrow \chi(T)$; $T_1(T)$; $T_1T\chi_d$	Yoshimura et al. (1984b)
$CeCo_2$	0.05–10	NQR; $T_1(T)$, $T < T_{sc} = 0.95$ K: enhancement, gap	Kitaoka et al. (1985c)
$Y_{1-x}Gd_xCo_2$	4.2–220	$K(T) \leftrightarrow \chi(T)$; $K(x)$	Hirosawa et al. (1979)
$Y(Ni_{1-x}Co_x)_2$	4.2–300	$K(x, T)$; $T_1T(x, T)$	Nagai et al. (1988b)
$Lu(Co_{1-x}Al_x)_2$	4.2	$x = 0$–0.08: $K \leftrightarrow \chi$; $x = 0.06$–0.12: coexisting PM/FM	Endo et al. (1988)
$GdCo_4B_4$	77–300	$\nu_Q \approx 2$ MHz; $K \leftrightarrow \chi$; $\alpha_{iso} = -800$ Oe μ_B^{-1}	Ueda et al. (1984)
(b) Magnetically ordered states			
R_4Co_3	4.2	R = Y: line profile $f(H_0)$; Co I non-magnetic, Co II weak-magnetic moment; R = Gd: ν_{res}(6h/2d/1b) = 45.5/62.5/(57) MHz; AF field dependence	Figiel et al. (1981)
Y_4Co_3	1.3	NQR: 1.7, 2.5, 3.7 MHz	Wada et al. (1983)
Y_4Co_3	2.1–4.2	ν(zero field) = 18 MHz	
	1.5	NQR: 1.7, 2.55, 3.7, (6.3) MHz; ν_Q(2d) = 0.85 MHz, η(2d) = 0; ν_Q(6h) = 1.40 MHz, η(6h) = 0.9; K_{iso}(2d) = 1.30%; K_{iso}(6h)≈1.6–1.9%	Takigawa et al. (1983c)
GdX: Co	4.2	X = Zn/Cd; 1 at.%; $H_{res} = -102.3/-102.0$ kOe	Kasamatsu et al. (1988)
$GdCo_2$	≤4.2	$H_{res} = 60.7$ kOe	Taylor and Christopher (1969)
$GdCo_2$	1.4–260	$H_{res}(1.4\text{ K}) = +61.3$ kOe	Wang et al. (1974)

TABLE B12 (cont'd)

Compound	Temperature (K)	Remarks	Reference
$GdCo_2$	1.3–335	T-dependent splitting; changes at 200 K ($\neq$[100]); 300 K (intensity)	Cannon et al. (1976)
$SmCo_2$	1.4	$H_{res} = +44$ kOe	Vijayaraghavan et al. (1977)
RCo_2	4.2	R = Nd, Gd, Tb, Ho: line splittings	Rubinstein et al. (1981)
RCo_2	1.5, 4.2	R = Pr, Nd, Sm, Gd, Tb, Dy, Ho, Er, Tm: ν_Q, $H_{res}(\theta)$, easy axis	Hirosawa and Nakamura (1982a)
RCo_2	4.2	(review); R = Pr, Nd, Sm, Gd, Tb, Dy, Ho, Er, Tm; 3%(R = Gd) to 26%(R = Pr) of Co moment orbital; $Tb_{1-x}Y_xCo_2$: satellites, H_N(Tb) = +42 kOe	Hirosawa and Nakamura (1982e)
$HoCo_2$	4–65	T = 15 K: [110]→[100] easy-axis change	Guimarães et al. (1987)
$Gd_{1-x}R_xCo_2$	4.2	$0 \leq x \leq 0.6$: R = Y; $0 \leq x \leq 0.06$: R = Dy; $0 \leq x \leq 0.4$: Ni	Taylor and Christopher (1969)
$Y_{1-x}Gd_xCo_2$	4.2, 77, 196, 273	$0.1 \leq x \leq 1$: $H_{res} = 61.4 \rightarrow 44.6$ kOe; $(\Delta H_{res}/H_{res})_{1\rightarrow 0.5} = 27\%$	Yoshie (1977, 1978)
$Y_{1-x}Gd_xCo_2$	1.6, 4.2	$0 \leq x \leq 1$: $\nu_{res}(x)$ (magnetically ordered), $K(x, T)$ (paramagnetic state)	Hirosawa et al. (1979)
$R_{1-x}Y_xCo_2$	1.5, 4.2	R = Pr: $0 \leq x \leq 0.6$: satellites, R = Ho: $0 \leq x \leq 0.5$: wall spectrum, non-magnetic Co for $n \geq 3$	Hirosawa and Nakamura (1982d)
$Tb_{1-x}Y_xCo_2$	4.2	$x \leq 0.10$: nn dominant $H_N^R = 43$ kOe	Hirosawa and Nakamura (1982a)
$Tb_{1-x}Dy_xCo_2$	4.2	spin reorient.; $0 \leq x \leq 0.3$: [111], $0.8 \leq x \leq 1$: [100]; intermediate x: non-collinear	Hirosawa and Nakamura (1982b)
$Dy_{1-x}Y_xCo_2$	4.2	$0 \leq x \leq 0.7$: resolved satellites	Yoshimura et al. (1984a)
$Er_{1-x}Y_xCo_2$	4.2	$0 \leq x \leq 0.1$ (satellite)	Yoshimura et al. (1984a)
$Gd(Fe_{1-x}Co_x)_2$	4.2	$x = 1$: $H_{res} = 67.0$ kOe; $x = 0.1$: 170 kOe	Belov et al. (1974)
$Gd(Fe_{1-x}Co_x)_2$	4.2	$\nu(x = 0.1/0.3/0.8\text{–}1.0) = 165/158/72\text{–}62$ MHz	Belov et al. (1976)
$Y(Fe_{1-x}Co_x)_2$	4.2	$x = 0.05$: $H_{hf} = -166$ kOe	Oppelt and Buschow (1976)
$Y(Fe_{1-x}Co_x)_2$	4.2, 77	$0 \leq x \leq 1$; small x: satellites; $0.98 \geqslant x \geqslant 0.9$: $\nu_{res} \approx 80$ MHz; $1 \geqslant x \geqslant 0.98$: $\nu(H)$, non-magnetic Co	Yamada and Ohmae (1980)

$Gd(Co_{1-x}Ni_x)_2$	4.2	$0 \leq x \leq 0.6$; $\mu_{Co} \approx 1.0\ \mu_B$	Tanaka et al. (1980)
$Gd(X_{1-x}Co_x)_2$	4.2	X = Al, Mn, Fe, Ni; $0 \leq x \leq 1$	Ichinose (1987)
$Ho(Co_{1-x}X_x)_2$	4.2	X = Al, Cu; $x < 0.2$; $\nu_{res}(x = 0) = 70.5, 51.5$ MHz	Englich et al. (1989)
$Lu(Co_{1-x}Al_x)_2$		$x = 0.08, 0.12$: coexisting FM/PM	Endo et al. (1988)
$Gd_{1-x}Y_x(Fe_{1-y}Co_y)_2$	77	$0 \leq x \leq 1$; $y = 0.3, 0.5$; $\nu(x, T)$; $\lvert H_{4f}\rvert \leq 10$ kOe	Ichinose et al. (1982)
$Y(Fe_{0.9}Co_{0.1})_2H_x$	1.7	$x = 0, 4.0$: $\nu = 170, 110$ MHz	Fujii et al. (1983)
$NdCo_3$	4.2	6c/18h/3b: −85/−50/−35 kOe	Streever (1975a)
YCo_3	4.2	spectrum	Figiel et al. (1977)
YCo_3	77	resonance line shape	Yoshie (1977)
$SmCo_3$	4.2	$18h_2/18h_1/3b/6c$: −78/−65/−57/+28 kOe	Yoshie and Nakamura (1990)
$GdCo_3$	4.2	$H_0 \leq 55$ kOe; H_{res}(3b/6c/18h) = 80/−58/−80 kOe	Yoshie and Nakamura (1988a)
$Gd_{1-x}Y_xCo_3$	4.2	$0 \leq x \leq 0.2$: (18h)-satellite; $H_{4f} = 44$ kOe	Yoshie and Nakamura (1988a)
$YCo_{3-x}Ni_x$	4.2	$0 \leq x \leq 1$; domain signals; $H_{res}(x = 0)$ = +35, +61, −42 kOe (3b(I), 6c(II), 18h (III) site);. $x \geq 0.65$: paramagn. Co	Yoshie et al. (1985a)
$Gd(Co_{1-x}X_x)_3$	4.2	$H_0 \leq 55$ kOe; X = Fe, $x = 0.1, 0.2, 0.3$: Fe→(18h); X = Ni, $x = 0.5$: Ni→(6c)	Yoshie and Nakamura (1988a)
$DyCo_{3-x}X_x$	4.2	$x = 0, 0.3$; X = Ni, Fe; domain signals; site assignment (3b, $18h_1$, 6c, $18h_2$), field depence	Yoshie and Nakamura (1989b)
$R(Fe_{1-x}Co_x)_3H_y$	77	R = Y, Gd; $x = 0.1, 0.3$; $y = 0.\ 0.61, 0.95$: $H_{I,III}$ decreasing, H_{II} increasing with y	Fujiwara et al. (1983)
Gd_2Co_7	77	$H_{res} = 59.3$(I, 3b), 66.7(III, 6c), 74.2 (I, 6c), 196(IV, 9e), 212 kOe(V, 18h)	Ueno et al. (1971)
Y_2Co_7	77	resonance line shape (≈45 MHz)	Yoshie (1977)
Y_2Co_7	4.2	spectrum	Figiel et al. (1977)
$GdCo_2Si_2$	4.2	ordered/PM	Figiel et al. (1989)
RCo_4B	4.2	R = Y/Nd; $H_{eff} = 31/25$ kOe (6i); 40/38 kOe (2c)	Kapusta et al. (1990)
YCo_5	4.2	spectrum	Figiel et al. (1977)
YCo_5	1.5	$H_{ani} \approx 57$ kOe (spin echo modulation, $H_{mod} = 0.1$ Oe, 80 kHz)	Searle et al. (1977)
YCo_5	1.5	wall center signals, $f(H)$	Kunkel and Searle (1981)
$LaCo_5$	4.2	$\nu_{res}(H_0$, domain); H_{hf}(3g/2c) = −74/+7.5 kOe	Yoshie and Nakamura (1988b)
$NdCo_5$	4.2	H_{res}(2c/3g) = −128/−106 kOe	Streever (1975a)
$SmCo_5$	1.4	$H_{res} = 197(Co_I), 178(Co_{II})$ kOe	Vijayaraghavan et al. (1977)
$SmCo_5$	4.2	$H_{\parallel}/H_{\perp} = -114/-176(-159/-132)$ kOe for 2c(3g) site	Streever (1978)

TABLE B12 (cont'd)

Compound	Temperature (K)	Remarks	Reference
$GdCo_5$	4.2	$\nu(x, H)$; 2c site: orbital moment	Yoshie et al. (1985b)
RCo_5	4.2	R = Y, Ce, Pr, Nd, Sm, Gd, Tb, Dy, Ho: domain-NMR ($H_0 \leq 55$ kOe); preferential (2c)-site occupation in $R(Co_{1-x}Ni_x)_2$ for site assignment; large orbital contribution to H_{hf}(2c)	Yoshie et al. (1987)
$NdCo_5$	4.2	$H_{res} = +21$ kOe (2c), -41 kOe ($3g_2$), -76 kOe ($3g_1$) -144 kOe (6l); large orbital moment; (2c)	Yoshie and Nakamura (1989a)
$Gd_{1-x}Y_xCo_5$	77	$0 \leq x \leq 1$; $H(Gd \rightarrow Co_{I,II}, x = 0) =$ 180/167.5 kOe	Yoshie et al. (1976)
$Gd_{1-x}Y_xCo_5$	4.2	$\nu(x, H)$; $x = 0.3, 0.5, 0.7, 1$	Yoshie et al. (1985b)
$Y_{1-x}Dy_xCo_5$	77	$0 \leq x \leq 0.5, 1.0$; $\Delta H_{4f} \leq 3$ kOe	Yoshie (1977)
$Y_{1-x}Ho_xCo_5$	293	$0 \leq x \leq 0.5, 1.0$; $\Delta H_{4f} \approx 0$	Yoshie (1977)
$Y(Fe_xCo_{1-x})_5$		Fe – Fe pair (AF exchange)	Inomata (1976b)
$GdCo_{5-x}Ni_x$	4.2	$\nu(x, H)$; $x = 1, 2, 3, 4$	Yoshie et al. (1985b)
$R(Co_{1-x}Ni_x)_5$	4.2	R = Y, Tb, Dy, Ho; $0 \leq x \leq 0.2$; domain signals ($H_0 < 55$ kOe); H_{hf}(R = Y, 2c/3g) = +15/−92 kOe	Yoshie et al. (1988a)
$R(Co_{1-x}Ni_x)_5$	4.2	R = Ce, (Sm); $0 \leq x \leq 0.3$; H_{hf}(2c/3g) = +61, (68)/−70, (−61) kOe	Yoshie et al. (1988b)
YCo_{5+x}	4.2	$x = 0, 0.3$: $\Delta H_{ani}^{I,II} = 26, 9$ kOe	Laforest et al. (1983)
RCo_5H_x	4.2	$0 \leq x \leq 0.46(1.0)$ for R = Y(Gd); H position, spectral changes	Yamaguchi et al. (1980)
$La_{1-x}Y_xCo_5H_y$	77	$x = 0, 0.2$; H→ Co electron transfer	Fujiwara et al. (1988)
$R_2Co_{14}B$	4.2	R = Y, Nd: narrow lines; site assignment, ν_Q	Kapusta et al. (1986)
$R_2Co_{14}B$	4.2, 30	R = *Y*, Pr, Nd; wall spectra, simulations	Wójcik et al. (1990)
$Y_2Co_{14}B$	4.2	$\nu = 110, 152, 159, 167.5, 187$ MHz; ν_Q	Figiel et al. (1987b)
$Y_2Co_{14}B$	4.2	site assignment, sign moments, orbital character	Berthier et al. (1988b)
$Nd_2Co_{14}B$	4.2	$\nu = 127, 130.6, 133, 162.6, 172.8, 184.2$ MHz; ν_Q	Figiel et al. (1987b)
$Nd_2Co_{14}B$	2–77	Spin reorientation; T(onset) = 32 K; hyperfine anistropy for c, k_2, k_1	Panissod et al. (1989)
$(Y_{1-x}Nd_x)_2Co_{14}B$	4.2	$0 \leq x \leq 1$; easy axis; orbital contribution	Kapusta and Figiel (1988)
$Nd_2Co_{14-x}Fe_xB$	4.2–77	$0 \leq x \leq 0.878$; $\nu_{res}(x)$, $H_{res}(x)$	Jedryka et al. (1988)
$Nd_2(Co_{1-x}X_x)_{14}B$	4.2	X = Mn, $x \leq 0.2$/X = Fe, $0 \leq x \leq 0.9$: H_{hf}(site, x)	Ichinose et al. (1988a)

$Nd_2(Co_{1-x}Fe_x)_{14}B$	4.2–32	4c = uniaxial hf anisotropy large (38.6 kOe) $x = 0$: basal plane hf anisotropy	Wójcik et al. (1989a)
$Nd_2(Co_{1-x}Fe_x)_{14}B$	4.2–77	$0.001 \leq x \leq 0.10$; canting versus c	Fedryka et al. (1990)
RCo_4B_4	1.3	R = Gd, Tb, Dy; AF, zero field; spin structure	Ueda et al. (1984)
Nd_2Co_{17}	4.2	6c/18f/9d/18h: −221/−187/−171/−161 kOe	Streever (1975a)
R_2Co_{17}	77	R = Ce, Pr, Gd, Tb, Dy, Ho: $H_{hf}(Co_{I\sim IV})$	Inomata (1976a)
Y_2Co_{17}	4.2	spectrum	Figiel et al. (1977)
R_2Co_{17}	77	R = Y, Gd; $H_{dip} \leq 12.3$ kOe	Figiel and Jaszczewski (1980)
R_2Co_{17}	4.2	R = Y, Nd	Kapusta et al. (1986)
$(Gd_{1-x}Y_x)_2Co_{17}$	77–430	$0 \leq x \leq 1$; $H_{A,B,C}(x, T)$	Nagai et al. (1976)
$(Y_{1-x}Gd_x)_2Co_{17}$	4.2	$0 \leq x \leq 1$; $\nu_{res,I}(9d, 6g) = 96 \rightarrow 74.5$ MHz	Figiel (1982b)
$(Y_{1-x}Gd_x)_2Co_{17}$	4.2	$x = 0, 0.1$: spin echo defocusing ↔ anisotropic hyperfine interaction	Machowska and Nadolski (1988)
$Y_2(Fe_xCo_{1-x})_{17}$		$x = 0$: $\nu = 170, 176, 200, 219$ MHz	Inomata (1976b)
$Gd_2(Co_{1-x}Fe_x)_{17}$	4.2, (77)	$0 \leq x \leq 0.7$: easy axis, site occupation; ν_Q(77 K, 169/195 MHz) = 1.23/3.0 MHz; $\nu_{res}(x = 0(0.7)) = 78, 169, 180, 195(169, 183, 201, 245)$ MHz	Kawakami (1981)
$Y_2(Co_{1-x}X_x)_{17}$	77	X = Al, Cu; $0 \leq x \leq 0.15$; $x = 0$: $\nu_{I,II,III,IV} = 203, 166, 219, 174$ MHz	Inomata (1981)
$R_2(Co_{1-x}Mn_x)_{17}$	4.2	R = Y, Gd; $0 \leq x \leq 1$	Figiel et al. (1982)
$R_2(Co_{1-x}Mn_x)_{17}$	4.2	R = Y, Gd; $x \leq 0.2$: easy-axis reorientation, orbital contribution	Figiel (1982a)
$LaCo_{13}$	4.2	$H^{I}_{res} = 135$ kOe; $H^{II}_{res} = 168, 180, 187$ kOe	Wójcik et al. (1989b)
$RCo_{12}B_6$	4.2	R = Y: $\nu_{res} = 26.7, 39.4, 49.5$ MHz; 7 lines $\nu_c = 76.2$ MHz, $\nu_Q = 1.85$ MHz; R = Gd: $\nu_{res} = 20, 38, 80.5$ MHz	Erdmann et al. (1988a)

TABLE B13

Nuclear magnetic resonance of the nucleus ^{61}Ni in an intermetallic compound with a magnetically ordered state. Nuclear data: ^{61}Ni, $I = \frac{3}{2}$, natural abundance 1.3%, $\gamma/2\pi = 0.3799$ MHz kOe^{-1}, $Q = +0.16 \times 10^{-24}$ cm^2

Compound	Temperature (K)	Remarks	Reference
GdCd:Ni	4.2	1 at.%; $H_{res} = 117$ kOe	Kasamatsu et al. (1988)

TABLE B14

Nuclear magnetic resonance of the nuclei ^{63}Cu and ^{65}Cu in intermetallic compounds. Nuclear data: ^{63}Cu, $I = \frac{3}{2}$, natural abundance 69.1%, $\gamma/2\pi = 1.1285$ MHz kOe^{-1}, $Q = -0.222 \times 10^{-24}$ cm^2; ^{65}Cu, $I = \frac{3}{2}$, natural abundance 30.9%, $\gamma/2\pi = 1.2090$ MHz kOe^{-1}, $Q = -0.195 \times 10^{-24}$ cm^2.

Compound	Temperature (K)	Remarks	Reference
(a) Paramagnetic states			
ScCu	77, 300	$K = 0.22, 0.224\%$	Seipler et al. (1977)
RCu	140–430	R = Y, Gd, Tb, Dy, Ho, Er: ^{63}K(YCu) = +0.15%, $K(T)$, $J_{sf} \approx -0.21$ eV	de Wijn et al. (1968)
YCu	1.5–300	$^{63}K = 0.20\%$, $T_1T = 1.5$ s K	von Meerwall et al. (1975)
LuCu	76, 300	$K = 0.222\%$	Schmidt (1973)
$Ce_{1.03}InCu_2$	0.6–35	$\Delta H_{hf}(T)$; $T_1(T)$	Nakamura et al. (1988d)
$Ce_{1.03}InCu_2$	0.3–200	$K(\chi)$, 4.2 K $\leq T \leq$ 50 K: $\alpha = -10.3$ kOe μ_B^{-1}, $\Delta H(T)$; $T_{N1} = 1.6$ K, $T_{N2} = 1.1$ K; zero-field signal at 0.3 K(1–7 MHz)	Nakamura et al. (1988c)
$CeInCu_2$		$T_N \approx 2.3$ K; $\Delta H(T)$, $T_2(T)$	Takagi et al. (1988a)
$CeCu_4$	140–400	$K(T)$; $^{63}K_0 = 0.204\%$; $J_{sf} = -0.01043$ eV	Pop et al. (1979a)
$PrCu_4$	140–400	$K(\chi)$; $^{63}K_0 = 0.209\%$; $J_{sf} = -0.00365$ eV	Pop et al. (1979b)
$NdCu_4$	140–400	$K(T)$; $^{63}K_0 = 0.2104\%$; $J_{sf} = -0.00246$ eV	Pop et al. (1980)
RCu_2Si_2	77–520	R = Y, La, Ce, Pr, Sm, Eu, Gd, Er, Tm, Yb: $(e^2q^{63}Q)(T)$	Sampathkumaran et al. (1979b, c, 1980a, 1981)
$LaCu_2Si_2$	1.35–1.5	T_1	MacLaughlin et al. (1984)
$CeCu_2Si_2$	0.35–1.35	NQR(^{63}Cu, 3.43 MHz): $T_1(T)$, T_2, T_2^*	MacLaughlin et al. (1984)
$CeCu_2Si_2$	0.065–77	NQR: no enhancement of $1/T_1$ for $T < T_c = 0.67$ K	Kitaoka et al. (1984)

$CeCu_2Si_2$	0.05–100	T_1(NQR); NMR: $1/T_1 \sim T^3$ ($0.1\,K < T < 0.6\,K$)($< T_c$)	Kitaoka et al. (1985c)
$CeCu_xSi_2$	0.1–100	$x = 1.99, 2.02$; $^{63}T_1T$; NMR, NQR	Kitaoka et al. (1986)
$CeCu_2Si_2$	0.4, 1.3	$^{63}K(T)$, ($K_\parallel$, $K_\perp$)	Ueda et al. (1987)
$YbCu_2Si_2$	4.2–200	SC; $K_\parallel$, $K_\perp \leftrightarrow \chi(T)$ non-linear for $T \leqslant 100$ K; $T \leqslant 10$ K: NMR + NQR; $\nu_Q(T)$; ν_Q(4.2 K; NQR) = 2.572 MHz; $K_0(\parallel) = 0.11\%$, $K_0(\perp) = 0.15\%$	Shimizu et al. (1987)
RCu_2Ge_2	300	R = Y, La, Ce, Pr, Sm, Gd, Er, Tm, Yb: ($e^2q^{63}Q$), K_{iso}	Sampathkumaran et al. (1979b, 1980a, 1981)
RCu_5	100–300	R = Tb, Dy, Ho, Er, Tm: $^{63}K(T)$; $J_{sf} \approx -0.11$ eV	Buschow et al. (1970)
$CeCu_5$	140–400	$K(T)$; $^{63}K_0 = 0.235\%$; $J_{sf} = +0.0039$ eV	Pop et al. (1979a)
$PrCu_5$	140–400	$K(\chi)$; $^{63}K_0 = 0.235\%$; $J_{sf} = +0.00221$ eV	Pop et al. (1979b)
$NdCu_5$	140–400	$K(T)$; $^{63}K_0 = 0.233\%$; $J_{sf} = -0.00135$ eV	Pop et al. (1980)
$LaCu_6$	4.2–80	spectrum, $T_1(T)$	Shimizu et al. (1985a)
$CeCu_6$		$J_{sf} = -0.012$ eV	Pop et al. (1974)
RCu_6	140–470	R = Ce, Pr, Nd, Gd: $K(\chi)$ linear, $J_{sf} < 0$, R = Sm: van Vleck type	Coldea and Pop (1975)
$CeCu_6$	0.06–30	NQR(^{63}Cu), T_1; $T < 0.2$ K: $T_1T = 0.011$ s K	Kitaoka et al. (1985b)
$CeCu_6$	4.2–150	$T_1(T)$	Shimizu et al. (1985a)
$CeCu_6$	0.06–30	T_1T; NQR (^{63}Cu)	Kitaoka et al. (1986)
(b) Magnetically ordered states			
GdX:Cu	4.2	X = Zn/Cd; 1 at.%; $H_{res} = 131/126$ kOe	Kasamatsu et al. (1988)
$Ce_{1.03}InCu_2$	0.4–35	$\Delta H_{hf}(Cu) = f(T)$	Nakamura et al. (1988d)

TABLE B15

Nuclear magnetic resonance of the nucleus ^{67}Zn in intermetallic compounds with magnetically ordered states. Nuclear data: ^{67}Zn, $I = \frac{5}{2}$, natural abundance 4.1%, $\gamma/2\pi = 0.2663\ \text{MHz kOe}^{-1}$, $Q = +0.150 \times 10^{-24}\ \text{cm}^2$.

Compound	Temperature (K)	Remarks	Reference
GdZn	4.2	$\nu_{res} = 46.8$ MHz	Oppelt et al. (1972a)
GdZn	4.2–180	$H_{hf}(T) \leftrightarrow M_s(T)$	Herbst et al. (1974)
RZn	1.4, 4.2	R = Gd, Tb, Ho, Er: $H_{hf} = -181.9/-150.2/-74.0/-46.6$ kOe	Eckrich et al. (1976)
GdZn	1.6	SC; $K = -0.56\%$	Kropp et al. (1984)
$Gd_{1-x}R_xZn$	4.2	R = Y, La: Zn satellite lines	Eckrich et al. (1972)
$Gd_{0.9}R_{0.1}Zn$	4.2	R = Sc, Y, La, Ce, Pr, Nd, Sm, Tb, Dy, Ho, Er: $H_{nn}(R)$	Eckrich et al. (1973, 1976)
$R_{0.9}La_{0.1}Zn$	4.2	R = Gd, Tb, Ho: $H_{nn}(R)$	Eckrich et al. (1976)
$Gd_{1-x}Ho_xZn$	4.2	$0 \leq x \leq 1$: $H_{nn}(x)$	Eckrich et al. (1976)
$GdZn_{1-x}Mg_x$	4.2	$0 \leq x \leq 1$: $\nu_{res}(x)$	Buschow and Oppelt (1974)
$GdZn_{1-x}Ag_x$	4.2	$\nu_{res}(x)$	Oppelt et al. (1972a)
$GdZn_{1-x}Ag_{0.5x}In_{0.5x}$	4.2	$\nu_{res}(x)$	Oppelt et al. (1972a)
$GdZn_{1-x}Cd_x$	4.2	$\nu_{res}(x)$	Oppelt et al. (1972a)
$GdZn_{1-x}In_x$	4.2	$\nu_{res}(x)$	Oppelt et al. (1972a)

TABLE B16

Nuclear magnetic resonance of the nucleus ^{75}As in intermetallic compounds with paramagnetic states. Nuclear data: ^{75}As, $I = \frac{3}{2}$, natural abundance 100%, $\gamma/2\pi = 0.7292\ \text{MHz kOe}^{-1}$, $Q = +0.314 \times 10^{-24}\ \text{cm}^2$.

Compound	Temperature (K)	Remarks	Reference
RAs	1.5–600	R = Sc, Y, La, Ce, Pr, Nd, Sm, Gd, Tm: $K(T)$	Jones (1969)
CeAs	7.5–200	$K(\chi)$ non-linear	Myers and Narath (1973b)
CeAs	14–194	$d(\ln K)/dp$, $p \leq 4$ kbar	Weaver and Schirber (1976a)
PrAs	4.2–300	$K(p)$, $p \leq 4$ kbar	Weaver and Schirber (1976b)

TABLE B17

Nuclear magnetic resonance of the nucleus ^{91}Zr in intermetallic compounds. Nuclear data: ^{91}Zr, $I = \frac{5}{2}$, natural abundance 11.2 %, $\gamma/2\pi = 0.3958$ MHz kOe^{-1}.

Compound	Temperature	Remarks	Reference
$Zr_{1-x}Gd_xZn_2$		$0 \leq x \leq 0.015$; $K(x, T) \leftrightarrow \chi(T)$; $\alpha = -38$ kOe μ_B^{-1}	Asanuma and Yamadaya (1968)
$Tb_xZr_{1-x}Fe_2$	77–300	$0 \leq x \leq 0.2$; ν_{res} ($x = 0$, 77 K) = 46.65 MHz; no satellites	Nikitin et al. (1988)
$Sc_{1-x}Zr_xFe_2$	4.2	$0 \leq x \leq 0.8$: -143.7 kOe $< H_{inf} \leq -128.7$ kOe	Pokatilov et al. (1989)

TABLE B18

Nuclear magnetic resonance of the nucleus ^{103}Rh in intermetallic compounds. Nuclear data: ^{103}Rh, $I = \frac{1}{2}$, natural abundance 100%, $\gamma/2\pi = 0.1340$ MHz kOe^{-1}.

Compound	Temperature (K)	Remarks	Reference
(a) Paramagnetic states			
ScRh	77, 300	$K = 0.862, 0.896\%$	Seipler et al. (1977)
YRh	77, 300	$K = 1.44, 1.48\%$	Seipler et al. (1977)
$LaRh_2$	4.2	$K = +0.78\%$	Seitchik et al. (1965)
RRh_4B_4	1.5–4.2	R = Y, Sm, Lu: K_{iso}; T_1T(Y, Lu) = 25 s K	Kohori et al. (1984)
(b) Magnetically ordered states			
$Gd_{1-x}La_xRh$	2, 4.2	$0 \leq x \leq 0.1$: $H_N(x)$	Dormann and Buschow (1976)
$GdRh_2$	4.2	$H_{res} = (56 \pm 5)$ kOe	Dormann and Buschow (1973)

TABLE B19

Nuclear magnetic resonance of the nucleus ^{107}Ag and ^{109}Ag in intermetallic compounds. Nuclear data: ^{107}Ag, $I = \frac{1}{2}$, natural abundance 51.4%, $\gamma/2\pi = 0.1723\,\text{MHz kOe}^{-1}$, ^{109}Ag, $I = \frac{1}{2}$, natural abundance 48.6%, $\gamma/2\pi = 0.19807\,\text{MHz kOe}^{-1}$.

Compound	Temperature (K)	Remarks	Reference
(a) Paramagnetic states			
ScAg	77, 300	$K = 0.345, 0.35\%$	Seipler et al. (1977)
RAg	77, 300	R = Y, La: $K(T)$	Schmidt (1973)
YAg	300	$K = +(0.345 \pm 0.005)\%$	Buschow and Oppelt (1974)
LaAg	1.5–300	$^{109}K = 0.25\%$	von Meerwall et al. (1975)
(b) Magnetically ordered states			
$GdZn_{1-x}Ag_x$	4.2	$\nu_{res}(x)$	Oppelt et al. (1972a)
$GdZn_{1-x}Ag_{0.5x}In_{0.5x}$	4.2	$\nu_{res}(x)$	Oppelt et al. (1972a)
$GdAg_{1-x}In_x$	4.2	$0.3 \leqslant x \leqslant 0.65$: $\nu_{res}(x)$	Oppelt et al. (1972a)

TABLE B20

Nuclear magnetic resonance of the nuclei ^{111}Cd and ^{113}Cd in intermetallic compounds. Nuclear data: ^{111}Cd, $I = \frac{1}{2}$, natural abundance 12.9%, $\gamma/2\pi = 0.9028\,\text{MHz kOe}^{-1}$; ^{113}Cd, $I = \frac{1}{2}$, natural abundance 12.3%, $\gamma/2\pi = 0.9444\,\text{MHz kOe}^{-1}$.

Compounds	Temperature (K)	Remarks	Reference
(a) Paramagnetic states			
YbCd	76, 300	$0.26\% < K < 0.29\%$	Schmidt (1973)
(b) Magnetically ordered states			
GdCd	4.2	$H_{hf} = -318.3\,\text{kOe}$	Eckrich et al. (1976)

TABLE B21

Nuclear magnetic resonance of the nucleus ^{115}In in intermetallic compounds with paramagnetic states. Nuclear data: ^{115}In, $I = \frac{9}{2}$, natural abundance 95.8%, $\gamma/2\pi = 0.93295$ MHz kOe^{-1}, $Q = +0.861 \times 10^{-24}$ cm^2.

Compound	Temperature (K)	Remarks	Reference
La_3In	14–300	$K(14\,K) = -0.155\%$, $K(300\,K) = +0.058\%$	Heiniger et al. (1973)
$La_3X_{1-x}X'_x$	4–300	X, X′ = Al, Ga, In, Sn, Tl: $K(x, T)$	Descouts et al. (1975)
La_3InC	4–300	$K(T)$	Descouts et al. (1975)
YbIn	76, 300	$K = 0.402\%, 0.419\%$	Schmidt (1973)
$LaAg_{0.75}In_{0.25}$	76, 300	$K = -0.01\%, -0.04\%$	Schmidt (1973)
$RInAg_2$	4–300	R = Y: $K_0 = +0.3\%$ R = Ce, Pr, Nd, Sm, Gd, Tb, Dy, Ho, Er, Tm, Yb: $K(T) \leftrightarrow \chi(T)$; α(Ce, Pr, Nd, Tm) = −104, −98, −98, −44 kOe μ_B^{-1}	Nambudripad et al. (1986)
$Ce_{1.03}InCu_2$	1.3–100	$K(\chi)$; 4.2–50 K: $\alpha = +2.9$ kOe μ_B^{-1}; $\Delta H(T)$	Nakamura et al. (1988c)

TABLE B22

Nuclear magnetic resonance of the nuclei ^{117}Sn and ^{119}Sn in intermetallic compounds with paramagnetic states. Nuclear data: ^{117}Sn, $I = \frac{1}{2}$, natural abundance 7.7%, $\gamma/2\pi = 1.517$ MHz kOe^{-1}; ^{119}Sn, $I = \frac{1}{2}$, natural abundance 8.7%, $\gamma/2\pi = 1.587$ MHz kOe^{-1}.

Compound	Temperature (K)	Remarks	Reference
CeNiSn	0.38–250	$^{119}k(T)$; $T_1(T)$	Kyogaku et al. (1990)
RSn_3	77–300	R = La, Ce, Pr, Nd, Sm, Eu, Yb: $^{119}K_{iso}(T)$, $K_{\parallel}(T)$; K_{iso}(La) = +0.643%	Barnes et al. (1965)
RSn_3	90–300	R = La, Ce, Pr, Nd, Sm: $K \leftrightarrow \chi$; K(La) = 0.62%, $J_{sf} = -0.07$ eV	Rao and Vijayaraghavan (1965)
RSn_3	77–400	R = La, Ce, Pr, Nd, Sm, Yb: $K(T)$, J_{sf}	Borsa et al. (1967)
$LaSn_3$	1.6–300	$K_{iso} = +0.640\%$, $T_1T = 0.033$ s K	Welsh et al. (1971b)
$La(Sn_{1-x}In_x)_3$	1.6, 4.2	$K(x, T)$, $T_1T(x)$	Toxen et al. (1973)
$CeSn_3$	1.2–300	$K(T)$, T_1T	Malik et al. (1975)
$CeSn_3$		$K(\chi)$ non-linear, modified for $T < T_{max} = 130$ K; $K_0 = -0.25\%$; $\alpha = 37$ kOe μ_B^{-1}	MacLaughlin (1981)
$SmSn_3$	77–300	$K(T)$	Malik (1970)
$SmSn_3$	77–400	$K(T)$ analysis	Malik and Vijayaraghavan (1971a, b)
$SmSn_3$	300	K	de Wijn et al. (1973)
$SmSn_3$	15–300	$K(T)$	Malik et al. (1977)

TABLE B23

Nuclear magnetic resonance of the nuclei ^{121}Sb and ^{123}Sb in intermetallic compounds with paramagnetic states. Nuclear data: ^{121}Sb, $I = \frac{5}{2}$, natural abundance 57.3%, $\gamma/2\pi = 1.019\,\text{MHz kOe}^{-1}$, $Q = -0.53 \times 10^{-24}\,\text{cm}^2$; ^{123}Sb, $I = \frac{7}{2}$, natural abundance 42.7%, $\gamma/2\pi = 0.5518\,\text{MHz kOe}^{-1}$, $Q = -0.68 \times 10^{-24}\,\text{cm}^2$.

Compound	Temperature (K)	Remarks	Reference
RSb	1.5–600	R = Sc, Y, La, Sm, Tm: $K(T)$	Jones (1969)

TABLE B24

Nuclear magnetic resonance of the nucleus ^{191}Ir and ^{193}Ir in intermetallic compounds with magnetically ordered states. Nuclear data: ^{191}Ir, $I = \frac{3}{2}$, natural abundance 38.5%, $\gamma/2\pi = 0.07318\,\text{MHz kOe}^{-1}$, $Q = 0.78 \times 10^{-24}\,\text{cm}^2$; ^{193}Ir, $I = \frac{3}{2}$, natural abundance 61.5%, $\gamma/2\pi = 0.07961\,\text{MHz kOe}^{-1}$, $Q = 0.70 \times 10^{-24}\,\text{cm}^2$.

Compound	Temperature (K)	Remarks	Reference
$GdIr_2$	4.2	$\nu_{res} = 29.0/31.5\,\text{MHz}$	Dormann and Buschow (1973)
$Gd_{1-x}R_xIr_2$	4.2	$0 \leq x \leq 0.2$: easy axis discussion	Dormann et al. (1976)

TABLE B25

Nuclear magnetic resonance of the nucleus ^{195}Pt in intermetallic compounds. Nuclear data: ^{195}Pt, $I = \frac{1}{2}$, natural abundance 33.7%, $\gamma/2\pi = 0.9094$ MHz kOe^{-1}.

Compound	Temperature (K)	Remarks	Reference
(a) Paramagnetic states			
RPt_2	80–400	R = La, Ce, Pr, Nd: $K(T) \rightarrow J_{sf}$	Vijayaraghavan et al. (1968a, b)
$SmPt_2$	4–300	$K(T)$	Malik (1970)
$CePt_{2-x}Rh_x$	77–300	$0 \leq x \leq 1.75$: $K(T)$	Sampathkumaran et al. (1983)
RPt_3	77–570	R = La, Ce, Pr: K, $\Delta H \leftrightarrow \chi$	Grover et al. (1977)
RPt_5	80–400	R = La, Ce, Pr, Nd: $K_{I,II}(T) \rightarrow J_{sf}$	Vijayaraghavan et al. (1968a, b)
$LaNi_{5-x}Pt_x$	4.2, 77, 300	$0 \leq x \leq 5$: $K(x)$, $T_1(x)$	Weisman et al. (1975)
(b) Magnetically ordered states			
$SmPt_2$	1.4	$H_{res} = -400$ kOe	Vijayaraghavan et al. (1977)
$EuPt_2$	4.2	$\nu_{res} = 80.8$ MHz	Kropp et al. (1979b)
$GdPt_x$	4.2	$2 \leq x \leq 3$; $H_{hf}(x = 2) = -217.2$ kOe; site occupation analysis	Dormann et al. (1977b)
$Gd_{1-x}R_xPt_2$	4.2	R = Sc, La; $0 \leq x \leq 0.2$; $H_{nn} = -35.3$ kOe	Dormann et al. (1977b)

TABLE B26

Nuclear magnetic resonance of the nuclei ^{203}Tl and ^{205}Tl in intermetallic compounds with paramagnetic states. Nuclear data: ^{203}Tl, $I = \frac{1}{2}$, natural abundance 29.5%, $\gamma/2\pi = 2.433$ MHz kOe^{-1}; ^{205}Tl, $I = \frac{1}{2}$, natural abundance 70.5%. $\gamma/2\pi = 2.457$ MHz kOe.

Compound	Temperature (K)	Remarks	Reference
La_3Tl	6.5–300	$K(T)$; $K(300) = +0.319\%$, $K(6.5\text{ K}) = -0.265\%$	Heiniger et al. (1973)
$La_3X_{1-x}X'_x$	4–300	X,X′ = In, Tl, Pb: $^{205}K(x, T)$	Descouts et al. (1975)
La_3TlC		^{205}K	Descouts et al. (1975)

TABLE B27
Nuclear magnetic resonance of the nucleus ^{207}Pb in intermetallic compounds with paramagnetic states. Nuclear data: ^{207}Pb, $I = \frac{1}{2}$, natural abundance 21.1%, $\gamma/2\pi = 0.8874$ MHz kOe^{-1}.

Compound	Temperature (K)	Remarks	Reference
$LaPb_3$	1.5–77	K, T_1T	Welsh et al. (1975)

TABLE B28
Nuclear magnetic resonance of the nucleus ^{209}Bi in intermetallic compounds with paramagnetic states. Nuclear data: ^{209}Bi, $I = \frac{9}{2}$, natural abundance 100%, $\gamma/2\pi = 0.6842$ MHz kOe^{-1}, $Q = -0.46 \times 10^{-24}$ cm^2.

Compound	Temperature (K)	Remarks	Reference
RBi	1.5–600	R = Y, Sm: $K(T)$	Jones (1969)

References

Aarts, J., F.R. de Boer and D.E. MacLaughlin, 1983, Phys. B (Amsterdam) **121B**, 162.

Abe, H., H. Yasuoka and A. Hirai, 1966, J. Phys. Soc. Jpn. **21**, 77.

Abe, T., 1975, J. Phys. Soc. Jpn. **38**, 1782.

Abragam, A., 1961, The Principles of Nuclear Magnetism (Oxford University Press, London).

Ait-Bahammou, A., F. Hartmann-Boutron, C. Meyer, Y. Gros and Y. Berthier, 1986, Hyperfine Int. **28**, 577.

Al-Assadi, K.F., I.S. Mackenzie and M.A.H. McCausland, 1984, J. Phys. F **14**, 525.

Alves, K.M.B., N. Alves, A.P. Guimarães, I.S. Mackenzie and J.W. Ross, 1986, J. Magn. & Magn. Mater. **54–57**, 501.

Alves, K.M.B., N. Alves, L.C. Sampaio, S.F. da Cunha and A.P. Guimarães, 1990, J. Appl. Phys. **67**, 5867.

Andres, K., and E. Bucher, 1968, Phys. Rev. Lett. **21**, 1221.

Aono, M., and S. Kawai, 1979, J. Phys. Chem. Solids **40**, 797.

Arif, S.K., and M.A.H. McCausland, 1975, J. Phys. F **5**, L247.

Arif, S.K., J.W. Ross and M.A.H. McCausland, 1977, Phys. B (Amsterdam) **86–88B**, 158.

Armitage, J.G.M., T. Dumelow, P.C. Riedi and J.S. Abell, 1989, J. Phys.: Condens. Matter **1**, 3987.

Asanuma, M., and T. Yamadaya, 1968, J. Appl. Phys. **39**, 1244.

Asayama, K., Y. Kitaoka and Y. Kohori, 1988a, J. Magn. & Magn. Mater. **76 & 77**, 449.

Asayama, K., Y. Kitaoka and Y. Kohori, 1988b, J. Phys. (Paris) Colloq. **49**, C8-2125.

Ayling, S.H., and D.C. Creagh, 1977, J. Mater. Sci. **12**, 2128.

Bahlouli, H., 1986, Phys. Lett. A **118**, 209.

Bajaj, M.M., 1976, Phys. Lett. A **56**, 390.

Bandyopadhyay, B., K. Ghoshray, A. Ghoshray and N. Chatterjee, 1990, J. Phys.: Condens. Matter **2**, 1253.

Barash, Y.B., and J. Barak, 1984, J. Phys. F **14**, 1531.

Barash, Y.B., J. Barak and N. Kaplan, 1982, Phys. Rev. B **25**, 6616.

Barash, Y.B., J. Barak and A. Grayevsky, 1983, Phys. Lett. A **95**, 252.

Barbara, B., and Y. Berthier, 1977, Phys. B (Amsterdam) **86–88B**, 1385.

Barnes, R.G., 1979, NMR, EPR and Mössbauer Effect: Metals, Alloys and Compounds, in: Handbook on the Physics and Chemistry of Rare Earths, Vol. 2, eds K.A. Gschneidner and L. Eyring (North-Holland, Amsterdam) ch. 18, pp. 387–505.

Barnes, R.G., and E.D. Jones, 1967, Solid State Commun. **5**, 285.

Barnes, R.G., and R.G. Lecander, 1967, J. Phys. Soc. Jpn. **22**, 930.

Barnes, R.G., and B.K. Lunde, 1970, J. Phys. Soc. Jpn. **28**, 408.
Barnes, R.G., and B.K. Lunde, 1975, AIP Conf. Proc. **24**, 217.
Barnes, R.G., W.H. Jones Jr and T.P. Graham, 1961, Phys. Rev. Lett. **6**, 221.
Barnes, R.G., F. Borsa and D. Peterson, 1965, J. Appl. Phys. **36**, 940.
Barnes, R.G., B.J. Beaudry and R.G. Lecander, 1966, J. Appl. Phys. **37**, 1248.
Barnes, R.G., R.B. Creel and D.R. Torgeson, 1970, J. Chem. Phys. **53**, 3762.
Barnes, R.G., W.C. Harper, S.O. Nelson, D.K. Thome and D.R. Torgeson, 1976, J. Less Common Metal **49**, 483.
Barnes, R.G., B.J. Beaudry, R.B. Creel and D.R. Torgeson, 1980, Solid State Commun. **36**, 105.
Bauer, M., and E. Dormann, 1990, Phys. Lett. A **146**, 55.
Belahkovsky, M., J. Pierre and D.K. Ray, 1972, Phys. Rev. B **6**, 939.
Belahkovsky, M., J. Pierre and D.K. Ray, 1973, Proc. 10th Rare Earth Res. Conf. Carefree, Arizona (USAEC: Techn. Inf. Center) p. 228.
Belorizky, E., and Y. Berthier, 1985, Phys. B (Amsterdam) **130B**, 474.
Belorizky, E., and Y. Berthier, 1986, J. Phys. F **16**, 637.
Belorizky, E., Y. Berthier, R.A.B. Devine, P.M. Levy and J.J. Niez, 1979, J. Phys. (Paris) Colloq. **40**, C5-56.
Belorizky, E., J.J. Niez and P.M. Levy, 1981, Phys. Rev. B **23**, 3360.
Belorizky, E., Y. Berthier and R.A.B. Devine, 1984, J. Magn. & Magn. Mater. **44**, 313.
Belorizky, E., J.P. Gavigan, D. Givord and H.S. Li, 1988, Europhys. Lett. **5**, 349.
Belov, K.P., V.A. Vasil'kovskii, N.M. Kovtun, A.K. Kupriyanov and S.A. Nikitin, 1974, JETP Lett. **20**, 304.
Belov, K.P., V.A. Vasil'kovskii, N.M. Kovtun, A.K. Kupriyanov and S.A. Nikitin, 1976, Sov. Phys. Solid State **18**, 1307.
Belov, K.P., V.A. Vasil'kovskii, N.M. Kovtun, A.K. Kupriyanov, S.A. Nikitin and V.F. Ostrovskii, 1981, JETP Lett. **33**, 581.
Berthier, Y., and E. Belorizky, 1984, Solid State Commun. **49**, 1099.
Berthier, Y., and E. Belorizky, 1986, J. Magn. & Magn. Mater. **54–57**, 1235.
Berthier, Y., and R.A.B. Devine, 1978, J. Phys. F **8**, L113.
Berthier, Y., and R.A.B. Devine, 1979a, J. Appl. Phys. **50**, 2321.
Berthier, Y., and R.A.B. Devine, 1979b, J. Appl. Phys. **50**, 7504.
Berthier, Y., and R.A.B. Devine, 1979c, J. Phys. (Paris) Colloq. **40**, C5-116.
Berthier, Y., and R.A.B. Devine, 1980a, Phys. Rev. B **21**, 3844.
Berthier, Y., and R.A.B. Devine, 1980b, J. Magn. & Magn. Mater. **15–18**, 703.
Berthier, Y., and R.A.B. Devine, 1981, J. Appl. Phys. **51**, 2071.
Berthier, Y., J. Barak and B. Barbara, 1975, Solid State Commun. **17**, 153.
Berthier, Y., R.A.B. Devine and B. Barbara, 1977, Phys. Rev. B **16**, 1025.
Berthier, Y., R.A.B. Devine, B. Barbara and M.F. Rossignol, 1978a, Phys. Rev. B **18**, 1504.
Berthier, Y., R.A.B. Devine and E. Belorizky, 1978b, Phys. Rev. B **17**, 4137.
Berthier, Y., R.A.B. Devine and R.A. Butera, 1981, in: Nuclear and electron resonance spectroscopies applied to materials science, eds E.N. Kaufmann and G.K. Shenoy, Proc. Annual Meeting of the Materials Research Society, Boston, MA, 1980 (North-Holland, New York) p. 449.
Berthier, Y., T. de Saxce, D. Fruchart and P. Vulliet, 1985, Phys. B (Amsterdam) **130B**, 520.
Berthier, Y., M. Boge, G. Cjzek, D. Givord, C. Jeandey, H.S. Li and J.L. Oddou, 1986a, J. Magn. & Magn. Mater. **54–57**, 589.
Berthier, Y., D. Gignoux, R. Kuentzler and A. Tari, 1986b, J. Magn. & Magn. Mater. **54–57**, 479.
Berthier, Y., J. Deportes, M. Horvatic and P. Rouault, 1988a, J. Phys. (Paris) Colloq. **49**, C8-261.
Berthier, Y., N. Nassar and T. Vadieu, 1988b, J. Phys. (Paris) Colloq. **49**, C8-585.
Besnus, M.J., A. Herr, K. Le Dang, P. Veillet, A.S. Schaafsma, I. Vincze, F. van der Woude, F. Mezei and G.H.M. Calis, 1982, J. Phys. F **12**, 2393.
Besnus, M.J., M. Benakki, A. Braghta, H. Danan, G. Fischer, J.P. Kappler, A. Meyer and P. Panissod, 1988, J. Magn. & Magn. Mater. **76 & 77**, 471.
Bond, W.L., 1954, Rev. Sci. Instrum. **25**, 401.
Borsa, F., and G. Olcese, 1973, Phys. Status Solidi a **17**, 631.

Borsa, F., R.G. Barnes and R.A. Reese, 1967, Phys. Status Solidi **19**, 359.
Borsa, F., G. Olcese and B.G. Silbernagel, 1973, in: Proc. XVII Congr. Ampere, ed. V. Hovi (North-Holland, Amsterdam) p. 326.
Bose, M., K. Roy and A. Basu, 1980, J. Phys. C **13**, 3951.
Bowden, G.J., 1978, J. Phys. F **8**, L73.
Bowden, G.J., P. Miles, J. Pope and K.N.R. Taylor, 1977, Phys. B (Amsterdam) **86–88B**, 179.
Bowden, G.J., J.M. Cadogan, K.R. Doolan, P.J. Martinson and J.M. Pope, 1982, J. Phys. F **12**, 363.
Bowden, G.J., J.M. Cadogan, W.M. Fairbairn and D.A. Griffin, 1983, J. Phys. F **13**, 191.
Bowman Jr, R.C., D.M. Gruen and M.H. Mendelsohn, 1979, Solid State Commun. **32**, 501.
Boyd, E.L., and R.J. Gambino, 1964, Phys. Rev. Lett. **12**, 20.
Bruker, 1989, Almanac (printed in W.-Germany 10. 1988, Bruker Analytische Messtechnik GmbH) p. 76, 77 and 93–96.
Bucher, E., K. Andres, F.J. di Salvo, J.P. Maita, A.C. Gossard, A.S. Cooper and G.W. Hull Jr, 1975, Phys. Rev. B **11**, 500.
Budnick, J.I., and S. Skalski, 1967, Nuclear Magnetic Resonance in Some Magnetically Ordered Systems, in: Hyperfine Interactions, eds A.J. Freeman and R.B. Frankel (Academic Press, New York) ch. 10, p. 724.
Budnick, J.I., R.E. Gegenwarth and J.H. Wernick, 1965, Bull. Am. Phys. Soc. **10**, 317.
Buschow, K.H.J., 1979, Rep. Prog. Phys. **42**, 1373.
Buschow, K.H.J., and A. Oppelt, 1974, J. Phys. F **4**, 1246.
Buschow, K.H.J., A.M. van Diepen and H.W. de Wijn, 1967, Phys. Lett. A **24**, 536.
Buschow, K.H.J., A.M. van Diepen and H.W. de Wijn, 1970, J. Appl. Phys. **41**, 4609.
Buschow, K.H.J., A.M. van Diepen and H.W. de Wijn, 1971, J. Appl. Phys. **42**, 4315.
Buschow, K.H.J., U. Goebel and E. Dormann, 1979, Phys. Status Solidi b **93**, 607.
Butler, M.A., 1973, Int. J. Magn. **4**, 131.
Campbell, I.A., 1969, J. Phys. C **2**, 1338.
Cannon, J.A., J.I. Budnick and T.J. Burch, 1975, Solid State Commun. **17**, 1385.
Cannon, J.A., J.I. Budnick, T.J. Burch, K. Raj and I. Wang, 1976, J. Magn. & Magn. Mater. **3**, 255.
Carter, G.C., and J.C. Swartz, 1971, J. Phys. Chem. Solids **32**, 2415.
Carter, G.C., L.H. Bennett and D.J. Kahan, 1977, Metallic Shifts in NMR (Pergamon Press, Oxford) Part I-IV, Progress in Materials Science, Vol. 20.
Cherchernikov, V.I., V.I. Nedel'ko and A.V. Vedyaev, 1969, Sov. Phys.-JETP **28**, 255.
Chock, E.P., R.A.B. Devine, S.A. Dodds, R. Orbach and L. Tippie, 1977, J. Phys. F **7**, 1097.
Chu, P.-J., B.C. Gerstein, H.D. Yang and R.N. Shelton, 1988, Phys. Rev. B **37**, 1796.
Clark, W.G., 1964, Rev. Sci. Instrum. **35**, 316.
Coldea, M., and I. Pop, 1975, Acta Phys. Pol. A **48**, 359.
Creyghton, J.H.N., P.R. Locher and K.H.J. Buschow, 1973, Phys. Rev. B **7**, 4829.
Crisan, M., 1986, Phys. Lett. A **115**, 69.
de Azevedo, W.M., I.S. Mackenzie and Y. Berthier, 1985, J. Phys. F **15**, L243.
de Gennes, P.G., 1962, J. Phys. Radium **23**, 510.
de Wijn, H.W., A.M. van Diepen and K.H.J. Buschow, 1967, Phys. Rev. **161**, 253.
de Wijn, H.W., K.H.J. Buschow and A.M. van Diepen, 1968, Phys. Status Solidi **30**, 759.
de Wijn, H.W., A.M. van Diepen and K.H.J. Buschow, 1970, Phys. Rev. B **1**, 4203.
de Wijn, H.W., A.M. van Diepen and K.H.J. Buschow, 1973, Phys. Rev. B **7**, 524.
de Wijn, H.W., A.M. van Diepen and K.H.J. Buschow, 1976, Phys. Status Solidi b **76**, 11.
Degani, J., and N. Kaplan, 1973, Phys. Rev. B **7**, 2132.
Descouts, P., B. Perrin and A. Dupanloup, 1975, in: Magnetic Resonance and related Phenomena, eds P.S. Allen, E.R. Andrew and C.A. Bates, Proc. XVIII Congr. Ampere, Nottingham 1974 (North-Holland, Amsterdam) p. 335.
Devine, R.A.B., and Y. Berthier, 1979, Phys. Rev. B **19**, 5939.
Devine, R.A.B., and Y. Berthier, 1981, J. Magn. & Magn. Mater. **25**, 135.
Dintelmann, F., and K.H.J. Buschow, 1971, Z. Angew. Phys. **31**, 181.
Dintelmann, F., E. Dormann and K.H.J. Buschow, 1970, Solid State Commun. **8**, 1911.
Dormann, E., 1972, Festkörperprobleme XII/Adv. Solid State Phys., ed. O. Madelung (Pergamon-Vieweg, Braunschweig) p. 487.
Dormann, E., 1977, J. Magn. & Magn. Mater. **6**, 87.
Dormann, E., and K.H.J. Buschow, 1973, Phys. Status Solidi b **59**, 411.

Dormann, E., and K.H.J. Buschow, 1976, J. Appl. Phys. **47**, 1662.
Dormann, E., and K.H.J. Buschow, 1977, Phys. B (Amsterdam) **86–88B**, 75.
Dormann, E., and U. Dressel, 1989, Hyperfine Int. **51**, 961.
Dormann, E., K.H.J. Buschow, K.N.R. Taylor, G. Brown and M.A.A. Issa, 1973, J. Phys. F **3**, 220.
Dormann, E., L. Schaafhausen and K.H.J. Buschow, 1976, J. Magn. & Magn. Mater. **2**, 177.
Dormann, E., M. Huck and K.H.J. Buschow, 1977a, J. Magn. & Magn. Mater. **4**, 47.
Dormann, E., M. Huck and K.H.J. Buschow, 1977b, Z. Phys. B **27**, 141.
Dormann, E., U. Goebel, H. Kropp and K.H.J. Buschow, 1980, J. Magn. & Magn. Mater. **15–18**, 658.
Dormann, E., H. de Graaf, R.C. Thiel and K.H.J. Buschow, 1982, J. Magn. & Magn. Mater. **30**, 231.
Dormann, E., U. Dressel, H. Kropp and K.H.J. Buschow, 1984, J. Magn. & Magn. Mater. **45**, 207.
Dormann, E., U. Dressel and U. Meister, 1986, J. Magn. & Magn. Mater. **54–57**, 507.
Dressel, U., and E. Dormann, 1988, J. Phys. (Paris) Colloq. **49**, C8-455.
Dressel, U., U. Meister, E. Dormann and K.H.J. Buschow, 1988, J. Magn. & Magn. Mater. **74**, 91.
Dumelow, T., and P.C. Riedi, 1987, Hyperfine Int. **35**, 1061.
Dumelow, T., P.C. Riedi, P. Mohn, K. Schwarz and Y. Yamada, 1986, J. Magn. & Magn. Mater. **54–57**, 1081.
Dumelow, T., D.K. Fowler, O. Prakash and P.C. Riedi, 1987, Hyperfine Int. **34**, 411.
Dumelow, T., P.C. Riedi, J.S. Abell and O. Prakash, 1988, J. Phys. F **18**, 307.
Durand, J., 1959, Rev. Sci. Instrum. **30**, 840.
Ebner, C., and C.C. Sung, 1973, Phys. Rev. B **8**, 5226.
Eckrich, K., E. Dormann, A. Oppelt and K.H.J. Buschow, 1972, Phys. Lett. A **41**, 23.
Eckrich, K., E. Dormann, A. Oppelt and K.H.J. Buschow, 1973, Int. J. Magn. **5**, 75.
Eckrich, K., E. Dormann, A. Oppelt and K.H.J. Buschow, 1976, Z. Phys. B **23**, 157.
Edwards, D.M., 1976, J. Phys. F **6**, L185.
Eidelman, O., D. Fekete and N. Kaplan, 1978, J. Phys. F **8**, L67.
Endo, K., M. Iijima, A. Shinogi, T. Goto and T. Sakakibara, 1988, J. Phys. (Paris) Colloq. **49**, C8-265.
Englich, J., H. Stěpánková, V. Sechovsky and H. Lütgemeier, 1989, Hyperfine Int. **50**, 729.
Erdmann, K., and M. Rosenberg, 1989, J. Magn. & Magn. Mater. **82**, 273.
Erdmann, K., P. Deppe, M. Rosenberg and K.H.J. Buschow, 1987, J. Appl. Phys. **61**, 4340.
Erdmann, K., M. Rosenberg and K.H.J. Buschow, 1988a, J. Appl. Phys. **63**, 4113.
Erdmann, K., M. Rosenberg and K.H.J. Buschow, 1988b, J. Appl. Phys. **63**, 4116.
Erdmann, K., M. Rosenberg and K.H.J. Buschow, 1988c, J. Phys. (Paris) Colloq. **49**, C8-583.
Erdmann, K., Th. Sinnemann, M. Rosenberg and K.H.J. Buschow, 1989, J. Less Common Metal **146**, 59.
Erdmann, K., M. Rosenberg and K.H.J. Buschow, 1990, J. Magn. & Magn. Mater. **83**, 315.
Fekete, D., A. Grayevskey, N. Kaplan and E. Walker, 1975, Solid State Commun. **17**, 573.
Fertig, W.A., D.C. Johnston, L.E. DeLong, R.W. McCallum, M.B. Maple and B.T. Matthias, 1977, Phys. Rev. Lett. **38**, 987.
Figiel, H., 1982a, J. Magn. & Magn. Mater. **27**, 303.
Figiel, H., 1982b, J. Magn. & Magn. Mater. **29**, 117.
Figiel, H., 1983, Zesz. Nauk. Akad. Gorniczo-Hutn. Mat. Fiz. Chem. v. **937**(8), p. 1.
Figiel, H., and M. Jaszczewski, 1980, J. Magn. & Magn. Mater. **15–18**, 673.
Figiel, H., A. Oppelt, E. Dormann and K.H.J. Buschow, 1976, Phys. Status Solidi a **36**, 275.
Figiel, H., A. Oppelt, E. Dormann and K.H.J. Buschow, 1977, Phys. B (Amsterdam) **86–88B**, 77.
Figiel, H., E. Gratz and Cz. Kapusta, 1981, J. Magn. & Magn. Mater. **23**, 123.
Figiel, H., K. Lemańska, A. Lemański, A. Kulak and A. Semkowicz, 1982, Acta Phys. Pol. A **61**, 99.
Figiel, H., A.C. Barata and A.P. Guimarães, 1987a, Phys. Status Solidi b **139**, 311.
Figiel, H., D. Fowler, T. Dumelow, P.C. Riedi and Cz. Kapusta, 1987b, J. Magn. & Magn. Mater. **65**, 83.
Figiel, H., Cz. Kapusta, G. Sachs and K. Latka, 1989, Hyperfine Int. **51**, 967.
Follstaedt, D.M., W.J. Meyer and A. Narath, 1977, Phys. B (Amsterdam) **86–88B**, 507.
Fradin, F.Y., 1970, J. Phys. Chem. Solids **31**, 2715.

Fujii, H., J. Fujimoto, S. Takeda, T. Hihara and T. Okamoto, 1983, J. Magn. & Magn. Mater. **31–34**, 223.

Fujiwara, K., K. Ichinose, H. Nagai and A. Tsujimura, 1983, J. Magn. & Magn. Mater. **31–34**, 707.

Fujiwara, K., K. Ichinose, H. Nagai and A. Tsujimura, 1988, J. Phys. (Paris) Colloq. **49**, C8-519.

Fukushima, E., and S.B.W. Roeder, 1981, Experimental Pulse NMR (Addison-Wesley, MA).

Fukushima, E., V.O. Strubeing and H.H. Hill, 1975, J. Phys. Soc. Jpn. **39**, 921.

Gegenwarth, R.E., J.I. Budnick, S. Skalski and J.H. Wernick, 1966, J. Appl. Phys. **37**, 1244.

Gegenwarth, R.E., J.I. Budnick, S. Skalski and J.H. Wernick, 1967, Phys. Rev. Lett. **18**, 9.

Gehring, G.A., and A.B. Walker, 1981, J. Phys. C **14**, 5523.

Goebel, U., and E. Dormann, 1979, J. Magn. & Magn. Mater. **13**, 219.

Goebel, U., E. Dormann and K.H.J. Buschow, 1975, J. Phys. F **5**, 2198.

Goebel, U., E. Dormann and K.H.J. Buschow, 1977, J. Magn. & Magn. Mater. **6**, 166.

Göring, R., B. Schnabel and O.J. Zogał, 1980, Phys. Status Solidi a **59**, K147.

Gossard, A.C., and V. Jaccarino, 1962, Proc. Phys. Soc. **80**, 877.

Gossard, A.C., V. Jaccarino and J.H. Wernick, 1964, Phys. Rev. **133**, A881.

Grover, A.K., L.C. Gupta and R. Vijayaraghavan, 1977, Phys. B (Amsterdam) **86-88B**, 81.

Grover, A.K., S.K. Malik, R. Vijayaraghavan and K. Shimizu, 1979, J. Appl. Phys. **50**, 7501.

Guimarães, A.P., K.M.B. Alves, N. Alves and E. Gratz, 1987, J. Appl. Phys. **61**, 3985.

Gupta, L.C., D.E. MacLaughlin, Ch. Tien, C. Godart, M.A. Edwards and R.D. Parks, 1983, Phys. Rev. B **28**, 3673.

Hăgan, C., and I. Pop, 1986, J. Magn. & Magn. Mater. **58**, 78.

Halstead, T.K., 1974, J. Solid State Chem. **11**, 114.

Halstead, T.K., N.A. Abood and K.H.J. Buschow, 1976, Solid State Commun. **19**, 425.

Heiniger, F., E. Bucher, J.P. Maita and P. Descouts, 1973, Phys. Rev. B **8**, 3194.

Herbst, U., J. Schraub, E. Dormann and K.H.J. Buschow, 1974, Phys. Status Solidi b **61**, K101.

Hioki, T., and Y. Masuda, 1977, J. Phys. Soc. Jpn. **43**, 1200.

Hiraoka, K., T. Hihara, T. Shigeoka, H. Fujii and T. Okamoto, 1987, J. Magn. & Magn. Mater. **70**, 255.

Hirosawa, S., and Y. Nakamura, 1982a, J. Magn. & Magn. Mater. **25**, 284.

Hirosawa, S., and Y. Nakamura, 1982b, J. Phys. Soc. Jpn. **51**, 1162.

Hirosawa, S., and Y. Nakamura, 1982c, J. Phys. Soc. Jpn. **51**, 2464.

Hirosawa, S., and Y. Nakamura, 1982d, J. Phys. Soc. Jpn. **51**, 2819.

Hirosawa, S., and Y. Nakamura, 1982e, J. Appl. Phys. **53**, 2069.

Hirosawa, S., T. Tsuchida and Y. Nakamura, 1979, J. Phys. Soc. Jpn. **47**, 804.

Ichinose, K., 1987, J. Phys. Soc. Jpn. **56**, 2908.

Ichinose, K., K. Fujiwara, H. Yoshie, H. Nagai and A. Tsujimura, 1982, J. Phys. Soc. Jpn. **51**, 3853.

Ichinose, K., K. Fujiwara, H. Yoshie, H. Nagai and A. Tsujimura, 1983, J. Phys. Soc. Jpn. **52**, 4318.

Ichinose, K., K. Fujiwara, H. Yoshie, H. Nagai and A. Tsujimura, 1984a, J. Phys. Soc. Jpn. **53**, 2741.

Ichinose, K., K. Fujiwara, H. Yoshie, H. Nagai and A. Tsujimura, 1984b, J. Phys. Soc. Jpn. **53**, 4359.

Ichinose, K., K. Fujiwara, H. Yoshie, H. Nagai and A. Tsujimura, 1985, J. Phys. Soc. Jpn. **54**, 1103.

Ichinose, K., K. Fujiwara, M. Oyasato, H. Nagai and A. Tsujimura, 1988a, J. Phys. (Paris) Colloq. **49**, C8-595.

Ichinose, K., K. Fujiwara, M. Oyasato, H. Nagai and A. Tsujimura, 1988b, J. Phys. (Paris) Colloq. **49**, C8-1101.

Inomata, K., 1976a, J. Phys. Soc. Jpn. **41**, 1890.

Inomata, K., 1976b, Jpn. J. Appl. Phys. **15**, 821.

Inomata, K., 1981, Phys. Rev. B **23**, 2076.

Ishii, H., 1988, J. Phys. (Paris) Colloq. **49**, C8-2055.

Jaccarino, V., 1961, J. Appl. Phys. **32**, 102S.

Jaccarino, V., and L.R. Walker, 1965, Phys. Rev. Lett. **15**, 258.

Jaccarino, V., B.T. Matthias, M. Peter, H. Suhl and J.H. Wernick, 1960, Phys. Rev. Lett. **5**, 251.

Jedryka, E., M. Wójcik, P. Panissod, M. Rosenberg, S. Hirosawa and M. Sagawa, 1988, J. Phys. (Paris) Colloq. **49**, C8-587.

Jedryka, E., M. Wójcik, P. Panissod and K.H.J. Buschow, 1990, J. Appl. Phys. **67**, 4586.
Jena, P., and D.J. Lam, 1978, Phys. Rev. B **17**, 1.
Johnston, D.C., and B.G. Silbernagel, 1980, Phys. Rev. B **21**, 4996.
Jones, E.D., 1967, Phys. Rev. Lett. **19**, 432.
Jones, E.D., 1968, J. Appl. Phys. **39**, 1090.
Jones, E.D., 1969, Phys. Rev. **180**, 455.
Jones, E.D., and J.I. Budnick, 1966, J. Appl. Phys. **37**, 1250.
Jones, E.P., and D.L. Williams, 1962, Phys. Lett. **1**, 109.
Jones Jr, W.H., T.P. Graham and R.G. Barnes, 1963, Phys. Rev. **132**, 1898.
Joon, E.R., I.A. Heinmaa and A.V. Skripov, 1989, Solid State Commun. **71**, 1061.
Kakol, Z., and H. Figiel, 1986, Phys. Status Solidi b **138**, 151.
Kaplan, N., E. Dormann, K.H.J. Buschow and D. Lebenbaum, 1973, Phys. Rev. B **7**, 40.
Kaplan, N., D.L. Williams and A. Grayevsky, 1980, Phys. Rev. B **21**, 899.
Kapusta, Cz., and H. Figiel, 1988, J. Phys. (Paris) Colloq. **49**, C8-559.
Kapusta, Cz., Z. Kakol, H. Figiel and R. Radwanski, 1986, J. Magn. & Magn. Mater. **59**, 169.
Kapusta, Cz., N. Spiridis and H. Figiel, 1990, J. Magn. & Magn. Mater. **83**, 153.
Kasamatsu, Y., K. Kojima, T. Hihara and T. Kamigaichi, 1988, J. Phys. (Paris) Colloq. **49**, C8-389.
Kasaya, M., F. Iga, M. Takigawa and T. Kasuya, 1985, J. Magn. & Magn. Mater. **47 + 48**, 429.
Kasuya, T., 1956, Progr. Theor. Phys. **16**, 45.
Kasuya, T., M. Kasaya, K. Takegahara, T. Fujita, T. Goto, A. Tamaki, M. Takigawa and H. Yasuoka, 1983, J. Magn. & Magn. Mater. **31–34**, 447.
Kawakami, M., 1981, J. Phys. F **11**, 267.
Kawakami, M., S. Kunii, K. Mizuno, M. Sugita, T. Kasuya and K. Kume, 1981, J. Phys. Soc. Jpn. **50**, 432.
Kawakami, M., K. Mizuno, S. Kunii, T. Kasuya, H. Enokiya and K. Kume, 1982, J. Magn. & Magn. Mater. **30**, 201.
Kawakami, M., H.G. Bohn, H. Lütgemeier, S. Kunii and T. Kasuya, 1983, J. Magn. & Magn. Mater. **31–34**, 415.
Khodosov, E.F., and I.I. Khodos, 1971, Sov. Phys. Solid State **12**, 2213.
Khodosov, E.F., V.K. Prokopenko and A.I. Linnik, 1974, Sov. Phys. Solid State **16**, 157.
Kitaoka, Y., K. Ueda, T. Kohara and K. Asayama, 1984, Solid State Commun. **51**, 461.
Kitaoka, Y., H. Arimoto, Y. Kohori and K. Asayama, 1985a, J. Phys. Soc. Jpn. **54**, 3236.
Kitaoka, Y., K. Fujiwara, Y. Kohori, K. Asayama, Y. Onuki and T. Komatsubara, 1985b, J. Phys. Soc. Jpn. **54**, 3686.
Kitaoka, Y., K. Ueda, T. Kohara, K. Asayama, Y. Onuki and T. Komatsubara, 1985c, J. Magn. & Magn. Mater. **52**, 341.
Kitaoka, Y., K. Ueda, K. Fujiwara, H. Arimoto, H. Iida and K. Asayama, 1986, J. Phys. Soc. Jpn. **55**, 723.
Kohara, T., Y. Kohori, K. Kumagai and K. Asayama, 1983, Phys. Lett. A **96**, 425.
Kohori, Y., K. Kumagai and K. Asayama, 1983a, J. Phys. Soc. Jpn. **52**, 2910.
Kohori, Y., M. Matsumura, T. Kohara, K. Kumagai and K. Asayama, 1983b, J. Magn. & Magn. Mater. **31–34**, 495.
Kohori, Y., Y. Kitaoka, K. Kumagai and K. Asayama, 1984, J. Phys. Soc. Jpn. **53**, 780.
Kohori, Y., T. Kohara, K. Asayama and K. Kumagai, 1985, J. Phys. Soc. Jpn. **54**, 409.
Kohori, Y., T. Kohara, K. Asayama, N. Satoh, H. Yashima, H. Mori and T. Satoh, 1986, J. Magn. & Magn. Mater. **54–57**, 437.
Koi, L.D., 1969, Phys. Lett. A **28**, 671.
Kopp, J.P., and D.S. Schreiber, 1967, J. Appl. Phys. **38**, 1373.
Kropp, H., 1983, Knight-Shift Messungen an ferromagnetisch geordneten Einkristallen, Ph.D. Thesis (D17), Technische Hochschule Darmstadt, D-61 Darmstadt, Fed. Rep. Germany, unpublished.
Kropp, H., E. Dormann and K.H.J. Buschow, 1979a, Solid State Commun. **32**, 507.
Kropp, H., W. Zipf, E. Dormann and K.H.J. Buschow, 1979b, J. Magn. & Magn. Mater. **13**, 224.
Kropp, H., E. Dormann, A. Grayevsky and N. Kaplan, 1983, J. Phys. F **13**, 207.
Kropp, H., E. Dormann, U. Köbler and W. Assmus, 1984, J. Phys. F **14**, 2177.
Kumagai, K., and K. Asayama, 1975, J. Phys. Soc. Jpn. **39**, 543.
Kumagai, K., and F.Y. Fradin, 1983a, Phys. Rev. B **27**, 2770.
Kumagai, K., and F.Y. Fradin, 1983b, J. Magn. & Magn. Mater. **31–34**, 523.
Kumagai, K., T. Matsuhira and K. Asayama, 1978, J. Phys. Soc. Jpn. **45**, 422.

Kumagai, K., Y. Inoue and K. Asayama, 1979, J. Phys. Soc. Jpn. **47**, 1363.
Kumagai, K., Y. Inoue and K. Asayama, 1980, Solid State Commun. **35**, 531.
Kumagai, K., K. Kon and F.Y. Fradin, 1985, J. Magn. & Magn. Mater. **52**, 452.
Kume, K., and H. Yamagishi, 1964, J. Phys. Soc. Jpn. **19**, 414.
Kunkel, H.P., and C.W. Searle, 1981, Phys. Rev. B **23**, 65.
Kyogaku, M., Y. Kitaoka, H. Nakamura, K. Asayama, T. Takabatake, F. Teshima and H. Fujii, 1990, J. Phys. Soc. Jpn. **59**, 1728.
Laforest, J., R. Lemaire, H. Nagai and A. Tsujimura, 1983, Solid State Commun. **48**, 941.
Lawrence, J.M., P.S. Riseborough and R.D. Parks, 1981, Rep. Prog. Phys. **44**, 1.
Levin, R., A. Grayevsky, D. Shaltiel, V. Zevin, D. Davidov, D.L. Williams and N. Kaplan, 1979, Solid State Commun. **32**, 855.
Levy, P.M., 1969, Solid State Commun. **7**, 1813.
Lewicki, A., Z. Tarnawski, Cz. Kapusta, A. Kolodziejczyk, H. Figiel, J. Chmist, Z. Lalowicz and L. Sniadower, 1983, J. Magn. & Magn. Mater. **36**, 297.
Lysak, M.J., and D.E. MacLaughlin, 1985, Phys. Rev. B **31**, 6963.
Machowska, E., and S. Nadolski, 1988, Solid State Commun. **68**, 215.
MacLaughlin, D.E., 1976, Solid State Phys. **31**, 1.
MacLaughlin, D.E., 1977, J. Low Temp. Phys. **26**, 111.
MacLaughlin, D.E., 1980, J. Magn. & Magn. Mater. **15–18**, 695.
MacLaughlin, D.E., 1981, in: Valence Fluctuations in Solids, eds L.M. Falicov, W. Hanke and M.B. Maple (North-Holland, Amsterdam) p. 321.
MacLaughlin, D.E., 1985, J. Magn. & Magn. Mater. **47 + 48**, 121.
MacLaughlin, D.E., 1989, Hyperfine Int. **49**, 43.
MacLaughlin, D.E., and M. Daugherty, 1972, Phys. Rev. B **6**, 2502.
MacLaughlin, D.E., and R.R. Hewitt, 1978, J. Appl. Phys. **49**, 2121.
MacLaughlin, D.E., M. Daugherty and K. Parvin, 1973, Solid State Commun. **12**, 5.
MacLaughlin, D.E., H. Alloul and M. Daugherty, 1976, Solid State Commun. **18**, 901.
MacLaughlin, D.E., F.R. de Boer, J. Bijvoet, P.F. de Châtel and W.C.M. Mattens, 1979, J. Appl. Phys. **50**, 2094.
MacLaughlin, D.E., O. Peña and M. Lysak, 1981, Phys. Rev. B **23**, 1039.
MacLaughlin, D.E., Ch. Tien, L.C. Gupta, J. Aarts, F.R. de Boer and Z. Fisk, 1984, Phys. Rev. B **30**, 1577.
Makihara, Y., H. Fujii, K. Hiraoka and T. Hihara, 1988, J. Phys. (Paris) Colloq. **49**, C8-1087.
Malik, S.K., 1970, Phys. Lett. A **31**, 33.
Malik, S.K., and R. Vijayaraghavan, 1971a, J. Phys. (Paris) Colloq. **32**, C1-1028.
Malik, S.K., and R. Vijayaraghavan, 1971b, Phys. Lett. A **34**, 67.
Malik, S.K., R. Vijayaraghavan, S.K. Garg and R.J. Ripmeester, 1975, Phys. Status Solidi b **68**, 399.
Malik, S.K., R. Vijayaraghavan, S.K. Garg and R.J. Ripmeester, 1977, Solid State Commun. **21**, 245.
Malik, S.K., S.K. Dhar, R. Vijayaraghavan, K. Shimizu and W.E. Wallace, 1982a, in: The rare earths in modern science and technology, Vol. 3, eds G.J. McCarthy, H.B. Silber and J.J. Rhyne, 15th Rare Earth Conference, Rolla, MO, 1981 (Plenum Press, New York) p. 385.
Malik, S.K., S.K. Dhar, R. Vijayaraghavan and W.E. Wallace, 1982b, J. Appl. Phys. **53**, 8074.
Maple, M.B., 1983, J. Magn. Magn. Mater **31–34**, 479.
Martynova, L.F., V.I. Cherchernikov and V.I. Nedel'ko, 1976, Fiz. Met. Metalloved. [Phys. Met. Metallogr. **41**, 1298].
Masuda, Y., and M. Hashimoto, 1971, J. Phys. Soc. Jpn. **31**, 1661.
Matsui, K., and Y. Masuda, 1977, J. Phys. Soc. Jpn. **43**, 1169.
Matsumura, M., K. Asayama and K. Kumagai, 1982, Solid State Commun. **42**, 641.
McCausland, M.A.H., and I.S. Mackenzie, 1980, Nuclear Magnetic Resonance in Rare Earth Metals (Taylor & Francis, London) reprinted from Adv. Phys. **28**(3), 305, 1979.
McHenry, M.R., B.G. Silbernagel and J.R. Wernick, 1972, Phys. Rev. B **5**, 2958.
McMorrow, D.F., C. Carboni and M.A.H. McCausland, 1986, J. Magn. & Magn. Mater. **54–57**, 485.
McNiff Jr, E.J., and S. Shapiro, 1963, J. Phys. Chem. Solids **24**, 939.

Meyer, C., F. Hartmann-Boutron, Y. Gros, Y. Berthier and J.L. Buevoz, 1981, J. Phys. (Paris) **42**, 605.
Miles, P., M.A.A. Issa, K.N.R. Taylor and G.J. Bowden, 1977, J. Phys. F **7**, 2421.
Moore, J.M., W.G. Clark, J. Sanny, W.H. Wong, W.A. Hines, D.P. Yang and M. Schlott, 1990, Phys. B (Amsterdam) **163**, 522.
Moriya, T., 1977, Phys. B (Amsterdam) **86–88B**, 356.
Myers, S.M., and A. Narath, 1971, Phys. Rev. Lett. **27**, 641.
Myers, S.M., and A. Narath, 1973a, Phys. Rev. B **7**, 4776.
Myers, S.M., and A. Narath, 1973b, Solid State Commun. **12**, 83.
Myers, S.M., and A. Narath, 1974, Phys. Rev. B **9**, 227.
Nadolski, S., E. Machowska and E. Burzo, 1989, Solid State Commun. **71**, 97.
Nagai, H., 1989, Hyperfine Int. **51**, 1003.
Nagai, H., H. Yoshie, T. Unate, A. Tsujimura and J. Deportes, 1976, J. Phys. Soc. Jpn. **41**, 1907.
Nagai, H., Y. Ikami, H. Yoshie and A. Tsujimura, 1981, J. Phys. Soc. Jpn. **50**, 1873.
Nagai, H., H. Yoshie and A. Tsujimura, 1983, J. Phys. Soc. Jpn. **52**, 1122.
Nagai, H., K. Kojima and H. Yoshie, 1988a, J. Phys. (Paris) Colloq. **49**, C8-535.
Nagai, H., M. Takigawa and H. Yasuoka, 1988b, J. Phys. Soc. Jpn. **57**, 3690.
Nakamura, H., Y. Kitaoka, K. Asayama and J. Flouquet, 1988a, J. Phys. Soc. Jpn. **57**, 2644.
Nakamura, H., Y. Kitaoka, K. Asayama and J. Flouquet, 1988b, J. Magn. & Magn. Mater. **76 + 77**, 465.
Nakamura, H., Y. Kitaoka, K. Asayama, Y. Onuki and T. Komatsubara, 1988c, J. Phys. Soc. Jpn. **57**, 2276.
Nakamura, H., Y. Kitaoka, K. Asayama, Y. Onuki and T. Komatsubara, 1988d, J. Magn. & Magn. Mater. **76 + 77**, 467.
Nakamura, H., Y. Kitaoka, K. Yoshimura, Y. Kohori, K. Asayama, M. Shiga and Y. Nakamura, 1988e, J. Phys. (Paris) Colloq. **49**, C8-257.
Nakamura, H., H. Wada, K. Yoshimura, M. Shiga, Y. Nakamura, J. Sakurai and Y. Komura, 1988f, J. Phys. F **18**, 981.
Nambudripad, N., K.V. Gopalakrishnan, L.C. Gupta and R. Vijayaraghavan, 1986, J. Magn. & Magn. Mater. **54–57**, 1201.
Narath, A., 1967, Nuclear Magnetic Resonance in Magnetic and Metallic Solids, in: Hyperfine Interactions, eds A.J. Freeman and R.B. Frankel (Academic Press, New York) ch. 7, p. 287.
Narath, A., and T. Fromhold Jr, 1967, Phys. Lett. A **25**, 49.
Niculescu, V., I. Pop and M. Rosenberg, 1971, Phys. Lett. A **34**, 265.
Niculescu, V., I. Pop and M. Rosenberg, 1972, Phys. Status Solidi b **53**, 701.
Niculescu, V., I. Pop and M. Rosenberg, 1973a, J. Phys. Chem. Solids **34**, 961.
Niculescu, V., I. Pop and M. Rosenberg, 1973b, Acta Phys. Pol. A **43**, 279.
Nikitin, S.A., V.A. Vasil'kovskii, N.M. Kovtun, A.K. Kupriyanov and V.F. Ostrovskii, 1975a, Sov. Phys. Solid State **16**, 2031.
Nikitin, S.A., V.A. Vasil'kovskii, N.M. Kovtun, A.K. Kupriyanov and V.F. Ostrovskii, 1975b, Sov. Phys.-JETP **41**, 285.
Nikitin, S.A., V.A. Vasil'kovskii, N.M. Kovtun and A.K. Kupriyanov, 1976, Sov. Phys.-JETP **42**, 1125.
Nikitin, S.A., A.Kh.M. Bisliev and A.K. Kupriyanov, 1988, Bull. Acad. Sci. USSR, Phys. Ser. **52**, 75.
Ohno, T., Y. Kishimoto, Y. Yamada, Y. Michihiro and T. Kanashiro, 1989, J. Phys. Soc. Jpn. **58**, 50.
Okamoto, T., H. Fujii, Y. Makihara, T. Hihara and Y. Hashimoto, 1986, J. Magn. & Magn. Mater. **54–57**, 1087.
Oliveira, I.S., and A.P. Guimarães, 1988, J. Phys. (Paris) Colloq. **49**, C8-371.
Oppelt, A., and K.H.J. Buschow, 1973, J. Phys. F **3**, L212.
Oppelt, A., and K.H.J. Buschow, 1976, Phys. Rev. B **13**, 4698.
Oppelt, A., E. Dormann and K.H.J. Buschow, 1972a, Phys. Status Solidi b **51**, 275.
Oppelt, A., E. Dormann and K.H.J. Buschow, 1972b, Int. J. Magnetism **3**, 55.
Oppelt, A., A. Merkel and K.H.J. Buschow, 1976, Phys. Status Solidi a **37**, K205.
Oppelt, A., J. Schäfer, G. Wiesinger and K.H.J. Buschow, 1977, J. Magn. & Magn. Mater. **6**, 163.
Orlov, V.G., 1985, Sov. Phys. Solid State **27**, 1432.
Orlov, V.G., 1986, J. Magn. & Magn. Mater. **61**, 337.
Panissod, P., M. Benakki and A. Qachaou, 1988, J. Phys. (Paris) Colloq. **49**, C8-685.

Panissod, P., E. Jedryka, M. Wójcik and J.I. Budnick, 1989, Phys. Rev. B **40**, 2606.
Parks, R.D., 1985, Hyperfine Int. **25**, 565.
Peña, O., M. Lysak, D.E. MacLaughlin and Z. Fisk, 1981a, Solid State Commun. **40**, 539.
Peña, O., D.E. MacLaughlin, M. Lysak and Z. Fisk, 1981b, J. Appl. Phys. **52**, 2152.
Phua, T.-T., B.J. Beaudry, D.T. Peterson, D.R. Torgeson, R.G. Barnes, M. Belhoul, G.A. Styles and E.F.W. Seymour, 1983, Phys. Rev. B **28**, 6227.
Pieper, M.W., H. Lütgemeier and W. Zinn, 1984, Solid State Commun. **50**, 125.
Pieper, M.W., H. Lütgemeier and W. Zinn, 1986, Z. Phys. B **63**, 369.
Pokatilov, V.S., V.V. Sadchikov and O.V. Utenkova, 1985, Sov. Phys. Dokl. **30**, 250.
Pokatilov, V.S., V.V. Golikova and E.F. Sidokhin, 1989, Sov. Phys.-JETP **68**, 1202.
Pop, I., M. Coldea and V. Niculescu, 1974, Czech. J. Phys. B **24**, 1398.
Pop, I., M. Coldea and W.E. Wallace, 1978, J. Solid State Chem. **26**, 115.
Pop, I., E. Rus, M. Coldea and O. Pop, 1979a, J. Phys. Chem. Solids **40**, 683.
Pop, I., E. Rus, M. Coldea and O. Pop, 1979b, Phys. Status Solidi a **54**, 365.
Pop, I., E. Rus and O. Pop, 1980, J. Phys. Chem. Solids **41**, 1315.
Potenziani II, E., 1985, J. Appl. Phys. **58**, 2764.
Prakash, O., M.A. Chaudhry, J.W. Ross and M.A.H. McCausland, 1983, J. Magn. & Magn. Mater. **36**, 271.
Prakash, O., D.St.P. Bunbury and M.A.H. McCausland, 1984, Z. Phys. B **58**, 39.
Quinn, R.K., and H.T. Weaver, 1976, J. Solid State Chem. **16**, 197.
Raizman, A., D. Zamir and R.M. Cotts, 1985, Phys. Rev. B **31**, 3384.
Rao, V.U.S., and R. Vijayaraghavan, 1965, Phys. Lett. **19**, 168.
Ray, D.K., 1974, Solid State Commun. **15**, 1471.
Riedi, P.C., and G.D. Webber, 1983, J. Phys. F **13**, 1057.
Riedi, P.C., T. Dumelow and J.S. Abell, 1985, Phys. B (Amsterdam) **130B**, 449.
Riedi, P.C., T. Dumelow and J.S. Abell, 1988, J. Phys. (Paris) Colloq. **49**, C8-451.
Rosenberg, M., P. Deppe, M. Wójcik and H. Stadelmaier, 1985, J. Appl. Phys. **57**, 4124.
Rosenberg, M., P. Deppe, K. Erdmann, M. Sostarich and H. Stadelmaier, 1986, J. Magn. & Magn. Mater. **54–57**, 599.
Ross, J.W., O. Prakash and M.A.H. McCausland, 1983, J. Phys. F **13**, L95.
Roth, S., 1978, Appl. Phys. **15**, 1.
Rubinstein, M., L.J. Swartzendruber and L.H. Bennett, 1979, J. Appl. Phys. **50**, 2046.
Rubinstein, M., P. Lubitz and N.C. Koon, 1981, J. Magn. & Magn. Mater. **24**, 288.
Ruderman, M.A., and C. Kittel, 1954, Phys. Rev. **96**, 99.
Sampathkumaran, E.V., L.C. Gupta and R. Vijayaraghavan, 1979a, Phys. Lett. A **70**, 356.
Sampathkumaran, E.V., L.C. Gupta and R. Vijayaraghavan, 1979b, J. Phys. C **12**, 4323.
Sampathkumaran, E.V., L.C. Gupta and R. Vijayaraghavan, 1979c, Phys. Rev. Lett. **43**, 1189.
Sampathkumaran, E.V., L.C. Gupta and R. Vijayaraghavan, 1980a, J. Magn. & Magn. Mater. **15–18**, 977.
Sampathkumaran, E.V., L.C. Gupta, R. Vijayaraghavan, T.K. Hatwar, M.N. Ghatikar and B.D. Padalia, 1980b, Mater. Res. Bull. **15**, 939.
Sampathkumaran, E.V., L.C. Gupta and R. Vijayaraghavan, 1981, in: Valence Fluctuations in Solids, eds L.M. Falicov, W. Hanke and M.B. Maple (North-Holland, Amsterdam), p. 241.
Sampathkumaran, E.V., L.C. Gupta and R. Vijayaraghavan, 1982a, Phys. Lett. A **88**, 180.
Sampathkumaran, E.V., L.C. Gupta, R. Vijayaraghavan, Le Dang Khoi and P. Veillet, 1982b, J. Phys. F **12**, 1039.
Sampathkumaran, E.V., L.C. Gupta and R. Vijayaraghavan, 1983, J. Magn. & Magn. Mater. **31–34**, 413.
Sampathkumaran, E.V., I. Stang, R. Vijayaraghavan, G. Kaindl and K. Lüders, 1985, Phys. Rev. B **31**, 6099.
Satoh, K., Y. Kitaoka, H. Yasuoka, S. Takayanagi and T. Sugawara, 1981, J. Phys. Soc. Jpn. **50**, 351.
Schirber, J.E., and H.T. Weaver, 1979, J. Phys. (Paris) Colloq. **40**, C5-124.
Schmidt, V.H., 1973, Proc. 10th Rare Earth Res. Conf. Carefree, Arizona (USAEC: Techn. Inf. Center) Vol. II, p. 1007.
Schmitt, D., and P.M. Levy, 1984, Phys. Rev. B **29**, 2850.

Schreiber, D.S., 1965, Phys. Rev. A **137**, 860.
Schreiber, D.S., and R.M. Cotts, 1963, Phys. Rev. **131**, 1118.
Searle, C.W., H.P. Kunkel, C. Kupca and I. Maartense, 1977, Phys. Rev. B **15**, 3305.
Seipler, D., B. Bremicker, U. Goebel, H. Happel, H.E. Hoenig and B. Perrin, 1977, J. Phys. F **7**, 599.
Seitchik, J.A., V. Jaccarino and J.H. Wernick, 1965, Phys. Rev. A **138**, 148.
Shaltiel, D., A.C. Gossard and J.H. Wernick, 1965, Phys. Rev. A **137**, 1027.
Shamir, N., N. Kaplan and J.H. Wernick, 1971, J. Phys. (Paris) Colloq. C1, **32**, C1-902.
Shaw, K.I., I.S. Mackenzie and M.A.H. McCausland, 1983, J. Phys. F **13**, 1735.
Shen, L., J.P. Kopp and D.S. Schreiber, 1969, Phys. Lett. A **29**, 438.
Shevchenko, V.I., A.N. Pogorelyi and V.I. Perepelitsa, 1983, Sov. Phys. Solid State **25**, 1269.
Shevchenko, V.I., A.N. Pogorelyi and V.I. Perepelitsa, 1987, Fiz. Met. Metalloved. **64**, 1018.
Shiga, M., H. Wada and Y. Nakamura, 1983, J. Magn. & Magn. Mater. **31–34**, 119.
Shiga, M., H. Wada, K. Yoshimura and Y. Nakamura, 1986, J. Magn. & Magn. Mater. **54–57**, 1073.
Shimizu, K., 1982, J. Phys. Soc. Jpn. **51**, 2703.
Shimizu, K., 1985a, J. Phys. Soc. Jpn. **54**, 1154.
Shimizu, K., 1985b, J. Phys. Soc. Jpn. **54**, 2009.
Shimizu, K., and S. Okeya, 1986, J. Phys. Soc. Jpn. **55**, 1062.
Shimizu, K., S.K. Dhar, R. Vijayaraghavan and S.K. Malik, 1981, J. Phys. Soc. Jpn. **50**, 1200.
Shimizu, T., M. Takigawa, H. Yasuoka, Y. Onuki and T. Komatsubara, 1985a, J. Phys. Soc. Jpn. **54**, 470.
Shimizu, T., M. Takigawa, H. Yasuoka and J.H. Wernick, 1985b, J. Magn. & Magn. Mater. **52**, 187.
Shimizu, T., H. Yasuoka, Z. Fisk and J.L. Smith, 1987, J. Phys. Soc. Jpn. **56**, 4113.
Silbernagel, B.G., and J.H. Wernick, 1973, Phys. Rev. B **7**, 4787.
Silbernagel, B.G., V. Jaccarino, P. Pincus and J.H. Wernick, 1968, Phys. Rev. Lett. **20**, 1091.
Sinneman, Th., M.U. Wisniewski, M. Rosenberg and K.H.J. Buschow, 1990, J. Magn. & Magn. Mater. **83**, 259.
Sinnemann, Th., K. Erdmann, M. Rosenberg and K.H.J. Buschow, 1989, Hyperfine Int. **50**, 675.
Slichter, C.P., 1978, Principles of Magnetic Resonance (Springer, Berlin).
Smith, W.C., R.G. Barnes and D.R. Torgeson, 1971, Bull. Am. Phys. Soc. **16**, 315.
Speight, P.A., K.R. Jeffrey and J.A. Courtney, 1974, J. Phys. E **7**, 801.
Stakelon, T.S., and D.M. Follstaedt, 1978, Rev. Sci. Instrum. **49**, 45.
Streever, R.L., 1975a, AIP Conf. Proc. 24, Magn. Magn. Mater. 1974 (AIP, New York) p. 462.
Streever, R.L., 1975b, Phys. Rev. B **12**, 4653.
Streever, R.L., 1978, Phys. Lett. A **65**, 360.
Streever, R.L., 1979, Phys. Rev. B **19**, 2704.
Takagi, S., T. Kimura, N. Sato, T. Satoh and T. Kasuya, 1988a, J. Phys. Soc. Jpn. **57**, 1562.
Takagi, S., A. Oyamada and T. Kasuya, 1988b, J. Phys. Soc. Jpn. **57**, 1456.
Takigawa, M., H. Yasuoka, Y. Kitaoka, T. Tanaka, H. Nozaki and Y. Ishizawa, 1981, J. Phys. Soc. Jpn. **50**, 2525.
Takigawa, M., H. Yasuoka, T. Tanaka and Y. Ishizawa, 1983a, J. Phys. Soc. Jpn. **52**, 728.
Takigawa, M., H. Yasuoka, T. Tanaka, Y. Ishizawa, M. Kasaya and T. Kasuya, 1983b, J. Magn. & Magn. Mater. **31–34**, 391.
Takigawa, M., H. Yasuoka, Y. Yamaguchi and S. Ogawa, 1983c, J. Phys. Soc. Jpn. **52**, 3318.
Tanaka, Y., T. Tsuchida and Y. Nakamura, 1980, J. Phys. Soc. Jpn. **48**, 1092.
Tari, A., 1978, Phys. Status Solidi a **46**, 173.
Taylor, K.N.R., 1971, Adv. Phys. **20**, 551.
Taylor, K.N.R., and J.T. Christopher, 1969, J. Phys. C **2**, 2237.
Toxen, A.M., R.J. Gambino and L.B. Welsh, 1973, Phys. Rev. B **8**, 90.
Tse, P.K., A.T. Aldred and F.Y. Fradin, 1979, Phys. Rev. Lett. **43**, 1825.
Tucker, J.W., 1974, Solid State Commun. **15**, 1679.
Turov, E.A., and M.I. Kurkin, 1969, Sov. Phys.-Solid State **10**, 2551.
Ueda, K., Y. Kitaoka, Y. Kohori, T. Kohara, K. Asayama, K. Kumagai, H.C. Ku and F. Acker, 1984, J. Phys. Soc. Jpn. **53**, 2674.
Ueda, K., Y. Kitaoka, H. Yamada, Y. Kohori, T. Kohara and K. Asayama, 1987, J. Phys. Soc. Jpn. **56**, 867.
Ueno, N., H. Nagai and A. Tsujimura, 1971, J. Phys. Soc. Jpn. **31**, 1275.

van Diepen, A.M., H.W. de Wijn and K.H.J. Buschow, 1967, J. Chem. Phys. **46**, 3489.
van Diepen, A.M., H.W. de Wijn and K.H.J. Buschow, 1968a, Phys. Lett. A **26**, 340.
van Diepen, A.M., H.W. de Wijn and K.H.J. Buschow, 1968b, Phys. Status Solidi **29**, 189.
van Diepen, A.M., K.H.J. Buschow and H.W. de Wijn, 1969, J. Chem. Phys. **51**, 5259.
Vasil'kovskii, V.A., N.M. Kovtun, A.K. Kupriyanov, S.A. Nikitin and V.F. Ostrovskii, 1974, Sov. Phys.-JETP **38**, 342.
Vasil'kovskii, V.A., N.M. Kovtun, A.K. Kupriyanov, S.A. Nikitin and V.F. Ostrovskii, 1981a, Sov. Phys.-JETP **53**, 185.
Vasil'kovskii, V.A., N.M. Kovtun and V.F. Ostrovskii, 1981b, Sov. Phys.-Solid State **23**, 1750.
Vasil'kovskii, V.A., A.A. Gorlenko, N.M. Kovtun and V.M. Siryuk, 1983, Sov. Phys.-JETP **58**, 782.
Vasil'kovskii, V.A., A.A. Gorlenko, A.K. Kupriyanov and V.F. Ostrovskii, 1988, Sov. Phys.-Solid State **30**, 794.
Vijayaraghavan, R., S.K. Malik and V.U.S. Rao, 1968a, Phys. Rev. Lett. **20**, 106.
Vijayaraghavan, R., V.U.S. Rao, S.K. Malik and V.R. Marathe, 1968b, J. Appl. Phys. **39**, 1086.
Vijayaraghavan, R., K. Shimizu, J. Itoh, A.K. Grover and L.C. Gupta, 1977, J. Phys. Soc. Jpn. **43**, 1854.
von Meerwall, E.D., D.S. Schreiber and J.A. Kaeck, 1975, Solid State Commun. **16**, 1219.
Wada, H., H. Nakamura, K. Yoshimura, Y. Nakamura and M. Shiga, 1987, J. Magn. & Magn. Mater. **70**, 134.
Wada, S., T. Kohara, K. Asayama, Y. Kitaoka, Y. Kohori and N. Ishikawa, 1983, Solid State Commun. **48**, 5.
Waind, P.R., I.S. Mackenzie and M.A.H. McCausland, 1983, J. Phys. F **13**, 1041.
Wang, I., T.J. Burch, J.I. Budnick, J.J. Murphy and J.A. Cannon, 1974, AIP Conf. Proc. **18**, 437.
Weaver, H.T., 1972a, J. Chem. Phys. **56**, 3193.
Weaver, H.T., 1972b, Phys. Rev. B **5**, 1663.
Weaver, H.T., and J.E. Schirber, 1976a, Phys. Rev. B **13**, 1363.
Weaver, H.T., and J.E. Schirber, 1976b, Phys. Rev. B **14**, 951.
Weaver, H.T., J.E. Schirber and B. Morosin, 1977, Solid State Commun. **23**, 785.
Webber, G.D., and P.C. Riedi, 1981, J. Phys. E **14**, 1159.
Weisman, I.D., L.H. Bennett, A.J. McAlister and R.E. Watson, 1975, Phys. Rev. B **11**, 82.
Welsh, L.B., R.J. Gambino and A.M. Toxen, 1971a, J. Appl. Phys. **42**, 1545.
Welsh, L.B., A.M. Toxen and R.J. Gambino, 1971b, Phys. Rev. B **4**, 2921.
Welsh, L.B., C.L. Wiley and F.Y. Fradin, 1975, Phys. Rev. B **11**, 4156.
Winter, H., D. Shaltiel and E. Dormann, 1990, J. Magn. & Magn. Mater. **87**, 181.
Wójcik, M., E. Jedryka, P. Panissod, S. Hirosawa and M. Sagawa, 1989a, J. Magn. & Magn. Mater. **80**, 19.
Wójcik, M., E. Jedryka and M. Slepowroński, 1989b, Hyperfine Int. (Proc. NMM'88, A-14).
Wójcik, W., E. Jedryka, P. Panissod and K.H.J. Buschow, 1990, J. Magn. & Magn. Mater. **83**, 243.
Yamada, Y., and A. Ohmae, 1980, J. Phys. Soc. Jpn. **48**, 1513.
Yamaguchi, M., S. Sasaki and T. Ohta, 1980, J. Less Common Met. **73**, 201.
Yoshie, H., 1977, J. Phys. Soc. Jpn. **43**, 862.
Yoshie, H., 1978, J. Phys. Soc. Jpn. **44**, 1158.
Yoshie, H., and Y. Nakamura, 1988a, J. Phys. Soc. Jpn. **57**, 3157.
Yoshie, H., and Y. Nakamura, 1988b, J. Phys. Soc. Jpn. **57**, 3649.
Yoshie, H., and Y. Nakamura, 1989a, J. Phys. Soc. Jpn. **58**, 2603.
Yoshie, H., and Y. Nakamura, 1989b, J. Phys. Soc. Jpn. **58**, 3431.
Yoshie, H., and Y. Nakamura, 1990, J. Phys. Soc. Jpn. **59**, 1902.
Yoshie, H., M. Matsushima, N. Miyagi, T. Unate, H. Nagai and A. Tsujimura, 1976, J. Phys. Soc. Jpn. **41**, 481.
Yoshie, H., T. Fujii, H. Nagai, A. Tsujimura and Y. Nakamura, 1985a, J. Phys. Soc. Jpn. **54**, 2725.
Yoshie, H., M. Shiga and Y. Nakamura, 1985b, J. Phys. Soc. Jpn. **54**, 1116.
Yoshie, H., K. Ogino, H. Nagai, A. Tsujimura and Y. Nakamura, 1987, J. Magn. & Magn. Mater. **70**, 303.
Yoshie, H., K. Ogino, H. Nagai, A. Tsujimura and Y. Nakamura, 1988a, J. Phys. Soc. Jpn. **57**, 1063.
Yoshie, H., K. Ogino, H. Nagai, A. Tsujimura and Y. Nakamura, 1988b, J. Phys. Soc. Jpn. **57**, 2525.
Yoshimura, K., and Y. Nakamura, 1983, J. Magn. & Magn. Mater. **40**, 55.

Yoshimura, K., and Y. Nakamura, 1984, J. Phys. Soc. Jpn. **53**, 3611.
Yoshimura, K., S. Hirosawa and Y. Nakamura, 1984a, J. Phys. Soc. Jpn. **53**, 2120.
Yoshimura, K., T. Shimizu, M. Takigawa, H. Yasuoka and Y. Nakamura, 1984b, J. Phys. Soc. Jpn. **53**, 503.
Yoshimura, K., M. Shiga and Y. Nakamura, 1986a, J. Phys. Soc. Jpn. **55**, 3585.
Yoshimura, K., M. Takigawa, H. Yasuoka, M. Shiga and Y. Nakamura, 1986b, J. Magn. & Magn. Mater. **54–57**, 1075.
Yoshimura, K., H. Nakamura, M. Takigawa, H. Yasuoka, M. Shiga and Y. Nakamura, 1987, J. Magn. & Magn. Mater. **70**, 142.
Yoshimura, K., Y. Yoshimoto, M. Yamada, M. Mekata, K. Fukamichi and H. Yasuoka, 1988, J. Phys (Paris) Colloq. **49**, C8-317.
Yosida, K., 1957, Phys. Rev. **106**, 893.
Zevin, V., and N. Kaplan, 1975, Phys. Rev. B **12**, 4604.
Zhang, Y.D., J.I. Budnick, D.P. Yang, E. Potenziani II, A.T. Pedziwiatr, W.E. Wallace and M. Sagawa, 1988, J. Appl. Phys. **64**, 5586.
Zhang, Y.D., J.I. Budnick, D.P. Yang, E. Potenziani II, A.I. Pedziwiatr, W.E. Wallace and M. Sagawa, 1989, J. Magn. & Magn. Mater. **79**, 136.
Zogał, O.J., 1979, Phys. Status Solidi a **53**, K203.
Zogał, O.J., 1983, Phys. Status Solidi b **117**, 717.

Handbook on the Physics and Chemistry of Rare Earths, Vol. 14
edited by K.A. Gschneidner Jr. and L. Eyring

Chapter 95

LIGHT SCATTERING IN INTERMETALLIC COMPOUNDS

EBERHARD ZIRNGIEBL
Bayer AG, ZF-TPE6, Geb. E41, 5090 Leverkusen, Fed. Rep. Germany

GERNOT GÜNTHERODT
2. Physikalisches Institut, RWTH Aachen, 5100 Aachen, Fed. Rep. Germany

Contents

List of symbols and acronyms:

BIS	bremsstrahlung isochromatic spectroscopy	E_s	scattered electric field vector
c_B	bulk modulus	E_x	interconfigurational excitation energy
CC	configurational crossover	FWHM	full width at half maximum
CEF	crystalline electric field	Γ_7	doublet CEF state
Δ	CEF splitting	Γ_8	quartet CEF state
E_i	incident electric field vector	Γ_c	charge fluctuation rate

Γ_s	spin fluctuation rate	J	total angular momentum
T_f	interconfigurational fluctuation temperature	Q	valence of R ion
		R	rare earth
ICF	interconfigurational fluctuations	T_c	superconductor transition temperature
IV	intermediate valence		
	L_{III} $2p_{3/2}$ core level	V	unit cell volume
LA	longitudinal acoustic	XPS	X-ray photoelectron spectroscopy
LO	longitudinal optic		

1. General remarks

The advent of light scattering being applied to the spectroscopic investigation of metals occurred about a decade ago. Case studies have focused on layered charge-density-wave materials, superconductors, graphite intercalation compounds, thin metallic layers and metallic superlattices. Reviews of these topics can be found in the books edited by Cardona and Güntherodt (1982b, 1989).

In this article we give a status report on the progress that has been made in applying light scattering to various rare-earth (R) intermetallic compounds with the emphasis on Kondo- and intermediate valence-type materials. In this field of research, light scattering can now provide detailed information about localized electronic excitations [such as crystalline electric field (CEF) excitations, spin–orbit-split (J) multiplet excitations], phononic and elastic properties. This has not been an easy task, since for the materials under investigation the penetration depth of the light is of the order of about 100 Å, yielding a rather small scattering volume. In particular we want to show how light (Raman and Brillouin) scattering has become a valuable complementary tool compared to neutron scattering with the advantages of high resolution ($\leq$0.5 meV), strict symmetry selection rules, high (<1000 meV) as well as extremely small (>0.03 meV) observable energy losses, small usable sample size ($\leq$1 mm^3) and independence of rare-earth isotope. Moreover, Brillouin scattering from surface wave excitations of metals offers the possibility of determining the elastic constants of small (<1 mm^3) or irregularly shaped samples, which otherwise are not accessible by ultrasonic measurements. The disadvantage of light scattering being limited to small wavevectors of the excitations, is irrelevant in the case of localized electronic excitations. Difficulties owing to the small penetration depth of the light can be overcome by careful surface preparation techniques, such as cleaving or fracturing under an inert-gas atmosphere.

The paper will be organized according to the types of excitations in rare-earth intermetallics that have been investigated successfully by light scattering. Starting with intraconfigurational and interconfigurational localized electronic excitations in sect. 2.2 we turn to crystal-field excitations in sect. 2.3. Section 3 is devoted to lattice dynamics in rare-earth intermetallics, that is the investigation of optical phonon modes by Raman scattering and the investigation of elastic constants by Brillouin scattering. Finally, in sect. 4 we shall deal with modes of electronic as well as phononic character resulting from strong electron–phonon coupling.

2. Light scattering from 4f localized electronic excitations

2.1. *Introduction*

Among the various classes of lanthanide intermetallic compounds those exhibiting intermediate-valence or Kondo behavior have received much attention over the last decade. The occurrence of two different energetically degenerate configurations of the lanthanide atoms ($4f^n5d^16s^2$ and $4f^{n+1}6s^2$), together with the strongly localized character of the 4f shell are responsible for this seemingly irregular pattern of properties exhibited by these compounds. Despite the near degeneracy of the 4f, 5d and 6s binding energies allowing for 4f interconfigurational excitations ($4f^{n+1}6s^2 \rightarrow 4f^n5d^16s^2$), the spatial localization of the 4f electrons inside the filled 5s and 5p orbitals of the Xe cores, as discussed, e.g., by Goldschmidt (1978), is the reason why the 4f states largely retain their highly correlated, atomic nature after compound formation. These particular properties of the 4f shell, apart from being the cause of some of the most interesting aspects of lanthanide research, are also the source of the problems posed towards a quantitative description of the electronic structure of these materials. These problems arise because of the inadequacy of the conventional methods of band structure calculation for handling correlated many-electron states. On the other hand, descriptions of the intermediate valence 4f shell on the basis of an ionic picture, characterized by singlet-ion intraconfigurational J-multiplet level excitations and crystal-field excitations, taking into account hybridization perturbatively is the appropriate way to describe Kondo and intermediate-valence (IV) behavior (Müller-Hartmann et al. 1984, Kasuya 1985, Gupta and Malik 1987). The ionic picture was promoted for the first time in the interconfigurational fluctuation (ICF) model (Hirst 1970).

In this model the interaction between two 4f configurations, both described by their J-multiplet level structure, is parameterized first by the interconfiguration excitation energy (E_x), denoting the energy difference between the ground states of the two J-multiplet systems, and second by the fluctuation temperature (T_f) or interconfigurational mixing width. This model has been applied to the analysis and interpretation of experimental data (Wohlleben 1984, Röhler et al. 1982a, Wittershagen and Wohlleben 1985). A schematic picture of this model is given in fig. 1. In any case these modified low lying many-particle electronic excitations (J multiplet level excitations, crystal-field excitations, interconfigurational excitations) profoundly influence the thermodynamic and transport properties of IV and Kondo compounds. Their experimental determination serves not only as a spectroscopic test of microscopic theories but is an indispensable prerequisite of any understanding of the fascinating and numerous macroscopic properties of these compounds.

A more comprehensive presentation of the many experimental and theoretical aspects of IV and Kondo compounds as well as a compilation of the original references can be found in a number of conference proceedings and review articles as given, e.g., by Wachter and Boppart (1982), Müller-Hartmann et al. (1984), Kasuya (1985) and Gupta and Malik (1987).

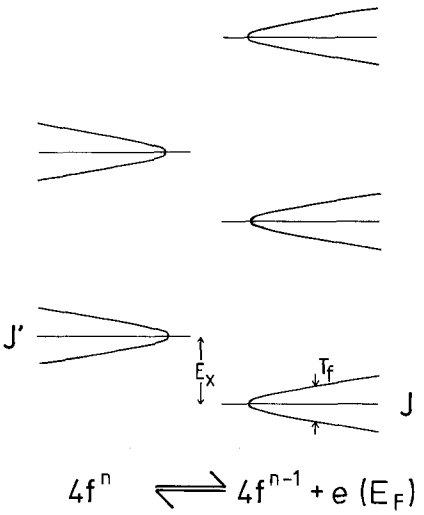

Fig. 1. Schematic energy level diagram of the interconfigurational fluctuation (ICF) model describing valence fluctuations between two 4f configurations ($4f^n$, $4f^{n-1}$), characterized by their Jmultiplet level structure. The basic parameters of the ICF model E_x and T_f denote the interconfigurational excitation energy and interconfigurational mixing width, respectively.

The application of Raman scattering to the lanthanide Kondo and IV compounds has resulted in a fruitful area of research as judged from its contributions to the understanding of these materials and from the large number of publications. In this section we review Raman scattering experiments that deal with the determination of intraconfigurational excitations (J-multiplet and crystal-field-level excitations), as well as interconfigurational excitation energies of valence unstable lanthanide compounds.

2.2. *Electronic Raman scattering in $Sm_{1-x}Y_xSe$ and $Sm_{1-x}Y_xS$*

Raman scattering in rare-earth chalcogenides has been reviewed by Güntherodt and Merlin (1984b). The Sm chalcogenides will be mentioned in this section for the sake of comparison with stable valence reference compounds and for demonstrating the configurational crossover from stable to fluctuating valence. Spin–orbit- and crystal-field-split levels of 4f states of lanthanide ions in insulating hosts have been extensively studied by Koningstein (1967) and Koningstein and Grünberg (1971) by means of electronic Raman scattering. In this subsection we discuss electronic Raman scattering from 4f spin–orbit-split levels in $Sm_{1-x}R_xSe$ and $Sm_{1-x}R_xS$ solid solutions in the vicinity of the 4f configuration crossover from stable valence to the intermediate-valence (IV) state. Such investigations have a direct bearing not only on the valence fluctuation problem, but also on the fundamentals of Raman scattering.

The ground state of Sm^{2+} in the Sm monochalcogenides is $4f^6(^7F_J = 0, 1, \ldots, 6)$, with a 0.6 eV wide spin–orbit-split ^7F_J multiplet. Electronic Raman scattering from the different J-multiplet levels of cleaved (100) faces of semiconducting SmSe (Güntherodt et al. 1981a) is shown in fig. 2. The odd-J levels show up for perpendicular incident ($\boldsymbol{E}_i$) and scattered ($\boldsymbol{E}_s$) polarization vectors, where-

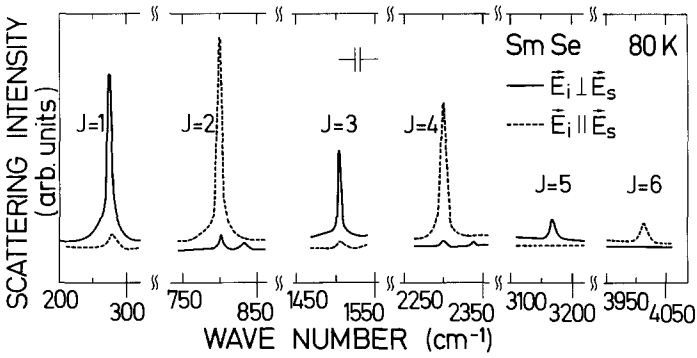

Fig. 2. Electronic Raman scattering from the (Sm^{2+}) $4f^6(^7F_J)$ configuration of SmSe at 80 K under 5145 Å laser excitation using backscattering from a cleaved (100) face; $\boldsymbol{E}_i \| \boldsymbol{E}_s$: $\Gamma_1^+ + 4\Gamma_{12}^+$; $\boldsymbol{E}_i \perp \boldsymbol{E}_s$: $\Gamma_{25}^+ + \Gamma_{15}^+$, with $\boldsymbol{E}_{i(s)}$ the electric field vector of the incident (scattered) photon.

as the opposite is true for the even-J levels. It has been shown for the case of SmS that the $J = 1$ peak (and in principle the $J = 3, 5$ peaks) appears only in the antisymmetric Γ_{15}^+ component (Güntherodt et al. 1978). The scattering intensity from either odd- or even-J levels decreases monotonically with increasing J-values as seen in fig. 2. This has been attributed to the higher J levels approaching the 4f–5d excitation gap (the excitation to the $J = 6$ level near 4010 cm^{-1} coincides with the 0.5 eV gap of SmSe). This conclusion is further supported by the fact that the $J \geq 3$ levels are not observed in SmS, which shows a 4f–5d gap of about 1200 cm^{-1} (0.15 eV).

Electronic Raman scattering has been observed in SmS, SmSe and SmTe by Nathan et al. (1975) and Smith et al. (1976), with particular emphasis on the temperature dependence of the singlet–triplet ($J = 0 \rightarrow 1$) excitation. In all three compounds the $J = 0 \rightarrow 1$ transition has been found to shift to a lower frequency upon cooling below room temperature. This temperature dependence of the singlet–triplet excitation could be fitted by results obtained in the random-phase approximation (Wang and Cooper 1968, 1969) using the free-ion spin–orbit coupling constant ($\lambda = 293.5\ cm^{-1}$) and by introducing an exchange interaction energy θ. The latter was found to decrease from 44 cm^{-1} in SmS to 8 cm^{-1} in SmTe. This seems to parallel a decreasing 5d admixture into the $4f^6$ ground state with increasing f–d excitation gap from SmS to SmTe.

Substitution of the cation in the solid solution system $Sm_{1-x}R_xSe$ by, e.g., Y or La reduces the lattice parameter and the 4f–5d excitation gap, without yielding the transition into the metallic intermediate-valence phase (Gronau 1979). In fig. 3 we show the polarized Raman spectra of $Sm_{1-x}Y_xSe$ at 80 K for $x = 0$, 0.25, 0.50, 0.75 and 1.0, obtained by Güntherodt et al. (1981a). For the sake of completeness, $Sm_{0.95}La_{0.05}Se$ has also been included. For the latter sample one observes below 200 cm^{-1} first-order defect-induced Raman scattering from acoustic and optical phonons which is absent in pure SmSe. The $J = 1$ peak of $Sm_{0.95}La_{0.05}Se$ has drastically broadened compared to that of pure SmSe at

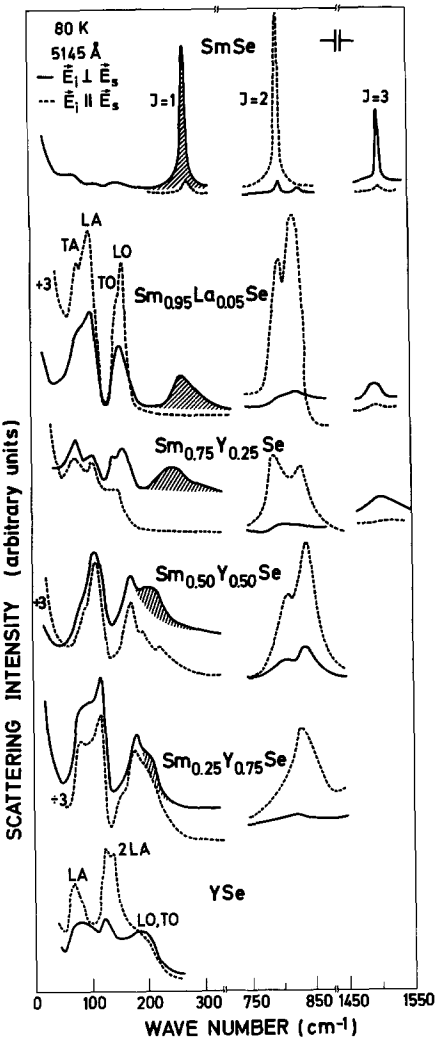

Fig. 3. Electronic Raman scattering from the J-multiplet levels of $Sm_{1-x}Y_xSe$ at 80 K for $0 \leq x \leq 1.0$; for $x = 0.05$, the La-substituted $Sm_{0.95}La_{0.05}Se$ is shown. The scattering configuration is the same as in fig. 2. The hatched area indicates the electronic scattering from the $J = 0 \rightarrow 1$ excitation. Phonon scattering is seen below 200 cm^{-1}.

275 cm^{-1} and has shifted to 266 cm^{-1}. The $J = 1$ peak is broadened further with increasing x and merges with the optical phonon density of states for $x \geq 0.50$. For $x = 0.75$, the $J = 1$ peak has shifted to about 210 cm^{-1} and is barely seen. The $J = 3$ peak of SmSe in fig. 3 does not shift with increasing x, but becomes strongly broadened and finally can no longer be resolved for $x \geq 0.50$. On the other hand, the persistence of the peak related to the $J = 2$ level up to $x = 0.75$ indicates that the 4f–5d gap is still finite, i.e., of the order of 0.1 eV (800 cm^{-1}). This is consistent with the fact that $Sm_{1-x}Y_xSe$ for all values of x does not undergo a transition into the homogeneous intermediate-valence phase (Gronau 1979). Otherwise, the intensity changes and the splittings of the $J = 2$ level with increasing x are unexplained.

The solid solution system $Sm_{1-x}Y_xS$ was first investigated using Raman scattering by Smith et al. (1976) and Tsang (1976) for concentrations near ($x \leq 0.15$) and beyond ($x > 0.15$) the configuration crossover (CC). Polarized Raman spectra by Güntherodt et al. (1981a) have shown a clear separation into phonon and electronic "magnetic" Raman scattering and the evolution with CC. Figure 4 shows the polarized Raman spectra of cleaved (100) faces of $Sm_{1-x}Y_xS$ for $x = 0$, 0.10 and 0.25 at 80 K. The case of $Sm_{0.85}Gd_{0.15}S$ has also been included, since the very same sample can be investigated in its non-transformed black phase (near CC) and in its pressure-transformed ($p > 4$ kbar) gold phase (beyond CC). For SmS ($x = 0$) in fig. 4, phonon scattering is shown by the dashed line below 300 cm^{-1}, whereas electronic scattering from the $J = 1$ level is represented by the solid line (hatched area) near 275 cm^{-1}. Electronic scattering from the $J = 2$ level is shown by the dashed line near 780 cm^{-1}. The $J \geq 3$ levels are not observed. With increasing x (≤ 0.15) the $J = 1$ level is reduced in intensity, strongly broadened and shifts to 250 cm^{-1} for $x = 0.15$. In the same sequence the $J = 2$ level is subject to strong broadening. Beyond CC ($x \geq 0.15$) no contributions from the $J = 0 \rightarrow 1$ and $J = 0 \rightarrow 2$ excitations could be identified, contrary to previous unpolarized Raman measurements (Tsang 1976). In the latter no distinction could be made between the electronic and the phonon contributions. The dominant phonon scattering intensity of, e.g., $Sm_{0.75}Y_{0.25}S$ near 250 cm^{-1}, will be discussed in more detail in sect. 3.

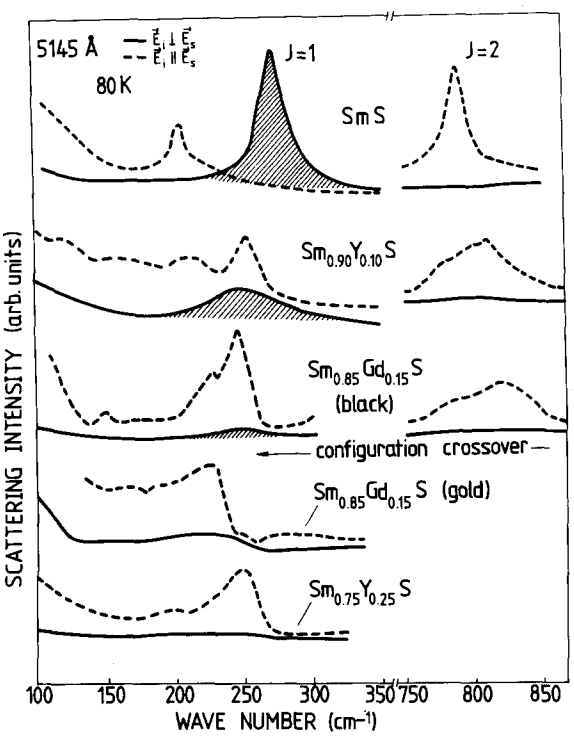

Fig. 4. Polarized Raman spectra of $Sm_{1-x}Y_xS$ ($x = 0$, 0.10, 0.25) and of $Sm_{0.85}Gd_{0.15}S$ in the "black" and pressure-transformed ($p > 4$ kbar) "gold" phase at 80 K. The scattering configuration is the same as in fig. 2. Dashed line below 300 cm^{-1}, phonon scattering; hatched area, electronic scattering form the $J = 0 \rightarrow 1$ excitation.

From the Raman scattering data in fig. 4 it can be concluded that the broadening of the $J = 1$ peak must have exceeded at least 200 cm^{-1} (25 meV) FWHM in order to be no longer resolved. On the other hand, a peak near 31 meV (250 cm^{-1}) found in neutron scattering on powdered $Sm_{0.75}Y_{0.25}S$ has been attributed to scattering from the $J = 0 \rightarrow 1$ excitation (Mook et al. 1978b). More recent neutron scattering experiments on polycrystalline $Sm_{0.75}Y_{0.25}S$ also revealed an inelastic magnetic excitation near 38 meV attributed to a modified $J = 0 \rightarrow J = 1$ transition (Holland-Moritz et al. 1988). At present there is no answer to this apparent discrepancy, perhaps pointing to a drastic reduction of the electronic Raman scattering cross-section of $Sm_{1-x}Y_xS$ induced by the valence mixing near the configuration crossover.

2.3. *Electronic Raman scattering in $EuPd_2Si_2$ and $EuCu_2Si_2$*

Eu-based group IV systems have been studied quite extensively as model compounds since their fluctuation temperature is quite often in the range of 100 K, thus on the one hand being large enough to induce quite dramatic modifications in the thermodynamic as well as the transport properties of the compound under investigation and, on the other hand, being small enough to retain the basic multiplet structure of the $Eu^{2+}4f^6(^7F_J)$ electronic structure. Moreover, Eu-based compounds serve as model systems because of the rather simple ground states of the two 4f configurations participating in the valence fluctuation process: Eu^{2+} ($4f^7$) has only the $J = S = \frac{7}{2}$ pure spin configuration without any CEF splitting and Eu^{3+} ($4f^6$) has a $J = 0$ ground state. The $J = 1$ state of Eu^{3+} lies about 550 K (De Shazer and Dieke 1963) above the $J = 0$ ground state and can be thermally populated, thus offering the possibility of a strong modification of the valence fluctuation process by temperature variation. Moreover, for Eu-based group IV compounds the investigation of the valence and its temperature dependence is easily feasible by the Mössbauer and L_{III} edge absorption spectroscopies. In particular, IV $EuPd_2Si_2$ (Sampathkumaran et al. 1981, Schmiester et al. 1982) as well as $EuCu_2Si_2$ (Bauminger et al. 1973, Röhler et al. 1982a) are sufficiently well characterized to establish helpful relationships between the thermodynamic data and the spectroscopic results.

Raman scattering measurements were carried out on freshly fractured polycrystals of $EuPd_2Si_2$ between 300 and 4.2 K (Zirngiebl et al. (1985a). In fig. 5 the Raman spectra of $EuPd_2Si_2$ obtained with 5309 Å laser excitation are shown for selected temperatures. At the top of the figure are shown the J-multiplet levels observed by electronic Raman scattering in SmSe (Güntherodt et al. 1981a). The maxima observed in $EuPd_2Si_2$ are close in energy to the J-multiplet levels of SmSe. This is to be expected, since the J-levels of Eu^{3+} should be the same as those of the Sm^{2+} $4f^6$ (^7F_J configuration). The J-multiplet levels of IV $EuPd_2Si_2$ at 300 K are quite broad compared to the J-levels of divalent SmSe. Upon cooling to 200 K, the J-levels of $EuPd_2Si_2$ undergo an asymmetric broadening which is most clearly seen for the $J = 3$ and $J = 4$ levels. This broadening develops into a well pronounced splitting at 145 K, which is best seen in the case of the $J = 2$, 3 and 4

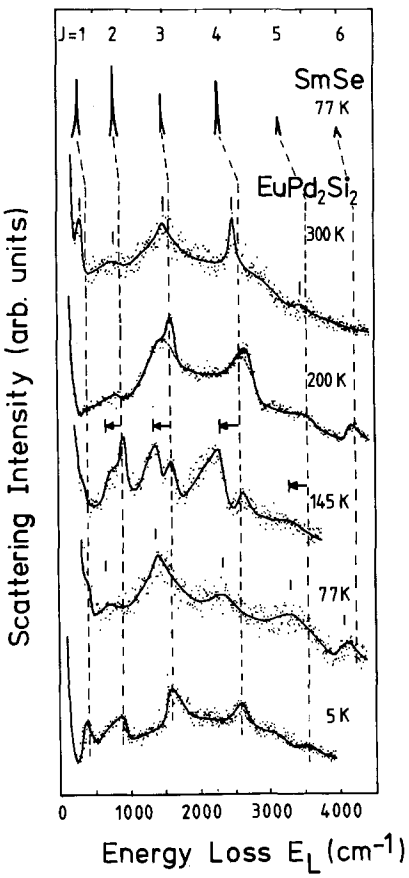

Fig. 5. Raman spectra of $EuPd_2Si_2$ at different temperatures under 5309 Å laser excitation. Vertical dashed guide lines mark the intraconfigurational excitations ($E_{L,intra}$) of the $Eu^{3+}4f^6(^7F_J)$ configuration; solid lines through spectra are guide lines to the eye. Top of the figure: electronic Raman scattering due to the $Sm^{2+}4f^6(^7F_J)$ configuration of SmSe.

levels (arrows in fig. 5). At 77 K the splitting of individual J-levels has disappeared, yielding a single broadened peak for each one of the J-levels. The spectrum at 4.2 K reveals well defined J-multiplet levels similar to the spectrum at 300 K. The reproducibility of the spectral features in fig. 5 is slightly affected, presumably by local strains giving rise to frequency shifts of the levels up to 3%. The overall background in fig. 5 arises mainly from sample imperfections causing luminescence emission.

Figure 6 shows the Raman spectra of freshly fractured $EuCu_2Si_2$ at selected temperatures (300, 77 and 4 K) under 5309 Å laser excitation (Zirngiebl et al. 1986a). At room temperature one observes a broad background of luminescence emission, which is also present in the low-temperature spectra. The double-peak structure near 2700 cm^{-1} is close to the energy of the $J = 0 \rightarrow 4$ transition of the free Eu^{3+} ion (Dieke and Crosswhite 1963). By cooling down to 77 K broad structures emerge near 800 and 1800 cm^{-1}, and the double-peak structure near 2700 cm^{-1} becomes even more pronounced. For the latter the splitting vanishes at 4 K, and the other peaks become more clearly pronounced. Moreover, at 4 K a

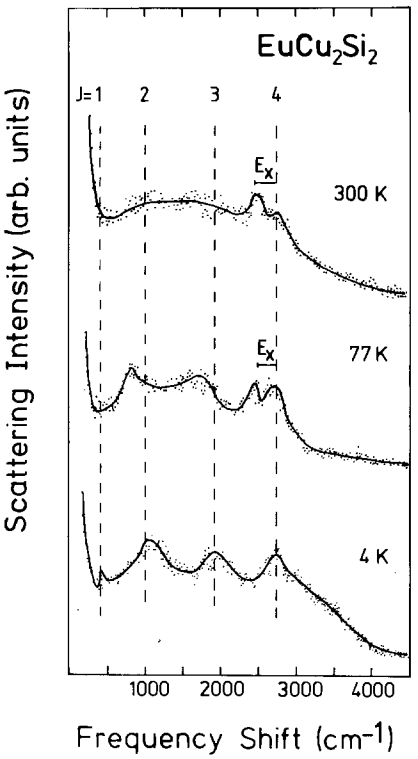

Fig. 6. Raman spectra of $EuCu_2Si_2$ at different temperatures under 5309 Å laser excitation. Vertical dashed lines mark the intraconfigurational excitations ($E_{L,\mathrm{intra}}$) of the free Eu^{3+} ion having the $4f^6(^7F_{J=0\cdots6})$ configuration. Solid lines through spectra are guides to the eyes.

fourth peak near 400 cm^{-1} can be resolved from the background. For comparison the J-level excitations of the free Eu^{3+} ion (Dieke and Crosswhite 1963) are indicated by the dashed vertical lines in fig. 6 for $J = 1$ to $J = 4$.

In fig. 7 we show a schematic energy-level diagram explaining the electronic Raman scattering from the J-multiplet levels in an IV Eu compound by applying the interconfigurational fluctuation model of intermediate valence (Hirst 1970, see fig. 1) to Raman scattering from IV Eu compounds. The (Eu^{2+}) $4f^7$ and (Eu^{3+}) $4f^6 + e^-$ configurations are nearly degenerate and separated by E_x. When $E_x \neq 0$, two sets of inelastic energy losses $E_{L,\mathrm{intra}}$ and $E_{L,\mathrm{inter}} = E_{L,\mathrm{intra}} - E_x$ are observable in Raman spectroscopy for the J-multiplet levels of the $4f^6$ configuration. These are the intraconfigurational excitations ($E_{L,\mathrm{intra}}$) of the $J = 1, \ldots, 6$ levels with respect to the ($4f^6$) $J = 0$ initial state and the interconfigurational excitations ($E_{L,\mathrm{inter}}$) with respect to the ($4f^7$) $J = 0$ initial state. The interconfigurational excitation energy E_x itself should also show up with respect to the $J = 0$ initial state. The inelastic scattering intensity of the interconfigurational excitations ($4f^7 \rightarrow 4f^6 + e^-$) is obtained in second-order perturbation theory and should be stronger than for the magnetic-dipole-allowed intraconfigurational excitations ($J = 0 \rightarrow J \neq 0$). The latter contribute to the scattering cross-section in third-order perturbation theory involving spin–orbit coupling.

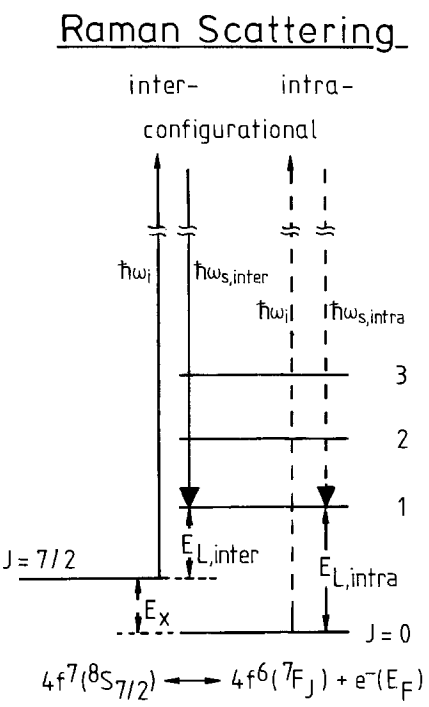

Fig. 7. Schematic representation of the electronic Raman scattering process in an intermediate-valence Eu compound showing an interconfigurational excitation energy $E_x \neq 0$. Indicated are the *intra*configurational energy losses ($E_{L,\text{intra}}$) and the *inter*configurational energy losses ($E_{L,\text{inter}} = E_{L,\text{intra}} - E_x$) of the incident photon $\hbar\omega_i$, with respect to the $J = 0$ and $J = \frac{7}{2}$ initial state, respectively.

We now turn to the interconfigurational excitation energy E_x and its temperature dependence, which is given by the common, rigid shift of all interconfigurational excitations ($E_{L,\text{inter}}$) with respect to the intraconfigurational J-multiplet excitations ($E_{L,\text{intra}}$). The latter have been indicated in figs 5 and 6 by the dashed vertical lines. For the case of $EuPd_2Si_2$ at 300 K the more intense interconfigurational excitations $E_{L,\text{inter}}$ (indicated by tick marks) are slightly shifted to lower energy with respect to the dashed lines, implying that $E_x \simeq 50\,\text{cm}^{-1}$ (70 K). At 200 K a further increase of E_x ($E_x \simeq 150$ K) is indicated by the asymmetric broadening of the peaks at their low-energy side. The clearest evidence for a pronounced increase in E_x ($E_x \simeq 350$ K) is found in the spectrum at 145 K, in which the $E_{L,\text{intra}}$ and $E_{L,\text{inter}}$ peaks are clearly split. At 77 K this splitting has disappeared, although the energy positions of the dominant interconfigurational excitations $E_{L,\text{inter}}$ (see tick marks) imply that E_x is still about the same as at 145 K. The spectrum at 5 K again shows rather narrow peaks near the positions of the dashed lines, implying that E_x is about of the order of the room temperature value. The temperature dependence of the E_x of $EuPd_2Si_2$, which is directly revealed in our Raman spectra, is plotted in fig. 8a.

Unlike $EuPd_2Si_2$, in the case of $EuCu_2Si_2$, $E_{L,\text{inter}}$ and $E_{L,\text{intra}}$ can only be distinguished at 300 and 77 K for the $J = 4$ level. For $J = 1$, 2 and 3 they cannot be separated due to the large inherent linewidths. From the $E_{L,\text{intra}}$ and $E_{L,\text{inter}}$ excitations of the $J = 4$ level one deduces an E_x of about 400 K at $T = 300$ K and $E_x \approx 320$ K at 77 K. Only one set of excitations is observable at 4 K, yielding an

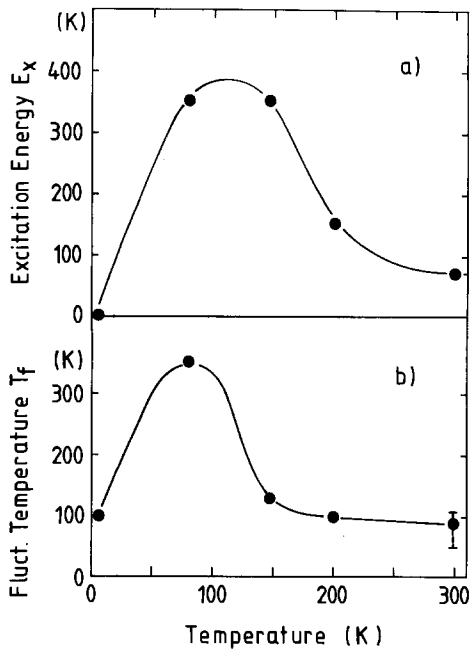

Fig. 8. Temperature dependence of (a) the interconfigurational excitation energy (E_x) and (b) the upper limit of the fluctuation temperature T_f of $EuPd_2Si_2$ as directly revealed in the Raman spectra of fig. 5.

E_x smaller than the linewidth of the narrowest peak ($J = 1$). Hence we obtain $E_x \leqslant 80$ K (see fig. 9a).

We shall now consider the temperature dependence of T_f, which characterizes the quantum mechanical mixing of the two 4f configurations (see bottom of fig. 1). This information is mainly contained in the spectral width of the Raman peaks. Although for $EuPd_2Si_2$ the experimentally observed widths of the different J-levels differ significantly at 300 K, their additional variations upon cooling below 300 K are very similar. Since we observe the joint mixing width of the initial and final states in the scattering process, we ascribe the temperature-dependent common contribution to the width of all the energy-loss peaks primarily to T_f of the initial state (ground state). The upper limit of T_f of the ground state of $EuPd_2Si_2$ is set by the narrowest energy-loss peak observable, i.e., $J = 1$ at 300 and 5 K, and $J = 3$ at all other temperatures. The values of T_f of $EuPd_2Si_2$ and $EuCu_2Si_2$ inferred from the spectral features are presented in figs. 8b and 9b, respectively, as a function of temperature. It has to be pointed out that these spectroscopically deduced values of E_x and T_f show good qualitative agreement with those obtained by Schmiester et al. (1982) for $EuPd_2Si_2$ and by Röhler et al. (1982a) for $EuCu_2Si_2$ (see also Röhler et al. 1982b) on quite different experimental grounds. By use of the ionic ICF model, Schmiester et al. (1982) have deduced the temperature dependence of E_x and T_f for $EuPd_2Si_2$ from the Mössbauer isomer shift and the magnetic susceptibility.

Moreover, for $EuPd_2Si_2$ there is at least basic agreement between the Raman scattering and the magnetic neutron scattering (Holland-Moritz et al. 1987)

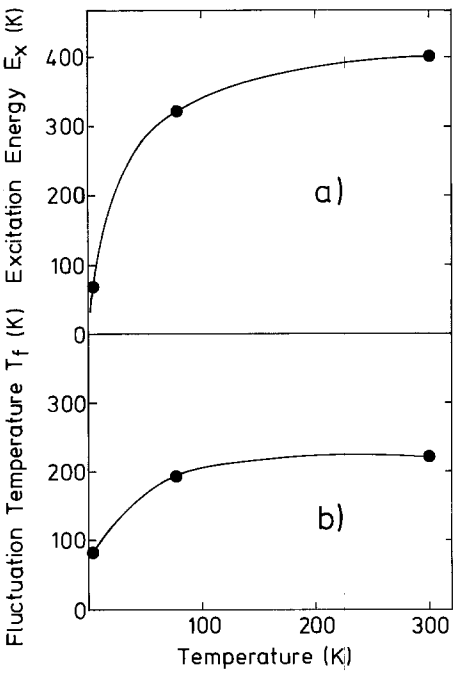

Fig. 9. Temperature dependence of (a) the interconfigurational excitation energy E_x and (b) an upper limit of the fluctuation temperature T_f of $EuCu_2Si_2$ as directly revealed in the Raman spectra of fig. 6.

concerning the temperature dependence of T_f and the existence of a $J = 0 \rightarrow J = 1$ transition of the Eu^{3+} configuration. Differences concerning the detailed transition energy of the $J = 0 \rightarrow 1$ excitation and the low-temperature behavior are unresolved and await further clarification on more theoretical grounds taking into account the different scattering mechanisms of neutron and Raman scattering.

2.4. *Electronic Raman scattering in CeS_{1+x} and $CePd_3$*

J-multiplet level excitations have also been observed in intermetallic Ce compounds (Mörke et al. 1986, Zirngiebl et al. 1985b). The *J*-multiplet structure of Ce^{3+} ions is simple compared to that of Eu^{3+}, since it consists only of the $J = \frac{5}{2}$ to $J = \frac{7}{2}$ transition at an energy of about 2150 cm^{-1} (Dieke and Crosswhite 1963). Both *J*-multiplet levels can be split by crystalline electric fields (CEF), which act more strongly on the Ce $4f^1$ electron than on those in Eu due to the more extended 4f radius of Ce compared to Eu. Nevertheless, especially at low temperatures, only the transitions out of the ground state (CEF-split ground state of the $J = \frac{5}{2}$ configuration) into the CEF-split states of the $J = \frac{7}{2}$ configuration should be observable, with the lowest transition energy being at roughly 2150 cm^{-1}.

We shall first discuss the results of Mörke et al. (1986) obtained on a series of stable valence CeS_{1+x} compounds. CeS has the NaCl structure and the first-order Raman effect is forbidden by symmetry at the zone center. However, defects can break the translational symmetry of the lattice leading to a relaxation of the

q-selection rule. The result is a weighted one-phonon density of states as found, e.g., in LaS (Mörke 1985). An example of CeS is shown in fig. 10 at the bottom. The Th_3P_4 crystal structure, within which Ce_2S_3 and Ce_3S_4 crystallize, can accommodate cations (M) and anions (S) in various stoichiometries with the nominal compositions M_2S_3 and M_3S_4. In the M_3S_4 compounds both sublattices are filled, whereas in the M_2S_3 compounds only the M sublattice contains vacancies. Therefore, it is better to denote this compound as $M_{2.67}S_4$. For trivalent rare-earth ions the R_3S_4 and R–S samples are metallic, whereas the R_2S_3 compounds are semiconductors. The three Ce_yS_4 samples investigated had the following compositions according to wet chemical analysis:

$Ce_4S_4 = Ce_{1.00}S_{1.00}$, $a_0 = 5.7772$ Å,
$Ce_{2.996}S_4$, $a_0 = 8.622$ Å,
$Ce_{2.717}S_4$, $a_0 = 8.625$ Å.

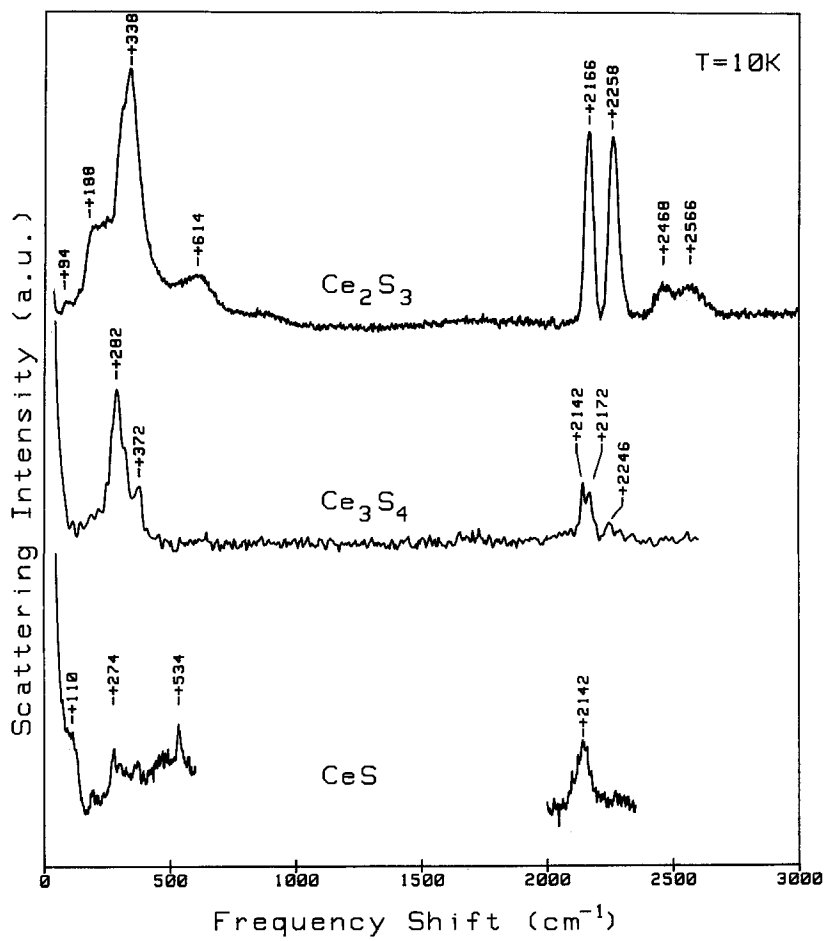

Fig. 10. Raman spectra of the series Ce_2S_3, Ce_3S_4 and CeS at 10 K. Of particular interest are the CEF-split J-multiplet excitations above 2000 cm^{-1}, after Mörke et al. (1986).

The second compound will be quoted as Ce_3S_4 and the last one as Ce_2S_3. Figure 10 shows the Raman spectra of all three compounds (Mörke et al. 1986). In the low-frequency range from 90 cm^{-1} to 650 cm^{-1} one observes light scattering from Raman-active phonons, defect-induced phonon density of states scattering and electronic Raman scattering from excitations within the $J = \frac{5}{2}$ multiplet. Additional features are seen near 2200 cm^{-1}, with their scattering intensity decreasing by going from the semiconducting Ce_2S_3 to metallic Ce_3S_4 and CeS. These excitations are interpreted as electronic transitions from the ground state of the $J = \frac{5}{2}$ configuration to the four doublets of the $J = \frac{7}{2}$ configuration. With increasing metallic behavior not only does the Raman scattering intensity decrease, but also the overall crystal-field splitting decreases due to the increasing shielding of the sulphur charges by conduction electrons and by a change in the site symmetry. The site symmetry of Ce in CeS in cubic (m3m), while in the other two compounds the Ce site symmetry is tetragonal ($\bar{4}$). The decrease of the overall crystal-field splitting is confirmed by magnetic susceptibility measurements, which show a drastic decrease of the crystal-field splitting of the $J = \frac{5}{2}$ ground state (Mörke et al. 1986).

The investigation of J-multiplet excitations of Ce has been extended to intermediate-valence $CePd_3$ by Zirngiebl and co-workers (Zirngiebl et al. 1985b). Figure 11 shows the Raman spectrum of $CePd_3$ at 5 K for 5309 A (2.3 eV) laser excitation. A broad maximum is found near 2600 cm^{-1} (325 meV) as indicated by the dashed guide line. The full width at half maximum (FWHM) amounts to about 250 meV. Superimposed on this broad maximum is a relatively sharp peak near 2050 cm^{-1} (256 meV) with a FWMH of 48 meV. The two maxima in fig. 11 always appear in the Raman spectra for different laser excitation energies at the same energy loss ΔE_R with respect to the incident photon energy $\hbar\omega_i$. Thus they are identified as electronic excitations (ΔE_R) with respect to the initial state in

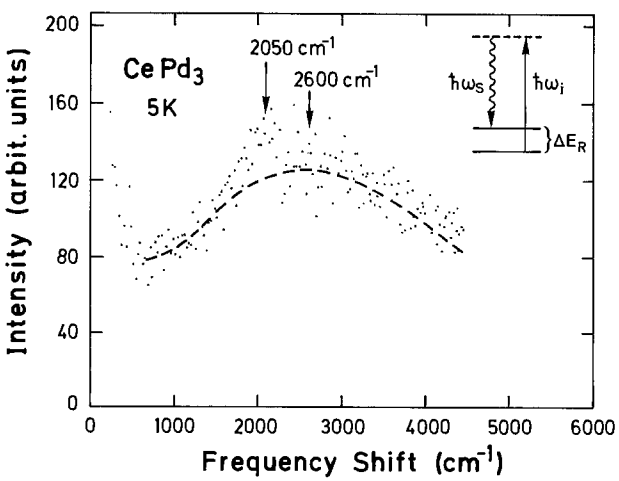

Fig. 11. Raman spectrum of $CePd_3$ at 5 K, showing the $4f^1 \rightarrow 4f^0$ excitation near 2600 cm^{-1} (dashed guide line) and the $J = \frac{5}{2} \rightarrow \frac{7}{2}$ excitation near 2050 cm^{-1}. Inset: the energy difference between the incident ($\hbar\omega_i$) and the scattered ($\hbar\omega_s$) photon yields the energy ΔE_R of the Raman excitation.

Raman scattering (see inset of fig. 11). Within the nomenclature introduced for the interpretation of Raman scattering results of IV $EuPd_2Si_2$ the broad maximum near 2600 cm^{-1} in fig. 11 is attributed to the $4f^1 \rightarrow 4f^0$ interconfigurational excitation energy E_x of about 325 meV. The one-electron occupied $4f^1$ state above E_F has been observed in BIS (bremsstrahlung isochromatic spectroscopy) near 450 meV (Baer et al. 1981), in good agreement with our findings. Both results indicate that the $4f^1$ level is well below the Fermi level, placing $CePd_3$ into the class of Kondo-like compounds and not into the class of strong IV compounds like $EuPd_2Si_2$, for which E_x is more than an order of magnitude smaller. The FWHM $\approx$ 250 meV of the interconfigurational excitation obtained in Raman scattering is smaller, by about a factor of three, than that in BIS, most probably due to the much better spectral resolution of Raman scattering. This value is of the order of magnitude of the estimated f–d hybridization width of $CePd_3$ with $\Delta \approx 100$ meV from optical data at 4.2 K and $\Delta \approx 150$ meV from X-ray photoemission (XPS) data (Fuggle et al. 1983).

The peak near 2050 cm^{-1} in fig. 11 coincides with the $^2F_{5/2} \rightarrow {}^2F_{7/2}$ intra-ionic excitation energy of the Ce^{3+} $4f^1$ configuration. This confirms the previous tentative assignment in infrared spectroscopy (Hillebrands et al. 1982) and proves that ionic configurations may still be preserved in IV compounds. The FWHM $\approx$ 48 meV is of the same order of magnitude as $2T_f \approx 2\Gamma_s/2 \approx 38$ meV as obtained from quasielastic magnetic neutron scattering (Loewenhaupt and Holland-Moritz 1979a).

2.5. *Light scattering from CEF excitations in RB_6*

The investigation of CEF levels in lanthanide intermetallic compounds is a classic domain of magnetic neutron scattering (Fulde and Loewenhaupt 1988). The normal energy range of CEF level splitting is of the order of 100 K and is best suited for inelastic magnetic scattering experiments. From the transition energies and intensities one can identify quite unambiguously CEF level schemes, especially for cubic compounds within the systematic treatment given by Lea, Leask and Wolf (Lea et al. 1962).

There is, however, a large number of examples, where due to the limited energy range available (the production rate of high-energy neutrons ($E > 50$ meV) is quite low at reactors) or due to the limited energy resolution of neutron scattering, light scattering can be a complementary tool in the investigation of CEF level schemes. In the following we shall discuss some of these cases where light scattering has helped to clarify unresolved questions.

2.5.1. *CeB_6*

The dense Kondo compound CeB_6 was first reported by Fisk in 1969 (Fisk 1969). In spite of the large body of thermal, magnetic and elastic data on CeB_6, which has accumulated over the following years various diverging speculations have entered the literature concerning the CEF excitations (for a review see Zirngiebl et al. (1984)). Their absence in direct spectroscopic measurements

(Horn et al. 1981a) has been puzzling ever since. This led to a wide variety of proposed CEF splittings ranging from 10 K (Goto et al. 1983) to more than 400 K (Horn et al. 1981b) and gave rise to conjectures about anomalous broadening or splitting effects (Horn et al. 1981b, Fujita et al. 1980, Hanzawa and Kasuya 1984). This unresolved CEF level scheme was even more puzzling as CeB_6 crystallizes in the cubic CaB_6 structure (space group O_h^1), where the sixfold-degenerate ground state $4f^1$ ($J = \frac{5}{2}$) of Ce^{3+} is expected to split only into two levels (a Γ_7 doublet and a Γ_8 quartet), giving rise to only one CEF excitation.

The first spectroscopic insight into the CEF level scheme of CeB_6 finally came from inelastic magnetic neutron scattering using high-energy incident neutrons up to 185 meV (Loewenhaupt and Carpenter 1983). An inelastic magnetic excitation was found near 530 K, still not yet allowing for a final conclusion about the CEF level scheme. This inelastic magnetic excitation has been further investigated by Raman spectroscopy (Zirngiebl et al. 1984), taking advantage of the high resolution as compared to neutron spectroscopy. The Raman measurements have been carried out on (100) faces of CeB_6 between 300 and 4.2 K using 5309 Å Kr^+ laser excitation. At room temperature an inelastic excitation at 372 cm^{-1} (530 K) was found as shown in fig. 12. Below 20 K the peak shifts by about 10 cm^{-1} to higher energies. At 4.2 K it is much narrower and has an energy of 382 cm^{-1} (fig. 12). The intensity of the peak does not change between 4.2 and 300 K because of the high excitation energy (530 K) compared to the sample temperature. Therefore, one cannot distinguish between a CEF excitation and a phonon by the intensity variation alone. However, the unusually large peak shift and its onset below 20 K rules out a phononic excitation since no lattice anomaly has been observed in this temperature range (Fujita et al. 1980). In addition, the nonmagnetic reference compound LaB_6 shows no excitation in that energy range at

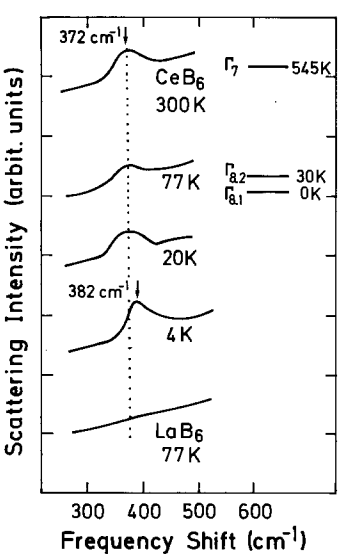

Fig. 12. Raman scattering intensities of CeB_6 and LaB_6 at different temperatures showing the Ce^{3+} Γ_8–Γ_7 CEF transition. Inset: derived CEF level scheme of CeB_6.

any temperature (see fig. 12 for, e.g., 77 K). Hence, Zirngiebl and co-workers concluded that the excitation near 372 cm^{-1} in CeB_6 corresponds to the Γ_8–Γ_7 CEF transition within the $4f^1$ configuration.

In order to further corroborate their CEF level assignment a symmetry analysis by polarized Raman measurements was performed as shown in fig. 13. For comparison the well known three Raman-active phonons appearing above 600 cm^{-1} have been included. The 372 cm^{-1} peak appears in the $\Gamma_3^+(E_g)$ and the $\Gamma_5^+(T_{2g})$ symmetry components. This is consistent with a Γ_8–Γ_7 transition because the direct symmetry product of the initial and final states $|\Gamma_8> \otimes <\Gamma_7| = \Gamma_3^+ \oplus \Gamma_4^+ \oplus \Gamma_5^+$ contains the experimentally observed symmetries.

From the symmetry analysis it cannot be decided which is the electronic ground state. However, Zirngiebl and co-workers deduced this information from the anomalous shift of the 372 cm^{-1} peak in fig. 12 for temperatures below 20 K. This behavior is explained by a non-Kramers ground state of Γ_8 symmetry, which is split into two doublets $\Gamma_{8,1}$ and $\Gamma_{8,2}$ with a separation of about 30 K. At temperatures well above 30 K, transitions from both $\Gamma_{8,1}$ doublets to the high-lying Γ_7 level are possible, yielding the measured mean transition energy of 372 cm^{-1} (530 K). A double-peak structure could not be resolved even in Raman scattering (experimental resolution 3 cm^{-1}) because of the large inherent width of the peaks. Upon cooling well below 30 K the upper doublet $\Gamma_{8,2}$ becomes thermally depopulated and the scattering takes place between the lower $\Gamma_{8,1}$

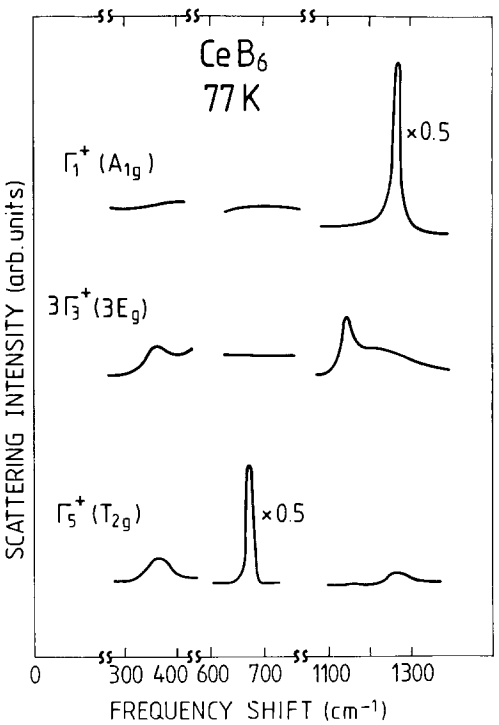

Fig. 13. Symmetry analysis of the Γ_8–Γ_7 CEF transition and the Raman-active phonons of CeB_6 at 77 K.

doublet and the Γ_7 level. This yields a shift of the observed transition energy upon cooling by $\frac{1}{2}(E_{8,2} - E_{8,1}) = 15\,\mathrm{K} = 10\,\mathrm{cm}^{-1}$ towards higher energy. The new CEF level scheme derived from the Raman measurements is shown in the inset of fig. 12, providing so far the most simple interpretation of the measured thermal, elastic and magnetic data (Zirngiebl et al. 1984).

2.5.2. *NdB_6*

The Hund's rule 4f ground state of the $Nd^{3+}(^4I_{9/2})$ is tenfold degenerate and splits when in a cubic crystal surrounding into two Γ_8 quartets and a Γ_6 doublet. The corresponding three-level CEF scheme of NdB_6 has been investigated by several experimental methods, yielding very different results (Westrum et al. 1965, Fisk 1976). A CEF level scheme has also been proposed on the basis of neutron scattering (Loewenhaupt and Prager 1986). Within the examined energy range of 50 meV (=400 cm^{-1}) one broad magnetic excitation was detected at 12 meV (=95 cm^{-1}). From the temperature dependence of the scattering intensity of the excitation and by comparison with the Lea–Leask–Wolf parameters of other RB_6 compounds the following level scheme was deduced: the ground state has $\Gamma_8^{(2)}$ symmetry, the first excited state at 12 meV has $\Gamma_8^{(1)}$ symmetry and the Γ_6 state lies 24 meV above the ground state. The excitation at 24 meV was not observed in neutron scattering because of the small transition matrix element $\Gamma_8^{(2)} \leftrightarrow \Gamma_6$. Therefore three possible transitions can give rise to only one peak in the neutron scattering spectrum. This determination of the CEF level scheme is plausible. It would, however, be more desirable to separate in energy the two transitions $\Gamma_8^{(2)} \rightarrow \Gamma_8^{(1)}$ and $\Gamma_8^{(1)} \rightarrow \Gamma_6$ within the peak at 12 meV.

Raman scattering on NdB_6 has been reported by Pofahl et al. (1986). The Raman measurements were carried out on the (110) face of a NdB_6 single crystal which was prepared using the arc floating zone technique (Verhoeven et al. 1976). The measurements were performed as a function of temperature between 300 K and 7 K, with the sample under vacuum. Several different laser wavelengths (5145 Å, 5130 Å, 5682 Å) were used.

In fig. 14 the Raman spectra of the magnetic compounds CeB_6 and NdB_6 and of the non-magnetic compound LaB_6 are shown. The well known Raman-active T_{2g} phonon of the rare-earth hexaborides is seen in all three spectra near 680 cm^{-1}, together with the phonon density of states near 180 cm^{-1}. The additional peak at 372 cm^{-1} in the spectrum of CeB_6 was attributed to the CEF excitation $\Gamma_8(0\,\mathrm{K}) \rightarrow \Gamma_7(545\,\mathrm{K})$ as discussed in sect. 2.5.1. The extra peak at 95 cm^{-1} in the spectrum of NdB_6 coincides with that observed in neutron scattering and was the subject of more detailed examinations, such as symmetry analysis and temperature dependence. As the peak does not show up in the Raman spectra of either LaB_6 or CeB_6 it is reasonable to associate it with excitations within the $4f^3$ configuration of the Nd^{3+} ion.

Polarized Raman measurements and special crystal orientations have been used by Pofahl et al. (1986) to analyze the mode symmetries as shown in fig. 15. It is possible to determine by group theory the symmetry of the different CEF transitions:

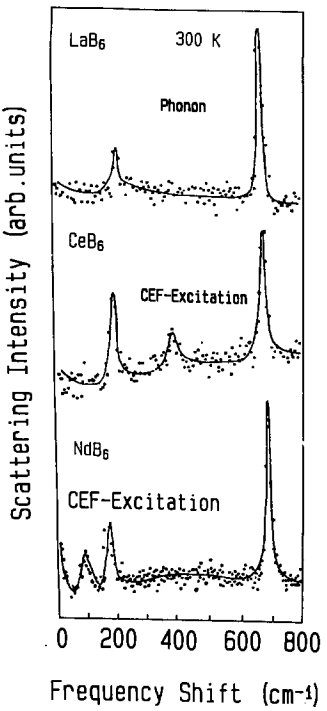

Fig. 14. Unpolarized Raman spectra of different RB_6 (R = La, Ce, Nd). Magnetic excitations are observed in CeB_6 near 372 cm^{-1} and in NdB_6 near 95 cm^{-1}. In all three spectra one observes the Raman-active T_{2g} phonon near 680 cm^{-1} and a phonon density of states near 180 cm^{-1}.

$$\Gamma_8 \otimes \Gamma_8 = \Gamma_1 \oplus \Gamma_2 \oplus \Gamma_3 \oplus 2\Gamma_4 \oplus 2\Gamma_5;$$
$$\Gamma_6 \oplus \Gamma_8 = \Gamma_3 \oplus \Gamma_4 \oplus \Gamma_5.$$

In the case of cubic crystal symmetry the Γ_1, Γ_3 and Γ_5 symmetry components are Raman allowed. In fig. 15 the well known vibrations of the B_6 octahedra have been included to demonstrate the corresponding symmetry. The peak near 95 cm^{-1} appears only in Γ_5 symmetry with the Γ_1 and Γ_3 components being zero. The symmetry analysis is consistent with the identification of the 95 cm^{-1} line as due to a crystal-field excitation, but does not allow a separation of the two transitions.

Figure 16 shows the temperature dependence of the magnetic excitation of NdB_6 near 95 cm^{-1} together with the phonon density of states near 170 cm^{-1} (Pofahl et al. 1986). At 300 K the peak at 95 cm^{-1} is the center of two transitions $\Gamma_8^{(2)} \rightarrow \Gamma_8^{(1)}$ and the $\Gamma_8^{(1)} \rightarrow \Gamma_6$. The excitation $\Gamma_8^{(2)} \rightarrow \Gamma_6$ (24 meV = 190 cm^{-1}) is neither observable in Raman scattering nor in neutron scattering due to the small transition matrix element (Loewenhaupt and Prager 1986). By cooling from 300 K down to 7 K, Pofahl and co-workers find a shift of the center of the excitation from 95 cm^{-1} to 92 cm^{-1} and a decrease in the linewidth of the peak from 36 cm^{-1} to 16 cm^{-1} (fig. 16).

Measuring with a high resolution of 2 cm^{-1} and by extending the measurement time by a factor of about ten, Pofahl and co-workers could resolve at 300 K, as

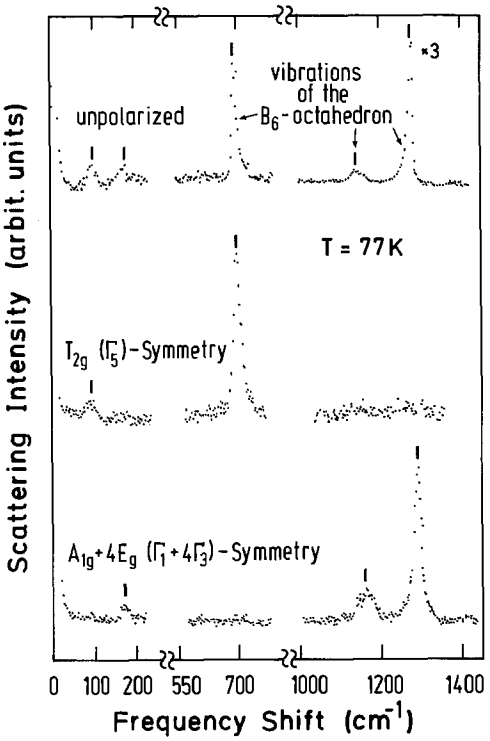

Fig. 15. Symmetry analysis of the CEF transitions and the Raman-active phonons of NdB_6 for the (110) face at 77 K. The unpolarized spectrum is shown at the top.

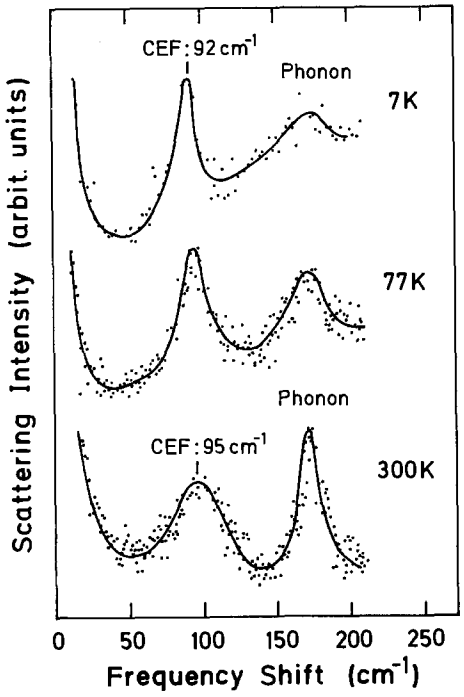

Fig. 16. Raman scattering intensities of NdB_6 at different temperatures. The peak at 170 cm^{-1} corresponds to the phonon density of states and decreases upon cooling due to the Bose factor. By cooling down from 300 K to 7 K the center of the CEF transitions shifts from 95 cm^{-1} to 92 cm^{-1}.

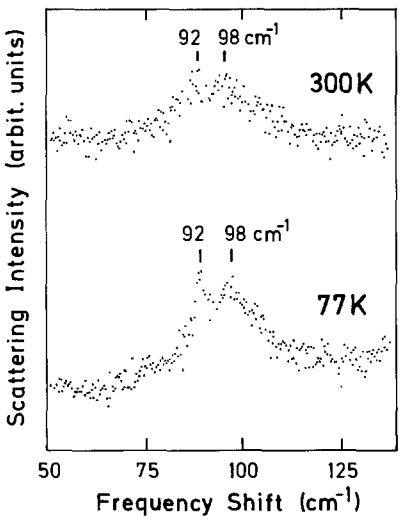

Fig. 17. Raman spectra of the CEF transitions of NdB_6 at 300 K and 77 K measured with a high instrumental resolution of 2 cm^{-1} (=0.25 meV).

well as 77 K, two peaks at 92 cm^{-1} and at 98 cm^{-1} as shown in fig. 17. At room temperature both peaks have the same intensity. At 77 K the intensity of the excitation at 98 cm^{-1} has decreased compared to that of the peak at 92 cm^{-1}. These experimental results can only be explained by a CEF level scheme with the $\Gamma_8^{(1)}$ state 92 cm^{-1} above the $\Gamma_8^{(2)}$ ground state and the Γ_6 state 98 cm^{-1} above the $\Gamma_8^{(1)}$ state. At 300 K both Γ_8 states are nearly equally populated, yielding comparable intensities of the two peaks at 92 cm^{-1} and 98 cm^{-1} in fig. 17. At low temperatures (77 K), the $\Gamma_8^{(1)}$ state is less populated than the $\Gamma_8^{(2)}$ state, yielding an increased intensity of the $\Gamma_8^{(2)} \rightarrow \Gamma_8^{(1)}$ excitation at 92 cm^{-1} compared to the $\Gamma_8^{(1)} \rightarrow \Gamma_6$ excitation near 98 cm^{-1}. Taking into account the observation of two peaks of equal intensity at high temperatures and the non-observance of a third one due to its weak intensity, one can find only one point in the Lea–Leask–Wolf scheme of Nd^{3+} for cubic crystal fields that fits all the results: hence Pofahl and co-workers obtained $x = -0.82$ and $W = -2.76\,cm^{-1}$. The resulting levels, together with the transition probabilities between the levels, are indicated in fig. 18.

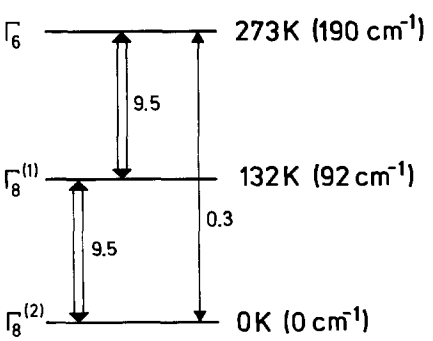

Fig. 18. CEF level scheme of NdB_6 with the values of the corresponding transition matrix elements indicated.

2.6. *Light scattering from CEF excitations in $CeCu_2Si_2$*

A great deal of attention has been recently afforded to "heavy-fermion" systems, a group of intermetallic compounds which behave like localized f-moment systems at high temperatures, but yet display many features of a simple Fermi-liquid at low temperatures [for a review of the activities on these materials, see Stewart (1984), and Grewe and Steglich (chapter X in this handbook)]. Of special interest are three such materials, $CeCu_2Si_2$ (Steglich et al. 1979b), UBe_{13} (Ott et al. 1983) and UPt_3 (Stewart et al. 1984), which have been shown to possess a superconducting ground state in which the heavy f electrons are thought to participate in spite of their room temperature predisposition towards localized magnetism. Given its evident importance, the 4f-electronic excitation spectrum of $CeCu_2Si_2$ has been widely investigated by neutron scattering to characterize the magnetic fluctuations of the 4f electrons and the effects of the CEF on the Ce multiplet. CEF excitations were first observed with levels reported by Horn et al. (1981b) at 140 K and 364 K (100 cm^{-1} and 260 cm^{-1}, respectively), whereas subsequent neutron scattering studies, while clearly observing the peak at higher energy, have been unable to confirm the lower energy transition (Stassis et al. 1986, Johnson et al. 1985).

Electronic Raman scattering experiments on oriented single-crystal samples of $CeCu_2Si_2$ were performed by Cooper et al. (1986) using a polarized 4880 or 5145 Å line of an argon laser as an excitation source.

In tetragonal surrounding the Ce^{3+} ($J = \frac{5}{2}$) multiplet is expected to split into the three doublets with two of Γ_7 symmetry and one of Γ_6 symmetry. Electronic transitions between these levels should manifest the symmetries allowed by the direct products of these states:

$$\Gamma_7 \otimes \Gamma_7 = \Gamma_1^+ \oplus \Gamma_2^+ \oplus \Gamma_5^+ \quad (A_{1g} \oplus A_{2g} \oplus E_g),$$

$$\Gamma_7 \otimes \Gamma_6 = \Gamma_3^+ \oplus \Gamma_4^+ \oplus \Gamma_5^+ \quad (B_{1g} \oplus B_{2g} \oplus E_g).$$

Cooper et al. (1986) reported on the observation of crystal-field excitations of $CeCu_2Si_2$ as being a broad hump centered roughly at 290 cm^{-1} in the Raman spectra of $CeCu_2Si_2$ as shown in fig. 19. For comparison the spectrum of the isostructural d-band metal $LaCu_2Si_2$ is also shown, exhibiting no Raman signal around 290 cm^{-1}, thus strongly confirming the interpretation of the 290 cm^{-1} excitation in $CeCu_2Si_2$ as being due to 4f electrons. This identification is further supported by the temperature dependence of the $A_{2g} + B_{1g}$ spectrum (Cooper et al. 1986). As expected of electronic transitions, the crystal-field peak at 290 cm^{-1} narrows and becomes stronger as the temperature is lowered, mimicking the sharpening Fermi factor. The appearance of the crystal-field peak in the $(A_{2g} + B_{1g})$- as well as the $(A_{2g} + B_{2g})$- symmetry-type Raman spectra confirms that it has the symmetry of the purely antisymmetric representation of the $CeCu_2Si_2$ space group, A_{2g}, characteristic of a Γ_7–Γ_7 transition. No evidence of a Γ_7–Γ_6 transition is seen according to Cooper and co-workers (Cooper et al. 1986).

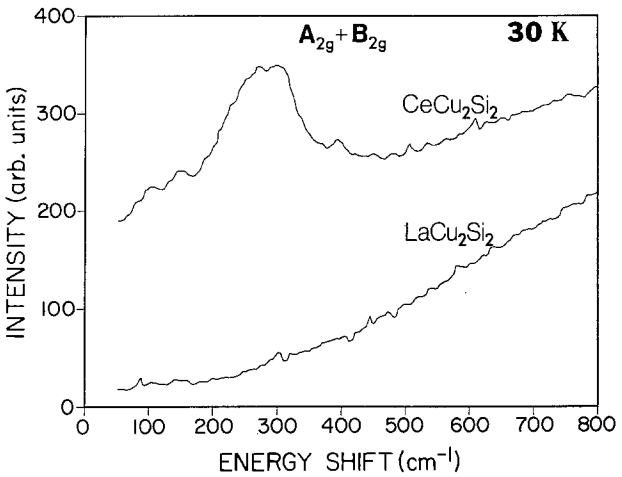

Fig. 19. Comparison of $A_{2g}+B_{2g}$ spectrum of $CeCu_2Si_2$ (upper) with that of $LaCu_2Si_2$ (lower) at 30 K. Resolution, 10 cm^{-1}. After Cooper et al. (1986).

The temperature dependence of the crystal-field linewidth [full width at half maximum (FWHM)] observed by Cooper et al. (1986) is shown in fig. 20. This temperature dependence has been calculated only for cubic Kondo systems (Becker et al. 1977, Lopes and Coqblin 1986), but the results adequately describe the general features of the observed linewidth in anisotropic $CeCu_2Si_2$. In these models, the dominant damping mechanism at high temperatures ($\Delta \ll T$, with Δ the crystal-field splitting) results from elastic scattering (i.e., the creation of electron–hole pairs) within each of the crystal-field levels, giving a linear dependence of linewidth on temperature (Lopes and Coqblin 1986):

$$\Gamma = 4\pi[n(E_F)]^2(|J_{77}|^2 + 2|J_{88}|^2)T, \quad \Delta \ll T.$$

Here, J_{77} and J_{88} are exchange integrals between electrons within the Γ_7 and Γ_8 crystal-field levels, respectively, while $n(E_F)$ is the conduction-band density of states at the Fermi energy.

At low temperatures ($T \ll \Delta$), damping chiefly results from transitions between the crystal-field levels, promoted by the exchange interaction between the conduction electrons and the Ce^{3+} 4f electron. This leads to a saturation of the linewidth at sufficiently low temperatures, as described by Lopes and Coqblin (1986)

$$\Gamma = 4\pi[n(E_F)]^2\left(|J_{78}|^2\Delta\frac{1+2e^{-\Delta/T}}{1-e^{-\Delta/T}}\right), \quad T \ll \Delta.$$

The crystal-field splitting is described by Δ in this relation, while J_{78} is the exchange term between the Γ_7 and Γ_8 levels.

An informal application of these results to $CeCu_2Si_2$ ($\Delta = 406$ K), presuming equal exchange terms and a weak splitting of the Γ_8 level, indicates that these two mechanisms should be of roughly equal importance down to about 160 K. Below this temperature, the inelastic damping term quickly begins to predominate. This

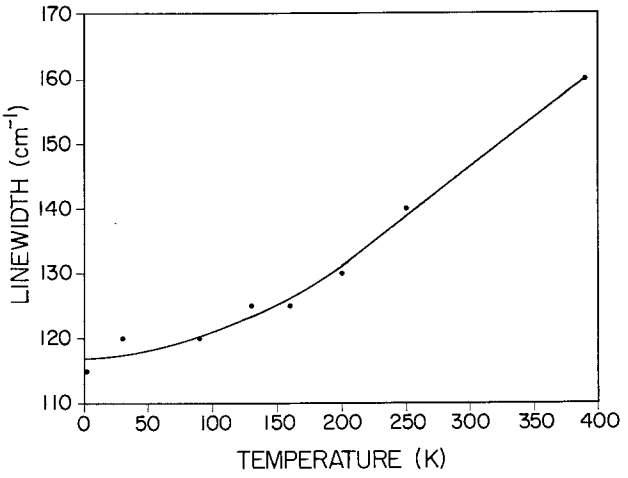

Fig. 20. Observed crystal-field linewidth (FWHM) vs. temperature for the A_{2g} crystal-field peak in $CeCu_2Si_2$. Resolution: $10\,cm^{-1}$. Line drawn is a guide to the eye. After Cooper et al. (1986).

behavior is reflected in the linewidth, observed by Cooper et al. (1986), wherein one notes a linear dependence above 200 K, with saturation occurring at lower temperatures (see fig. 20).

3. Phonon Raman scattering

3.1. *Introduction*

The primary interest in investigating mixed-valence materials using Raman scattering arose from the estimate (Varma 1976) that the inverse timescale of the 4f charge fluctuations inducing volume changes of up to 15%, may be of the order of the phonon frequencies. Hence, early Raman scattering experiments in intermediate-valence materials by Güntherodt et al. (1977a, 1978, 1981b, c), Treindl and Wachter (1979, 1980) and Stüsser et al. (1981, 1982) were concerned with the investigation of phonon anomalies and their relation to the electron–phonon interaction. In particular, polarized Raman scattering (Güntherodt et al. 1981b, c, Kress et al. 1981) has provided an experimental test of the relative importance of the different charge deformabilities introduced in the lattice dynamical model calculations (Güntherodt et al. 1981b, Kress et al. 1981, Bilz et al. 1979).

The interaction of phonons with the 4f electrons in IV compounds has been studied theoretically in different and complementary terms by a large number of authors (Ghatak and Bennemann 1978, Grewe and Entel 1979, Bennemann and Avignon 1980, Entel and Sietz 1981, Miura and Bilz 1986, Wakabayashi 1980, Matsuara et al. 1980). On the other hand, the experimental evidence for phonon frequency renormalizations due to valence fluctuations is on the whole rather limited. Phonon anomalies have been observed only for some IV compounds of Sm (Mook et al. 1978a, 1982, Hillebrands and Güntherodt 1983, Güntherodt et al. 1978), of Tm (Mook and Holtzberg 1981, Treindl and Wachter 1979), of Yb

(Güntherodt et al. 1983, 1985a) and only in two cases of Ce (Güntherodt et al. 1983, 1985b, Blumenröder et al. 1985). Moreover, no consistent interpretation of these observed anomalies has been given so far based on microscopic concepts. Therefore, we shall review the accumulated data only in the framework of some phenomenological ideas first introduced by Zirngiebl and co-workers (Zirngiebl et al. 1986b, Mock et al. 1986). We shall discuss the behavior of acoustic and optical phonon mode frequencies $\hbar\omega$ in IV compounds according to the following classification regimes: $\hbar\omega \gg \Gamma_c$ and $\hbar\omega \leq \Gamma_c$, where Γ_c denotes the charge fluctuation rate. For $\hbar\omega \gg \Gamma_c$ the phonon "sees" a static mixture of divalent ions. The mode frequency behavior in alloys of stable divalent and trivalent R ions as found, e.g., in $Gd_{1-x}Eu_xB_6$ by Ishii et al. (1976a) is shown in fig. 21 and varies nearly linearly as a function of the averaged valence. On the basis of this result one expects the phonon mode frequencies of the IV compound to be intermediate between those of the divalent and trivalent reference compounds according to the valence mixing ratio. In the phonon frequency range characterized by $\hbar\omega \leq \Gamma_c$, however, the phonon should soften compared to the stable valence reference compounds, because the charge fluctuation rate can easily follow the movement of the ions and thereby soften the lattice.

It has been emphasized (Mock et al. 1986) that besides a systematic understanding of the occurrence or absence of elastic and phonon anomalies in different IV compounds the concept introduced above allows for a first experimental estimate of charge fluctuation rates. The direct experimental investigation of these has not been feasible, unlike the magnetic relaxation rates, which have been investigated intensively by quasielastic neutron scattering (Holland-Moritz et al.

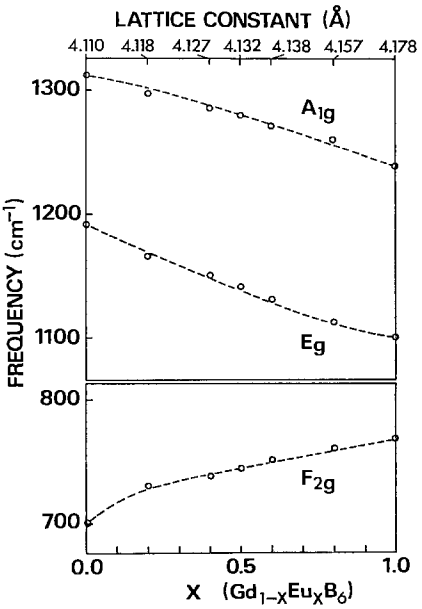

Fig. 21. Observed frequencies of the three Raman-active modes of $Gd_{1-x}Eu_xB_6$ plotted as a function of x. The lattice constants of $Gd_{1-x}Eu_xB_6$ are indicated at the top of the figure. After Ishii et al. (1976a).

1982). In the following we review Raman and Brillouin scattering from phonons in different IV compounds and their stable valence reference compounds, emphasizing the resulting estimate of the charge fluctuation rate in the IV compound under investigation. A compilation of the different crystal structures and corresponding vibrational mode symmetries of various types of valence fluctuating materials is given in table 1.

3.2. RB_6 ($R = Y, La, Ce, Nd, Sm, Eu, Gd$)

The RB_6 compounds, including the IV compound SmB_6 (Menth et al. 1969) and the Kondo compound CeB_6 (Winzer and Felsch 1978), crystallize in the simple cubic space group O_h^1 (Tanaka et al. 1977) as shown in fig. 22a, together with three Raman-active vibrations of the boron octahedron in fig. 22b. Typical Raman spectra of LaB_6 and CeB_6 are shown in fig. 23. One observes the three Raman-active modes near 1300 cm^{-1} (A_{1g}), 1150 cm^{-1} (E_g) and 690 cm^{-1} (T_{2g}) (Ishii et al. 1976b, Scholz et al. 1976) as well as the first-order symmetry-forbidden scattering intensity near 200 cm^{-1} (Mörke et al. 1981). From a comparison with the measured phonon dispersion of LaB_6 (Smith et al. 1985) the latter scattering intensity has been assigned to a T_{1u} optical mode (Zirngiebl et al. 1986b). The other low-frequency phonons are due to the acoustic branches whose long-wavelength limit is described by the elastic constants and, in particular, by the bulk modulus c_B. The elastic properties are accessible by Brillouin scattering or ultrasonic measurements.

TABLE 1
Vibrational mode symmetries of phonon modes in valence fluctuating materials.

Structure	Space group	Valence fluctuating materials	Acoustic	Infrared	Raman	Other optical modes
$ThCr_2Si_2$	I4/mm (D_{4h}^{17}) tetragonal	$CeCu_2Si_2$ $EuCu_2Si_2$ $YbCu_2Si_2$	$\Gamma_3^- + \Gamma_5^-$	$2\Gamma_3^- + 2\Gamma_5^-$	$\Gamma_1^+ + \Gamma_2^+ + 2\Gamma_5^+$	
Cu_3Au	Pm3m (O_h^1) cubic	$CePd_3$, $CeSn_3$	Γ_4^-	$2\Gamma_4^-$		Γ_5^-
CaB_6	Pm3m (O_h^1) cubic	SmB_6, CeB_6	Γ_4^-	$2\Gamma_4^-$	$\Gamma_1^+ + \Gamma_3^+ + \Gamma_5^+$	$\Gamma_4^+ + \Gamma_5^-$
NaCl	Fm3m (O_h^5) cubic	SmS (metallic) SmSe, SmTe, TmSe, TmTe, YbS, YbSe, YbTe	Γ_4^-	Γ_4^-		
$NaZn_{13}$	Fm3c (O_h^6) cubic	$CeBe_{13}$	Γ_4^-	$6\Gamma_4^-$	$2\Gamma_1^+ + 4\Gamma_3^+ + 4\Gamma_5^+$	$2\Gamma_2^+ + 5\Gamma_4^+ + \Gamma_1^- + \Gamma_2^- + 2\Gamma_3^- + 6\Gamma_5^-$
$MgCu_2$	Fd3m (O_h^7) cubic	$CeAl_2$ $YbAl_2$	Γ_4^-	$2\Gamma_4^-$	Γ_5^+	$\Gamma_2^- + \Gamma_3^- + \Gamma_5^-$

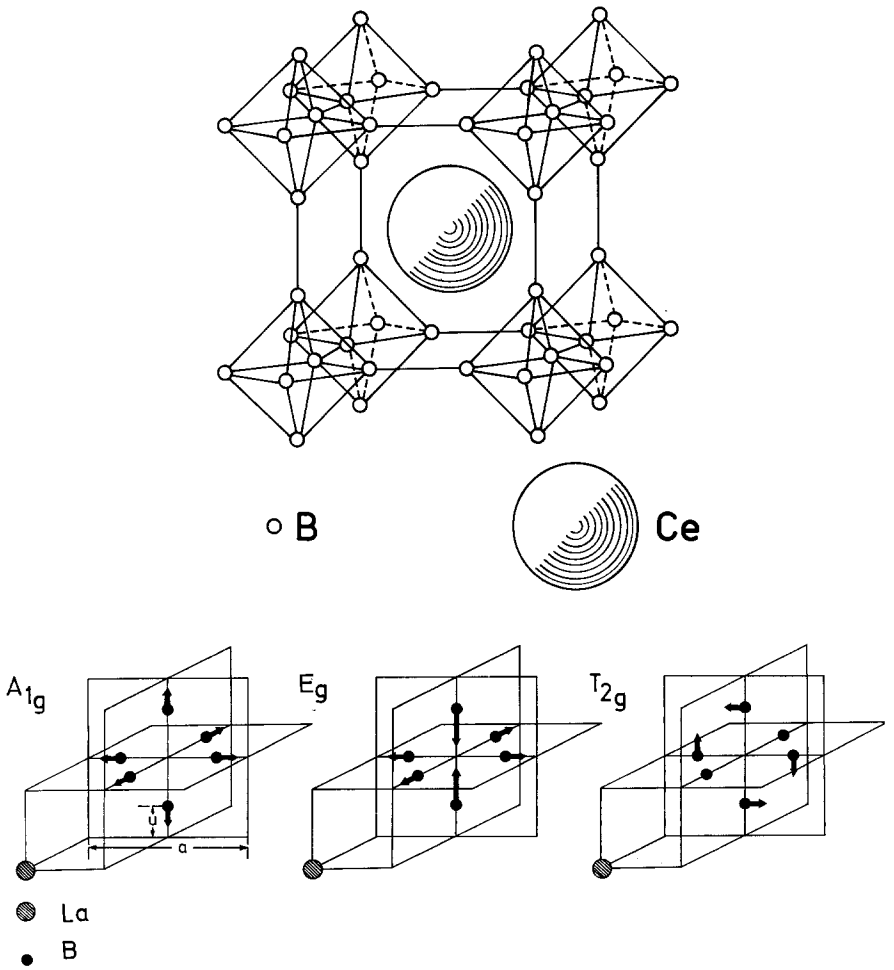

Fig. 22. (a) Structure of simple cubic CeB_6 belonging to the space group O_1^h. (b) Eigenvectors of the three Raman-active phonon modes. After Scholz et al. (1976).

In fig. 24 the frequencies of the different symmetry modes of the series RB_6 at room temperature are plotted as a function of the lattice parameter a_0 (Zirngiebl et al. 1986b). The stable trivalent RB_6 show a linear variation of the mode frequencies with a_0 as indicated by the solid lines. The reference lines for the stable divalent RB_6 (dashed lines) are fixed by EuB_6 and have been drawn parallel to the solid lines. The frequencies of the A_{1g}, E_g and T_{2g} modes of IV SmB_6 show up in between the stable divalent and trivalent reference lines according to its valence mixing ratio. On the other hand, the T_{1u} mode of SmB_6 shows a softening with respect to the coinciding stable valence reference lines. This softening has already been discussed in the literature (Mörke et al. 1981), but not in such a general framework as presented here.

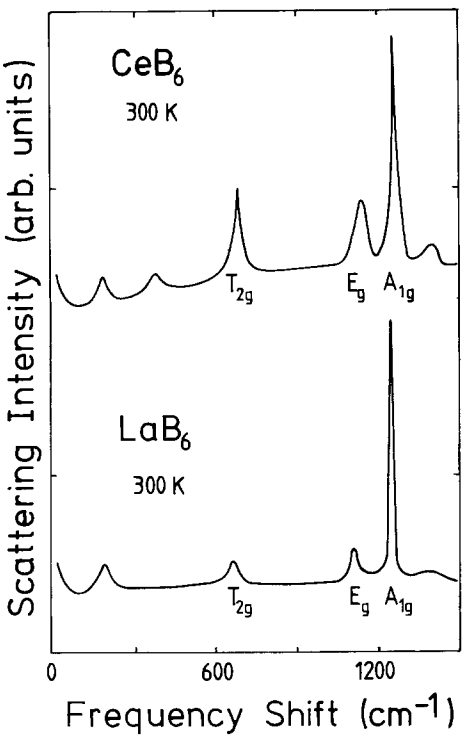

Fig. 23. Room temperature Raman spectrum of CeB_6 and LaB_6.

Figure 25 shows the bulk modulus of RB_6 (King et al. 1981) at room temperature as a function of Q/V, where Q denotes the valence and V the unit cell volume. SmB_6 exhibits a significant softening of the bulk modulus compared to the stable valence reference line.

These spectroscopic results can be summarized by the concept, introduced above, of comparing the phonon frequencies with the charge fluctuation rate (Zirngiebl et al. 1986b). The three highest lying phonon modes (A_{1g}, E_g and T_{2g}) of SmB_6 show their frequencies ($>650\,cm^{-1}$) between the stable divalent and trivalent references line, exhibiting the behavior of an alloy of stable divalent and trivalent R ions. On the other hand, the low lying T_{1u} phonon mode and the bulk modulus of SmB_6 show a softening compared to the reference lines. Therefore it has to be concluded that the charge fluctuation rate is above $200\,cm^{-1}$ (280 K) and well below $650\,cm^{-1}$ (920 K). This is the same order of magnitude one arrives at by scaling the calculated charge fluctuation rate (Müller-Hartmann 1981) by the spin fluctuation rate $\Gamma_s \approx 100$ K, which has been determined from the magnetic susceptibility (Maple and Wohlleben 1971). Hence one obtains a value of $\Gamma_c = 350$ K.

From the behavior of the T_{2g} mode frequency of SmB_6 compared to the divalent and trivalent reference lines a value of the valence, $v = 2.65$, can be deduced which is in good agreement with the value of 2.7 deduced from other measurements (Maple and Wohlleben 1971, Vainshtein et al. 1965).

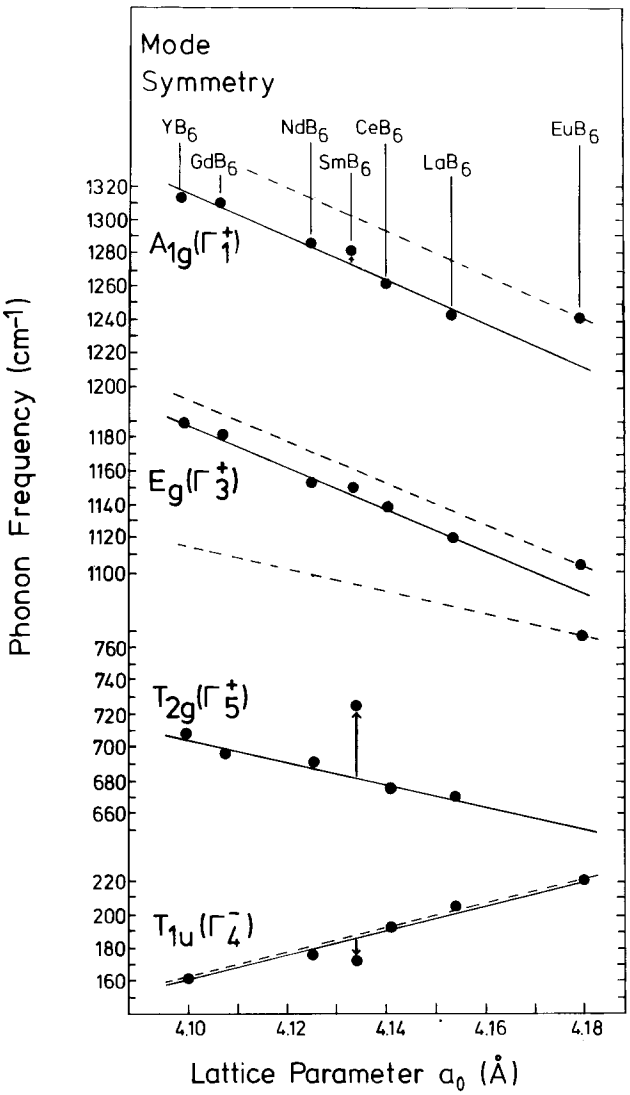

Fig. 24. Various phonon mode frequencies of RB_6 compounds as a function of the lattice parameter.

3.3. *RAl_2 (R = Y, La, Ce, Eu, Gd, Dy, Yb)*

The lattice dynamics of RAl_2 have been examined experimentally by Raman spectroscopy (Güntherodt et al. 1983, 1985b) and in the case of $CeAl_2$, $LaAl_2$ and YAl_2 by inelastic neutron scattering (Reichardt and Nücker 1983, 1985, Yeh et al. 1981). Moreover, the bulk moduli have been determined from lattice parameter measurements under pressure (Penney et al. 1981). Of particular interest within the RAl_2 series are $CeAl_2$, which is a Kondo compound (Steglich et al. 1979a) and $YbAl_2$, which is an intermediate-valence compound (Penney et al. 1981).

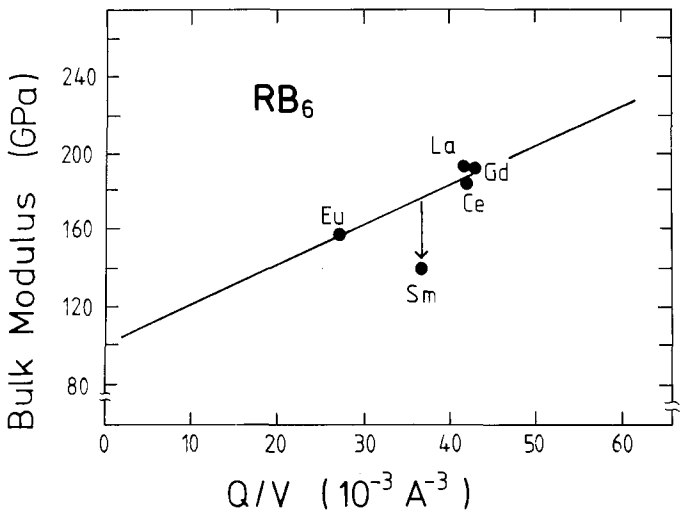

Fig. 25. Bulk modulus of various RB_6 compounds plotted as a function of Q/V (Q is the valence of the R ion and V is the unit cell volume). After King et al. (1981).

The Raman spectra of RAl_2 (R = La, Ce, Eu, Gd, Tb, Dy, Yb) have been measured at room temperature (Güntherodt et al. 1983) with a spectral resolution of $4\,cm^{-1}$. A mode in the frequency range from $95\,cm^{-1}$ ($YbAl_2$) to $118\,cm^{-1}$ ($GdAl_2$) in fig. 26a is identified as the Γ'_{25} phonon, which has been plotted in fig. 26b as a function of the lattice parameter, together with the other $q = 0$ optical phonon mode frequencies available from inelastic neutron scattering of $CeAl_2$, $LaAl_2$ and YAl_2. For the Γ'_{25} (Γ_5^+ or T_{2g}) phonon mode frequencies of the stable valence compounds RAl_2 one observes a linear variation with the lattice parameter. For $CeAl_2$ one observes (in the sequence of decreasing frequencies) a hardening of the $\Gamma_{15}(t)$, Γ'_{12}, Γ_{25} and $\Gamma_{15}(l)$ modes compared to the reference lines of stable trivalent RAl_2, whereas the Γ'_{25} mode shows a softening compared to the reference lines. For $YbAl_2$, where only the Γ'_{25} phonon has been investigated, one observes a softening of the Γ'_{25} mode compared to the stable valence reference line. (For the notation $\Gamma_{15}(t)$ and $\Gamma_{15}(l)$ see caption of fig. 26b.)

Figure 27 shows the bulk modulus of RAl_2 at room temperature as a function of the density of valence electrons Q/V. $CeAl_2$ and, even more pronounced, $YbAl_2$ show a softening of the bulk modulus compared to the stable valence reference line.

A consistent interpretation of these experimental data can be given on the basis of the model, introduced above, which assumes a charge relaxation rate Γ_c of roughly $120\,cm^{-1}$ for $CeAl_2$. Phonons with $\hbar\omega \gg \Gamma_c$ show a hardening due to a "static" mixture of trivalent and tetravalent Ce ions, whereas phonons with $\hbar\omega \leq \Gamma_c$ exhibit a softening compared to the stable valence reference lines. By the same reasoning one can give at least a lower boundary for the charge relaxation rate of $YbAl_2$, i.e., $\Gamma_c \geq 100\,cm^{-1}$.

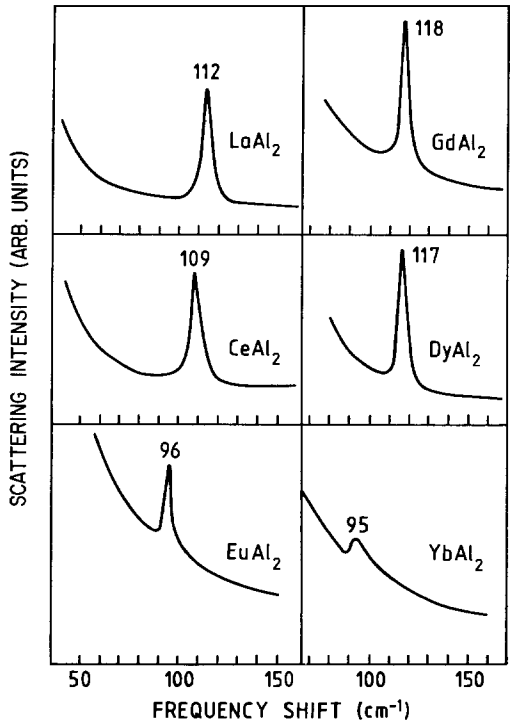

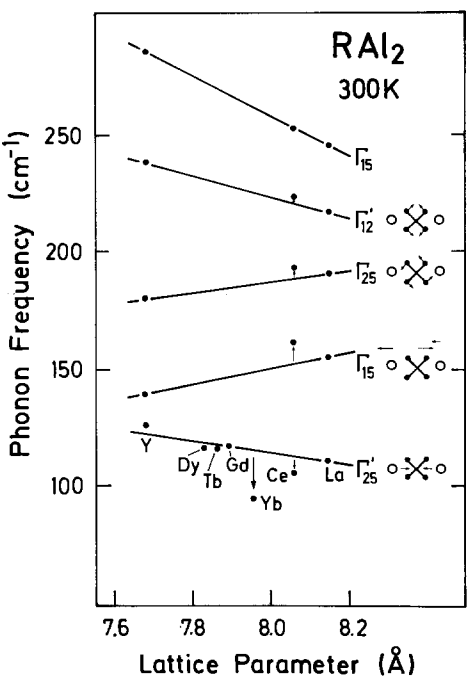

Fig. 26. (a) Unpolarized Raman spectra of RAl_2 at 300 K showing the Γ'_{25} (T_{2g}) phonon mode. (b) Phonon frequencies (in decreasing order) of the Γ_{15}(t), Γ'_{12}, Γ_{25}, Γ_{15}(l) and Γ'_{25} symmetry modes of various RAl_2 compounds taken from Raman scattering (Güntherodt et al. 1983) or neutron scattering (Reichardt and Nücker 1983, 1985, Yeh et al. 1981); $\Gamma_{15}(t)$, transverse configuration in the (110) plane; Γ_{15}(l), longitudinal configuration.

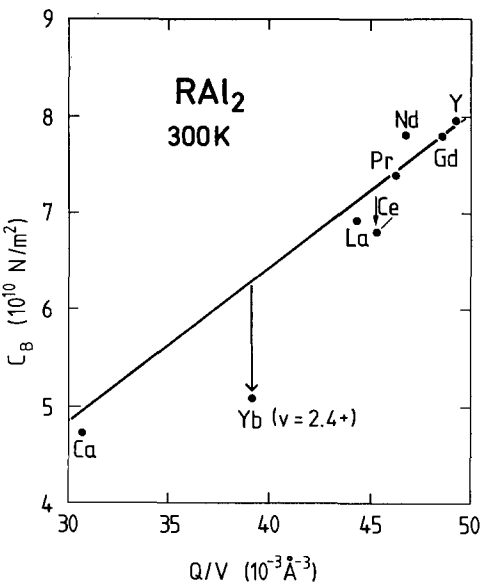

Fig. 27. Bulk modulus of various RAl_2 compounds plotted as a function of Q/V (Q is the valence of the R ion and V is the unit cell volume). After Penney et al. (1981).

3.4. *RCu_2Si_2 (R = Y, La, Ce, Tb, Tm)*

Within the RCu_2Si_2 series $CeCu_2Si_2$ has received a great deal of attention due to its heavy-fermion superconductivity (Steglich et al. 1979b, Stewart 1984). The origin of the pairing mechanism is still quite controversial; it is suggested as being purely electronic in nature (spin fluctuations) as well as being classically phononic (Razafimandimby et al. 1985). In any case, both the dependence of T_c on atomic volume (Steglich 1985) and the evidence for elastic anomalies (Mock and Güntherodt 1985) found in $CeCu_2Si_2$ illustrate that the lattice is also an important factor in the novel properties of this system and makes the investigation of the lattice dynamics by light scattering especially worthwhile. Raman scattering experiments of RCu_2Si_2 have been reported by Cooper et al. (1986). All of their light scattering experiments have been conducted in a near-backscattering geometry using a polarized 4880 or 5145 Å line of an argon laser utilizing a triple-stage spectrograph (with a filter as well as a dispersive stage) in conjunction with a multichannel as well as a single-channel detection system.

The RCu_2Si_2 compounds crystallize in the tetragonal $ThCr_2Si_2$ structure (space group $D_{4h}^{17} - I4/mmm$) with a unit cell depicted in fig. 28 (Rossi et al. 1979). The Raman-active phonons associated with RCu_2Si_2 are $A_{1g} + B_{1g} + 2E_g$ ($\Gamma_1^+ + \Gamma_3^+ + 2\Gamma_5^+$). From the site symmetries Si and Cu in $CeCu_2Si_2$, it is known that the A_{1g} phonon involves only Si atoms, while the B_{1g} phonon is purely a Cu mode. Both Si and Cu, however, participate in the two E_g phonons. The Ce atom, sitting at a site of inversion symmetry, is consequently not involved in any Raman-active modes.

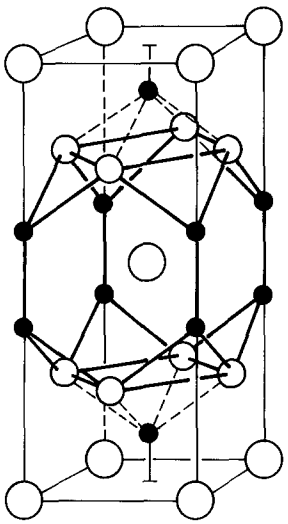

Fig. 28. $CeCu_2Si_2$ unit cell (D_{4h}^{17} – I4/mmm space group).

As an example, the two A_{1g} modes of $CeCu_2Si_2$ near 304 cm^{-1} and 398 cm^{-1} and the B_{1g} mode near 151 cm^{-1} are shown in fig. 29. In addition, fig. 30 shows the two E_g modes of $CeCu_2Si_2$ as functions of temperature. The appearance of two A_{1g} modes rather than the one mode allowed has been attributed to a static disorder of Cu ions on Si lattice sites (Cooper et al. 1986). This seems reasonable as firstly the observed energies of the two A_{1g} peaks are consistent with a simple scaling of the Cu and Si masses, and as secondly the large widths associated with both of these peaks indicates some degree of disorder in the material. Evidence for substantial disorder is particularly interesting in light of the peculiar volume

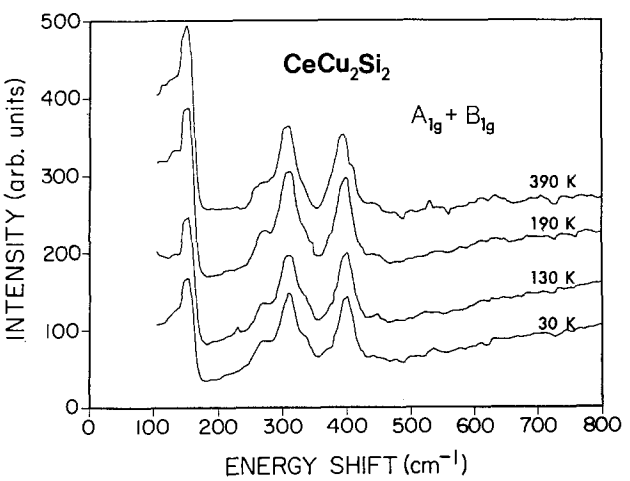

Fig. 29. $A_{1g} + B_{1g}$ spectra of $CeCu_2Si_2$ at 390 K. Resolution: 10 cm^{-1}. The spectra have been shifted upwards by 70 arb. units. After Cooper et al. (1986).

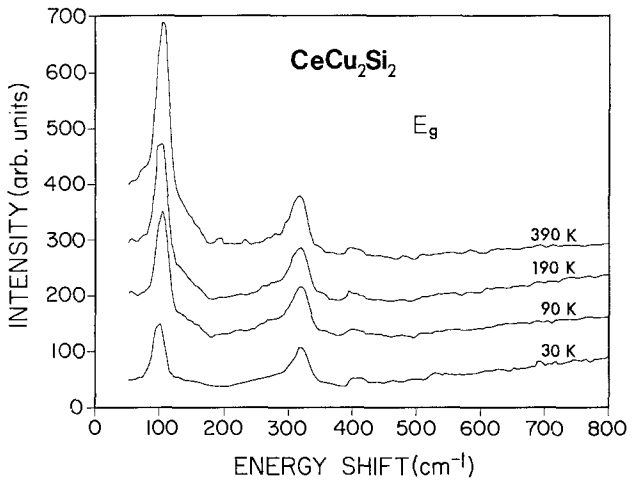

Fig. 30. E_g spectra of $CeCu_2Si_2$ at various temperatures. Resolution: 10 cm^{-1}. The spectra have been offset. After Cooper et al. (1986).

dependence of T_c noted in $CeCu_2Si_2$ (Steglich 1985). Specifically, compared with stoichiometric $CeCu_2Si_2$, Cu-rich $CeCu_{2.2}Si_2$ has been shown to display a compressed lattice and a high value of T_c ($T_c = 0.68$ K), while Cu-deficient $CeCu_{1.9}Si_2$ manifests an expanded lattice and an absence of superconductivity.

The observed phonon frequency data for RCu_2Si_2 are summarized in fig. 31, where they are displayed as a function of the unit cell volume. Within the experimental resolution the phonon frequencies of $CeCu_2Si_2$ lie on the stable valence reference line given by $LaCu_2Si_2$ and $GdCu_2Si_2$, whereas for intermediate-valence $YbCu_2Si_2$ (Holland–Moritz et al. 1982) a small softening of the B_{1g} mode and a small hardening of the A_{1g}(Si) mode compared to the stable valence reference line is observed. For the RCu_2Si_2 compounds, in addition to the

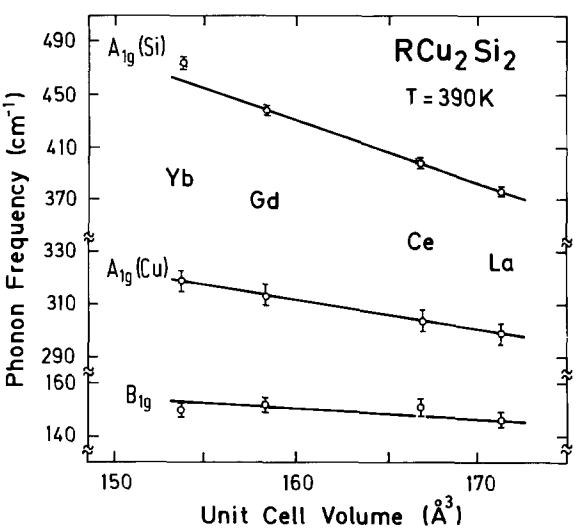

Fig. 31. Phonon frequencies of various RCu_2Si_2 as a function of the unit cell volume (see text).

data of the $q = 0$ Raman-active modes (Cooper et al. 1986), there are data available on the low-energy part ($E < 300$ K) of the phonon density of states (Holland-Moritz and Zirngiebl 1986). In fig. 32 the peak positions in the phonon density of states below $E = 300$ K are given as a function of the unit cell volume for various RCu_2Si_2. A phonon softening is observed for $CeCu_2Si_2$ and even more dramatic for $YbCu_2Si_2$, both compared to the stable valence reference line. It should be pointed out, especially for the case of $CeCu_2Si_2$, that one needs a whole set of stable valence reference compounds to infer the "stable valence behavior". It is not sufficient just to compare $LaCu_2Si_2$ and $CeCu_2Si_2$, which are in this case quite similar in phonon frequencies, thus concealing the phonon anomalies of $CeCu_2Si_2$.

Anomalous lattice dynamics of $CeCu_2Si_2$ as well as intermediate-valence $EuCu_2Si_2$ and $YbCu_2Si_2$ can also be inferred from their bulk moduli compared to the stable valence reference compounds. Figure 33 shows the bulk modulus of various RCu_2Si_2 compounds as a function of the rare-earth charge density Q/V, Q denoting the rare-earth valence and V denoting the unit cell volume (Mock et al. 1985). A drastic softening of the bulk modulus of the intermediate-valence RCu_2Si_2 compounds compared to the stable valence reference line is inferred. Within the model introduced above of electron–phonon coupling in rare-earth intermediate-valence compounds, the lower limit of the charge fluctuation rates of $CeCu_2Si_2$ and $YbCu_2Si_2$ can be estimated to be at least 200 K.

3.5. *RBe_{13} (R = La, Ce, Gd, Tb, Yb, Lu)*

Within the RBe_{13} series the IV $CeBe_{13}$ with its valence of 3.04 (Wohlleben and Röhler 1984a) has received a lot of attention. Due to its nearly integral valence rather large charge relaxation rates have been conjectured for this compound

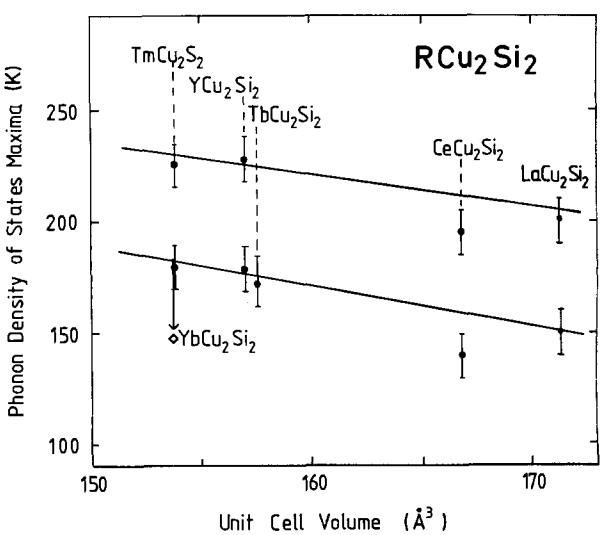

Fig. 32. Energies of maxima in the phonon density of states as observed by neutron scattering (Holland-Moritz and Zirngiebl 1986) for various RCu_2Si_2 compounds as a function of the unit cell volume.

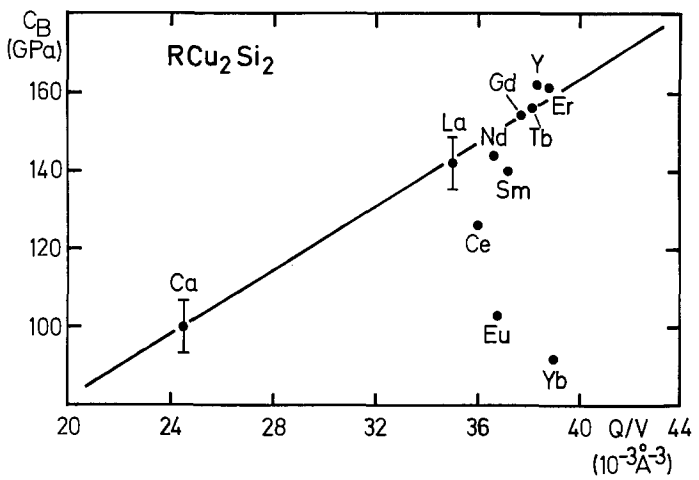

Fig. 33. Bulk modulus of various RCu_2Si_2 compounds plotted as a function of Q/V (Q is the valence of the R ion and V is the unit cell volume).

(Müller-Hartmann 1981). As the phonon modes of $CeBe_{13}$ are to be expected at rather high frequencies due to the light Be atoms, a still considerable electron–phonon coupling was suspected (Blumenröder et al. 1985). The first observations of Raman-active phonon modes in intermetallic RBe_{13} (R = La, Ce, Gd, Tb, Yb, Lu) and $Ce_{1-x}La_xBe_{13}$ ($x = 0.0$, 0.1, 0.23, 0.55, 0.8, 1.0) have been reported by Blumenröder and co-workers (Blumenröder et al. 1985). The RBe_{13} compounds crystallize in the cubic $NaZn_{13}$ structure (space group O_h^6), exhibiting ten ($q = 0$) Raman-active modes: $2\Gamma_1^+ + 4\Gamma_3^+ + 4\Gamma_5^+$. Figure 34 shows as an example the Raman spectra of $LaBe_{13}$, $CeBe_{13}$ and $Ce_{0.77}La_{0.23}Be_{13}$ at 300 K. One observes seven modes, except in $LaBe_{13}$ where the two modes near 500 cm^{-1} are degenerate. The mode assignment as given by Blumenröder and co-workers (Blumenröder et al. 1985) is also given in fig. 34. Figure 35 summarizes the Raman spectroscopic results of RBe_{13}. As a function of the lattice parameter the frequencies of the different phonon modes observed are plotted together with the Debye temperature deduced from specific heat measurements (Besnus et al. 1983). The stable valence reference compounds $LaBe_{13}$, $GdBe_{13}$, $TbBe_{13}$ and $LuBe_{13}$ show a linear variation with lattice constant as indicated in fig. 35 by the solid lines. No anomaly is observed for $YbBe_{13}$, which has been assumed to be of intermediate valence ion the basis of Mössbauer spectroscopy (Eynatten et al. 1983).

On the other hand, the two Γ_1^+ modes of $CeBe_{13}$ show a softening of about 2% with respect to the reference line. All other symmetry modes of $CeBe_{13}$ do not show any anomaly. This applies also to the bulk modulus of $CeBe_{13}$, partly indicative of the behavior of the long-wavelength acoustic phonons as shown in fig. 36. As a function of Q/V the bulk modulus of the RBe_{13} compounds follows a straight line with $CeBe_{13}$ right on it (Mock et al. 1985). However, an even stronger softening of the two Γ_1^+ modes is found upon Ce dilution in

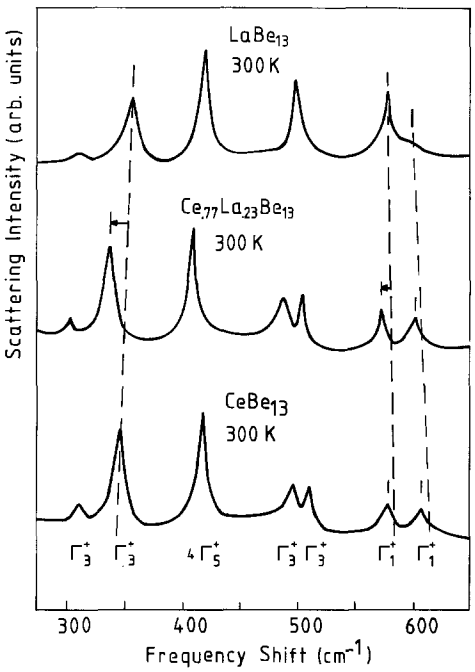

Fig. 34. Raman spectra of $LaBe_{13}$, $Ce_{0.77}La_{0.23}Be_{13}$ and $CeBe_{13}$ at room temperature; the behavior of the stable valence reference compounds is indicated for three modes by the dashed lines. The mode symmetry assignment for $CeBe_{13}$ is given at the bottom.

$Ce_{1-x}La_xBe_{13}$ as seen for all measured compositions $0.1 \leq x \leq 0.8$ in fig. 35. However, contrary to $CeBe_{13}$ this mode softening in $Ce_{1-x}La_xBe_{13}$ for $0.1 \leq x \leq 0.8$ is also observed for all other symmetry modes with respect to the average behavior of the reference materials. The phonon softening in $Ce_{1-x}La_xBe_{13}$ for $0.1 \ll x \leq 0.8$, independent of the mode symmetry is also reflected by the behavior of the Debye temperature Θ_D (Besnus et a. 1983), which is displayed at the bottom of fig. 35. No temperature dependent phonon anomaly has been observed for the optical phonons of $CeBe_{13}$, contrary to the anomalous softening of the bulk modulus upon cooling down below 350 K (Lenz et al. 1984).

By calibrating the theoretical ratio (Müller-Hartmann 1981) of charge to spin relaxation rates by the experimental spin relaxation rate $\frac{1}{2}\Gamma_s = 20$ meV of $CeBe_{13}$ (Holland-Moritz et al. 1982) the charge relaxation rate exceeds the highest phonon frequencies by about a factor of ten. This manifests itself in the small softening (2%) of the two Γ_1^+ modes of $CeBe_{13}$ (see fig. 35). The dilution of Ce in $Ce_{1-x}La_xBe_{13}$ leads to a reduction of all relaxation rates, indicated by the decreasing susceptibility maximum (Besnus et al. 1983). Similarly, a reduction of the fluctuation temperature T_f from about 150 K ($0.0 < x < 0.7$) to about 50 K ($x \geq 0.8$) has been deduced from thermal expansion measurements (Kaspers 1983). Consequently, the charge relaxation rate will be lowered, coming closer to the optical phonon frequencies. This is reflected in the further softening of the Γ_1^+ modes with increasing x. The concurrent softening of all other $q \approx 0$ symmetry modes stems from their long-wavelength phase-coherent averaging over primarily local (Γ_1^+) breathing-type charge fluctuations. This effect is obviously more

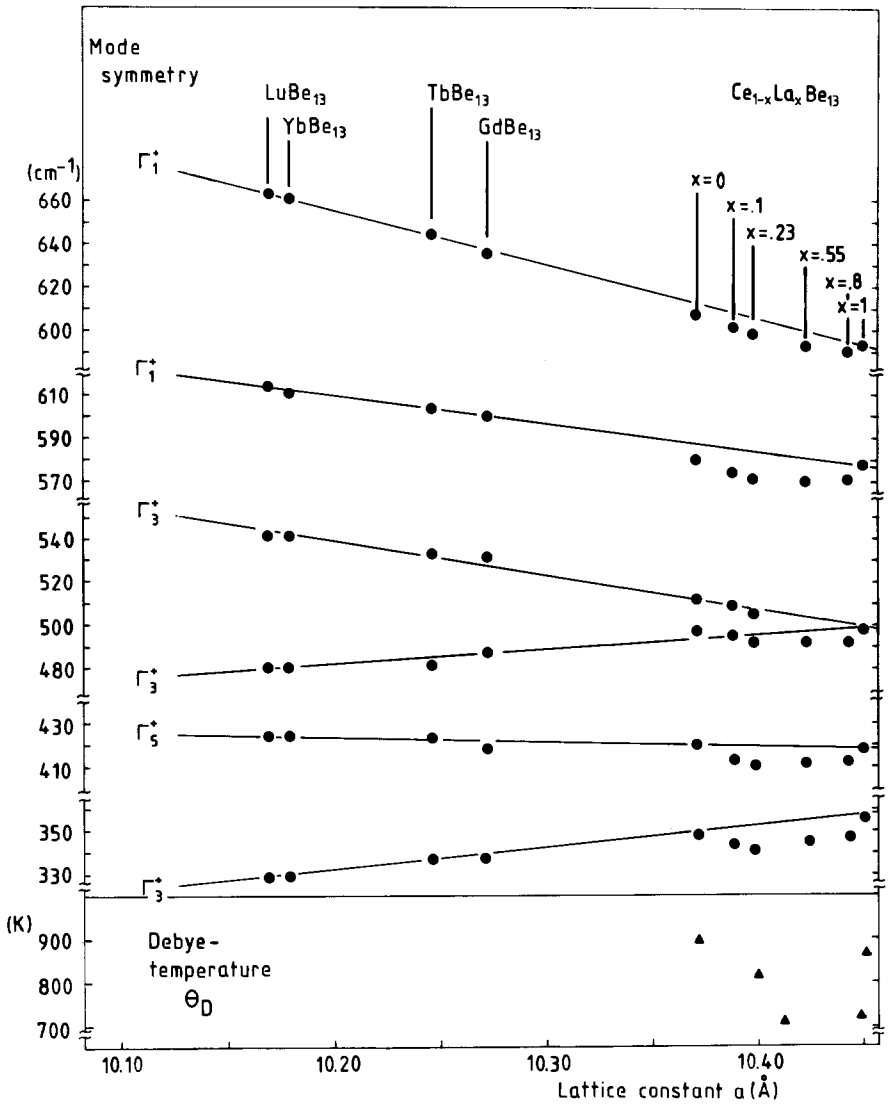

Fig. 35. Frequencies of the Raman-active phonon modes and the Debye temperature Θ_D (from Besnus et al. 1983) of various RBe_{13} and $Ce_{1-x}La_xBe$ compounds as a function of the lattice parameter.

pronounced for short-wavelength zone boundary phonons, which contribute most to Θ_D (see fig. 35) due to their high density of states.

3.6. *RS* (*R* = *Y*, *La*, *Pr*, *Sm*, *Eu*, *Gd*, *Yb*)

Among the various classes of rare-earth compounds the fcc (NaCl type) R-monosulphides are the simplest from a structural and magnetic-exchange point

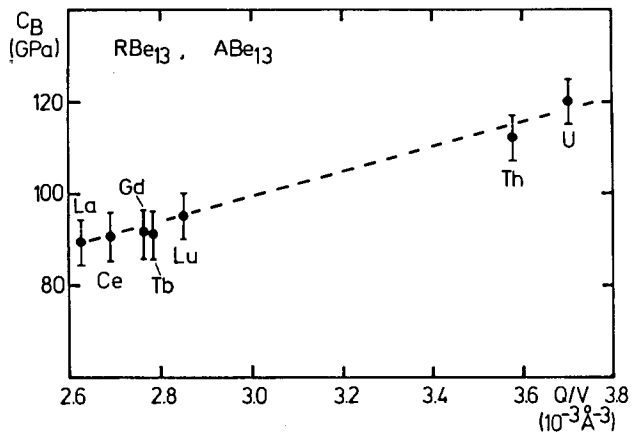

Fig. 36. Bulk modulus of various RBe_{13} and ABe_{13} compound (A = actinide) plotted as a function of Q/V (Q is the valence of the R or A ion and V the unit cell volume) as given by Mock and Güntherodt (1985).

of view. Although closely related in their chemical aspects, the RS show strongly different electronic, magnetic and optical properties along with the filling of the 4f shell; RS can be ferromagnetic semiconductors (EuS), metallic antiferromagnets (GdS), superconductors (LaS) or exhibit valence fluctuations after a semiconductor–metal transformation induced by external pressure (SmS) or by lattice pressure ($Sm_{1-x}Y_xS$). The interest in Raman studies of this class of compounds arose mainly from the intriguing possibility of investigating widely different types of electron–phonon couplings within one chemical structure. As first-order Raman scattering is symmetry forbidden in these fcc compounds, the observation of Raman scattering in these compounds is unusual by itself and has been attributed to strong coupling between excitons and LO phonons in YbS (Merlin et al. 1978) or to defect-induced Raman scattering in GdS (Güntherodt et al. 1977b), which is modified due to strong intra-ionic charge deformabilities in superconducting YS and in valence fluctuating SmS and $Sm_{0.75}Y_{0.25}S$ (Güntherodt et al. 1981d, Kress et al. 1981, Güntherodt and Merlin 1984). For EuS a strong interaction between the phonon and spin systems has been found to be responsible for the observed Raman scattering induced by spin disorder as well as the coupled magnon–phonon Raman scattering (Merlin et al. 1977, Güntherodt et al. 1979, Zeyher and Kress 1979, Güntherodt and Zeyher 1984). All these results have been extensively reviewed by Güntherodt and Merlin (1984) and Güntherodt and Zeyher (1984), and will not be discussed in further detail here. In the following we shall focus on the phononic properties of intermediate-valence, metallic SmS and $Sm_{0.75}Y_{0.25}S$ with respect to the stable valence reference compounds and we view these results in the more general framework of electron–phonon coupling in IV compounds as discussed in sect. 3.1.

The intermediate-valence phase of the solid solution system $Sm_{1-x}Y_xS$ with $x \geq 0.15$ was the first striking example of anomalous electron–lattice interactions

associated with valence fluctuations. The bulk modulus is soft for $x \geq 0.15$ due to the anomalous elastic constant $c_{12} < 0$ (Penney et al. 1975). Strong phonon anomalies have been identified in the [111] direction from the Γ to the L point of $Sm_{0.75}Y_{0.25}S$ (Güntherodt et al. 1981c, Mook et al. 1978a, 1982, Bilz et al. 1979, Entel et al. 1979, Mook and Holtzberg 1981). In addition to the LA phonon anomaly for $0 < k < \frac{3}{4}k_L$ associated with the soft bulk modulus, a corresponding anomaly was found for the LO phonon breathing mode near the L point. In addition, there is an anomaly near the Γ point of similar magnitude to that near the L point (Bilz et al. 1979).

The polarized Raman spectrum of a cleaved single crystal of $Sm_{0.75}Y_{0.25}S$ (Güntherodt et al. 1981c) is shown in the upper part of fig. 37. The Raman spectrum is dominated by the Γ_1^+ scattering intensity near 250 cm^{-1} and the weaker one near 85 cm^{-1}, superimposed on the rising background. The one-phonon density of states (bold lines) derived from the fit (Bilz et al. 1979) of the measured phonon dispersion (Mook et al. 1978a) is shown in the lower part of fig. 37. The shaded area results from weighting the density of states with the Γ_1^+ breathing cluster deformability, which represents the dominant electron–phonon matrix element in the Raman scattering process. Obviously, the TO phonon density of states near 270 cm^{-1} does not contribute to the shaded area. The

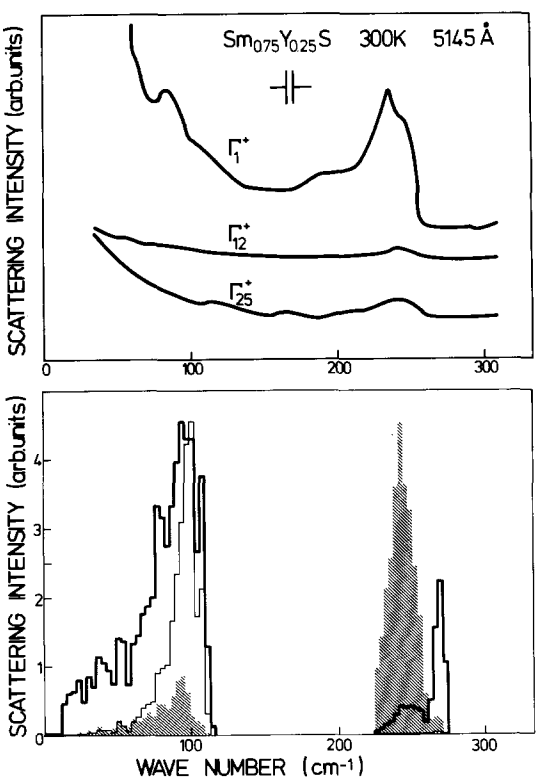

Fig. 37. Upper part: polarized Raman spectra of $Sm_{0.75}Y_{0.25}S$ at 300 K. Lower part: calculated one-phonon density of states weighted by $[n(qj)+1]/\omega(qj)$ (thick solid line); shaded area, Γ_1^+(Sm) contribution; thin solid line, Γ_{12}^+(S) contribution.

largest contribution is due to the LO phonon breathing mode near the L point. The small shaded area in the acoustic phonon region near 90 cm^{-1} is due to the Γ_1^+ deformability of the Sm ion induced by the longitudinal breathing motion of the surrounding Sm ions. The shaded areas in fig. 37 describe the measured Raman spectrum very well, except for the shoulder in the Γ_1^+ spectrum near 190 cm^{-1} which will be discussed in sect. 4. The assumption of a quadrupolar (Γ_{12}^+) deformability of the S ion, previously used in the lattice dynamical model (Bilz et al. 1979), yields the thin-line acoustic-phonon contribution near 100 cm^{-1} in the lower part of fig. 37. However, since the measured Γ_{12}^+ spectrum does not show any intensity near 100 cm^{-1}, such a local Γ_{12}^+ charge-density distortion is unrealistic. Thus, it had to be attributed to residual effects of screened Coulomb interactions (Güntherodt et al. 1981c). The absence of scattering intensity in the Γ_{25}^+ spectrum in fig. 37 indicates that intersite Sm–Sm or S–S interactions are negligible. Hence, the assumption of a local electron–lattice interaction, i.e., of Sm–S interactions only, in the lattice dynamical model for $Sm_{0.75}Y_{0.25}S$ (Bilz et al. 1979) is corroborated experimentally.

The very same Γ_1^+ charge deformability of the mixed-valence Sm ion due to $4f^{n+1} \leftrightarrow 4f^n5d^1$ excitations used for the description of the Raman intensities in fig. 37 has been used to describe the phonon anomalies (Bilz et al. 1979). Therefore we can conclude that the dominant Γ_1^+ scattering intensities of $Sm_{0.75}Y_{0.25}S$ near 250 cm^{-1} and 85 cm^{-1}, respectively, arise mainly from the LO and LA phonon anomalies in the [111] direction, emphasizing scattering from L-point phonons. The available data on the LO(L) phonon frequencies of RS are depicted in fig. 38 as a function of the lattice parameter. The LO(L) phonons of intermediate-valence metallic SmS and $Sm_{0.75}Y_{0.25}S$ lie between the divalent reference line given by YbS and EuS, and the trivalent reference line spanned by YS, GdS, PrS and LaS, thus exhibiting the behavior of an alloy of divalent and trivalent Sm ions. Figure 39 shows the bulk modulus of several RS compounds at room

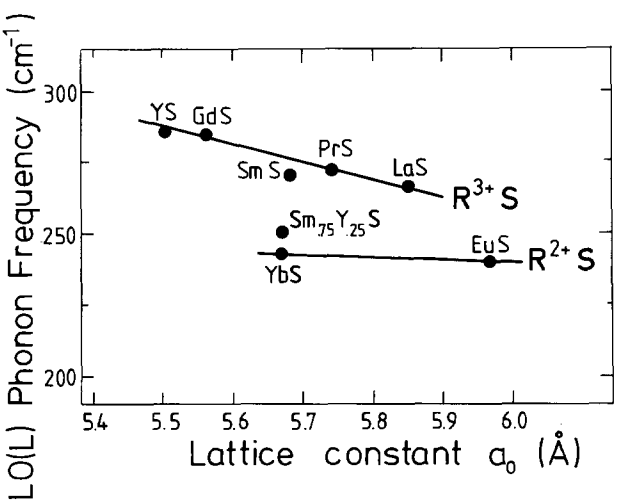

Fig. 38. LO(L) phonon frequencies as a function of the lattice parameter of various RS compounds.

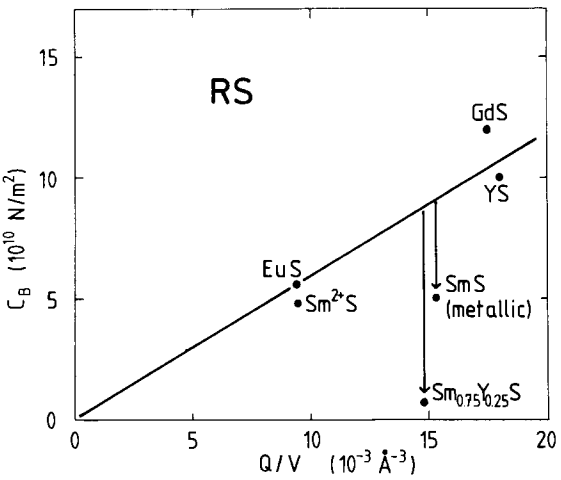

Fig. 39. Bulk modulus of various RS compounds plotted as a function of Q/V (Q denotes the valence of the R ion and V the unit cell volume).

temperature as a function of Q/V, where Q denotes the valence and V the unit cell volume. Metallic SmS as well as $Sm_{0.75}Y_{0.25}S$ exhibit a significant softening of the bulk modulus compared to the stable valence reference line (Jayaraman et al. 1974).

Interpreting these data within the framework given in sect. 3.1 we can estimate a charge fluctuation rate of roughly $100\,cm^{-1}$, well below the optical phonon frequencies, but within the range of the acoustic phonons. From the position of the LO(L) phonon frequencies of metallic SmS as well as $Sm_{0.75}Y_{0.25}S$ between the divalent and trivalent reference lines one can estimate valences of 2.8 and 2.3, respectively, which agree quite well with the valences deduced from L_{III} spectroscopy as given by Allen et al. (1980) and by Weber et al. (1989), respectively.

The concept of sect. 3.1 has been tested further by analysis of the temperature dependence of the dispersion of the longitudinal acoustic phonons of $Sm_{0.75}Y_{0.25}S$ in the [111] direction as given by Mook et al. (1978a) and Mook and Holtzberg (1981). This branch exhibits at 300 K the strongest anomaly near 2.0 THz ($q = 0.2$ in fig. 40a). Upon cooling from 300 to 200 K the frequencies below 2 THz at $q = 0.1$ and $q = 0.2$ (fig. 40a) show a softening and from 200 K down to 50 K a hardening. On the other hand, the frequencies above 2 THz $q = 0.3$ and $q = 0.35$ (fig. 40a) show only a hardening from 300 to 50 K. This experimental observation has been complemented by measurements of the temperature dependence of the elastic constants of $Sm_{0.75}Y_{0.25}S$ (Mock et al. 1986). This has been made feasible by means of Brillouin scattering, whereas ultrasonic techniques fail because of the large lattice expansion upon cooling. It was found that with decreasing temperature from 300 to 4.2 K the elastic constant c_{11} decreases by 20%, c_{12} increases by 24%, but c_{44} is temperature independent. This results in an overall softening of the bulk modulus c_B, with $c_B = c_L$ ([111]) $- \frac{4}{3}c_{44}$, by 30% upon cooling from 300 to 4.2 K, with the strongest variation near 200 K as shown in fig. 40b.

These results can be understood by assuming a Γ_c which decreases with decreasing temperature. The different temperature dependence of the phonon

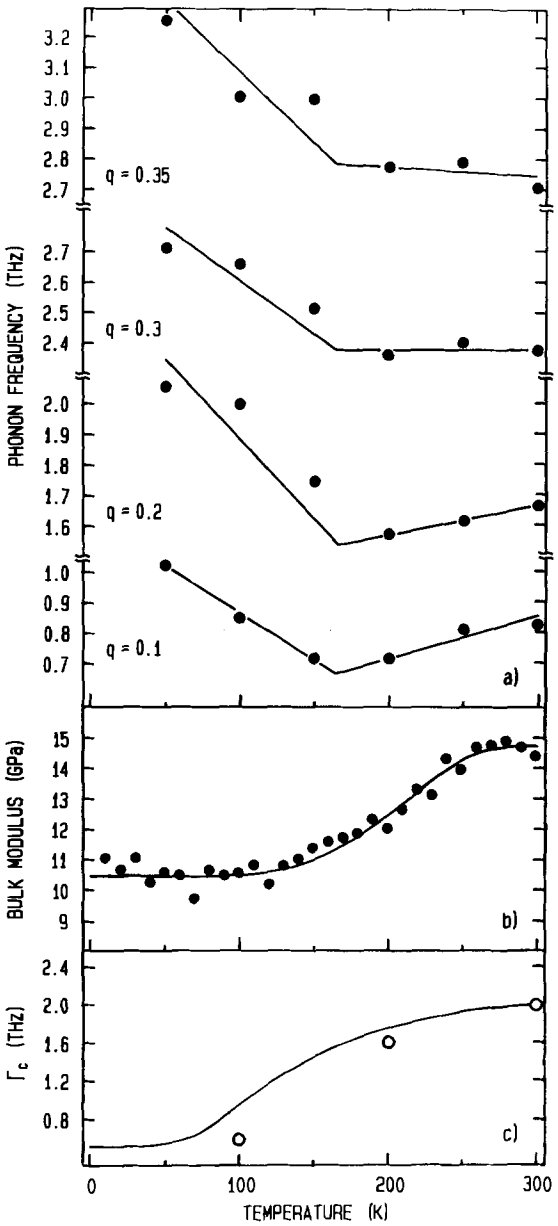

Fig. 40. (a) Temperature dependence of the longitudinal acoustic-phonon frequencies of $Sm_{0.75}Y_{0.25}S$ in the [111] direction for four different values of the wavevector q (see Mook et al. 1981). (b) Temperature dependence of the bulk modulus c_B of $Sm_{0.75}Y_{0.25}S$ measured by Brillouin scattering. c_B continues to soften upon cooling below 200 K, unlike the behavior of the phonon mode frequencies for $q \geq 0.1$ (fig. 40a). (c) Temperature dependence of the charge relaxation rate Γ_c derived from the experimental data in figs. 40a and 40b (open circles) and calculated from theory (Schmidt and Müller-Hartmann 1985) (solid line). The theoretical curve has been matched at 300 K to the experimental value.

frequencies in fig. 40a between 300 and 200 K indicates a Γ_c which lies roughly above 1.6 THz and below 2.4 THz (cf. Table 2, $\Gamma_c \approx 2.0 \pm 0.5$ THz). Upon cooling from 300 to 200 K, Γ_c is assumed to decrease, resulting in a softening of the low-frequency modes at $q = 0.1$ and 0.2 because of an increasing resonant coupling. On the contrary, the higher-frequency modes at $q = 0.3$ and 0.35 are either independent of temperature or harden slightly between 300 and 200 K. The

hardening of all phonon modes in fig. 40a upon cooling below 200 K can be explained by Γ_c decreasing below 0.7 THz, thus crossing the phonon modes at $q = 0.1$ and $q = 0.2$. This temperature dependence of Γ_c is corroborated by the maximum in the phonon linewidths near 150 K which is most pronounced for $q = 0.2$ (Mook and Holtzberg 1981). Moreover, the continuous softening of the bulk modulus from 300 to 4.2 K (fig. 40b), i.e., of the longitudinal acoustic mode in the [111] direction in the $q \approx 0$ limit, is consistent with the decrease in Γ_c. In fig. 40c we compare the experimentally deduced Γ_c (open circles) with the values predicted by theory (solid line) as given by Schmidt and Müller-Hartmann (1985). Scaling the calculated $\Gamma_c(T)$ by $\Gamma_c(T = 300\,\mathrm{K}) \approx 2.0\,\mathrm{THz}$ yields a rather good agreement.

To summarize the results discussed above one should emphasize that, from a comparison of the LO(L) phonon frequencies of IV metallic SmS and $Sm_{0.75}Y_{0.25}S$ with those of their stable valence reference compounds in the RS series, a reasonable estimate of charge relaxation rates can be given. Moreover, in the case of intermediate-valence Sm ($Sm^{2+} \leftrightarrow Sm^{3+} + e^-$) with the J-multiplet splitting of the Sm^{2+}-configuration well within the range of thermal energies, temperature-dependent changes of the valence and charge fluctuation rates are to be expected (Schmidt and Müller-Hartmann 1985). The valence changes have been observed for, e.g., $Sm_{0.75}Y_{0.25}S$ by Weber et al. (1989, and references cited therein). The temperature dependence of the charge fluctuation rate has been deduced from the temperature dependence of phonon anomalies by Mock et al. (1986), in quite good agreement with the theoretical predictions by Schmidt and Müller-Hartmann (1985). To complete the survey on phonon Raman data of RS compounds we should finally mention that semiconducting, divalent SmS shows a pronounced softening of the LO(L) phonon mode by 17% below the divalent reference line (at a_0 of EuS in fig. 38), (Güntherodt et al. 1977c, 1978), whereas the bulk modulus shows only a slight anomaly (see fig. 39). Within the picture of phonon anomalies in rare-earth IV compounds discussed in sect. 3.1 one can conclude that semiconducting SmS already exhibits charge fluctuations of the order of 200–300 cm^{-1} although it is assumed to be nearly divalent.

In another model calculation as given by Baba et al. (1980) the renormalization of the phonon frequencies of SmS has been expressed as a function of the energy gap between the $4f^6$ level and the bottom of the conduction band. A larger phonon softening has been obtained for the semiconducting phase because of the smaller energy gap, as compared to the metallic phase with a larger (although negative) gap. The microscopic origin of the renormalization has been attributed to the phonon-induced on-site f–d hybridization interaction which is enhanced for the smaller energy gap of the semiconducting phase of SmS.

3.7. *RSe* (*R* = *Y*, *La*, *Sm*, *Eu*, *Gd*, *Tm*, *Yb*)

Within the fcc RSe series TmSe exhibits quite unique properties, since it shows intermediate-valence behavior (Bucher et al. 1975, Campagna et al. 1974, Launois et al. 1980) in combination with low-temperature magnetic order

(Bucher et al. 1975, Ott et al. 1974, Triplett et al. 1974, Bjerrum Moeller et al. (1977). Another interesting feature is that one can adjust the degree of valence mixing by the composition of Tm_xSe (Batlogg et al. 1979). It has thus been observed that the valence of Tm can be varied between nearly 3^+ for $Tm_{0.87}Se$ and 2.7^+ for $Tm_{1.05}Se$. The intermediate-valence behavior of Tm is particularly interesting as it is due to the two magnetic 4f configurations involved ($4f^{12}$ and $4f^{13}$); two different magnetic relaxation rates have been predicted (Müller-Hartmann 1981). Only one magnetic relaxation rate has been observed so far using magnetic neutron scattering (Grier and Shapiro 1981, Holland-Moritz 1983), which makes an experimental estimate of the charge relaxation rate particularly worthwhile in comparison to the theoretical predictions.

Raman scattering in TmSe was first investigated by Treindl and Wachter (1979, 1980) and also by Stüsser et al. (1981). The connection between strong Raman intensities and phonon anomalies due to strong electron–phonon coupling (see also Klein 1982) is clearly illustrated by comparing the Raman spectra of cleaved (100) faces of the superconductor YSe with intermediate-valence TmSe and semiconducting SmSe as given by Stüsser et al. (1981) and depicted in fig. 41. The

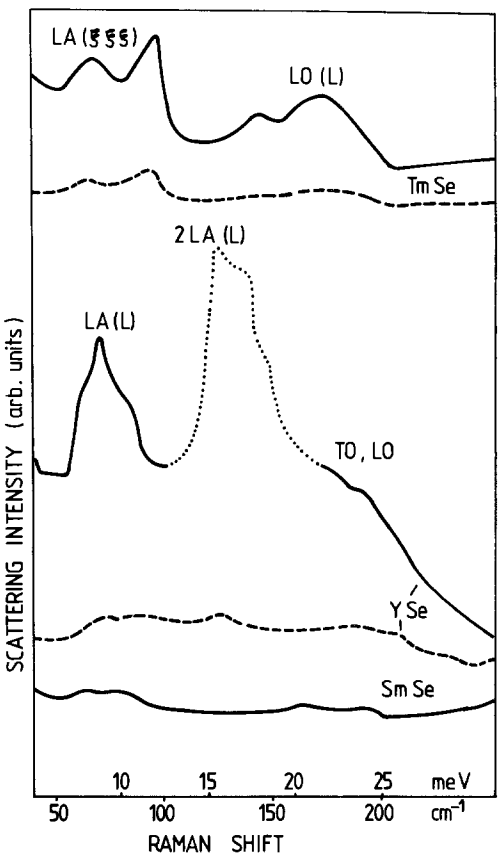

Fig. 41. Raman spectra of cleaved (100) faces of TmSe, YSe and SmS at 300 K using 5309 Å (TmSe) and 5145 Å (YSe, SmSe) laser excitation. Unpolarized spectrum for SmSe; polarized spectra for TmSe and YSe with $\boldsymbol{E}_i \| \boldsymbol{E}_s$ ($\Gamma_1^+ + 4\Gamma_{12}^+$) and $\boldsymbol{E}_i \perp \boldsymbol{E}_s$ ($\Gamma_{25}^+ + \Gamma_{15}^+$), where $\boldsymbol{E}_{i(s)}$ is the incident (scattered) electric field vector.

unpolarized Raman spectrum of SmSe does not show any appreciable scattering intensity in the range of the acoustic and optical phonon frequencies. In addition to a presumably low defect concentration, this result is consistent with the absence of significant phonon anomalies in this 0.5 eV f–d gap semiconductor. On the other hand, the one-phonon scattering intensity of YSe for $\boldsymbol{E}_i \| \boldsymbol{E}_s$ (solid line) is enhanced for acoustic phonons near 70 cm^{-1} as compared to the weak intensity from optical phonons near 180 cm^{-1} (the dotted line indicates second-order scattering). This result emphasizes the strong Raman intensity associated with the LA(L) phonon anomaly. On the other hand, for TmSe the $\boldsymbol{E}_i \| \boldsymbol{E}_s$ spectrum (solid line) shows about equal intensities for acoustic and optical phonons. The similarity with the spectrum of $Sm_{0.75}Y_{0.25}S$ in fig. 37 becomes evident by comparing the maxima of the latter near 85 cm^{-1} and 245 cm^{-1}, respectively, with those of TmSe near 70 cm^{-1} and 175 cm^{-1} in fig. 41. The latter two frequencies coincide with the LA and LO phonon anomalies of TmSe in the [111] direction (Mook and Holtzberg 1981). Hence it can be concluded from fig. 41 that in superconducting or intermediate-valence NaCl-type compounds, the Raman intenisty consists of a one-phonon density of states weighted by specific matrix elements of the electron–phonon coupling which are enhanced near the phonon anomalies.

Inspecting the LO(L) phonon frequencies of TmSe more closely,LO(L) phonon softening has been found in going from $Tm^{3+}_{0.87}Se$ to $Tm^{2.7+}_{1.05}Se$ (Treindl and Wachter 1979). This softening increases linearly with increasing valence mixing. These data have been summarized in fig. 42 where the LO(L) phonon frequencies of Tm_xSe together with those of various stable valence RSe compounds have been plotted as a function of the lattice parameter. The LO(L) phonon frequencies have been taken from the literature (Stüsser et al. 1981, Boppart et al. 1981, Güntherodt and Zeyher 1984, Güntherodt and Merlin 1984 and references cited therein). The stable divalent reference line is given by YbSe, EuSe and SmSe and the trivalent reference line is given by LaSe, GdSe, YSe and $Tm_{0.87}Se$.

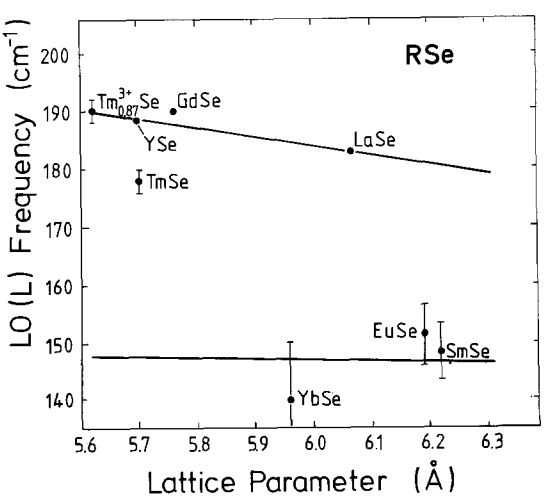

Fig. 42. LO(L) phonon frequencies of various RSe compounds as a function of the lattice parameter.

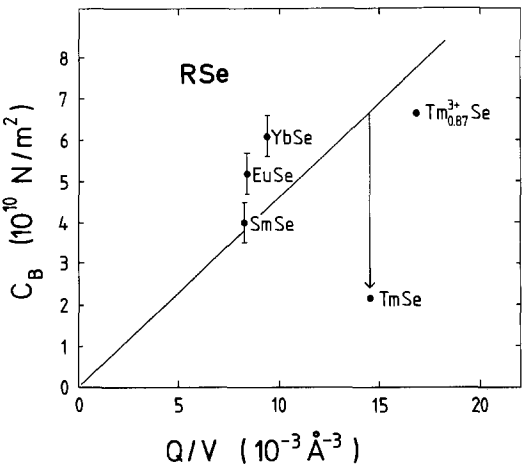

Fig. 43. Bulk modulus of various RSe compounds plotted as a function of Q/V (Q denotes the valence and V the unit cell volume).

The LO(L) phonon frequency of intermediate-valence $Tm_{1.0}Se$ lies between the divalent and trivalent reference lines according to its valence mixing ratio, indicating a charge relaxation rate well below the optical phonon frequencies. On the other hand, the bulk modulus of $Tm_{1.0}Se$ shows a distinct softening compared to the stable valence references as can be seen from fig. 43, where the bulk moduli of several RSe compounds are plotted as a function of Q/V (Q denoting the valence and V the unit cell volume). The bulk modulus of SmSe, EuSe and YbSe has been taken from Jayaraman et al. (1974) and that of $Tm_{1.0}Se$ and $Tm_{0.87}Se$ from Boppart et al. (1981). From the optical phonon anomaly of $Tm_{1.0}Se$ and its soft bulk modulus one can estimate a charge relaxation rate of the order of 50–100 cm^{-1}. This is even more interesting as Treindl and Wachter (1979) find a phonon Raman peak near 60 cm^{-1} which increases in intensity with increasing valence mixing from $x = 0.97$ to $x = 1.05$ and which is absent in $Tm_{0.87}Se$. The 60 cm^{-1} peak, which appears to be connected with the intermediate-valence state, has been attributed to either an anomaly in the LA phonon branch or to a localized low-energy electronic excitation near 60 cm^{-1} which may interact with the LA phonon branch. Although no such distinct localized electronic excitation was found in neutron scattering experiments of TmSe for temperatures above 100 K (Mook and Holtzberg 1981, Loewenhaupt and Holland-Moritz 1978), a charge relaxation rate of the order of 60 cm^{-1} might well induce strong anomalies within this phonon frequency range resulting in a flattening of the LA phonon dispersion around 60 cm^{-1} as assumed by Boppart et al. (1981) as well as an enhancement of the Raman scattering cross-section of these LA phonons (increase of the phonon-induced charge deformability) as has been emphasized by Stüsser et al. (1981).

3.8. *Conclusions*

The above analysis of all IV compounds investigated so far with respect to elastic and phononic properties is summarized schematically in fig. 44. The

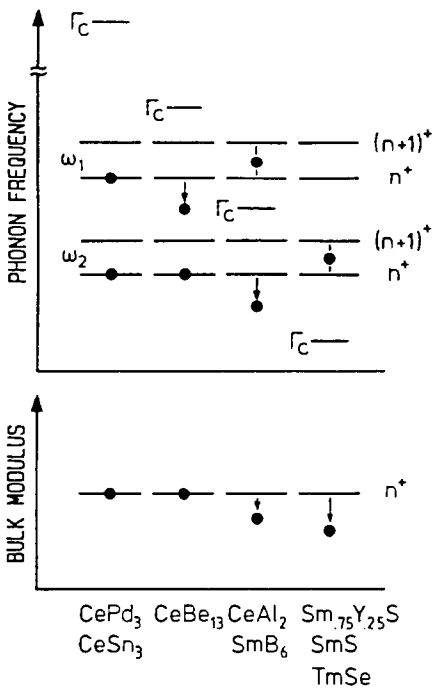

Fig. 44. Schematic representation of the influence of different charge relaxation rates Γ_c of IV rare-earth ions on the frequencies of the optical phonon modes (e.g., ω_1 and ω_2) and on the $q \approx 0$ longitudinal acoustic-phonon modes, represented by the bulk modulus c_B (see text). For the stable n^+- and $(n+1)^+$-valent rare-earth compounds we show generalized reference lines. Four typical cases are shown with the representative samples given at the bottom.

behavior of the long-wavelength ($q \approx 0$) acoustic phonons is represented by the bulk modulus c_B, which is a measure of the isotropic compression of the material and thus has the same (breathing) symmetry as the charge fluctuations. For IV compounds c_B probes anomalies of the longitudinal acoustic phonons. For the optical phonons, two mode frequencies (ω_1, ω_2) are shown schematically for the n^+- and $(n+1)^+$-valent reference compounds. The order of magnitude of Γ_c has been indicated. The different compounds listed at the bottom of fig. 44 can be classified according to the following four different cases:

(i) Intermediate-valence $CeSn_3$ and $CePd_3$ show neither elastic nor optical-phonon anomalies with respect to their trivalent reference compounds (Pintschovius et al. 1980, Blaschko et al. 1984, Severing 1985). This is explained by a value of Γ_c which is far above the highest optical-phonon branches, so that no coupling occurs between Γ_c and the phonons.

(ii) In the case of $CeBe_{13}$ only the two highest-lying optical ($q \approx 0$) phonons of Γ_1^+ symmetry ($\hbar\omega = 610\,\mathrm{cm}^{-1}$ and $\hbar\omega = 580\,\mathrm{cm}^{-1}$, both represented by $\hbar\omega_1$ in fig. 44) exhibit a softening, whereas the other four optical ($q \approx 0$) phonons (represented by $\hbar\omega_2$ in fig. 44) show no anomalies with respect to their reference lines (see discussion in sect. 3.5). Also, the bulk modulus does not exhibit any anomaly (Mock et al. 1985). Hence, Γ_c lies above, but close to, $\hbar\omega_1$.

(iii) The high-frequency optical ($q \approx 0$) phonons ($\hbar\omega > 650\,\mathrm{cm}^{-1}$) of SmB_6 (represented schematically by $\hbar\omega_1$ in fig. 44) are intermediate between the n^+ and $(n+1)^+$ reference lines, whereas both the low-energy optical phonons ($\hbar\omega < 200\,\mathrm{cm}^{-1}$, represented by $\hbar\omega_2$ in fig. 44) and the bulk modulus become soft as

TABLE 2
Experimentally determined charge relaxation rates Γ_c at room temperature compared to the theoretical values (Müller-Hartmann 1981), which have been scaled by the measured spin relaxation rates Γ_s. References for the values of Γ_s and the valence have been summarized by Zirngiebl (1986) and by Zirngiebl and Güntherodt (1990). ($\triangleq$ means "corresponds to".)

Compound	Valence	Γ_s (K)	Γ_c (theory) (K)	Γ_c (exp.) (K)
SmB_6	2.7	100	300	300–600
$CeAl_2$	3.02	58	1800	200
$YbAl_2$	2.4	400	600	>180
$CeCu_2Si_2$	3.05	70	2100	>200
$YbCu_2Si_2$	2.9	40	360	>200
$CeBe_{13}$	3.04	230	6000	$\gg$900
$CeSn_3$	3.02	250	10000	$\gg$300
$CePd_3$	3.26	200	1000	$\gg$300
$CeNi_2Ge_2$	3.07	120	1500	$\gg$400
$YbNi_2Ge_2$	2.89	90	800	$\gg$400
Sms (metal)	2.8	100	110	120
TmSe	2.58	10	60	120
$Sm_{1-x}Y_xS$ ($x = 0.25$)	2.4	50	80 ($\triangleq$ 1.6 THz)	100 ($\triangleq$ 2.0 THz)

discussed in sect. 3.2. From this it follows that $\hbar\omega_2 < \Gamma_c < \hbar\omega_1$. The same refers to $CeAl_2$ with the exception that the 4^+-valent reference line is not known quantitatively.

(iv) The fcc structures SmS, $Sm_{0.75}Y_{0.25}S$ and TmSe show longitudinal optical-phonon frequenices near the L point of the Brillouin zone which interpolate between the n^+ and $(n+1)^+$ reference lines according to the valence mixing ratio. On the other hand, these compounds exhibit a soft bulk modulus. Thus Γ_c lies between the acoustic and optical-phonon branches as discussed in sections 3.6 and 3.7. The analysis of the phonon anomalies in the different IV compounds investigated up to now give the numerical values of Γ_c listed in table 2. We have also listed theoretical values of the charge relaxation rates obtained by scaling the theoretically predicted (Müller-Hartmann 1981) ratio Γ_c/Γ_s by the experimentally determined spin relaxation rate Γ_s from the magnetic susceptibility or neutron scattering. There is reasonable agreement between theoretical and experimental values of Γ_c. Major discrepancies arise only for the "Kondo" systems $CeAl_2$ and $CeCu_2Si_2$. These discrepancies may be due to neglecting crystalline electric-field effects in the theoretical model.

4. Light scattering from "phonon bound states"

4.1. *Introduction*

As described in sect. 3 phonon Raman scattering in IV rare-earth compounds has been concerned quite intensively with phonon frequency renormalizations due

to strong electron–phonon coupling. However, a coupling of phonons to charge relaxation rates in IV compounds may not only cause phonon softening or a resonance enhancement of the Raman scattering cross-section but may also shift the spectral weight from the phonon mode into a lower frequency phonon satellite. The existence of such a phonon bound state due to the strong coupling of localized electronic excitations (or fluctuations) to phonons would indicate a breakdown of the Born–Oppenheimer approximation, which decouples the electronic and phononic systems. The following sections will be devoted to a systematic discussion of the various "phonon bound states" so far observed in Raman scattering from metallic rare-earth compounds. Emphasis will be put on a comparison of the Raman scattering results with the neutron scattering results from nominally the same phonon mode. Due to the different timescales probed by both methods (timescale of Raman scattering: 10^{-15} s, neutron scattering: 10^{-13} s) "phonon bound states" may show up rather differently in both methods. In the following we shall discuss the three systems, where phonon bound states are claimed as being observed, namely $Sm_{0.75}Y_{0.25}S$ and related compounds (Stüsser et al. 1982), $Tm_{1.0}Se$ and related compounds (Stüsser et al. 1982) and $CeAl_2$ (Güntherodt et al. 1985b). For a more general discussion of these compounds we refer to sections 3.6, 3.7 and 3.3, respectively.

4.2. *$Sm_{0.75}Y_{0.25}S$ and related compounds*

Raman scattering has been performed by Stüsser et al. (1982) for the intermediate-valence phases of the solid solution systems $Sm_{1-x}R_xS$ (R = Y, La, Pr, Gd, Tb, Dy, Tm; $0.15 < x < 1.0$). A mode independent of cation mass has been observed in between the gap of the acoustic- and optical-phonon branches for all Sm concentrated ($x < 0.5$) intermediate-valence phases. The Raman spectra of $Sm_{1-x}R_xS$ with R = Y, Pr, Gd, Dy in the upper part of fig. 45 show at 300 K a maximum of the scattering intensity near 200 cm^{-1}. This "gap mode" for $x < 0.50$ is due to first-order scattering as demonstrated by its temperature dependence (fig. 45 for $Sm_{0.78}Gd_{0.22}S$). For $x > 0.5$ the intensity observed in, e.g., $Sm_{0.25}Dy_{0.75}S$ at 300 K near 180 cm^{-1} (dashed line) is due to second-order scattering by phonons as proved by its quenching at 80 K. The absence of a significant defect in cation mass in $Sm_{1-x}R_xS$ with R = Pr, Gd, Dy rules out an interpretation of the "gap mode" as a local vibrational mode of the substituted cations.

The symmetry analysis of the "gap mode" intensity of, e.g., $Sm_{0.78}Gd_{0.22}S$ in the lower part of fig. 45 shows the dominance of the Γ_1^+ (A_{1g}) component, which is consistent with the behavior of the LO(L) phonon near 260 cm^{-1}. Moreover, the "gap mode" frequency appears to follow shifts of the LO(L) phonon frequency upon varying the cation masses. Hence the "gap mode" observed by Raman scattering in $Sm_{1-x}R_xS$ can be considered as a phonon "bound state" of the LO(L) phonon contributing to the scattering cross-section due to the coupling of low-frequency charge fluctuations to the lattice vibrations. Similarly, in neutron scattering experiments on IV $Sm_{0.75}Y_{0.25}S$ at room temperature a dispersionless "gap mode" at about $\hbar\omega = 175$ cm^{-1} (21.9 meV) is found which has been assigned

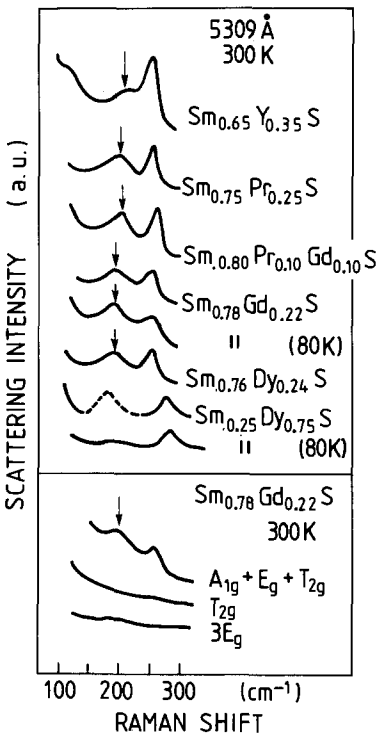

Fig. 45. Raman spectra of (100) cleaved intermediate-valence $Sm_{1-x}R_xS$ with R = Y, Pr, Gd and Dy at 300 K. Upper part: unpolarized spectra; spectra at 80 K for $x = 0.22$ Gd and $x = 0.75$ Dy, respectively, prove first- and second-order scattering (dashed line) at 300 K. The "gap mode" is seen near 200 cm^{-1}. Lower part: polarized Raman spectra of $Sm_{0.78}Gd_{0.22}S$ at 300 K.

to a localized vibrational mode of the lighter Y ions compared to Sm (Mook et al. 1978a). The frequency position of this "localized" mode agrees well with a simple mass scaling argument.

$$\omega = (m_{Sm}/m_Y)^{1/2}\omega_{LA(L)}$$

where $\omega_{LA(L)}$ denotes the frequency of the longitudinal acoustic phonons at the zone boundary L. However, since defect-induced Raman scattering should be rather weak (compare fig. 41) and since the frequency of the neutron and Raman "gap mode" differ by 25 cm^{-1}, which is way outside the experimental resolution, we conclude that they are not the same entity and have to be attributed to different origins.

Finally it seems interesting to compare the LO(L) frequencies as measured by Raman and neutron scattering (see table 3). The neutron scattering value of the LO(L) phonon frequency is soft compared to that measured by Raman scattering. The neutron LO(L) phonon frequency, on the other hand, compares quite well with the average of the Raman LO(L) phonon frequency and the "bound state" frequency weighted by the scattering intensity.

TABLE 3
Frequencies of some phonons as measured by neutron scattering compared to Raman scattering; frequencies of phonon "bound states" observed simultaneously in Raman scattering as well as the average of the Raman LO(L) frequency and the Raman "bound state" weighted by the Raman-scattering-intensity.

Phonon	Neutron scattering (cm^{-1})	Raman scattering (cm^{-1})	Raman "bound state" (cm^{-1})	Average (cm^{-1})
LO(L) phonon of $Sm_{0.75}Y_{0.25}S$	234	253	200	228
LO(L) phonon of TmSe	159	178	142	160
Γ_5^+ phonon of $CeAl_2$ (300 K)	108	109	71	108
Γ_5^+ phonon of $CeAl_2$ (77 K)	97	109	71	99
Γ_5^+ phonon of $CeAl_2$ (25 K)		109	71	82
Γ_5^+ phonon of $CeAl_2$ (4 K)	80	109	71	80

4.3. *TmSe and related compounds*

For TmSe similar results have been obtained as for the "bound state" of $Sm_{1-x}R_xS$. In particular, the peak near 145 cm^{-1} in the Raman spectrum of TmSe in fig. 46 has also been identified by Stüsser et al. (1982) as a "gap mode" between the acoustic- and optical-phonon dispersions. Moreover, from its first-order scattering nature (Stüsser et al. 1981, Treindl and Wachter 1979), its dominant A_{1g} symmetry (Stüsser et al. 1981), ruling out any involvement of TO phonons (Güntherodt et al. 1981b, Bilz et al. 1979), as well as from its frequency shift in parallel to that of the LO(L) phonons in $TmSe_{0.85}Te_{0.15}$ (see fig. 46), the "gap mode" can be identified as a bound state of the LO(L) phonon, analogously to the case of $Sm_{1-x}R_xS$. In the case of TmSe no localized phonon mode in the gap between acoustic- and optical-phonon branches has been observed by neutron scattering (Mook et al. 1982). Due to missing disorder this was to be expected. However, comparing LO(L) phonon frequencies as measured by Raman and neutron scattering we find again the following discrepancy: the LO(L) phonon measured by neutron scattering is soft compared to the Raman value but compares quite well with the intensity-weighted average of the Raman LO(L) phonon frequency and the Raman "bound state" frequency (see table 3).

4.4. *$CeAl_2$*

The Kondo system $CeAl_2$ has attracted continuous interest over the past decade due to its anomalously strong coupling between the elastic and magnetic (elec-

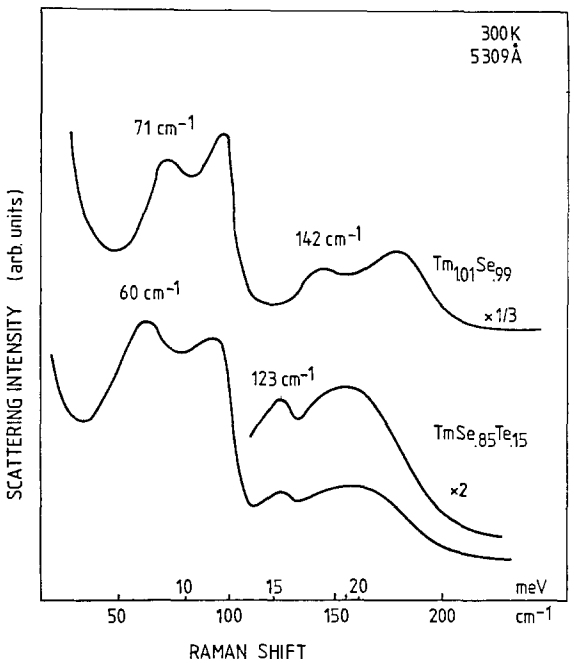

Fig. 46. Unpolarized Raman spectra of a (100) cleaved $Tm_{1.01}Se_{0.99}$ crystal and a $TmSe_{0.85}Te_{0.15}$ single crystal at 300 K.

tronic) subsystems. This results in a wide variety of unusual phenomena like, e.g., the pronounced softening of the c_{44} elastic mode as observed by Lüthi and Lingner (1979) and the splitting of the Γ_8 crystalline electric field (CEF) level (Loewenhaupt et al. 1979). These features have been interpreted in a model proposed by Thalmeier and Fulde (1982) taking into account the large magneto-elastic coupling between the energetically degenerate Γ_8 CEF level and the Γ_5^+ (T_{2g}) optical phonon. Raman scattering of $CeAl_2$ has been performed by Güntherodt et al. (1983) and Güntherodt et al. (1985b) as a function of temperature down to 5 K in order to characterize the Γ_5^+ phonon. The results are shown in fig. 47. The Raman peak near 109 cm^{-1} at 300 K does not show a significant shift upon cooling to 5 K. Below 77 K a new peak emerges near 71 cm^{-1} (8.9 meV) with a full width at half maximum of 15 cm^{-1}. This additional peak is not observed in the non-magnetic reference compound $LaAl_2$. The peak position coincides with the lower one of the inelastic transitions observed in neutron scattering (Loewenhaupt et al. 1979).

The most obvious assignment of this new Raman peak "phonon bound state" to the transition indicated as $\tilde{\Gamma}_7 - \tilde{\Gamma}_{8(2)}$ by Thalmeier and Fulde (1982) (see inset of fig. 47) poses a severe problem: since in the theory both $\tilde{\Gamma}_{8(i)}$ levels are composed symmetrically of phonon and CEF states, there exists no justification why one should not also observe the high lying $\tilde{\Gamma}_{8(1)}$ CEF level. Another inconsistent feature in this context of the new Raman peak is the fairly large intensity, pointing to phononic rather than electronic scattering, making an interpretation of this new mode as a "bound state" of the Γ_5^+ phonon quite straightforward.

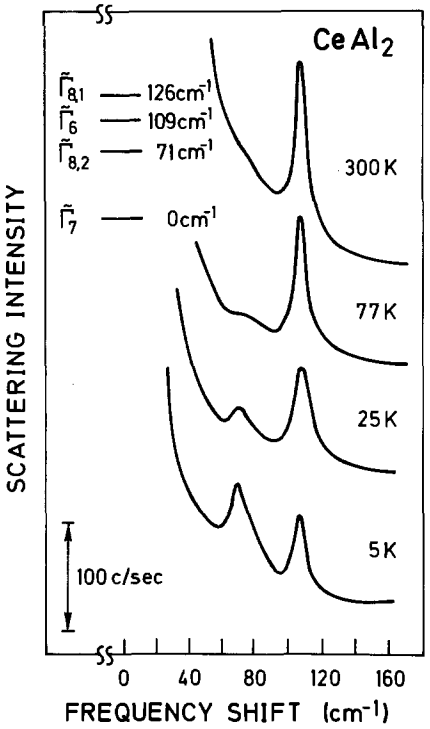

Fig. 47. Raman scattering cross-section of $CeAl_2$ as a function of temperature. Inset: magnetoelastically coupled phonon–CEF system (see Thalmeier and Fulde 1982).

In contrast to the Raman scattering results a temperature-dependent softening of the Γ_5^+ mode is observed between 300 and 5 K in phononic neutron scattering (Reichart and Nücker 1983). This has been attributed by Thalmeier (1984) to the temperature dependence of the vertex corrections, which have to be taken into account in higher-order perturbation theory. The vertex corrections yield a temperature-dependent renormalization of the Γ_5^+ phonon frequency proportional to the difference in occupation of the Γ_7 and Γ_8 CEF levels.

Comparing Raman and neutron scattering results concerning the Γ_5^+ phonon of $CeAl_2$ one can summarize: as soon as one observes the "phonon bound state" in Raman scattering the Γ_5^+, as observed by neutron scattering, is soft compared to its Raman counterpart. However, for all temperatures the Raman-intensity-weighted average of the Raman Γ_5^+ phonon energy and the "bound state" energy compares quite well with the Γ_5^+ phonon energy obtained by neutron scattering (see table 3).

4.5. *Conclusions*

To reconcile the diverging Raman and neutron scattering results the following point of view has been taken by Güntherodt et al. (1985b): similarly to the valence fluctuations between two integral valence states ($4f^n \leftrightarrow 4f^{n-1} + e^-$) in IV rare-earth compounds the systems $CeAl_2$, TmSe and $Sm_{0.75}Y_{0.25}S$ show

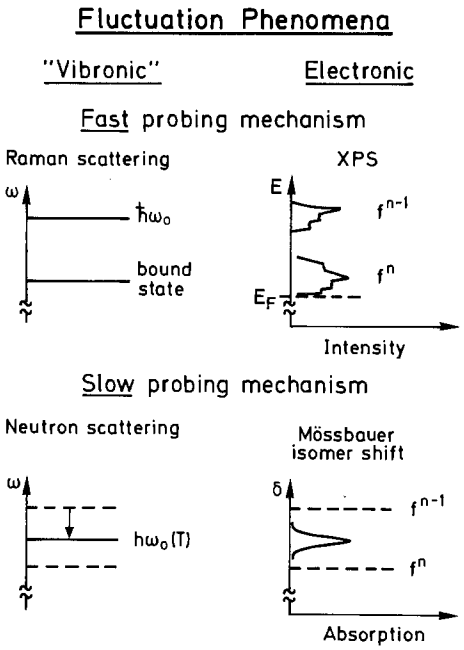

Fig. 48. Comparison of the different experimental methods probing the time-scale of "phononic" as well as electronic fluctuations (see text).

"phononic fluctuations" between a bare phonon and its renormalized bound state. Raman against neutron scattering from these phononic fluctuations are explained analogously as are XPS (X-ray *p*hotoelectron *s*pectroscopy) data against Mössbauer isomer shifts from valence fluctuations. The fast probing mechanism "Raman scattering" gives in analogy to XPS an instantaneous picture of the dynamical mixture of the two states, while the slow probing mechanism "neutron scattering" in analogy to Mössbauer isomer shifts yields an average over the two fluctuating states (see also fig. 48).

5. Final conclusions

In this chapter we have presented an overview of the rather diverse features observed by Raman scattering in metallic rare-earth compounds, ranging from purely electronic excitations to phonons and strongly coupled electron–phonon excitations. From the materials' point of view, Raman scattering has proved to be a useful tool to get started on rare-earth materials at a stage where their purity, perfection, size or isotope composition do not yet allow for investigations by neutron scattering. Thus Raman scattering investigations of rare-earth compounds have served to advance the understanding of new physical phenomena such as valence fluctuations of rare-earth ions in solids.

The field of Raman scattering in rare-earth intermediate-valence compounds has now reached a certain degree of maturity and understanding so that a lot of the activity has shifted to Raman and Brillouin scattering investigations of heavy-fermion compounds and high-temperature superconductors. The exciting

results of Raman scattering in these two classes of materials will be reviewed, respectively, by Zirngiebl and Güntherodt (1990), and by Thomsen (1990) in the forthcoming volume VI of *Light Scattering in Solids* (in the Springer Series "Topics in Applied Physics").

Acknowledgements

The authors would like to express their gratitude to M. Barth, B. Batlogg, S. Blumenröder, H. Brenten, M. Croft, B. Hillebrands, A. Jayaraman, R. Mock, G. Pofahl, N. Stüsser and J.D. Thompson for their cooperation and participation in various stages of the experimental work. We would like to thank Z. Fisk, P. Fulde, E. Holland-Moritz, M. Loewenhaupt, B. Lüthi, E. Müller-Hartmann, P. Thalmeier, and D. Wohlleben for many stimulating discussions.

The preparation, characterization and supply of samples by W. Assmus, M. Beyss, E. Bucher, Z. Fisk, F. Holtzberg, E. Melczer, A. Meyer, E.V. Sampathkumaran, J. Smith and K. Winzer are gratefully acknowledged. We are obliged to M. Jürss-Nysten, I. Kürten, M. Löhrer and H. Mattke for help in preparing the manuscript.

References

Allen, J.W., R.M. Martin, J.B. Boyce and F. Holtzberg, 1980, Phys. Rev. Lett. **44**, 1275.

Baba, K., M. Kobayashi, H. Kaga and I. Yokota, 1980, Solid State Commun. **35**, 175.

Baer, Y., H.R. Ott, J.C. Fuggle and L.E. De Long, 1981, Phys. Rev. B **5384**.

Batlogg, B., H.R. Ott, E. Kaldis, W. Thöni and P. Wachter, 1979, Phys. Rev. B **19**, 247.

Bauminger, E.R., D. Froindlich, J. Nowik, S. Ofer, I. Felner and I. Mayer, 1973, Phys. Rev. Lett. **30**, 1053.

Becker, K.W., P. Fulde and J. Keller, 1977, Z. Phys. B **28**, 9.

Bennemann, K.H., and M. Avignon, 1980, J. Magn. & Magn. Mater. **15–18**, 947.

Besnus, M.J., J.P. Kappler and A. Meyer, 1983, Solid State Commun. **48**, 835.

Bilz, H., G. Güntherodt, W. Kleppmann and W. Kress, 1979, Phys. Rev. Lett. **43**, 1998.

Bjerrum Moeller, H., S.M. Shapiro and R.J. Birgeneau, 1977, Phys. Rev. Lett. **39**, 1021.

Blaschko, O., G. Krexner, L. Pintschovius, W. Assmus and G. Ernst, 1984, Solid State Commun. **51**, 971.

Blumenröder, S., E. Zirngiebl, G. Güntherodt, A. Jayaraman, B. Batlogg, A. Meyer and Z. Fisk, 1985, J. Magn. & Magn. Mater. **47&48**, 318.

Boppart, H., A. Treindl and P. Wachter, 1981, in: Valence Fluctuations in Solids, eds L.M. Falicov, W. Hanke and M.B. Maple (North-Holland, Amsterdam) p. 103.

Brenten, H., E. Zirngiebl, M.S. Wire, S. Blumenröder, G. Pofahl, G. Güntherodt and Z. Fisk, 1987, Solid State Commun. **62**, 387.

Bucher, E., K. Andres, F.J. DiSalvo, J.P. Maita, A.C. Gossard, A.S. Cooper and G.W. Hull, 1975, Phys. Rev. B **11**, 500.

Campagna, M., E. Bucher, G.K. Wertheim, D.N.E. Buchanan and L.P. Longinotti, 1974, Phys. Rev. Lett. **32**, 885.

Cardona, M., and G. Güntherodt, 1982a, Light Scattering in Solids II, in: Topics in Applied Physics, Vol. 50 (Springer, Heidelberg, Berlin, New York).

Cardona, M., and G. Güntherodt, 1982b, Light Scattering in Solids III, in: Topics in Applied Physics, Vol. 51 (Springer, Heidelberg).

Cardona, M., and G. Güntherodt, 1984, Light Scattering in Solids IV, in: Topics in Applied Physics, Vol. 54 (Springer, Heidelberg).

Cardona, M., and G. Güntherodt, 1989, Light Scattering in Solids V, in: Topics in Applied

Physics, Vol. 66 (Springer, Heidelberg, Berlin, New York, Tokyo).
Cooper, S.L., M.V. Klein, Z. Fisk and J.L. Smith, 1986, Phys. Rev. B **34**, 6235.
De Shazer, L.G., and G.H. Dieke, 1963, J. Chem. Phys. **38**, 2190.
Dieke, G.H., and H.M. Crosswhite, 1963, Appl. Opt. **2**, 675.
Entel, P., and M. Sietz, 1981, Solid State Commun. **39**, 249.
Entel, P., N. Grewe, M. Sietz and K. Kowalski, 1979, Phys. Rev. Lett. **43**, 2002.
Eynatten, G., C.F. Wang, L.S. Fritz and S.S. Hanna, 1983, Z. Phys. B **51**, 37.
Fisk, Z., 1969, Ph.D. Thesis (University of California, San Diego, CA) unpublished.
Fisk, Z., 1976, Solid State Commun. **18**, 221.
Fuggle, J.C., F.U. Hillebrecht, Z. Zolnierek, R. Lässer, Ch. Freiburg, O. Gunnarsson and K. Schönhammer, 1983, Phys. Rev. B **27**, 7330.
Fujita, T., M. Suzuki, T. Komatsubara, S. Kunii, T. Kasuya and T. Oktsaka, 1980, Solid State Commun. **35**, 569.
Fulde, P., and M. Loewenhaupt, 1988, in: Modern Problems in Condensed Matter Sciences, Vol. 22, part I, eds A.S. Borovik-Romanov and S.K. Sinha (North-Holland, Amsterdam).
Ghatak, S.K., and K.H. Bennemann, 1978, J. Phys. F **8**, 571.
Goldschmidt, Z.B., 1978, in: Handbook on the Physics and Chemistry of Rare Earths, Vol. 1, eds K.A. Gschneidner Jr, and L. Eyring (North-Holland, Amsterdam) p. 1.
Goto, T., A. Tamaki, S. Kunii, T. Nakajima, T. Fujimura, T. Kasuya, T. Komatsubara and S.B. Woods, 1983, J. Magn. & Magn. Mater. **31–34**, 419.
Grewe, N., and P. Entel, 1979, Z. Phys. B **33**, 331.
Grier, B.H., and S.M. Shapiro, 1981, in: Valence Fluctuations in Solids, eds L.M. Falicov, W. Hanke and M.B. Maple (North-Holland, Amsterdam) p. 325.
Gronau, M., 1979, Ph.D. Thesis (Ruhr-Universität, Bochum) unpublished.
Güntherodt, G., and R. Merlin, 1984b, Light Scattering in Solids IV, in: Topics in Applied Physics, Vol. 54, eds M. Cardona and G. Güntherodt (Springer, Berlin, Heidelberg, New York, Tokyo) p. 243.
Güntherodt, G., and R. Zeyher, 1984a, Light Scattering in Solids IV, in: Topics in Applied Physics, Vol. 54, eds M. Cardona and G. Güntherodt (Springer, Berlin, Heidelberg, New York, Tokyo) p. 203.
Güntherodt, G., R. Merlin, A. Frey and F. Holtzberg, 1977a, in: Lattice Dynamics, ed. M. Balkanski (Flammarion, Paris) p. 130.
Güntherodt, G., P. Grünberg, E. Anastassakis, M. Cardona, H. Hackfort and W. Zinn, 1977b, Phys. Rev. B **16**, 3504.
Güntherodt, G., R. Keller, P. Grünberg, A. Frey, W. Kress, R. Merlin, W.B. Holzapfel and F. Holtzberg, 1977c, in: Valence Instabilities and Related Narrow Band Phenomena, ed. R.D. Parks (Plenum Press, New York) p. 321.
Güntherodt, G., R. Merlin, A. Frey and M. Cardona, 1978, Solid State Commun. **27**, 551.
Güntherodt, G., R. Merlin and P. Grünberg, 1979, Phys. Rev. B **20**, 2834.
Güntherodt, G., A. Jayaraman, E. Anastassakis, E. Bucher and H. Bach, 1981a, Phys. Rev. Lett. **46**, 855.
Güntherodt, G., A. Jayaraman, H. Bilz and W. Kress, 1981b, in: Valence Fluctuations in Solids, eds L.M. Falicov, W. Hanke and M.B. Maple (North-Holland, Amsterdam) p. 121.
Güntherodt, G., A. Jayaraman, W. Kress and H. Bilz, 1981c, Phys. Lett. A **82**, 26.
Güntherodt, G., A. Jayaraman, B. Batlogg and M. Croft, 1983, Phys. Rev. Lett. **51**, 2330.
Güntherodt, G., S. Blumenröder, B. Hillebrands, R. Mock and E. Zirngiebl, 1985a, Z. Phys. B **60**, 423.
Güntherodt, G., E. Zirngiebl, S. Blumenröder, A. Jayaraman, B. Batlogg and M. Croft, 1985b, J. Magn. & Magn. Mater. **47&48**, 315.
Gupta, L.C., and S.K. Malik, 1987, Valence Fluctuations and Heavy Fermions (Plenum Press, New York, London).
Hanzawa, K., and T. Kasuya, 1984, J. Phys. Soc. Jpn. **53**, 1809.
Hillebrands, B., and G. Güntherodt, 1983, Solid State Commun. **47**, 681.
Hillebrands, B., G. Güntherodt, R. Pott, W. König and A. Breitschwert, 1982, Solid State Commun. **43**, 891.
Hirst, L.L., 1970, Phys. Kondens. Mater. **11**, 255.
Holland-Moritz, E., 1983, J. Magn. & Magn. Mater. **38**, 253.
Holland-Moritz, E., and E. Zirngiebl, 1986, unpublished results.

Holland-Moritz, E., D. Wohlleben and M. Loewenhaupt, 1982, Phys. Rev. B **25**, 7482.
Holland-Moritz, E., E. Braun, B. Roden, B. Perscheid, E.V. Sampathkumaran and W. Langel, 1987, Phys. Rev. **35**, 3122.
Holland-Moritz, E., E. Zirngiebl and S. Blumenröder, 1988, Z. Phys. B **70**, 395.
Horn, S., E. Holland-Moritz, M. Loewenhaupt, F. Steglich, H. Scheuer, A. Benoit and J. Flouquet, 1981a, Phys. Rev. B **23**, 3171.
Horn, S., F. Steglich, M. Loewenhaupt, H. Scheuer, W. Felsch and K. Winzer, 1981b, Z. Phys. B **42**, 125.
Ishii, M., M. Aono, S. Muranaka and S. Kawai, 1976a, Solid State Commun. **20**, 437.
Ishii, M., T. Tanaka, E. Bannai and S. Kauni, 1976b, J. Phys. Soc. Jpn. **41**, 1075.
Jayaraman, A., A.K. Singh, A. Chatterjee and S. Usha Devi, 1974, Phys. Rev. B **9**, 2513.
Johnson, S.M., J.A.C. Bland, P.J. Brown, A. Benoit, H. Capellmann, J. Flouquet, H. Spille, F. Steglich and K.R.A. Ziebeck, 1985, Z. Phys. B **59**, 900.
Kaspers, W., 1983, Ph.D. Thesis (University of Cologne) unpublished.
Kasuya, T., 1985, Crystalline field and anomalous mixing effects in f-electron systems (North-Holland, Amsterdam).
King Jr, H.E., S.J. La Placa, T. Penney and Z. Fisk, 1981, in: Valence Fluctuations in Solids, eds L.M. Falicov, W. Hanke and M.B. Maple (North-Holland, Amsterdam) p. 333.
Klein, M.V., 1982, Light Scattering in Solids III, in: Topics in Applied Physics, Vol. 51, eds M. Cardona and G. Güntherodt (Springer, Berlin, Heidelberg, New York) p. 121.
Koningstein, J.A., 1967, J. Chem. Phys. **46**, 2811.
Koningstein, J.A., and P. Grünberg, 1971, Can. J. Chem. **44**, 2336.
Kress, W., H. Bilz, G. Güntherodt and A. Jayaraman, 1981, J. de Physique Colloq. **42**, C6-3.
Launois, H., M. Rewiso, E. Holland-Moritz, R. Pott and D. Wohlleben, 1980, Phys. Rev. Lett. **44**, 1271.
Lea, K.R., M.J.M. Leask and W.P. Wolf, 1962, J. Phys. Chem. Solids **23**, 1381.
Lenz, D., H. Schmidt, S. Ewert, W. Boksch, R. Pott and D. Wohlleben, 1984, Solid State Commun. **52**, 759.
Loewenhaupt, M., and J.M. Carpenter, 1983, Bull. Am. Phys. Soc. **28**, 286.
Loewenhaupt, M., and E. Holland-Moritz, 1978, J. Magn. & Magn. Mater. **9**, 50.
Loewenhaupt, M., and E. Holland-Moritz, 1979a, J. Appl. Phys. **50**, 7456.
Loewenhaupt, M., and M. Prager, 1986, Z. Phys. B **62**, 195.
Loewenhaupt, M., B.D. Rainford and F. Steglich, 1979, Phys. Rev. Lett. **42**, 1709.
Lopes, L.C., and B. Coqblin, 1986, Phys. Rev. B **33**, 1804.
Lüthi, B., and C. Lingner, 1979, Z. Phys. B **34**, 157.
Maple, M.B., and D. Wohlleben, 1971, Phys. Rev. Lett. **27**, 511.
Matsuara, T., R. Kittler and K.H. Bennemann, 1980, Phys. Rev. B **21**, 3467.
Menth, A., E. Buehler and T.H. Geballe, 1969, Phys. Rev. Lett. **22**, 295.
Merlin, R., R. Zeyher and G. Güntherodt, 1977, Phys. Rev. Lett. **39**, 1215.
Merlin, R., G. Güntherodt, R. Humphreys, M. Cardona, R. Suryanarayanan and F. Holtzberg, 1978, Phys. Rev. B **17**, 4951.
Miura, M., and H. Bilz, 1986, Solid State Commun. **59**, 143.
Mock, R., and G. Güntherodt, 1985, J. Magn. & Magn. Mater. **47&48**, 312.
Mock, R., B. Hillebrands, H. Schmidt, G. Güntherodt, Z. Fisk and A. Meyer, 1985a, J. Magn. & Magn. Mater. **47&48**, 312.
Mock, R., E. Zirngiebl, B. Hillebrands and G. Güntherodt, 1986, Phys. Rev. Lett. **57**, 1040.
Mook, H.A., and F. Holtzberg, 1981, in Valence Fluctuations in Solids, eds L.M. Falicov, W. Hanke and M.B. Maple (North-Holland, Amsterdam) p. 113.
Mook, H.A., R.M. Nicklow, T. Penney, F. Holtzberg and M.W. Shafer, 1978a, Phys. Rev. B **18**, 2925.
Mook, H.A., T. Penney, F. Holtzberg and M.W. Shafer, 1978b, J. de Physique Colloq. **39**, C6, Suppl. 8, 837.
Mook, H.A., D.B. McWhan and F. Holtzberg, 1982, Phys. Rev. B **25**, 4321.
Mörke, I., 1985, Ph.D. Thesis (ETH Zürich) unpublished.
Mörke, I., V. Dvorak and P. Wachter, 1981, Solid State Commun. **40**, 331.
Mörke, I., E. Kaldis and P. Wachter, 1986, Phys. Rev. B **33**, 3392.
Müller-Hartmann, E., 1981, in Springer Series in Solid-State Sciences, Vol. 29, ed. T. Moriya (Springer, Heidelberg) p. 178.
Müller-Hartmann, E., B. Roden and D. Wohl-

leben, 1984, Proc. 5th Int. Conf. on Valence Fluctuations, in: J. Magn. & Magn. Mater. **47&48**.

Nathan, M.I., F. Holtzberg, J.E. Smith Jr, J.B. Torrance and J.C. Tsang, 1975, Phys. Rev. Lett. **34**, 467.

Ott, H.R., K. Andres and E. Bucher, 1974, AIP Conf. Proc. **24**, 40.

Ott, H.R., H. Rudigier, Z. Fisk and J.L. Smith, 1983, Phys. Rev. Lett. **50**, 1595.

Penney, T., R.L. Melcher, F. Holtzberg and G. Güntherodt, 1975, AIP Conf. Proc. **29**, 392.

Penney, T., B. Barbara, R.L. Melcher, T.S. Plaskett, H.E. King Jr and S.J. LaPlaca, 1981, in: Valence Fluctuations in Solids, eds L.M. Falicov, W. Hanke and M.B. Maple (North-Holland, Amsterdam) p. 341.

Pintschovius, L., E. Holland-Moritz, D.K. Wohlleben, S. Stöhr and J. Liebertz, 1980, Solid State Commun. **34**, 953.

Pofahl, G., E. Zirngiebl, S. Blumenröder, H. Brenten, G. Güntherodt and K. Winzer, 1986, Z. Phys. B **66**, 339.

Razafimandimby, H., P. Fulde and J. Keller, 1984, Z. Phys. B **54**, 111.

Reichart, W., and N. Nücker, 1983, J. Phys. F **14**, L135.

Reichart, W., and N. Nücker, 1985, unpublished.

Röhler, J., D. Wohlleben, G. Kaindl and H. Balster, 1982a, Phys. Rev. Lett. **49**, 65.

Röhler, J., D. Wohlleben and G. Kaindl, 1982b, in: Valence Instabilities, eds P. Wachter and H. Boppart (North-Holland, Amsterdam) p. 341.

Rossi, P., R. Marazza and R. Feno, 1979, J. Less Common Metal **66**, 17.

Sampathkumaran, E.V., L.C. Gupta, R. Vijayaraghavan, K.V. Gopalakrishnan, R.G. Pillay and H.G. Devare, 1981, J. Phys. C **14**, L237.

Schmidt, H.J., and E. Müller-Hartmann, 1985, Z. Phys. B **60**, 363.

Schmiester, G., B. Perscheid, G. Kaindl and J. Zukrowsky, 1982, in: Valence Instabilities, eds. P. Wachter and H. Boppart (North-Holland, Amsterdam) p. 219.

Scholz, H., W. Bauhofer and K. Ploog, 1976, Solid State Commun. **18**, 1539.

Severing, A., 1985, Ph.D. Thesis (University of Cologne) unpublished.

Smith, H.G., G. Dolling, S. Kunii, M. Kasaya, B. Liu, K. Takegahara, T. Kasuya and T. Goto, 1985, Solid State Commun. **53**, 15.

Smith Jr, J.E., F. Holtzberg, M.I. Nathan and J.C. Tsang, 1976, in: Light Scattering in Solids, eds M. Balkanski, R.C.C. Leite and S.P.S. Porto (Flammarion, Paris) p. 31.

Stassis, C., B. Batlogg, J.P. Remeika, J.D. Axe, G. Shirane and Y.J. Uemura, 1986, Phys. Rev. B **33**, 1680.

Steglich, F., 1985, in: Theory of Heavy Fermions and Valence Fluctuations, eds T. Kasuya and T. Sato (Springer, Berlin) p. 23.

Steglich, F., C.D. Bredl, M. Loewenhaupt and K.D. Schotte, 1979a, J. Phys. **40**, C5-301.

Steglich, F., J. Aarts, C.D. Bredl, W. Lieke, D. Meschede, W. Franz and J. Schäfer, 1979b, Phys. Rev. Lett. **43**, 1982.

Stewart, G.R., 1984, Rev. Mod. Phys. **56**, 755.

Stewart, G.R., Z. Fisk, J.O. Willis and J.L. Smith, 1984, Phys. Rev. Lett. **52**, 679.

Stüsser, N., M. Barth, G. Güntherodt and A. Jayaraman, 1981, Solid State Commun. **39**, 965.

Stüsser, N., G. Güntherodt, A. Jayaraman, K. Fischer and F. Holtzberg, 1982, in: Valence Instabilities, eds P. Wachter and H. Boppart (North-Holland, Amsterdam) p. 69.

Tanaka, T., J. Yoshimoto, M. Ishii, E. Banai and S. Kawai, 1977, Solid State Commun. **22**, 203.

Thalmeier, P., 1984, J. Phys. C **17**, 4153.

Thalmeier, P., and P. Fulde, 1982, Phys. Rev. Lett. **49**, 1588.

Thomsen, Ch., 1990, Light Scattering in Solids VI, in: Topics in Applied Physics, eds M. Cardona and G. Güntherodt (Springer, Heidelberg, Berlin, New York, Tokyo) to be published.

Treindl, A., and P. Wachter, 1979, Solid State Commun. **32**, 573.

Treindl, A., and P. Wachter, 1980, Solid State Commun. **36**, 901.

Triplett, B.B., N.S. Dixon, P. Boolchand, S.S. Hanna and E. Bucher, 1974, J. de Physique Colloq. **35**, C6-653.

Tsang, J.C., 1976, Solid State Commun. **18**, 57.

Vainshtein, E.E., S.M. Blochin and Yu.B. Paderno, 1965, Sov. Phys.-Solid State **6**, 2318.

Varma, C.M., 1976, Rev. Mod. Phys. **48**, 219.

Verhoeven, J.D., D.E. Gibson, M.A. Noac and R.J. Conzemius, 1976, J. Cryst. Growth **36**, 115.

Wachter, P., and H. Boppart, 1982, Valence Instabilities (North-Holland, Amsterdam).

Wakabayashi, N., 1980, Phys. Rev. B **22**, 5833.

Wang, Y.L., and B.R. Cooper, 1968, Phys. Rev. **172**, 539.

Wang, Y.L., and B.R. Cooper, 1969, Phys. Rev. **185**, 696.

Weber, W., E. Holland-Moritz and K. Fischer, 1989, Europhys. Lett. **8**, 257.

Westrum, E.F., H.L. Cleaver, J.T.S. Andrews and G. Feick, 1965, in: Rare Earth III, ed. L. Eyring (Gordon and Breach, New York) p. 597.

Winzer, K., and W. Felsch, 1978, J. de Physique Colloq. **39**, C6-832.

Wittershagen, B., and D. Wohlleben, 1985, J. Magn. & Magn. Mater. **47&48**, 79.

Wohlleben, D., 1984, in: Physics and Chemistry of Electrons and Ions in Condensed Matter, NATO ASI Series, Vol. 130C, eds J.V. Acrivos, N.F. Mott and A.D. Yoffe (D. Reidel, Dordrecht) p. 85.

Wohlleben, D., and J. Röhler, 1984a, J. Appl. Phys. **55**, 1904.

Yeh, C.T., W. Reichardt, B. Renker, N. Nücker and M. Loewenhaupt, 1981, J. de Physique Colloq. **42**, C6-371.

Zeyher, R., and W. Kress, 1979, Phys. Rev. B **20**, 2850.

Zirngiebl, E., 1986, Ph.D. Thesis (University of Cologne) unpublished.

Zirngiebl, E., and G. Güntherodt, 1990, Light Scattering in Solids VI, in: Topics in Applied Physics, eds M. Cardona and G. Güntherodt (Springer, Heidelberg, Berlin, New York, Tokyo) to be published.

Zirngiebl, E., B. Hillebrands, S. Blumenröder, G. Güntherodt, M. Loewenhaupt, J.M. Carpenter, K. Winzer and Z. Fisk, 1984, Phys. Rev. **30**, 4052.

Zirngiebl, E., S. Blumenröder, G. Güntherodt, A. Jayaraman, B. Batlogg and M. Croft, 1985a, Phys. Rev. Lett. **54**, 213.

Zirngiebl, E., S. Blumenröder, G. Güntherodt and W. Assmus, 1985b, J. Magn. & Magn. Mater. **47&48**, 72.

Zirngiebl, E., S. Blumenröder, G. Güntherodt and E.V. Sampathkumaran, 1986a, J. Magn. & Magn. Mater. **54–57**, 343.

Zirngiebl, E., S. Blumenröder, R. Mock and G. Güntherodt, 1986b, J. Magn. & Magn. Mater. **54–57**, 359.

Handbook on the Physics and Chemistry of Rare Earths, Vol. 14
edited by K.A. Gschneider, Jr. and L. Eyring

Chapter 96

THE ELECTRON–PHONON INTERACTION IN INTERMETALLIC COMPOUNDS

P. THALMEIER
Institut Laue–Langevin, F-38042 Grenoble, France

B. LÜTHI
Physikalisches Institut, Universität Frankfurt, D-6000 Frankfurt, Fed. Rep. Germany

Contents

1. Introduction

The electron–phonon coupling in rare-earth (R) compounds can lead to very interesting low-temperature effects in many physical quantities connected with elastic or vibrational degrees of freedom, e.g., in the elastic constants, thermal expansion, magnetostriction and phonon frequencies. The physical nature of these effects depends crucially on the type of electronic ground state and low lying excited states in these compounds.

In insulators, one has only to consider the spectrum of localized, partly filled $4f^n$ states of R ions. The lowest states are the crystalline electric field (CEF) levels of the relevant Russell–Saunders *LSJ* ground state multiplet. Electron-phonon coupling to CEF states is commonly known as "magnetoelastic coupling" and it arises from the strain modulation of the energies of CEF states. In insulators, e.g., the R vanadates, arsenates and phosphates, this coupling can lead to cooperative Jahn–Teller phase transitions in which the degeneracy of the lowest CEF multiplet is lifted and accompanied by a lattice distortion. This subject is already well represented in several reviews, Elliott et al. (1972), Gehring and Gehring (1975) and Melcher (1976).

Therefore in this review we shall focus on the electron–phonon coupling in metallic R compounds. They have shifted to the center of interest in the last ten years because of new phenomena such as valence fluctuations, Kondo lattice behavior and the formation of heavy-electron bands. The varying degree of hybridization between 4f states and conduction electron states leads to low lying electronic states whose character is very different from the localized states due to many-body effects. Consequently they lead to a rich variety of electronic and elastic or vibrational anomalies at low temperatures.

1.1. *Electronic structure of rare-earth compounds*

We first give a qualitative discussion of electronic states in rare-earth intermetallics. In a simplified picture which applies to Ce($4f^1$) compounds the nature of the electronic states is determined by two parameters:

(i) the position of the 4f level $E_f < 0$ with respect to the Fermi level $E_F = 0$;
(ii) the average hybridization of mixing strength $V(k_F)$ of 4f states and 5d6s conduction electrons.

In the case of $Ce^{3+}(4f^1)$ the charge transfer excitation $4f^1 \rightleftharpoons 4f^0 + e^-$ (conduction electron) therefore, requires an energy $|E_f|$ and has a width $N_f\Gamma$ ($\Gamma = \pi N_c(0)V^2$) due to hybridization, where $N_c(0)$ is the conduction electron density of states at $E_F = 0$ and N_f the degeneracy of the 4f level.

Depending on the ratio $N_f\Gamma/|E_f|$, two limiting cases, the local-moment and the strongly mixed-valent regime, can be distinguished.

1.1.1. *Case A: the local-moment regime*

If $E_f < 0$, $N_f\Gamma < |E_f|$ one is in the local-moment regime with nearly integer occupation of the 4f level. In this limit the hybridization can be transformed away

in first order (Schrieffer and Wolff 1966) leaving an effective interaction between the 4f shell and the conduction electrons which is described by the Coqblin–Schrieffer Hamiltonian for $Ce^{3+}(4f^1)$ or $Yb^{3+}(4f^{13})$. This is an exchange-type Hamiltonian (Coqblin and Schrieffer 1969) with an effective exchange constant $I^1_{ex} \simeq -V^2/|E_f| < 0$ between 4f- and s-type conduction electrons which is always negative. The total sf interaction is given by $I_{ex} = I^1_{ex} + I^0_{ex}$, where $I^0_{ex} > 0$ is the direct sf exchange constant. Depending on the sign of I_{ex} one observes a very different low-temperature behaviour of the electronic excitations.

1.1.1.1. *Ferromagnetic case* ($I_{ex} > 0$). Here the sf interaction simply leads to a broadening of the CEF excitations between CEF-split 4f levels E_{fm} where m denotes any of the CEF states. Thus the transitions $\Delta_{mm'} = E_{fm} - E_{fm'} \neq 0$, acquire a temperature-dependent linewidth $\Gamma_{mm'} \sim [N_c(0)I_{ex}]^2\Delta_{mm'}$. For zero-energy transitions the 'Korringa' or 'quasielastic' linewidth $\Gamma_{mm'} \sim [N_c(0)I_{ex}]^2 T$ vanishes for $T \to 0$. Crystal-field splittings $\Delta_{mm'}$ and linewidths $\Gamma_{mm'}$ are much smaller than the hybridization width Γ (fig. 1). Nevertheless they can be observed by inelastic neutron scattering experiments where the 4f occupation is unchanged. In contrast,

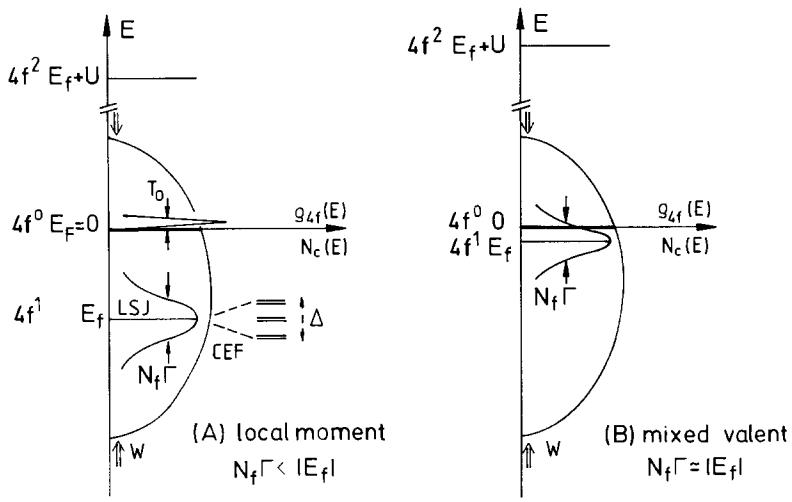

Fig. 1. Schematic energy diagram for electronic states in cerium intermetallic compounds. Conduction electron DOS $N_c(E)$ is shown as a semi-elliptic function with band width W. The Fermi level is at $E_F = 0$. The $4f^1$ level is at an energy E_f below and the $4f^2$ level at energy $E_f + U$ far above the Fermi energy where U is the on-site Coulomb repulsion of f electrons. In addition, the spin–orbit splitting (not shown) and CEF splitting Δ of E_f may exist. Hybridization (V) with conduction electrons affects the spectral density $\rho_{4f}(E)$ of the $4f^1 \to 4f^0$ excitations as indicated. There are two principal cases. (A) *The local-moment case*: there is a charge fluctuation peak at E_f of width $N_f\Gamma = \pi N_f V^2 N_c(0)$ and a narrow Kondo resonance peak above the Fermi level with a width $T_0 \sim T_K$ (Kondo temperature). The latter occurs only at low temperatures ($T < T_0$). The $4f^1$ level occupation n_f is close to one. (B) *The mixed-valent case*. the $4f^1$ level is near the Fermi energy, and real charge fluctuations lead to a sizable depopulation. As a consequence no resonance peak and no CEF levels exist. The order of magnitude for the various quantities is given by $U \simeq 10$ eV, $W \simeq 5$ eV, $|E_f| \simeq 2$ eV, $N_f\Gamma \simeq 0.5$ eV, $\Delta \simeq 10^{-2}$ eV (100 K), $T_0 \simeq 5$ K. Features in this diagram are not drawn to scale.

$N_f\Gamma$ is the linewidth of a real $4f^1 \rightarrow 4f^0$ excitation, as in a photoemission experiment which changes the 4f occupation.

1.1.1.2. *Antiferromagnetic case* ($I_{ex} < 0$). Here the sf interaction saturates the moment of the 4f states below a 'Kondo temperature' $T_K = W \exp((\pi E_f / N_f \Gamma)$, ($E_f < 0$, W is the conduction band width) leading to a many-body singlet ground state with a Pauli-type susceptibility. In the impurity case this can be interpreted as the formation of 'Kondo resonance' states above the Fermi level whose position and width is of the order of T_K. The linewidths $\Gamma_{mm'}$ for quasielastic transitions ($E_{fm} = E_{fm'}$) no longer tend to zero but saturate at a value close to T_K. In concentrated 'Kondo lattice' compound the single-ion Kondo resonance states may form quasiparticle bands due to coherence effects in a translationally invariant system. These bands are extremely narrow and their band width is of order T_K. Consequently the effective masses m^* of these 'heavy electrons' or 'heavy fermions' are very large compared to the free-electron mass. However, if effective intrinsic exchange interactions are strong enough there may instead be a magnetically ordered ground state with reduced moments.

1.1.2. *Case B*: *The strongly mixed-valent case*

If $|E_f| \sim N_f\Gamma$ one is in the strongly mixed-valent (MV) regime. In Ce-based MV compounds charge fluctuations $4f^1 \rightleftharpoons 4f^0 + e^-$ are then possible as real processes and are characterized by a charge fluctuation time $\hbar/\Gamma$. This constrasts to the previous situation (sect. 1.1.1) where only virtual charge fluctuations are possible and the characteristic timescale for Kondo compounds is provided by the larger 'spin fluctuation time' $\hbar/k_B T_K$. In the strongly MV compounds charge fluctuations destroy the CEF levels and also the magnetic moment of the 4f shell. One observes only a quasielastic line in neutron scattering experiments, Loewenhaupt and Holland-Moritz (1979). This is also true for the more general MV case such as Sm-based compounds where one has fluctuations between the nearly degenerate $(4f^n)(5d6s)^m$and $(4f^{n-1})(5d6s)^{m+1}$ configurations. Theoretically the MV case is described by the 'Anderson lattice' model which contains the original sf hybridization term and the intrasite Coulomb interaction U of the 4f electrons which is responsible for the energy difference between different $4f^n$ configurations. The energy diagrams for the local moment and mixed-valent case is drawn in fig. 1, which applies to Ce compounds.

Many aspects of the physics of intermetallic R compounds have already been covered in review articles. The normal CEF compounds are the central topic in Fulde and Peschel (1972), Fulde (1978a), and Fulde and Loewenhaupt (1986). Mixed-valent compounds are reviewed in Wohlleben and Coles (1973), Varma (1976) and Lawrence et al. (1981) and the more recent and rapidly evolving field of heavy-fermion compounds are discussed in Stewart (1984), Brandt and Moshchalkov (1984), Steglich (1985), Lee et al. (1986) and Fulde et al. (1988).

One should note that the local-moment Kondo case (sect. 1.1.1) and the strongly mixed-valent case (sect. 1.1.2) represent extreme limits and many R

compounds fall in between. Ce and Yb intermetallics can exhibit both behaviours and some Sm and Eu compounds and alloys belong to the strongly mixed-valent compounds. Most other R intermetallics are in the local-moment regime with E_f several electron volts below the Fermi level, their sf exchange constant I_{ex} is positive and therefore no Kondo behaviour is observed. In the modern theoretical view which has evolved from work on the Anderson (lattice) model it has become clear that there is a continuous transition as a function of the parameters E_f and V between the local-moment regime and the strongly mixed-valent regime.

1.2. *Electron–phonon coupling mechanism*

The qualitative knowledge of the electronic structure allows us to identify possible electron–lattice coupling mechanisms in the R compounds. We discuss them separately for the two regions introduced above:

1.2.1. *Case (A)*

There are two contributions: a deformation potential coupling and a magnetoelastic coupling. The former is due to the strain dependence of the conduction electron energies. Its relevant energy scale is the band width W. This term partly determines the background elastic constants and is also the origin of magnetoacoustic quantum oscillations. The other important contribution is due to the strain (ε_Γ) dependence, $E_m(\varepsilon_\Gamma)$, of the CEF levels. Because the energy scale is now $\Delta_{mm'} \sim 10^2$ K this coupling can produce strong temperature anomalies in the elastic constants, thermal expansion, phonon frequencies etc. below room temperature. It is a similar type of magnetoelastic coupling as in insulating R compounds.

In addition to the above contributions heavy-fermion compounds exhibit a special case of deformation potential coupling for heavy quasiparticle states at temperatures below T_K. It is characterized by an electronic 'Grüneisen parameter' Ω. This is a measure for the volume strain dependence of T_K. Microscopically it is mostly due to the volume strain dependence of the sf-hybridization strength V. Because the energy scale for this coupling is T_K one can expect elastic anomalies for temperatures $\leqslant T_K$ which are superposed on the magnetoelastic effects that have a temperature scale $\Delta_{mm'}$, which is generally much larger than T_K ($\leqslant$10 K).

1.2.2. *Case (B)*

In the strongly mixed-valent regime there are no CEF states, because Γ, the charge fluctuation width is usually larger than the typical CEF splittings. Therefore, there is no magnetoelastic coupling mechanism. The deformation potential coupling to the strongly hybridized conduction states at the Fermi level (fig. 1) is important if the temperature scale Γ is not too far above room temperature. Then volume strain coupling to charge fluctuations leads to anomalies in the bulk modulus and also in the phonon modes that have breathing character and whose frequency is comparable to the charge flucutation rate Γ.

Our review article will be organized according to the various types of electron–

phonon couplings introduced above. In sect. 2 we discuss magnetoelastic effects in conventional CEF-split stable-moment systems. This includes the various types of anomalies observed in the elastic constants and related phenomena; special emphasis will be placed on the effects in an external magnetic field. We shall discuss single ion as well as cooperative effects, especially quadrupolar phase transitions. In sect. 3 we give an introductory discussion of the deformation potential coupling and its consequences in R intermetallics with normal conduction electrons (magneto-acoustic quantum oscillations and anomalous temperature dependence of elastic constants). In sect. 4 this is applied to the recently investigated and more difficult electron–phonon interaction effects in cerium-based heavy-electron compounds. Phenomenological as well as microscopic theories of these effects are discussed and compared with experiment. Finally, we review elastic and phonon anomalies in the strongly mixed-valent compounds.

1.3. *Experimental methods*

A variety of experimental techniques are available for the investigation of the electron–lattice interaction. For static phenomena such as thermal expansion and magnetostriction one can use dilatometric and X-ray techniques. For dynamic effects such as elastic constant measurements, ultrasonic propagation and phonon dispersion the methods of sound velocity and attenuation measurements, and inelastic neutron or light scattering are available. In addition high-pressure work can give valuable information for some quantities.

Since we show extensive thermal expansion and sound velocity results we briefly review these two methods and refer to existing review articles for the others mentioned above. These are, e.g., for X-rays, Azaroff (1968); for inelastic neutron scattering, Dolling (1974); for light scattering, the review by Sandercock (1982) and the series on light scattering in solids edited by Cardona (1975) and Cardona and Güntherodt (1982).

1.3.1. *Thermal expansion measurements*

For thermal expansion and magnetostriction measurements the most commonly used method nowadays is the capacitive method. It has the advantage of high accuracy even with small samples and it can be used without corrections in external magnetic fields. Therefore, it is suitable for the study of both thermal expansion and magnetostriction especially at low temperatures. Capacitance bridges of high sensitivity are commercially available (e.g., General Radio, Type 1615-A). Various sample holders for capacitive length measurements are described in the literature: Brändli and Griessen (1973), Ott and Lüthi (1977), and Pott and Schefzyk (1982). A typical capacitance thermometer has a sensitivity of the order of 10^{-9} for relative length changes. This is sufficient to investigate length changes due to varying temperature and magnetic fields.

1.3.2. *Sound velocity and attenuation measurements*

There is a wide variety of different methods to measure sound velocities and

attenuation. For general reviews see Edmonds (1981), Bolef and Miller (1971) and Truell et al. (1969). One has to distinguish between absolute and relative measurements.

In the case of absolute velocity measurements one takes a crystal of given orientation with plane-parallel polished end faces. Piezoelectric transducers are bonded on these faces. An electromagnetic pulse of typical length 1 μs at 10–1000 MHz excites a longitudinal or transverse sound wave pulse which propagates back and forth in the sample. By measuring the time delay between the onset of the transit pulse and the first few echoes one can determine the absolute velocity with an accuracy of typically 1–2% for crystals of sufficient length. For a critical discussion and a new method to determine absolute velocities see Hock and Wesner (1989).

Relative velocity measurements can be performed with high sensitivity by using phase-sensitive methods. The phase of an echo pulse can be measured by mixing it with the generator signal (homodyne) or with a local oscillator signal (heterodyne). Both types are used in our laboratory, see Heil et al. (1984), Moran and Lüthi (1969). Using a boxcar and an integrator an automatic frequency tuning system keeps the phase always at zero. The relative frequency shift is then equal to the fractional sound velocity change (apart from a length change of the sample). In this way temperature- and magnetic-field-dependent sound velocity effects can be measured with a typical accuracy of one part in 10^6. By using a phase shifter and mixing the 0° and 90° signals both the relative sound velocity and the attenuation can be measured [see, e.g., Wallace and Garland (1986)].

2. Magnetoelastic effects in stable-moment compounds

These effects are due to the coupling of strains to CEF-split 4f states (Fulde 1978a, Lüthi 1980a). Therefore we shall first recapitulate some basic facts about the origin and symmetry classification of CEF states (sect. 2.1). For a more complete survey we refer to Hutchings (1964) and to review articles cited in the introduction. After this the microscopic origin and the Hamiltonians for magnetoelastic and interionic interactions will be discussed (sect. 2.2). Their influence on elastic properties, single ion as well as co-operative effects, will be discussed in sect. 2.3 (theory) and sect. 2.4 (experimental results). In sect. 2.5 we review the CEF effects on thermal expansion and magnetostriction. Section 2.6 is devoted to magnetoelastic effects in an external magnetic field, especially to symmetry breaking experiments. Finally in sect. 2.7 we discuss effects due to coupling of CEF states and high-frequency phonons.

2.1. *Crystalline electric field (CEF) states*

A free R ion with valence 2^+ or 3^+ has a partly filled $4f^n$ shell screened by the Xe core. The 4f states can be well classified within the Russell–Saunders *LS*

coupling scheme with the $(2J+1)$-fold degenerate ground state $^{2S+1}L_J$ determined by Hund's rules. The 4f occupation and ground states for the R series are listed in table 1. If an R ion is placed into a metallic matrix it experiences an electric field set up by the charges of surrounding ions and screened by conduction electrons. The full rotational symmetry of the free ions is therefore reduced to the appropriate point group symmetry of the R ions. In most cases discussed here it is the cubic group O_h and sometimes the hexagonal group D_{6h}. This results in a splitting of the degenerate ground state into CEF multiplets. Due to efficient screening by the $5p^6 6s^2$ shell, the crystalline electric field acts only as a weak perturbation of the 4f electrons, and is much smaller than the intra-atomic interactions (fig. 2). Therefore it does not mix states that belong to different LSJ multiplets and can be restricted to the relevant ground state multiplet of table 1. Using the Wigner–Eckart theorem the CEF potential can then be replaced by an effective CEF Hamiltonian which acts within the $(2J+1)$-fold degenerate ground state multiplet. It is commonly written in terms of Stevens operator equivalents, Stevens (1952) and Hutchings (1964), which are lth-order polynomials in the total angular momentum operators J_x, J_y and J_z:

$$H_{\mathrm{CEF}} = \sum_{l,m} B_l^m O_l^m, \quad l \leq 6, |m| \leq l . \tag{1}$$

The B_l^m are the CEF parameters. For cubic symmetry one has

$$H_{\mathrm{CEF}} = B_4^0(O_4^0 + 5O_4^4) + B_6^0(O_6^0 - 21O_6^4) . \tag{2}$$

This CEF Hamiltonian is determined by cubic symmetry alone. The physical problem is the determination of the CEF parameters B_4^0 and B_6^0. Ab initio calculations for these parameters have had only very limited success, even in

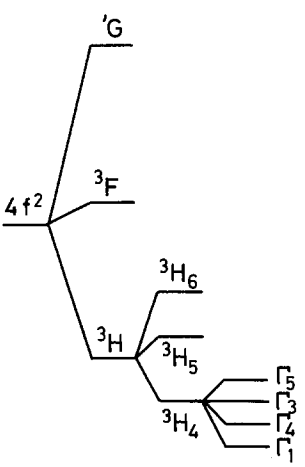

Fig. 2. Energy splittings for Pr^{3+} in octahedral symmetry. Typical magnitudes of overall splittings are also given.

TABLE 1
Ground state properties of R ions.

Ion	No. of 4f electrons	$\langle r^2 \rangle$ 4f (Å^2)	α_J ($\times 10^2$)	Ground state $^{2S+1}L_J$	g_J	Cubic CEF states
Ce^{3+}	1	0.3666	−5.71	$^2F_{5/2}$	6/7	$\Gamma_7 + \Gamma_8$
Pr^{3+}	2	0.3350	−2.10	$^3H_4$	4/5	$\Gamma_1 + \Gamma_3 + \Gamma_4 + \Gamma_5$
Nd^{3+}	3	0.3120	−0.643	$^4I_{9/2}$	8/11	$\Gamma_6 + 2\Gamma_8$
(Pm^{3+})	4	0.2899	0.771	$^5I_4$	3/5	$\Gamma_1 + \Gamma_3 + \Gamma_4 + \Gamma_5$
Sm^{3+}	5	0.2728	4.13	$^6H_{5/2}$	2/7	$\Gamma_7 + \Gamma_8$
En^{3+}	6	0.2569	0	$^7F_0$	0	Γ_1
Gd^{3+}	7	0.2428	0	$^8S_{7/2}$	2	$\Gamma_6 + \Gamma_7 + \Gamma_8$
Tb^{3+}	8	0.2302	−1.01	$^7F_6$	3/2	$\Gamma_1 + \Gamma_2 + \Gamma_3 + \Gamma_4 + 2\Gamma_5$
Dy^{3+}	9	0.2188	−0.635	$^6H_{15/2}$	4/3	$\Gamma_6 + \Gamma_7 + 3\Gamma_8$
Ho^{3+}	10	0.2085	−0.272	$^5I_8$	5/4	$\Gamma_1 + 2\Gamma_3 + 2\Gamma_4 + 2\Gamma_5$
Er^{3+}	11	0.1991	0.254	$^4I_{15/2}$	6/5	$\Gamma_6 + \Gamma_7 + 3\Gamma_8$
Tm^{3+}	12	0.1905	1.01	$^3H_6$	7/6	$\Gamma_1 + \Gamma_2 + \Gamma_3 + \Gamma_4 + 2\Gamma_5$
Yb^{3+}, Tm^{2+}	13	0.1826	3.17	$^2F_{7/2}$	8/7	$\Gamma_6 + \Gamma_7 + \Gamma_8$

insulators [for a review see Newman (1971)]. The simplest way to calculate B_4^0 and B_6^0 is given by the point-charge model which leads to $B_l^0 \sim q^* \langle r^l \rangle$ where q^* is the effective (screened) neighbour ion charge and $\langle r^l \rangle$ the lth moment of the radial 4f wavefunction. In the semimetallic R pnictides the radial moments correlate well with the experimentally determined B_4^0 CEF parameters throughout the R series, Birgeneau et al. (1971). A similar trend was found for the RAl_2 series and dilute R alloys with $LaAl_2$, YAl_2 and $ScAl_2$ (Frick and Loewenhaupt 1985). However, the absolute magnitude and sometimes even the sign of the CEF parameters is not predicted correctly by the point-charge model. Therefore B_4^0 and B_6^0, which depend only on J, are taken as empirical parameters to be determined by inelastic neutron scattering, Fulde and Loewenhaupt (1986). The possible types of cubic multiplets for any given ground state J are listed in table 1. Figure 2 shows a particular CEF sequence for $Pr^{3+}(J=4)$. The energies of the CEF multiplets Γ_α for any J can be obtained from the LLW tables (Lea et al. 1962). The CEF states $|\Gamma_\alpha^r\rangle$ of a multiplet $\alpha(r$ is the degeneracy index) form a representation of the (cubic) point group. For Kramers (J half-integer) and non-Kramers (J integer) ions in a cubic CEF one has the following representations (table 1):

$$\begin{aligned} &\text{non-Kramers, } \Gamma_1(1), \Gamma_2(1), \Gamma_3(2), \Gamma_4(3), \Gamma_5(3)\,; \\ &\quad \text{Kramers, } \Gamma_6(2), \Gamma_7(2), \Gamma_8(4)\,. \end{aligned} \tag{3}$$

The degeneracies are given in parentheses. Multiplets of Kramers ions are at least twofold degenerate. Each CEF state can be given as a linear combination of free-ion $|J, M\rangle$ states. For Ce^{3+} $(J = \frac{5}{2})$ one has for the Kramers doublet and quartet (cubic point group),

$$\begin{aligned} |\Gamma_7\rangle &= a|\pm\tfrac{5}{2}\rangle - b|\mp\tfrac{3}{2}\rangle\,, \\ |\Gamma_8\rangle &= \begin{cases} |\pm\frac{1}{2}\rangle & a = \sqrt{\frac{1}{6}} \\ b|\pm\frac{5}{2}\rangle + a|\mp\frac{3}{2}\rangle, & b = \sqrt{\frac{5}{6}} \end{cases}. \end{aligned} \tag{4}$$

For $J = \frac{5}{2}$, only the fourth-order term in H_{CEF} is present and the splitting energy is directly given by $\Delta = 360 B_4^0$. The sign of $B_4^0(\pm)$ determines the ground state $\Gamma_7(+)$ or $\Gamma_8(-)$. For larger J, the sixth-order term in the H_{CEF} is important and one has to consult the LLW tables. Similar tables for lower than cubic symmetry have been given by Walter (1984). The real-space 4f-charge densities corresponding to the cubic Γ_7 and Γ_8 states are shown in fig. 3 for illustration. Simple thermodynamic manifestations of CEF states, e.g., the Schottky anomaly in the specific heat will be discussed in sections 2.4 and 2.5.

2.2. *Magnetoelastic and interionic coupling of 4f ions*

Distortions of the local environment of 4f ions change the crystal-field potential and therefore the energies of the CEF states. This change is called the "magnetoelastic coupling energy". The distortions may be homogeneous if generated by external stresses or inhomogeneous if generated by sound waves or phonons. For

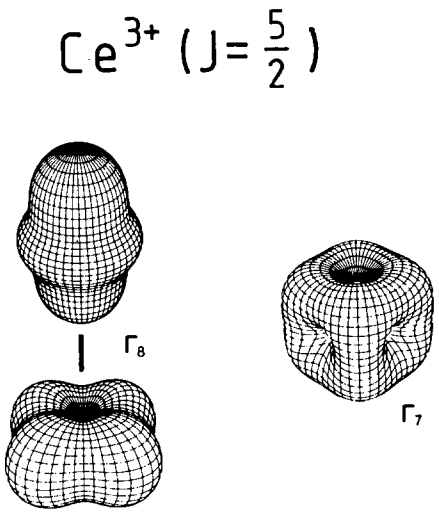

Fig. 3. Contours of equal 4f charge densities for a Ce^{3+} ion in the cubic Γ_7 and Γ_8 states. (After Walter 1985.)

small distortions the coupling can be obtained by expanding the CEF potential in terms of local strain coordinates. In this way one obtains microscopic expressions for the coupling constants (Dohm and Fulde 1975, Morin and Schmitt 1981a). Alternatively one may classify the possible contributions according to their symmetry character and treat the corresponding coupling strengths as phenomenological parameters to be determined from experiment, e.g., the temperature dependence of the elastic constants. In many cases, especially for the Pr and Tm intermetallics it is necessary to include the interionic quadrupolar coupling of 4f ions to obtain quantitative agreement. This coupling is also essential for the description of the cooperative Jahn–Teller effect and for quadrupolar phase transitions. In intermetallic R compounds it is predominantly caused by a strong aspherical Coulomb interaction of conduction electrons with 4f shells.

2.2.1. *The magnetoelastic interaction*

In the continuum limit the local deformation of a crystal can be described by the gradient of the displacement field $\boldsymbol{u}(i, t) = \tilde{\boldsymbol{R}}_i(t) - \boldsymbol{R}_i$ where $\tilde{\boldsymbol{R}}_i$ and $\boldsymbol{R}_i$ are the temporary and equilibrium lattice positions, respectively. The gradient tensor is given by $V_{kl}(i) = \partial u_k(i)/\partial R_i^l$ with $k, l = x, y, z$. The general deformation can be described as a pure strain deformation η followed by a rotation $\boldsymbol{D}$

$$(\boldsymbol{I} + \boldsymbol{V}) = \boldsymbol{D}(\boldsymbol{I} + 2\boldsymbol{\eta})^{1/2} . \tag{5}$$

For small deformations, when second-order terms in V_{kl} "finite-strain effects" can be neglected, $\boldsymbol{\eta}$ and $\boldsymbol{D}$ are simply given by the symmetric and antisymmetric parts of

$$\begin{aligned} &\boldsymbol{V}\colon \eta_{kl} = \varepsilon_{kl},\ D_{kl} = \delta_{kl} + \omega_{kl}, \text{ with} \\ &\varepsilon_{kl} = \tfrac{1}{2}(V_{kl} + V_{lk}), \qquad \omega_{kl} = -\omega_{lk} = \tfrac{1}{2}(V_{kl} - V_{lk}) . \\ &\text{(strain tensor)} \qquad\qquad \text{(rotational tensor)} \end{aligned} \tag{6}$$

Contributions to the magnetoelastic interaction that contain the rotational tensor are important only in an external magnetic field. This will be considered separately in sect. 2.6. For the moment we consider only pure strain contributions. In cubic crystals the components of $\boldsymbol{\varepsilon}$ can be grouped to form irreducible representations ε_Γ of the cubic point group (Thalmeier and Fulde 1975, du Tremolet de Lacheisserie et al. 1978):

$$\begin{aligned}
&\Gamma_1\colon \varepsilon_{\Gamma_1} \equiv \varepsilon_v = (\varepsilon_{xx} + \varepsilon_{yy} + \varepsilon_{zz}) \\
&\Gamma_3\colon \varepsilon_{\Gamma_3} = (\varepsilon_2, \varepsilon_3) = ((\varepsilon_{xx} - \varepsilon_{yy})/\sqrt{2}, (2\varepsilon_{zz} - \varepsilon_{xx} - \varepsilon_{yy})/\sqrt{6}) \\
&\Gamma_5\colon \varepsilon_{\Gamma_5} = (\varepsilon_{yz}, \varepsilon_{zx}, \varepsilon_{xy})\,. \qquad (7)
\end{aligned}$$

The three components of the rotational tensor $\boldsymbol{\omega}$ form a Γ_4 representation. A Γ_2 representation is possible only in higher than linear order. These symmetry strains are shown in fig. 4. $\varepsilon_{\Gamma_1} = \varepsilon_v$ corresponds to the fully symmetric volume strain. Deformations of the local environment lead to deformations of the 4f-charge cloud, microscopically one therefore has a coupling of strains to multipolar operators O_Γ^l of the 4f shell. These are polynomials in J_x, J_y and J_z of degree $l = 2$, 4 and 6 which again transform as irreducible point-group representations. In the cubic case the quadrupolar ($l = 2$) operators are:

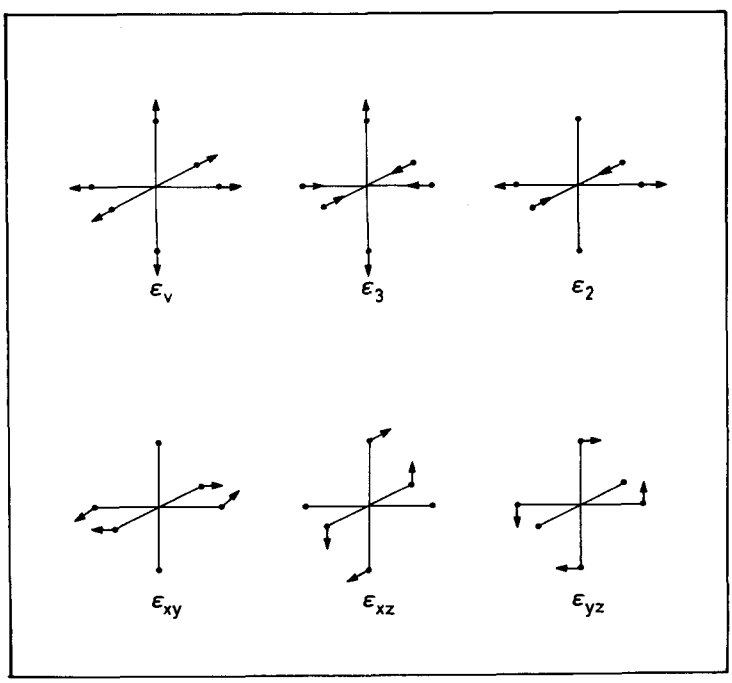

Fig. 4. Symmetry strains for cubic symmetry.

$$\Gamma_3\colon O_{\Gamma_3} = (O_2, O_3) = ((J_x^2 - J_y^2)/\sqrt{2}, (2J_z^2 - J_x^2 - J_y^2)/\sqrt{6})\,;$$

$$\Gamma_5\colon O_{\Gamma_5} = (O_{yz}, O_{xz}, O_{xy}) = (J_yJ_z + J_zJ_y, J_xJ_z + J_zJ_x, J_xJ_y + J_yJ_x)\,. \tag{8}$$

All other representations require higher multipolar ($l = 4, 6$) operators. The O_Γ^l are not to be confused with the individual O_l^m operators in the CEF potential [eq. (1)]. The latter are in general *not* cubic representations. However, the O_Γ^l can be expressed as linear combinations of the O_l^m. The magnetoelastic Hamiltonian has to be invariant under the relevant point group. To first order in the local strains this leads to (Callen and Callen 1963)

$$H_{\mathrm{me}} = -\sum_i \sum_{\Gamma_i l} g_\Gamma^l \varepsilon_\Gamma(i) O_\Gamma^l(i)\,. \tag{9}$$

This shorthand notation implies that the summation runs over $\Gamma = (\alpha, r)$ where α is the type of representation and r is the degeneracy index ($1 \leq r \leq d_\alpha$, d_α = dimension of Γ_α). The magnetoelastic coupling constants g_Γ^l cannot depend on r if H_{me} is to be invariant. In most cases it is sufficient to include only quadrupolar terms ($l = 2$) in $\mathrm{H_{me}}$, therefore the l-index will be suppressed in what follows. There are, however, exceptions where higher-order ($l = 4$) contributions are essential. These will be discussed in sect. 2.4.2. The restriction to quadrupolar contributions is suggested by a simple point-charge calculation of $g_\Gamma^{(2)} = g_\Gamma$ (Mullen et al. 1974, Morin and Schmitt 1981a, b). One obtains for cubic structures:

$$g_\Gamma = \sigma_\Gamma \alpha_J \langle r^2 \rangle Ze^2/a^3\,. \tag{10}$$

The numerical factor σ_Γ depends only on the crystal structure and on the type of strain, e.g., $\sigma_{\Gamma_3} = 9/\sqrt{6}$, $\sigma_{\Gamma_5} = \frac{3}{2}$ for NaCl-type crystals. For $\alpha_J\langle r^2\rangle$ see table 1; Z is the effective neighbour charge and a the cubic lattice constant. For the higher multipolar couplings one obtains $g_\Gamma^{(4)} \approx \beta_J\langle r^4\rangle$ and $g_\Gamma^{(6)} \sim \gamma_J\langle r^6\rangle$. The α_J, β_J and γ_J can be found in Hutchings (1964) and the $\langle r^n\rangle$ in Freeman and Desclaux (1979). They decrease with increasing order of l which suggests the restriction to quadrupolar coupling. In addition to the linear strain coupling of H_{me}, quadratic contributions may be important. They will be discussed in sect. 2.6.

The displacement field $\boldsymbol{u}(\boldsymbol{R}_i)$ and its corresponding inhomogeneous strain field $\varepsilon_{kl}(i)$ can be expanded in phonon coordinates. One has

$$\varepsilon_{kl}(i) = -\mathrm{i}\sum_{q,\lambda} \frac{q_k e_l(q\lambda)}{(2M_c N_s \omega_{q\lambda})^{1/2}}\, \varphi_{q\lambda} \exp(\mathrm{i}\boldsymbol{q}\cdot\boldsymbol{R}_i)\,, \tag{11}$$

where $\boldsymbol{e}(\boldsymbol{q}\lambda)$ is the polarization vector of acoustic mode λ, ω_{ql} is the phonon frequency, M_c is the unit cell mass and $\varphi_{q\lambda} = a_{q\lambda} + a_{q\lambda}^\dagger$ are phonon operators. Inserting this into eq. (9) and retaining only quadrupolar terms one obtains the magnetoelastic Hamiltonian

$$H_{\mathrm{me}} = -\sum_\Gamma \sum_{q\lambda} g_\Gamma Q_\Gamma(q\lambda) O_\Gamma(-q) \varphi_{q\lambda}\,,$$

$$O_\Gamma(q) = N^{-1/2} \sum_i O_\Gamma(i) \exp(\mathrm{i}\boldsymbol{q}\cdot\boldsymbol{R}_i)\,. \tag{12}$$

The Fourier amplitudes $Q_\Gamma(\boldsymbol{q}\lambda) = -\mathrm{i}|\boldsymbol{q}|(2NM_c\omega_{\boldsymbol{q}\lambda})^{-1/2}\,\hat{Q}_\Gamma(\boldsymbol{q}\lambda)$ can be obtained from eq. (7), with $\hat{\boldsymbol{q}} = \boldsymbol{q}/|\boldsymbol{q}|$:

$$\hat{Q}_{\Gamma_3} = ((\hat{q}_x e_x - \hat{q}_y e_y)/\sqrt{2}, (2\hat{q}_z e_z - \hat{q}_x e_x - \hat{q}_y e_y)/\sqrt{6}) \tag{13}$$

$$\hat{Q}_{\Gamma_5} = (\tfrac{1}{2}(\hat{q}_y e_z + \hat{q}_z e_y), \quad \text{cyclic}) .$$

The $e_x = e_x(\boldsymbol{q}\lambda)$ etc. are components of the polarization vector. The effective coupling strength of the mode $\boldsymbol{q}\lambda$ to O_Γ is then given by $\xi_\Gamma(\boldsymbol{q}\lambda) = g_\Gamma Q_\Gamma(\boldsymbol{q}\lambda)$. According to its derivation via local strains this is only valid for long-wavelength acoustic phonons ($qa \ll 1$) for which $\xi_\Gamma \sim |\boldsymbol{q}|$. For larger $|\boldsymbol{q}|$ and also if λ corresponds to an optic mode, $\xi_\Gamma(\boldsymbol{q}\lambda)$ can no longer be written as a product $g_\Gamma Q_\Gamma$. However, the form of eq. (12) is valid for any mode and with $\xi_\Gamma(\boldsymbol{q}\lambda)$ replacing $g_\Gamma Q_\Gamma$ and summing over acoustic and optic branches it represents the most general form of linear phonon coupling to 4f states. Therefore we do not introduce a new name but generally call it "magnetoelastic coupling".

If the crystal is strained homogeneously by external stresses or by undergoing a cooperative Jahn–Teller transition, the total strain $\varepsilon_\Gamma(i) = \varepsilon_\Gamma + \hat{\varepsilon}_\Gamma(i)$ is the sum of homogeneous (ε_Γ) and inhomogeneous ($\hat{\varepsilon}_\Gamma$) local strains produced by phonons. Accordingly one has

$$H_{\mathrm{me}} = -\sum_{\Gamma,i} g_\Gamma \varepsilon_\Gamma O_\Gamma(i) - \sum_{\Gamma,\boldsymbol{q}\lambda} \xi_\Gamma(\boldsymbol{q}\lambda) O_\Gamma(-\boldsymbol{q}) \varphi_{\boldsymbol{q}\lambda} . \tag{14}$$

This separation is necessary if phonon coordinates are defined with periodic boundary conditions (Born and Huang 1954, Kanamori 1960 and Elliott et al. 1972).

2.2.2. *Effective quadrupolar interionic interactions*

It is well known that an on-site exchange interaction of conduction electrons and 4f electrons leads to an effective RKKY interaction between 4f moments on different sites (Kasuya 1966). In the heavy R metals this interaction is responsible for a variety of magnetically ordered phases and spin-wave excitations. For an extensive treatment, see Coqblin (1977). In the lighter R metals and in many R intermetallics where the CEF energies are comparable to the interionic exchange energies, e.g., in Pr or PrSb [reviewed by Jensen (1982)] the RKKY mechanism leads to the existence of 'magnetic exciton' bands as seen in inelastic neutron scattering.

In addition to the isotropic exchange interaction there are many more types of interaction between conduction electrons and electrons in the 4f shell, which are due to the finite spatial extent of the latter. The corresponding scattering operators transform as tensors in spin space and real space, and therefore can be classified according to their orbital rank $0 \leq \Lambda \leq 6$ (for f electrons; $l = 3$) and spin rank $\Sigma = 0, 1$ (Hirst 1978). Aside from the isotropic exchange scattering where $(\Lambda, \Sigma) = (0, 1)$ one has identified aspherical Coulomb scattering with $(\Lambda, \Sigma) = (2, 0)$ to be of major importance in R intermetallics. This was concluded from magnetotransport anisotropies in dilute R intermetallics, Fert et al. (1977). (See

discussions in sect. 2.4.3) Such a mechanism is due to the quadrupolar moment of the 4f charge distribution. The theory of quadrupolar and higher multipolar sf interactions has been extensively discussed by Teitelbaum and Levy (1976). The aspherical Coulomb scattering in cubic systems is given by

$$H_{\rm ac} = \sum_{\Gamma,i} \sum_{\boldsymbol{k},\boldsymbol{q},\sigma} I_\Gamma(\boldsymbol{q}) O_\Gamma(i) c^\dagger_{\boldsymbol{k}\sigma} c_{\boldsymbol{k}+\boldsymbol{q}\sigma} \exp(\mathrm{i}\boldsymbol{q}\cdot\boldsymbol{R}_i)\,, \tag{15}$$

with

$$I_\Gamma(\boldsymbol{q}) = \frac{(4\pi)^{3/2}}{V} e^2 C_\Gamma q^{-2} F_2(q) K_\Gamma(\hat{\boldsymbol{q}})$$

giving the scattering strength. A summation over the components of the cubic representations Γ is implied. Quadrupolar operators O_Γ are given in eq. (8). The $c^\dagger_{\boldsymbol{k}\sigma}$ create free conduction electrons. Here C_Γ is a constant, $K_\Gamma(\hat{\boldsymbol{q}})$ is a cubic harmonic and $F_2(q) = \langle j_2(qr)\rangle_{4\rm f}$ is the radial average of a Bessel function. In close analogy to the RKKY mechanism, $H_{\rm ac}$ leads to an effective interionic quadrupolar interaction in second-order perturbation theory. It has the form

$$H_{\rm Q} = -\tfrac{1}{2} \sum_{ij} K_\Gamma(i,j) O_\Gamma(i) O_\Gamma(j)\,, \tag{16}$$

where a scalar product of the O_Γ operators is implied. The interaction parameters $K_\Gamma(i, j)$ are given by

$$K_\Gamma(i,j) = \frac{1}{N_s} \sum \hat{K}_\Gamma(\boldsymbol{q}) \exp[\mathrm{i}\boldsymbol{q}\cdot(\boldsymbol{R}_j - \boldsymbol{R}_i)]\,, \qquad \hat{K}_\Gamma(\boldsymbol{q}) = K_\Gamma(\boldsymbol{q}) - \bar{K}_\Gamma\,, \tag{17}$$

where the "self-energy" term $\bar{K}_\Gamma = N_s^{-1} \Sigma_{\boldsymbol{q}} K_\Gamma(\boldsymbol{q})$ has been subtracted because it only leads to a contribution of the order of $O^2_\Gamma(i)$, which can be absorbed in the CEF potential. Consequently, we have $K_\Gamma(i, i) = 0$. The Fourier components $K_\Gamma(\boldsymbol{q})$ are obtained from second-order perturbation theory in $H_{\rm ac}$:

$$K_\Gamma(\boldsymbol{q}) = \sum_{\boldsymbol{k}} |I^{nn'}_\Gamma(\boldsymbol{k}, \boldsymbol{k}+\boldsymbol{q})|^2 \frac{f_{kn}(1 - f_{k+qn'})}{E_{k+qn'} - E_{kn}}\,. \tag{18}$$

Here the interaction has been generalized to include band (n, n') effects for conduction electrons. An ab-initio calculation of the tetragonal $K_{\Gamma_3}(\boldsymbol{q})$ and trigonal $K_{\Gamma_5}(\boldsymbol{q})$ Fourier transform for DyZn was performed by Schmitt and Levy (1984) starting from APW calculations for the conduction electron bands. The result is shown in fig. 5. Note that the maxima for the $K_\Gamma(\boldsymbol{q})$ occur at the zone boundary points of the simple cubic Brillouin zone, that is the interaction is of 'antiferroquadrupolar' type. If it is strong enough it may lead to an AFQ phase transition as is the case in CeB_6 or $TmGa_3$. In TmZn and TmCd $K_{\Gamma_3}(\boldsymbol{q})$ has its maximum at the zone center $\boldsymbol{q} = 0$, these compounds therefore show a ferroquadrupolar ordering. Unfortunately the quadrupolar $K_\Gamma(\boldsymbol{q})$ cannot be obtained easily from inelastic neutron scattering in the same way as the exchange Fourier transform is obtained from spin-wave or magnetic exciton dispersion. For a discussion of this point see Levy and Trammell (1977). The effective interaction

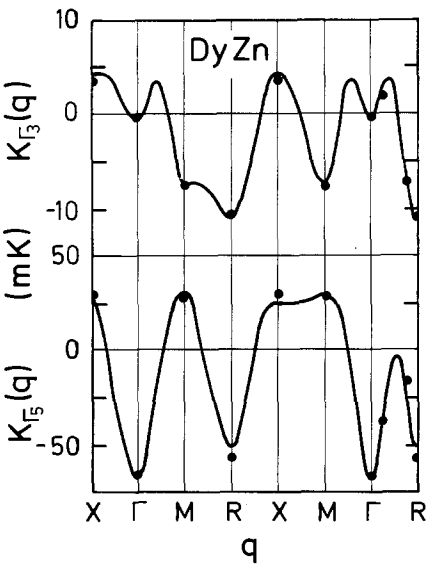

Fig. 5. Fourier transforms, $K_{\Gamma_5}(\boldsymbol{q})$ and $K_{\Gamma_3}(\boldsymbol{q})$, of the trigonal and tetragonal quadrupolar interactions in cubic DyZn. Points are calculated. Full curves are least square fits with a Fourier series (Schmitt and Levy 1984).

as a function of the R ion separation $|\boldsymbol{R}_i - \boldsymbol{R}_j|$ displays the same type of oscillatory behavior as the RKKY interaction and decays as $|\boldsymbol{R}_i - \boldsymbol{R}_j|^{-3}$ for large distances (Teitelbaum and Levy 1976).

In the context of elastic properties the essential quantities are the "quadrupolar coupling constant" $g'_\Gamma = \hat{K}_\Gamma(\boldsymbol{q}=0)$ and possibly $\hat{K}_\Gamma(\boldsymbol{q}_0)$ with $\boldsymbol{q}_0$ the zone boundary wavevector. The g'_Γ are important in explaining the temperature dependence of elastic constants and the ordering temperatures T_Q for ferroquadrupolar phase transitions. Likewise the $\hat{K}_\Gamma(\boldsymbol{q}_0)$ determine T_Q for antiferroquadrupolar ordering (see sect. 2.4).

Finally, it should be noted that the phonon part in eq. (14) also leads to an effective quadrupolar interaction between 4f ions if the phonon coordinates are eliminated in second-order perturbation theory. This 'virtual phonon exchange' mechanism is important in insulators, see Orbach and Tachiki (1967). In R intermetallics such as TmZn and TmCd, however, the electronic origin of effective interactions is now established, Levy et al. (1979).

2.3. *Elastic constants and sound velocities: theory*

We first want to recall some basic facts of the theory of elasticity. In the harmonic approximation the lattice energy of a crystal has contributions due to homogeneous strains and to harmonic phonons:

$$H_L = H_{el} + H_{ph} = \tfrac{1}{2}\sum_\Gamma c^0_\Gamma \varepsilon^2_\Gamma + \tfrac{1}{2}\sum_{q\lambda} \omega_{q\lambda}(a^\dagger_{q\lambda}a_{q\lambda} + \tfrac{1}{2})\,. \tag{19}$$

Here c^0_Γ are the symmetry elastic constants. They can be expressed in terms of the contracted elastic constants c^0_{ij} that correspond to the Cartesian strain components

ε_{kl} and read for cubic symmetry

$$c^0_{\Gamma_1} = c^0_B d = \tfrac{1}{3}(c^0_{11} + 2c^0_{12}), \qquad c^0_{\Gamma_3} = \tfrac{1}{2}(c^0_{11} - c^0_{12}), \qquad c^0_{\Gamma_5} = c^0_{44}. \tag{20}$$

For a non-Bravais lattice (e.g., diamond structure) H_L may also have contributions due to product terms of homogeneous strains and optic phonon coordinates (sect. 2.4.1).

2.3.1. *Anharmonic interactions*

In a perfectly harmonic crystal the elastic constants would be strictly independent of temperature. However, due to the existence of third- and fourth-order anharmonic terms in the crystal potential there is a coupling between the homogeneous strains and the phonon coordinates. This will lead to a background temperature dependence of the elastic constants. It can be described within a quasiharmonic approximation (Ludwig 1967), in which the anharmonic contributions to the crystal potential are implicitly included by assuming a strain dependence $\omega_{q\lambda}(\varepsilon_{kl})$ of the phonon frequencies which can be characterized by the phonon Grüneisen parameters,

$$\gamma_{kl} = -\frac{\partial \ln \overline{\omega^2}}{\partial \varepsilon_{kl}}, \qquad \Gamma_{klk'l'} = -\frac{\partial^2 \ln \overline{\omega^2}}{\partial \varepsilon_{kl}\, \partial \varepsilon_{k'l'}}, \tag{21}$$

where $\overline{\omega^2}$ is the average squared phonon frequency. This leads to a strain- and temperature-dependent quasiharmonic free energy ($F_0 = H_{el}$),

$$F_a(\varepsilon_{kl}, T) = F^0 + kT \sum_{q\lambda} \ln[2 \sinh(\beta \hbar \omega_{q\lambda}/2)]. \tag{22}$$

The isothermal elastic constants are given by

$$c^a_{ij} = c^a_{(kl)(k'l')} = \frac{1}{V}\left(\frac{\partial^2 F_a}{\partial \varepsilon_{kl}\, \partial \varepsilon_{k'l'}}\right)_T, \tag{23}$$

where V is volume and the contraction rules $(kl) \to i$, $(11) \to 1$, $(22) \to (2)$, $(33) \to 3$, $(23) \to 4$, $(13) \to 5$ and $(12) \to 6$ have been implied. From eqs. (22, 23) one derives

$$c^a_{ij}(T) = c^0_{ij} - \frac{1}{2V}\Gamma_{klk'l'} U(T) + \frac{1}{4V}\gamma_{kl}\gamma_{k'l'}[U(T) - TC_V(T)] \tag{24}$$

$$C_V = \left(\frac{\partial U}{\partial T}\right)_V, \qquad U(T) = \int \mathrm{d}\omega\, D(\omega) \hbar \omega [n(\omega) + \tfrac{1}{2}].$$

Here U and C_V are the lattice internal energy and the specific heat respectively, $D(\omega)$ is the phonon density of states (DOS) and

$$n(\omega) = (1 - e^{\beta \hbar \omega})^{-1}$$

is the phonon occupation. In general, $c^a_{ij}(T)$ shows a monotonic decrease with increasing temperature starting at $c^a_{ij}(0)$. The latter is not equal to c^0_{ij} in eq. (24) due to strain interaction with the zero-point motion, i.e., because of $U(0) > 0$.

For the high- and low-T behaviour of $\Delta c_{ij}^{a}(T) = c_{ij}^{a}(0) - c_{ij}^{a}(T)$ we obtain with eq. (24)

$$\Delta c_{ij}^{a}(T) \sim T^4, \quad T \ll \theta_D$$
$$\Delta c_{ij}^{a}(T) \sim T, \quad T \gg \theta_D \,, \tag{25}$$

where θ_D is the Debye temperature. In the discussion of magnetoelastic or other anomalies in the $c_{ij}(T)$ of R compounds this anharmonic background T-dependence must always be subtracted. This is done in practice by measuring elastic constants in the isostructural La compounds and correcting for the mass difference of the corresponding R compound. An example of the anharmonic T-dependence in $LaAl_2$, Schiltz and Smith (1974), is given in fig. 6.

The elastic constants determine the acoustic phonon dispersion for long wavelengths according to the equations of motion in the continuum limit:

$$\rho \frac{\partial^2 u_k}{\partial t^2} = \frac{\partial \sigma_{lk}}{\partial R_l} \,, \tag{26}$$

where ρ is the mass density $\boldsymbol{R}$ is the position of the volume element and $\boldsymbol{\sigma}$ is the symmetric stress tensor given by Hooke's law

$$\sigma_{kl} = c_{klk'l'} \varepsilon_{k'l'} \,, \tag{27}$$

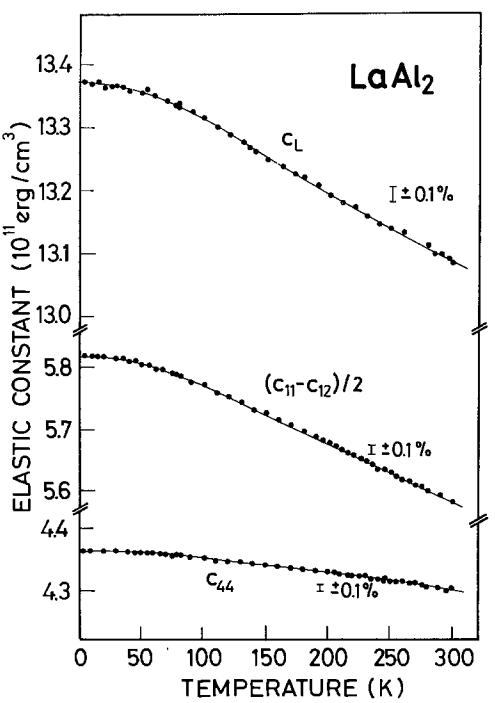

Fig. 6. Temperature dependence of elastic constants for $LaAl_2$ (Schiltz and Smith 1974).

This leads to sound modes with eigenfrequencies $\omega_{q\lambda}$ given by

$$(\rho\omega^2\delta_{kl} - c_{klk'l'}q_kq_l)e_l = 0\,, \tag{28}$$

where $\boldsymbol{e}(\boldsymbol{q})$ is the polarization vector. For symmetry directions like [100] and [110] in cubic systems some of the three solutions $\omega_{qs} = V_s(\hat{\boldsymbol{q}})|\boldsymbol{q}|$, where $s = 1, 2, 3$ is the polarization index and $\hat{\boldsymbol{q}} = \boldsymbol{q}/|\boldsymbol{q}|$ generate only one type of symmetry strain. The corresponding sound velocity is therefore given by only one symmetry elastic constant, e.g., for the transverse (T) modes we have for one Γ_5 c_{44} mode

$$\boldsymbol{k}\|[100]\,, \qquad \boldsymbol{e}\|[010], [001]\,, \qquad v_{\mathrm{T}} = (c_{44}/\rho)^{1/2}$$

for the Γ_3 $c_{11} - c_{12}$ mode,

$$\boldsymbol{k}\|[110]\,, \qquad \boldsymbol{e}\|[1\bar{1}0]\,, \qquad v_{\mathrm{T}} = [(c_{11} - c_{12})/\rho]^{1/2} \tag{29}$$

and for the other Γ_5 c_{44} mode

$$\boldsymbol{k}\|[110]\,, \qquad \boldsymbol{e}\|[001]\,, \qquad v_{\mathrm{T}} = (c_{44}/\rho)^{1/2}\,.$$

For longitudinal modes in cubic systems the velocities are $v = (c_{11}/\rho)^{1/2}$ for propagation along the [100] direction and $v_{\mathrm{L}} = [(c_{11} + c_{12} + 2c_{44})/2\rho]^{1/2}$ along the [110] direction. The bulk modulus c_{B} is given by $c_{\mathrm{B}} = \frac{1}{3}(c_{11} + 2c_{12})$.

2.3.2. *Theory of single-ion magnetoelastic effects*

In the following we review a simple thermodynamic calculation for the magnetoelastic contribution to the temperature dependence of the elastic constants in the single-ion approximation. We start from eq. (22) and include the free energy F of CEF-split 4f states. For the symmetry constants we obtain

$$c(T) = c_\Gamma^0(T) + \frac{1}{V}\left(\frac{\partial^2 F_{\mathrm{e}}}{\partial\varepsilon_\Gamma^2}\right)_T\,, \tag{30}$$

where we have now renamed $c_{ij}^{\mathrm{a}}(T) \to c_{ij}^0(T)$, i.e., the anharmonic effects are now already included in the "background" elastic constants. The electronic free energy of N_{s} non-interacting R ions

$$F_{\mathrm{e}}(T, \varepsilon_\Gamma) = -N_{\mathrm{s}}k_{\mathrm{B}}T \ln \sum_n \exp[-E_n(\varepsilon_\Gamma)/k_{\mathrm{B}}T] \tag{31}$$

depends on the strain via strain-dependent CEF levels $E_n(\varepsilon_\Gamma)$ [$n = (\alpha r)$ is a collective index for both multiplets and their degenerate states]. In second-order perturbation theory with respect to the Hamiltonian H_{me} of homogeneous strains one has [eqs. (9, 14)]

$$E_n(\varepsilon_\Gamma) = E_n - g_\Gamma\varepsilon_\Gamma\langle n|O_\Gamma|n\rangle + g_\Gamma^2\varepsilon_\Gamma^2 \sum_{n\neq m} \frac{|\langle n|O_\Gamma|m\rangle|^2}{E_n - E_m}\,. \tag{32}$$

It has been assumed that the states of a given multiplet are chosen such that O_Γ is already diagonal in this subspace. The E_n are unperturbed CEF energies.

According to eqs. (30, 31) one obtains, Lüthi (1976), ($\beta = 1/k_B T$)

$$c_\Gamma(T) = c_\Gamma^0(T) + \frac{N_s}{V}\left[\left\langle\frac{\partial^2 E}{\partial \varepsilon_\Gamma^2}\right\rangle - \beta\left\langle\left(\frac{\partial E}{\partial \varepsilon_\Gamma}\right)^2\right\rangle + \beta\left\langle\frac{\partial E}{\partial \varepsilon_\Gamma}\right\rangle^2\right]; \tag{33}$$

the terms in parentheses are called "Van Vleck" and "Curie" ($\sim 1/k_B T$) contributions respectively. They are thermal averages of the strain derivatives of eq. (32) according to the definition

$$\langle A\rangle = \sum_n p_n \langle n|A|n\rangle$$

$$p_n = Z_{CEF}^{-1}\exp(-\beta E_n), \qquad Z_{CEF} = \sum_n \exp(-\beta E_n). \tag{34}$$

The p_n are occupation probabilities for CEF levels and Z_{CEF} is their partition function. With eq. (32), eq. (33) finally yields

$$c_\Gamma(T) = c_\Gamma^0\left(1 - \frac{g_\Gamma^2}{c_\Gamma^0 v_c}\chi_\Gamma(T)\right), \tag{35}$$

where $v_c = V/N_s$ is the volume per R ion and the quadrupolar single-ion susceptibility χ_Γ is given by

$$\chi_\Gamma(T) = \sum_{n\neq m}\frac{p_n - p_m}{E_m - E_n}|\langle n|O_\Gamma|m\rangle|^2 + \frac{1}{k_B T}\sum_n p_n|\langle n|\hat{O}_\Gamma|n\rangle|^2, \tag{36}$$

with $\hat{O}_\Gamma = O_\Gamma - \langle O_\Gamma\rangle$. The first term, χ_Γ^{VV}, and second term, χ_Γ^C, are again Van-Vleck- and Curie-type contributions, respectively. They originate in the mixing of states belonging to different CEF multiplets (χ_{VV}) and in the splitting of multiplets by an applied external strain (χ_C). Equations (35, 36) are the fundamental expressions for discussing the T-dependent elastic constants in R compounds which have weak interionic interactions so that the single-ion approximation is correct. The R pnictides fit rather well into this picture (see sect. 2.4.1).

The T-dependences of χ_Γ and c_Γ are qualitatively different for CEF systems with (a) singlet or Kramers doublet ground states (Γ_1, Γ_6 and Γ_7 in cubic crystals) with $\langle\Gamma_\alpha|O_\Gamma|\Gamma_\alpha\rangle = 0$ and for those with (b) orbitally degenerate ground states (Γ_3, Γ_4, Γ_5, Γ_8) for which $\langle\Gamma_\alpha|O_\Gamma|\Gamma_\alpha\rangle \neq 0$. For $T \ll |E_m - E_n| \neq 0$

$$\chi_\Gamma(T) = \begin{cases}\chi_\Gamma^{VV}(0)\\ \chi_\Gamma^{VV}(0) + \dfrac{C(\Gamma,\Gamma_\alpha)}{k_B T},\end{cases} \tag{37}$$

where

$$C(\Gamma,\Gamma_\alpha) = \frac{1}{d_\alpha}\sum_{n\in\Gamma_\alpha}|\langle n|O_\Gamma|n\rangle|^2$$

and d_α is the ground state multiplet degeneracy, In case (a) the depression of $c_\Gamma(T)$ saturates at a finite value for $T\to 0$ determined by $\chi_\Gamma^{VV}(0)$. In case (b), however, $c_\Gamma(T)$ goes soft due to the presence of the Curie term $\chi_\Gamma(T)$ of eq. (37). This ultimately leads to a Jahn–Teller effect, i.e., a lattice distortion

accompanied by a lifting of the ground state degeneracy. However, to understand the cooperative nature of this effect the inclusion of effective quadrupolar interactions is necessary.

2.3.3. *Cooperative effects in the elastic constants and finite-frequency phenomena*

In many R compounds, especially the Tm intermetallics the elastic constants show strong deviations from the single-ion theory as expressed in eq. (35). This is due to the influence of strong quadrupolar interactions between R ions (sect. 2.2.2). If H_Q [eq. (16)] is treated in mean-field approximation, i.e.,

$$H_Q^{mf} = -\hat{K}_\Gamma(\boldsymbol{q}=0)\langle O_\Gamma\rangle \sum_i O_\Gamma(i)$$

it can be added to H_{me} as another single-ion term. The same procedure as at the end of sect. 2.3.2 then leads to an expression for $c_\Gamma(T)$ which contains the effects of quadrupolar interactions (Levy 1973). As shown in appendix A by a different method the basic equation which now determines the temperature dependence of elastic constants is

$$\left(\frac{v^2}{v_0^2}\right)_\Gamma = \frac{c_\Gamma}{c_\Gamma^0} = \frac{1-(\tilde{g}_\Gamma^2 + g_\Gamma')\chi_\Gamma(T)}{1-g_\Gamma'\chi_\Gamma(T)}\,, \tag{38}$$

where $\tilde{g}_\Gamma^2 = g_\Gamma^2/c_\Gamma^0 v_c$, $g_\Gamma' = \hat{K}_\Gamma(0)$ and $\chi_\Gamma(T)$ is the isothermal single-ion susceptibility of eq. (36). Furthermore $c_\Gamma = v_\Gamma^2\rho$ etc.

This equation has been used by many authors, e.g., Levy (1973), Moran et al. (1973), Lüthi et al. (1973a), Mullen et al. (1974) and others to explain the T-dependence of elastic constants for a large variety of R compounds which have non-negligible quadrupolar interactions (see sect. 4.3.). Such a formula was used before for transition-metal compounds and actinide compounds, Allen (1968), Kataoka and Kanamori (1972), Kino et al. (1973), Thomas (1977) and Kugel and Khomskii (1982). Note that $c_\Gamma(T)$ may go soft at a temperature T_c given by

$$1-(\tilde{g}_\Gamma^2 + g_\Gamma')\chi_\Gamma(T_c) = 0\,. \tag{39}$$

This will certainly happen if there is an orbitally degenerate CEF ground state because its corresponding Curie term in $\chi_\Gamma(T)$ diverges for low T and the numerator in eq. (38) will always vanish. Depending on whether the magnetoelastic coupling $\tilde{g}_\Gamma^2$ is larger or smaller than the quadrupolar coupling g_Γ' one talks about a "Jahn–Teller phase transition" or a "quadrupolar phase transition" at T_c, respectively, (Levy et al. 1979). In both cases the CEF ground state splits and the crystal distorts below T_c (sect. 2.4.3). According to the discussion given in appendix A the isothermal $c_\Gamma(T)$ of eq. (38) are measured in an ultrasonic experiment as long as $\omega \ll \tau_{nn}^{-1}$, the inverse relaxation time for population changes of CEF levels. In the vicinity and below a Jahn–Teller or quadrupolar transition, however, this relaxation no longer happens independently at each site but is determined by collective thermodynamic transport processes which are governed by conservation laws. They are characterized by much longer relaxation times

which determine how fast equilibrium is reached within and between thermodynamic subsystems, i.e., CEF excitations, conduction electrons and phonons. In this case one expects deviations from isothermal elastic constants already at much lower frequencies. Until now this has only been observed in insulators, namely $TbVO_4$ (Sandercock et al. 1972), but not for metallic R compounds. A phenomenological expression for the frequency dependent elastic constants was suggested in this reference and also discussed by Young (1975).

2.4. *Temperature dependence of elastic properties: a discussion of experimental results*

In this section we present experimental results on the temperature dependence of elastic constants for intermetallic rare-earth compounds in which magnetoelastic effects due to the presence of crystal fields are dominant. There are systematic studies of these effects for given structures across the rare-earth series. Examples are the rare-earth monopnictides, especially the rare-earth antimonides (RSb), the rare-earth dialuminides (RAl_2) and rare-earth compounds with the CsCl structure. From such experiments one obtains the single-ion magnetoelastic coupling constants g_Γ across the series and in a few cases the quadrupolar coupling constant g'_Γ [eq. (38)] too. The case of a cooperative Jahn–Teller effect will be treated separately in sect. 2.4.3. The examples presented here can be explained mostly with the single-ion strain susceptibility χ_Γ [eq. (35) instead of eq. (38)],

$$c_\Gamma = c_\Gamma^0(1 - \tilde{g}_\Gamma^2 \chi_\Gamma), \qquad \tilde{g}_\Gamma^2 = g_\Gamma^2 / v_c c_\Gamma^0 . \tag{35a}$$

Here Γ is the symmetry index, g_Γ the magnetoelastic coupling contant, v_c volume per R ion and χ_Γ the strain susceptibility per ion (see sect. 2.3.).

It should be emphasized again that c_Γ^0, the background elastic constant, is also temperature dependent due to the anharmonic phonon interaction as discussed in sect. 2.3. [eq. (25) and fig. 6]. For extracting the crystal-field effects and estimating $c_\Gamma^0(T)$ one takes the recourse to extrapolation procedures by linearly approximating $c_\Gamma^0(T)$ at higher temperatures and taking c_Γ^0 to be approximately independent of temperature at low temperatures ($T < 20\,\mathrm{K}$). In the transition region the T^4 law holds; in some cases the corresponding La or Lu compounds give a good estimate of $c_\Gamma^0(T)$. For a typical behaviour of c_Γ^0 see fig. 6.

The rare-earth atoms in compounds contribute three ($5d^1 6s^2$) valence electrons per atom which hybridize into bands. Because the 5d-like bands are quite narrow their contribution to the elastic constants should also be considered. This will be done in sect. 3. It is sufficient to mention here that these deformation potential effects have little or no effect on $c_\Gamma^0(T)$ for the system discussed here, as simple density of states considerations will show (see sect. 3.2).

2.4.1. *Survey of elastic constant results: single-ion effects*

After the above remarks we shall now survey several classes of rare-earth compounds.

2.4.1.1. *Rare-earth antimonides RSb.* Among the rare-earth monopnictides the RSb system has been studied in greatest detail. For a discussion of physical properties of the pnictides see Hulliger (1979).

In the RSb manifest crystal-field effects have been observed. They were among the first compounds to be investigated (Lüthi et al. 1973b, Mullen et al. 1974). The RSb compounds are well characterized substances with rather small electrical conductivities (Hulliger 1979). The crystal-field splittings have been determined by inelastic neutron scattering spectroscopy (Birgeneau et al. 1973). Therefore, crystal-field effects in the elastic constants have been measured and interpreted quantitatively.

As a representative example we show the results for TmSb in fig. 7. Pronounced CEF effects are seen for both the $c_{11} - c_{12}$ and c_{44} modes. Tm^{3+} in TmSb has a singlet ground state followed by a Γ_5 triplet 25 K above. Magnetic measurements, (Cooper and Vogt 1970) and neutron scattering indicate negligible exchange between the Tm ions and no dispersion for the CEF levels, making TmSb an ideal compound for studying single-ion CEF and magnetoelastic effects (see sections 2.5 and 2.6). The results in fig. 7 show a shallow minimum for $c_{11} - c_{12}$ around 40 K and a pronounced minimum for c_{44} at 12 K.

These anomalies are typical for CEF effects on elastic constants and can be

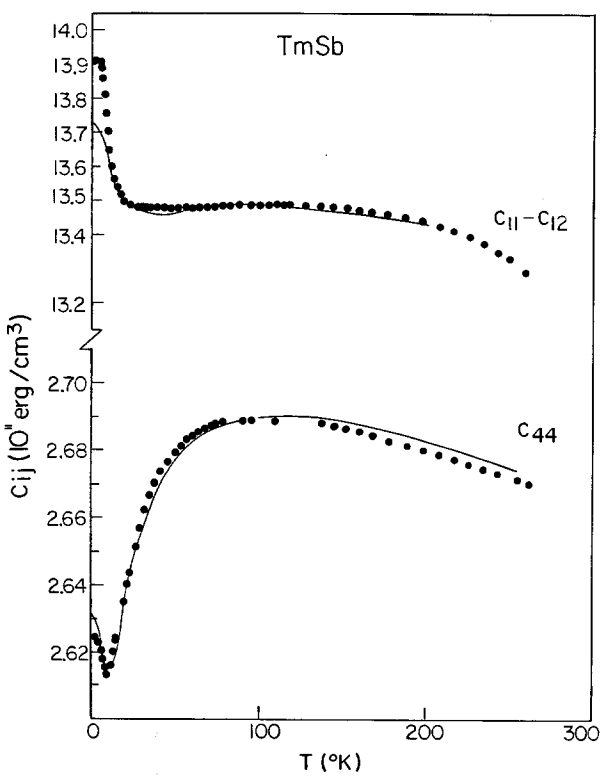

Fig. 7. Temperature dependence of elastic constants $c_{11} - c_{12}$ and c_{44} for TmSb. Full lines are calculations based on eqs. (35) and (36) (Mullen et al. (1974).

interpreted quantitatively using eqs. (33) and (35). For a temperature $T > 25$ K the Γ_5 triplet state is still populated and the Curie term in the strain susceptibility with its strong temperature dependence still contributes because the diagonal quadrupolar matrix elements $\langle \Gamma_5 | O_{\Gamma_3} | \Gamma_5 \rangle$ and $\langle \Gamma_5 | O_{\Gamma_5} | \Gamma_5 \rangle$ are different from zero. For $T < 25$ K Γ_5 is depopulated and the ground state Γ_1 can only contribute via Van Vleck terms [off-diagonal quadrupolar matrix elements, first term in eq. (36)]. A strain susceptibility fit using eq. (37) leads to a good agreement between experiment and calculations. Both minima are well reproduced. At the lowest temperatures there is a small quantitative discrepancy between theory and experiment, which is often observed. The origin may be due to impurities in these compounds. The strain susceptibility fits yield the magnetoelastic coupling constants $|g_{\Gamma_3}|$ and $|g_{\Gamma_5}|$.

In fig. 8 these coupling constants are plotted together with those from other compounds. Actually we plot g_{Γ_3}/α_J. The reason is that g_Γ is composed of two factors $g_\Gamma = \alpha_J \langle r^2 \rangle C_\Gamma$ where $\alpha_J \langle r^2 \rangle$ is characteristic for the R ion and C_Γ is due to its environment (see sect. 2.2.1). By dividing by α_J we obtain the influence from the crystalline environment on the R ion, which should not change much across the R series [see fig. 8 and Lüthi (1980b)]. In the RSb compounds no quadrupolar effects are observed. The elastic anomalies are of single-ion magnetoelastic origin, except for HoSb where one also observes critical effects above T_N (Mullen et al. 1974, Jensen et al. 1980). Some of the compounds SmSb, GdSb, TbSb, DySb, HoSb and ErSb have low-temperature magnetic phase transitions, in the case of an orbitally degenerate ground state (Tb^{3+}, Dy^{3+}, Ho^{3+}) they are also accompanied by a structural deformation of tetragonal or trigonal type at T_N, Lévy 1969, Stevens and Pytte 1973, Bucher et al. 1972). For SmSb (Sm^{3+}, $J = \frac{5}{2}$) the Γ_7–Γ_8 splitting of 65 K was determined from the CEF effects on $c_{11} - c_{12}$ and c_{44}, and from the specific heat results (Mullen et al. 1974). These elastic constant anomalies are typical for compounds with Sm^{3+} ions (SmSb) and Ce^{3+} ions

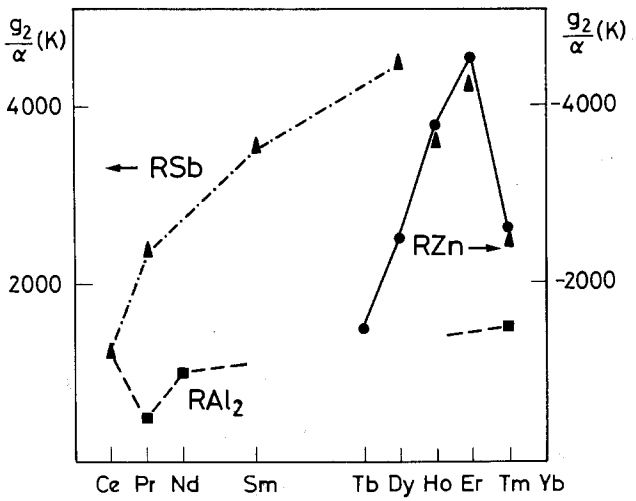

Fig. 8. Magnetoelastic coupling contant g_2/α_J corresponding to a tetragonal strain, for RSb, RZn and RAl_2 ($g_2 = g_{\Gamma_3}$).

($CeAl_2$, $CePb_3$) with a Γ_7 ground state. For CeSb, Goto et al. (1985) the relatively high T_N of 18 K and the strong short-range-order effects prevent the observation of similar anomalies. The plot of g_{Γ_3}/α_J in fig. 8 shows that g_{Γ_3} scales approximately with the Stevens factor α_J since g_{Γ_3}/α_J varies only within a factor of three across the RSb series. The disagreement between theory and experiment for c_{44} in PrSb will be discussed in sect. 2.4.2.

Other pnictides have been less thoroughly investigated. There is a short report on CeBi, Lüthi (1974), where a magnetic transition at 25 K hinders the observation of CEF effects on elastic constants, similar to the case of CeSb. The case of TbP should be mentioned because it is a thoroughly investigated singlet ground state system (Koetzler et al. 1979, Loidl et al. 1979). A strong softening of c_{44} down to the antiferromagnetic transition temperature $T_N = 7$ K leads to a coupling constant $\tilde{g}^2_{\Gamma_5} = 1$ mK (Bucher et al. 1976). Actually for TbP the quadrupolar coupling constant is dominant and it is in good agreement with that determined from magnetic measurements (Koetzler et al. 1979). A comparative magnetic study of various Tb pnictides has also been performed [TbP, TbAs, TbSb, TbBi, Koetzler and Raffius (1980)]. The beautiful analysis of quadrupolar against fluctuation-driven magnetic phase transition for TbP should be especially mentioned, Koetzler (1984).

2.4.1.2. *Rare-earth dialuminides RAl_2.* The magnetic properties of RAl_2 have been reviewed before, see Kirchmayer et al. (1980). The Laves R compounds also have interesting electron–phonon coupling effects. In particular, the RFe_2, notably amongst them $TbFe_2$ (Clark 1980), have giant magnetoelastic coupling constants. This is partly due to the Laves C-15 structure, which gives rise to an optical mode of even symmetry T_{2g} involving the two rare-earth ions per unit cell (Cullen and Clark 1977), i.e., a zone center optic mode has the same symmetry as the c_{44} strain.

In the RAl_2 series $CeAl_2$ is the most interesting case for the electron–phonon interaction (Lüthi and Lingner 1979, Thalmeier and Fulde 1982). At the other end of the series $YbAl_2$ is a typical mixed-valence compound with an anomalously low bulk modulus (Penney et al. 1982). $YbAl_2$ does not exhibit any CEF effects. It will be discussed in sect. 4.5. The elastic and magnetoelastic coupling constants g_{Γ_3}/α_J (Lingner and Lüthi 1983) are also plotted in fig. 8. Again as for the RSb, g_{Γ_3}/α_J varies little across the series.

The electron–phonon Hamiltonian used for the explanation of magnetoelastic effects, eq. (14), has to be generalized for RAl_2 because of the strain–optic-phonon coupling mentioned above. This leads to an additional mixed term in the lattice potential

$$H_L = c^0_\Gamma \varepsilon^2_\Gamma + E_\Gamma Q_\Gamma \varepsilon_\Gamma + \tfrac{1}{2}\omega_0^2 Q^2_\Gamma \,, \tag{40}$$

In our case $\Gamma = \Gamma_5$ and $Q = (2\omega_0)^{-1/2}\varphi^\Gamma$ is the $q = 0$ T_{2g} optical phonon coordinate and ω_0 its frequency. The magnetoelastic interaction is again [eq. (14)],

$$H_{me} = -\sum_i g_\Gamma \varepsilon_\Gamma O_\Gamma(i) - \sum_i A_\Gamma Q_\Gamma O_\Gamma(i) \,, \tag{41}$$

where $A_\Gamma = (2\omega_0)^{1/2}\xi_\Gamma$. If Q_Γ is treated as a classical variable it can be eliminated from the free energy $F(\varepsilon_\Gamma, Q_\Gamma)$ by minimization. Then one obtains [Lüthi et al. 1979, Lüthi and Lingner 1979, Schmidt (private communication)]

$$c_{44} = c_{44}^0 - E_\Gamma^2/\omega_0^2 - v_c^{-1}(g_\Gamma - A_\Gamma E_\Gamma/\omega_0^2)^2\chi_\Gamma \,. \tag{42}$$

If $E_\Gamma A_\Gamma < 0$ one has an enhanced coupling constant $g_\Gamma^{\text{eff}} = g_\Gamma + |A_\Gamma E_\Gamma|/\omega_0^2$. This enhancement may contribute to the large coupling constant $(\tilde{g}_{\Gamma_5}^{\text{eff}}) = 368$ mK found in $CeAl_2$ (see also sect. 2.7).

2.4.1.3. *CsCl-structure materials.* Perhaps the best studied materials, with respect to magnetoelastic and quadrupolar interactions, are the CsCl-structure materials (TmCd, TmZn etc.). The Grenoble group (Morin, Schmidt and collaborators), in particular, has done a variety of investigations on these simple cubic compounds. In addition to elastic constant measurements, as discussed before, they have applied other techniques to illustrate the electron–phonon coupling mechanisms:

(i) In the so-called parastriction method (Morin et al. 1980a), one measures the anisotropic strain in the presence of a magnetic field, induced by the magnetoelastic interaction. This is the well known magnetostriction in the paramagnetic region. By applying the magnetic field along symmetry directions and measuring the field-dependent strain parallel to the field ($\varepsilon_\parallel$) and perpendicular to the field ($\varepsilon_\perp$) one can eliminate any possible volume strain. Calculating the induced anisotropic strains for $\boldsymbol{B}$ parallel to [001] and [111] one obtains magnetoelastic and quadrupolar coupling constants for concentrated systems. Therefore, this method is equivalent and complementary to the measurement of the elastic constant. A typical example is shown in fig. 9.

(ii) Another method is the determination of the third-order magnetic susceptibility (Morin and Schmitt 1981b). Similar to the parastriction method, a magnetic field induces a quadrupole moment which affects the magnetic susceptibility in higher order. Plotting the induced magnetization M as M/B against B^2 yields the third-order susceptibility as the initial slope. From such measurements one obtains the total coupling constant $g_\Gamma' + \tilde{g}_\Gamma^2$. A typical example is shown in fig. 10.

It should be emphasized that the quantitative interpretation of all these methods relies on the molecular field approximation, ie., it neglects any fluctuation effects. The same remark holds for the treatment of the ordered phase, the phase diagram obtained using exchange and quadrupolar interactions (Koetzler et al. 1979, Morin and Schmitt 1983).

For our purpose of a survey, comparative investigations of different systems are especially valuable. For example, a variety of Tm compounds (TmZn, TmCd, TmCu, TmAg, TmMg) have been studied, see Giraud et al. (1985). Another series are the RCd compounds (Aléonard and Morin 1984) and the RZn compounds (Morin et al. 1977). Of these compounds two, TmCd and TmZn, are particularly interesting because they undergo a structural phase transition at a

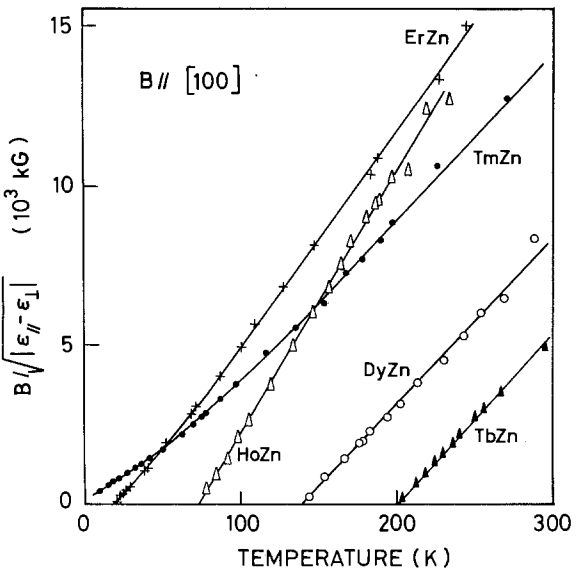

Fig. 9. Parastriction: temperature variation of $B/(\varepsilon_{\parallel} - \varepsilon_{\perp})^{1/2}$ for tetragonal strain in RZn. The full lines are calculated dependences (Morin et al. 1980a).

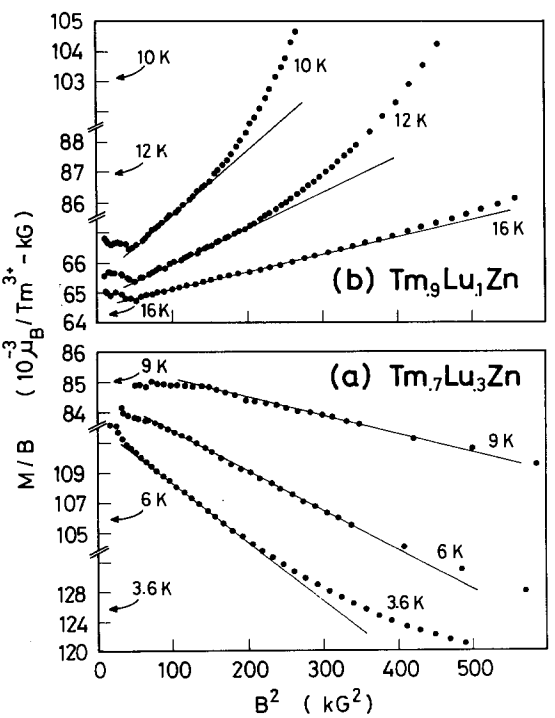

Fig. 10. Third-order susceptibility: M/B plotted against B^2 for $Tm_{0.7}Lu_{0.3}Zn$ and $Tm_{0.9}Lu_{0.1}Zn$ at different temperatures. The straight lines correspond to the linear parts of the curves (Morin and Schmitt 1979).

temperature T_Q higher than the magnetic phase transition. This structural transition will be discussed in more detail in sect. 2.4.3. A comparison of the various coupling constants determined from the different experiments will be given for TmCd and TmZn in sect. 2.4.3, table 3. In addition, the magnetoelastic coupling constant g_{Γ_3}/α_J for the RZn system is shown in fig. 8 together with coupling constants from the other series discussed above. Again g_{Γ_3}/α_J for the CsCl-type compound does not change very much across the series.

2.4.1.4. *The rare-earth hexaborides* (RB_6). This class of compounds has been studied in less detail. Experiments have been performed for CeB_6 (Goto et al. 1983, Lüthi et al. 1984), $Ce_xLa_{1-x}B_6$ (Winter et al. 1986), and for NdB_6 and PrB_6 (Tamaki et al. 1985a, b), see also Pofahl et al. (1987). CeB_6 is a dense Kondo compound and will be discussed in sect. 4. Of particular interest for our purpose are the measurements of the dilute $Ce_xLa_{1-x}B_6$ compounds with $x = 1\%$, 3% and 10%. In fig. 11 we show the temperature dependence of the symmetry modes c_{44}, $c_{11} - c_{12}$ for these compounds together with a single-ion strain susceptibility fit (Winter et al. 1986). Above $T = 2\,\mathrm{K}$ the agreement is very good. The magnetoelastic coupling constants deduced from this fit agree, within the limits of error, with those of the concentrated compound CeB_6 (Lüthi et al. 1984).

The dilute hexaborides are a nice example illustrating that a single-ion approxi-

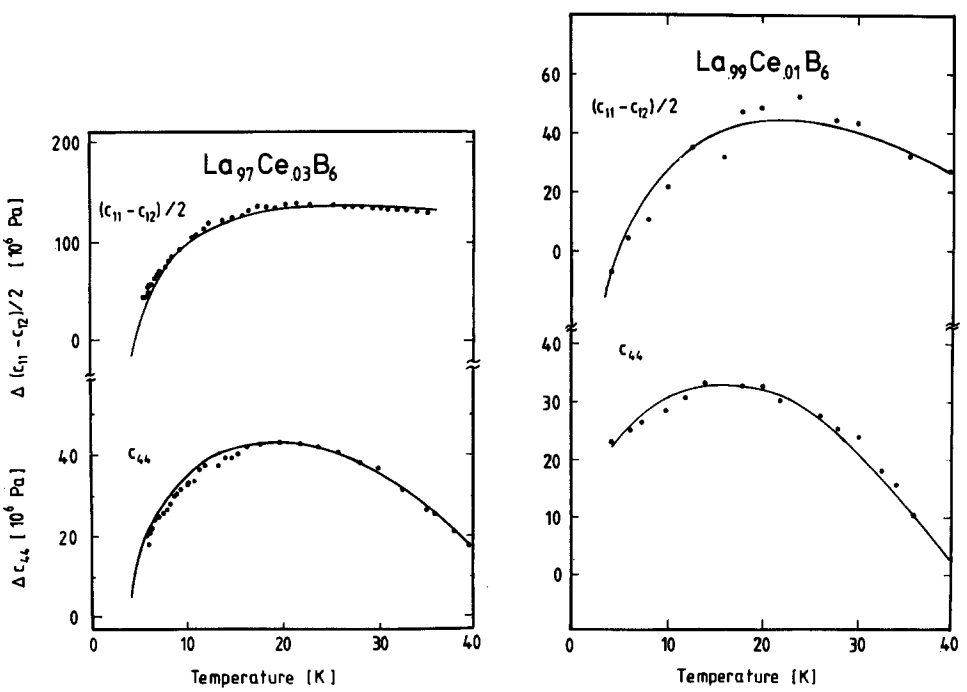

Fig. 11. Differences of elastic symmetry constants of $La_{0.097}Ce_{0.03}B_6$ and $La_{0.99}Ce_{0.01}B_6$ from those of LaB_6 as functions of temperature. The solid line is a theoretical fit (Winter et al. 1986).

mation is never quite correct, even for concentrations as low as 1%. If the temperature is low enough ($T \sim 2$ K in this case) the effects of the quadrupolar interionic coupling can be seen in the elastic constants (Lemmens et al. 1989). From a low-temperature fit with eq. (38) one then obtains g'_Γ in the dilute series $La_{1-x}Ce_xB_6$ ($x = 0.01, 0.03, 0.1$) for the c_{44} and $c_{11} - c_{12}$ modes. Together with g'_Γ for the concentrated ($x = 0.5, 1.0$) systems the concentration dependences of the quadrupolar coupling constants g'_{Γ_3} and g'_{Γ_5} can be plotted as in fig. 12. On a logarithmic scale they are linear functions of concentration x with a slope of one third, e.g., $g'_\Gamma(x) \sim x^{1/3}$.

In contrast to $g'_\Gamma(x)$ the magnetoelastic coupling constants are independent of x and were found to be $g_{\Gamma_3} = 50$ K and $g_{\Gamma_5} = 190$ K, see Winter et al. (1986).

It is no accident that such studies of single-ion effects are performed with Ce^{3+} ions. The value of $\alpha_J\langle r^2\rangle$ for this ion is exceptionally large due to the spatial extent of its $4f^1$ wavefunction (see table 1). This was noticed before in a study of the CsCl-structure material $Ce_xLa_{1-x}Ag$ (Lüthi et al. 1982). However, the concentrated compound ($x = 1$) CeAg does not exhibit magnetoelastic effects because of strong anharmonic interactions that lead to a martensitic phase transformation at 15 K (Takke et al. 1981a).

2.4.1.5. *Rare-earth metals.* In the light rare-earth metals, especially in Pr, CEF effects can be observed, see Greiner et al. (1973). Lüthi et al. (1973b), and Palmer and Jensen (1978). However, the high magnetic transition temperatures prevent the observation of similar CEF effects in the elastic constants of the heavy R metals. The large magnetic anisotropy in these metals is, of course, a consequence of the strong CEF potential. This matter has been reviewed in a previous volume (Scott 1978), by Coqblin (1977) and by Rhyne (1972).

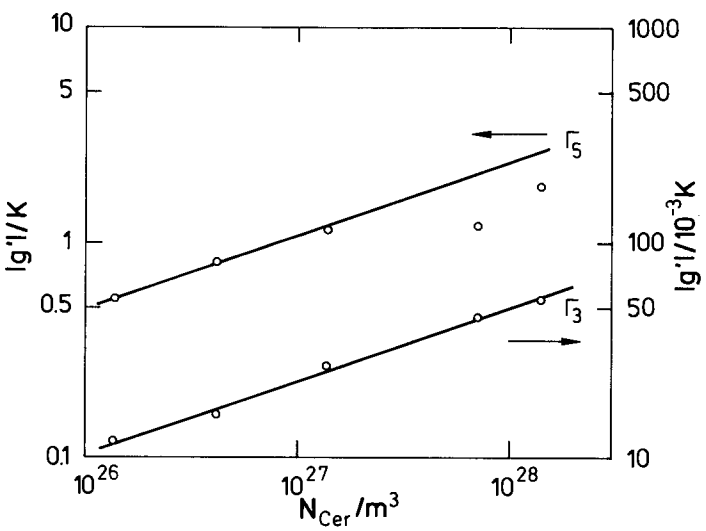

Fig. 12. Concentration dependence of quadrupolar constants $g'_{\Gamma_3} < 0$, and $g'_{\Gamma_5} < 0$ in $La_{1-x}Ce_xB_6$ ($x = 0.01, 0.03, 0.10, 0.5, 1.0$) (Lemmens et al. 1989).

2.4.2. *Higher-order effects*

Thus far we have discussed elastic constant effects due to magnetoelastic coupling described by quadrupolar ($l=2$) operators O_Γ^l. In analogy with the cubic crystal field Hamiltonian where one has $l=4$ and $l=6$ terms [eq. (2)] one can ask whether in addition one has $l=4$ coupling terms in the magnetoelastic Hamiltonian [eqs. (9), (14)]. So far such higher-order terms have been uniquely identified for two cases in the paramagnetic region: PrSb and $PrPb_3$ (Lüthi et al. 1982, Niksch et al. 1982b).

In PrSb the c_{44} mode exhibits a minimum at $T=25$ K, whereas the calculated quadrupolar strain susceptibility has a minimum at 60 K. With the addition of terms of the order of $O_\Gamma^{l=4}$ in the magnetoelastic Hamiltonian one obtains better agreement with the experiment (fig. 13).

Following Callen and Callen (1963) one can generalize the magnetoelastic Hamiltonian [eqs. (8), (9)] by including terms with $l=4$.

$$H_{\mathrm{me}} = -\sum_i \{\varepsilon_2[g_{\Gamma_3}^{(2)} O_2^2\sqrt{3} + g_{\Gamma_3}^{(4)} O_2^4]_i + \varepsilon_3[g_{\Gamma_3}^{(2)} O_3^2 + g_{\Gamma_3}^{(4)} O_3^4]_i + \varepsilon_{xy}[g_{\Gamma_5}^{(2)} O_{xy}^2 + g_{\Gamma_5}^{(4)} O_{xy}^4]_i + \cdots\}\,, \tag{43}$$

where

$$O_2^4 = \tfrac{1}{4}\{[7J_z^2 - J(J+1) - 5](J_+^2 + J_-^2) + (J_+^2 + J_-^2)[7J_z^2 - J(J+1) - 5]\}\,,$$

$$O_{xy}^4 = \tfrac{1}{4}\mathrm{i}\{[7J_z^2 - J(J+1) - 5](J_+^2 - J_-^2) + (J_+^2 - J_-^2)[7J_z^2 - J(J+1) - 5]\}\,.$$

The strain susceptibilities of these operators are again given by eq. (36). As a new free parameter one has the ratio $\delta = g_\Gamma^{(4)}/g_\Gamma^{(2)}$. This ratio is varied to obtain the best fit to the experiments. In fig. 13 the two cases of $PrPb_3$ ($c_{11}-c_{12}$ mode) and PrSb (c_{44} mode) are shown. In $PrPb_3$ $\delta = g_{\Gamma_3}^{(4)}/g_{\Gamma_3}^{(2)} = 1/135$ leads to the observed

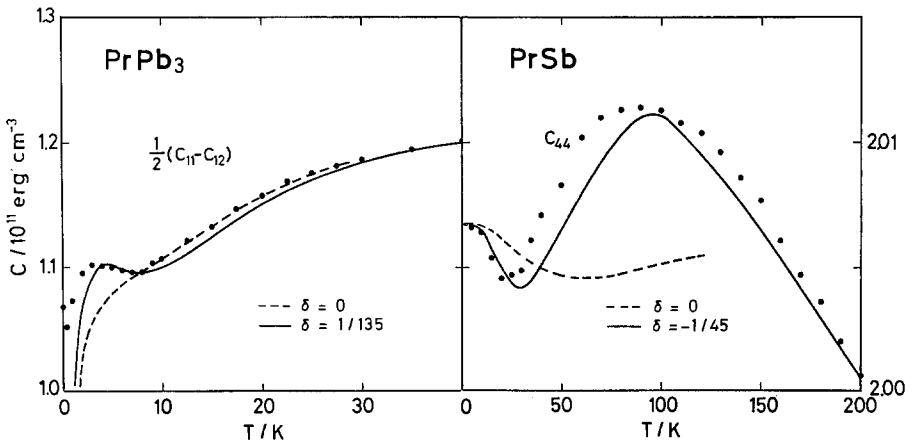

Fig. 13. Higher-order effects in $PrPb_3$ and PrSb. Temperature dependences of the $(c_{11}-c_{12})/2$ mode and the c_{44} mode. Dashed lines fit with quadrupolar strain susceptibility, full lines fit with higher-order susceptibility (Lüthi et al. 1982).

minimum in the $c_{11} - c_{12}$ mode at 7 K and in PrSb $\delta = g_{\Gamma_5}^{(4)}/g_5^{(2)} = -1/45$ shifts the c_{44} minimum from 60 K (with $l = 2$ quadrupolar strain susceptibility only) to the observed one at 25 K.

It should be emphasized that these effects occur in the paramagnetic region where other interactions such as the interionic quadrupole coupling cannot explain these additional structures in $c_\Gamma(T)$. It is not surprising that the Pr^{3+} ion leads to these higher-order effects. Pr^{3+} with $J = 4$, $L = 5$ and $S = 1$ has a large orbital contribution and therefore $l = 4$ contributions in the magnetoelastic coupling can become sizeable.

2.4.3. *The cooperative Jahn–Teller (CJT) effect and quadrupolar phase transitions*

A structural instability caused by the electron–phonon interaction with localized electrons was first investigated in transition-metal compounds, see Dunitz and Orgel (1957), Kataoka and Kanamori (1972), Gehring and Gehring (1975) and Kugel et al. (1982). This type of structural transition has been studied with a wide variety of techniques experimentally and theoretically after its discovery in insulating rare-earth compounds, namely the rare-earth zircons (Elliott et al. 1972, Melcher 1976, Gehring and Gehring 1975). Here we discuss the analogous structural transitions in R intermetallics.

In table 2 we list rare-earth compounds that have a structural transition at a temperature T_Q driven by the interactions discussed in sect. 2.3. Some of these compounds also have magnetic transitions at temperatures lower than T_Q. Common to all is a partial softening of a symmetry elastic constant. It can be described with the molecular field formula, eq. (38), discussed before. The fits, to experimental results for TmCd and TmZn are shown in fig. 14 (Lüthi et al. 1979). From this the quadrupolar coupling constant g'_{Γ_3} and the magnetoelastic coupling constant $\tilde{g}^2_{\Gamma_3}$ can be obtained. Figure 14 shows that eq. (38) describes the temperature dependence of the soft elastic mode (c_{Γ_3} in this case) very well. The inclusion of interionic quadrupolar interactions is necessary for intermetallic rare-earth compounds to describe the cooperative structural transition. In fact for TmCd and TmZn $g'_{\Gamma_3} > \tilde{g}^2_{\Gamma_3}$, as shown in table 3. This is in contrast to insulators where generally $g'_{\Gamma_3} < \tilde{g}^2_\Gamma$ (Lüthi 1980b), $DyVO_4$ and $CsCuCl_3$ being the excep-

TABLE 2
Intermetallic R compounds with cooperative Jahn–Teller or quadrupolar phase transitions

Material	Structure	T_Q (K)	T_N (K)	T_c (K)	Soft mode	Electronic ground state
TmCd	CsCl	3.16	—	—	$c_{11} - c_{12}$	Γ_5
TmZn	CsCl	8.55	—	8.12	$c_{11} - c_{12}$	Γ_5
$TmGa_3$	Cu_3Au	4.29	4.26	—		Γ_5
$PrPb_3$	Cu_3Au	0.37	—	—	$c_{11} - c_{12}$	Γ_3
$PrCu_2$	orthorhombic	7.3			c_{55}	singlet
CeB_6	cubic	3.35	2.31			Γ_8

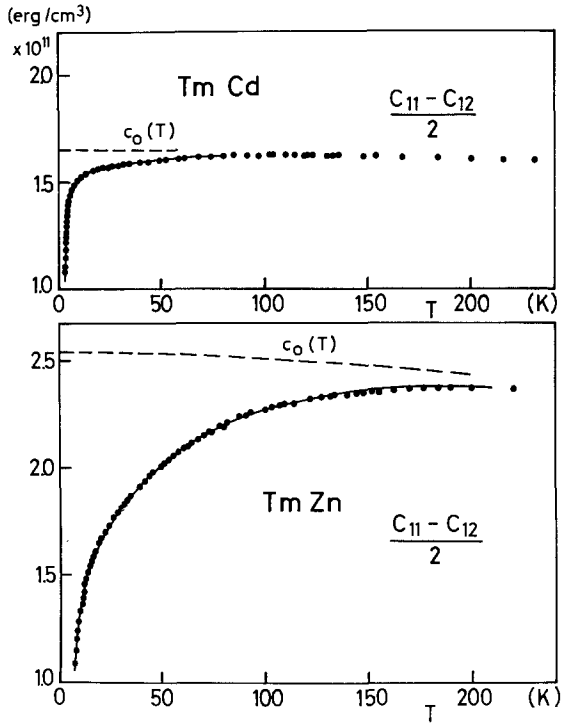

Fig. 14. Temperature dependence of $(c_{11} - c_{12})/2$ mode for TmCd and TmZn. Full line is a fit with eq. (38) (Lüthi et al. 1979).

tions. The appearance of strong interionic quadrupolar interactions in metallic systems means that, in addition to the sf-exchange interaction, an aspherical Coulomb scattering of conduction electrons by the quadrupolar moment of R ions is important here (see discussion in sect. 2.2.2). If $g'_\Gamma > \tilde{g}^2_\Gamma$ one speaks of quadrupolar-induced structural phase transitions, in the opposite case of a true cooperative Jahn-Teller effect, see Levy et al. (1979).

For TmCd and TmZn a variety of techniques have been applied to determine the important coupling constants g'_{Γ_3} and $\tilde{g}^2_{\Gamma_3}$; they are listed in table 3. In addition to the temperature dependence of the symmetry elastic constant $c_\Gamma(T)$, the parastriction method, the third-order susceptibility and the magnetic field dependence of the structural phase transition temperature $T_Q(B)$ have been used. The different experimental methods have been described in sect. 2.4.1. It is seen from table 3 that the coupling constants determined with these different methods are in good agreement with each other.

TABLE 3
Electron–phonon coupling constants for TmCd and TmZn (Γ_3 mode).

	$\tilde{g}^2$ (mK)	g' (mK)	$\tilde{g}^2 + g'$ (mK)			
			$c_{11} - c_{12}$	T_Q	$T_Q(B)$	Parastriction
TmCd	0.7	8.5	9.2	11.3	11.3	12
TmZn	3.6	24.3	27.9	25.5	25.7	25

Although TmCd and TmZn are the best characterized materials exhibiting a quadrupolar phase transition, there are other interesting examples (see table 2): $TmGa_3$ again has a quadrupolar-type phase transition at 4.29 K followed by an antiferromagnetic transition at 4.26 K (Czopnik et al. 1985, Morin et al. 1987). This means that the aspherical quadrupolar scattering is just a bit stronger than the RKKY interaction. $PrPb_3$ has the same Cu_3Au structure as $TmGa_3$. Strong higher-order magnetoelastic interactions (sect. 2.4.2) and the low transition temperature $T_Q = 0.37$ K prevent the determination of the quadrupolar coupling constant g'_Γ. In addition, the small structural distortion and CEF splitting could not be measured by neutron scattering techniques (Niksch et al. 1982b). An interesting case is $PrCu_2$ because the high-temperature orthorhombic crystal structure allows only singlet CEF states. Therefore the structural transition at $T_Q = 7.3$ K is of an induced nature, see Andres et al. (1976). The same is true for Pr_3Te_4 where the point symmetry is again low (Bucher et al. 1976). Finally, we mention CeB_6 where an elastic constant analysis has suggested an antiferroquadrupolar phase transition at 3.35 K ($g'_\Gamma < 0$ in analogy to antiferromagnetic $\Theta_N < 0$), Lüthi et al. (1984), which has been verified by neutron scattering experiments (Effantin et al. 1985). For CeB_6 see also sect. 4.

With the exception of CeB_6 all rare-earth compounds exhibiting structural transitions of quadrupolar type have Pr^{3+} or Tm^{3+} ions as rare-earth constituents. For both ions (Pr^{3+}: $J = 4$, $L = 5$; Tm^{3+}: $J = 6$, $L = 5$) the orbital angular momentum L is rather large, making aspherical Coulomb charge scattering a dominant mechanism which in turn leads to a large value of g'_Γ. This was also shown by magnetoresistance measurements in metals with rare-earth impurities (Fert et al. 1977), see discussion in sect. 2.2.2. Indeed for Pr^{3+} and Tm^{3+} the quadrupolar scattering dominates exchange scattering. The results of magnetoresistance measurements for the heavy R alloys are shown in fig. 15. It is seen that $|E_Q| > |E_{ex}|$ for the Tm ion.

There are examples of structural transitions of intermetallic rare-earth compounds where the magnetoelastic and/or quadrupolar interaction is not the responsible mechanism. A prominent example is CeAg which exhibits a structural transition at $T_Q = 15$ K followed by a ferromagnetic one at 7 K (Takke et al. 1981a). The strong softening of the c_{Γ_3} elastic constant follows a $(T - T_Q)^{-1}$ law similar to the $La_{1-x}In_xAg$ compounds (Knorr et al. 1980). In analogy, this martensitic type of transition is triggered by a softening of a zone boundary phonon caused by conduction-electron–phonon interaction. Somewhat related is the case of $PrAg_{1-x}Cu_x$ [see Abu-Aljarayesh et al. (1986) and references contained in it].

A structural phase transition driven by magnetoelastic and quadrupolar interactions can be well described by molecular field theory because the range of these interactions is large. Therefore the critical fluctuations near T_Q should be small. One test is, of course, the static response function $c_\Gamma(T)$ (fig. 14). Another is the ultrasonic attenutation near T_Q. There is only one experiment for TmZn which shows an attenuation $\alpha = B\omega^2(T - T_Q)^{-n}$ with exponent $n = 1.5$ in good agreement with theory, see Leung et al. (1979). Theoretical discussions of the attenution are also given by Leung and Huber (1979) and Becker et al. (1979).

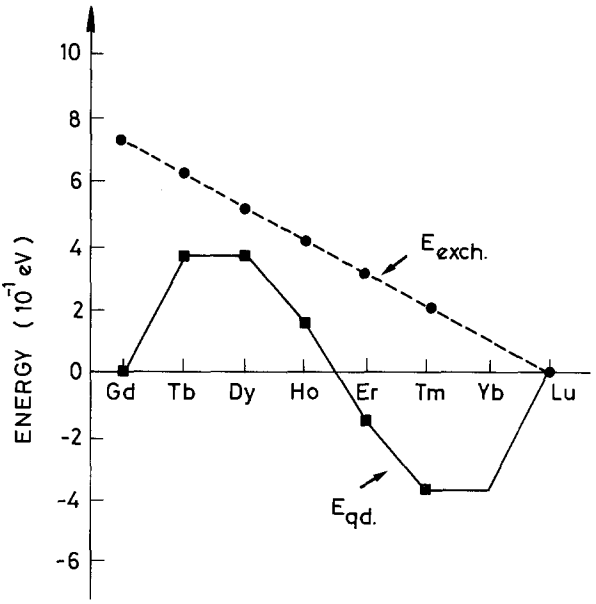

Fig. 15. Characteristic energies of quadrupolar interaction (E_{qd}) and of isotropic exchange (E_{exch}) for heavy rare-earth impurities in gold. E_{qd} is proportional to K_Γ, E_{exch} is proportional to $(g-1)J_{ex}$ (Fert et al. 1977).

So far we have studied elastic constants in the high-symmetry phase of the various compounds. The elastic constants play the role of an order parameter susceptibility [eqs. (35), (38)], indicating which type of structural phase transition can occur at lower temperatures. For $T < T_Q$, T_N only a few elastic constant measurements exist mostly because in a multidomain state they cannot contribute much to the knowledge of the ordered state. For example, in some pnictides (SmSmb, GdSb, DySb, ErSb), see Mullen et al. (1974), the elastic constants decrease with decreasing temperature for $T < T_N$ and increase only in an applied field where a single-domain state is formed. On the other hand, in HoSb the temperature dependences of $c_{11} - c_{12}$ and c_{44} are normal for $T < T_N$. For Jahn–Teller compounds only a few elastic constant measurements for $T < T_Q$ exist.

However, order parameter measurements for $T < T_Q$, T_N have been performed for a number of rare-earth compounds. In the first place one has to mention X-ray diffraction experiments for various monopnictides where tetragonal distortions were found in CeSb, NdSb, DySb, DyAs, DyP, HoSb, HoAs, HoP and HoN, and trigonal distortions in TbSb, TbAs, TbP and ErSb while no distortions were found in GdSb and TmSb (Lévy 1969). This is in complete agreement with the findings and analysis given in sect. 2.4.1. Unfortunately, the determination of T_Q in this work was not accurate enough so that the impression that $T_Q > T_N$ was given for several compounds. Subsequent work on DySb (Bucher et al. 1972), Tb monopnictides (Koetzler and Raffius 1980), RZn compounds (Morin et al. 1977), the monochalcogenides NdS, DyS, ErS (Tao et al. 1974) and others, however, have shown that for monopnictides and monochalcogenides $T_Q = T_N$ and for RZn $T_Q = T_c$ (except for TmZn).

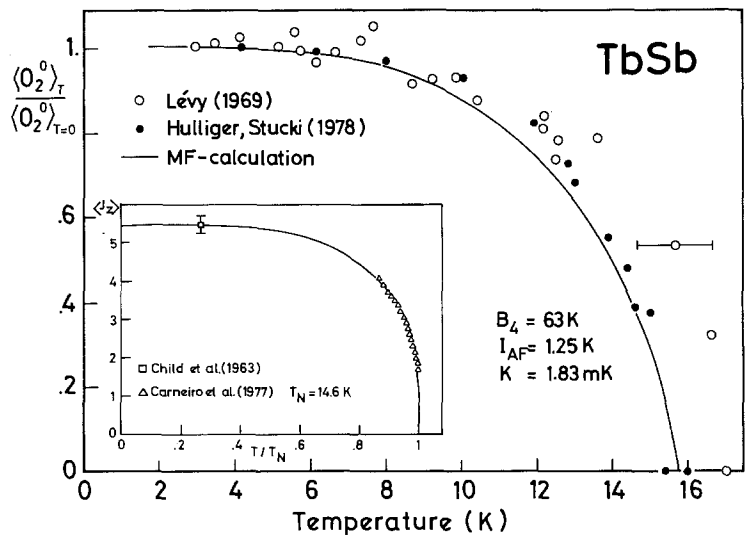

Fig. 16. Spontaneous trigonal distortion of TbSb normalized to saturation and magnetic moment (inset) compared to self-consistent computations (Koetzler and Raffius 1980).

As examples of direct order parameter measurements we show in figs. 16 and 17 results for TbSb and DyZn, respectively. In TbSb the trigonal distortion was measured using X-ray diffraction (Lévy 1969, Hulliger and Stucki 1978) and the results were interpreted with a trigonal molecular field distortion model, (Koetzler and Raffius 1980). In DyZn the length changes were measured parallel and perpendicular to the magnetization in a small magnetic field of 1 kOe. In both cases the quadrupolar order parameter for $T \leqslant T_N$, T_c was determined.

These few results indicate that the coupling constants obtained in the high-

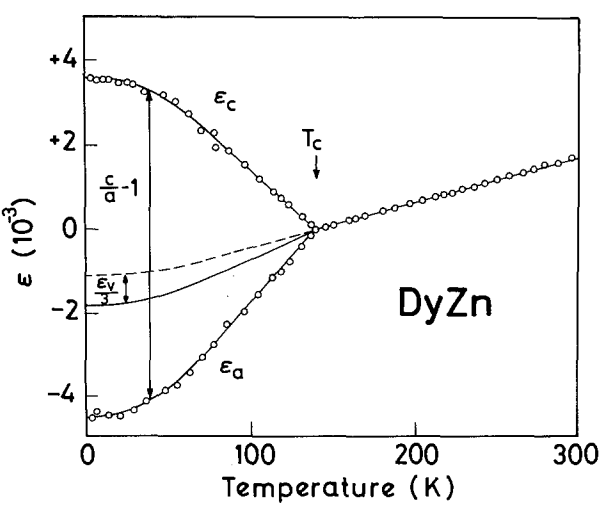

Fig. 17. Thermal variations of relative length changes ε_c, ε_a in DyZn. The paramagnetic curve is extrapolated down to 0 K, Morin et al. (1977).

symmetry phase ($T > T_Q$) via elastic constants, third-order susceptibility or parastriction experiments can explain the expected unit cell distortions for $T < T_Q$, even in the case $T_Q = T_N$ or $T_Q = T_c$.

2.5. *Thermal expansion and magnetostriction*

The magnetoelastic coupling in rare-earth compounds leads to pronounced effects in the various symmetry elastic constants as discussed previously in sections 2.3 and 2.4. We considered mainly cubic compounds where the elastic constants of Γ_3 and Γ_5 symmetry exhibit these effects. The Γ_1 symmetry elastic constant, i.e., the bulk modulus c_B is associated with the volume strain ε_v. It also shows magnetoelastic effects which, however, are caused by a coupling of ε_v to the higher multipolar operators $O^l_{\Gamma_1}(l \geq 4)$ allowed by cubic symmetry. Because they are fully symmetric their thermal average $\langle O^l_{\Gamma_1} \rangle$ is different from zero, which leads to a temperature dependence of the volume strain ε_v and therefore a magnetoelastic contribution to the thermal expansion. We shall discuss both $c_B(T)$ and $\beta(T)$ for cubic and hexagonal intermetallic R compounds.

The volume thermal expansion coefficient,

$$\beta = \frac{1}{V}\left(\frac{\partial V}{\partial T}\right)_p = \left(\frac{\partial \varepsilon_v}{\partial T}\right)_p = -\kappa V\left(\frac{\partial^2 F}{\partial V\, \partial T}\right), \tag{44}$$

can be calculated from H_{me} as, Ott et al. (1976, 1977) and Lüthi (1980a),

$$\beta = -\frac{\kappa}{v_c}\frac{1}{k_B T}\left(\langle E^2\gamma\rangle - \langle E\rangle\langle E\gamma\rangle\right). \tag{45}$$

Here $\kappa = c_B^{-1}$ is the compressibility, the averages are given by eq. (34) and $\gamma_n = -(\partial \ln E_n / \partial \ln V)$ define electronic Grüneisen parameters for a given CEF level. The close correspondence between β and the Schottky specific heat has been emphasized before (Ott et al. 1976, 1977, Lüthi 1980a). The latter is described by a corresponding formula

$$C = \frac{1}{v_c k_B T^2}\left(\langle E^2\rangle - \langle E\rangle^2\right). \tag{46}$$

As for elastic constants, the CEF effects in thermal expansion and the Schottky specific heat are especially pronounced in TmSb, see fig. 18. Equations (45) and (46) give a good fit to the data, (Ott and Lüthi 1976, 1977) with $\gamma_4 = \gamma_5 = -1.2$ as seen from fig. 18. The CEF Grüneisen parameters measuring the volume dependence of the CEF levels turn out to be of the order of one. In this way a number of cubic compounds have been studied so far: TmSb, PrSb, SmSb, ErSb, CeTe and TmTe (Ott and Lüthi 1977), and TmCu, TmZn and TmCd (Morin and Williamson 1984).

Of particular importance is the case of hexagonal substances where one finds thermal expansion coefficients of different signs depending on the crystallographic direction. In fig. 19 we show the case of $PrNi_5$ where the linear expansion

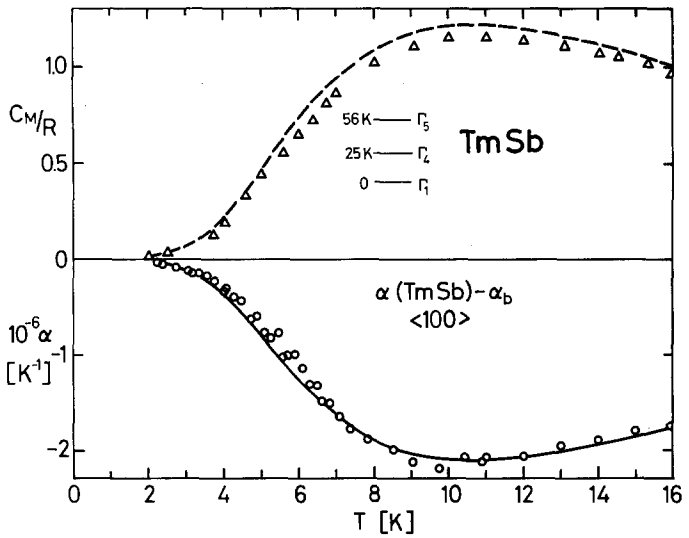

Fig. 18. Crystal-field effect on specific heat C_M and linear thermal expansion α for TmSb. Full and dashed lines are CEF calculations with the level scheme given in the inset and using eqs. (45) and (46) (Ott and Lüthi 1977).

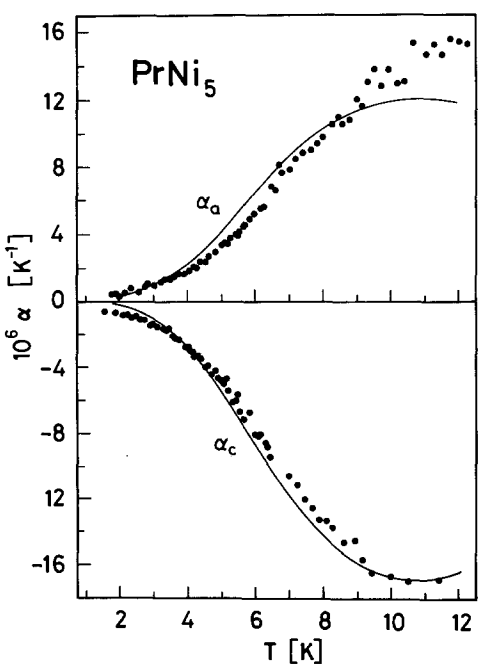

Fig. 19. Thermal expansion of $PrNi_5$. Solid lines indicate the CEF effect (Lüthi and Ott 1980).

coefficients α_a and α_c have opposite signs (Lüthi and Ott 1980). The equivalent magnetoelastic Hamiltonian (Callen and Callen 1965) is given by

$$H_{me} = -\sum_i [B_v \varepsilon_v O_2^0(i) + B_3 \varepsilon_3 O_2^0(i)] , \tag{47}$$

from which one can determine the temperature dependence of $\delta c/c = \varepsilon_{zz} = \frac{1}{3}(\varepsilon_v + \varepsilon_3)$ and $\delta a/a = \frac{1}{6}(2\varepsilon_v - \varepsilon_3)$ by calculating the strain-dependent energy levels and the equilibrium strains. The result is a similar expression as eq. (45) with prefactors that depend on the compliances for the different directions. The fit to experimental results for $PrNi_5$ as shown in fig. 19 is quite successful with a single set of CEF Grüneisen parameters. The opposite signs for α_a and α_c arise from different compliances. Other examples analyzed are Pr (Lüthi and Ott 1980) and Mg:R (de Jong et al. 1982).

Unlike thermal expansion, there is little information about CEF effects in the bulk modulus $c_B(T)$ because higher-order multipolar terms $l \geq 4$ in H_{me} are generally weak. For a critical discussion see Morin and Williamson (1984).

Finally, we discuss the parastriction (or magnetostriction) effect. In an applied magnetic field the magnetoelastic coupling induces strains because of the field dependence of the quadrupolar moments of the rare-earth ions according to

$$\varepsilon_\Gamma(B, T) = \frac{1}{c_\Gamma^0 v_c} g_\Gamma \langle O_\Gamma \rangle_{B,T} . \tag{48}$$

Neglecting the volume magnetostriction $\varepsilon_v(B)$ one can have tetragonal Γ_3 and trigonal Γ_5 strains depending on the direction in which the magnetic field is applied. The case of compounds has been mentioned in sect. 2.4.1 (parastriction method). There are also a number of experiments for various dilute R alloys. It is important to perform these experiments on single crystals in order to avoid averaging problems. Typical examples of single-crystal work are Ag:R, Au:R (Creuzet and Campbell 1981) and Y:Tb (Pureur et al. 1982). For the problem of averaging spontaneous symmetry strains in polycrystalline materials see the case of $LaAl_2$:Ce (Zieglowski et al. 1986). For a review see Creuzet and Campbell (1982). The volume magnetostriction is rather small and we shall discuss it only for unstable-moment compounds where the effects are larger (sect. 4).

2.6. *Magnetic field effects in sound propagation*

A magnetic field leads to a Zeeman splitting of CEF multiplets into singlets and also to a mixing of their wavefunctions resultings in new eigenstates. Because of the magnetoelastic interaction this can have profound consequences for ultrasound propagation. The most obvious is a field dependence of the elastic constants which may be due to the Zeeman splitting and/or to field-induced quadrupolar matrix elements. More dramatic are symmetry breaking effects caused by the field in which the twofold degeneracy of high symmetry sound modes (e.g., transverse modes along a cubic axis) is lifted by magnetoelastic interactions. These are known as the Voigt effect (magnetoacoustic birefringence), the Faraday effect and the rotational invariance effect depending

on the field direction as well as the propagation and polarization directions of the sound modes considered. The former can be understood with magnetoelastic interactions that are of first order in the strain ε_{kl} only, which were used up to now. The rotational invariance effects, however, are due to magnetoelastic interaction terms that include the rotational tensor ω_{kl} [eq. (6)]. To treat these contributions consistently, i.e., to ensure rotational invariance for zero field one has to include all terms up to second order in the rotational tensor. A short pedagogical review of these effects has been given by Fulde (1978b).

2.6.1. *Magnetic field dependence of elastic constants*

In a magnetic field one obtains Zeeman-split CEF levels with new eigenstates of the total Hamiltonian,

$$H_{\text{eff}} = H_{\text{CEF}} + g\mu_{\text{B}} B \sum_i J(i) . \tag{49}$$

These are admixtures of the zero-field CEF states. As an illustration the split level scheme for a $\Gamma_7(0)$–$\Gamma_8(\Delta)$ system is shown in fig. 20. In practice one is always in the limit $\mu_{\text{B}} B \ll \Delta$. The field-dependent elastic constants can be computed from eq. (35) or eq. (38) with the quadrupolar susceptibility given by eq. (36) where $E_n(B)$, $|n\rangle$ now denote the field-dependent Zeeman levels and eigenstates of H_{eff}. Note that now in general $\langle O_\Gamma \rangle \neq 0$, it is therefore essential to use $\hat{O}_\Gamma = O_\Gamma - \langle O_\Gamma \rangle$ in the Curie term of eq. (36) to ensure $\chi^{\text{c}}_\Gamma(T) \to 0$ as $T \to 0$ where only the lowest Zeeman level is populated. Two main causes for the field dependence of $c_\Gamma(T, B)$ can be distinguished:

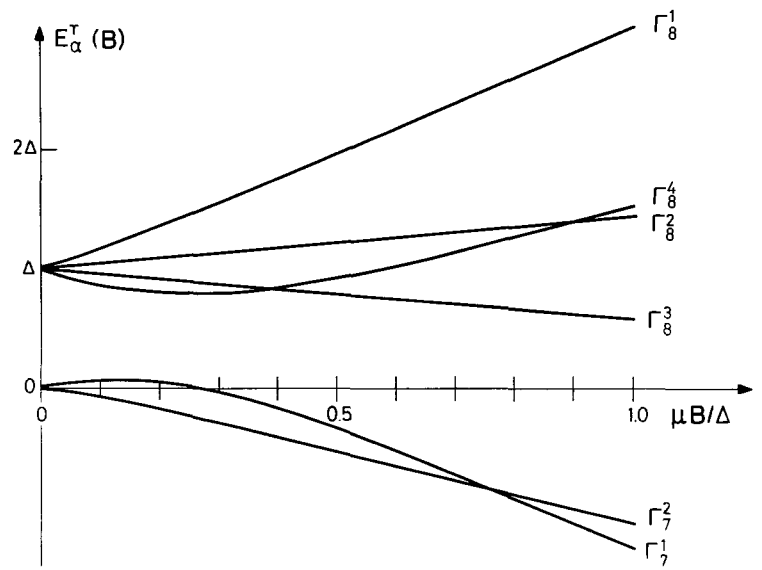

Fig. 20. Zeeman splitting of the Ce^{3+} ($J = \frac{5}{2}$) CEF states $\Gamma_7(0)$ and $\Gamma_8(\Delta)$ in a magnetic field parallel to a cubic axis.

(i) The ground state is orbitally degenerate and O_Γ has matrix elements. One therefore has a CJT transition at a temperature T_Q (see sect. 2.4.3). A Zeeman splitting of the ground state strongly reduces the Curie term in $\chi_\Gamma(T, B)$ and thus leads to a continuous increase in $c_\Gamma(T, B)$ with increasing field strength. If B is large enough it may completely suppress the softening of $c_\Gamma(T, B)$ above T_Q and thus prevent the CJT transition. For example, this type of behaviour has been found in HoSb (fig. 21) which has a Γ_3 ground state, Mullen et al. (1974). A different behaviour, namely $T_Q(B) > T_Q(0)$, has been observed, however, for TmCd and TmZn (Lüthi et al. 1979, Lüthi and Lingner 1979).

(ii) In a singlet ground state system the low-temperature behaviour of c_Γ is determined by Van Vleck contributions. Due to the mixing of CEF states in a magnetic field, selection rules for quadrupolar matrix elements may change leading to additional contributions in χ_Γ. This is especially pronounced in singlet ground state systems which have a field-induced quadrupolar matrix element to the first excited state like $|\langle\Gamma_1|O_\Gamma|\Gamma_4\rangle|^2 \sim B^2$ for small fields in Γ_1–Γ_4 systems (e.g., PrSb and TmSb). These field-induced transitions determine $c_\Gamma(T, B)$ at low temperatures. An example of this effect is shown in fig. 22 for Pr_3Te_4 which, however, has a lower than cubic symmetry with two singlets as lowest states (Bucher et al. 1976).

2.6.2. *Magnetoacoustic birefringence and Faraday rotation: theory*

Compounds with an n-fold rotation axis ($n > 2$) have doubly degenerate sound modes with propagation vector $\boldsymbol{k}$ along the symmetry axis. For example, in cubic systems with $\boldsymbol{k} \| [001]$ one has two degenerate c_{44} modes with $v = (c_{44}/\rho)^{1/2}$ whose

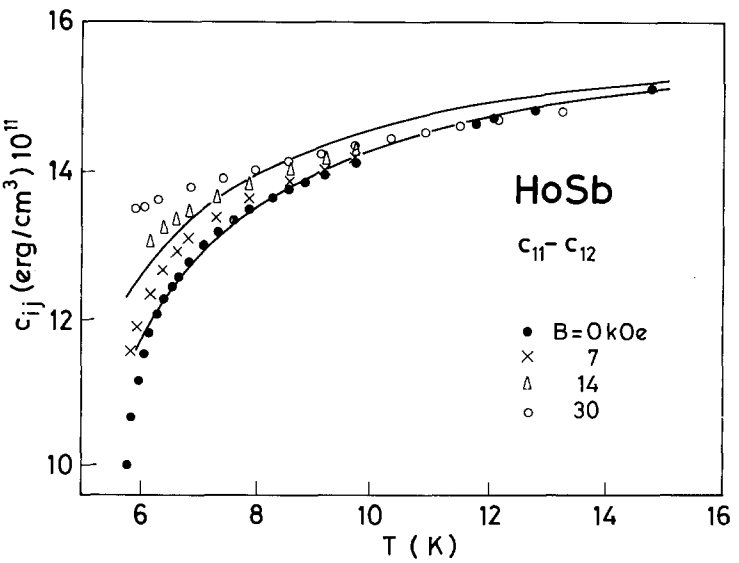

Fig. 21. Temperature and magnetic field dependences of $(c_{11} - c_{12})/2$ mode for HoSb (Mullen et al. 1974).

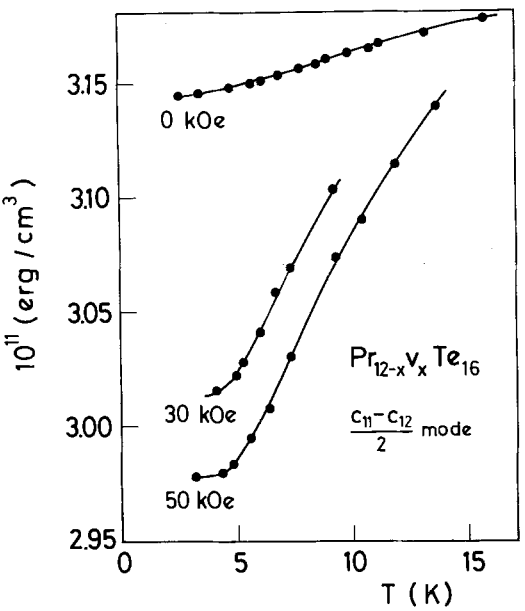

Fig. 22. Temperature and magnetic field dependences of $(c_{11} - c_{12})/2$ mode for Pr_3Te_3 (Bucher et al. 1976).

polarization e may be chosen perpendicular, e.g., $e_x = [100]$ and $e_y = [010]$. Due to the magnetoelastic coupling an applied field may lift this degeneracy; experimentally this is observed as a change of sound wave polarization along the propagation direction. Depending on whether $\mathbf{B} \perp \mathbf{k}$ or $\boldsymbol{B} \| \boldsymbol{k}$ one observes magnetoacoustic birefringence or Faraday rotation of soundwaves (fig. 23). The former is simply due to a different effect on $\boldsymbol{B}$ on the sound velocities $v_\parallel(B)$ and $v_\perp(B)$, corresponding to polarization parallel and perpendicular to the field. The latter is a real finite-frequency effect, it was predicted by Kochelaev (1962) for paramagnetic spin-$\frac{1}{2}$ systems and discussed in detail by Tucker (1973). The theory for CEF-split R systems was given by Thalmeier and Fulde (1978).

In the Voigt or Cotton–Mouton (CM) configuration the unequal sound velocities $v_\parallel(\boldsymbol{B})$ and $v_\perp(\boldsymbol{B})$ lead to different wave numbers $k_\parallel = \omega/v_\parallel$ and $k_\perp = \omega/v_\perp$ (ω is frequency) for the two eigenmodes with polarizations parallel and perpendicular to $\boldsymbol{B}$. To be specific we assume $\boldsymbol{B} \| [010]$ and $\boldsymbol{k} \| [001]$. The displacement field of a sound wave initially polarized along [110] at $z = 0$ is then given by

$$u(z, t) = [(\cos \tfrac{1}{2}\varphi)\boldsymbol{e}_+ + \mathrm{i}(\sin \tfrac{1}{2}\varphi)\boldsymbol{e}_-] \exp[\mathrm{i}(\omega t - kz)] ,$$

$$\boldsymbol{e}_\pm = 1/\sqrt{2}(\boldsymbol{e}_x \pm \boldsymbol{e}_y), \qquad k = \tfrac{1}{2}(k_\parallel + k_\perp), \qquad \varphi = (k_\parallel - k_\perp)z . \tag{50}$$

This describes an elliptically polarized sound wave with major axis $\boldsymbol{e}_\pm$ where the CM phase shift φ determines the ellipticity $u_y/u_x = \tan \frac{1}{2}\varphi$. The phase shift per unit length can be obtained experimentally and is given by

$$\varphi(B)/z = \omega \left(\frac{1}{v_\parallel} - \frac{1}{v_\perp} \right) \simeq \frac{2\pi}{\lambda v(0)} [v_\perp(B) - v_\parallel(B)] . \tag{51}$$

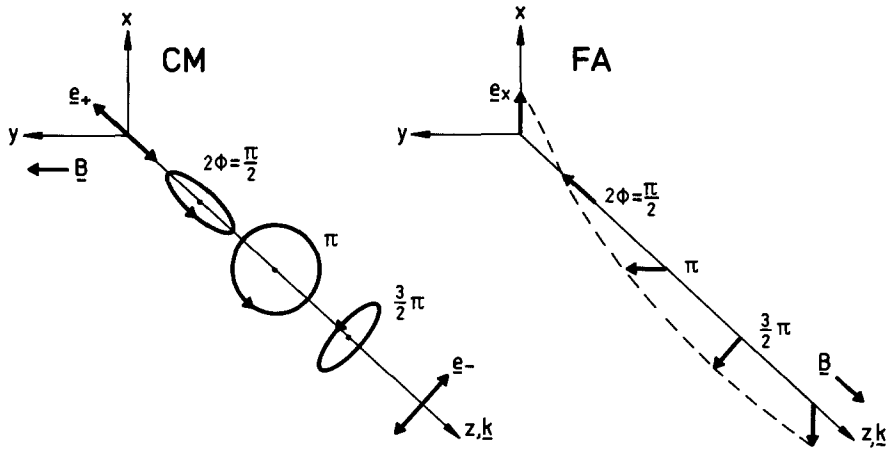

Fig. 23. The geometry of the propagation ($\boldsymbol{k}$), polarization ($\boldsymbol{e}$) and magnetic field ($\boldsymbol{B}$) vectors for the Voigt or Cotton–Mouton (CM) and Faraday (FA) effects. The change of polarization state of transverse c_{44} modes is indicated. For clarity the polarization is not shown in perspective. Φ is the CM or FA rotation angle.

The sound velocities $v_{\parallel}^2 = \rho c_{44}^{\parallel}$ and $v_{\perp}^2 = \rho c_{44}^{\perp}$ are given by eq. (35). The corresponding strain susceptibilities $\chi_{\Gamma_5}^{xz}(B)$ and $\chi_{\Gamma_5}^{yz}(B)$ are obtained from the Γ_5 quadrupolar operators $O_{xz} = J_x J_z + J_z J_x$ and $O_{yz} = J_y J_z + J_z J_y$, respectively. For zero field $\chi_{\Gamma_5}^{xz}$ and $\chi_{\Gamma_5}^{yz}$ and hence $v_{\parallel}$ and $v_{\perp}$ must be identical due to cubic symmetry; for $\boldsymbol{B} = B\boldsymbol{e}_y$ this symmetry is broken.

In the Faraday configuration ($\boldsymbol{B} \| \boldsymbol{k}$) the fourfold rotational symmetry around the cubic axis is preserved contrary to the previous situation. The lifting of the degeneracy is now directly due to the breaking of time-reversal invariance. The new eigenmodes are left- and right-handed circularly polarized, which are described by polarization vectors

$$\boldsymbol{e}_{\mathrm{L}} = \frac{1}{\sqrt{2}}(\boldsymbol{e}_x + \mathrm{i}\boldsymbol{e}_y), \qquad \boldsymbol{e}_{\mathrm{R}} = \frac{1}{\sqrt{2}}(\boldsymbol{e}_x - \mathrm{i}\boldsymbol{e}_y)\,. \tag{52}$$

The phase velocities (but not the group velocities) of the L and R modes will be different, therefore the difference of wave numbers $k_{\mathrm{L}} - k_{\mathrm{R}}$ for a sound frequency ω will itself be proportional to ω. This follows because it must change sign under time reversal, i.e., $\omega \to -\omega$ and $R \rightleftharpoons L$. A sound wave originally linearly polarized along $\boldsymbol{e}_x$ can be written as the superposition and L- and R-polarized modes. If their wave numbers k_{L} and k_{R} differ slightly the displacement field will be given by

$$\boldsymbol{u}(z, t) = (\cos\varphi \boldsymbol{e}_x + \sin\varphi \boldsymbol{e}_y)\exp[\mathrm{i}(\omega t - kz)]\,,$$
$$k = \tfrac{1}{2}(k_{\mathrm{L}} + k_{\mathrm{R}}), \qquad \varphi = \tfrac{1}{2}(k_{\mathrm{L}} - k_{\mathrm{R}})z\,. \tag{53}$$

This describes a linearly polarized sound wave whose polarization rotates during

propagation (fig. 23). The 'Faraday rotational angle' per unit length is φ/z and can be obtained from Dyson's equation for the L and R modes as

$$\varphi/z = \frac{\pi}{\lambda}\left(\frac{v_0}{v(B)}\right)^2 g_{\Gamma_5}^2 \,\mathrm{Im}\,\chi_{\Gamma_5}^{xz,yz}(\omega, B, T)\,. \tag{54}$$

The mixed quadrupolar susceptibility for O_{xz} and O_{yz} vanishes identically for $\boldsymbol{B} = 0$ because of cubic symmetry. One obtains, in explicit terms,

$$\begin{aligned}\varphi/z = {} & \frac{\pi}{\lambda}\left(\frac{v_0}{v(B)}\right)^2 g_{\Gamma_5}^2 \\ & \times \sum_{n,m}{}' \frac{\omega(p_n - p_m)}{(E_n - E_m)^2}\,\frac{1}{2\mathrm{i}}\,(\langle m|O_{xz}|n\rangle\langle n|O_{yz}|m\rangle - \langle n|O_{xz}|m\rangle \\ & \times \langle m|O_{yz}|n\rangle)\,.\end{aligned} \tag{55}$$

The summation is restricted to $E_n \neq E_m$. E_n and $|n\rangle$ are again the field-dependent eigenstates of H_{eff} [eq. (49)]. Note that the products in parentheses are purely imaginary. Furthermore, $v(B)$ is the renormalized sound velocity. In practice, one may have to include finite linewidths Γ_{nm} for the various contributions in eq. (55). The Faraday rotation should be of the order of ω^2, since $\lambda = 2\pi v/\omega$ contrary to the CM phase shift which is of the order of ω. It should be large in CEF systems with magnetic ground states and quadrupolar matrix elements, i.e., a Γ_8 ground state would be the most favourable. A model calculation for TmTe has been given (Thalmeier and Fulde 1978), but no experiments were performed on this compound. In $CeAl_2$, the only paramagnetic R system studied so far experimentally, there is a serious discrepancy to the above single-ion theory for φ/z as discussed below.

2.6.3. *Magnetoacoustic birefringence and Faraday experiments*

The first of these experiments was performed in insulators. The magnetoacoustic analogue of the Faraday effect was first observed in yttrium iron garnet (Matthews and LeCraw 1962), the analogue of the Cotton–Mouton or Voigt effect in gadolinium iron garnet (Lüthi 1965) and magnetite (Lüthi 1966). For a review see Lüthi (1980a).

In intermetallic rare-earth compounds there exist a few studies of magnetoacoustic birefringence and Faraday effects. In $CeAl_2$ the circular birefringence (Voigt effect) were observed (Lüthi and Lingner 1979) in the paramagnetic region at 4.3 K. Furthermore, in NdB_6 and PrB_6 the Voigt effect has been found, see Tamaki et al. (1985a).

In fig. 24 relative velocity changes for the various c_{44} modes in the presence of a magnetic field are shown in $CeAl_2$ in the Voigt geometry. With u_k denoting the displacement vector component the figure demonstrates very nicely the symmetry breaking due to a magnetic field: the strong effect for the (u_x, k_z) mode (c_{66} like) and the corresponding c_{44}-like modes (u_y, k_z) and (u_z, k_y) with magnetic field in the y-direction. In addition, the much smaller effect due to rotationally invariant

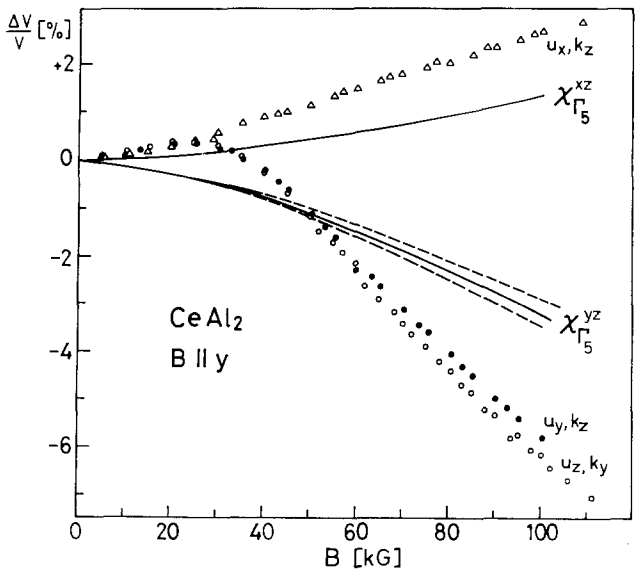

Fig. 24. Magnetic field dependence of the three c_{44} modes for $T = 4.3$ K in $CeAl_2$. Full lines are strain susceptibilities for (u_x, k_z) and (u_y, k_z) modes. Broken lines indicate rotationally invariant magnetoelastic interaction (Lüthi and Lingner 1979).

magnetoelastic effects for the two c_{44} modes (u_y, k_z) and (u_z, k_y) is also seen. It will be discussed in sect. 2.6.4. The symmetry breaking into c_{44} and c_{66} modes is due to the magnetoelastic interaction. The corresponding strain susceptibilities $\chi^{xz}_{\Gamma_5}$ and $\chi^{yz}_{\Gamma_5}$ are different and explain the experiment semiquantitatively. The lack of complete quantitative agreement between experiment and theory is probably due to the vicinity of the magnetic phase transition at $T_N = 3.8$ K and Kondo-like phenomena occurring in this compound at low temperatures (see sect. 4.1).

From the velocity difference of the modes (u_x, k_z) and (u_y, k_z) follows the linear birefringence of the medium. By placing the shear transducer in the xy-plane with polarization 45° to the x-, y-axes, the different velocities seen in fig. 24 give rise to an amplitude-modulated signal because of the resulting phase change.

The phase change is π for subsequent maxima and minima of the received acoustic signal in this Voigt geometry. In fig. 25 the amplitude signals for the two configurations (Voigt and Faraday) are shown for $CeAl_2$ at 4.3 K. Whereas the amplitude modulation is almost 100% in the Voigt case, the Faraday case shows a much weaker modulation effect. This may be significant for the understanding of the latter. From the extrema of the amplitude signals one can plot the phase φ/z as done in fig. 26. Five different frequencies were used to determine this phase curve. To obtain the total phase change we took a phase difference of $\frac{1}{2}\pi$ between subsequent minima and maxima for the Faraday effect and π for the Voigt effect. In fig. 26 we also make quantitative comparison with the results of fig. 25 using eq. (51). The full line shows a good agreement up to 7 T. The disagreement for $B > 7$ T arises from the splitting of the echoes due to the different velocity components (Lüthi and Lingner 1979).

Much more serious is the discrepany between theory and experiment in the case

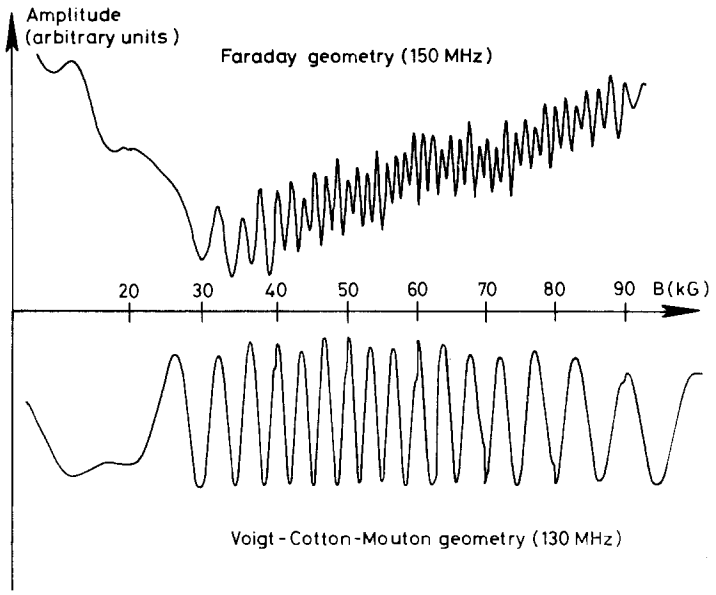

Fig. 25. Amplitude modulation for Faraday geometry and Voigt–Cotton–Mouton geometry in $CeAl_2$ (Lüthi and Lingner 1979).

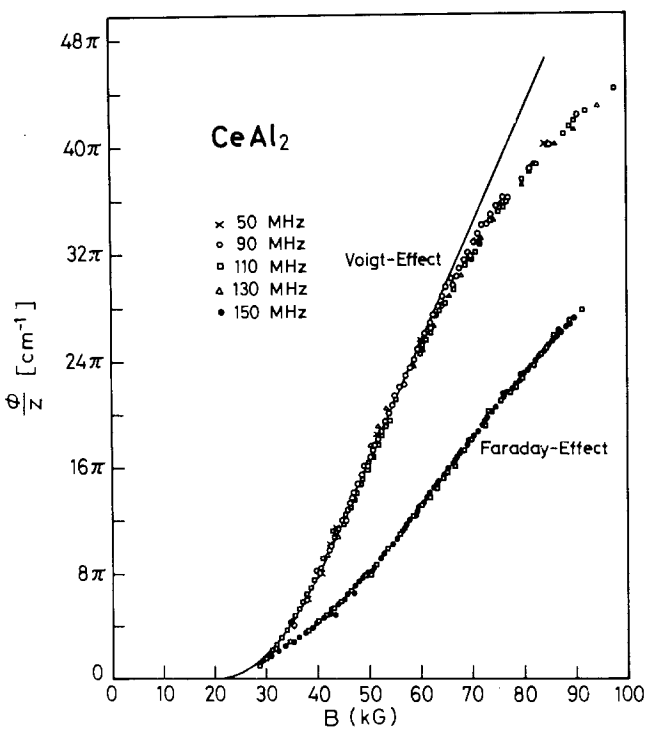

Fig. 26. Phase differences φ/z for the Cotton–Mouton and Faraday geometries for different frequencies and different echo numbers as functions of magnetic field (Lüthi and Lingner 1979).

of the Faraday effect. Whereas theory predicts a phase change proportional to ω^2 [eq. (55)] in the paramagnetic region, the results of fig. 26 lead to a strictly linear ω-dependence. This discrepany cannot be explained with the fluctuations caused by the vicinity to the magnetic phase transition and is as yet unexplained.

Another system studied with the Voigt effect is NdB_6 in the antiferromagnetic phase ($T_N = 8.6$ K) at 4.2 K (Tamaki et al. 1985a). Again the effect is proportional to the frequency. However, no further quantitative analysis was made. Magnetoacoustic birefringence experiments have also been performed with acoustic surface waves in $CeAl_2$. CEF effects have been observed for both $CeAl_2$ and SmSb in the surface acoustic wave velocity and the magnetoacoustic analogue of the Voigt birefringence effect has been also studied, see Lingner and Lüthi (1981). All these effects could be accounted for quantitatively by calculating renormalized elastic constants in the equation for the surface acoustic wave velocities.

One can expect, in analogy to sound waves, similar effects for optical phonons. The splitting of the E_g optical phonons in $Ce_xLa_{1-x}F_3$ using Raman scattering has indeed been observed for the Cotton–Mouton, Voigt and the Faraday geometries (Ahrens and Schaack 1980).

2.6.4. *Rotational invariance effects*

All previous discussions were restricted to magnetoelastic interactions that are of first order in the strain ε_{kl} only. Contributions of the rotational part ω_{kl} in the total deformation tensor [eq. (6)] to the interactions were neglected. The meaning of the rotational part is illustrated in fig. 27 for the case of transverse c_{44} modes in cubic crystals. Its neglect in the interaction between the 4f ions and the lattice leads to a magnetoelastic Hamiltonian which is not rotationally invariant. This invariance requires that the interaction of a magnetic ion with angular momentum $\boldsymbol{J}$, with the strained and rotated crystal is equal to the interaction of the purely strained crystal with the ion whose $\boldsymbol{J}$ has been rotated in the reverse sense. For $\boldsymbol{B} = 0$, neglect of rotational contributions has no consequences because

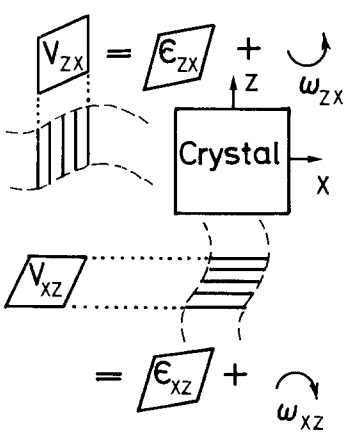

Fig. 27. Contributions to the total deformation tensor V_{kl} for two transverse c_{44} modes propagating along a cubic axis. The rotational part ω_{kl} has opposite sign for the (k_z, u_x) and (k_x, u_z) modes ($\omega_{zx} = -\omega_{xz}$).

in the long-wavelength limit the rotational tensor describes homogeneous rotations of the crystal which cannot influence the elastic constants. For a finite magnetic field, however, the quadrupolar moments are 'pinned' by the field and cannot rotate freely with the crystal, therefore the rotational contributions in the interaction should also influence the elastic constants. Rotationally invariant effects for sound propagation were first discussed by Melcher (1970, 1972). The complete theory of rotational effects has been developed by Dohm and Fulde (1975) who showed that it is necessary to include all terms up to second order in ω_{kl} in the interaction Hamiltonian. A restriction to linear rotational terms would lead to spurious effects in the elastic constants at zero field.

Here we concentrate on the discussion of rotational effects for the two c_{44} modes (u_x, k_z) and (u_z, k_x) which should still be degenerate in an external field $\boldsymbol{B} = B\hat{\boldsymbol{z}}$, if the interaction has only strain contributions. To derive the rotational interaction part we use an elegant method due to Goto et al. (1986), starting from the rotational invariance principle as formulated above

$$H(\boldsymbol{J}, \boldsymbol{\varepsilon}, \boldsymbol{\omega}) = H(\boldsymbol{D}^{-1}\boldsymbol{J}, \boldsymbol{\varepsilon}) . \tag{56}$$

Here $\boldsymbol{D}$ is the matrix for a rotation around $\hat{\boldsymbol{y}}$ by an angle ω_{zx}. Its components are $D_{xx} = D_{zz} = 1$ and $D_{zx} = -D_{xz} = \omega_{zx}$. The effect of this rotation can be described by a unitary operator $R(\omega_{zx}) = \exp(\mathrm{i}\omega_{zx}J_y)$ which acts on the CEF states. Then

$$H(\boldsymbol{J}, \boldsymbol{\varepsilon}, \boldsymbol{\omega}) = R^{+}H(\boldsymbol{J}, \boldsymbol{\varepsilon})R = R^{+}(H_{\mathrm{CEF}} + H_{\mathrm{str}})R . \tag{57}$$

Here

$$H_{\mathrm{str}} = -g_{\Gamma_5} \sum_i \varepsilon_{zx}(i) O_{zx}(i) \tag{58}$$

is the first-order strain contribution to H_{me} used previously. Expansion of eq. (57) up to second order in the rotation leads to a total magnetoelastic Hamiltonian $H_{\mathrm{me}} = H_{\mathrm{str}} + H_{\mathrm{rot}}$ with

$$H_{\mathrm{rot}} = -\sum_i [\omega_{zx}\Lambda_{zx} + g_{\Gamma_5}\varepsilon_{zx}\omega_{zx}\Omega_{zx} + \lambda_{zx}\omega_{zx}^2]_i , \tag{59}$$

and

$$\begin{aligned}
\Lambda_{zx} &= \mathrm{i}[J_y, H_{\mathrm{CEF}}] = 20B_4[(J_z^2 - J_x^2)(J_xJ_z + J_zJ_x) + (J_xJ_z + J_zJ_x)(J_z^2 - J_x^2)] , \\
\lambda_{zx} &= \tfrac{1}{2}\mathrm{i}[J_y, \Lambda_{zx}] = 40B_4[(J_x^2 - J_z^2)^2 - (J_xJ_z + J_zJ_x)^2] , \\
\Omega_{zx} &= \mathrm{i}[J_y, O_{zx}] = 2(J_z^2 - J_x^2) .
\end{aligned} \tag{60}$$

The explicit expressions are valid for a CEF potential

$$H_{\mathrm{CEF}} = -20B_4 \sum_{k \neq l} J_k^2 J_l^2 , \quad k, l = x, y, z ,$$

which has only fourth-order terms as, e.g., in Ce compounds. Note that H_{rot} does not contain any new coupling constants, all terms are determined by the strain coupling g_{Γ_5} and the CEF parameter B_4.

The effect of $H_{me} = H_{str} + H_{rot}$ on the elastic constants c_{zx} and c_{xz} for the modes (u_z, k_x) and (u_x, k_z) can be obtained in the usual way by Green's function techniques (Dohm and Fulde 1975) or calculation of the free energy as explained in sect. 2.3.1. (Wang and Lüthi 1977). The last term in H_{rot} together with H_{str} renormalizes both c_{zx} and c_{xz} by the same amount, however, the terms in H_{rot} which are linear in $\omega_{zx} = -\omega_{xz}$ lead to a correction equal in magnitude but opposite in sign for both constants. This is due to the opposite sense of rotation with respect to the field direction in both modes, see fig. 27. The difference is given by

$$\frac{c_{zx} - c_{xz}}{c_0} = \frac{N}{8c_0} (\chi_-(B, T) - \chi_+(B, T) + 4g_{\Gamma_5}\langle \Omega_{zx}\rangle) , \tag{61}$$

where $\chi_\pm$ are quadrupolar susceptibilities of the operators $O_\pm = g_{\Gamma_5} O_{zx} \pm \Lambda_{zx}$, respectively, and $\langle \Omega_{zx}\rangle$ denotes the thermal average. For zero field $\chi_+ = \chi_-$ and $\langle \Omega_{zx}\rangle = 0$, leading to identical $c_{xz} = c_{zx} = c_{44}$.

Furthermore, looking at c_{zx} and c_{xz} directly one may show (Dohm and Fulde 1975) that for $B = 0$ the contributions of the first term $\omega_{zx}\Lambda_{zx}$ and the last term $\lambda_{zx}\omega_{zx}^2$ cancel exactly. This shows the necessity of going beyond the linear approximation in ω_{kl} for a consistent theory without spurious rotational effects for zero field.

Sound propagation experiments testing rotational invariance were first performed by Melcher (1970, 1972) in MnF_2 at low temperatures in the antiferromagnetic state and later on for RVO_4 by Bonsall and Melcher (1976) and Goto et al. (1986), and in CuPt alloys by Rouchy et al. (1980). In intermetallic R compounds such experiments have been carried out in TmSb and Pr_3Te_4 (Wang and Lüthi 1977) and in $CeAl_2$ (Lüthi and Lingner 1979). For $CeAl_2$, c_{44} is given in fig. 24 together with a calculation based on eq. (61). Because of the vicinity of the magnetic phase transition ($T_N = 3.8$ K, experiment performed at 4.2 K) the agreement between theory and experiment is not complete.

A particularly clear example is TmSb, see Wang and Lüthi (1977). As pointed out in sect. 2.4 the single-ion picture is a very good approximation for this compound. In addition, crystal field parameters and magnetoelastic coupling constants have been experimentally determined (see, e.g., fig. 7). Therefore, no adjustable parameters are taken for a comparison of theory and experiment in fig. 28. The discrepancy between theory and experiment of about 20% is therefore considered to be very good. However, two words of caution are in place: as pointed out by Dohm (1976) second-order strain interactions are as important as rotational interactions and may also contribute to the strain susceptibilities. They can only be estimated using point-charge calculations. In addition in TmSb the B_6 terms in the CEF Hamiltonian are small but not negligible. This means that similar but more complicated terms than those in eq. (59) had to be included in the strain susceptibilities. They could well make up for the 20% difference observed in fig. 28.

In addition to the c_{44} mode discussed here and shown in figs. 24 and 28, rotationally invariant effects can also exist for the $c_{11} - c_{12}$ mode, Wang and Lüthi

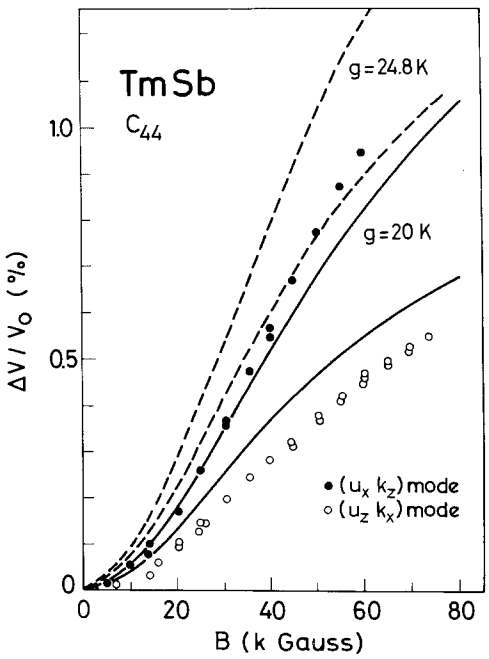

Fig. 28. Relative sound velocity changes for the c_{44} mode in TmSb at $T = 2$ K in high magnetic fields, indicating the magnetoelastic rotationally invariant effect (Wang and Lüthi 1977).

(1977). Again as in the case of magnetoacoustic birefringence, surface acoustic waves (SAW) can also be used to test the rotationally invariant magnetoelastic interaction. In $CeAl_2$ this effect for SAW was observed and found to be of the same order of magnitude as in the bulk case, see Lingner and Lüthi (1981) and Camley and Fulde (1981).

For ferromagnets, theories of rotational invariance effects have been developed (Southern and Goodings 1973, Rouchy and du Trémolet de Lacheisserie 1979). However, the situation is much more complicated than in paramagnets, see, e.g., Rouchy and du Trémolet de Lacheisserie (1979). Here one has an additional coupling of sound waves to spin waves and morphic effects due to the magnetization dependence on the crystallographic axis. One must also be sure to have a single-domain state. In ferromagnetic rare-earth metals such an investigation has not been performed in any detail. The only complete study of a ferromagnetic metal has been carried out for a Co–Pt alloy, see Rouchy et al. (1980).

Recently, the influence of dipolar interactions on rotational invariance effects has been studied by Jensen (1988). It was found that the agreement between theory and experiment for TmSb (fig. 28) is improved.

2.7. *Coupling of high-frequency phonons and CEF excitations*

The magnetoelastic anomalies in sound velocities as discussed in previous sections are only the long-wavelength limit of 4f electron–phonon coupling effects. Very interesting consequences of this coupling also occur for high-

frequency phonons, especially when they are in resonance with inelastic CEF transitions. The latter are, in addition, coupled by effective dipolar (exchange) and quadrupolar interactions and therefore form magnetic or quadrupolar "exciton" bands, respectively (for a review see Fulde and Loewenhaupt 1986). If the magnetoelastic coupling is not too strong one may observe "mixed-mode" excitations of (acoustic) phonons and excitons in the region of q-space where their dispersion curves cross. In inelastic neutron scattering experiments this is observed as an "anticrossing" or repulsion of phonon and exciton bands:

(i) The mixing of acoustic phonons with quadrupolar excitons has been observed in the insulating materials $PrAlO_3$ (Birgeneau et al. 1974). $TbVO_4$ (Hutchings et al. 1975) and $TmVO_4$ (Kjems et al. 1975). In the latter case an external magnetic field is needed to give a finite energy to the quadrupolar excitation. In intermetallic R compounds this type of mode mixing has never been observed directly. Indirect evidence for it has been claimed by Aksenov et al. (1983) in $PrNi_5$.

(ii) Mixing of phonons with magnetic excitons in an external magnetic field or in the molecular field of a ferromagnetically ordered compound. Without such a field, mixing cannot occur [in the random-phase approximation (RPA)] due to time reversal invariance.

Experimentally this has been found in dhcp Pr (Houmann et al. 1979, Jensen 1976) and $PrAl_2$ (Purwins et al. 1976). Various theoretical methods have been used to describe mixed-mode excitations: pseudospon techniques, (Elliott et al. 1972), diagrammatic methods (Thalmeier and Fulde 1975) and equation of motion techniques (Morin et al. 1980b, Aksenov et al. 1981). In the RPA all these methods lead to mixed excitations of infinite lifetime. Lifetime effects can be included in a phenomenological manner, see, e.g., Becker et al. (1981). For a microscopic treatment of linewidth effects beyond RPA the projection operator technique is more suitable (Huggins et al. 1984).

In this RPA mixed-mode picture one assumes that the self-energy corrections of local CEF excitations due to the interaction with phonons are simply constants. The shifted CEF excitations then turn into exciton bands caused by interionic interactions. However, if the interaction with phonons is very strong the dynamical nature of the self-energy may no longer be neglected and it may lead to a completely different excitation spectrum consisting of bound states between CEF excitations and phonons. Such a strong coupling excitation spectrum was indeed experimentally observed in $CeAl_2$ and also in its diluted alloys $Ce_xLa_{1-x}Al_2$ with $x \geq 0.07$ (Loewenhaupt et al. (1979). We shall discuss both mixed modes and bound states in the following.

2.7.1. *Mixed modes: phonons and excitons*

The quadrupolar exciton dispersion $\omega_Q(q)$ is given by the poles of the dynamical susceptibility $\chi_\Gamma(q, \omega)$ of the system of R ions coupled by quadrupolar interactions. Its theoretical derivations by diagrammatic methods is given in appendix A. Using eq. (A7) as obtained from fig. 59 one has for only one $K_\Gamma(q)$:

$$1 - K_\Gamma(q)\chi_\Gamma(q, \omega_Q(q)) = 0 . \tag{62}$$

For a two-level system Γ_α, Γ_β (like Γ_1, Γ_5 etc.) with non-vanishing quadrupolar matrix elements O^Γ_{nm} $(n, m \in \Gamma_\alpha, \Gamma_\beta)$ one obtains an exciton dispersion

$$\omega_Q^2(q) = \Delta^2\left(1 - \frac{2M_Q^2 K_\Gamma(q)}{\Delta} F(T)\right), \tag{63}$$

where $F(T) = p_\alpha(T) - p_\beta(T)$ is the thermal occupation [eq. (34)] difference of both levels and $\Delta = E_\beta - E_\alpha$, their CEF energy difference. For a singlet–singlet system one would have

$$F(T) = \tanh(\Delta/2T) .$$

Furthermore,

$$M_Q^2 = \sum_{n,m} |O^\Gamma_{nm}|^2$$

is the total Γ_α–Γ_β quadrupolar transition strength. As already mentioned in sect. 2.2.2, quadrupolar excitons unlike their magnetic counterparts cannot be observed directly by inelastic neutron scattering experiments because the scattering cross-section is determined by the dipolar dynamic susceptibility if one neglects magnetic octupole scattering contributions (Levy and Trammell 1977). However, if they form mixed-mode excitations with phonons of an appropriate polarization λ that produce local distortions of Γ-symmetry they should be visible in the phonon cross-section near the crossing point q_0 where $\omega_Q(q_0) = \omega_{q_0\lambda}$ (phonon frequency). The mixed-mode dispersions are given by the poles of $D(q, \lambda, \omega)$ in eq. (A10). For the two-level system above one obtains the two mixed-mode branches $\omega_\pm(q)$ as solutions of

$$(\omega^2 - \omega_{q\lambda}^2)(\omega^2 - \omega_Q^2(q)) = 4\Delta\omega_{q\lambda}|\xi_\Gamma(q, \lambda)|^2 M_Q^2 F(T) . \tag{64}$$

Here $\xi_\Gamma(q\lambda)$ is the coupling in the magnetoelastic Hamiltonian, eq. (14). At the crossing point $q = q_0$ the mixed modes show a splitting

$$\omega_+^2 - \omega_-^2 = 4|\xi_\Gamma(q_c\lambda)|M_Q[\Delta\omega_{q_0\lambda}F(T)]^{1/2} .$$

As mentioned previously this mixing of phonons and quadrupolar excitons due to magnetoelastic interactions has so far been found only in insulators but not in intermetallic R compounds.

The experimental situation is more favourable if we consider magnetic exciton bands. They result from magnetic CEF excitations coupled by an interionic (Heisenberg) exchange

$$H_{ex} = -\tfrac{1}{2}\sum_{ij} J_{ex}(i, j)\, J(i)\cdot J(j) . \tag{65}$$

In a completely analogous way to fig. 59 one obtains an RPA expression for the dynamic magnetic susceptibility

$$\chi_M(\boldsymbol{q}, \omega) = \frac{v(\omega)}{1 - I(\boldsymbol{q})v(\omega)}\,, \tag{66}$$

where

$$I(\boldsymbol{q}) = N_s^{-1} \sum_{ij} J_{ex}(i, j) \exp[i\boldsymbol{q} \cdot (\boldsymbol{R}_i - \boldsymbol{R}_j)]$$

and $v(\omega)$ is the dipolar single-ion susceptibility which is the equivalent of $\chi_\Gamma(\omega)$ in eq. (38) but now with dipolar matrix elements. For a two-level system Γ_α, Γ_β with non-vanishing matrix elements (e.g., Γ_1, Γ_4) one has ($v(\omega) = v_{zz}(\omega)$)

$$v(\omega) = \frac{2M^2\Delta}{\omega^2 - \Delta^2} F(T)\,, \tag{67}$$

with

$$M^2 = \sum_{nm} |J_z^{nm}|^2$$

and Δ, $F(T)$ as before. The magnetic exciton dispersion $\omega_M(\boldsymbol{q})$ is obtained from the poles of eq. (66) and is the same as in eq. (63) with $M_Q^2 K_\Gamma(\boldsymbol{q})$ replaced by $M^2 I(\boldsymbol{q})$. For zero magnetic field there is no coupling of phonons and the (in this case threefold degenerate) magnetic excitons within the RPA approximation. This situation is shown in fig. 29 for the Γ_1, Γ_4 model by broken lines. However, if an external field is applied or if a molecular field below a ferromagnetic phase transition is present a coupling is induced via susceptibilities of mixed dipolar–quadrupolar character (Thalmeier and Fulde 1975), e.g.,

$$w_\Gamma^z(\omega) = \sum_{E_n \neq E_m} \frac{O_{nm}^\Gamma J_{mn}^z}{\omega - (E_n - E_m) + i\eta} (p_n - p_m)\,, \qquad \omega \neq 0\,, \tag{68}$$

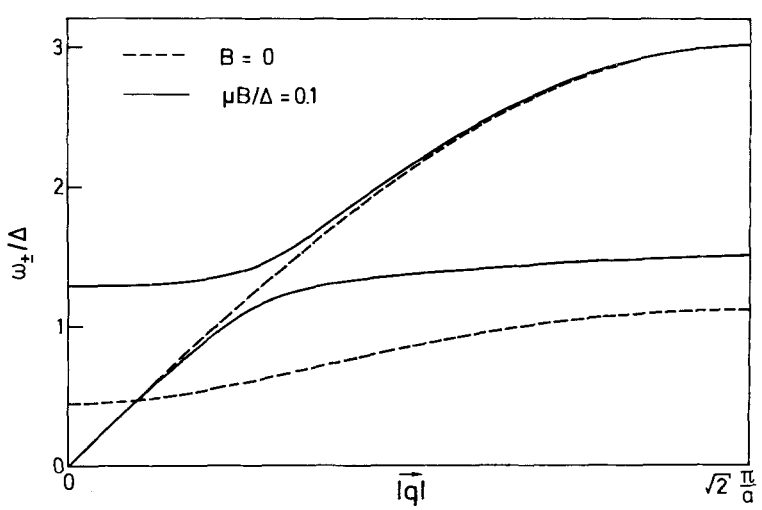

Fig. 29. Mixing of Γ_1 and Γ_4 magnetic excitons and the [101] transverse acoustic phonons in a magnetic field. A model parameter $\omega(q_0)/\Delta = 3$ where $q_0 = \sqrt{2}\pi/a$ was used (Thalmeier and Fulde 1975).

which is zero for zero field because $\boldsymbol{J}$ changes sign under time reversal whereas O_Γ does not. Now $|n\rangle$ and E_n are the eigenstates and energies of the mean-field Hamiltonian including H_{CEF} and a Zeeman term due to the molecular field $g\mu_{\mathrm{B}}B + I(0)\langle J_z\rangle$. In the Γ_1, Γ_4 model this field splits the three magnetic exciton branches, one of them mixes with the phonons and shows an anticrossing due to a non-vanishing contribution of the order of $w_\Gamma^z(\omega)^2[1 - I(\boldsymbol{g})v(\omega)]^{-1}$ in the phonon self-energy. One obtains a mixed-mode equation

$$[\omega^2 - \omega_{q\lambda}^2][\omega^2 - \omega_{\mathrm{M}}^2(q)] = 4\,\Delta\omega_{q\lambda}|\xi_\Gamma(q\lambda)|^2 M^2 \tilde{M}_{\mathrm{Q}}^2 G(B, T)\,, \tag{69}$$

where $G(B, T) \sim B^2$ for small ($\mu_{\mathrm{B}}B \ll \Delta$) fields and $\tilde{M}_{\mathrm{Q}} = O_\Gamma^{nn}$ is a diagonal quadrupolar matrix element for one ($n = 2$) of the three Γ_4 states. The mode mixing described by this equation thus occurs via field-induced quadrupolar matrix elements between Γ_1, Γ_4 states which have only dipolar matrix elements in zero field. The anticrossing of acoustic phonons and magnetic excitons is shown in fig. 29 for the Γ_1, Γ_4 model. The splitting increases linearly with B for small fields.

Experimentally this effect has been found in dhcp Pr (Houmann et al. 1979) and in $PrAl_2$ (Purwins et al. 1976). The latter has cubic site symmetry and the ground and first excited states are Γ_3 (0 K) and Γ_4 (27.4 K). It orders ferromagnetically at $T_{\mathrm{c}} = 33$ K. At low temperatures ($T \ll T_{\mathrm{c}}$) only three of the field-split Γ_3–Γ_4 magnetic excitons are seen (fig. 30) and those with $J_\pm$ polarization show a strong anti-crossing effect with a transverse acoustic phonon mode in the [001] direction. Detailed model calculations for this mixed-mode spectrum were performed by Aksenov et al. (1981) using an equation of motion approach.

2.7.2. *Bound state of CEF excitations and phonons*

In compounds with weak interionic exchange the magnetic exciton bands are quite flat and one observes essentially local excitations between CEF states in

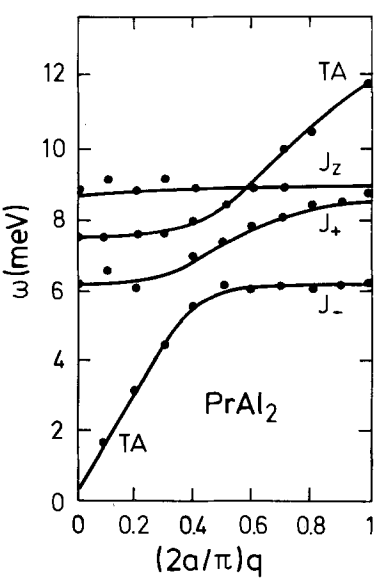

Fig. 30. Mixed-mode dispersions in ferromagnetic $PrAl_2$ at $T = 4.4$ K for the [001] direction. Full points represent experimental data from Purwins et al (1976), full curves are calculations by Aksenov et al. (1981), TA stands for transverse acoustic phonon, and J_z and $J_\pm$ are exciton branches with different polarizations.

inelastic neutron scattering experiments that allow the determination of the energies and symmetries of those states. The latter can be classified according to the representations of R-site symmetry which gives the possible number and types of multiplets for any R ion. With the help of LLW tables this can be done quite uniquely for any cubic system. Surprisingly this was not possible for the intermetallic compound $CeAl_2$ and some of its alloys. It showed a CEF excitation spectrum which was apparently incompatible with the tetrahedral site symmetry of Ce^{3+} ions, see Loewenhaupt et al. (1979a). It was found that this is due to a very large 4f electron–phonon coupling which leads to bound states between a CEF excitation and phonons (Thalmeier and Fulde 1982, Thalmeier 1984). Contrary to the systems discussed in sect. 2.7.1 the dynamical nature of the magnetoelastic self-energy of CEF excitations plays an essential role in this compound.

The intermetallic Laves phase $CeAl_2$ has a unit cell as shown in fig. 31. The Ce ions are in an almost integer 3+ valence state with $J = \frac{5}{2}$. Due to the tetrahedral site symmetry this should be split into a Γ_7 doublet and a Γ_8 quartet by the CEF. From the c_{44} elastic constant softening (Lüthi and Lingner 1979) a splitting $\Gamma_7(0) - \Gamma_8(\Delta)$ of $\Delta \simeq 100\,\mathrm{K}$ was deduced for the Ce^{3+} 4f states. However, inelastic neutron scattering, Loewenhaupt et al. (1979), revealed a striking anomaly: instead of a single $\Gamma_7 \rightarrow \Gamma_8$ transition in the magnetic cross-section, two clearly separated peaks at $\Delta_1 = 100\text{–}110\,\mathrm{K}$ and $\Delta_2 = 180\text{–}200\,\mathrm{K}$ have been found (fig. 32a). This seems to be in conflict with the cubic symmetry of the compound. However, a splitting of the Γ_8 quartet into two doublets due to a static lattice distortion was ruled out by X-ray diffraction, which showed that $CeAl_2$ is cubic with an accuracy of $\Delta a/a \simeq 10^{-5}$ (Steglich et al. 1979). The following experimental facts point to the origin of this anomalous magnetic excitation spectrum:

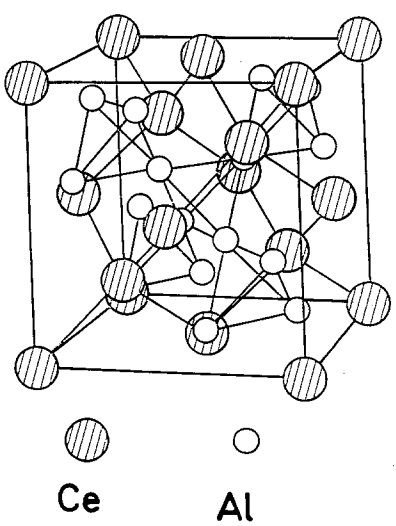

Fig. 31. Conventional cubic unit cell of RAl_2. The R ions form a diamond-type sublattice. The Al ions are placed on the corners of tetrahedrons. For $CeAl_2$ the lattice constant is $a = 8.062$ Å.

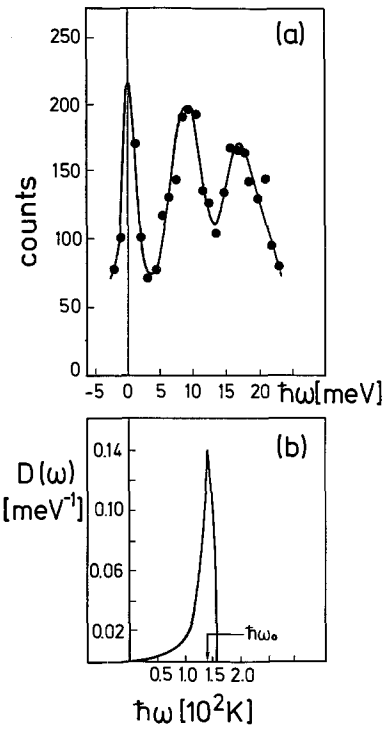

Fig. 32. (a) Magnetic scattering rate as a function of energy transfer in $CeAl_2$ at $T = 60$ K (Loewenhaupt et al. 1979a). (b) Phonon density of states of the lowest LA, TA and LO, TO modes in $CeAl_2$ at room temperature (Reichardt and Nücker 1984). Average energy $\hbar\omega_0 = 140$ K.

(i) The total intensity I_{in} of both inelastic lines has a value (relative to the quasielastic intensity I_{el}) that is equal to the value $I_{in}/I_{el} = 3.2$ expected for a conventional Γ_7–Γ_8 system. The Q-dependence of the scattering intensity is given by the magnetic form factor $F(Q)$.

(ii) Both inelastic peaks show only a weak dispersion. Recently this has been reanalyzed by polarized neutron scattering, Loewenhaupt et al. (1987), with the conclusion that interionic exchange is responsible for this dispersion.

(iii) The double-peak structure of the excitation spectrum does not change qualitatively in the alloys $La_{1-x}Ce_xAl_2$ ($x > 0.06$) and $Sc_{1-x}Ce_xAl_2$ ($x > 0.6$) where Ce is replaced by non-magnetic ions.

These observations suggest that one still observes localized excitations which can be understood within a single-ion picture. Neutron scattering experiments by Reichardt and Nücker (1984) gave the clue to the origin of the anomalous magnetic excitation spectrum. They showed that the phonon density of states at room temperature has a sharp peak at an energy $\hbar\omega_0 \simeq 140$ K (1 meV = 11.605 K), see fig. 32b. These phonons correspond to the vibrations of the heavy diamond-type Ce sublattice (fig. 31). Figure 32 shows that the sharp phonon peak lies just in between the inelastic magnetic excitations at Δ_1 and Δ_2. It should be mentioned that phonon and magnetic contributions to the total cross-section can be separated by the different Q (momentum transfer) dependences. If we assume

$\Delta = \frac{1}{2}(\Delta_1 + \Delta_2) \simeq 140\,\mathrm{K}$ for the original unperturbed CEF gap, we see from fig. 32b that in $CeAl_2$ the Γ_7–Γ_8 excitation is degenerate with a phonon band of width $\hbar\omega_b \simeq 40\,\mathrm{K}$ centered at $\hbar\omega_0 = 140\,\mathrm{K}$. A strong 'magnetoelastic' coupling between these modes then leads to the excitation spectrum observed in $CeAl_2$ which we discuss now.

The phonons of interest correspond to vibrations of the diamond-type Ce sublattice, i.e., three acoustic and three optical branches. These branches are very flat and almost degenerate near the zone boundary and thus produce a sharp peak in the phonon density of states at $\hbar\omega_0$ of width $\hbar\omega_b$. The magnetoelastic interaction of these phonon modes $(\boldsymbol{q}\lambda)$(λ is the branch index, $\boldsymbol{q}$ is the wavevector) can be decomposed into contributions transforming like the representations of the tetrahedral site group T_d. Point-charge calculations (Cullen and Clark 1977) and ultrasonic experiments (Lüthi and Lingner 1979) suggest that only Γ_5 (T_2)-type distortions are important. Then the model Hamiltonian is given by $H = H_0 + H_{me}$ with

$$H_0 = \sum_{\alpha r} E_\alpha |\Gamma_\alpha^r\rangle\langle\Gamma_\alpha^r| + \sum_{\boldsymbol{q}\lambda} \hbar\omega_{\boldsymbol{q}\lambda}(a_{\boldsymbol{q}\lambda}^+ a_{\boldsymbol{q}\lambda} + \tfrac{1}{2}) ,$$

$$H_{me} = -\sum_{\substack{\boldsymbol{q}\lambda s \\ i\tau}} g_s(\boldsymbol{q}\lambda, \tau)(a_{\boldsymbol{q}\lambda} + a_{\boldsymbol{q}\lambda}^+) O_s(\boldsymbol{R}_{i\tau}) \exp(-\mathrm{i}\boldsymbol{q}\cdot\boldsymbol{R}_{i\tau}) . \tag{70}$$

In H_0, α denotes the multiplet, r the degeneracy index and $E_\alpha^r = E_\alpha$ = multiplet energy ($E_7 = 0$, $E_8 = \Delta$). In H_{me} $\boldsymbol{R}_{i\tau}$ are the Ce^{3+} sites, g_s are the coupling constants and $\{O_s, s = 1, 2, 3\}$ are quadrupolar operators transforming like a Γ_5 triplet, $O_s = O_{\Gamma_5}^s$ ($s = yz, xz, xy$). The O_s [eq. (8)] describe which CEF transitions couple to phonons; the most important are the Γ_7–Γ_8 transitions which are characterized by a matrix element $\gamma_0 = (40)^{1/2}$.

We now consider the influence of this coupling on the CEF excitation spectrum. For this purpose we use Abrikosov's technique as described in appendix A. The renormalized pseudofermion Green's function asociated with any CEF state $|n\rangle = |\Gamma_\alpha^r\rangle$ is given by the Dyson equation of fig. 33. This leads to (basis index τ suppressed)

$$G(i, n, \omega_l) = [\mathrm{i}\omega_l - \lambda_i - E_n - \Sigma_c(i, n, \omega_l)]^{-1} , \tag{71}$$

in which Σ_c is the second-order (with respect to H_{me}) self-energy of a CEF pseudofermion state $|n\rangle$ which is due to the virtual excitation of phonons with arbitrary $(\boldsymbol{q}\lambda)$ and a simultaneous virtual transition $|n\rangle \leftrightarrow |m\rangle$. This formation of a virtual 'phonon cloud' occurs independently at any site i in the approximation of fig. 33. One has

$$\Sigma_c(i, n, \omega) = \beta^{-1} \sum_{\substack{m\omega' \\ \boldsymbol{q}\lambda, s}} |g_s(\boldsymbol{q}\lambda)|^2 |O_s^{nm}|^2 G_0(i, m, \omega') D_0(\boldsymbol{q}\lambda, \omega - \omega') . \tag{72}$$

Explicit calculation and analytic contintuation leads to (for $k_B T \ll \hbar\omega_0$):

$$\bar{\Sigma}_c(n, \omega) = \sum_{\boldsymbol{q}\lambda, sm} \frac{|g_s(\boldsymbol{q}\lambda)|^2 |O_{nm}^s|^2}{\omega - E_m - \omega_{\boldsymbol{q}\lambda} + \mathrm{i}\eta} ,$$

$$\bar{G}(n, \omega) = (\omega - E_n - \bar{\Sigma}_c(n, \omega) + \mathrm{i}\eta)^{-1} , \tag{73}$$

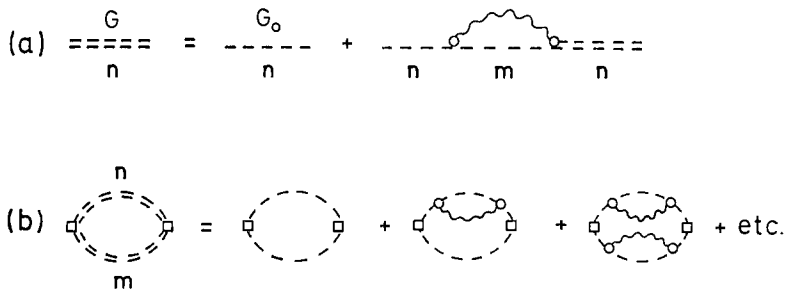

Fig. 33. (a) Dyson equation for the pseudofermion propagators of CEF states n, m (broken lines). Phonons are indicated by wavy lines. Open circles represent the magnetoelastic interaction vertex. (b) Bubble diagram for the dynamical magnetic susceptibility using renormalized propagators. Open squares represent the dipolar operator $\boldsymbol{J}$.

where we have defined $\bar{G}(n, \omega) = G(n, \omega + \lambda)$ and $\bar{\Sigma}_c(n, \omega) = \Sigma_c(n, \omega + \lambda)$. The site index has now been deleted. For zero coupling ($\bar{\Sigma}_c = 0$) $\bar{G}$ has poles at the unperturbed CEF energies E_n ($E_7 = 0$, $E_8 = \Delta$), i.e., its spectral function

$$S_c(n, \omega) = -\pi \operatorname{Im} \bar{G}(n, \omega)$$

is a δ-function at E_n. If H_{me} is included a finite self-energy will change this spectrum. For this purpose we assume an average coupling constant $g_s(\boldsymbol{q}\lambda) \to g_0$ in eq. (73). Then one obtains

$$\begin{aligned} \bar{\Sigma}_c(n, \omega) &= g_0^2 \sum_m \left(\sum_s |O_s^{nm}|^2 \right) H(\omega - E_m) \\ &= \bar{\Sigma}_1(n, \omega) + \mathrm{i}\bar{\Sigma}_2(n, \omega) , \end{aligned} \tag{74}$$

where

$$H(\omega) = H_1(\omega) + \mathrm{i}H_2(\omega) = \mathrm{P} \int \frac{D(\omega')}{\omega - \omega'} \, \mathrm{d}\omega' - \mathrm{i}\pi D(\omega) . \tag{75}$$

The real part $H_1(\omega)$ is the Hilbert transform of the phonon density of states which has an approximately triangular shape with the center at $\hbar\omega_0 = 140\,\mathrm{K}$ and a phonon band width of $\hbar\omega_b = 40\,\mathrm{K}$. The renormalized energies of CEF sates are then given by the solutions of

$$\omega - E_n - \bar{\Sigma}_1(n, \omega) = 0 . \tag{76}$$

If $\bar{\Sigma}_1(n, \omega)$ is small and only weakly frequency dependent around $\omega \simeq E_n$ the CEF energy is simply shifted by a small amount. This is the case for the Γ_7 state.

The more interesting case is the Γ_8 Green's function because the resonant ω-behaviour of $\bar{\Sigma}(\Gamma_8, \omega)$, which is due to virtual phonon emission, now becomes important. One has

$$g_0^{-2} \bar{\Sigma}(\Gamma_8, \omega) \simeq \gamma_0^2 H_1(\omega) - \mathrm{i}\pi\gamma_0^2 D(\omega) . \tag{77}$$

This leads to renormalized energies given by

$$\alpha^{-2}(\omega - \Delta) = H_1(\omega) , \qquad \alpha^2 = g_0^2 \gamma_0^2 . \tag{78}$$

The solutions of this equation can be found graphically as shown by Thalmeier (1984). Two cases are possible:

(i) For weak coupling (small) one has only a shifted ($\Delta' = \Delta + \alpha^2 H(\Delta)$) and broadened ($\Gamma \simeq \alpha^2 D(\Delta'))$ Γ_8 level.

(ii) For a sufficiently strong coupling (α^2 large) and if the bare level Δ is degenerate with phonons two solutions $\Delta_{1,2}$ exist above and below the phonon continuum. These solutions corresponds to a bound state (Δ_2) and antibound state (Δ_1) of a $\Gamma_7 \to \Gamma_8$ excitation and the phonons with $\omega_1 < \omega < \omega_2$, which we call $\tilde{\Gamma}_{82}$ and $\tilde{\Gamma}_{81}$ respectively. They lead to pole contributions in the renormalized Green's function according to

$$\bar{G}_b(\Gamma_8, \omega) = \frac{Z_1}{\omega - \Delta_1 + i\eta} + \frac{Z_2}{\omega - \Delta_2 + i\eta}\,, \tag{79}$$

where $Z_{1,2} = |1 - \alpha^2 H_1'(\Delta_{1,2})|^2$ are the weights of bound and antibound states poles. In the perfectly resonant case where $\Delta = \hbar\omega_0$ it follows that $Z_1 = Z_2$. Furthermore, $Z_1 + Z_2 < 1$ because part of the spectral density is associated with a cut of $\bar{G}(\Gamma_8, z)$ in the region where $D(\omega) > 0$. The coupling strength α must exceed a critical value in order that one has (anti)-bound state solutions. One obtains

$$\alpha_c = g_0^c \gamma_0 = \lambda \omega_b \left(1 + 2\left|\frac{\omega_0 - \Delta}{\omega_b}\right|\right)^{1/2},$$

$$\lambda = (2 \ln 2)^{1/2}/2\,, \qquad \gamma_0 = \sqrt{40}\,. \tag{80}$$

It is also useful to consider the dispersionless limit $\hbar\omega_b \to 0$ where CEF transitions couple to a local oscillator mode of unique energy $\hbar\omega_0$. In this case

$$H_1(\omega) = \mathrm{P} \int \frac{D(\omega')}{\omega - \omega'}\, \mathrm{d}\omega' = (\omega - \omega_0)^{-1}\,, \tag{81}$$

and the solutions of eq. (78) are given by

$$\Delta_{1,2} = \tfrac{1}{2}(\Delta + \hbar\omega_0) \pm [\tfrac{1}{4}(\Delta - \hbar\omega_0)^2 + g_0^2 \gamma_0^2]^{1/2}\,. \tag{82}$$

Furthermore, $Z_{1,2} \to \frac{1}{2}$ for $\hbar\omega_b \to 0$ and $\Delta = \hbar\omega_0$.

These bound states poles directly show up in the magnetic cross-section and explain the double-peak structure of fig. 32a. According to standard theory the magnetic cross-section is of the order of $F(Q^2)S(\omega)$ where $F(Q)$ is the 4f form factor and $S(\omega)$ the dynamic structure factor:

$$S(\omega) = (1 - \mathrm{e}^{-\beta\omega})^{-1}\, \mathrm{Im}\, v(\omega)$$

$$v(\omega) = \int_0^\infty \langle [J_z(t), J_z] \rangle\, \mathrm{e}^{\mathrm{i}(\omega + \mathrm{i}\eta)t}\,, \quad \eta \to 0\,. \tag{83}$$

The dynamic magnetic susceptibility can in principle be obtained from the renormalized $G(n, \omega)$ by the diagram shown in fig. 33b which leads to ($M_{nm} = \langle n|J_z|m\rangle$)

$$v(\omega) = -\beta^{-1} \sum_{\substack{nm \\ \omega'_\ell}} |M_{nm}|^2 G(m, \omega'_\ell) G(n, \omega_\ell + \omega'_\ell) \,. \tag{84}$$

This can easily be computed if one uses the pole approximation of eq. (79). One obtains δ-peaks in $\mathrm{Im}\, v(\omega)$ at $\omega = 0$, Δ_1, Δ_2 with respective intensities $|M_{77}|^2$, $Z_1|M_{78}|^2$ and $Z_2|M_{78}|^2$ at low temperatures (summation over degeneracies implied). If $\hbar\omega_0 \simeq \Delta$ and g_0 is appreciably larger than the minimum g_0^c, which is the case for $CeAl_2$, on has $Z_1 \simeq Z_2 \simeq \frac{1}{2}$. This explains naturally the observed intensity ratio because

$$\frac{I_{\mathrm{in}}}{I_{\mathrm{el}}} = \frac{Z_1|M_{78}|^2 + Z_2|M_{78}|^2}{|M_{77}|^2} \simeq \frac{|M_{78}|^2}{|M_{77}|^2} = 3.2 \,.$$

In reality the peaks in $S(\omega)$ are broadened by an exchange interaction of strength I_{ex} with conduction electrons. By including this effect $S(\omega)$ has been calculated within the dispersionless model (Thalmeier and Fulde 1982). The result is shown in fig. 34 for the symmetrical case $\hbar\omega_0 = \Delta$. The adjustable parameters are g_0 and I_{ex}. The coupling strength $g_0 = 6.3$ K is chosen such that the splitting $\Delta_1 - \Delta_2 = 80$ K corresponds to the observed double-peak structure and $I_{\mathrm{ex}}N_{\mathrm{c}}(0) = 0.06$ was obtained from the T-dependence of the quasielastic linewidth. There is good qualitative agreement between figs. 34 and 32a. To relate the coupling strength g_0 to the g_{Γ_5} obtained from the elastic constants $c_{44}(\mathrm{T})$ (Lüthi and Lingner 1979) one has to compare $g_{\Gamma_5}^2/c_{44}^0 v_{\mathrm{c}} = 368$ mK (v_{c} = volume per Ce atom) with $g_0^2/\hbar\omega_0 = 283$ mK. The difference is only thirty per cent; this underlines that both elastic anomalies and the magnetic double-peak spectrum in $CeAl_2$ have their origin in a very strong magnetoelastic coupling in this compound. In fact, g_{Γ_5} for $CeAl_2$ is larger by at least a factor of ten compared to the other RAl_2 compounds (Lingner and Lüthi 1983).

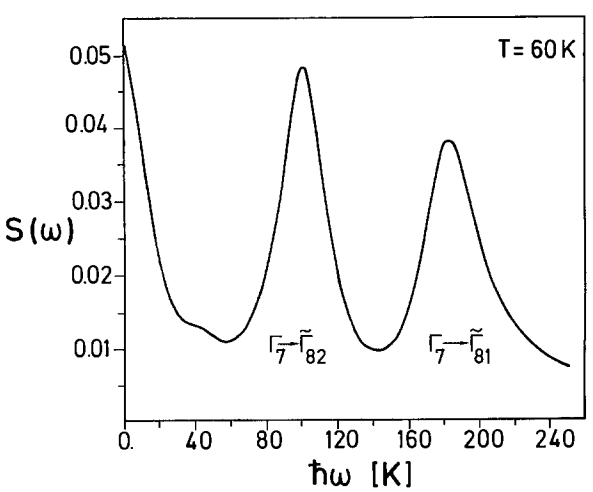

Fig. 34. Magnetic structure function for $CeAl_2$ calculated in the dispersionless model. Broadening of (anti-) bound state peaks is due to an exchange interaction with conduction electrons of strength $I_{\mathrm{ex}}N_{\mathrm{c}}(0) = 0.06$.

The average phonon energy $\hbar\omega_0 = 140$ K corresponds to the peak in the phonon density of states of the six lowest branches measured at room temperature where the renormalization due to magnetoelastic interaction is quite small. At lower temperatures (77 K, 4 K) some typical branches have also been investigated by neutron scattering (Reichardt and Nücker 1984) and a pronounced softening was found. Because it is absent in $LaAl_2$ it must be caused by magnetoelastic interactions in $CeAl_2$. A theoretical discussion has been given by Thalmeier (1984). The zone center Γ_5^+ optical phonon has been measured in great detail by Loewenhaupt and Reichardt (1984). Its temperature behaviour is given in fig. 35, which shows the softening very nicely. In addition one can notice a broadening of this phonon with decreasing temperature. This is very uncommon and probably also due to the increased effectiveness of magnetoelastic coupling at low temperature.

Furthermore, it should be noted that the presence of a bound state (but not the antibound state) has also been seen in Raman scattering experiments (Güntherodt et al. 1983, 1985). No phonon softening was observed, however. This discrepancy to neutron scattering results are attributed to different typical probing times for those techniques.

Finally, we mention that the effect bound states on the magnetization and

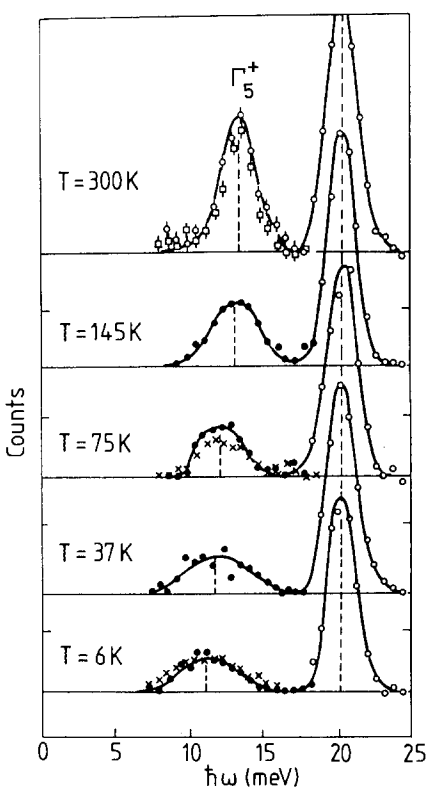

Fig. 35. Temperature dependence of the zone center Γ_5^+ phonons in $CeAl_2$. The data were obtained at different momentum transfers. The phonons at 20 meV (220 K), which involve vibrations of Ce and Al atoms, are temperature independent (Loewenhaupt and Reichardt 1984).

susceptibility has been investigated by Aarts et al. (1985). Using the bound state model they showed that their experimental data can be explained by using CEF parameters that before seemed to contradict other experiments.

3. Conduction electron–phonon coupling

The electronic structure of rare-earth atoms with the configuration $(Xe)4f^n5d^16s^2$ gives rise to conduction bands with 5d and 6s character in the intermetallic compounds. The d bands can have a rather large density of states. Therefore the coupling of phonons to these itinerant electrons can be quite strong. In this chapter we review experimental effects caused by the interaction of conduction electrons with sound waves. These experiments mainly concern the anomalous temperature dependence of symmetry elastic constants and the presence of magnetoacoustic quantum oscillations observed in sound velocity and attenuation.

We first introduce the concept of deformation potential coupling which is applied to calculate the temperature dependence of elastic constants, followed by a presentation and discussion of relevant experimental data. Afterwards we shall present examples for magnetoacoustic quantum oscillations in rare-earth intermetallics.

3.1. *Deformation potential coupling in rare-earth compounds*

Deformations of the lattice caused by sound waves or phonons modify the charge distribution and lattice potential, which leads to a coupling between the conduction electrons and the phonons. It causes a temperature dependence of elastic constants, provides an ultrasonic attenuation mechanism and is responsible for magnetoacoustic quantum oscillations in R intermetallics. It is very difficult to calculate the matrix elements of this interaction for phonons of arbitrary wavelength (Ziman 1960). In the long-wavelength limit, however, the influence on electronic states can be treated within a "deformation potential" approach. In this case the deformation can be described by a slowly varying local strain, therefore the electronic energy bands $E_\nu^0(\boldsymbol{k})$ (ν is the band index) are changed adiabatically to

$$E_\nu(\boldsymbol{k}, \boldsymbol{R}_i) = E_\nu^0(\boldsymbol{k}) + \sum_{k,l} d_{kl}^\nu(\boldsymbol{k})\varepsilon_{kl}(i)\,. \tag{85}$$

These position-dependent energy bands are only a useful concept if the wavelength is many times larger than the lattice spacing. The "deformation potential" d_{kl} $(\boldsymbol{k})$ (if the band index ν is suppressed) in this limit is identical to that for homogeneous strains. It can be split into two contributions. Consider a constant-energy surface (E) in $\boldsymbol{k}$-space. The induced strain ε_{kl} causes an adiabatic change $\Delta k_{\mathrm{n}}^{(1)}$ (n is the normal component) of wavevectors lying on the surface. The resulting surface is in general not yet a constant-energy surface and still has to relax by an amount $\Delta k_{\mathrm{n}}^{(2)}$ at every point. This will happen if $\omega\tau \ll 1$ holds for

the ultrasonic wave (τ is the conduction electron lifetime). Then the total change $\Delta k_n = \Delta k_n^{(1)} + \Delta k_n^{(2)}$ of every normal wavevector component is given by (Pippard 1960, Fawcett et al. 1980)

$$\Delta k_n = \sum_{kl} \lambda_{kl} \varepsilon_{kl} , \qquad \lambda_{kl}(\boldsymbol{k}) = -k_k n_l + r_{kl}(\boldsymbol{k}) , \tag{86}$$

where n_l are the components of the surface normal vector. The two contributions in λ_{kl} correspond to the $\Delta k_n^{(1)}$ and $\Delta k_n^{(2)}$ changes, respectively. A complete pointwise determination of $\lambda_{kl}(\boldsymbol{k})$ has not been performed for any metal but certain orbital averages can be obtained from the strain dependence of Fermi surface cross-sections in de Haas–van Alphen (dHvA) experiments, see Fawcett et al. (1980). Using $\Delta E = \hbar v_n(\boldsymbol{k}) \Delta k_n$ where $v_n(\boldsymbol{k}) = \hbar^{-1} (\partial E / \partial k_n)$ is the normal velocity component we obtain for the deformation potential:

$$d_{kl}(\boldsymbol{k}) = \frac{\partial E(\boldsymbol{k})}{\partial \varepsilon_{kl}} = \hbar v_n(\boldsymbol{k})[-k_k n_l + r_{kl}(\boldsymbol{k})] . \tag{87}$$

One can also form linear combinations d_Γ of these components that correspond to the symmetry strains ε_Γ. For isotropic bands with $E(k) = E(|\boldsymbol{k}|)$ the deformation potential d_{Γ_1} of a purely dilational strain $\varepsilon_{\Gamma_1} = \varepsilon_V = \varepsilon_{xx} + \varepsilon_{yy} + \varepsilon_{zz}$ has no relaxational part of the order of r_{kl} because ε_V only changes the radius or constant-energy spheres, not their shape. One then has

$$d_{\Gamma_1} = -\frac{n}{N_c(E_F^0)} = -\tfrac{2}{3} E_F^0 , \tag{88}$$

where n is the electron density and E_F^0 the Fermi energy in the unstrained crystal. The last identity holds only for parabolic bands. To study the influence of a deformation potential coupling on elastic constants one needs to compute the strain dependence of the conduction electron free energy (sect. 3.2). In this quantitiy band energies always enter as counted from the strain-dependent Fermi energy $E_F(\varepsilon_\Gamma) = E_F^0 + \bar{d}_\Gamma \varepsilon_\Gamma$, $\bar{d}_\Gamma = \partial E_F / \partial \varepsilon_\Gamma$ where $\bar{d}_\Gamma$ is an average of $d_\Gamma(\boldsymbol{k})$ over the Fermi surface, in which case

$$\begin{aligned} &E(\boldsymbol{k}) - E_F = E^0(\boldsymbol{k}) - E_F^0 + D_\Gamma(\boldsymbol{k}) \varepsilon_\Gamma , \\ &D_\Gamma(\boldsymbol{k}) = d_\Gamma(\boldsymbol{k}) - \bar{d}_\Gamma . \end{aligned} \tag{89}$$

This can be written as

$$D_\Gamma(\boldsymbol{k}) = \bar{\Omega}_\Gamma E_F - \Omega_\Gamma(\boldsymbol{k}) E(\boldsymbol{k}) , \tag{90}$$

where

$$\Omega_\Gamma(\boldsymbol{k}) = \frac{-\partial ln\, E(\boldsymbol{k})}{\partial \varepsilon_\Gamma} = -\frac{d_\Gamma(\boldsymbol{k})}{E(\boldsymbol{k})}$$

is called the 'electronic Grüneisen parameter' of conduction bands subject to a symmetry strain ε_Γ. Note that $\bar{\Omega}_\Gamma = -\bar{d}_\Gamma / E_F$ is not equal to the Fermi surface average of $\Omega(\boldsymbol{k})$. Because in general $\Omega_\Gamma(\boldsymbol{k}) \neq \bar{\Omega}_\Gamma$ for a $\boldsymbol{k}$-vector on the Fermi surface, $D_\Gamma(\boldsymbol{k})$ will be non-zero on it. However, for an isotropic band $\Omega_\Gamma(\boldsymbol{k}) = \bar{\Omega}_\Gamma$

on the Fermi surface and in the vicinity one can approximate in eq. (90):

$$D_\Gamma(\boldsymbol{k}) \simeq \bar{\Omega}_\Gamma(E_F - E(\boldsymbol{k}))\,. \tag{91}$$

This vanishes at the Fermi surface, therefore the deformation potential coupling to a single isotropic band does not influence elastic constants (see sect. 3.2). It leads to an observable effect for

(i) degenerate isotropic bands (spherical Fermi surface) with different $\bar{\Omega}_\Gamma^{(\nu)}$ (ν is the band index); this is commonly called 'band Jahn–Teller coupling'.

(ii) a single anisotropic band with anisotropic deformation potential coupling $d_\Gamma(\boldsymbol{k}) \neq \bar{d}_\Gamma$. This situation is illustrated in fig. 36.

The deformation potential is subject to restrictions required by crystal symmetry (Gray and Gray 1976). One has

$$\sum_{\{\boldsymbol{k}\}} d_\Gamma(\boldsymbol{k}) = 0, \qquad \text{for } \Gamma \neq \Gamma_1$$
$$\bar{d}_\Gamma = 0\,, \tag{92}$$

where $\{\boldsymbol{k}\}$ denotes the star of the $\boldsymbol{k}$-vector and Γ is the fully symmetric representation. For cubic symmetry $\varepsilon_{\Gamma_1} = \varepsilon_V$ is the only dilatational (volume changing) strain. Thus eq. (92) holds for any volume conserving strain (tetragonal, trigonal) in cubic systems. An illustration for the star sum rule in eq. (92) is given in fig. 36b.

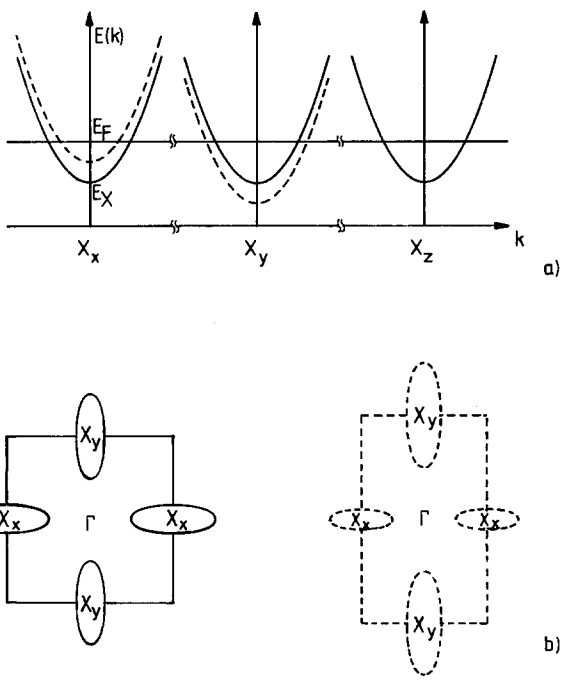

Fig. 36. Illustration of the effect of an orthorhombic strain on electron pockets at the three X-points in LaAg. Full lines, unstrained state; dashed lines, strained state. (a) $E(k)$ for the three X-points, (b) X-point Fermi surface pockets (Niksch et al. 1987).

The most detailed information about the deformation potential is obtained from the analysis of strain dependence of extremal cross-sectional area $A(\varepsilon_\Gamma)$ in dHvA experiments (Griessen and Sorbello 1974, Fawcett et al. 1980). For volume conserving strains one has

$$\left(\frac{\partial A}{\partial \varepsilon_\Gamma}\right)_{E_F} = \int \frac{d_\Gamma(\boldsymbol{k})}{\hbar v_n(\boldsymbol{k})}\, \mathrm{d}l_{\boldsymbol{k}} = \int \lambda_\Gamma(\boldsymbol{k})\, \mathrm{d}l_{\boldsymbol{k}}\,, \tag{93}$$

where $\mathrm{d}l_{\boldsymbol{k}}$ is the line element of the extremal orbit and $\lambda_\Gamma(\boldsymbol{k})$ denotes the symmetry combinations of components in eq. (86). Ab initio calculations of these orbital averages within KKR and OPW band structure methods have been attempted for noble metals. See the references given above. The derivatives in eq. (93) also determine the amplitude of magnetoacoustic quantum oscillations (MAQO) as discussed in sect. 3.3.

3.2. *Deformation potential coupling and elastic constants*

In intermetallic rare-earth compounds the residual resistivity is of the order $1\ \mu\Omega\,\mathrm{cm}$, which leads to electronic relaxation times smaller than 10^{-12} s. For a sound wave propagating in such a material with frequency $\omega/2\pi < 100\,\mathrm{MHz}$ this means that $\omega\tau \ll 1$ and $ql \ll 1$ where ω, q are the frequency and wavevector of sound wave, respectively. The ultrasonic attenuation has been calculated in the various limits (Akhiezer et al. 1957, Pippard 1960), for a review see Rayne and Jones (1970). In the limits given above the ultrasonic attenuation for both longitudinal and transverse waves is proportional to $q^2 l$. The attenuation coefficient for longitudinal waves expressed with $\bar{d}_\Gamma$ as introduced above [eq. (89)] and the density of states $N_c(0)$ is ($E_F \equiv 0$)

$$\alpha_l = A_0\, \frac{\bar{d}_\Gamma^2 N_c(0)}{\rho v v_F}\, q^2 l\,, \tag{94}$$

where A_0 is a factor of order one. Equation (94), shows that unless $N_c(0)$ and the frequency $\omega = vq$ are very large, α_l is very small (Lüthi 1985) and of little significance.

However, elastic constants can show observable effects. In the limits given above the electrons experience a quasi-static strain induced by the sound wave. The resulting energy shift $d_\Gamma(\boldsymbol{k})\varepsilon_\Gamma$ is the net shift with electron relaxation processes already included, as discussed in sect. 3.1. One can calculate the isothermal elastic constants using the free-energy density of band electrons, (Ziman 1960):

$$F_{el} = nE_F - k_B T \sum_{\boldsymbol{k}} \ln\left[1 + \exp\left(\frac{E_F - E(\boldsymbol{k})}{k_B T}\right)\right], \tag{95}$$

where E_F is the Fermi energy and n is the number of electrons per unit volume. If the particle number is conserved,

$$\frac{\partial n}{\partial \varepsilon_\Gamma} = \frac{\partial}{\partial \varepsilon_\Gamma} \sum_{\boldsymbol{k}} f_{\boldsymbol{k}} = 0\,,$$

one obtains eq. (89)

$$\bar{d}_\Gamma = \frac{\partial E_F}{\partial \varepsilon_\Gamma} = \sum_k f_k(1-f_k)d_\Gamma(\boldsymbol{k}) \Big/ \sum_k f_k(1-f_k)\,. \tag{96}$$

With

$$\frac{\partial F_F}{\partial \varepsilon_\Gamma} = \sum_k f_k \frac{\partial E(\boldsymbol{k})}{\partial \varepsilon_\Gamma}$$

one obtains for the isothermal elastic constant

$$c_\Gamma = \frac{\partial^2 F}{\partial \varepsilon_\Gamma^2} = c_\Gamma^0 + \sum_k f_k \frac{\partial^2 E(\boldsymbol{k})}{\partial \varepsilon_\Gamma^2} - \frac{1}{k_B T} \sum_k f_k(1-f_k) D_\Gamma^2(\boldsymbol{k})\,, \tag{97}$$

and with (96)

$$c_\Gamma = c_\Gamma^0 + \sum_k f_k \frac{\partial^2 E(\boldsymbol{k})}{\partial \varepsilon_\Gamma^2} - \frac{1}{k_B T} \sum_k d_\Gamma^2(\boldsymbol{k}) f_k(1-f_k) + \frac{1}{k_B T} \frac{\left[\sum_k d_\Gamma(\boldsymbol{k}) f_k(1-f_k)\right]^2}{\sum_k f_k(1-f_k)}\,. \tag{98}$$

Here

$$f_k = \left[1 + \exp\left(\frac{E(\boldsymbol{k}) - E_F}{k_B T}\right)\right]^{-1}$$

is the Fermi distribution function and c_0 denotes the background elastic constant. Equation (98) has the same structure as eq. (33) of sect. 2.3. The first term with the second derivative $\partial^2 E(\boldsymbol{k})/\partial \varepsilon_\Gamma^2$ corresponds to the Van Vleck term and the rest with the strong $1/T$ temperature dependence to the Curie term. In deriving eq. (98) particle conservation was assumed, i.e., $\partial n/\partial \varepsilon_\Gamma = 0$, from which we obtain the strain dependence of the Fermi level $\partial E_F/\partial \varepsilon_\Gamma$ [eq. (96)].

To evaluate eq. (98) additional assumptions have to be made. For our purposes we shall discuss two models: the so-called rigid band and the Grüneisen parameter models. The latter will be important for intermetallic compounds with unstable rare-earth ions. We shall postpone its discussion until sect. 4.

In the rigid-band model one assumes that $d_\Gamma(\boldsymbol{k}) = \bar{d}_\Gamma$ is independent of $\boldsymbol{k}$, i.e., a given band shifts as a whole under the influence of a strain ε_Γ. Consequently, the Van Vleck term does not contribute. In a rigid one-band model the deformation potential coupling does not lead to any change in the elastic constant because $D_\Gamma(\boldsymbol{k}) = 0$, eqs. (89) and (97) , which is equivalent to a concellation of the two last terms in eq. (98). The reason is that due to particle conservation the energy band and the Fermi energy shift correspondingly.

In a rigid two-band model (A, B) with constant density of states N_A, N_B one obtains

$$c_\Gamma = c_\Gamma^0 - (\bar{d}_A - \bar{d}_B)^2 \frac{N_A N_B f_A f_B}{N_A f_A + N_B f_B}\,, \tag{99}$$

and for the special case of $N_{A,B} = N_c(0)$, $\bar{d}_A = -\bar{d}_B = \bar{d}_\Gamma$, $n = 2N_c(0)(E_F - E_0)$

one obtains the so-called band Jahn–Teller formula

$$c_\Gamma = c_\Gamma^0 - 2\bar{d}_\Gamma^2 N_c(0)\left[1 - \exp\left(\frac{-(E_F - E_0)}{k_B T}\right)\right]. \tag{100}$$

E_0 is the bottom of the conduction band and $N_c(0)$ the DOS at E_F. Such a formula was successfully applied to the temperature dependence of c_{Γ_3} in the A15 compounds, see Testardi (1974).

The name "band Jahn–Teller effect" suggests that one deals with degenerate bands of say e_g or t_{2g} symmetry. However, such a degeneracy is not necessary. What one needs are only identical Fermi surface pieces which deform differently under the action of a symmetry strain. This is shown in a simple but realistic example in figs. 36a, b. We show a two-dimensional cross-section of the Fermi surface and the change of the Brillouin zone under the symmetry strain $\varepsilon_{\Gamma_3} = \varepsilon_{xx} - \varepsilon_{yy}$. This orthorhombic strain has an opposite effect on the Fermi surface pieces A and B. In fig. 36b this is shown for $E(\boldsymbol{k})$ in the two cases. In the limit $\omega\tau \ll 1$ the different Fermi surface pieces are in equilibrium and eqs. (99) and (100) can be interpreted without using band Jahn–Teller concepts. Such a situation actually occurs in LaAg, an intermetallic compound discussed thoroughly by Niksch et al. (1987). It is a consequence of the sum rule eq. (92).

Equation (100) shows that effects on $c_\Gamma(T)$ can be expected if $E_F - E_0$ is of the order of $k_B T$, i.e., the energy difference between Fermi energy and bottom or top of the band should be typically smaller than 500 K. This condition, together with a large $\bar{d}_\Gamma$ and a large density of states, is important in order to observe deformation potential effects in $c_\Gamma(T)$. These ideas will now be discussed more quantitatively.

Anomalous temperature dependences of elastic constants due to deformation potential coupling has been observed before in d-band metals. Examples are Pd (Rayne 1960) and Pd_xAg_{1-x} (Walker et al. 1970). Here we discuss these effects for intermetallic rare-earth compounds. In figs. 37 and 38 we show temperature dependences of elastic constants for LaAg (Assmus et al. 1978, Knorr et al. 1980) and for the Th_3P_4 structure material La_3S_4 (Wruk et al. 1985), respectively. In both figures it is seen that the $c_{11} - c_{12}$ mode has an anomalous temperature dependence.

In LaAg the $c_{11} - c_{12}$ mode can be fitted with eq. (100) over a region of more than 400 K. While the deformation potential coupling constant is of the same order as those found from magnetoacoustic quantum oscillations, the Fermi energy $E_F - E_0$ needed for the fit in fig. 37 is somewhat smaller than that obtained from band structure calculations (Niksch et al. 1987). $\bar{d}_\Gamma N_c(0)$ for LaAg is too small to induce a structural transition. The $LaAg_xIn_{1-x}$ system exhibits a structural transition (Ihrig et al. 1973); however, as shown by inelastic neutron scattering this structural transition is not due to deformation potential coupling because the soft mode is a zone corner phonon (Knorr et al. 1980).

The same conclusions hold for the Th_3P_4 structure materials La_3S_4, La_3Se_4, Pr_3Se_4 and Pr_3Te_4 illustrated in fig. 38. The $c_{11} - c_{12}$ mode of these materials exhibits strong softening that can be described quantitatively by formula (100).

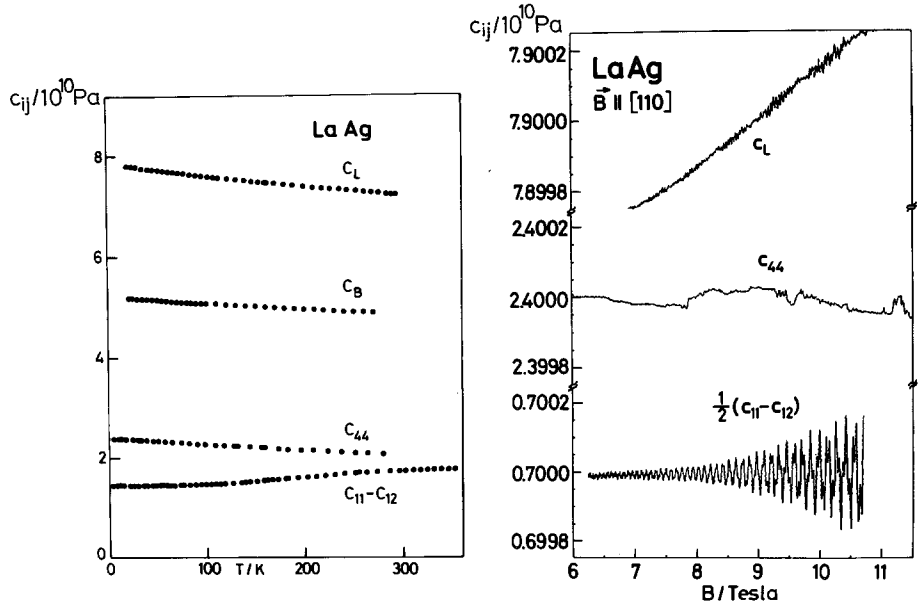

Fig. 37. Temperature and magnetic field dependences of various elastic modes for LaAg (Niksch et al. 1987).

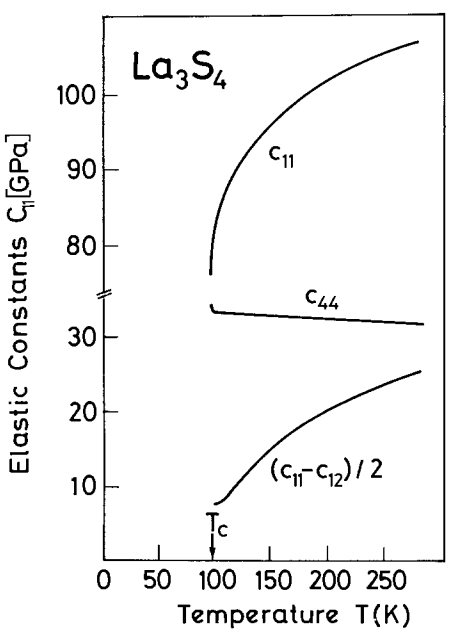

Fig. 38. Temperature dependence of various elastic modes above T_c for La_3S_4, Wruk et al. (1985).

TABLE 4
Density of states, $N_c(E_F)$, for various compounds.

Material	LaSb	LuN	LaS	LaAg	La_3Se_4
Structure	NaCl	NaCl	NaCl	CsCl	Th_3P_4
γ(mJ K^{-2} mol^{-1})	0.95	0.6	3.28	7.7	6.3
N_c(eV^{-1} atom^{-1})	0.2	0.13	1.39	1.65	0.9

However, the first-order structural transition temperatures T_Q are too high for this mechanism to be operative. A remarkable sensitivity on the stoichiometry of T_Q has been noted (Bucher et al. 1976). Since the Th_3P_4 structure is rather complicated, so are the phonon spectra and the band structure; a quantitative analysis is therefore very difficult.

Deformation potential coupling constants are of the order of E_F, (Ziman 1960). To observe deformation potential effects in the temperature dependence of elastic constants several conditions have to be met as discussed above: $d_\Gamma^2 N_c(0)$ must be large and $E_F - E_0$ has to be of the order of $k_B T$. This excludes normal metals and only d-band metals with rather narrow bands can exhibit this behavior. Typical examples have been given above. In intermetallic rare-earth compounds simple density of states arguments show why elastic constant effects can be observed only for CsCl-type and Th_3P_4-type materials. In table 4 electronic specific heat values are listed for various rare earth compounds. This is an updated list of a previous work, see Lüthi et al. (1982). This table indicates that monopnictides and monochalcogenides have smaller values of γ than CsCl- and Th_3P_4-structure materials, i.e., the 5d band of the former structure is more hybridized than in the latter.

3.3. *Magnetoacoustic quantum oscillations (MAQO)*

De Haas–van Alphen (dHvA)-type quantum oscillations as observed in the sound velocity and sound attenuation provide important information about the Fermi surface and the electron–phonon interaction (Roberts 1968, Fawcett et al. 1980). This technique has been successfully applied to intermetallic rare-earth compounds as discussed below. Recent progress in dHvA techniques for heavy-fermion materials (Taillefer et al. 1987, Reinders et al. 1986) should make similar MAQO experiments also possible. Compounds studied so far are LaAg, LaB_6, $LaAl_2$, RB_6, $CeSn_3$, CeB_6, $CeCu_6$ and $CePb_3$.

The free-energy expression for conduction electrons in a magnetic field with quantized Landau levels was given by Lifshitz and Kosevich (1956):

$$F_{osc} = G\cos\left(\frac{c\hbar A_{ex}}{eB} + \gamma\right),$$

$$G = 2k_B T\left(\frac{eB}{2\pi c\hbar}\right)^{3/2} \frac{(A''_{ex})^{-1/2}}{\sinh(2\pi^2 k_B T/\hbar\omega_c)} \exp\left(\frac{2\pi^2 k_B X}{\hbar\omega_c}\right), \qquad (101)$$

where A_{ex} is the extremal Fermi surface cross-section, $\omega_c = eB/m^*c$ is the cyclotron frequency and X is the Dingle temperature (Shoenberg 1984).

One obtains the isothermal velocity change $c_{osc} = \partial^2 F_{osc}/\partial \varepsilon_\Gamma^2$,

$$c_{osc} = g(B, T)\cos(FB^{-1} + \gamma)$$

$$g(B, T) = \left(\frac{\partial A_{ex}}{\partial \varepsilon_\Gamma}\right)^2 G\,, \qquad F = \frac{c\hbar A_{ex}}{e}\,, \tag{102}$$

where the strain dependence of the extremal Fermi surface cross-sectional area $\partial A/\partial \varepsilon_\Gamma$ is the coupling constant. For parabolic bands eq. (93) leads to

$$\frac{\partial A}{\partial \varepsilon_\Gamma} = \frac{2\pi m^*}{\hbar^2}\,\frac{\partial E_F}{\partial \varepsilon_\Gamma} = \frac{2\pi m^*}{\hbar^2}\,\bar{d}_\Gamma\,. \tag{103}$$

Equation (102) shows that MAQO can provide important information about the electronic parameters (extremal Fermi surface cross-sectional area, effective masses, electronic relaxation times) and about the electron–phonon interaction (strain derivatives of the cross-sectional area for different symmetry strains). With the help of this technique, combined with de Haas–van Alphen susceptibility measurements, one can put the deformation potential interaction and the temperature dependence of the elastic constants, discussed above in sect. 3.2, on a solid basis. In the following we discuss some compounds.

3.3.1. *LaAg*

Of all the intermetallic rare-earth compounds this is the compound which has been studied most thoroughly with MAQO techniques (Niksch et al. 1982a, c, 1987): dHvA oscillations and MAQO have been measured for a whole range of magnetic field directions. Figure 37 gives a comparison between $c_\Gamma(T)$ and $\Delta c_{osc}(B)$, indicating that only the Γ_3 mode exhibits an anomalous temperature dependence and MAQO. The longitudinal mode

$$c_L = c_B + \tfrac{1}{3}c_{11} - c_{12}/2 + c_{44}$$

shows oscillations with the weight of the Γ_3 mode in the linear combination. Using eq. (102) and performing a Fourier analysis we obtain values for the frequencies $F = c\hbar A/e$ as given in fig. 39. They are compared with a scalar relativistic band structure calculation with the spin–orbit interaction included. It is seen that the agreement between experiment and calculation is quite satisfactory. Although not all Fermi surface sections could be observed, the good agreement with sizeable parts of the Fermi surface makes the band structure calculation reliable.

The effective mass ratios measured are of the order of one. The deformation potential coupling constants vary between 0.5×10^4 K and 3.8×10^4 K. That deduced from the temperature dependence is 10^4 K. From the band structure for LaAg it was conjectured that the phase transition in the LaAgIn compounds could be due to a nesting feature of the Fermi surface, which gives large electron–phonon matrix elements for the observed M-point phonons (Knorr et al. 1980, Niksch et al. 1987).

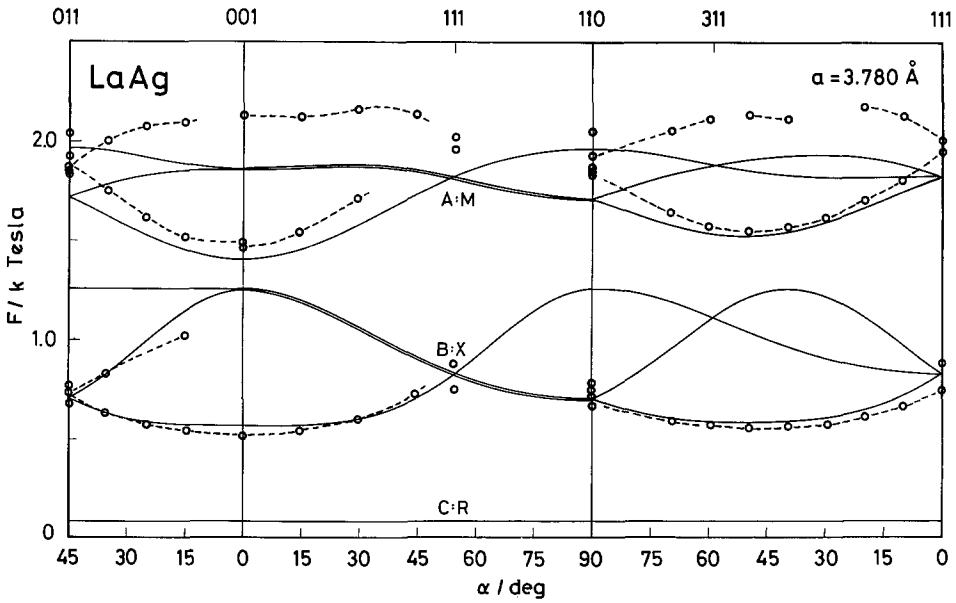

Fig. 39. Measured de Haas–van Alphen frequencies for LaAg as a function of field direction together with the calculated values (full lines) (Niksch et al. 1987).

The fact that only the Γ_3 strain has an appreciable electron–phonon coupling can be understood from the simple coupling argument in sect. 3.2 (fig. 36). The observed Fermi surface pieces as the X and M points (fig. 39) are sensitive to Γ_3 strains but not to Γ_5 strains (Niksch et al. 1987).

3.3.2. LaB_6

Magnetoacoustic quantum oscillations have been observed in this compound for the c_{11} mode (Lüthi et al. 1984) and for the c_{44}, and the $c_{11} - c_{12}$ modes (Suzuki et al. 1985a, Ewert et al. 1987). The observed frequencies are very small, however, typically $F \sim 5$–6 T. They arise from tiny flat electron ellipsoids within the necks along the [110] directions in the simple cubic Brillouin zone (Suzuki et al. 1985a, Onuki et al. 1988). Until now, higher frequencies have not been observed in MAQO techniques.

An interesting observation was made for LaB_6 (Suzuki et al. 1985a), as shown in fig. 40. MAQO have been measured for the c_{44} and $c_{11} - c_{12}$ modes for the geometries $(\boldsymbol{k} \| \boldsymbol{B}, \boldsymbol{e} \perp \boldsymbol{B})$ and $(\boldsymbol{k} \perp \boldsymbol{B}, \boldsymbol{e} \| \boldsymbol{B})$ where $\boldsymbol{e}$ denotes the polarization vector. For the c_{44} mode the MAQO look almost the same but not for the $c_{11} - c_{12}$ mode. While the oscillation frequency is the same for the two geometries because they involve the same orbit, the amplitudes for the two cases are rather different. This might be the analogue of the rotational invariance phenomenon discussed in the case of the magnetoelastic interaction in sect. 2.6. Here it would be caused by deformation potential coupling to itinerant electrons. A quantitative theory is still lacking.

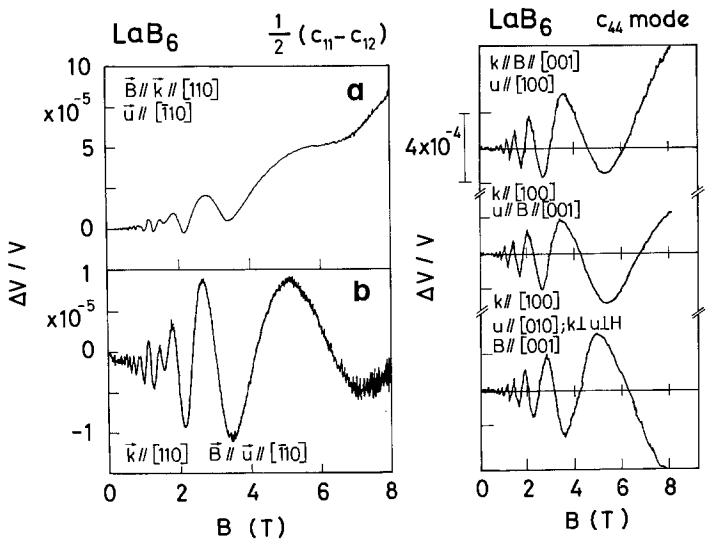

Fig. 40. Acoustic quantum oscillations in LaB_6 for the $(c_{11} - c_{12})/2$ and c_{44} modes for different geometries (Suzuki et al. 1985a).

3.3.3. *Dilute alloys*: $La_{1-x}Ce_xB_6$

The temperature and field dependences of MAQO (and also dHvA) amplitudes is commonly described by the Lifshitz–Kosevich (LK) formula, eq. (102), which is then used to extract values for m^* and τ from experimental data. However, this can only be valid if the conduction electron lifetime is a constant for electron energies in a shell $|E - E_F| < k_B T$ around the Fermi level, see, e.g., Shoenberg (1984). This assumption is well justified for pure metals like, e.g., LaB_6. Here the lifetime is due to electron–phonon scattering and hence $\tau(E)$ varies on an energy scale set by the Debye temperature Θ_D that is usually much larger than the temperature T at which the MAQO experiments are performed ($T < 10\,\mathrm{K}$).

However, in the case of a dilute alloy with unstable-moment inpurities (e.g., Ce^{3+}) many-body effects lead to the existence of narrow Kondo resonance states above the Fermi level as discussed in detail in sect. 4. This leads to a strongly energy-dependent scattering rate for conduction electrons $\Gamma(E) = 1/\tau(E)$ that is directly proportional to the density of many-body resonance states (see fig. 46). The energy scale for the $\tau(E)$ dependence is now the Kondo temperature T_K which can be comparable with T. Therefore, in this case one should expect that MAQO and dHvA amplitudes may deviate from the LK formula. Experimentally this effect has been quite elusive. One of the rare cases where it was actually observed is the dilute alloy $La_{1-x}Ce_xB_6$ ($x = 0.10$), see Thalmeier et al. (1987). Figure 41 shows the T-dependence of MAQO amplitudes for a very small extremal area with $F = 6.5\,\mathrm{T}$ or

$$A_{ex} = (2\pi e/h)F = 6.2 \times 10^{12}\,\mathrm{cm}^{-2}\,,$$

which presumably corresponds to the ellipsoid structures in the Fermi surface

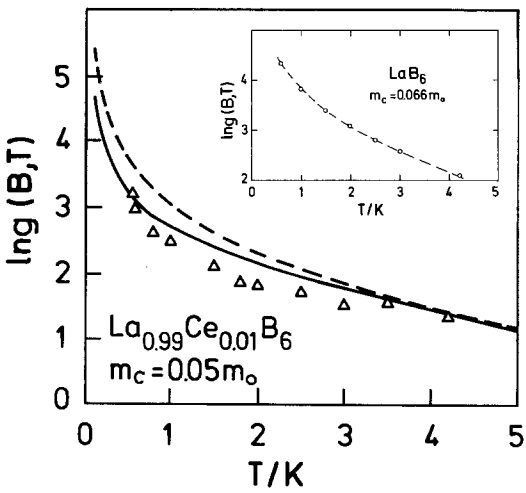

Fig. 41. Logarithm of MAQO amplitude as function of temperature for $B = 2.78$ T. (a) Triangles, experimental results; (b) dashed curve, behaviour acording to LK formula; (c) full curve, results according to eq. (104). An effective mass $m_c = 0.05m_0$ was used for the fit. Inset shows corresponding results for pure LaB_6 fitted with the LK formula and $m_c = 0.066m_0$.

mentioned before as obtained in band structure calculations on LaB_6 (Harima et al. 1989). The experimental results (triangles) are seen to disagree strongly with the dashed curve predicted by the LK formula. In the temperature range relevant in fig. 41 the (LaCe)B_6 alloys also display a variety of 'Kondo anomalies' in the thermodynamic and transport properties, e.g., Bickers et al. (1985). Thus it seems likely that the anomalous MAQO amplitude is also caused by the many-body effects due to scattering by Ce impurities. In a phenomenological approach one can describe this anomaly by assuming that eq. (102) is still valid if one uses an effective Dingle temperature $X(T)$ which itself depends on temperature, see fig. 42. For the dilute $La_{0.99}Ce_{0.01}B_6$ a strong T-dependence of $X(T)$ is obtained with a maximum around 1 K. For comparison the observed Dingle temperature of pure LaB_6 is constant as it should be. In a proper microscopic description of MAQO amplitudes one must include the effect of a resonant scattering rate $\Gamma(E) = 1/\tau(E)$. This leads to an expression (Engelsberg and Simpson 1970),

$$g(B, T) = \sum_{n=0}^{\infty} \exp\left(-\frac{2\pi}{\hbar\omega_c}\left[\omega_n + \zeta(\mathrm{i}\omega_n)\right]\right), \tag{104}$$

where $\omega_n = (2n+1)\pi k_B T$ and $\zeta = \mathrm{i}\Sigma(\mathrm{i}\omega_n)$ where Σ is the analytically continued electron self-energy. The essential part $\zeta'(\mathrm{i}\omega_n)$ is derived as (Thalmeier et al. 1987),

$$\zeta'(\mathrm{i}\omega_n) = \frac{\alpha_0 \hat{\delta} n_r(T)(\omega_n + \Gamma_r)}{(\omega_n + \Gamma_r)^2 + \varepsilon_r^2}\,. \tag{105}$$

Here $\alpha_0 = \frac{1}{2}cT_0/N_c(0)$ determines the strength of the impurity scattering (c is the

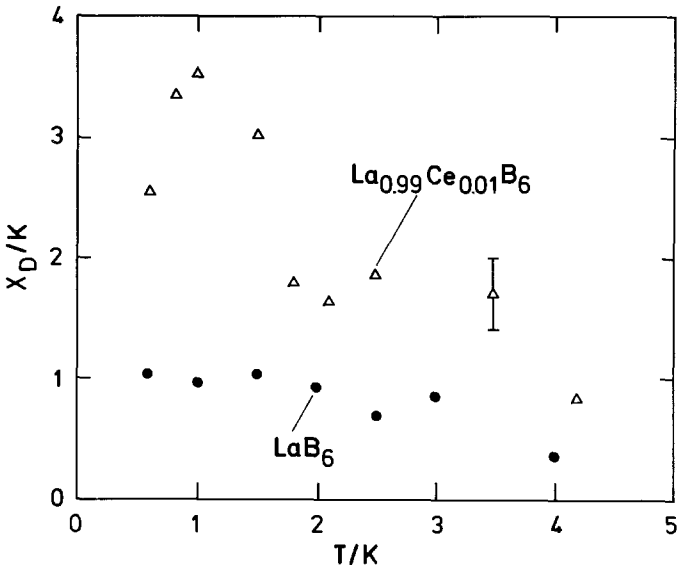

Fig. 42. Effective Dingle temperature $X(T)$ of $La_{0.99}Ce_{0.01}B_6$ as function of temperature in comparison to the constant X of pure LaB_6. An absolute shift of X has been applied for all points to match the data at $T = 4$ K (Thalmeier et al. 1987).

concentration) and $\hat{\delta}n_r(T)$, which is the normalized resonance weight (fig. 46), determines the temperature dependence. Furthermore, ε_r, Γ_r and $T_0 \sim T_K$ are the parameters that characterize the resonance DOS (see sect. 4.2.1). If $\zeta(i\omega_n)$ were taken as constant the LK formula [eqs. (101), (102)] is readily retained. A proper numerical evaluation of eqs. (104) and (105) with $c = 0.01$, $T_0 = 1$ K and $N_c(0) = 0.098\,\text{eV}^{-1}$, i.e., $\alpha_0 = 72.7\,\text{K}^2$ leads to the full curve in fig. 41. The depression of the MAQO amplitude by resonant scattering is seen to have the proper magnitude; however, the overall T-dependence is not reproduced very well. This is possibly due to polarization effects by the external field of $B \simeq 3$ T that would require a spin- and field-dependent $\zeta'_\sigma(i\omega_n, B)$ while eq. (105) is only strictly valid for zero field.

3.3.4. *$CeSn_3$*

Preliminary studies have also been made for the compound $CeSn_3$ that is a borderline case between a mixed-valent compound and a Kondo lattice compound (see sect. 4). MAQO have been observed for the c_{11}, c_{44} and $(c_{11} - c_{12})$ modes (Niksch et al. 1985, Suzuki et al. 1987a). Because the experiments were performed for $T > 1$ K only small Fermi surface pieces have been observed with normal electron masses. Heavy masses observed by conventional de Haas–van Alphen experiments (Johannsen et al 1984) have not be detected so far. As in the case of LaB_6 the $c_{11} - c_{12}$ mode also exhibits for $CeSn_3$ the rotational invariance phenomenon (Suzuki et al. 1987a).

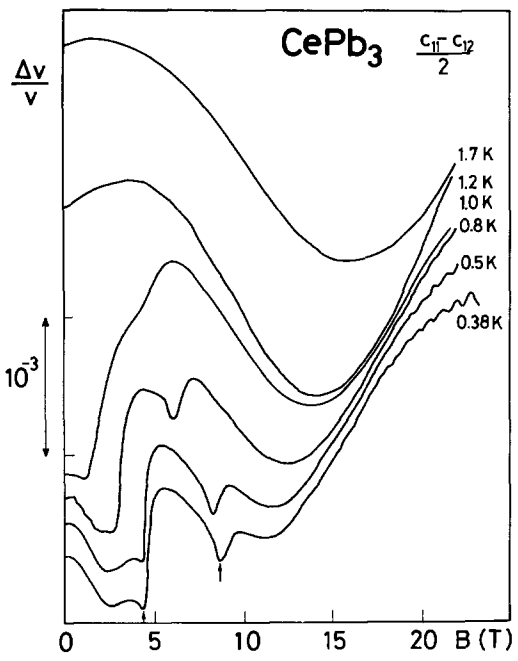

Fig. 43. Relative velocity change for $(c_{11} - c_{12})/2$ mode as a function of magnetic field for various temperatures (Nikl et al. 1987).

3.3.5. *$CePb_3$*

Recently MAQO experiments have also been performed for the Kondo lattice compound $CePb_3$, see Nikl et al. (1987). Figure 43 shows relative velocity changes for the $c_{11} - c_{12}$ mode for $\boldsymbol{B} \| \boldsymbol{k}$ in the temperature range between 0.38 K to 1.7 K. For magnetic fields from 18–23 T a clear MAQO with frequency $F = 617$ T is observed with an effective mass $m^*/m = 4.3$. More extensive experiments have to be performed in order to determine the Fermi surface geometry. The complicated B–T phase diagram will be discussed in sect. 4.

Very little work on other systems has been done. MAQO were found in $LaAl_2$ and $CeNi_5$. Unsuccessful attempts to find MAQO have been performed for $CePd_3$, $LaPd_3$, $PrPb_3$ and $YbAl_2$ (Niksch 1986, Lüthi 1986).

Very recently MAQO work has been performed for heavy-fermion compounds also below 100 mK. In CeB_6 an oscillation with $F = 1.26$ MG and an effective mass of $m = 7.2 m_0$ was found (Suzuki et al. 1987b). In $CeCu_6$ at $T \leq 510$ mK and for fields $B \leq 8$ T oscillations were found which, however, do not follow eq. (102), indicating an instability under a magnetic field, see Goto et al. (1987). Finally, MAQO have also been observed in $SmCu_6$ (Endoh et al. 1987).

It is clear that MAQO technique is very powerful and that in coming years such research will be done especially in heavy-fermion compounds using low temperatures and high magnetic fields.

4. Unstable-moment compounds

The instability of magnetic moments in intermetallic R compounds belongs to the most interesting many-body phenomena in condensed matter physics. It is very widespread among cerium compounds but also exists in Yb, Eu and Sm compounds. Many of these compounds have a non-magnetic ground state despite the existence of free 4f moments at elevated temperatures; this observation gave the name to the class of compounds discussed in this chapter. In simplified terms the Curie-like high-temperature susceptibility saturates below a "fluctuation temperature T^*" in an enhanced Pauli-type susceptibility characteristic for a non-magnetic Fermi liquid ground state. As already mentioned in the introduction the microscopic origin of this behaviour lies in the interplay between the hybridization of localized 4f and itinerant (5d6s) electrons and the intrasite Coulomb repulsion of 4f electrons. Unstable-moment systems can roughly and somewhat arbitrarily be divided into two classes: (A) Kondo lattice and (B) mixed-valent (MV) compounds.

(A) In this case the 4f level lies well below the Fermi level (fig. 1), charge fluctuations are suppressed and the 4f occupation n_f is almost integral. The fluctuation temperature T^* is then given by the single-ion Kondo temperature T_K which is of the order of 1–10 K in Ce compounds. Furthermore, below T_K coherent heavy-electron bands may develop in some compounds with thermal effective masses up to $m^* = 200m_0$ and a band width of the order of T_K. In other cases to be discussed later, moment instability and heavy-band formation is ultimately intercepted by the magnetic order of already reduced moments. There are also compounds where the heavy electron bands develop a spin splitting with very small resulting magnetic moments, $\mu \leqslant 0.1\mu_B$, below T^*.

Heavy-fermion systems have been extensively investigated recently and several review articles exist, see Stewart (1984), Steglich (1985), Lee et al. (1986), Fulde et al. (1988) and Fisk et al. (1988).

(B) In MV compounds the 4f level is closer to the Fermi level and real charge fluctuation processes lead to a non-integer occupation n_f. T^* ranges from a few hundred Kelvins in the weakly MV compounds to a few thousand Kelvins in the strongly MV compounds. In the latter case, T^* corresponds directly to the hybridization width Γ. Reviews have been cited in the introduction.

We first begin with a short survey of the basic experimental evidence in sect. 4.1. The basic physical properties of the unstable-moment systems will be surveyed. In order to discuss their elastic and lattice dynamical properties that are of central interest here an outline of current theoretical concepts to describe unstable-moment systems, especially heavy-fermion compounds is given first (sect. 4.2). Because in heavy-electron compounds T_K is much smaller than the CEF splittings they exhibit magnetoelastic anomalies as described in sect. 2. However, in addition, Grüneisen parameter coupling to the heavy-electron bands leads to elastic effects below T_K. For a few typical Ce compounds this is studied within a microscopic model calculation in sect. 4.3. A more complete discussion

of the elastic properties for heavy-electron compounds based on a phenomenological approach and a scaling ansatz are given in the following, sect. 4.4. Finally, sect. 4.5, electron–phonon coupling in MV compounds will be discussed. Due to their large values of T^* no CEF effects survive, and Grüneisen parameter coupling is present although less spectacular. On the other hand, MV compounds show interesting anomalies in high-frequency phonons of the breathing type caused by their coupling to charge fluctuations in the 4f shell.

4.1. *Basic experimental properties of unstable moments*

We want to recall experimental evidence for the two unstable-moment regimes: the local-moment regime leading to Kondo and Kondo lattice behaviour and the mixed-valent case. In the introduction we have given a qualitative discussion of the two cases. In the first part we want to give general evidence for these phenomena. In doing so we rely heavily on existing review articles. In the second part we give typical evidence for electron–phonon coupling effects.

As pointed out in the theoretical sect. 4.2 the two regimes are characterized by two quite different fluctuation temperatures. In the single-ion Kondo case or the Kondo lattice case the Kondo temperature is typically $T_K < 10\,K$. This implies by virtue of $T_K \sim 1 - n_f$ [eq. (113)] almost integral valence, and anomalies of the physical quantities only at low temperature $T < T_K$. On the other hand, the mixed-valent regime (n_f non-integer) has a fluctuation temperature typically larger than $T^* \geqslant 100\,K$. Therefore, anomalies can be observed even at room temperature as discussed below.

4.1.1. *Mixed-valence case, general experimental evidence*

A detailed experimental review on this subject can be found in Lawrence et al. (1981). One of the most frequently used methods to determine a mixed-valent compound and its valency is a lattice constant measurement. This technique assumes the validity of Vegard's law, i.e., the linearity between lattice constant and valence, as well as knowledge of the lattice constants $a_0(n)$ and $a_0(n-1)$ of compounds where the rare earth is in the configurations $4f^n$ and $4f^{n-1}$, respectively. In this way the intermediate valency of Ce compounds (α-Ce, $CeBe_{13}$, $CePd_3$), of Sm compounds (SmS, SmB_6), of Tm compounds (TmSe) and of Yb compounds ($YbAl_2$) was determined [see Lawrence et al. (1981) and Penney (1984)].

In addition, other experimental techniques help to characterize this mixed-valence state. Related to the anomalous lattice constants the thermal expansion also shows pronounced anomalies in the same temperature range as the magnetic susceptibility. Transport properties give additional information. Of great significance are spectroscopic techniques. The field of photoemission (X-ray and ultraviolet spectroscopy and bremsstrahlung isochromat spectroscopy) has matured considerably, see Gunnarson-Schönhammer (1987). In some cases intraconfigurational and interconfigurational excitations could be resolved with Raman spectroscopy (Güntherodt et al. 1981). The isomer shift in Mössbauer spectroscopy helps to determine the valence (Coey and Massenat 1977, Nowik 1977)

and the quasielastic linewidths in neutron scattering give a measure of the fluctuation temperature, see Loewenhaupt et al. (1979b).

4.1.2. *Kondo alloys and Kondo lattice compounds*

As mentioned in the introduction dilute alloys with Ce^{3+} impurities and some Ce compounds belong to this category. A relevant review can be found by Maple et al. (1978), and references listed in the introduction to sect. 4. Because of the small fluctuation temperature only low-energy methods can help to characterize this state (thermodynamic properties, transport properties, ultrasonics).

Typical Kondo-like resistivities of Ce^{3+} impurities have been observed in Y by Sugawara and Eguchi (1967), in YLa by Winzer (1977), in $LaAl_2$ by Felsch et al. (1975) and in LaB_6 by Samwer and Winzer (1976).

Kondo-like resistivities can also be observed in concentrated Kondo compounds. Typical examples are $CeAl_3$ (Buschow et al. 1971), $CeAl_2$ (Buschow et al. 1969), $CeCu_2Si_2$, (Steglich et al. 1985) and $CeSn_3$ (Gschneidner et al. 1985). A characteristic property is the low-temperature specific heat or its γ-value, $\gamma = C/T$, which has very large values of the order of $1\ \mathrm{J\,Mol^{-1}\,K^{-2}}$ (see table 5). This large value for γ, expressed in electron density of states or effective masses m^*/m (of the order of 200) have led to the name of heavy-fermion compounds (Stewart 1984).

In this chapter we want to focus on the electron–phonon effects in the mixed-valence and heavy-fermion compounds. In the mixed-valence compounds one usually observes an extremely low bulk modulus c_B (table 6). As an example the case of $Sm_xY_{1-x}S$ is given in fig. 44, see Penney and Melcher (1976). In addition, the so-called Poisson ratio ν is negative in these compounds (see table 6). Analogously, certain phonon branches exhibit anomalies. A detailed discussion and explanation of these facts and related experiments will be given in sect. 4.5.

TABLE 5
Physical properties of unstable Ce compounds.

Material	γ (mJ mol^{-1} K^{-2})	T_K (K)	T_Q (K)	T_N (K)	T_{SL} (K)	Crystal structure
$CeAl_3$	1200	3	—	—	—	hex. Ni_3Sn
$CeCu_6$	1450	4	—	—	—	orthorh.
$CeRu_2Si_2$	385	15	—	—	—	tetr.
$CeCu_2Si_2$	1100	5	—	—	0.7	tetr.
$CeAl_2$	135	6	—	3.8	—	C-15
CeAg			15	5.3 (T_c)	—	CsCl
CeZn						CsCl
CeB_6	260	7	3.3	2.1		CaB_6
$CePb_3$	225	2	—	1.1		Cu_3Au
$CeIn_3$	260		—	10	—	Cu_3Au
$CeSn_3$	42	260	—	—	—	Cu_3Au
$CePd_3$		220	—	—	—	Cu_3Au
$CeBe_{13}$		340				$NaZn_{13}$

TABLE 6
Bulk modulus c_B and Poisson ratio ν for unstable-moment compounds.

Material	Temperature at which c_B, ν are given (K)	c_B (10^{11} erg cm^{-3})	Poisson ratio, ν
$Sm_{0.75}Y_{0.25}S$	300	0.83	−0.671
SmB_6	300	9.33	−0.195
TmSe	300	2.17	−0.467
$Ce_{0.74}Th_{0.26}$	150	0.1	−0.75
$CeBe_{13}$	150	8.16	0.005
$YbAl_2$	290	4.67	0.102
$CePd_3$	300	10.25	0.312
CeB_6	290	16.8	0.033
$CeAl_3$	0.5	4.58	0.175
$CeAl_2$	300	6.89	0.168
UTe	300	3.45	−0.16
UPt_3	300	20.9	0.19–0.48
UBe_{13}	300	16.1	0.05
Cu	300	14.45	0.42

In the case of Kondo lattices strong temperature-dependent anomalies in thermal expansion and longitudinal elastic constants are observed. As an example we show in fig. 45 for $CeAl_3$ the γ-value, $\gamma(T)$, the thermal expansion coefficient, $\beta(T)$, and the bulk modulus, $c_B(T)$. All quantities exhibit distinct anomalies for $T < 1$ K. The important point to be made and discussed later is that the so-called Grüneisen parameter $\Omega = \beta c_B / C$ can have gigantic values for small T in such compounds (e.g., in $CeAl_3$ $\Omega = -220$ for $T < 0.5$ K). The thermal expansion can also be large for mixed-valence compounds, however, the magnitude characterized by Ω is almost an order of magnitude smaller than for Kondo lattice

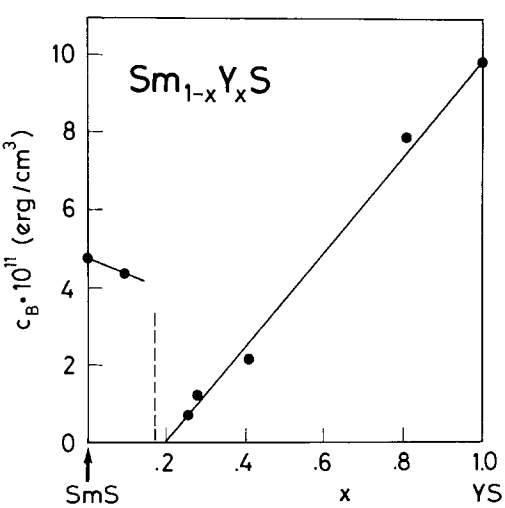

Fig. 44. Bulk modulus for $Sm_{1-x}Y_xS$ at 300 K as a function of x (Penney and Melcher 1976).

TABLE 7
Electronic Grüneisen parameter for various substances.

Material	Temperature at which Ω is given (K)	Ω
Cu	2	1.4
Pd	4	2.5
TmSb	<20	1
$CeAl_3$	<0.5	−200
$CeCu_6$	<1	$\Omega_a = 70$, $\Omega_c > 120$
$CeRu_2Si_2$	<5	$\Omega_a = \Omega_c = 120$
$CeCu_2Si_2$	<8	75
$CeSn_3$	<50	10
CeNi	<50	10–20
UPt_3	10	65
UBe_{13}	<10	94

compounds (see table 7 and fig. 45). For concentrated Ce compounds that have no low-temperature phase transition ($CeAl_3$, $CeCu_6$, $CeRu_2Si_2$) longitudinal elastic constants exhibit strong anomalies in the temperature dependence, whereas transverse elastic modes only exhibit crystal-field effects for $T > T_K$. The anomalies for the longitudinal modes can be described again with a Grüneisen parameter coupling. In addition, strong magnetic field effects are observed in longitudinal elastic constants and magnetostriction as discussed below (sect. 4.4).

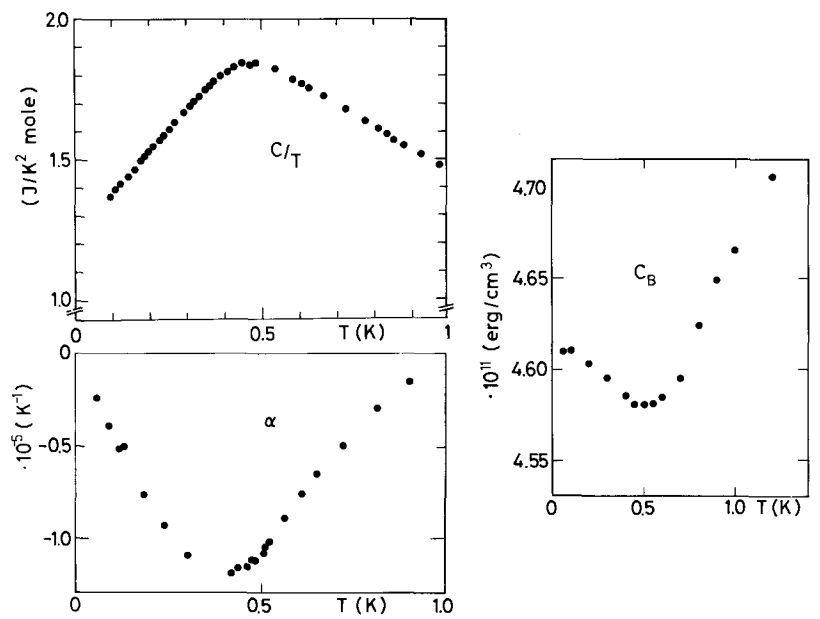

Fig. 45. Specific heat, thermal expansion and bulk modulus for $CeAl_3$ at very low temperatures. Adapted from Andres et al. (1975), Ribault et al. (1976) and Niksch et al. (1980).

4.2. *Origin and theory of unstable moments and quasiparticle bands*

A theoretical description of electron-phonon coupling effects in unstable-moment compounds demands a thorough understanding of their electronic excitation spectrum. It has already been qualitatively described in the introduction. In this section we give a firmer theoretical foundation to these concepts for the 4f impurity case as well as the periodic lattice of 4f ions in a metallic compound. For the Ce or Yb systems the physics for these two cases is adequately described by the (degenerate) Anderson and Anderson lattice Hamiltonians respectively. For a single impurity it reads ($n_m = f_m^\dagger f_m$)

$$H_A = \sum_{km} E_k c_{km}^\dagger c_{km} + \sum_m E_m n_m + \sum_{km} V(k)(c_{km}^\dagger f_m + f_m^\dagger c_{km}) + U \sum_{m \neq m'} n_m n_{m'} . \tag{106}$$

Here $c_m^\dagger$ and f_m create conduction electrons in total angular momentum states m around the impurity site and a 4f electron at the site, respectively, with band energies E_k and 4f energies $E_f^m \equiv E_m < 0$. They are split due to spin–orbit coupling and a CEF potential. Furthermore, $V(k) \cong V(k_F)$ is the hybridization strength of localized 4f and conduction electrons and U is the on-site Coulomb interaction which sets the largest energy scale in the problem (fig. 1). The total number of 4f states involved is N_f, thus $1 \leq m \leq N_f$. The ground state degeneracy is denoted by N. For Ce compounds one has $N_f = 14$ due to the $J = \frac{5}{2}, \frac{7}{2}$ angular momentum multiplets. They are separated by a spin–orbit energy $\Delta_{so} \simeq 0.25$ eV. Depending on the degree of CEF splitting of the lowest multiplet ($J = \frac{5}{2}$) one has a ground state degeneracy $N = 6$ (no CEF splitting), $N = 4$ (cubic Γ_8 ground state) or $N = 2$ (Kramers doublets). In the Kondo limit with E_f sufficiently far below the Fermi level, a Schrieffer–Wolff transformation of H_A leads to the Coqblin–Schrieffer–Hamiltonian (Coqblin and Schrieffer 1969), where the hybridization and Coulomb terms are eliminated and replaced by an effective exchange-type sf scattering of strength $I_{ex} \sim |V|^2/E_f < 0$ ($U \gg |E_f|$). Both Hamiltonians can be treated with a variety of methods.

(*i*) *The impurity model.* Bethe ansatz techniques yield exact solutions and from these thermodynamic quantities have been computed (Wiegmann 1980, Andrei 1980), also including orbital degeneracy and CEF effects (Schlottmann 1983, 1984, Okiji and Kawakami 1986). However, dynamical quantities cannot be computed with this technique. For this purpose approximate $1/N$ expansion methods for a generalized $U = \infty$ Anderson model have been developed (Coleman 1984, Read 1985, Cox 1985) which allow the computation of the electron excitation spectrum. For a review, see Bickers (1987). Its most important feature is a Kondo resonance just above the Fermi level whose width is of order T_K. It is responsible for all the low-temperature ($T < T_K$) thermodynamic and transport anomalies in dilute Kondo alloys. Thermodynamic quantities derived from this agree well with the exact Bethe ansatz solutions (Cox et al. 1986).

A self-consistent perturbation theory which leads to similar results has also been developed, e.g., Kuramoto (1983) and Kojima et al. (1984). A different variational approach has been used by Gunnarson and Schönhammer (1983, 1987) to discuss high-energy properties like photoemission spectra.

(*ii*) *the Lattice problem.* For the Anderson or Kondo lattice model that can be used to describe the MV and HF compounds the theory is much less developed. The $1/N$ expansion has been used to derive a phase diagram for the Kondo lattice (Lacroix and Cyrot 1979, Lacroix 1985). It is determined by a competition of the Kondo effect which tends to compensate the individual 4f moments below T_K because of an effective antiferromagnetic sf exchange $I_{ex} < 0$ and the associated interionic RKKY interaction, which tends to order the 4f moments at low temperatures. If $\alpha = |I_{ex}| N_c(0)$ exceeds a critical value α_c the ground state of the Kondo lattice is non-magnetic. A schematic phase diagram was given by Lacroix (1985). From theory one expects a critical parameter $\alpha_c > 0.5$ to achieve a non-magnetic ground state. The experimental values in cerium compounds are always smaller than this. Furthermore, anisotropy seems to favor a non-magnetic state because the cubic Kondo compounds $CeAl_2$, $CeIn_3$, $CePb_3$ and CeB_6 are all magnetic whereas the non-cubic compounds $CeAl_3$, $CeCu_6$, $CeCu_2Si_2$ and $CeRu_2Si_2$ are all non-magnetic or have moments $\mu \ll \mu_B$ (Vettier et al. (1986), (see table 5). It is not certain that the Kondo lattice model is appropriate for the non-magnetic Ce compounds; the effect of charge fluctuations, i.e., non-integer 4f occupation may be essential for the existence of a non-magnetic state, see Lacroix (1987).

In this case the Anderson lattice model is a more appropriate starting point. A qualitative phase diagram for the $U = \infty$ Anderson model was suggested by Ohkawa (1985) with a non-magnetic ground state if the 4f occupation n_f is smaller than a critical value estimated as $n_f^{cr} \simeq 0.9$–0.99. Assuming a non-magnetic state, Coleman (1985) has derived the excitation spectrum for this model by using a mean-field approximation that is exact only for $N \to \infty$. In the Kondo limit he obtains narrow quasiparticle bands whose width is of the order of T_K. They are identified with the heavy-electron bands found in several Ce compounds as discussed in sect. 4.2.2. An attempt to compute the excitation spectrum of the Anderson lattice model beyond mean-field theory for all temperatures has been made by Kuramoto et al. (1987) and Kim et al. (1987).

A different approach was used by Razafimandimby et al. (1984), d'Ambrumenil and Fulde (1985) and Fulde et al. (1988) for the Kondo lattice to calculate quasiparticle bands. They start from the observation, Nozières (1974), that for $T \ll T_K$ a Fermi liquid description can be used for the scattering by Kondo ions. Its phase shift is assumed to have a resonant behaviour around the Fermi energy, with T_K defining the energy scale. A periodic lattice of resonant scattering centers then leads to narrow quasiparticle bands, which have been calculated within the KKR formalism. In the simplest approximation they are equivalent to those obtained from the mean-field approximation of the Anderson lattice. The method of Razafimandimby et al. has been used for a realistic

semi-empirical calculation of heavy-electron bands in $CeAl_3$ and $CeCu_2Si_2$ (Sticht et al. 1986, Zwicknagl 1988).

4.2.1. *Excitation spectrum of the Anderson impurity, the Kondo resonance*

For Ce-based systems the intrasite Coulomb interaction U is large compared to all other relevant energies (fig. 1). and will be taken to be infinite for simplicity. In this case the last term in eq. (106) may be dropped if one introduces the boundary condition that only $4f^0$ and $4f^1$ configurations can occur at any impurity site, $4f^2$ states are completely suppressed. This infinite-U constraint can be incorporated into the model by introducing a charge carrying slave-boson field b_i at site $\boldsymbol{R}_i$ with $[b_i, b_i^\dagger] = 1$ such that the above constraint is now equivalent to a conservation law for the total charge $Q = (\Sigma_m f_m^\dagger f_m + b^\dagger b)$ at every impurity site. In the Bose field representation the $U = \infty$ "generalized" Anderson Hamiltonian then reads (Coleman 1984):

$$\tilde{H} = \sum_{km} E_k c_{km}^\dagger c_{km} + \sum_m E_f f_m^\dagger f_m + \sum_{km} \frac{\tilde{V}}{\sqrt{N}} (c_{km}^\dagger f_m b^\dagger + \text{hc}) + \lambda \Big(\sum_m f_m^\dagger f_m + b^\dagger b\Big) . \tag{107}$$

Here we have only included the N-fold degenerate 4f states that constitute the members of the lowest CEF multiplet ($1 \leq m \leq N$) at E_f. This is appropriate for discussing low-energy and low-temperature phenomena, provided the Kondo temperature T_K is much smaller than the excitation energy to higher CEF multiplets. In the Hamiltonian above a rescaled hybridization $\tilde{V} = \sqrt{N} V$, which leads to $\tilde{\Gamma} = N\Gamma$ ($\Gamma = \pi N_c(0) V^2$) has been used that is convenient for implementing the $1/N$ expansion. This Hamiltonian can be treated with conventional field theoretical methods. We identify $f_m^\dagger|0\rangle$ and $b^\dagger|0\rangle$ with the physical states $|4f^1, m\rangle$ and $|4f^0\rangle$ respectively, where $|0\rangle$ is the vacuum state. Thus $b^\dagger$ creates a 4f hole. The total f charge Q commutes with H; therefore its corresponding state space consists of subspaces of definite total charge $Q = 0, 1, 2, \ldots$. By construction the space of physical (f^0, f^1) configurations corresponds to the $Q = 1$ subspace. Therefore, a fourth term with a Lagrange parameter λ is added in eq. (107), which is used to project to the physical subspace by taking λ to infinity at the end of the calculations. In appendix B we describe how the calculations are actually performed. Here we only discuss the result for the $4f^1 \to 4f^0$ excitation spectrum, which is denoted as $\rho_{4f}^m(\omega)$. Its properties can be described as follows (see also introduction to sect. 1).

4.2.1.1. *Case A: Local moment regime* ($N\Gamma < |E_f|$). For $T < T_K$ there are two contributions to ρ_{4f}^m.

(i) A broad 'charge fluctuation' peak at an energy corresponding to a relaxed 4f level near E_f. Its width is given by $\tilde{\Gamma} = N\Gamma$ because the Hamiltonian defined above includes only hybridization with the 4f ground state. One should keep in mind, however, that the width seen in a real photoemission experiment is given by $N_f\Gamma$.

(ii) The second contribution is a narrow "spin fluctuation" peak or "Kondo" resonance at an energy $T_0 = aW \exp(\pi E_f/\tilde{\Gamma}) = aT_K$ above the Fermi level, with a resonance width $\Gamma_r \ (T=0) = \pi T_0/N$. Except for a numerical factor $a = (\tilde{\Gamma}/\pi N|E_f|)^{1/N}$ of order unity, T_0 equals the Kondo temperature T_K. The Kondo resonance is caused by an infrared singularity whose physical origin lies in the collective excitation of the low-energy particle–hole pairs that accompany the decay of a 4f hole. The weight $\delta n_r(T)$ of the resonance vanishes for $T \gg T_K$ and has a zero-temperature limit of

$$\delta n_r(0) = \frac{\pi T_0}{\tilde{\Gamma}} \ll 1 .$$

Therefore, the occupied charge fluctuation peak carries most of the weight and the 4f occupation number

$$n_f(T) = \sum_m \int d\omega \, \rho_{4f}^m(\omega) f(\omega) \tag{108}$$

is only slightly less than one in the local-moment regime. An example for $\rho_{4f}^m(\omega)$ is given in fig. 46 that clearly shows these features. From the numerical solutions (Cox 1985) one concludes that the Kondo resonance around $\omega \simeq 0$ (the Fermi level) may be approximated by a Lorentzian

$$\rho_r(\omega) = \frac{\pi^{-1}\Gamma_r(T)\,\delta n_r(T)}{(\omega - \varepsilon_r)^2 + \Gamma_r^2(T)} = \delta n_r(T)\rho_r^0(\omega) , \tag{109}$$

where $\varepsilon_r = T_0$ is the resonance position and $\Gamma_r(T)$ its width, which increases with temperature according to a power law. The resonance weight $\delta n_r(T)$ decreases monotonically with increasing temperatures as shown in the inset of fig. 46. The

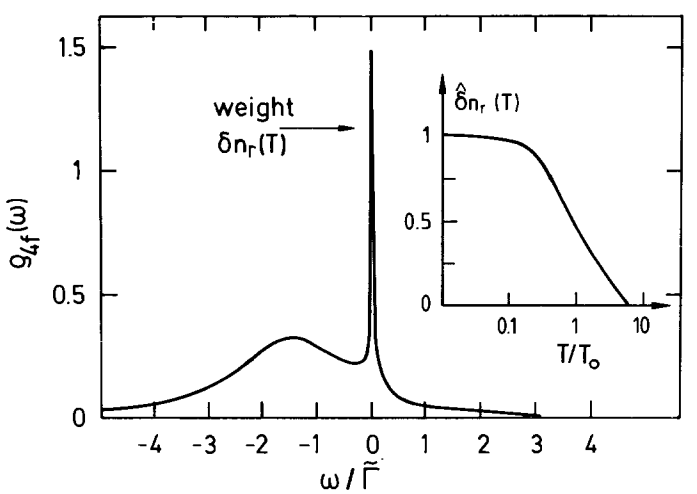

Fig. 46. Spectral density ρ_{4f} of $4f^1 \rightarrow 4f^0$ excitations for a degeneracy of $N=6$ with parameters $W/\tilde{\Gamma} = 10$, $|E_f|/\tilde{\Gamma} = 2$. Here $\tilde{\Gamma} = \pi \tilde{V}^2 N_c(0) = N\Gamma$, where $\tilde{V}$ is the rescaled hybridization strength in eq. (107). (From Coleman 1984.) Inset shows the temperature variation of the normalized Kondo resonance weight $\delta \hat{n}_r(T) = \delta n_r(T)/\delta n_r(0)$. This is a universal function of T/T_0, independent of model parameters in the Kondo regime. (From Cox 1985.)

resonance becomes sharper as the degeneracy N increases and the value of $|E_f|$ increases; i.e., as the 4f level lies deeper below the Fermi level.

4.2.1.2. *Case B: the strongly MV regime.* Now the charge fluctuation peak has moved near to the Fermi level thus making real $4f^1 \rightleftharpoons 4f^0 + e^-$ processes possible (see fig. 1). This leads to a decrease in the 4f occupation, $n_f(0)$, and to a vanishing of the Kondo resonance peak. However, there is no sharp separation between the MV and local-moment regimes; the transition is gradual. Down to $n_f(0) \simeq 0.86$ the Kondo resonance still dominates the low-energy properties (Cox 1985).

Knowing the excitation spectrum one can compute the thermodynamic properties. In the local-moment regime they exhibit low-temperature ($T \leqslant T_K$) "Kondo anomalies" that are due to the resonance states. For example, the static magnetic susceptibilty $\chi(T)$, the specific heat, various transport coefficients and also dynamical quantities (photoemission spectra, dynamical structure function for neutron scattering) have been calculated (Bickers et al. 1985, Cox et al. 1986). An excellent model system for comparison with experimental data are the dilute $(La, Ce)B_6$ alloys because of a fourfold degenerate Γ_8 ground state of cerium (Zirngiebl et al. 1984).

4.2.2. *Quasiparticle bands in the Anderson lattice*

It is suggestive that the narrow Kondo resonance states of individual 4f impurities will form heavy quasiparticle bands in a periodic lattice of 4f ions. A satisfactory microscopic theory of heavy-band formation has yet to be developed. The Hamiltonian of eq. (107) can be generalized to the lattice by introducing a Bose field b_i at every lattice site. However, in this model it is no longer practicable to restrict to physical states with $Q_i = 1$ at every site. The most successful approach so far consists in a mean-field approximation for the Bose field (Coleman 1985, 1987, Newns and Read 1987) that is valid for large N and $T \ll T_K$. It can be applied both for the impurity and the lattice model. It starts from the observation that in the limit $N \to \infty$ with $Q_i/N = q_0$ fixed, the rescaled Bose fields $\tilde{b}_i = b_i/\sqrt{N}$ become classical variables. The square $|\langle \tilde{b}_i \rangle|^2$ is the probability of having a $4f^0$ configuration at site i and its availability for hybridization with conduction electrons. Therefore they can be considered as moving in a classical field $\sigma_i = \langle \tilde{b}_i \rangle$ governed by an effective single-particle Hamiltonian:

$$
\begin{aligned}
H_{\mathrm{mf}} = & \sum_{km} E_k c^\dagger_{km} c_{km} + \sum_{mi} E_f f^\dagger_{im} f_{im} \\
& + \sum_{kmi} \tilde{V}(k)[\sigma_i c^\dagger_{km} f_{im} \exp(-i\boldsymbol{k}\cdot\boldsymbol{R}_i) + \sigma_i^* f^\dagger_{im} c_{km} \exp(i\boldsymbol{k}\cdot\boldsymbol{R}_i)] \\
& + \lambda \sum_i \left(\frac{1}{N} \sum_m f^\dagger_{im} f_{im} + |\sigma|^2 - q_0 \right).
\end{aligned} \tag{110}
$$

To avoid the difficulty of projecting to appropriate angular momentum channels

in the lattice, it is assumed that conduction electrons have a spin S with $N = 2S + 1$.

The minimum free energy resulting from $H_{\rm mf}$ corresponds to a constant and homogeneous field $\sigma = r_0 e^{i\varphi}$ whose overall phase is set to zero. The minimum conditions lead to self-consistent equations for the amplitude r_0 and the Lagrange parameter λ in terms of the mean-field expectation values. They are evaluated by introducing quasiparticle states created by $a^\dagger_{kms}$ ($s = \pm$) which diagonalize $H_{\rm mf}$ to

$$H_{\rm mf} = \sum_{kms} \varepsilon_{ks} a^\dagger_{kms} a_{kms} ,$$

with

$$c_{km} = \sum_s u^s_k a_{kms} , \qquad f_{km} = \sum_s v^s_k a_{kms} , \tag{111}$$

where

$$f_{km} = N_s^{-1/2} \sum_i f_{im} \exp(-i\boldsymbol{k}\cdot\boldsymbol{R}_i) .$$

There are two quasiparticle states per spin channel. Defining $\tilde{E}_{\rm f} = E_{\rm f} + \lambda$ as the renormalized f level one obtains the quasiparticle dispersion $\varepsilon_s(k)$:

$$\varepsilon_\pm(k) = \tfrac{1}{2}(\tilde{E}_{\rm f} + E_k) \pm [\tfrac{1}{4}(\tilde{E}_{\rm f} - E_k)^2 + r_0^2 \tilde{V}(k)^2]^{1/2} , \tag{112}$$

where $\tilde{V}_{\rm e}(k) = r_0(T)\tilde{V}(k)$ is the effective hybridization. Note that each of the quasiparticle bands is still N-fold degenerate. Umklapp terms, which would lead to a dispersion of the renormalized f level, have been neglected.

The minimum conditions for $T = 0$ now lead to, Coleman (1985),

$$\tilde{E}_{\rm f} = E_{\rm f} + \lambda = W \exp(\pi E_{\rm f}/\tilde{\Gamma}) = T_{\rm K} ,$$

$$r_0^2(0) = 1 - n_{\rm f}(0) = q_0 \pi T_{\rm K}/\Gamma \ll 1 . \tag{113}$$

The first equation shows that the center of the quasiparticle bands lies at an energy $T_{\rm K}$ above the original conduction band Fermi level. This should be compared with the position $T_0 = aT_{\rm K}$ of the Kondo resonance in the impurity model. The second equation simply results from the charge constraint $Q_i/N = q_0$, which is now enforced only on the average in contrast to the impurity model. The occupation $n_{\rm f}(0)$ is obtained by setting q_0 equal to the actual value of $1/N$. The quasiparticle bands ε_{ks} are the result of a hybridization with an effective strength $\tilde{V}_{\rm e} = r_0(T)\tilde{V}$. Here $r_0^2(T)$ is the average fraction of sites without f occupation, which are therefore available for hybridization with conduction states. This is a crude way to describe the electronic correlations which give rise to the narrow quasiparticle bands. The density of states $N^*(\varepsilon)$ of the quasiparticle (qp) bands given by eq. (112) is shown in fig. 47. It shows two narrow spikes and a hybridization gap both with a width of $O(T_{\rm K})$. The Fermi level is pinned in a region of large $N^*(\varepsilon)$ where the states have mostly f-like character but are nevertheless true coherent band states. They can be assigned an effective mass m^* via $m^*/m = N^*(0)/N_{\rm c}(0) \gg 1$, which justifies calling them heavy-electron bands. From specific heat experiments one obtains masses of $m^*/m \sim 200$ (Stewart 1984). The existence of a true hybridization gap is an artefact of this model that

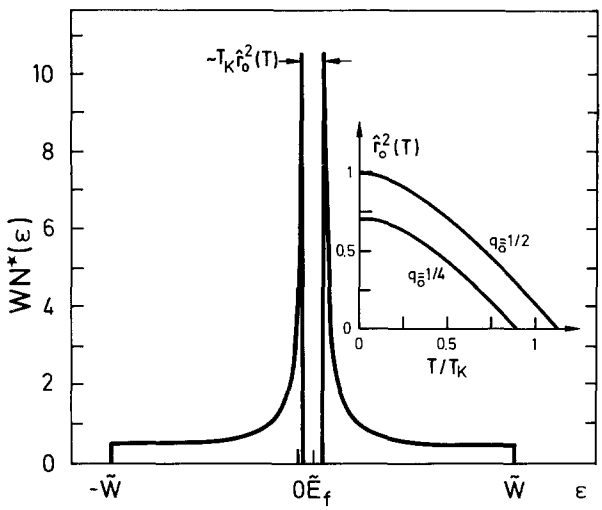

Fig. 47. Schematic quasiparticle density of states $N^*(\varepsilon)$ as obtained from the mean-field dispersion, eq. (112). They lead to a hybridization gap centered around $\tilde{E}_f = T_K$ and two peaks in $N^*(\varepsilon)$ whose width and separation is also of order T_K. The Fermi level (0) is pinned in this region. The temperature dependence of the effective hybridization $\tilde{V}_e^2$ is given by the function $\hat{r}_0^2(T) = r_0^2(T)/r_0^2(0, N=2)$ as shown in the inset (Coleman 1987). $\tilde{W}$ is a slightly renormalized band width [a square DOS of width W has been used for the bare $N_c(\varepsilon)$].

neglects the influence of anisotropy and fluctuations. It is probable that in reality even for $T = 0$ only a 'pseudogap' structure with two peaks but non-vanishing $N^*(\varepsilon)$ in between them exists. Specific heat data in $CeAl_3$, $CeCu_6$ and other compounds have been analyzed with such a model (Bredl et al. 1984).

The effective hybridization is temperature dependent and vanishes at the transition temperature T_K (see insert of fig. 47). Above this temperature quasiparticle bands cease to exist and in this mean-field model one is left with bare 4f and conduction band states. This phase transition is an artificial feature of the mean-field approximation. It will be suppressed by fluctuations in the phase φ of the Bose field and a smooth cross-over from the strong coupling ($T \ll T_K$) to the weak coupling regime ($T \geqslant T_K$) results. For low temperatures, $T \ll T_K$ one can go one step beyond the mean-field theory, which corresponds to the $N = \infty$ limit and includes fluctuations to order $1/N$ (Coleman 1987, Millis and Lee 1987a). This leads to effective interactions between the heavy quasiparticles. They may actually cause an instability of the normal, non-magnetic mean-field ground state. The true ground state may be completely different, e.g., superconducting or magnetically ordered (Tesanovich and Valls 1986, Auerbach and Levin 1986, Doniach 1987, Millis et al. 1987b). The assignment of a single m^* as discussed above is much oversimplified. In reality the masses of heavy quasiparticles are rather anisotropic as seen in table 8 which gives the results of dHvA experiments in $CeCu_6$ see Reinders et al. (1986). A similar result was found for UPt_3 (Taillefer et al. 1987).

TABLE 8
Extremal Fermi surface areas F and effective masses for $CeCu_6$ (from Reinders et al. 1986).

$F[T]$	m^*/m_0
1300 ± 20	24 ± 2
1034 ± 75	40 ± 2
740 ± 10	23 ± 1
638 ± 10	14 ± 1
210 ± 10	...
122 ± 2	6.0 ± 0.2
40 ± 4	11 ± 3

4.3. *Microscopic theory of electron–phonon coupling in heavy-fermion compounds*

The effects of electron–phonon coupling on sound propagation in heavy-electron (HF) compounds can be studied within a similar phenomenological model of deformation potential coupling characterized by Grüneisen parameters as has already been discussed for normal R intermetallics (sect. 3). This approach will be used in sect. 4.4. However, in principle that is only valid for $T \ll T_K$ where well defined quasiparticle bands exist. If the temperature is raised these coherent states are destroyed and evolve into incoherent resonant states at higher temperature ($T \geq T_K$). The corresponding effect on electron–phonon coupling has been considered within a microscopic theory (Thalmeier 1987, 1988).

Microscopically, an important contribution to the Grüneisen parameter coupling in HF Ce compounds comes from a strong volume dependence of the sf-hybridization strength $V(k)$ (Allen and Martin 1982, Razafimandimby et al. 1984). Therefore, sound waves of compressional character, e.g., longitudinal modes modulate the mixing term in the Hamiltonian of eq. (107) and consequently couple to electronic states. For small displacements one can write

$$\tilde{V}(u_i) = \tilde{V} + \left(\frac{\partial \tilde{V}}{\partial \varepsilon_v}\right) \varepsilon_v(i) , \qquad \varepsilon_v(i) = \operatorname{div} \boldsymbol{u}_i , \tag{114}$$

where $\boldsymbol{u}_i$ is the phonon displacement field and $\varepsilon_v(i)$ the corresponding local volume strain. Transformation to phonon coordinates leads to

$$\varepsilon_v(i) = -\mathrm{i} \sum_{q\lambda} (2N_s M_c \omega_{q\lambda})^{-1/2} (\boldsymbol{q} \cdot \boldsymbol{e}_{q\lambda}) \varphi_{q\lambda} \exp(\mathrm{i}\boldsymbol{q} \cdot \boldsymbol{R}_i) . \tag{115}$$

Insertion into the mixing part of eq. (107) yields an additional term,

$$H_{ph}^{r} = -\sum_{km,q\lambda} \frac{\gamma_{q\lambda}}{\sqrt{N}} \varphi_{q\lambda} c_{km}^{\dagger} (b^{\dagger} f_m) + \mathrm{hc} , \tag{116}$$

describing the phonon coupling to the interacting electronic system, i.e., ultimate-

ly to the resonant states at site $\boldsymbol{R}_i = 0$. The coupling constant is given by ($\tilde{V} = \sqrt{N}V$):

$$\gamma_{qs} = \mathrm{i}\tilde{V}' \frac{(\boldsymbol{q}\cdot\boldsymbol{e}_{q2})}{(2M_cN_s\omega_{q2})^{1/2}}, \qquad \tilde{V}' = \left(\frac{\partial\tilde{V}}{\partial\varepsilon_v}\right)_{k_F}. \tag{117}$$

Because it was assumed that $\tilde{V}$ depends only on the volume changing strain $\varepsilon_v = \varepsilon_{xx} + \varepsilon_{yy} + \varepsilon_{zz}$, a scalar product $(\boldsymbol{q}\cdot\boldsymbol{e}_{q2})$ appears in eq. (117) and therefore $\gamma_{qT} = 0$ for transverse modes and $\gamma_{qL} = \mathrm{i}\tilde{V}'|\boldsymbol{q}|\,(2M_cN_s\omega_{qL})^{-1/2}$ for the longitudinal modes. In the long-wavelength limit it is convenient to define $|\gamma_L|^2 := |\gamma_{qi}|^2/v_0 q$ ($q = |\boldsymbol{q}|$), where v_0 is the longitudinal background sound velocity. Using $v_0^2 = c_0/\rho$ and $\rho = M_c/v_c$ (c_0 is the longitudinal elastic constant, ρ is the mass density, M_c is the unit cell mass, v_c is the volume per Ce atom and N_s is the number of Ce atoms) one obtains

$$|\gamma_L|^2 = \tilde{V}'^2/2c_0v_cN_s\,. \tag{118}$$

Here c_0v_c has the meaning of an elastic energy scale. One can relate this to the more phenomenological Grüneisen parameter Ω. Since $T_K \sim \exp(E_f/N_c(0)\tilde{V}^2)$ one obtains

$$\tilde{V}'^2 = \tilde{V}^2\left(\frac{\tilde{\Gamma}}{2\pi E_f}\right)^2\Omega\,, \qquad \Omega = -\frac{1}{T_K}\left(\frac{\partial T_K}{\partial\varepsilon_v}\right). \tag{119}$$

The impurity Hamiltonian H_{ph}^{r} describes the promotion of an f electron into the conduction band by absorbing (emitting) a phonon and creating a $4f^0$ hole. If this coupling is generalized to the lattice model within the mean-field approximation one obtains from H_{mf} [eq. (110)]:

$$H_{ph}^{qp} = -\sum_{q\lambda}\sum_{\substack{km\\ss'}}(r_0\gamma_{q\lambda}u_k^s v_{k-q}^{s'})a_{kms}^{\dagger}a_{k-qms'}\varphi_{q\lambda} + \mathrm{hc}\,. \tag{120}$$

Here the transformation to the quasiparticle operators of eq. (111) has already been performed. As before only the longitudinal modes have a non-vanishing coupling:

$$\tilde{\gamma}_{qL}^{ss'}(\boldsymbol{k}) = r_0(T)\gamma_{qL}u_k^s v_{k-q}^{s'}\,; \qquad \gamma_{qL} = \frac{\mathrm{i}\tilde{V}'(\boldsymbol{q}\cdot\boldsymbol{e}_{qL})}{2N_sM\omega_{qL}}\,. \tag{121}$$

Due to these interactions, H_{ph}^{r} and H_{ph}^{qp}, the phonon frequencies are renormalized by virtual-electron excitations. As indicated before this is done separately in the quasiparticle and resonance regimes. In the former ($T \leqslant T_K$) the phonons will be renormalized by the coupling to quasiparticle hole excitations. This leads to a longitudinal phonon self-energy:

$$\pi(qz) = N_s|\gamma_{qL}|^2r_0^2(T)\int \mathrm{d}\varepsilon\,\mathrm{d}\omega\; N_c(\varepsilon)\rho_{fp}^0(\omega)\frac{f(\varepsilon) - f(\omega)}{z + \varepsilon - \omega}\,, \tag{122}$$

where $z = \nu + \mathrm{i}\eta$ and $f(\omega) = (\mathrm{e}^{\beta\omega} + 1)^{-1}$ and the f-projected DOS is given by

$$\rho_{fp}^0(\omega) = N_s^{-1}\sum_{ks}|v_k^s|^2\delta(\omega - \varepsilon_k^s)\,. \tag{123}$$

It will be approximated by a Lorentzian corresponding to a pole $z_0 = -T_0 + i\Gamma_r$ in the complex-energy plane.

In the long-wavelength limit the renormalized and bare longitudinal phonon frequencies Ω_{qL} and ω_{qL} are given by $\Omega_{qL} = v|q|$ and $\omega_{qL} = v_0 q$ where v_0 and v are the background (including magnetoelastic contributions) and the renormalized sound velocities, respectively. Then

$$\frac{v(T)}{v_0} = \left(\frac{c(T)}{c_0}\right)^{1/2} = 1 + \frac{\pi'(q,0)}{v_0|q|}, \tag{124}$$

where $c_0 = v_0^2/\rho$ and $c = v^2/\rho$ are the longitudinal elastic constants, and ρ is the mass density. Because no relaxation mechanism was included $c(T)$ describes the elastic constants in the isolated regimes. Using eq. (122) it is given by

$$\left(\frac{c(T)}{c_0}\right)^{1/2} = 1 - \Theta(T)\left[\ln\left(\frac{\beta W}{2\pi}\right) - \operatorname{Re}\,\psi\left(\tfrac{1}{2} - i\frac{\beta z_0}{2\pi}\right)\right]. \tag{125}$$

Here $\psi(z) = d\ln\Gamma(z)/dz$ is the digamma function and W is the band width of the Lorentzian conduction electron density of states. Furthermore, $\Theta(T)$ is the effective temperature-dependent coupling strength of the longitudinal sound waves to quasiparticles. It may be written as

$$\Theta(T) = \frac{1}{8\pi}\left(\frac{\tilde{\Gamma}}{E_f}\right)^2 \Omega^2\left(\frac{aT_K}{c_0 v_c}\right) r_n^2(T). \tag{126}$$

The Grüneisen parameter Ω has been introduced via eqs. (118) and (119). Similar formulae hold in the resonance regime ($T \geqslant T_K$) and an interpolation may be used for intermediate temperatures (Thalmeier 1987).

Note that c_0 is the longitudinal background elastic constant, which is obtained by extrapolation from the high-T magnetoelastic region down to $T = 0$. The maximum depression at $T = 0$ due to coupling to quasiparticles is from eq. (125):

$$\frac{\Delta c(0)}{c_0} = \frac{1}{4\pi}\left(\frac{\tilde{\Gamma}}{E_f}\right)^2 \Omega^2\left(\frac{aT_K}{c_0 v_c}\right)\ln\left(\frac{W}{T_K}\right). \tag{127}$$

The temperature dependence of $c(T)$ is given by a monotonic function of T/T_K only.

The theoretical value of $c_L(T)$ has been compared with the experimental results for some Ce compounds, namely $CeCu_6$, $CeRu_2Si_2$ and $CeAl_3$. There are essentially two parameters to be fixed: T_K and Ω which determine the onset and depth of the $c_L(T)$ depression. The quasiparticle DOS was approximated by the Lorentzian resonance DOS as indicated after eq. (123). The theoretical curve is not very sensitive to this assumption. For E_f and W standard Ce values are used, and $\tilde{\Gamma}$ is computed from T_K, E_f and W. Because of the low symmetry of all the compounds the Ce^{3+} ($J = \frac{5}{2}$) splits into three Kramers doublets, e.g., $E_{\pm 3/2}(0\,K)$, $E_{\pm 5/2}(18\,K)$ and $E_{\pm 1/2}(90\,K)$ in $CeAl_3$, therefore the effective degeneracy is $N = 2$. This is one reason why the theory can only qualitatively describe the experiments. Because the crystal-field splittings are quite large compared to the Kondo temperatures in all compounds the magnetoelastic anomalies as described

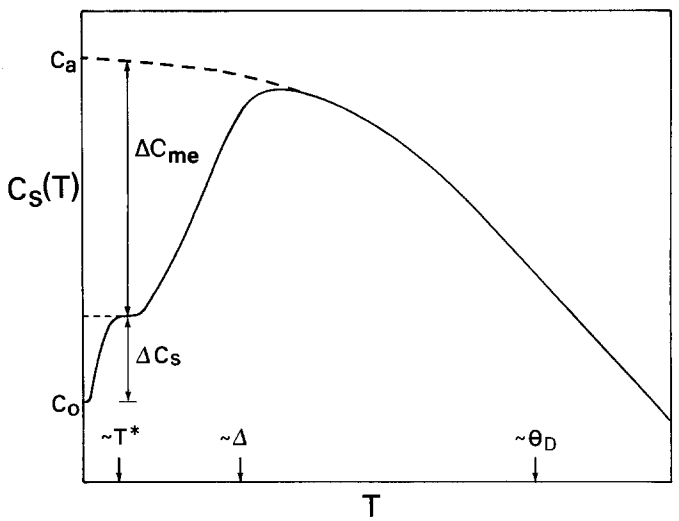

Fig. 48. Schematic temperature variations of adiabatic longitudinal elastic constants in Ce HF compounds. In the various regimes $c_s(T)$ is determined by anharmonic effects ($T \simeq \theta_D$), magnetoelastic coupling ($T \sim \Delta$ = CEF gap) and Grüneisen parameter coupling ($T < T^*$). c_a, c_0 are extrapolations from the anharmonic and magnetoelastic regimes, respectively.

in sect. 2.3 have already reached a plateau when the depression due to the Grüneisen parameter coupling sets in, (see figs. 48 and 51).

This is clearly seen for $c_{11}(T)$ in $CeCu_6$ (fig. 49). Here $T_K = 4.4\,K$ is most reasonable and $\Omega = 57$ was deduced from the maximum depression $\Delta c_{11}(0)/c_{11}(0) \simeq 0.11\%$. This is fairly close to the value of $\Omega = 71$ used by Weber et al. (1987). The comparison of experimental data and theory is given in fig. 49.

The compound $CeRu_2Si_2$ also shows a well developed depression caused by coupling to heavy quasiparticles. The same procedure as above leads to values of

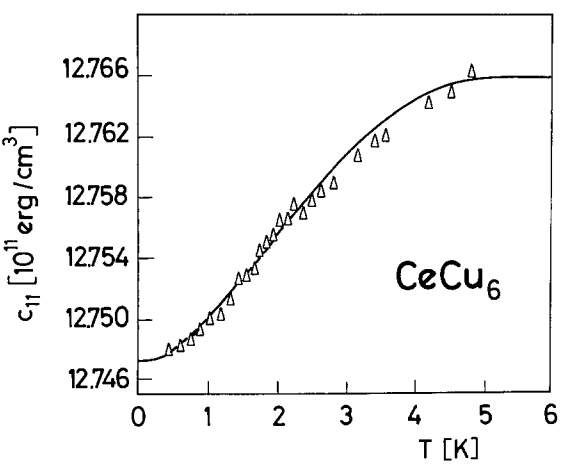

Fig. 49. Temperature dependence of the longitudinal elastic constant c_{11} in $CeCu_6$. Data points are from Weber et al. (1987). Full line: model calculation with $\Omega = 57$, $T_K = 4.4\,K$, $W = 2\,eV$, $E_f = \frac{2}{3}W$, $N = 2$, $c_0 = 12.766 \times 10^{11}\,erg\,cm^{-3}$ and $v_c = 1.05 \times 10^{-22}\,cm^3$.

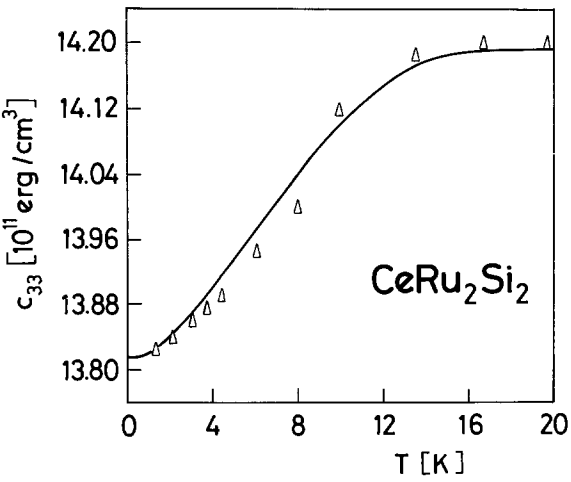

Fig. 50. Temperature dependence of the longitudinal elastic constant c_{33} in $CeRu_2Si_2$. Data points are from Weber et al. (1989). Full line: calculation with $\Omega = 115$, $T_K = 14$ K, $W = 2$ eV, $E_f = \frac{2}{3}W$, $N = 2$, $c_0 = 14.195 \times 10^{11}$ erg cm^{-3} and $v_c = 0.788 \times 10^{-22}$ cm^3.

$T_K = 14$ K and $\Omega = 115$. The latter agrees well with the value of $\Omega = 120$ obtained by Kouroudis et al. (1987). It leads to a maximum depression $\Delta c_{33}(0)/c_{33}(0) = 2.7\%$. The comparison of data and theory is shown in fig. 50.

The first evidence of Grüneisen parameter coupling in elastic constants was originally found in polycrystalline $CeAl_3$, and in $CeSn_3$ (Takke et al. 1981b). The same comparison as above leads for $CeAl_3$ to $T_K = 3$ K and $|\Omega| = 230$. The depression obtained is $\Delta c_L(0)/c_L(0) \simeq 2\%$. The sign of Ω (compare sect. 4.4) cannot be determined in this context. The agreement for $CeAl_3$ is less satisfactory because $c_L(T)$ and the bulk modulus $c_B(T)$ (fig. 45) show an additional minimum at $T \simeq 0.5$ K, whereas the theoretical curve is always monotonically increasing.

It should be emphasized that in the present microscopic context Ω is a constant independent of temperature and has to be compared to the $T = 0$ value of the phenomenological Grüneisen parameter $\Omega(T)$, which is obtained directly from thermal expansion experiments as discussed in the following section. It is possible that an improved theory which includes vertex corrections and fluctuations beyond the mean-field model would lead to a strongly renormalized and temperature-dependent Grüneisen parameter.

4.4. *Phenomenological treatment of electron–phonon coupling in heavy-fermion systems*

In the introduction (sect. 1.2) as well as in sections 4.1 and 4.3 we discussed the main electron–phonon coupling mechanism in heavy-fermion systems. Here we give another discussion for the anomalous cerium compounds, leaving the case of mixed valence to sect. 4.5. In contrast to the previous sect. 4.3 the discussion here is phenomenological and not microscopic. However, we discuss scaling approaches as well as physical effects typical for the large Grüneisen parameter coupling occurring in these systems.

4.4.1. *Crystal-field effects and phase transitions*

In cerium heavy-electron compounds one observes for $T > T_K$ magnetoelastic effects in elastic constants as described in sect. 2 (Lüthi 1985, Lüthi and Yoshizawa 1987). As examples we show the various elastic constants for $CeCu_6$ (fig. 51). The c_{11}, c_{33} and c_{44} modes exhibit clear CEF effects (Weber et al. 1987, Suzuki et al. 1985b). For the other modes the strain susceptibility is too small. Other examples for CEF effects on elastic constants are $CeAl_2$ (Lüthi and Lingner 1979), $CeAl_3$ (Niksch et al. 1980), CeB_6 (Lüthi et al. 1984, Goto et al. 1985), $CePb_3$ (Nikl et al. 1987), $CeRu_2Si_2$ (Kouroudis et al. 1987), LaCeAg (Lüthi et al. 1982) and $CeIn_3$ (Gao et al. 1985). For $T < T_K$ the Van Vleck part of the strain susceptibility can still be operative because only the low lying excitations of the CEF-split $J = \frac{5}{2}$ system are strongly modified by the Kondo interactions.

For the cerium compounds with a cubic crystal structure ($CeAl_2$, CeB_6, $CePb_3$, CeAg) one observes low-temperature magnetic and structural phase transitions (see table 5). $CeAl_2$ was discussed in detail in sect. 2.6, see also sect. 4.5. CeB_6 has two consecutive phase transitions, one of the antiferroquadrupolar character at 3.35 K and a lower magnetic one at 2.31 K.These transitions and the CEF level scheme were investigated with Raman scattering (Zirngiebl et al. 1984), with ultrasound (Lüthi et al. 1984) and with neutrons (Effantin et al. 1985). The B–T

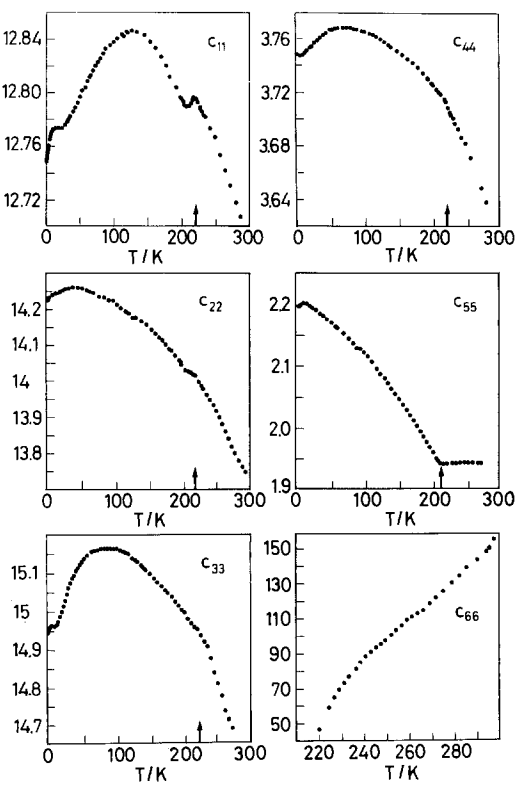

Fig. 51. Elastic constants for $CeCu_6$ as a function of temperature (Weber et al. 1987), in units of 10^{11} erg cm^{-3} except for c_{66} (10^8 erg cm^{-3}).

phase diagram has not been explained completely at the present time. $CePb_3$ has a very large negative magnetoresistance (Lin et al. 1985) which, however, does not lead to field-induced superconductivity (Welp et al. 1987). $CePb_3$ exhibits a magnetic phase transition (Vettier et al. 1986) and a complicated B–T phase diagram (fig. 43), (Nikl et al. 1987), which has not been discussed theoretically yet. The case of CeAg was briefly dealt with in sect. 2.4.3. Here the structural phase transition is of martensitic type, Takke et al. (1981a), see also Morin (1988).

As mentioned already at the beginning of this section, a small magnetic moment has been observed for some low-symmetry crystals at low temperatures ($CeAl_3$, $CeCu_2Si_2$).

4.4.2. *Grüneisen parameter coupling*

For $T < T_K$ a Grüneisen parameter coupling for longitudinal strains is dominant in the cases where no magnetic or structural phase transitions occur (see tables 5, 7), i.e., for $CeCu_6$, $CeAl_3$ and $CeRu_2Si_2$. For the cubic cases $CeAl_2$, CeB_6, $CePb_3$, $CeIn_3$ and CeAg experimental evidence for Grüneisen parameter coupling is difficult to obtain because of the low-temperature phase transitions. Electronic Grüneisen parameters have been introduced before for transition metals (Chandrasekhar and Fawcett 1971) where they are, however, small.

Introducing the deformation potential coupling $E_k = E_k^0 + d_\Gamma(k)\varepsilon_\Gamma$ as in sect. 3.1 [see eq. (89)], one can define $d_{\Gamma_1}(k) = -\Omega_k E_k^0$ or $\Omega_k = -\partial \ln E_k / \partial \varepsilon_v$ [(eq. (90)]. The coupling constant is of order $d_{\Gamma_1} \sim \Omega E_F \sim \Omega T_K$. For a one-band model the Grüneisen parameter Ω is equivalent to the usual definition in terms of thermodynamic quantities (Wallace 1972),

$$\Omega = \frac{\beta c_B}{C} \tag{128}$$

with β is the volume thermal expansion and C is the specific heat. For a two-band model, see below. According to eq. (128) Ω is determined solely from experimental quantities and is thus model independent. With $\beta(T)$ and $C(T)$ Ω will in general also be temperature dependent.

Notice that Ω can have very large values for heavy-fermion systems for $T < T_K$ where β and C are predominantly of electronic origin. In table 7 we list the Ω-values at low temperatures for normal metals Cu and Pd, for CEF-split localized electrons, for mixed-valence systems and for heavy electrons. It is seen that Ω is of order unity for the former cases and very large for heavy electrons. In figs. 52 and 53 we show $\Omega(T)$ for $CeAl_3$ and $CeCu_6$, respectively. These values were obtained from eq. (128) and from the scaling relations described below. In fact the large absolute values of $\Omega(T)$ for $T \ll T_K$ in $CeAl_3$ were the starting point for the thorough investigation of the electron–phonon coupling in heavy-fermion materials (Takke et al. 1981b, Flouquet et al. 1982). It is interesting to note that $\Omega(T \to 0)$ determined from eq. (128) or from scaling relations agrees very well with the corresponding Ω used in the microscopic theory (Thalmeier 1987) as illustrated in table 7. The large negative values of $\Omega(T)$ in $CeAl_3$ for $T \ll T_K$ have

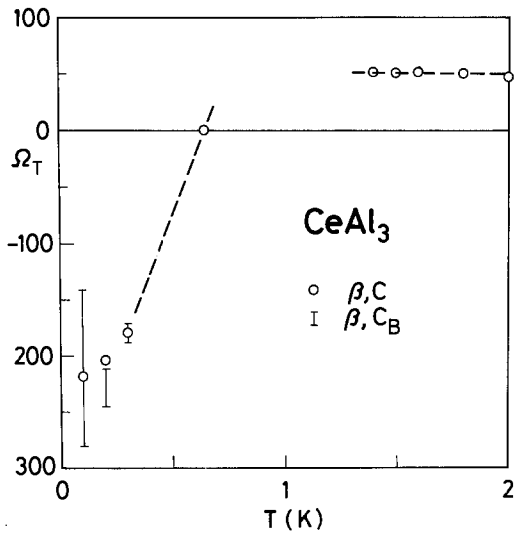

Fig. 52. Grüneisen parameter as a function of temperature for $CeAl_3$ (Takke et al. 1981b).

been the subject of theoretical investigations (Fetisov and Khomskii 1985, Bastide and Lacroix 1986, Lang et al. 1987).

4.4.3. *Sound propagation effects*

The heavy-fermion state with its high density of quasiparticle states and large Grüneisen parameters has a profound influence on sound propagation and thermal properties. Here we mention some typical effects (Yoshizawa et al. 1986, Lüthi and Yoshizawa 1987, Becker and Fulde 1986, 1987a, b).

(a) Using the relation

$$\left(\frac{\mathrm{d}T}{\mathrm{d}\varepsilon}\right)_S = -\left(\frac{\partial T}{\partial S}\right)_\varepsilon \left(\frac{\partial S}{\partial \varepsilon}\right)_T$$

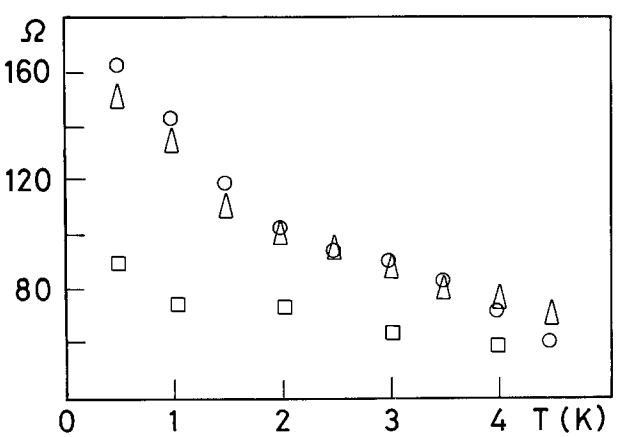

Fig. 53. Grüneisen parameter as a function of temperature for $CeCu_6$: □, $\Omega(c_{11})$; Δ, $\Omega(c_{33})$; ○, $\Omega(\beta)$ (Weber et al. 1987, Ott 1987).

one can write for the average Grüneisen parameter Ω:

$$\Omega = \frac{\beta c_B}{C} = -\left(\frac{\partial \ln T}{\partial \varepsilon_v}\right)_S . \tag{129}$$

This means that a strain wave is accompanied by a temperature wave. With $\Omega \sim 100$, $\varepsilon_v \sim 10^{-4}$ and $T = 1\,\mathrm{K}$, this leads to a temperature amplitude $\Delta T \sim 10\,\mathrm{mK}$ that should be detectable. The resulting temperature gradient ∇T can also be of importance for ultrasonic attenuation effects (Müller et al. 1986).

(b) In the heavy-fermion state the sound propagation is adiabatic. For $ql \ll 1$ a local thermodynamic state can be defined (q is wave number, l is electron mean free path) and the adiabatic sound propagation means that the sound wave period is much smaller than the energy diffusion time (Yoshizawa et al. 1986). Therefore $\omega\tau \ll (3/2\pi)(v_s/v_F)^2$, which is valid for heavy-fermion metals with electron relaxation times $\tau \sim 10^{-12}$ s and sound velocities v_s of the same order as the Fermi velocity v_F. The same estimate shows that for normal metals under the same conditions sound propagation is isothermal. Actually it has been argued that in heavy-fermion systems one is even in the isolated region, i.e., the sound wave period is much less than the particle diffusion time (Becker and Fulde 1987a, b).

(c) Another consequence is the large difference between the adiabatic and the isothermal longitudinal elastic constants. Because of $c_S - c_T = \beta^2 T c_B^2 / C = \Omega^2 TC$ one obtains a relative change in the elastic constant

$$\frac{c_S - c_T}{c_T} = \frac{\Omega^2 TC}{c_B} . \tag{130}$$

For the values used above this leads to $(c_S - c_T)/c_T \sim 1\%$ even at low temperatures of 1 K, whereas for a normal metal like Cu at 1 K $(c_S - c_T)/c_T \sim 10^{-8}$, i.e., the difference between c_S and c_T has no consequences in normal metals.

(d) The large difference between c_S and c_T leads to central-peak phenomena, i.e., an anomalously large Landau–Placzek ratio which determines the ratio of the quasielastic line and the Brillouin lines (Becker and Fulde 1986, 1987a, b). Experimental verification of this fact has been obtained recently for UPt_3 (Mock et al. 1989) but not yet for Ce compounds.

(e) Yet another important consequence is a possible ultrasonic attenuation mechanism similar to what is found in fluids, (Becker and Fulde 1986, 1987a, b, Pethick et al. 1987, Schotte et al. 1986). For UPt_3 an attenuation peak has been found at $T \sim 12$ K, but its origin is not yet entirely clear (Müller et al 1986). Such a peak has also been found in the heavy-electron cerium compound $CeRu_2Si_2$ (Weber et al. 1991).

4.4.4. *The scaling approach*

A simple description of the thermodynamic quantities such as the thermal expansion and the elastic constants can be given in the framework of Grüneisen parameter coupling by using scaling concepts. The first approach assumed a parametrization of the free energy $F(T, \varepsilon_v) = -kTNf(T/T_K)$ where the volume strain dependence enters only through $T_K(\varepsilon_v)$. The resulting electron–lattice

coupling is expressed by the Grüneisen parameter (Takke et al. 1981b)

$$\Omega = -\partial \ln T_K / \partial \varepsilon_v \,. \tag{131}$$

Relations between the isothermal elastic constant c_T, the thermal expansion β and the specific heat C can be obtained:

$$\begin{aligned} &\beta = \Omega C / c_B \,, \\ &c_T - c_T^0 = -\Omega^2 T C \,, \\ &c_T - c_T^0 = -\Omega c_B T \beta \,, \end{aligned} \tag{132}$$

where the first relation is identical to the original Grüneisen parameter definition, eq. (130). From two of the three eqs. (132) Ω can be determined experimentally. This has been done successfully for a number of systems, e.g., $CeAl_3$ and $CeSn_3$ (Takke et al. 1981b).

A generalization has been given using eq. (131) and taking as scaling parameter $\lambda = e^{-\Omega \varepsilon_v}$ (Yoshizawa et al. 1986). A coupling to the strain is then caused by a change in the energy scale of the electron states. The density of states of quasiparticles can be scaled as $N(E, \varepsilon_v) = N(E/\lambda, 0)/\lambda$. From this one can obtain expressions for the thermodynamic quantities. Within a two-band model for cubic systems one obtains (band indices 1, 2):

$$\begin{aligned} &\text{specific heat}\,, && C = C_1 + C_2 \,; \\ &\text{thermal expansion}\,, && \beta = (\Omega_1 C_1 + \Omega_2 C_2)/c_B \,; \\ &\text{elastic constant}\,, && c_S = \Omega_1^2 U_1 + \Omega_2^2 U_2 - T(\Omega_1 - \Omega_2)^2 C_1 C_2 / C \end{aligned} \tag{133}$$

and average Grüneisen parameter, $\Omega = (\Omega_1 C_1 + \Omega_2 C_2)/C$.

Evidence for a validity of the scaling approaches has been observed in a number of heavy-electron compounds. From the data of fig. 45 for $CeAl_3$ one can determine $\Omega(T)$ as shown in fig. 52. It is seen that the scaling relations, eq. (132), are well obeyed for $T < 0.5$ K and lead to the large absolute value of Ω (table 7). Using the two-band model eq. (133) one can also determine $\Omega(T)$ for $CeCu_6$ (fig. 53). Obviously for the c_{11} mode $\Omega(T)$ is close to the value obtained from the microscopic approach, sect. 4.3 and fig. 49. For the c_{33} mode, $\Omega(T)$ is close to the values obtained from thermal expansion results of a polycrystalline sample (Ott 1987). Another interesting compound is $CeRu_2Si_2$ (Haen et al. 1987): this is a tetragonal compound with a crystral structure as shown in fig. 54. Elastic constants can be fitted again using eq. (133) and as before $\Omega = 115$ is very close to the value used in the microscopic description (fig. 50) for c_{33}. Finally, it should be mentioned that a two-band scaling approach [eq. (133)] has been sucessfully applied to the heavy-fermion compound UPt_3 (Yoshizawa et al. 1986).

The phenomenological Grüneisen parameter electron–phonon coupling for the heavy-fermion compounds is very successful in describing the thermal expansion and temperature dependence of elastic constants. The parameters deduced from the different experiments agree with each other and they agree also with the parameters used in the microscopic description, sect. 4.3.

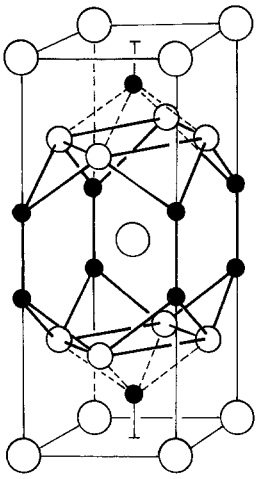

Fig. 54. Unit cell for $CeRu_2Si_2$ (Haen et al. 1985).

Since the heavy-fermion systems discussed are anisotropic ($CeCu_6$ orthorhombic–monoclinic, $CeRu_2Si_2$ tetragonal) one should introduce anisotropic Grüneisen parameters for the description of thermal expansion, elastic constants, magnetostriction etc. This can be done most conveniently by generalizing equation (133) to anisotropic Grüneisen parameters. In the case of tetragonal and hexagonal systems it is sufficient to introduce (Weber et al. 1990).

$$\Omega_a = -\frac{\partial \ln T_K}{\partial \varepsilon_{11}}, \qquad \Omega_c = -\frac{\partial \ln T_K}{\partial \varepsilon_{33}}. \tag{134a}$$

One obtains for the thermal expansion coefficients in the a-, c-directions,

$$\beta_i = \frac{d\varepsilon_{ii}}{dT} = \sum s_{ij} \frac{d^2F}{d\varepsilon_{jj}\, dT},$$

(Lüthi and Ott 1980, Weber et al. 1990),

$$\beta_a = (s_{11} + s_{12})\Omega_a C + s_{13}\Omega_c C,$$

$$\beta_c = 2s_{13}\Omega_a C + s_{33}\Omega_c C, \tag{134b}$$

where the s_{ij} are the elastic compliances (as used in sect. 2.5) and C the specific heat. Because the off-diagonal compliance components can also be negative this can lead to opposite signs in the thermal expansion coefficients as observed before $PrNi_5$ (fig. 19) and UPt_3. From eq. (134b) one obtains a very useful expression for the volume Grüneisen parameter by using

$$\Omega = \beta c_B / C = c_B(2\beta_a + \beta_c)/C$$

(Weber et al. 1989)

$$\Omega = c_B[2\Omega_a(s_{11} + s_{12} + s_{13}) + \Omega_c(s_{33} + 2s_{13})] \tag{135a}$$

with $c_B = 2c_{11} + 2c_{12} + 4c_{13} + c_{33}$.

Finally, for the elastic constants c_{11} and c_{33} one can obtain analogous anisotropic Grüneisen parameter expressions:

$$c_{11} = \Omega_a^2 U\,, \qquad c_{33} = \Omega_c^2 U\,. \tag{135b}$$

The aforementioned calculations have been performed with this formula. In addition, the values for Ω_a and Ω_c listed in table 7 have been obtained in this way. Finally, the fits given in figs. 49 and 50 using the microscopic approach correspond to expressions such as eq. (135b) (Thalmeier 1988).

4.4.5. *Magnetic field effects*

Another aspect to this Grüneisen parameter coupling in the Kondo lattice was added when magnetic field effects on elastic constants were investigated. Particularly convincing results were obtained for UPt_3 and $CeRu_2Si_2$ (Kouroudis et al. 1987). These compounds exhibit an anomaly in the magnetization at $B_c = 21\,\mathrm{T}$ and $B_c = 8.1\,\mathrm{T}$, respectively, i.e., a peak in the differential susceptibility for B along the easy axis (see table 9) (Franse et al. 1984, Besnus et al. 1985). For an explanation of this "metamagnetic behaviour", see Bruls et al. (1990a). Likewise the c_{11} mode for UPt_3 and the c_{33} mode for $CeRu_2Si_2$ exhibit very strong softening. Figure 54 shows the crystal structure of $CeRu_2Si_2$. In fig. 55 $c_{33}(T, B)$ for $CeRu_2Si_2$ is shown. At 1.3 K the relative velocity change at B_c (maximum susceptibility) is more than 15%. On the other hand, the c_{11} mode with magnetic field along the a-axis does not exhibit any field dependence.

One can explain these phenomena again with a Grüneisen parameter mechanism. Defining an appropriate thermodynamic potential

$$F = F_0 - \int M\,\mathrm{d}B$$

and taking the electron lattice coupling by scaling $M(B/B_c)$ with $\Omega_B = -\partial \ln B_c/\partial \varepsilon_v$ we obtain for the isothermal elastic constant $c = \partial^2 F/\partial \varepsilon_v^2$ approximately (Kouroudis et al. 1987):

$$c = c_0 - \Omega_B^2 B^2 \chi_m\,. \tag{136}$$

Here $\chi_m = \partial M/\partial B$ is the differential susceptibility and we have neglected terms

TABLE 9
Physical properties of UPt_3 and $CeRu_2Si_2$.

Material	UPt_3	$CeRu_2Si_2$
Crystal structure	hexagonal	tetragonal
specific heat γ-values (mJ mol^{-1} K^2)	420	380
Fluctuation temperature, T^*(K)	25	15
Magnetic easy direction	a, b-plane	c-axis
Critical field, B_c(T) for χ_m anomaly	20.35	8.07
Soft longitudinal acoustic mode	c_{11}	c_{33}
Magnetic Grüneisen parameter, Ω_B	65	117

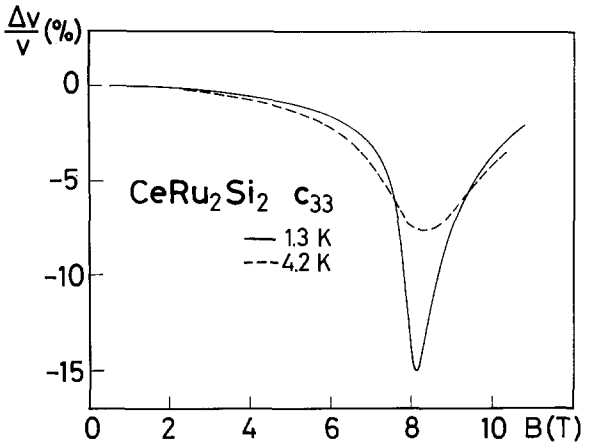

Fig. 55. Magnetic field dependence of longitudinal c_{33} mode in CRu_2Si_2 for different temperatures (Kouroudis et al. 1987).

with $\partial^2 B_c/\partial\varepsilon_v^2$. Formula (136) can also be obtained from a generalized scaling $F(T/T_K, B/B_c)$ by introducing

$$\Omega_T = -\frac{\partial \ln T_K}{\partial \varepsilon_v}, \qquad \Omega_B = -\frac{\partial \ln B_c}{\partial \varepsilon_v},$$

(Thalmeier and Fulde 1986). For $T \ll T_K$ and $\Omega_T = \Omega_B$, formula (136) is again obtained. It is seen that eq. (136) gives a very good description of the experimental results and the near equality of $\Omega_B = 117$ and $\Omega_T = 115$ used in fitting $c_{33}(T)$ in fig. 50. This shows the internal consistency of this description. Similar agreement is obtained for UPt_3.

The analysis of these magnetic-field-dependent results is again carried out using anisotropic Grüneisen parameters

$$\Omega_B^a = -\frac{\partial \ln B_c}{\partial \varepsilon_{11}}, \qquad \Omega_B^c = -\frac{\partial \ln B_c}{\partial \varepsilon_{33}},$$

(Weber et al. 1991) as outlined in sect. 4.4.4. For $CeRu_2Si_2$ the Grüneisen parameter Ω_B quoted above is Ω_B^a and Ω_B^c, respectively (see also tables 7 and 9). In analogy to eq. (135a) one can obtain similar formulae for the linear magnetostriction coefficients. The interesting point is that the magnetostrictive strains ε_a and ε_c should have opposite signs if β_a and β_c have opposite signs. Recent magnetostriction results for UPt_3 (de Visser et al. 1987) do not show this effect although the volume magnetostriction gives a volume Grüneisen parameter of the expected size. The discrepancy for the linear magnetostriction is not understood yet. In $CeRu_2Si_2$ linear thermal expansion and magnetostriction give the same sign, however (de Visser et al. 1987, Puech et al. 1988).

Apart from the soft c_{33} mode for $CeRu_2Si_2$ the c_{11} mode shows analogous soft behaviour for magnetic fields applied along the c-axis (Weber et al. 1988, Bruls et al. 1990a). The Grüneisen parameters obtained from this give $\Omega_B^a \sim \Omega_B^c$ (table 7).

In addition to the effects displayed in fig. 55 attenuation peaks have been observed as a function of field in $CeRu_2Si_2$ and UPt_3 (Weber et al. 1988, 1991). These effects can be accounted for with a Landau–Khalatnikov type of formula for the attenuation

$$\alpha = -(\Delta c/c)\omega^2\tau/2v_s ,$$

where it turns out that the relaxation time τ is very long ($\sim 10^{-9}$ s) for $CeRu_2Si_2$ and $T = 1.2$ K.

Finally various elastic modes exhibit oscillations in the presence of magnetic fields (Weber et al. 1987). The oscillations for the transverse modes in $CeRu_2Si_2$ and UPt_3 reported earlier, (Kouroudis et al. 1987), could, apart from a strong anomaly at B_c, no longer be observed in new crystals of larger size. They were due to mode conversion effects in the original crystals (Weber et al. 1991).

In addition, volume magnetostriction experiments have been performed for polycrystalline samples of the heavy-fermion materials $CeCu_6$ and $CeAl_3$, see Zieglowski et al. (1986). The approximate temperature and field dependences of the volume strain $\varepsilon_v \sim B^2/(T + T^*)^2$ can again be explained by a Grüneisen parameter coupling (Thalmeier and Fulde 1986). For these heavy-fermion materials the volume magnetostriction is much larger (because of the large value of Ω) than for R compounds with stable magnetic ions (sect. 2.5).

4.5. *Electron–lattice coupling in mixed-valence systems*

As discussed before (sections 1.1 and 4.1) magnetic ions with unfilled 3d or 4f shells are often found in different valence states. The resulting state is said to exhibit interconfigurational or valence fluctuations. Examples are Fe^{2+}–Fe^{3+} ions in spinel compounds (inhomogenous valence fluctuations) or Sm^{2+}–Sm^{3+} ions in cubic rare-earth compounds (homogeneous valence fluctuations). By applying pressure or by alloying a valence instability transition can occur (Parks 1976, Lawrence et al. 1981, Penney 1984). A famous example is SmS which collapses to an intermediate-valence state under pressure or by alloying with Y, As ect. Large volume changes can be observed with no change in lattice symmetry, because the trivalent and divalent ions have quite different ionic radii.

For a microscopic model that describes the valence transition one has to add the electronic and elastic energies. The appropriate "order parameter" for a valence transition is the volume strain ε_v and the associated "soft mode", the bulk modulus. But this is not all. Because of the large volume changes one can expect an anomalous Poisson ratio ν, i.e., an uniaxial pressure can give rise to lateral contraction, i.e., $\nu = -\varepsilon_\perp/\varepsilon_\parallel$ can become negative ($\varepsilon_\perp$, $\varepsilon_\parallel$ strains perpendicular and parallel to the applied pressure). This fact shows the strong contrast between the Kondo lattice (KL) and the mixed-valence (MV) compounds: in the former there is approximately particle conservation in the heavy-fermion band, whereas in the latter we have a transfer of f electrons to the conduction band thereby reducing the screening and making $\nu < 0$. The lateral strain $\varepsilon_\perp$ can be estimated as $\varepsilon_\perp = \delta n_f/(Z - n_f)$ with n_f, δn_f the number and its change under pressure of the f

electron and Z an effective number of unscreened nuclear charges of the ion (Lüthi 1985).

Examples of clear-cut effects for c_B and ν as discussed above are found in $Sm_{1-x}Y_xS$ (Penney et al. 1976), TmSe (Boppart et al. 1980), SmB_6, (Tamaki et al. 1985b) and $Ce_{1-x}Th_x$ (Wehr et al. 1981), (see table 6 and fig. 44). Less clear examples are $YbAl_2$ (Penney et al.), $CeBe_{13}$ (Lenz et al. 1984) and $CePd_3$, (Takke et al. 1981b).

In some of these compounds a small hybridization energy gap opens at the Fermi energy giving rise to a large increase in resistivity as discussed in sect. 1.2. In table 6 we list materials which can be classified as a mixed-valent compounds and Kondo lattice compounds. It is seen that c_B is usually small for MV materials compared to their two and three valent neighbors and normal for Kondo lattice (KL) compounds. Likewise the Poisson ratio ν is negative or exceptionally small for MV systems and positive for the KL case in agreement with the qualitative consideration given above.

Pressure studies have been performed on the SmS and $Sm_{1-x}Y_xS$ system with the aim of establishing the phase diagram. For a review see Jayaraman (1978) and Grewe et al. (1980). Furthermore, Sm substitution by Y gives analogous effects. As an example we show in fig. 44 the bulk modulus for $Sm_{1-x}Y_xS$ as a function of x (Penney et al. 1976). It is seen that at the semiconductor–metal transition for $x \sim 0.2$, c_B is practically zero. In addition some phonon modes in the measured phonon dispersion spectra of $Sm_{0.75}Y_{0.25}S$ exhibit anomalies (Mook et al. (1978). These are particularly strong for longitudinal phonons in the (111) direction as shown in fig. 56. The fact that $\omega_{LA}(k) < \omega_{TA}(k)$ for small k is again evidence for

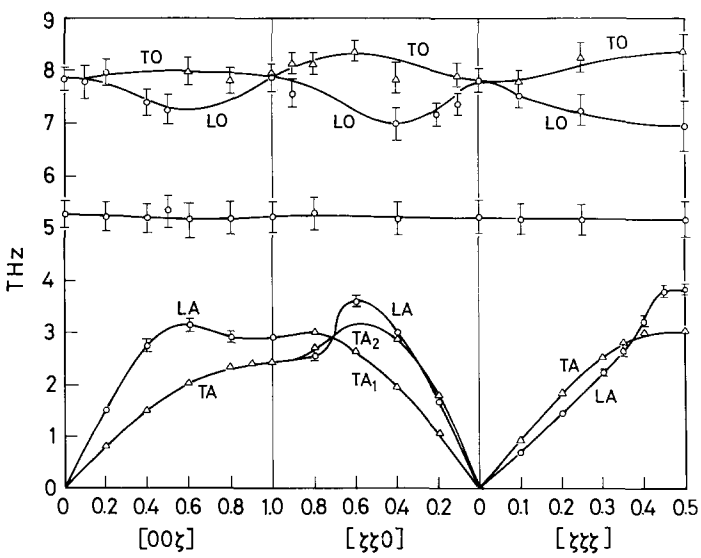

Fig. 56. Phonon spectra for the $Sm_{0.75}Y_{0.25}S$ system for various symmetry directions (Mook et al. 1978).

negative Poisson ratio ($c_{12} < -c_{44}$) (Lüthi 1985). From $\rho v_L^2 = \frac{1}{3}(c_{11} + 2c_{12} + 4c_{44})$ and $\rho v_T^2 = \frac{1}{3}(c_{11} + c_{44} - c_{12})$ follows for $v_L < v_T$ again $c_{12} < -c_{44}$, i.e., $\nu = c_{12}/(c_{11} + c_{12}) < 0$. Detailed calculations of the phonon dispersion spectra have been performed (Wakabayashi 1980, Bilz et al. 1979, Grewe et al. 1978, Pastor et al. 1987). The phase transition line $V(p)$ for SmS has been discussed elsewhere, see Hirst (1974). Another system which shows phonon anomalies as found by neutron scattering is $CePd_3$, see Severing et al. (1988).

TmSe is another interesting example for anomalous elastic properties. TmSe with the two magnetic configurations $4f^{13}(Tm^{2+})$ and $4f^{12}(Tm^{3+})$ exhibits an antiferromagnetic ordering at $T_N \sim 3$ K. As seen from table 6, c_B is small and $\nu < 0$. Very illustrative is the semiconductor–metal transition in the TmSe–TmTe system (Boppart 1985). In fig. 57 the phase diagram p–V–x exhibits close similarities to the common liquid–gas transition ($TmSe_{1-x}Te_x$). The critical point is givey by $x_c \sim 0.45$, $p_c \sim 0.8$ GPa. Because of the same symmetry between the two states a critical point is expected for this solid state transition. For $x < x_c$, one observes a first-order semiconductor–metal transition. The phase transition shows mean-field behaviour with classical critical exponents as expected for long-range elastic interactions with a soft bulk modulus at p_c.

Very similar behaviour to the TmSe–TmTe system has been observed for the $Ce_{1-x}Th_x$ system (Lawrence et al. 1977, 1981) with critical parameters $x_c = 0.265$ and $T_c = 148$ K. Again a very small bulk modulus and a negative Poisson ratio has been observed (Wehr et al. 1981).

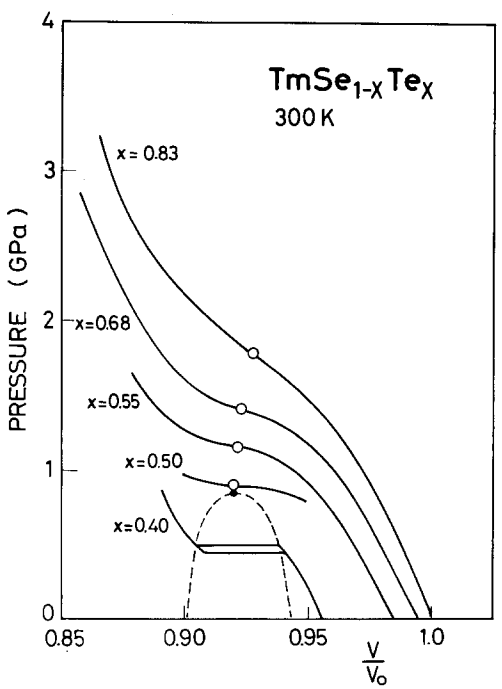

Fig. 57. The p–V phase diagram for $TmSe_{1-x}Te_x$ system at 300 K, (Boppart 1985).

In SmB_6 a considerable temperature softening of c_B of 5% is observed. In addition $\nu < 0$. Furthermore, a Debye-type dispersion of $c_{11} - c_{12}$ and c_{44} was observed for temperatures $100\,K < T < 200\,K$ (Tamaki et al. 1985b). These attenuation and dispersion effects are due to thermal hopping of 4f electrons between different Sm^{3+} and Sm^{2+} configurations.

The other examples of MV compounds are less spectacular in their electron–phonon effects. Both $YbAl_2$ and $CePd_3$ do not show very anomalous behaviour in c_B and ν. This is probably related to the particular crystal structure (Laves phase for $YbAl_2$ and Cu_3Au structure for $CePd_3$). Simple elastic force constant effects may overshadow the anomalous elastic behaviour in these cases.

Theories for electron–phonon effects in mixed-valence compounds, which take into account a breathing mode coupling of nearest neighbors to the rare-earth ion, have been developed (Sherrington and Molnar 1975, Hewson 1979). They were used to explain phonon spectra in systems like $Sm_{0.75}Y_{0.25}S$ (Mook et al. 1978).

More information can be gained from a discussion of the charge fluctuation rate. This can be calculated similar to the spin fluctuation rates (Müller-Hartmann 1981, Schmidt and Müller-Hartmann 1985). Unlike the spin fluctuation rates, which can be measured with quasielastic neutron scattering, charge fluctuation rates can be determined only indirectly via the phonon spectra. Depending on whether the phonon frequencies ω_q are larger than the charge fluctuation width Γ ($\hbar\omega_q > \Gamma$) or smaller ($\hbar\omega_q < \Gamma$) different effects can be observed, see Mock et al. (1986), and Zirngiebl et al. (1986). In the first case the lattice vibrations of the mixed-valent compound sample a static distribution of two-valent and three-valent ions and therefore the phonon frequencies are intermediate between the two integral-valent cases. A typical example are the Γ_1^+, Γ_3^+ and Γ_5^+ phonon modes ($\omega > 700\,cm^{-1}$) in SmB_6. In the other limit ($\hbar\omega_q < \Gamma$) one observes a softening of the phonon modes because the charge fluctuation can follow the movement of the ions. Examples for this behaviour are the Γ_4^- mode in SmB_6 ($\omega \sim 172\,cm^{-1}$) and, in the quasi-static limit, the softening of the bulk modulus in the compounds discussed above.

Of particular interest is the transition from the Kondo lattice regime to the mixed-valence state. This could be done by taking a KL compound and investigating its physical properties as a function of applied pressure. Such experiments have been performed for a number of substances. In $CeRu_2Si_2$, discussed in sect. 4.4, one observes an increase of the fluctuation temperature on applying pressure (Thompson et al. 1985). The increase is so large that crystal-field effects disappear. However, no transition to a mixed-valence state is observed. In $CeAl_2$ recent measurements, correcting previous experiments, again do not exhibit an abrupt transition from the KL to the MV state up to a pressure of 20 GPa (Vedel et al. 1987a). The bulk modulus (Penney et al. 1982, Lingner and Lüthi 1983) does not change substantially throughout the whole pressure range. From the reduction of the unit cell volume a continuous valence change can be deduced. Similar results have been found for $CeIn_3$ (Vedel et al. 1987a). Thus in Ce-compounds the γ–α transition, as discussed before for SmS and TmSe (fig. 57), does not take place. Therefore instead of a promotion model (4f→conduction

band) an explanation with a strong electronic Grüneisen parameter should be sought. A true γ–α transition has been observed in elemental Ce (Koshenmahi and Gschneidner 1978), its alloys with La and Th and in CeP (Vedel et al. 1987b).

5. Outlook

Whereas the electron–phonon interaction is well understood for stable R compounds as outlined in sections 2 and 3, this is not the case for unstable ions. Several developments can already be anticipated.

There is increasing evidence that most non-magnetic heavy-fermion compounds develop weak magnetic moments at low temperatures. For URu_2Si_2 at $T < 17.5$ K a magnetic moment of about 0.03 μ_B appears (Broholm et al. 1987) and $CeAl_3$ below 2 K develops a magnetic moment of 0.05 μ_B (Barth et al. 1987). This new development, carried out with the help of neutron scattering and μ-spin precession experiments, clearly contradicts standard ideas of the singlet ground state of heavy-fermion systems. On the other hand, $CeCu_6$ and $CeRu_2Si_2$ do not exhibit long-range magnetic order but pronounced magnetic correlations which saturate below their respective fluctuation temperature (Rossat-Mignod et al. 1988).

The question will then arise whether in the electron–phonon interaction additional terms of, e.g., exchange striction type will contribute to the Grüneisen parameter coupling.

With respect to the magnetic and thermal Grüneisen parameters Ω_B, Ω_T (sect. 4.4) it has recently been shown that $\Omega_B > \Omega_T$ for transition-metal compounds with strong Stoner enhancement, (Kaiser and Fulde 1988). Since the Sommerfeld–Wilson ratio,

$$R = \frac{1}{3}\left(\frac{\pi k_B}{\mu_B}\right)^2 \frac{\chi_m}{\gamma},$$

is small for heavy-fermion systems, $\Omega_B = \Omega_T$ is expected as has been observed in some cases (sect. 4.4.4). The relation between the enhancement factor and Ω_B may help to obtain a better microscopic understanding of the Grüneisen parameter.

Another important problem is the relation between heavy-electron masses as obtained from measurement of the specific heat γ-value and from the dHvA experiments. For example, in $CeCu_6$ the former shows a strong field dependence, Stewart et al. (1988) whereas the latter seems to be field independent (Reinders et al. 1986). For CeB_6, however, both the thermal and the cyclotron masses show pronounced field dependences (Joss et al. 1987).

Superconductivity in heavy-fermion cerium compounds has been observed only in $CeCu_2Si_2$, Steglich et al. (1979). Recently, single crystals of $CeCu_2Si_2$ of sufficiently good quality could be grown to perform acoustic experiments. Therefore, acoustic propagation could be studied as in, e.g., UPt_3 (Müller et al. 1987) or UBe_{13} (Golding et al. 1985). The first experiments determined the B–T phase diagram for the superconducting and magnetic phases for two crystals (Bruls et al. 1990b,c, Assmus et al. 1990). In a crystal with $T_c = 0.18$ K the two phases are

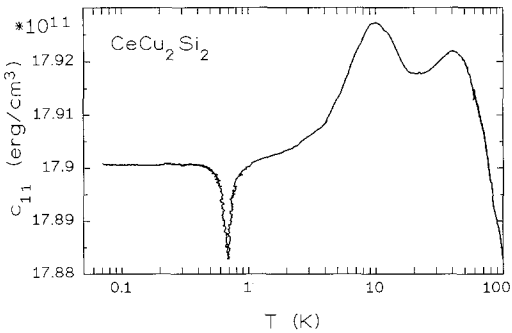

Fig. 58. C_{11} as a function of temperature for single-crystal $CeCu_2Si_2$ ($T_c = 0.7$ K).

separated, whereas with the one with $T_c = 0.7$ K the phase diagram looks much closer to the one determined from susceptibility and NMR experiments (Nakamura et al. 1988). Similar experiments, together with magnetoacoustic quantum oscillations, have been performed in URu_2Si_2 (Bruls et al. 1991). As a final illustration of the various elastic effects discussed in this review we show the global temperature variation of c_{11} (fig. 58) for single crystal $CeCu_2Si_2$ with a superconducting $T_c = 0.7$ K.

Recently, in analogy to the magnetic Kondo effect, a quadrupolar Kondo effect was suggested (Cox 1987). Prominent candidates for this effect to exist are the UBe_{13} and Ce systems with Γ_8 ground states. Clearly temperature- and magnetic-field-dependent elastic constants can help to clarify the situation of this effect.

Acknowledgement

Part of this work was supported by Sonderforschungsbereich 252, Darmstadt–Frankfurt–Mainz, F.R.G. One of us (P.T.) was supported by a Heisenberg Fellowship from the Deutsche Forschungsgemeinschaft. We thank W. Seitz for an excellent job of typing the manuscript.

Appendix A

In this appendix we discuss a very convenient method to calculate electron–phonon coupling effects for stable-moment compounds, i.e., with integer 4f occupation. It is based on diagrammatic perturbation theory and will be used extensively in sect. 2. It is especially suitable for the calculation of finite-frequency phenomena like quadrupolar excitons and their mixing with phonons (sect. 2.7). In this 'pseudofermion' method invented by Abrikosov (1965) and then adapted to CEF problems (Fulde and Peschel 1972) the transition operators $L_{nm} = |n\rangle\langle m|$ that form the "standard basis" for operators acting within a given CEF system are replaced by pseudofermion operators f_n according to $L_{nm} \to f_n^\dagger f_m$. Unlike the L_{nm} they obey Fermi commutation rules $\{f_n, f_m^\dagger\} = \delta_{mn}$. In this basis H_{CEF} and H_{me} of eqs. (2) and (9) read

$$\tilde{H}_{\mathrm{CEF}} = \sum_{i,n} (E_n + \lambda_i) f^{\dagger}_{ni} f_{ni} ,$$

$$H_{\mathrm{me}} = -N^{-1/2} \sum_{\Gamma,i} \sum_{\substack{q\lambda \\ n,m}} g_\Gamma Q_\Gamma(q, \lambda) O^{nm}_\Gamma(i) f^{\dagger}_{ni} f_{mi} \varphi_{q\lambda} \exp(-\mathrm{i} q \cdot R_i) , \tag{A1}$$

where we have replaced

$$O_\Gamma(i) \rightarrow \sum_{n,m} O^{nm}_\Gamma f^{\dagger}_{ni} f_{mi}$$

with $O^{nm}_\Gamma = \langle n | O_\Gamma | m \rangle$. However, this substitution introduces unphysical states where more than one CEF state is occupied simultaneously. These states can be projected out by taking the chemical potential $\lambda(i)$ to be added in H_{CEF} to infinity at every site i. This means that thermal averages are performed according to

$$\langle A \rangle = \lim_{\lambda_i \to \infty} Z^{-1} \exp(\beta \lambda_i) \langle A \rangle_{\lambda_i} \tag{A2}$$

at the end of any perturbation calculation. In this way only configurations with one occupied CEF state per site are left. Expressed differently, one is projecting to the physical subspace which has the "f charge"

$$Q_i = \sum_m f^{\dagger}_{mi} f_{mi} = 1 .$$

Using the pseudofermion representation for H_{me} and a similar one for H_{Q} we can now calculate the phonon propagator renormalized by this interaction:

$$D(q\lambda, \tau) = -\mathrm{i} \langle T \varphi_{q\lambda}(\tau) \varphi_{q\lambda}(0) \rangle . \tag{A3}$$

For this purpose we also need the bare pseudofermion propagator whose Fourier transform is $[\omega_l = \pi \beta^{-1}(2l+1)]$

$$G^0_n(i, \mathrm{i}\omega_l) = (\mathrm{i}\omega_l - \lambda_i - E_n)^{-1} , \tag{A4}$$

and the bare phonon propagator ($\nu_l = \pi \beta^{-1} l$)

$$D_0(q\lambda, \mathrm{i}\nu_l) = 2\omega_{q\lambda} [(\mathrm{i}\nu_l)^2 - \omega_{q\lambda}{}^2]^{-1} . \tag{A5}$$

If we restrict to modes which have $Q_\Gamma(q\lambda) \neq 0$ for only one Γ the self-energy of phonons due to $H_{\mathrm{me}} + H_{\mathrm{Q}}$ is given

$$\pi(q\lambda, \mathrm{i}\nu_l) = -g^2_\Gamma |Q_\Gamma(q, \lambda)|^2 \chi^{\mathrm{Q}}_\Gamma(q, \mathrm{i}\nu_l) . \tag{A6}$$

Here $\chi^{\mathrm{Q}}_\Gamma(q, \mathrm{i}\nu_l)$ is the dynamical quadrupolar susceptibility of the system of RE ions coupled by H_{Q}. In the RPA approximation whose corresponding diagrams are shown in fig. 59b we have ($\mathrm{i}\nu_l \rightarrow \omega + \mathrm{i}\eta$)

$$\chi^{\mathrm{Q}}_\Gamma(q, \omega) = \frac{\chi_\Gamma(\omega)}{1 - \hat{K}_\Gamma(q) \chi_\Gamma(\omega)} , \tag{A7}$$

where the dynamical single-ion susceptibility $\chi_\Gamma(\omega)$ is given by

$$\chi_\Gamma(\mathrm{i}\nu_l) = -\lim_{\lambda \to \infty} Z^{-1} \exp(\beta\lambda) \beta^{-1} \sum_{nm} \sum_{\omega_k} |\hat{O}^{nm}_\Gamma|^2 G^0_m(\mathrm{i}\omega_k) G^0_n(\mathrm{i}\omega_k + \mathrm{i}\nu_l) , \tag{A8}$$

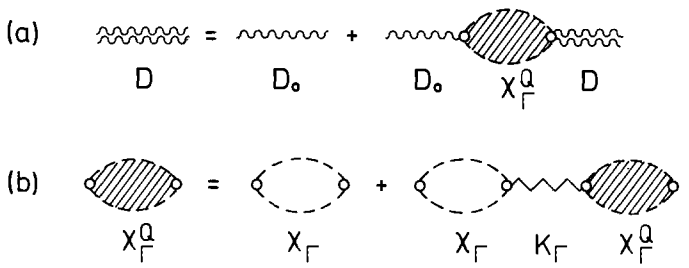

Fig. 59. (a) The Dyson equation [eq. (A10)] for the phonon propagator. (b) The RPA approximation for the quadrupolar susceptibility with respect to the quadrupolar interaction K_Γ, see eq. (A7). Circles represent the quadrupolar operators O_Γ.

corresponding to the first diagram in fig. 59. Summation and the identity

$$\hat{O}_\Gamma^{nm} = O_\Gamma^{nm}(1-\delta_{nm}) + \hat{O}_\Gamma^{nm}\delta_{nm}$$

leads to the final result ($i\nu_l \to \omega + i\eta$)

$$\chi_\Gamma(\omega) = \sum_{\substack{n,m \\ E_n \neq E_m}} |O_\Gamma^{nm}|^2 \frac{p_n - p_m}{\omega - (E_n - E_m) + i\eta} + \frac{1}{k_B T}\sum_n p_n |\hat{O}_\Gamma^{nn}|^2 \delta_{\omega,0} . \qquad \text{(A9)}$$

Together with eq. (A7) this defines the dispersion of collective quadrupolar excitations that is given by the zeros of the denominator in eq. (A7). The renormalized phonon propagator is now obtained by Dyson's equation (fig. 59a) as

$$D(\boldsymbol{q}\lambda, \omega)^{-1} = D_0^{-1}(\boldsymbol{q}, \lambda, \omega) - \pi(\boldsymbol{q}\lambda, \omega) . \qquad \text{(A10)}$$

The dynamics of the coupled phonons and quadrupolar excitons is determined by eqs. (A7), (A9) and (A10). The corresponding excitation spectrum of "mixed modes" is discussed in sect. 2.7.1.

We now focus on the low-frequency limit for sound waves. Note that $\chi_\Gamma(\omega)$ of eq. (A9) behaves singularly at $\omega = 0$, namely,

$$\chi_\Gamma^{\mathrm{I}}(T) = \lim_{\omega \to 0} \chi_\Gamma(\omega) \neq \chi_\Gamma(\omega = 0) = \chi_\Gamma(T)$$

with

$$\chi_\Gamma(T) = \chi_\Gamma^{\mathrm{I}}(T) + \frac{1}{k_B T}\sum_n p_n |\hat{O}_\Gamma^{nm}|^2 . \qquad \text{(A11)}$$

Here $\chi_\Gamma(T)$ is the isothermal susceptibility of eq. (36) and $\chi_\Gamma^{\mathrm{I}}(T)$ is the "isolated susceptibility" that is identical to the Van Vleck contribution $\chi_\Gamma^{\mathrm{VV}}(T)$ in eq. (36). They differ by the Curie contributions of the degenerate CEF states. The latter are due to the thermal repopulation of those states when they are split by a static external strain. Eq. (A9) seems to suggest that even an arbitrary small sound frequency, $\omega \neq 0$, is too high to allow for repopulation of states. Thus Curie terms would be absent and the isolated quadrupolar susceptibility would determine the T-dependence of the sound velocities at finite frequencies. However, this singular behaviour of $\chi_\Gamma(\omega)$ in eq. (A9) is an artifact of the RPA approximation used,

which assumes a coupling of sound waves to unperturbed "isolated" CEF excitations without a relaxation mechanism, which leads to a finite linewidth $\Gamma_{nm} = \hbar/\tau_{nm}$ of the CEF transition $|n\rangle \rightarrow |m\rangle$. Their inclusion (Young 1975) leads to a Curie contribution in eq. (A9) that is of the form

$$\chi_\Gamma^{\mathrm{C}}(\omega) = \frac{1}{k_{\mathrm{B}}T} \sum_n p_n |\hat{O}_{nn}|^2 \frac{1}{1 - \mathrm{i}\omega\tau_{nn}} . \tag{A12}$$

Now for $\omega \ll \tau_{nn}^{-1}$ $\chi_\Gamma(\omega) \rightarrow \chi_\Gamma(T)$, the isothermal susceptibility of eq. (36). Here τ_{nn} is a phenomenological relaxation time which determines how fast each level reaches its thermal equilibrium population. In metallic R compounds the dominating relaxation mechanism is the exchange interaction with conduction electrons. At low temperatures it leads to a Korringa behaviour $\hbar/\tau_{nn} \simeq cT$ for normal compounds [see, e.g., Becker et al. (1977)] and to a constant rate $\hbar/\tau_{nn} \sim T_{\mathrm{K}}$ for Kondo compounds. In any case one has $\omega\tau_{nn} \ll 1$ in the temperature ($T \geq 0.5\,\mathrm{K}$) and frequency ($\omega/2\pi \leq 100\,\mathrm{MHz}$) regions where ultrasonic experiments are performed. Therefore, it is the isothermal and not the isolated susceptibility which determines the sound velocities in this regime. From eq. (A10) we now obtain the renormalized phonon frequency $\omega_{q\lambda}^2 = (\omega_{q\lambda}^0)^2 + 2\omega_{q\lambda}^0 \pi(\boldsymbol{q}\lambda, \omega_{q\lambda})$. In the long-wavelength limit $\omega_{q\lambda}^0 = v_0(\hat{\boldsymbol{q}}\lambda)|\boldsymbol{q}|$ and $\omega_q = v(\hat{\boldsymbol{q}}\lambda)|\boldsymbol{q}|$, where v_0 and v are the background and renormalized sound velocities, respectively, ($\hat{\boldsymbol{q}} = \boldsymbol{q}/|\boldsymbol{q}|$). Using eqs. (A6) and (A7) this yields

$$\left(\frac{v^2}{v_0^2}\right)_{q\lambda} = 1 - \sum_\Gamma g_\Gamma^2 |\hat{Q}_\Gamma(\hat{\boldsymbol{q}}\lambda)|^2 \chi_\Gamma^{\mathrm{Q}}(0,0) . \tag{A13}$$

The $\hat{O}_\Gamma$ were defined by eq. (13). For sound modes ($\hat{\boldsymbol{q}}$, λ) that generate only one symmetry strain ε_Γ this simplifies to

$$\left(\frac{v^2}{v_0^2}\right) = \frac{c_\Gamma}{c_\Gamma^0} = \frac{1 - (\tilde{g}_\Gamma^2 + g_\Gamma')\chi_\Gamma(T)}{1 - g_\Gamma'\chi_\Gamma(T)} , \tag{A14}$$

where $\tilde{g}^2 = g_\Gamma^2/c_\Gamma^0 v_{\mathrm{c}}$, $g_\Gamma' = \hat{K}_\Gamma(0)$ and $\chi_\Gamma(T)$ is the isothermal single-ion susceptibility of eq. (36). Furthermore, $c_\Gamma = v_\Gamma^2/\rho$ etc. and v_{c} is the volume per R ion. This formula will be used extensively in sect. 2.4.

Appendix B

The computational technique used to treat the generalized Anderson impurity model in the slave boson representation will be described in some detail. For an extensive discussion see Coleman (1984). In Appendix A we represented the CEF states of stable $4f^n$ shells (i.e., with integer occupation n) by pseudofermions. In the present case of unstable shells with possible $4f^1$ and $4f^0$ configurations we need an additional slave boson field for the $4f^0$ state. The interesting physical quantities, static as well as dynamic, can be calculated in terms of the fully renormalized fermion and slave boson Matsubara Green's functions

$$G_\lambda^m(\tau) = \langle T f_m(\tau) f_m^\dagger \rangle_\lambda , \tag{B1}$$

and

$$D_\lambda(\tau) = \langle Tb(\tau)b^\dagger \rangle_\lambda .$$

The average is taken with respect to the grand canonical ensemble whose partition function is $Z_G(\beta, \lambda) = \mathrm{Tr}\exp(-\beta\tilde{H})$ [see eq. (107)]. These Green's functions are computed in a self-consistent perturbation expansion to all orders in $\tilde{V}/\sqrt{N}$. For a constant $\tilde{V}$ this amounts to a $1/N$-expansion of G and D to infinite order where vertex corrections are neglected (Coleman 1984). Their Fourier transforms are then given by

$$G^m_\lambda(\mathrm{i}\omega_n) = [\mathrm{i}\omega_n - E_f - \lambda - \Sigma^m_\lambda(\mathrm{i}\omega_n)]^{-1} ,$$

and

$$D_\lambda(\mathrm{i}\nu_n) = [\mathrm{i}\nu_n - \lambda - \pi_\lambda(\mathrm{i}\nu_n)]^{-1} . \tag{B2}$$

After taking the limit $\lambda \to \infty$ the fermion and boson self-energies Σ, π satisfy a set of coupled T-dependent integral equations central to this theory ($\mathrm{i}\omega_n \to \omega + \mathrm{i}\eta$ etc.):

$$\Sigma_m(\omega + \mathrm{i}\eta) = \frac{\tilde{V}^2}{N} \sum_k [1 - f(E_k)] D(\omega + E_k + \mathrm{i}\eta) ,$$

and

$$\pi(\nu + \mathrm{i}\eta) = \frac{\tilde{V}^2}{N} \sum_{k,m} f(E_k) G_m(\nu + E_k + \mathrm{i}\eta) . \tag{B3}$$

Their numerical solution yields the spectral functions

$$A_m(\omega) = -\pi^{-1} \,\mathrm{Im}\, G_m(\omega + \mathrm{i}\eta)$$

and

$$B(\nu) = -\pi^{-1} \,\mathrm{Im}\, D(\nu + \mathrm{i}\eta) ,$$

from which all the interesting quantities may be computed (Coleman 1984, Cox 1985). For example, the real electronic excitation spectrum is described by the "real" 4f Green's function

$$G^m_{4\mathrm{f}}(\tau) = \lim_{\lambda\to\infty} \langle Tb^\dagger(\tau) f_m(\tau) f^\dagger_m b \rangle_\lambda / \langle Q \rangle_\lambda , \tag{B4}$$

which has a spectral representation

$$G^m_{4\mathrm{f}}(\mathrm{i}\omega_n) = \int \frac{\rho^m_{4\mathrm{f}}(\omega')}{\mathrm{i}\omega_n - \omega'} \,\mathrm{d}\omega' . \tag{B5}$$

Here $\rho^m_{4\mathrm{f}}(\omega')$ describes the spectrum of electronic $4\mathrm{f}^0 \rightleftharpoons 4\mathrm{f}^1$ excitations; it is obtained as a convolution of $A_m(\omega)$ and $B(\nu)$:

$$\rho^m_{4\mathrm{f}}(\omega') = \int_{-\infty}^{\infty} \mathrm{d}\omega' \,[A^m_{\mathrm{f}}(\omega + \omega') B(\omega')][\mathrm{e}^{-\beta(\omega+\omega')} + \mathrm{e}^{-\beta\omega'}]/Z_{\mathrm{MV}}(\beta) , \tag{B6}$$

where

$$Z_{\mathrm{MV}}(\beta) = \int_{-\infty}^{\infty} \mathrm{d}\omega \left(\sum_m A^m_{\mathrm{f}}(\omega) + B(\omega) \right) \mathrm{e}^{-\beta\omega} \tag{B7}$$

is the partition function of the 4f impurity. An example for this spectrum is shown in fig. 46.

References

Aarts, J., F.R. de Boer and P.F. de Châtel, 1985, J. Magn. & Magn. Mater. **49**, 271.

Abrikosov, A.A., 1965, Physics **2**, 5.

Abu-Aljarayesh, I., J.S. Kouvel and T.O. Brun, 1986, Phys. Rev. B **34**, 240.

Ahrens, K., and G. Schaack, 1980, Z. Phys. B **40**, 45.

Akhiezer, A.I., M.I. Kaganov and G.Ia. Liubarskii, 1957, Sov. Phys-JETP **5**, 685.

Aksenov, V.L., Th. Frauenheim, N.M. Plakida and J. Schreiber, 1981, J. Phys F **11**, 905.

Aksenov, V.L., E.A. Goremychkin, E. Mühle, Th. Frauenheim and W. Bührer, 1983, Physica B **120**, 310.

Aléonard, R., and P. Morin, 1984, J. Magn. & Magn. Mater. **42**, 151.

Allen, J.W., and R. Martin, 1982, Phys. Rev. Lett. **49**, 1106.

Allen, S.J., 1968, Phys. Rev. **167**, 492.

Andrei, N., 1980, Phys. Rev. Lett. **45**, 379.

Andres, K., J.E. Graebner and H.R. Ott, 1975, Phys. Rev. Lett. **35**, 1779.

Andres, K., P.S. Wang, Y.H. Wong, B. Lüthi and H.R. Ott, 1976, AIP Conf. Proc. **34**, 222.

Assmus, W., R. Takke, R. Sommer and B. Lüthi, 1978, J. Phys. C **11**, L575, Corr. L 793.

Assmus, W., W. Sun, G. Bruls, D. Weber, B. Wolf, B. Lüthi, M. Lang, U. Ahlheim, A. Zahn and F. Steglich, 1990, Physica B **165&166**, 379.

Auerbach, A., and K. Levin, 1986, Phys. Rev. Lett. **57**, 877.

Azaroff, L.V., 1968, Elements of X-ray crystallography (McGraw-Hill, New York).

Barth, S., H.R. Ott, F.N. Gygax, B. Hitti, E. Lippelt, A. Schenck, C. Baines, B. van den Brandt, T. Konter and S. Manger, 1987, Phys. Rev. Lett. **59**, 2991.

Bastide, C., and C. Lacroix, 1986, Solid State Commun. **59**, 121.

Becker, K.W., and P. Fulde, 1986, Europhys. Lett. **1**, 669.

Becker, K.W., and P. Fulde, 1987a, Z. Phys. B **65**, 313.

Becker, K.W., and P. Fulde, 1987b, Z. Phys. B **67**, 35.

Becker, K.W., P. Fulde and J. Keller, 1977, Z. Phys. B **28**, 9.

Becker, K.W., P. Fulde, J. Keller and P. Thalmeier, 1979, J. Phys. Colloq. **C5**, 35.

Becker, P.J., G.A. Gehring, R. Gosh and M. Steiner, 1981, J. Phys. C **14**, 1945.

Besnus, M.J., J.P. Kappler, P. Lehmann and A. Meyer, 1985, Solid State Commun. **55**, 779.

Bickers, N.E., 1987, Rev. Mod. Phys. **59**, 845.

Bickers, N.E., D.L. Cox and J.W. Wilkins, 1985, Phys. Rev. Lett. **54**, 230.

Bilz, H., G. Güntherodt, W. Kleppmann and W. Kress, 1979, Phys. Rev. Lett. **43**, 1979.

Birgeneau, R.J., E. Bucher, L. Passell and K.C. Turberfield, 1971, Phys. Rev. B **4**, 718.

Birgeneau, R.J., E. Bucher, J.P. Maita, L. Passell and K.C. Turberfield, 1973, Phys. Rev. B **8**, 5345.

Birgeneau, R.J., J.K. Kjems, G. Shirane and L.G. van Uitert, 1974, Phys. Rev. B **10**, 2512.

Bolef, D.I., and J.G. Miller, 1971, in: Physical Acoustics, eds W.P. Mason and R.N. Thurston (Academic Press, New York) Vol. VIII.

Bonsall, L., and R.L. Melcher, 1976, Phys. Rev. B **14**, 1128.

Boppart, H., 1985, J. Magn. & Magn. Mater. **47&48**, 436.

Boppart, H., A. Treindl, P. Wachter and S. Roth, 1980, Solid State Commun. **35**, 483.

Born, M., and K. Huang, 1954, Dynamical Theory of Crystal Lattices (Oxford University Press).

Brändli, G., and R. Griessen, 1973, Cryogenics **13**, 299.

Brandt, N.B., and V.V. Moshchalkov, 1984, Adv. Phys. **33**, 373.

Bredl, C.D., S. Horn, F. Steglich, B. Lüthi and R.M. Martin, 1984, Phys. Rev. Lett. **52**, 1982.

Broholm, C., J.K. Kjems, W.J.L. Buyers, P. Matthews, T.T.M. Palstra, A.A. Menovsky and J.A. Mydosh, 1987, Phys. Rev. Lett. **58**, 1467.

Bruls, G., D. Weber, B. Lüthi, J. Flouquet and P. Lejay, 1990a, Phys. Rev. B **42**.

Bruls, G., D. Weber, G. Hampel, B. Wolf, I.

Kouroudis and B. Lüthi, 1990b, Physica B **163**, 41.
Bruls, G., B. Lüthi, D. Weber, B. Wolf and P. Thalmeier, 1990c, Phys. Scr., in press.
Bruls, G., D. Weber, B. Wolf, P. Thalmeier and B. Lüthi, 1991, to be published.
Bucher, E., R.J. Birgeneau, J.P. Maita, G.P. Felcher and T.O. Brun, 1972, Phys. Rev. Lett. **28**, 746.
Bucher, E., J.P. Maita, G.W. Hull Jr, L.D. Longinotti, B. Lüthi and P.S. Wang, 1976, Z. Phys. B **25**, 41.
Buschow, K.H.J., and H.J. van Daal, 1969, Phys. Rev. Lett. **23**, 408.
Buschow, K.H.J., H.J. van Daal, F.E. Maranzana and P.B. van Aken, 1971, Phys. Rev. B **3**, 1662.
Callen, E.R., and H.B. Callen, 1963, Phys. Rev. **129**, 578.
Callen, E.R., and H.B. Callen, 1965, Phys. Rev. A **139**, 455.
Camley, R., and P. Fulde, 1981, Phys. Rev. B **23**, 2614.
Cardona, M., 1975, Light Scattering in Solids, in: Topics in Applied Physics, Vol. 8 (Springer, Berlin).
Cardona, M., and G. Güntherodt, 1982, Light Scattering in Solids, in: Topics in Applied Physics, Vol. 50 & 51 (Springer, Berlin).
Chandrasekhar, B.S., and E. Fawcett, 1971, Adv. Phys. **20**, 775.
Clark, A.E., 1980, in: Ferromagnetic Materials, Vol. 1, ed. E.P. Wohlfarth (North-Holland, Amsterdam).
Coey, J.M.D., and O. Massenat, 1977, in: Valence Instabilities and Related Narrow Band Phenomena, ed. R.D. Parks (Plenum Press, New York).
Coleman, P., 1984, Phys. Rev. B **29**, 3035.
Coleman, P., 1985, J. Magn. & Magn. Mater. **47&48**, 323.
Coleman, P., 1987, Phys. Rev. B **35**, 5072.
Cooper, B.R., and O. Vogt, 1970, Phys. Rev. B **1**, 1218.
Coqblin, J., 1977, The Electronic Structure of Rare Earth Metals and Alloys: The Magnetic Heavy Rare Earths (Academic Press, New York).
Coqblin, J., and J.R. Schrieffer, 1969, Phys. Rev. **185**, 847.
Cox, D.L., 1985, Thesis (Cornell University).
Cox, D.L., 1987, Phys. Rev. Lett. **59**, 1240.
Cox, D.L., N.E. Bickers and J.W. Wilkins, 1986, J. Magn. & Magn. Mater. **54–57**, 333.
Creuzet, G., and I.A. Campbell, 1981, Phys. Rev. B **23**, 3375.
Creuzet, G., and I.A. Campbell, 1982, in: Crystalline Electric Field Effects in f-Electron Magnetism, eds R.P. Guertin, W. Suski and Z. Zolnierek (Plenum Press, New York).
Cullen, J.R., and A.E. Clark, 1977, Phys. Rev. B **15**, 4510.
Czopnik, A., N. Illiev, B. Stalinski, J. Madge, G. Bazaw and R. Pott, 1985, Physica B **130**, 262.
d'Ambrumenil, N., and P. Fulde, 1985, J. Magn. & Magn. Mater. **52**, 182.
de Jong, M.H., J. Bijvoet and P.F. de Châtel, 1982, in: Crystalline Electric Field Effects in f-Electron Magnetism, eds R.P. Guertin, W. Suski and Z. Zolnierek (Plenum Press, New York).
de Visser, A., L. Puech, W. Joss, A.A. Menovsky and J.J.M. Franse, 1987, Jpn. J. Appl. Phys., Suppl. **26–3**, 513.
Dohm, V., 1976, Z. Phys. B **23**, 153.
Dohm, V., and P. Fulde, 1975, Z. Phys. B **21**, 299.
Dolling, G., 1974, in: Dynamical of Solids, Vol. 1, eds G.K. Horton and A.A. Maradudin (North-Holland, Amsterdam).
Doniach, S., 1987, Phys. Rev. B **35**, 1814.
du Trémolet de Lacheisserie, E., P. Morin and J. Rouchy, 1978, Ann. Physique **3**, 479.
Dunitz, J.D., and L.E. Orgel, 1957, J. Phys. Chem. Solids **3**, 20.
Edmonds, P.E., ed., 1981, Ultrasonic, in: Methods of Experimental Physics, Vol. 19 (Academic Press, New York).
Effantin, J.M., J. Rossat-Mignod, P. Burlet, H. Bartholin, S. Kunii and T. Kasuya, 1985, J. Magn. & Magn. Mater. **47&48**, 145.
Elliott, R.J., R.T. Harley, W. Hayes and J.R.P. Smith, 1972, Proc. Roy. Soc. A **328**, 217.
Endoh, D., T. Goto, T. Suzuki, T. Fujimura, Y. Onuki and T. Komatsubara, 1987, J. Phys. Soc. Jpn. **56**, 4489.
Engelsberg, S., and G. Simpson, 1970, Phys. Rev. B **6**, 1657.
Ewert, S., S. Guo, P. Lemmens, D. Lenz, W. Sander, P. Thalmeier and K. Winzer, 1987, Jpn. J. Appl. Phys. Suppl. **26–3**, 537.
Fawcett, E., R. Griessen, W. Joss, M.J.G. Lee and J.M. Perz, 1980, in: Electrons at the Fermi Surface, ed. M. Springford (Cambridge University Press).
Felsch, W., K. Winzer and G.V. Minnigerode, 1975, Z. Phys. B **21**, 151.

Fert, A., and P.M. Levy, 1977, Phys. Rev. B **16**, 5052.
Fert, A., R. Asomoza, D.H. Sanchez, D. Spanjaard and A. Friedrich, 1977, Phys. Rev. B **16**, 5040.
Fetisov, E.P., and D.I. Khomskii, 1985, Solid State Commun. **56**, 403.
Fisk, Z., D.W. Hess, C.J. Pethick, D. Pines, J.L. Smith, J.D. Thompson and J.O. Willis, 1988, Science **239**, 133.
Flouquet, J., J.C. Lasjaunias, J. Peyrard and M. Ribault, 1982, J. Appl. Phys. **53**, 2127.
Franse, J.J.M., A. de Visser, A. Menovsky and P.H. Frings, 1985, J. Magn. & Magn. Mater. **52**, 61.
Freeman, A.J., and J.P. Desclaux, 1979, J. Magn. & Magn. Mater. **12**, 11.
Frick, B., and M. Loewenhaupt, 1985, Physica B **130**, 372.
Fulde, P., 1978a, in: Handbook on the Physics and Chemistry of Rare Earths, eds K.A. Gschneidner and L. Eyring (North-Holland, Amsterdam).
Fulde, P., 1978b, J. Appl. Phys. **49**, 1311.
Fulde, P., and M. Loewenhaupt, 1986, Adv. Phys. **34**, 589.
Fulde, P., and I. Peschel, 1972, Adv. Phys. **21**, 1.
Fulde, P., J. Keller and G. Zwicknagl, 1988, Solid State Phys. Vol. **41**, eds H. Ehrenreich and D. Turnbull (Academic Press, New York) p. 1.
Gao, Q.Z., E. Kanda, M. Sera, T. Goto and T. Kasuya, 1985, J. Magn. & Magn. Mater. **47&48**, 61.
Gehring, G.A., and K.A. Gehring, 1975, Rep. Progr. Phys. **38**, 1.
Giraud, M., P. Morin and D. Schmitt, 1985, J. Magn. & Magn. Mater. **52**, 41.
Golding, B., B. Batlogg, D.J. Bishop, W.H. Haemmerle, Z. Fisk, J.L. Smith and H.R. Ott, 1985, in: Proc. 2nd Int. Conf. Phonon Physics, eds J. Kollar, N. Kroo, N. Menyhard and T. Siklos (World Scientific, Singapore).
Goto, T., A. Tamaki, S. Kunii, T. Nakajima, T. Fujimura, T. Kasuya, T. Komatsubara and S.B. Woods, 1983, J. Magn. & Magn. Mater. **31–34**, 419.
Goto, T., A. Tamaki, T. Suzuki, S. Kunii, N. Sato, T. Suzuki, H. Kitazawa, T. Fujimura and T. Kasuya, 1985, J. Magn. & Magn. Mater. **52**, 253.
Goto, T., A. Tamaki, T. Fujimura and H. Unoki, 1986, J. Phys. Soc. Jpn. **55**, 1613.
Goto, T., T. Suzuki, Y. Oke, A. Tamaki, S. Sakatsume, T. Fujimura, Y. Onuki and T. Komatsubara, 1987, Jpn. J. Appl. Phys. Suppl. **26–3**, 525.
Gray, D.M., and A.M. Gray, 1976, Phys. Rev. B **14**, 669.
Greiner, J.D., R.J. Schiltz Jr, J.J. Tommies, F.H. Spedding and J.F. Smith, 1973, J. Appl. Phys. **44**, 3862.
Grewe, N., 1984, Solid State Commun. **50**, 19.
Grewe, N., P. Entel and H.J. Leder, 1978, Z. Phys. B **30**, 393.
Grewe, N., H.J. Leder and P. Entel, 1980, in: Festkörperprobleme XX, ed. J. Treusch (Vieweg, Braunschweig).
Griessen, R., and R.S. Sorbello, 1974, J. Low Temp. Phys. **16**, 237.
Gschneidner, K.A., S.K. Dhar, R.J. Stierman, T.W.E. Tsang and O.D. Masters, 1985, J. Magn. & Magn. Mater. **47&48**, 51.
Gunnarsson, O., and K. Schönhammer, 1983, Phys. Rev. B **28**, 4315.
Gunnarsson, O., and K. Schönhammer, 1987, in: Handbook on the Physics and Chemistry of Rare Earths, Vol. **10**, eds K.A. Gschneidner, L. Eyring and S. Hüfner (North-Holland, Amsterdam).
Güntherodt, G., A. Jayaraman, E. Anastassakis, E. Bucher and H. Bach, 1981, Phys. Rev. Lett. **46**, 855.
Güntherodt, G., A. Jayaraman, B. Batlogg, M. Croft and E. Melczer, 1983, Phys. Rev. Lett. **51**, 2330.
Güntherodt, G., E. Zirngiebl, S. Blumenröder, A. Jayaraman, B. Batlogg, M. Croft and E. Melczer, 1985, J. Magn. & Magn. Mater. **47&48**, 315.
Haen, P., J. Flouquet, F. Lapierre, P. Lejay and G. Remenyi, 1987, J. Low Temp. Phys. **67**, 516 and unpublished 1985.
Harima, H., O. Sakaki, T. Kasuya and Y. Yanase, 1988, Solid State Commun. **66**, 603.
Heil, J., I. Kouroudis, B. Lüthi and P. Thalmeier, 1984, J. Phys. C **17**, 2433.
Hewson, A.C., 1979, J. Magn. & Magn. Mater. **12**, 83.
Hirst, L.L., 1974, J. Phys. Chem. Solids **35**, 1185.
Hirst, L.L., 1978, Adv. Phys. **27**, 231.
Hock, R., and J. Wesner, 1989, J. Appl. Phys. **65**, 4564.
Houmann, J.G., B.D. Rainford, J. Jensen and A.R. Mackintosh, 1979, Phys. Rev. B **20**, 1105.

Huggins, J.G., P. Thalmeier and P. Fulde, 1984, J. Phys. C **17**, 5263.
Hulliger, F., 1979, in: Handbook on the Physics and Chemistry of Rare Earths, Vol. 4-II, eds K.A. Gschneidner Jr and L.R. Eyring (North-Holland, Amsterdam).
Hulliger, F., and F. Stucki, 1978, Z. Phys. B **31**, 391.
Hutchings, M.T., 1964, in: Solid State Phys. Vol. 16, eds F. Seitz and D. Turnbull (Academic Press, New York).
Hutchings, M.T., R. Scherm, S.H. Smith and S.R.P. Smith, 1975, J. Phys. C **8**, L393.
Ihrig, H., D.T. Vigren, J. Kübler and S. Methfessel, 1973, Phys. Rev. B **8**, 4525.
Ishizawa, Y., T. Tanaka, E. Bannai and S. Kawai, 1977, J. Phys. Soc. Jpn. **42**, 112.
Jayaraman, A., 1978, in: Handbook on the Physics and Chemistry of Rare Earths, eds K.A. Gschneidner and L. Eyring (North-Holland, Amsterdam) Vol. 9.
Jensen, J., 1976, J. Phys. C **9**, 111.
Jensen, J., 1982, J. Magn. & Magn. Mater. **29**, 47.
Jensen, J., 1988, Phys. Rev. B **37**, 9495.
Jensen, J., N. Hessel Andersen and O. Vogt, 1980, J. Phys. C **13**, 213.
Johannson, W.R., G.W. Crabtree, A.S. Edelstein and O.D. McMasters, 1981, Phys. Rev. Lett. **46**, 504.
Joss, W., J.M. van Ruitenbeek, G.W. Crabtree, J.L. Tholence, A.P.J. van Deursen and Z. Fisk, 1987, Phys. Rev. Lett. **59**, 1609.
Kaiser, A., and P. Fulde, 1988, Phys. Rev. B **37**, 5357.
Kanamori, J., 1960, J. Appl. Phys. **31**, 145.
Kasuya, T., 1966, Magnetism, Vol. IIb, eds G.T. Rado and H. Suhl (Academic Press, Amsterdam).
Kataoka, M., and J. Kanamori, 1972, J. Phys. Soc. Jpn. **32**, 113.
Kim, C.I., Y. Kuramoto and T. Kasuya, 1987, Solid State Commun. **62**, 627.
Kino, Y., M.E. Mullen and B. Lüthi, 1973, Solid State Commun. **12**, 275.
Kirchmayer, H.R., and C.A. Poldy, 1980, in: Handbook on the Physics and Chemistry of Rare Earths, Vol. 2, eds K.A. Gschneidner and L. Eyring (North-Holland, Amsterdam).
Kjems, J.K., W. Hayes and S.H. Smith, 1975, Phys. Rev. Lett. **35**, 1089.
Knorr, K., B. Renker, W. Assmus, R. Takke, B. Lüthi and H.J. Lauter, 1980, Z. Phys. B **39**, 151.
Kochelaev, B.I., 1962, Sov. Phys.-Solid State **4**, 1145.
Kojima, H., Y. Kuramoto and M. Tachiki, 1984, Z. Phys. B **54**, 293.
Koskenmaki, D.C., and K.A. Gschneidner Jr, 1978, in: Handbook on the Physics and Chemistry of Rare Earths Vol. 1, eds K.A. Gschneidner Jr and L.R. Eyring (North-Holland, Amsterdam).
Kötzler, J., 1984, Z. Phys. B **55**, 119.
Kötzler, J., and G. Raffius, 1980, Z. Phys. B **38**, 139.
Kötzler, J., G. Raffius, A. Loidl and C.M.E. Zeyen, 1979, Z. Phys. B **35**, 125.
Kouroudis, I., D. Weber, M. Yoshizawa, B. Lüthi, L. Puech, P. Haen, J. Flouquet, G. Bruls, U. Welp, J.J.M. Franse, A. Menovsky, E. Bucher and J. Hufnagl, 1987, Phys. Rev. Lett. **58**, 820.
Kugel, K.I., and D.I. Khomskii, 1982, Sov. Phys. Usp. **25**, 231.
Kuramoto, Y., 1983, Z. Phys. B **53**, 37.
Kuramoto, Y., 1989, Physica B **156&157**, 789.
Kuramoto, Y., C.I. Kim and T. Kasuya, 1987, Jpn. J. Appl. Phys. **26**, Suppl. 26–3, 459.
Lacroix, C., 1985, Solid State Commun. **54**, 991.
Lacroix, C., 1987, J. Magn. & Magn. Mater. **63&64**, 239.
Lacroix, C., and M. Cyrot, 1979, Phys. Rev. B **20**, 1969.
Lang, M., R. Schefzyk, F. Steglich and N. Grewe, 1987, J. Magn. & Magn. Mater. **63&64**, 79.
Lawrence, J.M., M.C. Croft and R.D. Parks, 1977, in: Valence Instabilities and Related Narrow Band Phenomena, ed. R.D. Parks (Plenum Press, New York).
Lawrence, J.M., P.S. Riseborough and R.D. Parks, 1981, Rep. Progr. Phys. **44**, 1.
Lea, K.R., J.M. Leask and W.P. Wolf, 1962, J. Phys. Chem. Solids **23**, 1381.
Lee, P.A., T.M. Rice, J.W. Serene, L.J. Sham and J.W. Wilkins, 1986, Comments Solid State Phys. **12**, 99.
Lemmens, P., S. Ewert, P. Thalmeier, D. Lenz and K. Winzer, 1989, Z. Phys. B **76**, 501.
Lenz, D., H. Schmitt, S. Ewert, W. Boksch, R. Pott and D. Wohlleben, 1984, Solid State Commun. **52**, 759.
Leung, K.M., and D.L. Huber, 1979, Phys. Rev. B **19**, 5483.
Leung, K.M., D.L. Huber and B. Lüthi, 1979, J. Appl. Phys. **50**, 1831.
Lévy, F., 1969, Phys. Kondens. Mat. **10**, 85.

Levy, P.M., 1973, J. Phys. C **6**, 3545.
Levy, P.M., and G.T. Trammell, 1977, J. Phys. C **10**, 1303.
Levy, P.M., P. Morin and D. Schmitt, 1979, Phys. Rev. Lett. **42**, 1417.
Lifshitz, I.M., and A.M. Kosevich, 1956, Sov. Phys.-JETP **2**, 636.
Lin, C.L., J. Teter, J.C. Crow, T. Mihalisin, J. Brooks, A.I. Abou-Aly and G.R. Stewart, 1985, Phys. Rev. Lett. **54**, 2541.
Lingner, C., and B. Lüthi, 1981, Phys. Rev. B **23**, 256.
Lingner, C., and B. Lüthi, 1983, J. Magn. & Magn. Mater. **36**, 86.
Loewenhaupt, M., and E. Holland-Moritz, 1979b, J. Magn. & Magn. Mater. **14**, 227.
Loewenhaupt, M., and W. Reichardt, 1984, ILL Report to Experiment No. 4-03-332.
Loewenhaupt, M., B.D. Rainford and F. Steglich, 1979a, Phys. Rev. Lett. **25**, 1709.
Loewenhaupt, M., W. Reichardt, R. Pynn and E. Lindley, 1987, J. Magn. & Magn. Mater. **63&64**, 73.
Loidl, A., K. Knorr, J.K. Kjems and B. Lüthi, 1979, Z. Phys. B **35**, 253.
Ludwig, W., 1967, in: Trends in Modern Physics, Vol. **43** (Springer, Berlin).
Lüthi, B., 1965, Appl. Phys. Lett. **6**, 234.
Lüthi, B., 1966, J. Appl. Phys. **37**, 990.
Lüthi, B., 1974, Proc. 1st Conf. Crystal Electric Field Effects in Metals and Alloys, ed. R.A.B. Devine (Université de Montreal).
Lüthi, B., 1976, AIP Conf. Proc. **34**, 7.
Lüthi, B., 1980a, in: Dynamical Properties of Solids, Vol. 3, eds G.K. Horton and A.A. Maradudin (North-Holland, Amsterdam).
Lüthi, B., 1980b, J. Magn. & Magn. Mater. **15–18**, 1.
Lüthi, B., 1985, J. Magn. & Magn. Mater. **52**, 70.
Lüthi, B., and C. Lingner, 1979, Z. Phys. B **34**, 157.
Lüthi, B., and H.R. Ott, 1980, Solid State Commun. **33**, 717.
Lüthi, B., and M. Yoshizawa, 1987, J. Magn. & Magn. Mater. **63&64**, 274.
Lüthi, B., M.E. Mullen, K. Andres, E. Bucher and J.P. Maita, 1973a, Phys. Rev. B **8**, 2639.
Lüthi, B., M.E. Mullen and E. Bucher, 1973b, Phys. Rev. Lett. **31**, 95.
Lüthi, B., R. Sommer and P. Morin, 1979, J. Magn. & Magn. Mater. **13**, 198.
Lüthi, B., M. Niksch, R. Takke, W. Assmus and W. Grill, 1982, in: Crystal Electric Field Effects in f-Electron Magnetism, eds Guertin, Suski and Zolnierek (Plenum Press, New York).
Lüthi, B., S. Blumenröder, B. Hillebrands, E. Zirngiebl, G. Güntherodt and K. Winzer, 1984, Z. Phys. B **58**, 31.
Maple, M.B., L.E. DeLong and B.C. Sales, 1978, in: Handbook on the Physics and Chemistry of Rare Earths, Vol. 1, eds K.A. Gschneidner Jr and L.R. Eyring (North-Holland, Amsterdam).
Matthews, H., and R.C. LeCraw, 1962, Phys. Rev. Lett. **8**, 317.
Melcher, R.L., 1970, Phys. Rev. Lett. **25**, 1201.
Melcher, R.L., 1972, in: Proc. Int. School of Physics, Enrico, Fermi, Varuma, ed. E. Burstein (Academic Press, New York) course LII.
Melcher, R.L., 1976, in: Physical Acoustics, Vol. XII, eds W.P. Mason and R.N. Thurston (Academic Press, New York).
Millis, A.J., and P.A. Lee, 1987a, Phys. Rev. B **35**, 3394.
Millis, A.J., M. Lavagna and P.A. Lee, 1987b, J. Appl. Phys. **61**, 3904.
Mock, R., and G. Güntherodt, 1989, Z. Phys. B **74**, 315.
Mock, R., E. Zirngiebl, B. Hillebrands, G. Güntherodt and F. Holtzberg, 1986, Phys. Rev. Lett. **57**, 1040.
Mook, H.A., R.M. Nicklow, T. Penney, F. Holtzberg and M.W. Shafer, 1978, Phys. Rev. B **18**, 2925.
Moran, T.J., and B. Lüthi, 1969, Phys. Rev. **187**, 710.
Moran, T.J., R.L. Thomas, P.M. Levy and H.H. Chen, 1973, Phys. Rev. B **7**, 3238.
Morin, P., 1988, J. Magn. & Magn. Mater. **71**, 151.
Morin, P., and D. Schmitt, 1979, Phys. Lett. A **73**, 67.
Morin, P., and D. Schmitt, 1981a, Phys. Rev. B **23**, 2278.
Morin, P., and D. Schmitt, 1981b, Phys. Rev. B **23**, 5936.
Morin, P., and D. Schmitt, 1983, Phys. Rev. B **27**, 4412.
Morin, P., and S.J. Williamson, 1984, Phys. Rev. B **29**, 1425.
Morin, P., J. Rouchy and E. du Trémolet de Lacheisserie, 1977, Phys. Rev. B **16**, 3182.
Morin, P., D. Schmitt and E. du Trémolet de Lacheisserie, 1980a, Phys. Rev. B **21**, 1742.
Morin, P., D. Schmitt, C. Vettier and J. Rossat-Mignod, 1980b, J. Phys. F **10**, 1575.
Morin, P., M. Giraud, P. Burlet and A. Czopnik, 1987, J. Magn. & Magn. Mater. **68**, 107.

Mullen, M.E., B. Lüthi, P.S. Wang, E. Bucher, L.D. Longinotti, J.P. Maita and H.R. Ott, 1974, Phys. Rev. B **10**, 156.
Müller, V., D. Maurer, K. de Groot, E. Bucher and H.E. Bömmel, 1986, Phys. Rev. Lett. **56**, 248.
Müller, V., C. Roth, D. Maurer, E. Scheidt, K. Lüders, E. Bucher and H. Bömmel, 1987, Phys. Rev. Lett. **58**, 1224.
Müller-Hartmann, E., 1981, in: Electron correlation and magnetism in narrow band systems, ed. T. Moriya (Springer, Berlin) p. 178.
Nakamura, H., Y. Kitaoka, H. Yamada and K. Asayama, 1988, J. Magn. & Magn. Mater. **76&77**, 517.
Newman, D.J., 1971, Adv. Phys. **20**, 197.
Newns, D.M., and N. Read, 1987, Adv. Phys. **36**, 799.
Nikl, D., I. Kouroudis, W. Assmus, B. Lüthi, G. Bruls and U. Welp, 1987, Phys. Rev. B **35**, 6864.
Niksch, M., 1986, Ph.D. Thesis (Universität Frankfurt).
Niksch, M., B. Lüthi and K. Andres, 1980, Phys. Rev. B **22**, 5774.
Niksch, M., B. Lüthi, W. Assmus and J. Kübler, 1982a, J. Magn. & Magn. Mater. **28**, 243.
Niksch, M., W. Assmus, B. Lüthi, H.R. Ott and J.K. Kjems, 1982b, Helv. Phys. Acta **55**, 588.
Niksch, M., B. Lüthi, W. Assmus and J. Kübler, 1982c, in: Superconductivity in d- and f-Band Metals, KFZ Karlsruhe.
Niksch, M., I. Kouroudis, W. Assmus and B. Lüthi, 1985, J. Magn. & Magn. Mater. **47&48**, 299.
Niksch, M., B. Lüthi and J. Kübler, 1987, Z. Phys. B **68**, 291.
Nowik, I., 1977, in: Valence Instabilities and Related Narrow-Band Phenomena, ed. R.D. Parks (Plenum Press, New York) p. 261.
Nozières, P., 1974, J. Low Temp. Phys. **17**, 31.
Ohkawa, F.J., 1985, J. Magn. & Magn. Mater. **52**, 217.
Okiji, A., and N. Kawakami, 1986, J. Magn. & Magn. Mater. **54–57**, 327.
Onuki, Y., Y. Kurosawa, T. Omi, T. Komatsubara, R. Yoshizaki, H. Ikeda, K. Maezawa, S. Wakabayashi, A. Umerawa, W.K. Kwok and G.W. Crabtree, 1988, J. Magn. & Magn. Mater. **76&77**, 37.
Orbach, R., and M. Tachiki, 1967, Phys. Rev. **158**, 524.
Ott, H.R., 1987, in: Progr. in Low Temp. Phys., Vol. XI, 215.
Ott, H.R., and B. Lüthi, 1976, Phys. Rev. Lett. **36**, 600.
Ott, H.R., and B. Lüthi, 1977, Z. Phys. B **28**, 141.
Palmer, S.B., and J. Jensen, 1978, J. Phys. C **11**, 2465.
Pastor, G., A. Caro and B. Alascio, 1987, Phys. Rev. B **36**, 1673.
Penney, T., 1984, in: Moment Formation in Solids, ed. W.J.L. Buyers (Plenum Press, New York).
Penney, T., and R.L. Melcher, 1976, J. Phys. Colloq. **37**, C4, 273.
Penney, T., B. Barbara, R.L. Melcher, T.S. Plaskett, H.E. King Jr and S.J. La Placa, 1981, in: Valence Fluctuations in Solids, ed. L.M. Falicov, W. Hanke and M.B. Maple (North-Holland, Amsterdam).
Penney, T., B. Barbara, T.S. Plaskett, H.E. King Jr and S.J. La Placa, 1982, Solid State Commun. **44**, 1199.
Pethik, C.J., D. Pines and K.F. Quader, 1987, Phys. Lett. A **125**, 485.
Pippard, A.B., 1960, Proc. Roy. Soc. A **257**, 165.
Pofahl, G., E. Zirngiebl, S. Blumenröder, H. Breuten, G. Güntherodt and K. Winzer, 1987, Z. Phys. B **66**, 339.
Pott, R., and R. Schefzyk, 1983, J. Phys. E **16**, 444.
Puech, L., J.M. Mignot, P. Lejay, P. Haen and J. Flouquet, 1988, J. Low Temp. Phys. **70**, 237.
Pureur, F., G. Creuzet and A. Fert, 1982, in: Crystalline Electric Field Effects in f-Electron Magnetism, eds R.P. Guertin, W. Suski and Z. Zolnierek (Plenum Press, New York).
Purwins, H.G., W.J.L. Buyers, T.M. Golden and E.C. Svensson, 1976, AIP Conf. Proc. **29**, 259.
Rayne, J.A., 1960, Phys. Rev. B **118**, 1515.
Rayne, J.A. and C.K. Jones, 1970, in: Physical Acoustics, Vol. VII, eds W.P. Mason and R.N. Thurston (Academic Press, New York).
Razafimandimby, H., P. Fulde and J. Keller, 1984, Z. Phys. B **54**, 111.
Read, N., 1985, J. Phys. C **18**, 2651.
Regnault, L.P. et al., 1988.
Reichardt, W., and N. Nücker, 1984, J. Phys. F **14**, L135.
Reinders, P.H.P., M. Springford, P.T. Coleridge, R. Boulet and D. Ravot, 1986, Phys. Rev. Lett. **56**, 1631.

Rhyne, J.J., 1972, in: Magnetic Properties of rare Earth Metals, ed. R.J. Elliott (Plenum Press, New York) p. 129.

Ribault, M., A. Benoit, J. Flouquet and J. Palleau, 1976, J. Phys. **40**, L-413.

Roberts, B.W., 1968, in: Physical Acoustics, Vol. IVB, ed. W.P. Mason (Academic Press, New York).

Rossat-Mignod, J., L.P. Regnault, J.L. Jacoud, C. Vettier, P. Lejay, J. Flouquet, E. Walker, D. Jaccard and A. Amato, 1988, J. Magn. & Magn. Mater. **76&77**, 376.

Rossat-Mignod, J., L.P. Regnault, J.L. Jacond, C. Vettier, P. Lejay, J. Flouquet, E. Walker, D. Jaccard and A. Amato, 1988, J. Magn. & Magn. Mater. **76&77**, 376.

Rouchy, J., and E. du Trémolet de Lacheisserie, 1979, Z. Phys. B **36**, 67.

Rouchy, J., E. du Trémolet de Lacheisserie, J.C. Genna and A. Waintal, 1980, J. Magn. & Magn. Mater. **21**, 69.

Samwer, K., and K. Winzer, 1976, Z. Phys. B **25**, 269.

Sandercock, J.R., 1982, in: Light Scattering in Solids III, eds M. Cardona and G. Güntherodt, Topics in Appl. Phys., Vol. 51 (Springer, Berlin).

Sandercock, J.R., S.B. Palmer, R.J. Elliott, W. Hayes, S.R.P. Smith and Y.P. Young, 1972, J. Phys. C **5**, 3126.

Schiltz, R.J., and J.F. Smith, 1974, J. Appl. Phys. **45**, 4681.

Schlottmann, P., 1983, Phys. Rev. Lett. **50**, 1697.

Schlottmann, P., 1984, Z. Phys. B **55**, 293.

Schmidt, H.J., and E. Müller-Hartmann, 1985, Z. Phys. B **60**, 363.

Schmitt, D., and P.M. Levy, 1984, Phys. Rev. B **29**, 2850.

Schotte, K.D., D. Förster and U. Schotte, 1986, Z. Phys. B **64**, 165.

Schrieffer, J.R., and P. Wolf, 1966, Phys. Rev. **149**, 491.

Scott, T.E., 1978, in: Handbook on the Physics and Chemistry of Rare Earths, Vol. 1, eds K.A. Gschneidner and L. Eyring (North-Holland, Amsterdam).

Severing, A., W. Reichardt, E. Holland-Moritz, D. Wohlleben and W. Assmus, 1988, Phys. Rev. B **38**, 1773.

Sherrington, D., and S. von Molnar, 1975, Solid State Commun. **16**, 1347.

Shoenberg, D., 1984, in: Magnetic oscillations in metals (Cambridge University Press).

Southern, B.W., and D.A. Goodings, 1973, Phys. Rev. B **7**, 534.

Steglich, F., 1985, in: Theory of Heavy Fermions and Valence Fluctuations, eds T. Kasuya and T. Saso, Springer Series in Solid-State Sciences, Vol. 62 (Springer, Berlin).

Steglich, F., P.D. Bredl, M. Loewenhaupt and K.D. Schotte, 1979, J. Phys. Colloq. **C5**, Suppl. 301.

Steglich, F., U. Ahlheim, J.J.M. Franse, N. Grewe, D. Rainer and U. Rauchschwalbe, 1985, J. Magn. & Magn. Mater. **52**, 54.

Stevens, K.W.H., 1952, Proc. Phys. Soc. A **65**, 209.

Stevens, K.W.H., and E. Pytte, 1973, Solid State Commun. **13**, 101.

Stewart, G.R., 1984, Rev. Mod. Phys. **56**, 755.

Stewart, G.R., B. Andraka, G. Quitman, B. Treadway, Y. Shapira and E.J. McNiff, 1988, Phys. Rev. B **37**, 3344.

Sticht, J., N. d'Ambrumenil and J. Kübler, 1986, Z. Phys. B **65**, 149.

Sugawara, T., and Y. Eguchi, 1967, Phys. Lett. A **25**, 668.

Suzuki, T., T. Goto, T. Fujimura, S. Kunii, T. Suzuki and T. Kasuya, 1985a, J. Magn. & Magn. Mater. **52**, 261.

Suzuki, T., T. Goto, A. Tamaki, T. Fujimura, Y. Onuki and T. Komatsubara, 1985b, J. Phys. Soc. Jpn. **54**, 2367.

Suzuki, T., T. Goto, A. Tamaki, T. Fujimura, H. Kitazawa, T. Suzuki and T. Kasuya, 1987a, J. Magn. & Magn. Mater. **63&64**, 563.

Suzuki, T., T. Goto, J. Sakatsume, A. Tamaki, S. Kunii, T. Kasuya and T. Fujimura, 1987b, Jpn. J. Appl. Phys., Suppl. 26-3, 525.

Taillefer, L., R. Newbury, G.G. Lonzarich, Z. Fisk and J.L. Smith, 1987, J. Magn. & Magn. Mater. **63&64**, 372.

Takke, R., N. Dolezal, W. Assmus and B. Lüthi, 1981a, J. Magn. & Magn. Mater. **23**, 247.

Takke, R., M. Niksch, W. Assmus, B. Lüthi, R. Pott, R. Schefzyk and D.K. Wohlleben, 1981b, Z. Phys. B **44**, 33.

Tamaki, A., T. Goto, M. Yoshizawa, T. Fujimura, S. Kunii and T. Kasuya, 1985a, J. Magn. & Magn. Mater. **52**, 257.

Tamaki, A., T. Goto, S. Kunii, M. Kasaya, T. Suzuki, T. Fujimura and T. Kasuya, 1985b, J. Magn. & Magn. Mater. **47&48**, 469.

Tao, L.J., J.B. Torrance and F. Holtzberg, 1974, Solid State Commun. **15**, 1015.

Teitelbaum, H.H., and P.M. Levy, 1976, Phys. Rev. B **14**, 3058.
Tesanovich, Z., and O.T. Vallis, 1986, Phys. Rev. B **34**, 1918.
Testardi, L.R., 1974, in: Physical Acoustics, Vol. X, eds W.P. Mason and R.N. Thurston (Academic Press, New York).
Thalmeier, P., 1984, J. Phys. C **17**, 4153.
Thalmeier, P., 1987, J. Phys. C **20**, 4449.
Thalmeier, P., 1988, J. Magn. & Magn. Mater. **76&77**, 299.
Thalmeier, P., and P. Fulde, 1975, Z. Phys. B **22**, 359.
Thalmeier, P., and P. Fulde, 1978, Z. Phys. B **29**, 299.
Thalmeier, P., and P. Fulde, 1982, Phys. Rev. Lett. **49**, 1588.
Thalmeier, P., and P. Fulde, 1986, Europhys. Lett. **1**, 367.
Thalmeier, P., P. Lemmens, S. Ewert, D. Lenz and K. Winzer, 1987, Europhys. Lett. **4**, 1177.
Thomas, H., 1977, in: Electron Phonon Interaction and Phase Transitions, ed. T. Riste (Plenum Press, New York) p. 245.
Thompson, J.D., J.O. Willis, L.C. Gupta, D.E. McLaughlin and C. Godart, 1985, Solid State Commun. **56**, 169.
Truell, R., C. Elbaum and B.C. Chick, 1969, in: Ultrasonic Methods in Solid State Physics (Academic Press, New York).
Tucker, J.W., 1973, J. Phys. C **6**, 255.
Varma, C.M., 1976, Rev. Mod. Phys. **48**, 219.
Vedel, I., A.M. Redon, J.M. Mignot and J.M. Leger, 1987a, J. Phys. F **17**, 849.
Vedel, I., A.M. Redon, J. Rossat-Mignod, O. Vogt and J.M. Leger, 1987b, J. Phys. C **20**, 3439.
Vettier, C., P. Morin and J. Flouquet, 1986, Phys. Rev. Lett. **56**, 1980.
Wakabayashi, N., 1980, Phys. Rev. B **22**, 5833.
Walker, E., J. Ortelli and M. Peter, 1970, Phys. Lett. A **31**, 24.
Wallace, D.C., 1972, in: Thermodynamics of Crystals (Wiley, New York).
Wallace, P.W., and C.W. Garland, 1986, Rev. Sci. Instr. **57**, 3085.
Walter, U., 1984, J. Phys. Chem. Solids **45**, 401.
Walter, U., 1985, Z. Phys. B **62**, 299.
Wang, P.S., and B. Lüthi, 1977, Phys. Rev. B **15**, 2718.
Weber, A., I. Kouroudis, B. Lüthi, G. Bruls, M. Yoshizawa, P. Haen, J. Flouquet, E. Bucher and J. Hufnagel, 1988, J. Magn. & Magn. Mater. **76&77**, 315.
Weber, D., M. Yoshizawa, I. Kouroudis, B. Lüthi and E. Walker, 1987, Europhys. Lett. **3**, 827.
Weber, D., G. Bruls, P. Thalmeier and B. Lüthi, 1991, to be published.
Wehr, H., K. Knorr and R. Feile, 1981, Solid State Commun. **40**, 507.
Welp, U., P. Haen, G. Bruls, G. Remenyi, J. Flouquet, P. Morin, A. Briggs, G. Cors and M. Karkut, 1987, J. Magn. & Magn. Mater. **63&64**, 28.
Wiegmann, P.B., 1980, Phys. Lett. A **80**, 163.
Winter, K.M., D. Lenz, H. Schmidt, S. Ewert, S. Blumenröder, E. Zirngiebl and K. Winzer, 1986, Solid State Commun. **59**, 117.
Winzer, K., 1977, Solid State Commun. **24**, 551.
Wohlleben, D.K., and B.R. Coles, 1973, Magnetism V, ed. H. Suhl (Academic Press, New York).
Wruk, N., J. Pelzl, K.H. Höck and G.A. Saunders, 1985, Proc. 2nd Int. Conf. Phonon Physics, eds J. Kollar, N. Kroo, N. Menyhard and F. Siklas (World Scientific, Singapore).
Yoshizawa, M., B. Lüthi and K.D. Schotte, 1986, Z. Phys. B **64**, 169.
Young, A.P., 1975, J. Phys. C **8**, 3158.
Zieglowski, J., H.U. Häfner and D. Wohlleben, 1986, Phys. Rev. Lett. **56**, 193.
Ziman, J., 1960, in: The Physics of Electrons and Phonons (Oxford University Press).
Zirngiebl, E., B. Hillebrands, S. Blumenröder, G. Güntherodt, M. Loewenhaupt, J.M. Carpenter, K. Winzer and Z. Fisk, 1984, Phys. Rev. B **30**, 4052.
Zirngiebl, E., S. Blumenröder, R. Mock and G. Güntherodt, 1986, J. Magn. & Magn. Mater. **54&57**, 359.
Zwicknagl, G., 1988, J. Magn. & Magn. Mater. **76&77**, 16.

Handbook on the Physics and Chemistry of Rare Earths, Vol. 14
edited by K.A. Gschneidner, Jr. and L. Eyring

Chapter 97

HEAVY FERMIONS

NORBERT GREWE and FRANK STEGLICH
Institut für Festkörperphysik, Technische Hochschule Darmstadt, D-6100 Darmstadt, FRG

Contents

List of symbols

AC	alternating current
ASR	Abrikosov–Suhl resonance
BCS	Bardeen–Cooper–Schrieffer
CDW	charge-density wave
CF	crystal field
DC	direct current
dHvA	de Haas–van Alphen
DOS	density of states
IV	intermediate valence
LDA	local-density approximation
LMTO	linear combination of muffin tin orbitals
LNCA	lattice non-crossing approximation
μSR	muon spin rotation
NCA	non-crossing approximation
NMR	nuclear magnetic resonance
RE	rare earth
RKKY	Ruderman–Kittel–Kasuya–Yosida

RPA	random-phase approximation
SDW	spin-density wave
Δ	Anderson's width ($=\pi V^2 N_F$); also: superconducting gap
$V, V_{k\sigma\alpha}$	hybridization matrix element
N_F	density of bare band-electron states at the Fermi level
E_F	Fermi level
$\gamma(\gamma_v)$	Sommerfeld coefficient of electronic specific heat (at constant volume) ($=\mathrm{Lim}_{T\to 0}\, C/T$); sometimes $\gamma(T) = C(T)/T$.
χ_0	Pauli susceptibility of band electrons
T	temperature; also: time reversal operator; also: unit "Tesla"
T_K	Kondo temperature (magnetic impurity)
T^*	characteristic temperature of a lattice periodic f-metal with magnetic moments
T_{coh}	coherence temperature, as defined via the approach to the low-temperature regime of an f-metal, where $\rho(T) \sim T^2$
T_c	superconducting to normal phase-transition temperature
T_N	antiferromagnetic to normal paramagnetic phase-transition (Néel-) temperature
k_B	Boltzmann constant
$\delta(\omega)$	Delta function
N_F^r	partial density of states at E_F in band r
$\hbar$	$h/2\pi$ (Planck constant)
m^*	effective mass for quasiparticles at E_F
k_F	Fermi wave number (used for an idealized, isotropic situation)
E_F^*	hypothetical Fermi energy, as calculated from k_F and m^* via free-electron formulae
x	concentration (per formula unit); also: dimensionless exchange-coupling constant $N_F J$
n_ℓ	number of localized electrons (per f-ion)
α	local quantum numbers as appropriate for one-particle f-shell excitations
δ_α	phase shift for band-electron scattering in channel α
$\Sigma_\alpha(\omega + i\eta)$	self energy of a local f-electron in state α with real part R_α and imaginary part-Δ_α
$G_\alpha(z)$	Green function of a local f-electron in state α
ϵ_α	excitation energy of an f-electron in state α
$N_\alpha(\omega)$	spectral density (DOS) of a local f-electron in state α at energy ω
B	magnetic induction ("field")
σ	pseudo-spin, as appropriate in the presence of spin–orbit coupling
N_F^*, N_{QP}	quasiparticle density of states at E_F (N_{QP} for local Fermi liquid only)
$z, \omega, \nu, \epsilon, E$	complex and real energy variables, general (z, ω, ν), local (ϵ) and band (E)
$\lvert M\rangle$	ionic many-body state with quantum numbers M for f-electrons
$\mathcal{P}_M(z)$	resolvent (Green function) of ionic state $\lvert M\rangle$, with a thermal average on band states [according to eq. (7)] only
E_0^c	total energy of band electrons in a specific unperturbed state
ϵ_M	unperturbed total energy of ionic state $\lvert M\rangle$
H	total Hamiltonian operator
$\Sigma_M(z)$	self energy associated with the resolvent $\mathcal{P}_M$
$\langle\cdots\rangle_{cond}$	thermal average with respect to conduction (band) electrons
$\mathcal{P}_M^{(0)}(z)$	unperturbed resolvent of ionic state $\lvert M\rangle$
E_G	threshold energy, connected with the onset of spectral weight in ionic resolvents $\mathcal{P}_M$
$\rho_M(\omega)$	spectral density (DOS) of ionic states as derived from the resolvent $\mathcal{P}_M$
U	Coulomb-repulsion strength of two f-electrons on the same ionic shell (Hubbard repulsion), also: electrical voltage
$\mathcal{Z}$	total partition function
$\mathcal{Z}_0^c$	unperturbed partition function of band electrons
$\beta = 1/k_B T$	inverse temperature in energy units; also: coefficient of the cubic specific-heat contribution $\sim T^3$
$T_{k\sigma,k'\sigma'}(z)$	scattering operator-matrix element (T-matrix) for band electrons off f-shells from band state $k\sigma$ to $k'\sigma'$ at energy z

$T_{k\sigma}(z)$	diagonal matrix element appropriate for a lattice-periodic system
$G_{k\sigma}(z)$	Green function of a band electron in state k,σ
k, q	(lattice-) wave vector
$G^{(0)}_{k\sigma}(z)$	unperturbed band electron Green function
$G_{k\alpha}(z)$	Green function of f-electrons in state k, α (derived from local state α) for a lattice-periodic system
$G^{\text{eff}}_{\alpha}(z)$	Green function of local f-electrons in state α for a fictitious ("effective") impurity, designed to mimic f-electrons in a lattice-periodic system
$\Sigma_{k\alpha}(z)$	self energy of f-electrons in state k, α for a lattice-periodic system
$\Sigma^{\text{eff}}_{\alpha}(z)$	self energy of local f-electrons in state α for a fictitious ("effective") impurity designed to f-electrons in a lattice-periodic system
I, I'	integral operators appearing in NCA (LNCA) equations
$f(\omega)$	Fermi function
$\tau(\omega)$	transport relaxation time
L^{l}_{m}	transport integrals, l and m indicating powers of τ and ω
Re, Im	real and imaginary parts of a complex quantity
a, α, α'	expansion coefficients of T^2 and $(E-E_F)^2$ terms
ρ	electrical resistivity
ρ_0	residual resistivity (value at T = 0 due to lattice imperfections)
p	hydrostatic pressure
J	quantum number for total f-shell angular momentum
Δ_{CF}	crystal-field splitting energy
$T_{\max}$	generally position of a maximum in a temperature-dependent experimental quantity, like, e.g., $C(T)$
$\chi(q, \nu)$	magnetic susceptibility due to the presence of f-moments
$\Gamma(T)$	width (FWHM) of the quasi-elastic line observed in magnetic neutron scattering
T^{c}	estimate for T^*, as derived from a comparison of the incremental experimental specific heat curve to a Bethe-ansatz calculation for impurity spin $S = \frac{1}{2}$
S	quantum number for f-shell spin-angular momentum
$\gamma_{\max}$	maximum value of the Sommerfeld coefficient $\gamma(T) = C(T)/T$
T^{γ}	position of $\gamma_{\max}$
$\Delta\rho$	incremental resistivity $\rho - \rho_{\text{ref.sys.}}$
ρ_m	magnetic resistivity
$S(T)$	thermoelectric power
$R_H(T)$	Hall coefficient
l	quantum number for (one-electron) orbital angular momentum; also: electron mean-free path
$\Delta\tilde{\rho}(B)$	magnetoresistivity $[=(\rho(B)-\rho(0))/\rho(0)]$
B_K	Kondo magnetic field
μ	magnetic saturation moment of an ion, like, e.g., U^{3+}
μ_s	magnetic saturation moment in a heavy-fermion compound
B_{eff}	scaling parameter for the magnetoresistivity of a Kondo lattice
B^*	characteristic magnetic field of a Kondo lattice in the Fermi liquid phase
T_x	crossing temperature for a sign change of $\Delta\tilde{\rho}(T, B)$ at fixed low field B as function of temperature
ΔM	oscillatory variation of the magnetization in the de Haas–van Alphen effect
ω_c	cyclotron frequency
e	absolute value of the electron charge
c	speed of light
V_0	equilibrium value of hybridization matrix element V for undistorted crystal unit cells
g_j	electron–phonon coupling constants
ΔX_j	(relative) ionic displacements
G	effective electron–phonon coupling constant for breathing interaction; also: symmetry group of the superconducting order parameter
f, f^+	f-electron destruction and creation operators
η_v	Grüneisen parameter
Vol	unit-cell volume
Γ_1^+	phonon mode
$\alpha(T)$	thermal-expansion coefficient;

	also: ultrasonic-attenuation coefficient
$\mathscr{J}$	effective exchange integral between local and band electron
m_0	bare electron mass
η_B	magnetic Grüneisen parameter
γ^*	fictitious value of the Sommerfeld coeffecient γ, when extrapolated through a phase transition to $T=0$
$K(q, \nu)$	(negative) contribution to the inverse susceptibility due to quasiparticle interactions
$\chi^{\mathrm{eff}}(\nu)$	susceptibility of local f-electrons for a fictitious ("effective") impurity, designed to mimic f-electrons in a lattice periodic system
$T^{\mathrm{eff}}_{k\sigma}(z)$	scattering operator diagonal matrix element, as derived via $G^{\mathrm{eff}}_{\alpha}(z)$ for a lattice periodic system
$G^{\mathrm{c}}_{k\sigma}(z)$	cumulant band Green function as defined in LNCA theory
g	gyromagnetic factor
μ_{B}	Bohr magneton
Π^{c}	local quasiparticle interaction vertex, depending on three external energy variables
$\rho^{\mathrm{eff}}_{\alpha}(\omega)$	spectral density of one-particle excitations (DOS) as derived from $G^{\mathrm{eff}}_{\alpha}$
$\rho^{\mathrm{c}}_{k\sigma}(\omega)$	spectral density of one-particle excitations (DOS) as derived from G^{c}_{α}
$K^{(\mathrm{h})}(q, \nu)$	contribution to $K(q, \nu)$ from high-energy quasiparticle-interaction processes only
$T^{(\mathrm{h})}_{\mathrm{m}}$	fictitious magnetic transition-temperature as calculated from high-energy quasiparticle-interaction processes only
$T^{(\mathrm{l})}_{\mathrm{m}}$	fictitious magnetic transition-temperature as calculated from low-energy quasiparticle-interaction processes only
$\boldsymbol{k}_{\mathrm{F}}$	wave vector from the Brillouin-zone center to a point on the Fermi surface
T_{RKKY}	energy scale characteristic for high-energy (RKKY) interaction processes
Y	abbreviation for $\chi^{\mathrm{eff}} K$
ω_0	characteristic magnetic excitation energy in neutron-scattering spectra; also: Josephson frequency
$\boldsymbol{a}_0$	characteristic magnetic modulation wave vector
t_{p}	normalized pressure-derivative of the Néel temperature
T_{m}	general symbol for a magnetic phase-transition temperature
ν_{μ}	muon Larmour frequency
c, a	crystallographic axes
R	ideal gas constant; also: electrical resistance
$C(C_v, C_p)$	heat capacity or specific heat (at constant volume or pressure)
$\Delta\alpha, \Delta G$ etc.	increment of a quantity α, G etc.
$B_{\mathrm{c2}}(T)$	upper critical magnetic field of a superconductor
Θ_{D}	Debye temperature
B_{c2}	(negative) slope of $B_{\mathrm{c2}}(T)$ at $T=T_{\mathrm{c}}$
ξ	superconducting coherence length
κ	$=\lambda/\xi$, Ginzburg–Landau parameter
λ	penetration depth of a magnetic field into a superconductor
$B_{\mathrm{c1}}(T)$	lower critical magnetic field of a superconductor
$\boldsymbol{A}$	vector potential
$\boldsymbol{v}^{\mathrm{s}}$	velocity of the superconducting condensate
φ	electric potential
$\boldsymbol{l}$	prefered axis of an anisotropic superconducting order parameter in a crystal
$P_{\parallel}, P_{\perp}$	projectors along and perpendicular to a given direction
$\boldsymbol{j}^{\mathrm{s}}$	superconducting current density
$\boldsymbol{n}^{\mathrm{s}}$	tensor of superconducting condensate density
$\boldsymbol{n}^{\mathrm{n}}$	density tensor of quasiparticle excitations in the presence of an anisotropic superconducting condensate
$\hbar\Gamma$	electron-scattering rate due to impurities
P	spatial inversion (parity operator)
$\kappa(T)$	thermal conductivity
$(T_1)^{-1}$	spin-lattice relaxation rate
γ_{s}	coefficient of the linear specific-heat term (in T) for an anisotropic superconducting state

λ_s	coefficient of the linear thermal-conductivity term (in T) for an anisotropic superconducting state
v_s	(average) sound velocity
v_F	(average) Fermi velocity
T_{c0}	superconducting transition temperature in the undoped material
T^ρ	position of the low-temperature maximum in the resistivity $\rho(T)$ of a Kondo-lattice system
R_n	normal-state resistance of a Josephson contact
$K(x)$	complete elliptical integral of the first kind
I_c	Josephson current
T_c^*	superconducting to normal transition temperature in a Josephson contact
$M_{\alpha\beta}$	tunnel matrix element for electrons through a barrier, connecting pseudo spin-states α and β on either side, respectively
v	electron velocity
$m_0, \boldsymbol{m}$	components of $\hat{M} \equiv (M_{\alpha\beta})$ along 1 and $\boldsymbol{\sigma}$, respectively
$\hat{\boldsymbol{\sigma}}$	vector of Pauli matrices (often supplemented by the two dimensional matrix **1**)
$I_c^{ss}, I_c^{st}, I_c^{tt}$	singlet–singlet, singlet–triplet and triplet–triplet components of the Josephson current I_c
$\Delta_0, \boldsymbol{\Delta}$	components of the superconducting order-parameter matrix in pseudo spin space along 1 and $\hat{\boldsymbol{\sigma}}$, respectively
B_M	position of the inflection point in a field-dependent magnetization curve $M(B)$
T_M	position of the maximum in a temperature dependent susceptibility curve $\chi(T)$
ΔC_0	specific-heat jump at the superconducting to normal transition in the undoped material

1. Introduction

In the field of transition-metal physics, the lanthanide systems are of particular interest: in some of them, the 4f states contribute to crystal binding via hybridization with the delocalized band states. In most lanthanide compounds, the contribution of 4f states to the binding energy is negligible due to a large valence-excitation energy. In these cases the direct exchange and crystal-field (CF) effects determine the low-temperature state, which mostly involves magnetic order. Lanthanide ions near the ends and the middle of the 4f series may exhibit a valence instability. In fact, there are several Ce, Sm, Eu or Yb compounds for which the valence-excitation energy is so small that hybridization of 4f states with Wannier orbitals at neighbouring sites can lead to a homogeneous intermediate-valent (IV) phase [for review articles on the IV phenomenon, see: Wohlleben and Coles (1973), Wohlleben (1976), Jefferson and Stevens (1978), Robinson (1979), Grewe et al. (1980), Lawrence et al. (1981)]. For this phenomenon the term valence fluctuations is often used, implying that charge fluctuations destabilize the local 4f moments. The result is non-magnetic behaviour characterized by enhanced Pauli paramagnetism.

The strength of these hybridization effects is measured by Anderson's width $\Delta = \pi V^2 N_F$ which involves an appropriate average of the hybridization matrix element V and the conduction-band density of states (DOS) N_F at the Fermi level E_F. In the IV phase, $\Delta = 10^{-2}$–10^{-1} eV is typically of the same order as the

valence-excitation energy. Roughly, hybridization causes scattering resonances near the Fermi level of an IV system leading to virtual bound states of width Δ and to an enhanced total DOS of order Δ^{-1}. For this reason Δ in many experimental properties has to be viewed as an effective band width. It is typically smaller than the conduction band width by up to a factor of 100. The result is a correspondingly drastic enhancement of the thermodynamic quantities, e.g., the Sommerfeld coefficient of the electronic specific heat, γ, and the Pauli susceptibility, χ_0. Values found for the prototypical IV compound $CePd_3$ are $\gamma = 37\,\mathrm{mJ\,K^{-2}\,mol^{-1}}$ and $\chi_0 = 2.5 \times 10^{-8}\,\mathrm{m^3\,mol^{-1}}$, which substantially exceed even the corresponding values $\gamma = 9.4\,\mathrm{mJ\,K^{-2}\,mol^{-1}}$ and $\chi_0 = 1.2 \times 10^{-8}\,\mathrm{m^3\,mol^{-1}}$ of the nearly magnetic d-band metal Pd.

Heavy-fermion compounds [for existing review articles, see: Stewart (1984), Brandt and Moshchalkov (1984), Varma (1985a), Steglich (1985a), Lee et al. (1986), Ott (1987), Fulde et al. (1988)] exhibit a considerably more stable 4f configuration although the 4f occupancy still deviates slightly from integral values. They derive their particularly interesting properties at low temperatures from dramatically sharper scattering resonances near E_F. The anomalies in γ and χ_0 are thus further enhanced by typically an order of magnitude over the IV systems. For $CeAl_3$, γ amounts to $1.6\,\mathrm{J\,K^{-2}\,mol^{-1}}$ and χ_0 to $4.5 \times 10^{-7}\,\mathrm{m^3\,mol^{-1}}$. In these systems, the valence-excitation energy usually exceeds the Anderson width considerably, and no simple explanation of this phenomenon in terms of a one-particle picture is available. The narrow scattering resonances at the Fermi level are due to many-body effects. They lead, within the framework of Landau's Fermi-liquid theory, to strongly renormalized electronic quasiparticles with, e.g., very heavy masses. The formation of the heavy quasiparticles takes place at low temperatures. In dilute alloys the characteristic energy $k_B T_K$ related to the width of the resonance at E_F is commonly connected with the Kondo effect. This "Kondo temperature" T_K is typically in the range of a few kelvins. In many respects, concentrated heavy-fermion systems show striking similarities with dilute Kondo systems. Most properties may again be understood via one characteristic energy scale T^*, which can be surprisingly close to the value of $k_B T_K$ of the corresponding dilute system. As in the dilute case the electrical resistivity of heavy-fermion compounds has a negative temperature coefficient above T^*. Hence, these materials have been labelled "Kondo lattices". Marked deviations from the saturated maximum of the Kondo-impurity resistivity as $T \to 0$ are generally found below T^*. The resistivity of such compounds exhibits a maximum near $T^* > 0$ and drops towards $T = 0$. In high-quality samples the resistivity decrease can be drastic and the residual value comparable to that found for pure transition metals. In a lattice-periodic system the ground state, even if not magnetic or superconducting, should be coherent, and the low-lying excitations should obey the well known laws of Landau's Fermi-liquid theory. In particular, the transition to a T^2-behaviour of the resistivity well below T^* defines a "coherence temperature" T_{coh}. Although a Fermi-liquid description of the low-temperature phase of heavy-fermion compounds is possible in principle, a straightforward application of the formulae of Sommerfeld's theory for a one-

component, non-interacting Fermi system can be quite misleading. The structure of quasiparticles results from an interplay of two kinds of very different electronic states, i.e., well localized ionic f-states and rather delocalized conduction-band states, both in general anisotropic. Thus, the number of Fermi-liquid parameters required to understand the experimental observations is not small as in simple metals, even transition metals. In addition, interactions between quasiparticles are apparently very important in heavy-fermion compounds. Energies due to interactions between the heavy quasiparticles can be as large as the effective band width $k_B T^*$ as inferred, e.g., from cooperative effects found in these systems. It has been unanimously proven that superconducting and magnetically ordered phases are formed within heavy-quasiparticle liquids. The corresponding ordering temperatures are again in the range of a few kelvins. Superconductivity of heavy fermions below $T_c = 0.7$ K was first discovered for $CeCu_2Si_2$ and $CeAl_2$, the latter being the prototypical magnetically ordered heavy-fermion system with $T_N = 3.9$ K. In both cases an explanation of these phenomena is not possible in a straightforward way via the application of standard theories.

In addition, the surprisingly high effective masses of the quasiparticles, in particular the exotic properties of the cooperative states of heavy-fermion systems, have triggered much excitement among solid-state physicists and initiated the development of novel theoretical concepts for highly correlated electron systems. A variety of interesting magnetic phenomena, e.g., modulated structures, spin-density waves (SDW) and reduced moments challenge the theory of magnetism in the whole span between localized-moment behaviour and the band magnetism of the heavy quasiparticles. For the superconducting heavy-fermion systems, strong deviations from BCS theory have been measured. This has not only invoked the investigation of strong coupling effects, but – because of the similarities with the phenomenology of liquid ^{3}He – also speculations about exotic superconducting states, notably triplet pairing. A particularly interesting possibility involves the pronounced magnetic tendencies of heavy-fermion systems to produce a non-phononic pairing mechanism for the superconducting phases. Magnetic order can even coexist with heavy-fermion superconductivity as found, e.g., in URu_2Si_2. Heavy-fermion behaviour demonstrates in a particularly pronounced fashion the impact of strong correlations on classical condensed-matter concepts. In view of such phenomena as the quantized Hall effect, metal–insulator transitions and high-T_c superconductivity the study of strong correlation effects opens an exciting perspective.

2. The normal, paramagnetic state

2.1. *About the origin of heavy masses*

The most important experimental quantity with which to recognize heavy-carrier masses is the Sommerfeld coefficient γ of the electronic specific heat. In Fermi-liquid theory (Abrikosov et al. 1963, Nozières 1964, Baym and Pethick

1978), γ is proportional to quasiparticle DOS at E_F or to the effective mass. The former connection follows from an exact equation (Luttinger 1960),

$$\gamma = \frac{\pi^2 k_B^2}{3} \sum_{k,r} \delta(E_F - \epsilon_k^r) . \tag{1}$$

Equation (1) expresses γ in terms of a sum over a partial DOS

$$N_F^r = \sum_k \delta(E_F - \epsilon_k^r)$$

for quasiparticle bands characterized by an index r, containing in general a pseudospin variable σ, which crosses the Fermi surface at E_F. It is quite common to extrapolate the quasiparticle bands down to $k = 0$ by assuming a parabolic free-electron dispersion,

$$\epsilon_k = \hbar^2 k^2 / 2m^* , \tag{2}$$

thereby defining m^* in terms of the total quasiparticle DOS

$$N_F = \sum_r N_F^r$$

at the Fermi surface. For this purpose, the true Fermi surface is replaced by a sphere that preserves the total volume. Then, the free-electron formula,

$$\gamma = \frac{\pi^2}{3} k_B^2 N_F = \frac{k_B^2}{3\hbar^2} k_F m^* , \tag{3}$$

is used to give m^*. At the same time a fictitious Fermi energy $E_F^* = \hbar^2 k_F^2 / 2m^*$ is introduced reflecting a changed energy scale for phenomena taking place near the Fermi surface. Note that the Fermi wave number k_F is determined by the conduction-electron concentration and the lattice constant alone and is typically of order 1 Å^{-1}. This corresponds to the fact that according to Luttinger's theorem (Luttinger and Ward 1960, Luttinger 1960) the volume inside the Fermi surface is not changed by interactions. In general, the fictitious energy E_F^* is larger than the characteristic energy scale $k_B T^* (\approx 10\,\text{K})$ found experimentally: employing, e.g., $\gamma \approx 1\,\text{J K}^{-2}\,\text{mol}^{-1}$, one obtains $E_F^* \approx 500\,\text{K}$ (Steglich et al. 1982). In addition, these numbers imply an effective mass m^* of order $300 m_0$, where m_0 is the bare-electron mass. It is to be emphasized that the natural limit for the validity of the Fermi-liquid picture used above is T^* rather than E_F^*: Fermi-liquid theory becomes exact only for $T \ll T^*$. Roughly, T^* is a measure for the width of those structures in the one-particles DOS near E_F that are induced by correlations. It determines the steepness of the quasiparticle dispersion and, therefore, scales with the inverse of m^* or N_F.

The temperature dependence of the Sommerfeld coefficient of the electronic specific heat is shown in fig. 1 for $Ce_xLa_{1-x}Cu_6$ with varying Ce concentrations (Onuki and Komatsubara 1987). It is striking that these data, in units per mole of Ce, are independent of x, falling on the same curve. This demonstrates that the correlation effects causing the steep increase of γ below 10 K are essentially due to a single-ion behaviour. This point is illustrated likewise by the susceptibility

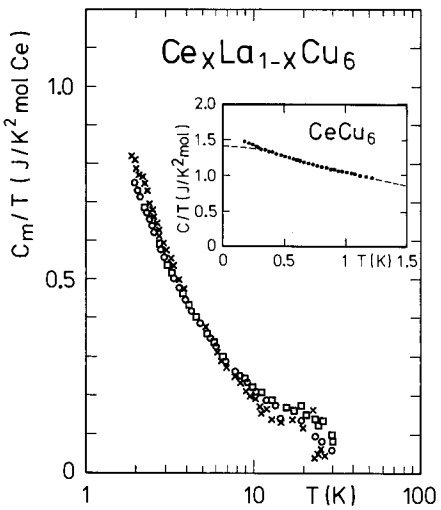

Fig. 1. Temperature dependence of 4f-derived specific heat per mole of cerium as C_m/T plotted against T for $Ce_xLa_{1-x}Cu_6$ with $x = 1$ (○), 0.8 (□) and 0.5 (×) (Onuki and Komatsubara 1987). Inset shows low-T data (Steglich et al. 1985). Dashed curve indicates result for an $S = \frac{1}{2}$ Kondo impurity with $T_K = 4.2$ K (Andrei et al. 1983).

data (see fig. 2), which show, when scaled to one mole of Ce, very few deviations up to 90 at.% Ce. Quite generally, thermodynamic data hint at the importance of single-ion effects: systematic deviations found on dilution could in all cases be understood quite conventionally, i.e., by changes of the lattice parameters. The most drastic variations have been found for $Ce_{1-x}La_xAl_2$ where T^* decreases by more than one order of magnitude upon dilution (Bredl et al. 1978a). Apparently, the main influence on this decrease derives from the larger La volume rather than from the elimination of the Ce–Ce interactions. This fact is substantiated in fig. 3 for $Ce_{1-x}Y_xAl_2$: dilution with smaller Y ions leads to an increase in T^*, in spite of the decrease in Ce concentration (Aarts et al. 1981).

As a result of the dominance of single-ion effects in the thermodynamics of heavy-fermion systems, the origin of heavy masses has to be traced back to the physics of strong local correlations as studied in connection with magnetic impurities in metals. In particular, the Kondo effect has been invoked (Kondo

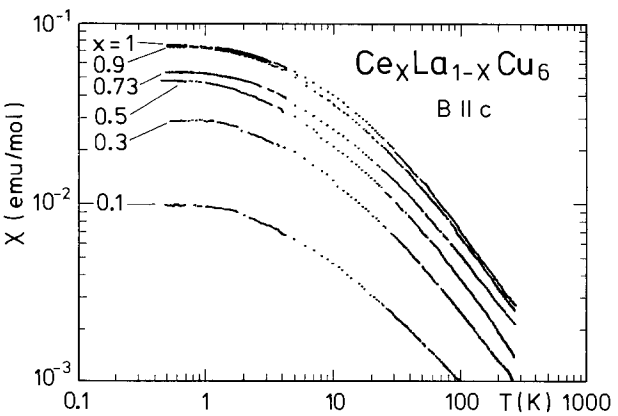

Fig. 2. Temperature dependence of the magnetic susceptibility per mole of formula unit for $Ce_xLa_{1-x}Cu_6$ (Onuki and Komatsubara 1987).

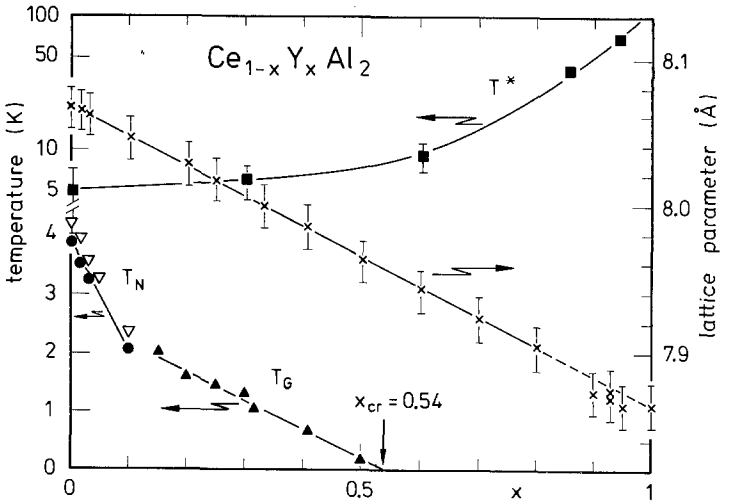

Fig. 3. Lattice parameter (right-hand scale) and characteristic temperatures (left-hand scale) of $Ce_{1-x}Y_xAl_2$ as functions of Y concentration. Characteristic temperatures are plotted on logarithmic scale (upper left) as obtained by neutron scattering (▀) and thermopower (■). Néel temperatures T_N as determined by specific heat (●) and susceptibility peaks at $B \leq 0.5$ T (▽), as well as the spin-glass temperatures T_G (▲) determined by zero-field susceptibility peaks, are plotted on a linear scale (lower left). Note that, for $x > x_{cr} = 0.54$, no cooperative magnetism exists and, for $x \geq 0.9$, the lattice parameters fall slightly below Vegard's straight line, indicating an IV state (Aarts et al. 1981).

1964, 1966, Grüner and Zawadowski 1974, Wilson 1975). The thermodynamics of a "Kondo impurity" has been calculated exactly in the framework of the s–d exchange model (Kondo 1964) via the Bethe-ansatz technique (Andrei et al. 1983, Tsvelik and Wiegmann 1983) and can be understood intuitively via a local Fermi-liquid picture (Nozières 1974). The corresponding theoretical specific-heat curve is shown for comparison in the inset of fig. 1, where the low-T data for $CeCu_6$ (Steglich et al. 1985) are displayed. The apparent good agreement with the experimental data above $T = 0.3$ K indicates the relevance of the Kondo effect for the heavy-fermion behaviour of these systems. The theory of the Kondo effect bears out the importance of one single energy scale T_K that allows an understanding of all the anomalous properties in a universal picture.

Many properties of the s–d model, or more generally of an underlying Anderson model (Anderson 1961, Schrieffer and Wolff 1966, Mühlschlegel 1968), can be understood as a consequence of the formation of a narrow resonance in the one-particle DOS near E_F, usually called Abrikosov–Suhl resonance (ASR) (Abrikosov 1965a, Suhl 1965, Grüner and Zawadowski 1972). Although the Kondo effect is of a true many-body nature and the calculational procedures become rather involved, the essence of this phenomenon can be easily understood: the formation of a singlet ground state requires the local magnetic moment to be screened by a spin polarization of the surrounding conduction electrons. This magnetic screening mechanism involves low-lying particle–hole excitations,

thereby introducing a narrow scattering resonance in the one-particle spectrum near E_F (Krishna-murthy et al. 1975, 1980a, b, Nozières 1978). A convenient tool for exploiting the consequences of the screening effect is given by Friedel's sum rule (Friedel 1952). In its most general form, which is based on Fermi-liquid theory (Langer and Ambegaokar 1961, Schrieffer and Mattis 1965, Langreth 1966, Yoshimori and Zawadowski 1982), it relates the total number n_ℓ of electrons localized due to the presence of a magnetic impurity to the scattering phase shifts δ_α with local quantum numbers α:

$$n_\ell = \frac{1}{\pi} \sum_\alpha \delta_\alpha \,. \tag{4}$$

Due to Anderson's compensation theorem (Anderson 1961), which holds for sufficiently structureless bands, n_ℓ may be identified with the number of electrons residing in the partially filled shell of the impurity. The phase shift δ_α in Fermi-liquid theory is given by

$$\arctan\left(\frac{\Delta_\alpha}{E_F - \epsilon_\alpha - R_\alpha}\right)$$

in terms of the self energy

$$\Sigma_\alpha(E_F + i\eta) = R_\alpha - i\Delta_\alpha$$

of the localized electrons. Via the standard relation

$$N_\alpha(\omega) = -\pi^{-1} \operatorname{Im} G_\alpha(\omega + i\eta) \,,$$

which connects the partial local DOS in channel α to the one-particle Green function G_α, one expresses N_α at E_F in terms of the phase shift (Langreth 1966, Haldane 1981):

$$N_\alpha(E_F) = \frac{1}{\pi\Delta_\alpha} \sin^2(\delta_\alpha) \,. \tag{5}$$

Equations (4) and (5) establish a relation between the DOS at E_F and the number of localized electrons. For a degenerate ionic doublet state ($B = 0$, $\alpha = \sigma$ labelling the z-component of the corresponding pseudospin) the result is

$$N_\sigma(E_F) = \frac{1}{\pi\Delta} \sin^2\left(\frac{\pi n_\ell}{2}\right) . \tag{6}$$

Typically, n_ℓ is near to one for Ce systems with the bare f-level well below E_F. Note that the Anderson width Δ is much smaller than that conduction-band width, so that $N_\sigma(E_F)$ is indeed large when compared with the bare conduction-band DOS. On the other hand, it should be clear that singlet formation via an indirect exchange coupling cannot transfer much spectral weight from the bare local level ϵ_α up to E_F. Thus, a narrow resonance near the Fermi level of maximum height $(\pi\Delta)^{-1}$ and width $k_B T_K \ll \Delta$ arises. It should be emphasized that the local DOS considered here is not the quasiparticle DOS that is used in Fermi-liquid theory to express thermodynamic quantities via free-particle for-

mulae and that is observed in thermodynamic measurements (see fig. 1). When applying Fermi-liquid formulae, back-flow effects at all energies are projected into the low-energy properties of the particles. Roughly, this leads to an increase of the spectral weight of order $k_B T_K/\Delta$ of the ASR to weight one of a full particle, corresponding to the increase of the resonance height of order $1/\Delta$ by a factor of $\Delta/k_B T_K$, i.e., to $1/k_B T_K$ (Kaga and Kubo 1988). The difference between $N_\sigma(E_F) \sim 1/\Delta$ and $N_{QP}(E_F) \sim 1/k_B T_K$ explains the difference between spectroscopic and thermodynamic data: whereas in photoelectron spectroscopy, which probes the bare local one-particle states with high energies (Gunnarson and Schönhammer 1987), an appropriate small spectral weight is found near E_F, the presence of heavy-mass quasiparticles dominates the thermodynamic, i.e., the low-energy, properties completely.

The preceding theoretical considerations refer to $T = 0$. They cannot be used to explain the pronounced temperature dependences of heavy-fermion properties. For the latter purpose one has to report to specific theoretical models that can be solved with the many-body techniques developed over the last few years. [For review articles see: Keiter and Morandi (1984), Bickers et al. (1987), Newns and Read (1987).] The temperature-dependent thermodynamic coefficients of the Anderson impurity model and some of its generalizations can be completely derived from the Bethe ansatz (Schlottmann 1985b, Desgrange and Rasul 1985, Okiji and Kawakami 1986, Coleman and Andrei 1986). Dynamic properties like one-particle spectra, including also the thermodynamics, can be studied to a good approximation by direct perturbation theory with respect to the hybridization between local and band states (Keiter and Kimball 1971, Keiter and Czycholl 1983, Grewe 1983a,b, Kuramoto 1983, Kuramoto and Kojima 1984, Lee and Zhang 1984, Zhang and Lee 1984, Coleman 1984, Bickers et al. 1985, Cox et al. 1985, 1986). The formation of the ASR as a function of temperature, e.g., is clearly borne out of such a calculation (Grewe 1983b, Kojima et al. 1984) see fig. 4a. The relevance of these model calculations of temperature-dependent one-particle excitation spectra for the physics of heavy-fermion materials has been beautifully demonstrated by high-resolution photoelectron spectroscopy (Patthey et al. 1987). The system $CeSi_2$ with a crystal-field doublet ground state and a characteristic temperature of about 35 K is at the verge of a valence instability and thus exhibits enough spectral weight near E_F to be observed with this technique. The structure found, including the temperature dependence as well as the spin–orbit and crystal-field (CF)-level splittings, can be fitted well by a perturbative calculation on the basis of a generalized Anderson impurity model, as demonstrated in fig. 5.

Calculations of the spectral properties for theoretical models containing a simplified version of f-shell dynamics usually aim at the resolvents $\mathcal{P}_M(z)$ of ionic many-body states $|M\rangle$ (Kuramoto 1983),

$$\mathcal{P}_M(z) = \left\langle M \middle| \left\langle \frac{1}{z + E_0^c - H} \right\rangle_{\text{cond}} \middle| M \right\rangle = [z - \epsilon_M - \Sigma_M(z)]^{-1} . \tag{7}$$

M denotes a collection of ionic quantum numbers, including the number of

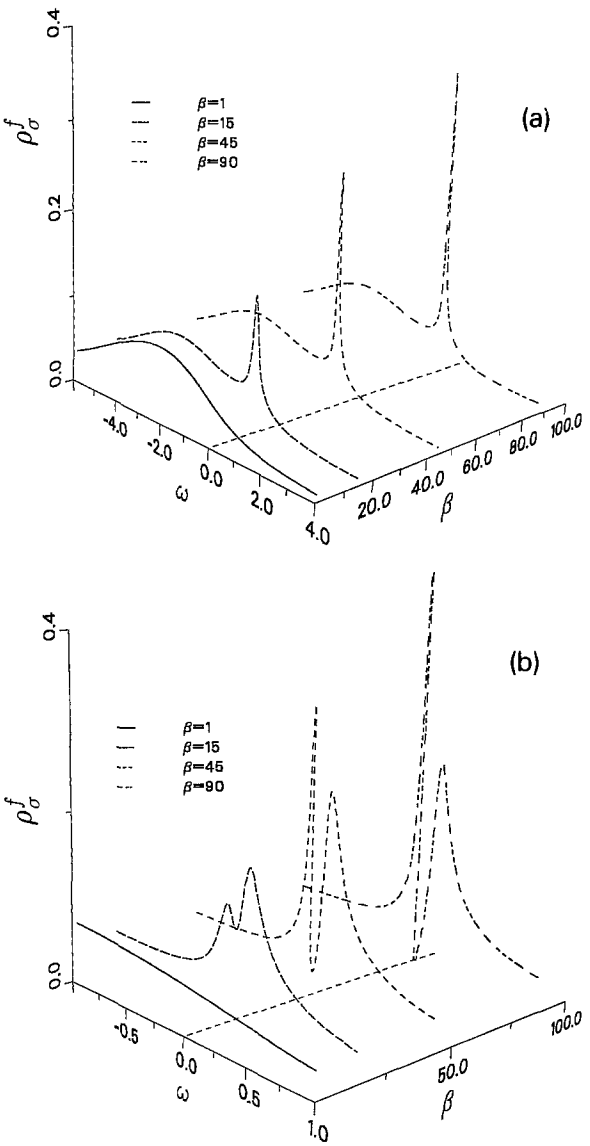

Fig. 4. Spectrum of localized electrons for an Anderson model with an ionic one-particle level at $\epsilon_1 = -3\Delta$ and an infinite Coulomb repulsion U, calculated at four different temperatures $k_B T = \Delta/\beta$. Energies are given in units of the Anderson width $\Delta = \pi V^2 N_F$. (a) NCA calculation for an impurity, $k_B T_K \approx 0.02\Delta$. At the lowest temperature $k_B T = \Delta/90 < k_B T_K$ the ASR near $\omega = 0$ is nearly saturated with a peak value of $\rho_0^f \approx (\pi\Delta)^{-1}$. The original ionic resonance at ϵ_1 is broadened on the scale Δ. (b) LNCA calculation for the lattice on an extended scale, showing the formation of a coherence gap in the ASR.

electrons n occupying the f shell and angular momenta according to Hund's rules as well as proper CF level indices. H is the full Hamiltonian, incorporating the f-shell dynamics, a set of bands and a hybridization between the two groups of states. $\mathscr{P}_M$ is to be interpreted like a propagator in ordinary quantum mechanics. It contains, in particular, all the information about the time evolution of states $|M\rangle$ and the corresponding spectral properties. The only non-standard feature of the definition (7) is the thermal average $\langle \cdots \rangle_{\text{cond}}$ over band states, which effectively reduces the problem to that of an ion in the complex potential $\Sigma_M(z)$.

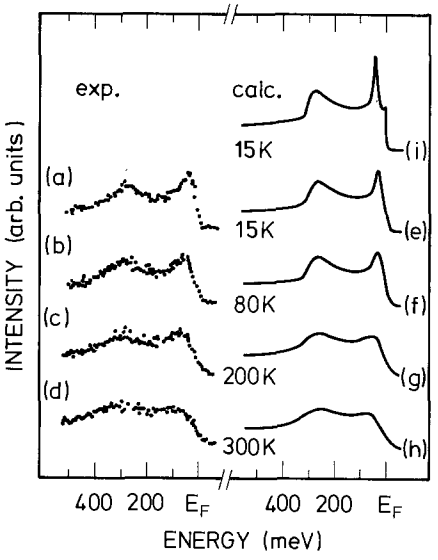

Fig. 5. Comparison between experimentally derived [(a)–(d)] and computed [(e)–(i)] f-spectra of $CeSi_2$ (Patthey et al. 1987). The theoretical curves (e)–(h) are the result of an NCA calculation for the corresponding temperatures including $4f^1$ spin–orbit and $4f^1_{5/2}$ crystal-field splittings. They also account, other than curve (i), for the instrumental resolution.

Since $|M\rangle$ is taken to be an eigenstate of the ionic part of H alone, Σ_M arises from the hybridization with band states. The shift of the energy variable z by the appropriate unperturbed band energies E_0^c under this trace leaves only the ionic part of the excitation energy and thus guarantees a uniquely defined ionic energy scale. Due to the repeated conversion of local electrons to band electrons via hybridization, the analytical character of the resolvents $\mathcal{P}_M$, which originally was determined by a simple pole at ϵ_M only, i.e., $\mathcal{P}_M^{(0)}(z) = (z - \epsilon_M)^{-1}$, changes drastically (Müller-Hartmann 1984). For all states $|M\rangle$ that can be constructed from the f-shell vacuum via hybridization processes from the band, a common threshold energy E_G develops which, e.g., appears in the spectra

$$\rho_M(\omega) = \pi^{-1} \operatorname{Im} \mathcal{P}_M(\omega - i\eta) .$$

Placing the Fermi level at $E_F = 0$, band electrons with energies $\epsilon < E_G$ experience no absorption when scattering on the f-shell at $T = 0$. Thus, E_G is the analogue (Menge and Müller-Hartmann 1988) of the long known threshold encountered in X-ray absorption (Haensel et al. 1969, 1970). In fact, the algebraic power law decay, which rules the ρ_M not too far above the threshold, is also connected to this well studied many-body problem (Nozières and de Dominicis 1969).

Numerical calculations of the ionic spectra ρ_M rely on a systematic skeleton expansion, defined via perturbation theory, with respect to the hybridization based on band states and ionic many-body states. This perturbation technique results in integral equations of the type $\Sigma_M = I(\{\mathcal{P}_{M'}\})$, which are usually solved in iteration procedures. The most recent version (Pruschke and Grewe 1989), which is appropriate for the Anderson model with finite or infinite Coulomb repulsion U, uses a generalization of the so-called non-crossing approximation (NCA) (Keiter and Kimball 1971). For an asymmetric Anderson model with $U = 3|\epsilon_1|$ it gives the spectral density of ionic states shown in fig. 6. The threshold

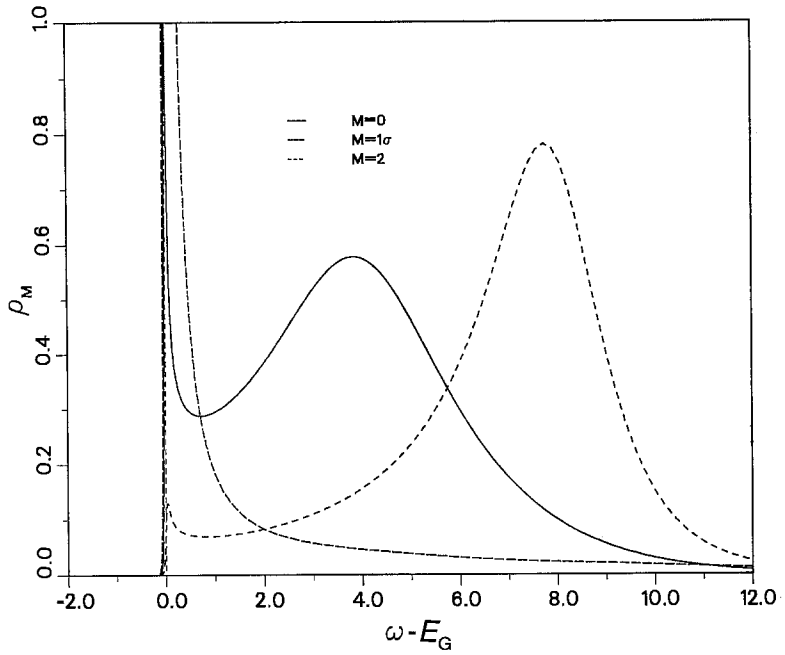

Fig. 6. Spectral density of ionic states for impurity-Anderson model with $\beta = 50$, i.e., $T \approx T_K$, and $\epsilon_1 = -3\Delta$, $U = 9\Delta$ (Pruschke and Grewe 1989). E_G is a common threshold energy, as known from the X-ray problem. The broad maxima in the $M = 0$ and $M = 2$ curves indicate resonances originating from the removal or addition of an electron in the $M = 1\sigma$ state, respectively. Units as in fig. 4.

energy E_G connects in the right way to the dynamic energy scale $k_B T_K$ as calculated from renormalization and Bethe-ansatz techniques. The decay exponents, however, come out slightly wrong in this approximation (Menge and Müller-Hartmann 1988). Thermodynamic data are obtained from the partition function, which is expressed via the ρ_M in an intuitive form (Grewe 1983a):

$$\mathscr{Z} = \mathscr{Z}_0^c \sum_M \int d\epsilon \, e^{-\beta\epsilon} \rho_M(\epsilon) \,. \tag{8}$$

The Boltzmann factor $e^{-\beta\epsilon}$ is weighted by the spectral density at energy ϵ for each renormalized ionic state $|M\rangle$. Likewise, ionic Green functions for f-electrons (Kuramoto 1983, Grewe 1983b, Pruschke and Grewe 1989) and local susceptibilities (Kuramoto 1983) are represented as convolutions of the ionic resolvents. The reconstruction of G_α with local one-particle quantum numbers α from such ionic Green functions is straightforward only in simple models for the f-shell dynamics. In realistic cases, complicated linear combinations have to be taken, according to the angular momentum and crystal-field coupling schemes encountered. For all of these quantities a generalized NCA, although not free from problems (Grewe and Keiter 1981, Grewe 1982, 1983b), resulting from the inaccurate threshold exponents of the $\mathscr{P}_M$, has turned out to be a sensible first

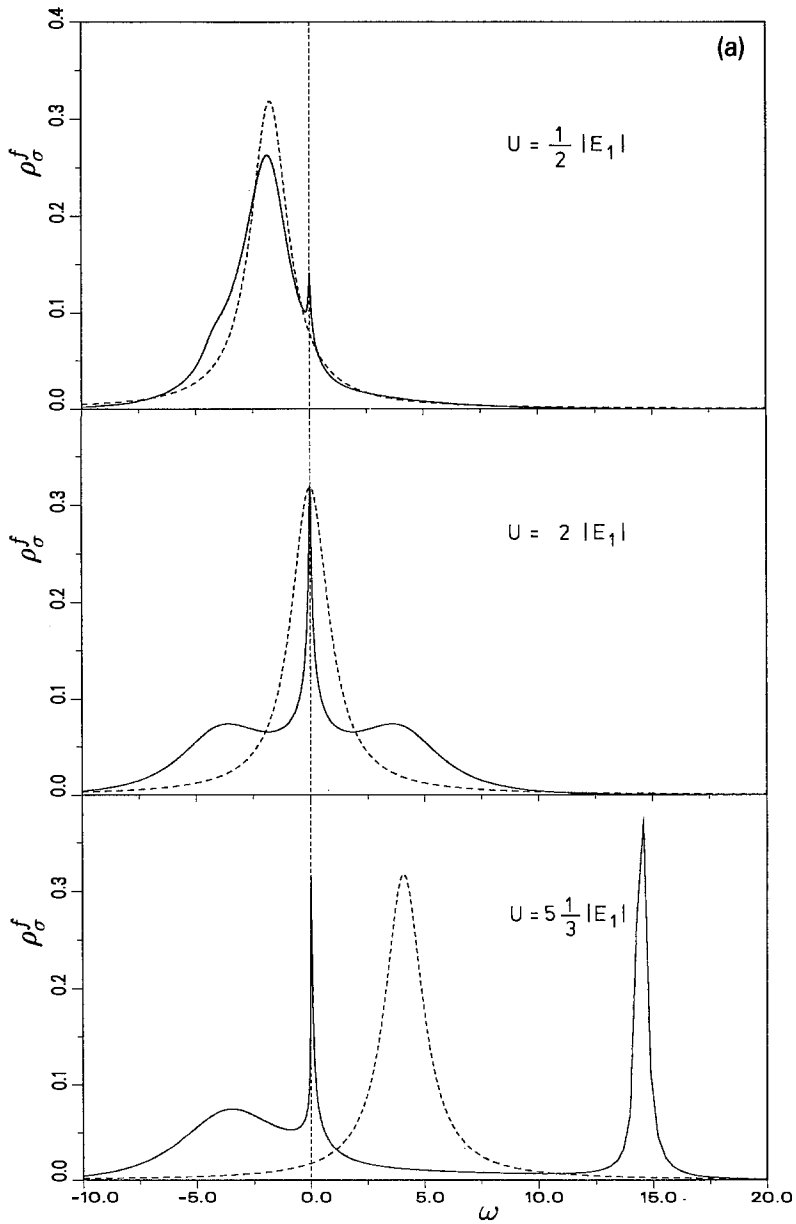

Fig. 7. The two sequences of pictures show the growth of correlations with increasing Coulomb parameter U in the Kondo regime $\epsilon_1 = -3\Delta$ of an Anderson impurity (a) and a lattice (b). The characteristic temperatures T_K and T^*, respectively, that vary with U and are largest for the impurity with $U = 16$ [last picture in (a)], i.e., $k_B T_K \approx 0.02\Delta$, exceed in all cases the temperature $k_B T = 0.02\Delta$ chosen. For the lattice, the band DOS (dark dashed) is shown in addition to the DOS of the localized electrons. Both curves exhibit simultaneous formation of the coherence gap with decreasing temperature. A comparison with the Hartree–Fock solution of the model (broken curves) gives an estimate of the many-body nature of all the features, which is small for $U < \Delta$ and very essential for large $U \gg \Delta$. Units as in fig. 4.

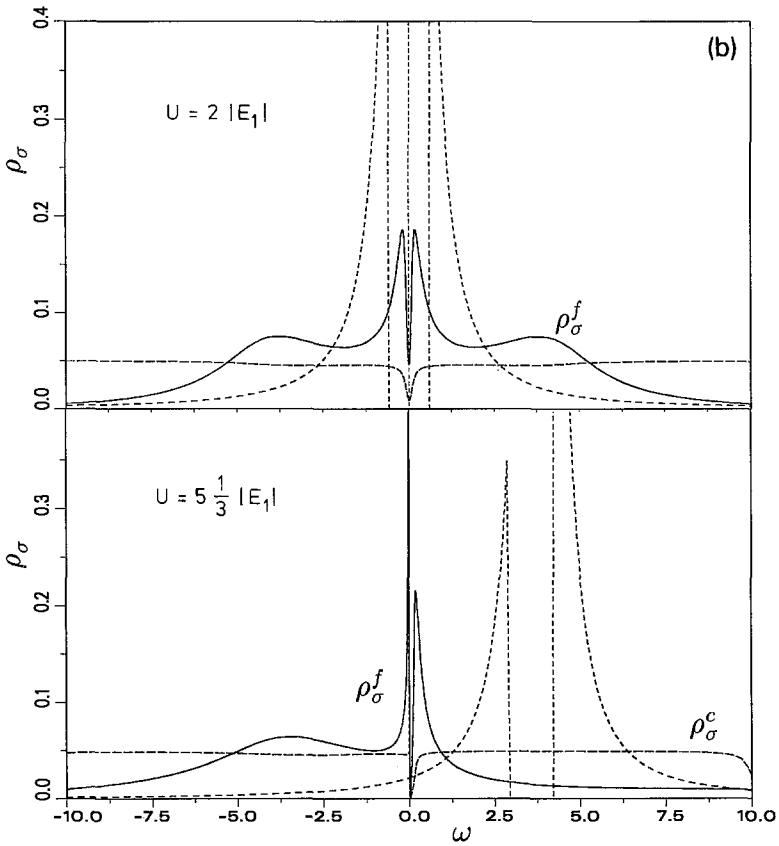

Fig. 7. (cont'd)

approximation (Kuramoto and Kojima 1984, 1985, Bickers et al. 1987, Pruschke and Grewe 1989). It is possible, e.g., to study the growth of correlations in the Kondo regime of the Anderson model, as the Coulomb parameter U increases. The sequence of pictures in fig. 7a visualizes the pronounced deviations of the one-particle spectrum of local electrons from the one obtained via the Hartree–Fock solution when U grows far beyond Δ. Clearly visibly is the formation of the ASR and the removal of weight belonging to the doubly-occupied states from the spectrum in the form of a narrow resonance, when $2\epsilon_1 + U$ exceeds the upper band edge. These results are based on a skeleton expansion for the Σ_M that includes vertex corrections beyond the simple NCA to account for finite-U effects (Pruschke and Grewe 1989, Pruschke 1989). Although it may be necessary and is, in fact, possible to go further beyond the NCA, a numerical evaluation of the resulting expanded system of integral equations seems difficult at the moment.

2.2. *The Kondo-lattice state and coherence*

Whereas the thermodynamic properties of heavy-fermion compounds are determined to a large degree by single-ion effects, transport properties reveal the

growing importance of coherence in the low-temperature state of heavy-fermion materials with increasing concentration of the f-ions. As an illustration, the incremental resistivity of $Ce_xLa_{1-x}Cu_6$ is shown in fig. 8 for varying Ce concentration x. In the dilute limit (low Ce concentration) one recognizes a negative temperature coefficient over more than four decades, with a nearly logarithmic dependence above the characteristic temperature of about 4 K. This is the hallmark of the Kondo effect. The behaviour of the resistivity can be traced to the presence of the ASR: since the T-matrix for band-electron scattering is directly proportional to the Green functions G_α of localized states (Langreth 1966),

$$T_{k\sigma,k'\sigma'}(z) = \sum_\alpha V_{k\sigma\alpha} V_{k'\sigma'\alpha} G_\alpha(z) , \tag{9}$$

the large imaginary part of G_α, i.e., $N_\alpha(E_F)$, causes strong resonant band-electron scattering at $E \approx E_F$ (Yosida and Yamada 1970, 1974, Yamada 1974, 1975).

In the Fermi-liquid phase of a periodic compound this strong resonant scattering disappears with $T \to 0$, as is observed, e.g., for $CeCu_6$, see fig. 8. The suppression of elastic local scattering has its formal correspondence in a vanishing imaginary part of the local-electron self-energy $\Sigma_{k\alpha}$ at E_F and $T = 0$ (Ohkawa 1984): the impurity contribution Δ_α is cancelled in the lattice by a corresponding term of non-local origin (Grewe 1982, Cox and Grewe 1988). Thus the T-matrix at E_F, being diagonal in k and proportional to the Green function $G_{k\alpha}$ for local states, has no imaginary part and quasiparticle decay cannot contribute to the resistivity at $T = 0$ (Yoshimori and Kasai 1983, Grewe and Pruschke 1985). The model calculation furnishing the one-particle spectrum of fig. 4a can be extended to the lattice (Grewe 1984a, 1987) and shows a corresponding decrease of the DOS in the middle of the ASR below a temperature T^*, i.e., the formation of a pseudogap, see fig. 4b. The disappearance of elastic scattering as well as gap formation for temperatures small compared with T^* both occur in approaching the coherent ground state of the system that obeys lattice-translational invariance (Martin 1982). The growth of correlations in the spectrum for local electrons with increasing U in the lattice is visualized in fig. 7b, where again the Hartree–Fock curves are shown for comparison.

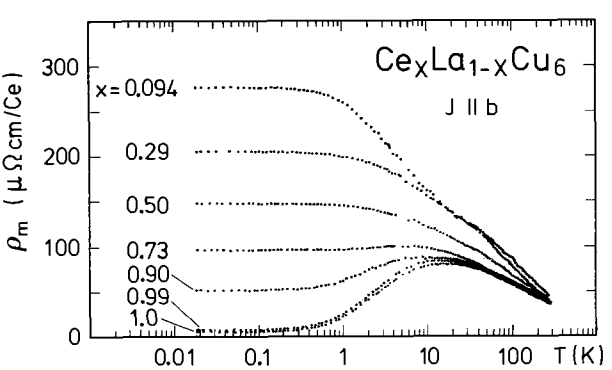

Fig. 8. Temperature dependence of the magnetic resistivity per mole of cerium for $Ce_xLa_{1-x}Cu_6$ (Onuki and Komatsubara 1987).

From a technical point of view, calculations for a lattice-periodic Anderson model in the Fermi-liquid phase account for the coherent action of many 4f-shells as scattering centers in the following way (Grewe 1987, Grewe et al. 1988):

(i) The T-matrix for band-electron scattering, defined by

$$G_{k\sigma}(z) = G^{(0)}_{k\sigma}(z) + G^{(0)}_{k\sigma}(z) T_{k\sigma}(z) G^{(0)}_{k\sigma}(z) , \tag{10}$$

is, as before, essentially the f-electron Green function,

$$T_{k\sigma}(z) = \sum_{\alpha} |V_{k\sigma\alpha}|^2 G_{k\alpha}(z) .$$

$G_{k\sigma}$ now includes the possibility that an electron, created on the f-shell at a first site 1 moves, after a hybridization process, via a band state to a second different site, and so on, until it is finally destroyed in the f-shell of the last site n. The resulting picture envisages $G_{k\alpha}$ as a sequence of local scattering events (Elliott et al. 1974, Grewe 1982):

$$G_{k\alpha}(z) = G^{\mathrm{eff}}_{\alpha}(z) + G^{\mathrm{eff}}_{\alpha}(z) \sum_{\sigma} V^{*}_{k\sigma\alpha} \left(G^{(0)}_{k\sigma}(z) - \frac{1}{N} \sum_{k} G^{(0)}_{k\sigma}(z) \right) V_{k\sigma\alpha} G^{\mathrm{eff}}_{\alpha}(z)$$

$$+ \cdots = \left[G^{\mathrm{eff}}_{\alpha}(z)^{-1} - \sum_{\sigma} |V_{k\sigma\alpha}|^2 \left(G^{(0)}_{k\sigma}(z) - \frac{1}{N} \sum_{k} G^{(0)}_{k\sigma}(z) \right) \right]^{-1} . \tag{11}$$

For simplicity, conservation of the local quantum numbers α has been assumed here, as well as pseudospin conservation.

(ii) The superscript of the Green function $G^{\mathrm{eff}}_{\alpha}$, which describes an ionic state α on an effective site of the lattice, indicates the modified local renormalizations as compared to the impurity problem: local electrons, when emitted into the band, can experience scattering off the f-shell at different lattice sites before they are reabsorbed. Thereby a different, effective, band DOS is probed locally that leads to a moderate increase of the lattice-energy scale $k_{\mathrm{B}}T^{*}$ (Kuramoto 1985, Grewe et al. 1988). This effect has been termed "collective enhancement of the Kondo effect" (Kim et al. 1987). The effective DOS can be expressed via a kind of renormalized band Green function, so that a complete self-consistency circle is obtained, leading to new equations of the form $\Sigma_M = I'(\{\mathcal{P}_M\})$ for the effective-site problem (Grewe 1987).

We illustrate the formation of coherence in the one-particle DOS again in fig. 9a for the band states. The calculation, like the ones before, is based on the lattice version of the NCA technique (LNCA), which has been outlined above. It leads to temperature-dependent spectra for both kinds of electrons, cf. also fig. 4b. The band states do not reflect the enhancement of the DOS, which is due to the local states, but they react simultaneously by the formation of a gap of the same size to the increase of local scattering at all lattice sites with decreasing temperature. Clearly the change in DOS near E_{F} reflects the characteristic temperature T^{*}, which can roughly be determined from the size of the gap. For comparison, a calculation for the IV regime of the periodic Anderson model is in addition shown in fig. 9b. The spectrum is less temperature dependent, due to the

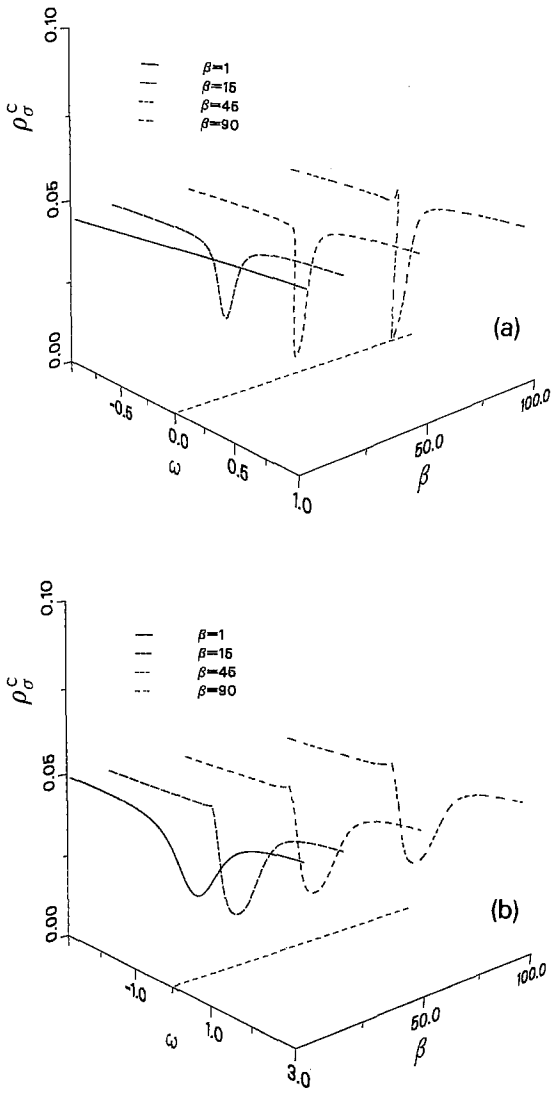

Fig. 9. Comparison of coherence gap formation in the band DOS for the Kondo regime (a) and the IV regime (b) of the Anderson lattice. Parameters are $U = \infty$ and $\epsilon_1 = -3\Delta$ (implying $k_B T^* \approx 0.03\Delta$) for (a), $\epsilon_1 = -0.5\Delta$ for (b), units as in fig. 4. The characteristic energy scales, $k_B T^*$ for (a) and Δ for (b), are apparent from the widths of the features as well as from the saturation behaviour of the temperature variations in the spectra. Considerable many-body effects become apparent even in the IV case, e.g., the temperature variation itself. For $\epsilon_1 \to 0$ the dynamic scale $k_B T^*$, however, merges with the scale Δ for one-particle resonant scattering.

reduced importance of many-body correlations, and the characteristic scale for both, temperature variation and size of the gap, has changed to Δ. Although infinite U has been assumed in these examples, the technique also works for reduced correlations, i.e., $U < \infty$ (Pruschke and Grewe 1989). Such model studies are useful for an understanding of the basic phenomena in heavy-fermion physics. They also lend support to semi-phenomenological approaches, like the renormalized band scheme, which improve on conventional band-structure calculations in the self-consistent LMTO (Jarlborg et al. 1983) or the LDA scheme (Oguchi and Freeman 1986) by accounting for a large effective-mass enhancement factor (Sticht et al. 1986, Strange and Newns 1986, Fulde et al. 1988). Here the proper

crystal structure is included in the calculation and detailed realistic Fermi surface structures can be obtained (Zwicknagl 1988, Hofmann and Keller 1989).

Transport coefficients are given in terms of the following moments of the transport relaxation time $\tau(\omega)$ (Abrikosov 1965, Kozarzewski 1973):

$$L_m^l = \int \mathrm{d}\omega \left(-\frac{\partial f}{\partial \omega}\right) \omega^m \tau(\omega)^l . \tag{12}$$

For a wavevector independent self-energy Σ in the carrier Green function

$$G_k(z) = [z - \epsilon_k - \Sigma(z)]^{-1} ,$$

and a smooth density of band states this τ is approximated by (Keiter and Kurkijärvi 1977, Yoshimori and Kasai 1983)

$$\tau(\omega) = \frac{1}{2 \operatorname{Im} \Sigma(\omega - \mathrm{i}\eta)} . \tag{13}$$

In the Fermi-liquid phase, the self-energy can be expanded as (Yoshimori and Kasai 1986, Yamada et al. 1987, Yoshimori 1976, Shiba 1975, Nozières 1974)

$$\operatorname{Im} \Sigma(T, \epsilon - \mathrm{i}\eta) = \alpha T^2 + \alpha'(\epsilon - E_\mathrm{F})^2 \tag{14}$$

near E_F and for low temperatures. In the presence of impurities Im Σ acquires a small energy- and temperature-independent residual value. Eq. (13) and (14) lead to a positive qudratic increase of the resisitivity of low temperatures, $\rho = \rho_0 + aT^2$, with $a \sim \alpha$ and α' independent of the impurity concentration (Grewe and Pruschke 1985, Cox and Grewe 1988). This behaviour is observed in all heavy-fermion compounds. For an example, see $CeCu_6$ (fig. 10).

Above T^*, the self-energy rapidly approaches that of independent impurities (Yoshimori and Kasai 1983). As a result, the resistivity exhibits a maximum near T^*, followed by the logarithmic decrease known from the dilute systems, see fig.

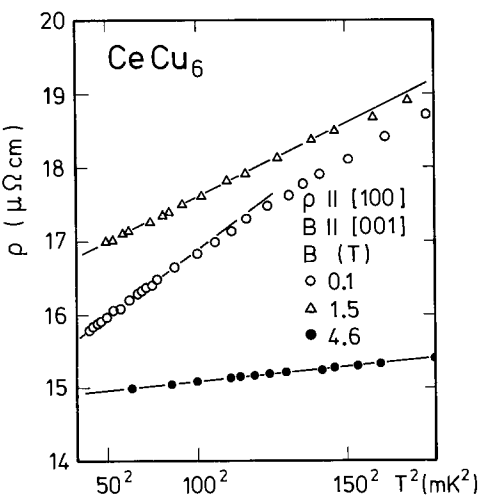

Fig. 10. Resistivity along the direction [100] as a function of T^2 for three different magnetic fields applied along [001] (Amato et al. 1987a).

8. In agreement with the strong energy dependence on the small scale T^*, the self-energy acquires strong variations due to lattice defects (Cox and Grewe 1988). According to fig. 8, the low-temperature coherent phase is efficiently disturbed by substitution of non-f ions. Given the smallness of T^*, the influence of an impurity in the coherent state will extend over several lattice spacings as a consequence of the uncertainty principle.

The pronounced effect of coherence in the resistivity can find its correspondence even in the thermodynamic properties: $CeAl_3$ shows, at temperatures much smaller than T^*, a maximum in the Sommerfeld coefficient $\gamma(T)$ (fig. 11), in striking contrast to the Bethe-ansatz result for a single Kondo ion (see dashed curve in the inset of fig. 1). According to the model calculation of fig. 4b, this can be attributed to the reduced DOS in the pseudogap of the Fermi-liquid phase. Such a qualitative argument (Bredl et al. 1984b) is supported by calculations of the quasiparticle band structures, using the LDA scheme combined with a strongly energy-dependent phase shift at E_F (Sticht et al. 1986, Strange and Newns 1986, Zwicknagl 1988). One typically finds pronounced features in the DOS, including such pseudogaps near E_F, cf. fig. 12. In the framework of band-structure theory the existence of flat portions of (quasiparticle) bands near E_F connected with pseudogaps is guaranteed by Luttinger's theorem (Luttinger 1960, Martin 1982). Without any local Coulomb repulsion of f-electrons, the Fermi energy E_F would be situated at the nearly dispersionless localized f-state, i.e., low in the band but consistent with a large value of the Fermi momentum. In the presence of the local interaction, E_F becomes shifted to a value fairly far above the f-energy in order to deplete the local level. In the corresponding formation of quasiparticle states, the conduction bands develop flat portions near the new E_F in order to guarantee conservation of the $\boldsymbol{k}$-space volume inside the Fermi surface (Brandow 1986, 1988).

It is interesting to study the formation of coherence under application of pressure, as has been done, e.g., in the case of $CeCu_6$ (Thompson 1987). In fig.

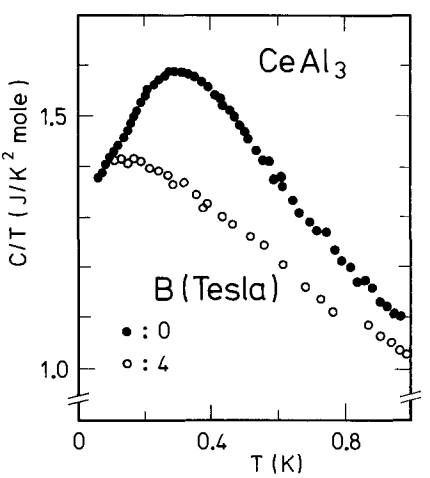

Fig. 11. Specific heat of $CeAl_3$ as C/T plotted against T at $B = 0$ and 4 T (Steglich 1985b).

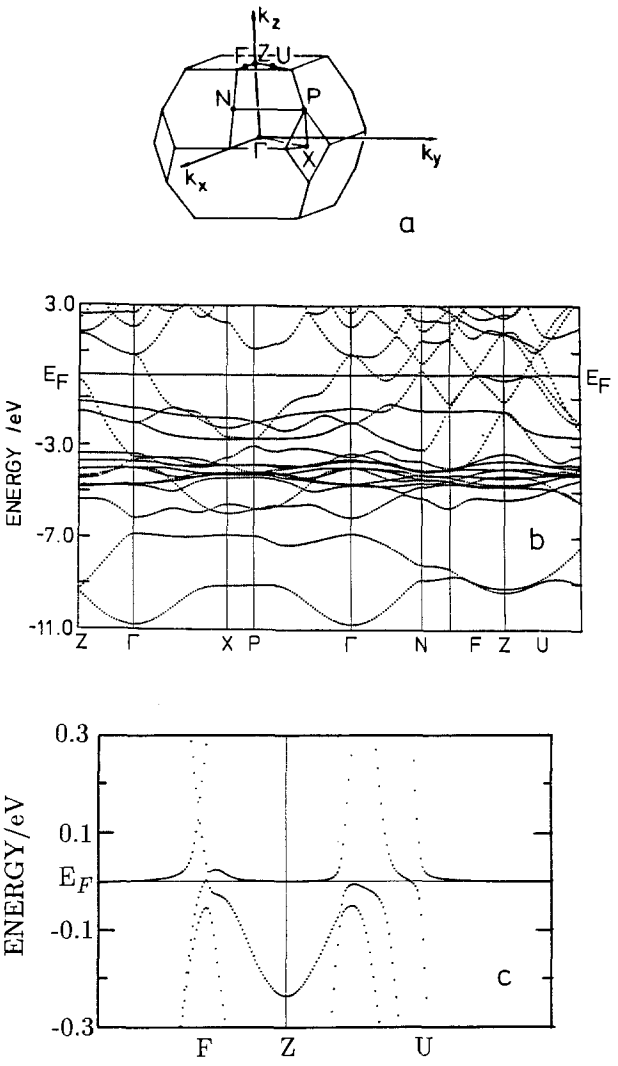

Fig. 12. Quasiparticle band structure of $CeCu_2Si_2$ (Sticht et al. 1986), derived from an LDA calculation augmented with an additional strongly energy-dependent f-scattering phase shift. (a) Brillouin zone of the body-centered tetragonal $CeCu_2Si_2$ crystal structure. (b) Quasiparticle bands on a large energy scale. Heavy-fermion bands form on the line representing the Fermi level E_F. (c) Neighbourhood of E_F with high energy resolution along some symmetry directions, shown in (a), with apparent hybridization gaps. The whole structure is highly anisotropic.

13 scaling is remarkably well obeyed at temperatures $T > T^*$, i.e., the normalized resistance curve R/R_{max} is a function of the reduced temperature $T/T^*(p)$ alone. This property even seems to apply for $T < T^*$, i.e., in the region where coherence effects start to have a distinct influence on scattering. It can be taken as support for theoretical considerations indicating that T^* also sets the scale for coherence effects (Grewe 1984a, Grewe et al. 1988). This fact should not be confused with the possible relevance of an independent scale $T_{coh} \ll T^*$, which is used to limit the small regime near $T = 0$, where a T^2-power law as characteristic for inelastic excitations in a coherent Fermi liquid close to its ground state is observed, see below. An increase of T^* with pressure is also established in $CeAl_3$ via measurements of the specific heat (Brodale et al. 1986). Since a plot of C/T against T

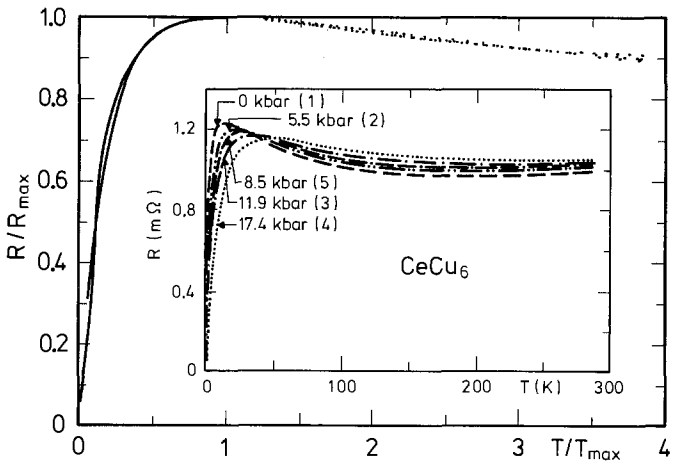

Fig. 13. Resistance normalized by its maximum value as a function of reduced temperature for $CeCu_6$ at five pressures (experimental sequence as indicated by the numbers in the parentheses) between 1 bar and 17.4 kbar. T_{max}, the temperature at which the resistance maximum occurs (inset), increases montonically with pressure from 15 to 51 K (Thompson 1987). The $p = 0$ value of T_{max} exceeds the characteristic temperature T^* by a factor of 3.5.

already develops a plateau at moderate pressure $p > 0$ (Brodale et al. 1986), a corresponding shift of the coherent region of the Fermi-liquid state is difficult to assert. In the actinide system UBe_{13}, on the other hand, the picture is consistent again, resembling the case of $CeCu_6$: scaling of R/R_{max} as a function of $T/T^*(p)$ exists from 1 K to well above T^* (Thompson 1987). $T^* = 2.3$ K, taken here as the position of the resistivity peak, shifts upwards with pressure, and so does the specific heat peak, which is located at 2.4 K at ambient pressure (Thompson 1987). The latter effect, in particular, demonstrates the increasing band-like behaviour in the coherent system of heavy quasiparticles.

2.3. *Energy scales*

The novel characteristic features of heavy-fermion physics involve the low-energy excitations. At high excitation energies or temperatures, heavy-fermion systems behave in accord with the well-known physics of conventional lanthanide systems such as Gd metal. In particular, most of the features seen in photoelectron spectroscopy can essentially be understood in terms of ionic energy schemes and normal band structures (Gunnarsson and Schönhammer 1983, 1987). These ionic energies result from the electrostatic interactions among the f-shell eletrons and their spin–orbit coupling (Hirst 1978). Thus, one finds localized magnetic moments according to Hund's rules. The corresponding effective Coulomb repulsion on the f-shell is of order 10 eV, the direct exchange coupling of order 1 eV, and the spin–orbit interaction of order 0.1 eV. Crystal-fields (CF) acting on the localized 4f-electrons of lanthanide ions are typically smaller by another order of

magnitude (Chan and Lam 1974, Fulde and Loewenhaupt 1985). This clear hierarchy of ionic energies is different from the 3d metals, where the order of spin–orbit and CF interactions is reversed. The light actinides, on the other hand, do not exhibit a good separtion of energy scales: CF effects on the less localized 5f-electrons are comparable to the action of spin–orbit coupling, and direct exchange interactions in general just barely exceed both, preventing the application of Hund's rules.

It is well known that the 5f-states of light actinides, e.g., U and Np, in a metallic environment are usually subject to considerable hybridization with neighbouring ligand states (Koelling et al. 1985, Crabtree 1985, Oguchi and Freeman 1986). Though according to the Hill plot (Hill 1970), direct 5f–5f wavefunction overlap is negligible in the actinide-based heavy-fermion compounds, e.g., UBe_{13} and $NpBe_{13}$, it is this 5f-ligand hybridization that gives rise to the concept of an intrinsic "5f-band width". Depending on the nature of the ligand atoms and their coordination, one expects – on the basis of modern band-structure theory – clear trends in the chemical and physical properties of 5f-compound materials (Freeman and Darby 1974), in accord with experiment. In the typical heavy-fermion systems, this mechanism at best gives narrow and highly correlated "f-bands": in the absence of considerable direct overlap between such ligand states, the system usually realizes the localized side of a Mott transition (Mott 1974, Brandow 1977) in these "f-bands". Therefore, it is in general a good starting point for understanding the physics of heavy-fermion compounds to consider the f-electrons as being localized and being subject to a rather weak hybridization with the broad conduction bands formed by a superposition of ligand states and the d-states of the respective lanthanide or actinide atom. Although this hybridization energy is definitely smaller for actinide compounds than the ionic energies mentioned above, i.e., CF and spin–orbit energies of order several tenths of an electron volt, it is the essential parameter in heavy-fermion physics. Variations both in the anisotropy and strength of the hybridization can result in drastic phenomenological differences between actinide-based heavy-fermion compounds (Crabtree 1985). As an illustration, the temperature dependence of the electrical resistivity of the two U-based heavy-fermion superconductors UBe_{13} and UPt_3 is shown in fig. 14. It is remarkable that the resistivity curve for UBe_{13} resembles that of the Ce-based heavy-fermion superconductor $CeCu_2Si_2$ which is also included in the figure. Since the 4f electrons in Ce-based systems are definitely well localized, this supports the local nature of the heavy-fermion phenomena in actinide-based compounds.

In contrast to the situation in lanthanide compounds, a unique characterization of the low-lying ionic energy levels for actinide heavy-fermion systems is generally not at hand. The case of U compounds is particularly intriguing. We shall argue below that in all known cases it is the conventional Kondo effect – properly modified for a lattice system – which provides the heavy masses; the essence of the argument being based on the sensitivity of magnetic probes and the consistency of different, i.e., the magnetic and non-magnetic characterizations of a characteristic low-energy scale. This implies a magnetic ionic ground state or, as may be

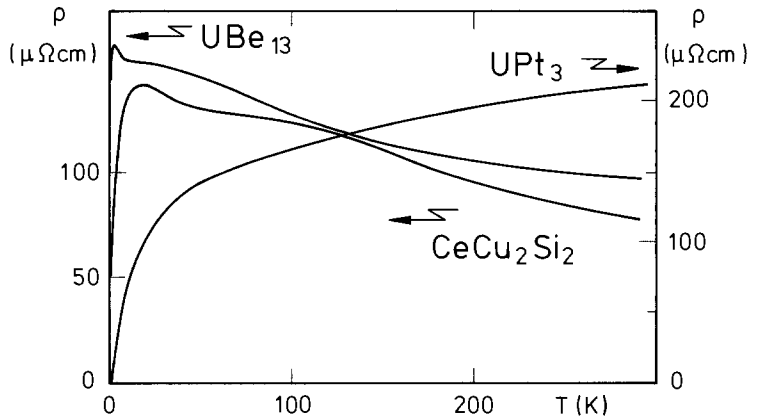

Fig. 14. Resistivity as a function of temperature for $CeCu_2Si_2$, UBe_{13} and UPt_3 (Steglich 1989).

considered for U^{4+}, at least low-lying magnetic levels. It has been pointed out, however, that a U^{4+} ion in a cubic, and possibly also tetragonal, environment could exhibit a non-Kramers ground doublet and no possibility for low-energy magnetic excitations. In this situation an alternative mechanism, called the "quadrupolar Kondo effect" could account for the heavyness of quasiparticles (Cox 1987b–1988), which originates from a coupling of ionic to band-electron electric quadrupole moments and may formally be mapped onto a multichannel Kondo problem. In addition to an apparent insensitivity to magnetic couplings – weak effects are only expected from Van Vleck contributions – the quadrupolar Kondo effect, e.g., involves a logarithmically divergent (quadrupolar) susceptibility and specific-heat coefficient $\gamma(T)$. Thus it should be possible to discriminate it experimentally from the conventional Kondo effect. Although in our opinion the evidence for, e.g., UBe_{13} as the strongest candidate is against this possibility, see, e.g., fig. 29 and the corresponding discussion of the magnetoresistance, the quadrupolar Kondo effect is an interesting concept that may well be important in the broader field of actinide physics.

In the following we concentrate on heavy fermions in Ce-based compounds. The Hund's rule ground state of Ce^{3+} ($J = \frac{5}{2}$) is sixfold degenerate. In the crystal environment it can potentially split into three Kramers doublets or, in cubic symmetry, into one Γ_7 doublet and one Γ_8 quartet. Inelastic magnetic neutron-scattering spectra on compounds like $CeAl_3$ (Murani et al. 1977), see fig. 15, and $CeCu_2Si_2$ (Horn et al. 1981a), are commonly understood in terms of CF splittings of typical order 100 K. Since for these metallic systems a simple interpretation of CF effects via point charges does not work, CF schemes are essentially of phenomenological character and not part of any a priori theory for heavy-fermion systems. In particular, hybridization and CF effects cannot necessarily be separated. Whereas in IV systems CF resonances are smeared out by the large hybridization, they are generally sharper and may well be identified in heavy-fermion systems. An extreme case is $CeRu_{2.16}Ge_2$ where, according to fig. 16a,

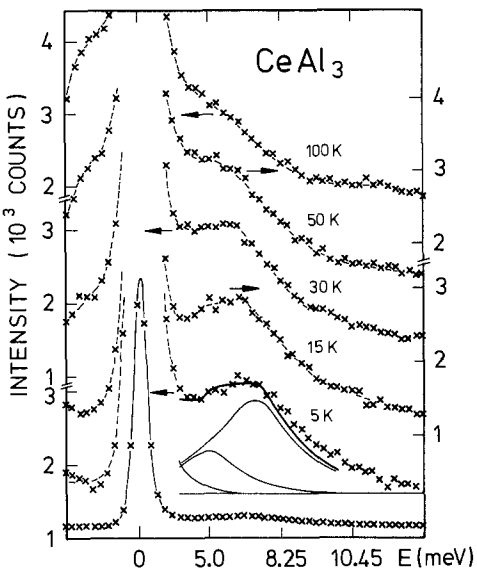

Fig. 15. Scattered intensity of time-of-flight spectra plotted against energy transfer, E, for polycrystalline $CeAl_3$. Thick continuous line shows result of fit constructed from various components indicated by fainter lines: flat background, nuclear elastic line, inelastic magnetic lines at $E = 5.2$ meV and 7.5 meV, respectively (Murani et al. 1977).

the CF excitations lie well above ($\Delta_{CF}/k_B \approx 500$ and 700 K) the low-temperature regime that is dominated by a ferromagnetic transition at $T_m \simeq 7$ K (Felten et al. 1987). Hybridization in this case does not significantly contribute to a broadening of the excited CF levels, which is demonstrated by a nearly perfect Schottky fit to the high-temperature specific-heat data (cf. solid curve). More typical is the case of $CeCu_2Ge_2$ where a lower-lying excited CF level ($\Delta_{CF}/k_B = 170$ K) gives rise to a considerably broadened specific-heat anomaly, see fig. 16b.

For $CeCu_{2.2}Si_2$ (Bredl et al. 1985) and $CeAl_3$ (de Boer et al. 1985) strong electronic correlations produce a pronounced anomaly at the low-temperature tail of the CF peak in C against T. The whole feature can still be explained via two separated energy scales: $k_B T^*$ and Δ_{CF}. The shape of this curve can be fitted surprisingly well by a superposition of the Bethe-ansatz result for spin $\frac{1}{2}$ and Kondo temperature $T^* = T_K = 9$ K and 4 K for $CeCu_{2.2}Si_2$ and $CeAl_3$, respectively, and the CF-derived Schottky anomaly for excitations into higher CF states. Within Bethe-ansatz theory the interference of Kondo effect and CF excitations has been taken into account (Schlottmann 1984a, b, 1985a, Desgranges and Rasul 1985, 1987, Okiji and Kawakami 1986, Desgranges 1987) and leads to curves very similar to the ones observed, see fig. 16. It is remarkable that the specific heats of the two U-based heavy-fermion superconductors resemble the Ce-data as is obvious from figs. 17a and 17b. Whereas CF effects are rarely observed in metallic U systems, UBe_{13} may well be compared with $CeCu_2Si_2$, and UPt_3 may be described by the theoretical curve in fig. 18 for $\Delta_{CF}/k_B T_K = 1$. In the Bethe-ansatz parts of these specific-heat fits the entropy corresponding to the CF ground states can be obtained from the area below the curve of C against $\ln T$ between $T \to 0$ and the peak position $T = T_m$, which amounts to almost half of the full value. For all systems mentioned before one finds the latter to be $R \ln 2$

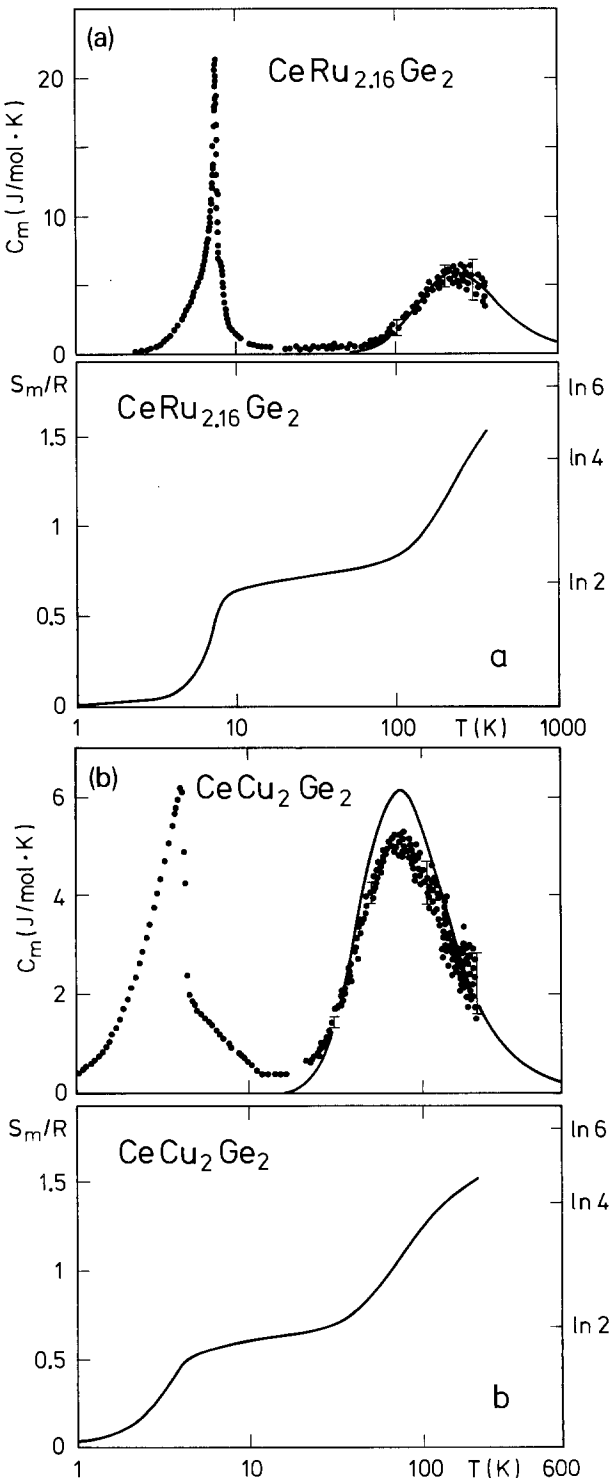

Fig. 16. Temperature dependence of 4f-derived specific heat, C_m, and entropy in units of the gas constant, S_m/R, for (a) $CeRu_{2.16}Ge_2$ and (b) $CeCu_2Ge_2$ (Felten et al. 1987). Solid curves in upper parts show Schottky anomalies corresponding to the CF splitting of Ce^{3+} given in the text.

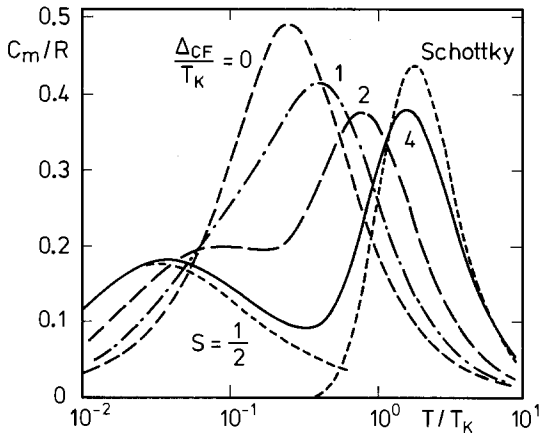

Fig. 17. 4f-derived specific heat for crystal-field-split doublet–doublet system in units of the gas constant, C_m/R, as a function of T/T_K (on a logarithmic scale) for different ratios $\Delta_{CF}/k_B T_K$. For comparison Bethe-ansatz result for $S = \frac{1}{2}$ and Schottky anomaly are also shown (Desgrange and Rasul 1985).

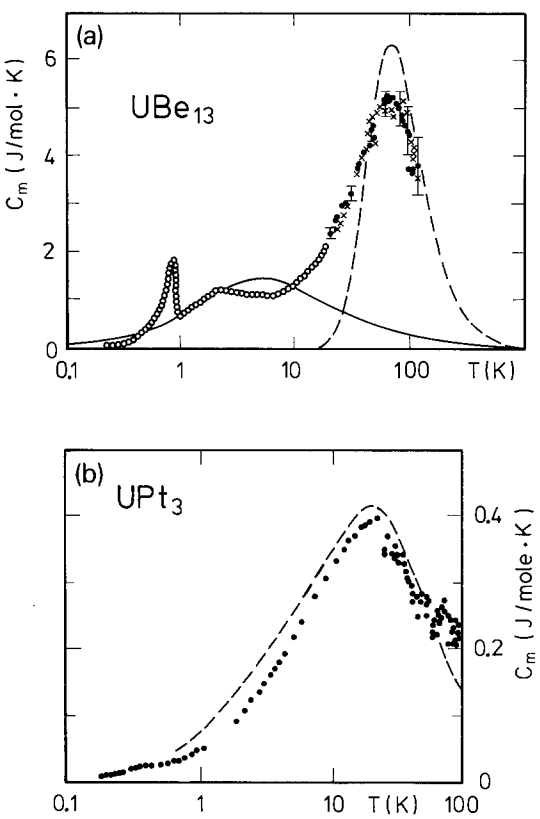

Fig. 18. The 5f-derived specific heat of (a) UBe_{13} (Felten et al. 1986) and (b) UPt_3 (Rietschel et al. 1988). Solid curve in (a) is Bethe-ansatz result for $S = \frac{1}{2}$ and $T_K = 7/8$ K, dashed one is Schottky anomaly for doublet–quartet splitting of $k_B \cdot 180$ K. Dashed curve in (b) is curve for $\Delta_{CF}/k_B T_K = 1$ from fig. 17.

corresponding to a doublet CF ground state. In addition, since T_{max} is related to T_K via $T_{max} = 0.66 T_K$ (Andrei et al. 1983), the characteristic low-energy scale $k_B T^* \approx k_B T_K \approx k_B 10\,\mathrm{K}$ lies well below the CF excitation energy $\Delta_{CF} \approx 100\,\mathrm{K}$.

The most important energy for heavy-fermion systems is the characteristic temperature T^*. It plays a number of different roles, depending on the particular question addressed.

(i) It separates a high-energy (temperature) from a low-energy (temperature) regime (Nozières 1974). The degrees of freedom in the former are still the magnetic moments of the 4f/5f shells and the conduction electrons, both with moderate renormalizations, and the dynamics can be derived via low-order perturbative corrections due to their mutual interactions. At excitation energies $\omega, k_B T < k_B T^*$, however, magnetic moments and conduction electrons appear as strongly coupled objects, itinerant though with highly increased mass and magnetic though only as objects obeying Fermi statistics, i.e., Pauli paramagnetic.

(ii) $k_B T^*$ plays the role of an internal binding energy for these new degrees of freedom, known as heavy fermions. It is, e.g., the energy needed to strip off the spin compensation cloud from the local moments, and as such is often addressed as a singlet–triplet excitation energy (Brandow 1988). Seen from the point of view of quasiparticle band structure theory it gives the energy spread of that part of the band structure near E_F, in which the dispersion is anomalously reduced by correlation effects, i.e., the quasiparticle-band width. An excitation of a quasiparticle beyond this range liberates it from the strong scattering off the local moments and from its participation in the spin-compensation clouds. It thus leaves essentially a low-mass band electron.

(iii) T^* also sets the scale for the magnitude of quasiparticle interactions at small energy transfer (Lee 1985, Grewe and Pruschke 1985, Zhang et al. 1987, Grewe 1987, Keller et al. 1989). This interaction strength reflects the local susceptibility, i.e., $\chi^{-1} \sim T^*$, of an f-moment bound to a spin-compensation cloud that retains a considerable magnetic polarizability. In simple terms, the corresponding local interaction mechanism can be described as follows: an external quasiparticle, placed on a lattice site, induces a magnetic moment on the local f-shell via the indirect exchange coupling mediated by the hybridization. In view of the spin-compensation cloud this may be regarded as an induced polarization of the composite object. A second quasiparticle then experiences a net exchange field on this site. Due to its local nature this direct quasiparticle interaction vanishes (in leading order) for equal spins as a consequence of the Pauli principle and is repulsive for opposite spins since then the second quasiparticle is subject to an exchange field of unfavourable direction (Lee 1985, Grewe 1987). As a consequence of this direct local interaction, indirect non-local quasiparticle interactions arise which may be the source of collective effects like magnetism and, possibly, superconductivity (Zhang et al. 1987, Grewe et al. 1988). The effective interactions are in general not connected to the single scale $k_B T^*$; they may introduce additional energy scales characteristic of collective effects.

(iv) T^* to a certain extent also marks the transition from single-ion to coherent-state behaviour (Lavagna et al. 1982a, Grewe 1984a, Brandow 1988,

Grewe et al. 1988). This is inevitable for a concentrated system since the compensation clouds extend over several lattice spacings and have to be superimposed constructively, in order to keep the admixture of states far from the Fermi level into the many-body ground state small (Nozières 1987). For the same reason this ground state should not be seen as a mere collection of local moments, each with its individual spin compensation cloud. The adjustment of single-particle states, enforced by the need for coherent spin compensation, introduces magnetic correlations between f-moments on different sites into the ground state. Singlet formation in the concentrated system is not a local process any more. It involves clusters of sites with characteristic diameter of the order of the lattice spacing divided by $(N_F k_B T^*)^{1/3}$, i.e., that of spin-compensation clouds. The temperature at which local elastic scattering becomes ineffective and the Fermi-liquid regime characterized, e.g., by a T^2-law for the resistivity is approached depends, however, on the detailed nature of the low-lying excitations, i.e., on the possible collective scales, as well. Therefore, a different kind of coherence temperature, called $T_{coh} < T^*$ in the foregoing section, in general is encountered in real lattice-periodic heavy-fermion systems.

In model calculations using, e.g., the LNCA technique in connection with the periodic Anderson model, T^* is most easily extracted from the width or the position of the ASR in the local one-particle spectral density (Kuramoto and Müller-Hartmann 1985, Bickers et al. 1987, Pruschke and Grewe 1989). It coincides with the Kondo temperature T_K for an f-impurity and acquires some modest corrections for the lattice case (Grewe et al. 1988). The aforementioned characterizations of T^* are, to a large degree, substantiated by such calculations, too. Collective effects in heavy-fermion systems pose a much harder problem for solid state theory, which has met only partial success until today.

$k_B T^*$ as the characteristic energy scale of heavy-fermion systems at low temperatures has been studied extensively with various experimental and theoretical methods. Neutron-scattering results have proven to be of particular importance. In fig. 19 the half width (HWHM), $\frac{1}{2}\Gamma(T)$, of the quasielastic magnetic neutron line is shown for a number of nearly trivalent Ce compounds. In contrast to the almost temperature-independent value of $\frac{1}{2}\Gamma(T)$ established for many IV systems (Loewenhaupt and Holland-Moritz 1979), a characteristic negative curvature is found for the trivalent counterparts. This T-dependence is also at variance with the Korringa behaviour, $\frac{1}{2}\Gamma(T) \sim T$, commonly observed for stable RE moment systems (cf. Fulde and Loewenhaupt 1985). In particular, a finite value for $\frac{1}{2}\Gamma$ is obtained as T approaches zero. The wavevector-independent contribution to $\frac{1}{2}\Gamma$ has been measured by neutron scattering down to ultralow temperatures for $CeAl_3$ (Murani et al. 1980), and $CeCu_6$ and $CeRu_2Si_2$ (Rossat-Mignod et al. 1988). It turns out as a good measure for the characteristic lattice Kondo temperature T^*, see table 1. Residual linewidths for other Ce compounds as extrapolated from $T > 2$ K are also listed in the table. Additional estimates for T^* are derived from different experimental information: T^c results from a comparison to the Bethe-ansatz specific-heat curve for an $S = \frac{1}{2}$ Kondo impurity (Andrei et al. 1983), the other two temperatures, T^ρ and T^s, from low-T maxima

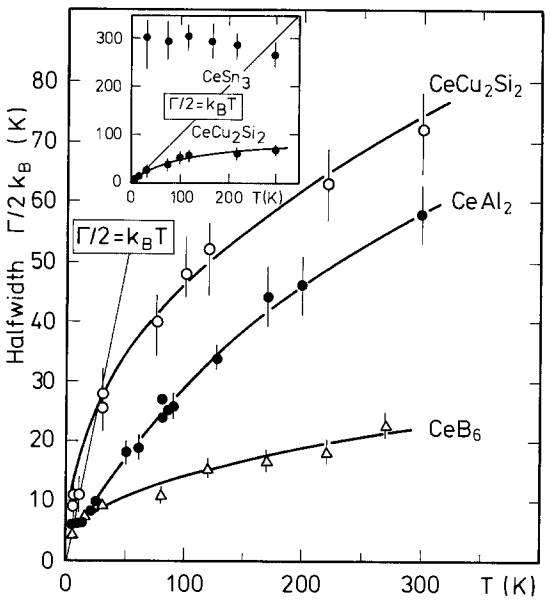

Fig. 19. Temperature dependence of the half width of the quasielastic magnetic neutron line for CeB_6, $CeAl_2$ and $CeCu_2Si_2$. Data of $CeCu_2Si_2$ are compared with the data of intermediate-valence $CeSn_3$ in the inset (Horn et al. 1981a). Thin straight line marks $\frac{1}{2}\Gamma(T) = k_B T$. The other lines are guides to the eye.

in the transport coefficients resistivity, $\rho(T)$, and thermopower, $S(T)$. Values of both the Sommerfeld coefficient and Pauli susceptibility included in table 1 give information about the quasiparticle DOS and roughly scale with the inverse of these temperatures.

In many heavy-fermion intermetallic compounds pronounced structures can even be found below the temperature scale T^*. These are connected with the onset of coherence and with cooperative phenomena in the heavy-electron liquid. In particular, magnetically ordered and superconducting phases will be discussed in separate sections (3 and 4, respectively). There exists a reciprocal relation between the carrier masses and the magnitude of the effective magnetic moments: the formation of the heavy-Fermi liquid exhausts the local magnetic degrees of freedom (Doniach 1977, Nozières 1985). On the other hand, conventional order among the local magnetic moments needs the band electrons as intervening particles and prevents them from forming a liquid (Rudermann and Kittel 1954, Kasuya 1956, Yosida 1957, Yosida and Watabe 1962, Goncalves da Silva and Falicov 1972). This competition between an RKKY phase and the magnetically compensated heavy-fermion phase is felt even at high temperatures. In many cases short-range antiferromagnetic correlations are frozen in at temperatures relatively high compared to T^* (see sect. 3).

In those cases where the magnetic moments are sufficiently quenched with decreasing temperature, the remaining residual interactions can be described as quasiparticle interactions in a heavy Fermi liquid (Grewe and Pruschke 1985, Auerbach and Levin 1986, Millis and Lee 1987, Zhang et al. 1987, Grewe et al. 1988, Höhn and Keller 1988). Thus, any magnetic ordering phenomenon well below T^* is to be understood as a collective effect in the coherent heavy-fermion bands. Here as well as in the heavy-fermion superconductors one can observe the

TABLE 1

Low-temperature single-site and lattice properties of some selected normal heavy-fermion compounds. Sommerfeld coefficient γ_0 (as $T \to 0$) and γ_{max} ($T = T^{\gamma}$), (intrinsic) Pauli susceptibility χ_0 (as $T \to 0$), characteristic temperature T^* as measured via T^{ρ} (position of $\rho(T)$ peak), T^{s} (position of $S(T)$ anomaly), T^{c} (derived from either $\gamma_0 = 0.68\ R/T^{c}$ or $T_{max} = 0.66\ T^{c}$, T_{max}: position of $C(T)$ peak (Andrei et al. 1983)) and $T^{n} = \Gamma/2k_B$ (as $T \to 0$), $\Gamma(T)$: quasielastic magnetic neutron line width (FWHM); /: not existing; n.d.: not determined; n.m.: evaluation not meaningful.

	γ_0	γ_{max}	χ_0	T^{ρ}	T^{s}	T^{c}	T^{n}	T^{γ}
System	(J/K^2 mol f-ion)		(10^{-9} m^3/mol f-ion)	(K)				
$CeCu_6$	1.6[a]	/	940[b]	10[c]	6d	4.2[d]	5[e]	/
$CeAl_3$	1.25[f]	1.6–1.83[f]	345[g]	35[h,*]	3.8[d]	3.8[g]	6[i]	0.32–0.47[f]
$CeCu_2Si_2$§	0.6[j,k]	0.8–1.25[j,k]	80[l,m]	20[n]	20[n]	9[o]	10[p]	0.35–0.42[j,k]
CePtSi	0.81[q]	0.84[q]	2390[q]	/	n.d.	6.7[q]	n.d.	0.5[q]
$CeRu_2Si_2$	0.35[d]	0.36[r]	200[s]	/	25[d]	16[d]	23[e]	2[r]
UBe_{13}	0.72–0.8[t,u]	/	190[t]	2.3[t]	<0.9[v]	7.1–7.9[t,u]	140[w,*]	/
UPt_3	0.425[x,y,z]	/	53(B‖c); 104(B⊥c)[α]	/	8[d,**]	80[β,†]	110[γ]	/
UAl_2	0.145[δ]	/	55[δ]	/	16[ε,**]	n.m.	280[φ]	/

[a]Satoh et al. (1988); [b]Ōnuki and Komatsubara (1987); [c]Ōnuki et al. (1984); [d]Steglich et al. (1985); [e]Rossat-Mignod et al. (1988); [f]Steglich (1985b); [g]de Boer et al. (1985); [h]Ott et al. (1985b); [i]Murani et al. (1980); [j]Bredl et al. (1984a); [k]Bredl (1985); [l]Lieke et al. (1982); [m]Steglich (1985a); [n]Franz et al. (1978); [o]Bredl et al. (1985); [p]Horn et al. (1981a); [q]Rebelsky et al. (1988); [r]Mayer (1986); [s]Thompson et al. (1985); [t]Ott et al. (1983); [u]Mayer et al. (1986a); [v]Gottwick et al. (1987); [w]Goldman et al. (1986); [x]Stewart et al. (1984a); [y]Franse et al. (1985); [z]Sulpice et al. (1986); [α]Frings et al. (1983); [β]Rietschel et al. (1988); [γ]Aeppli et al. (1988); [δ]Trainor et al. (1975); [ε]Armbrüster et al. (1979); [φ]Loewenhaupt et al. (1979).

§superconducting (poly- and single-crystalline) samples only.

*Probably due to CF-effects.

**Probably indicating "coherence effects".

†From comparison with theoretical result by Desgranges and Rasul (1985).

onset of coherence in various quantities. In the coherent regime, resonant scattering is frozen out and quasiparticle interactions dominate, leading to the characteristic Fermi-liquid form, eq. (14), of the self-energy. The coefficients α and α' in eq. (14) scale with $(T^*)^{-2}$ (Grewe and Pruschke 1985, Auerbach and Levin 1986, Cox and Grewe 1988) so that the scattering becomes small only at $T \ll T^*$. Thus, although in the most simple situation no additional energy scale T_{coh} enters, it is only in this regime that pronounced coherence effects are observed. In several compounds, e.g., the Sommerfeld coefficient $\gamma(T) = C(T)/T$ exhibits a maximum well below 1 K (cf. fig. 11). The decrease of $\gamma(T)$ for $T \to 0$ has been ascribed to the formation of a pseudogap in the quasiparticle density of states, which indicates coherence (Bredl et al. 1984a). The maximum value, γ_{max}, together with its position, T^{γ}, as observed for several compounds, is also listed in table 1. As has been mentioned above, the resistivity approaches its residual value via a T^2 law, which is much smaller than the unitarity limit, the latter setting the scale for the maximum value around T^*, cf. fig. 8. Even more pronounced features at low temperatures are found in two other transport properties: sign changes often occur in the thermopower (fig. 20) and negative peaks in the Hall constant (fig. 21). A straightforward explanation would invoke band-like behaviour of the quasiparticles (Sparn et al. 1985). This picture is supported by a

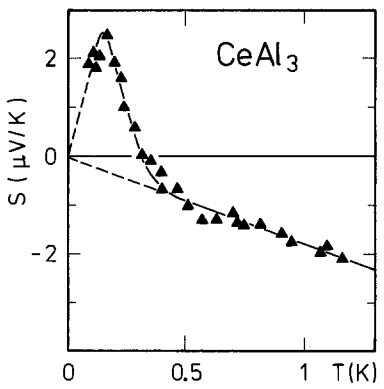

Fig. 20. Low-temperature thermopower as a function of temperature for $CeAl_3$ (Steglich et al. 1984). Solid line is guide to the eye. Dashed lines are extrapolations to $T = 0$.

sign change in the magnetoresistance, the latter being negative at elevated temperatures ($T > T^*$) as characteristic of local moments, but becomes positive for $T \to 0$ as expected for band electrons after the onset of coherence (Edelstein et al. 1977, Remenyi et al. 1983), see fig. 22. Further empirical features signalling the completion of the coherent low-temperature state have been reported for $T < T_{coh} \approx 0.2$ K in $CeCu_6$, e.g., a Korringa law in the spin–lattice relaxation rate (Onuki and Komatsubara 1987).

The preceding discussion of energy scales was based on a conceptually simple isotropic situation, essentially in order to point out the hierarchial structure of different physical phenomena. It is able to explain qualitatively a number of experimental findings. The necessary precautions may be characterized via the magnetic field dependence of the γ-coefficient as an example. For CeB_6, γ for not too small magnetic fields of $B > 1.5$ T (for lower fields CeB_6 is antiferromagnetically ordered) smoothly decreases with increasing B (fig. 23), and the corresponding characteristic scale B^* of a few tesla agrees well with the magnitude of the "Kondo field" $B_k = (k_B/g\mu_B)T^*$ [$T^* \simeq 3$ K, Horn et al. (1981b)]. One has to realize, however, that the strong anisotropy found in heavy-fermion systems may preclude such clear distinctions in most realistic cases. We would like to exemplify this fact via the magnetic field dependence of the linear specific-heat coefficient for $CeCu_6$ using fig. 24. In its orthorhombic low-T phase $CeCu_6$ exhibits strong anisotropies in most of its electronic properties (Amato et al. 1987b). A magnetic field parallel to the c-axis strongly reduces the heavy masses. The scale of this initial decrease of about 5 T compares well with $T^* \simeq 4$ K for the lattice Kondo temperature. The decrease, however, is reduced at higher fields and leaves a value of about 200 mJ K^{-2} mol^{-1} at $B = 23$ T (Stewart 1989). This insensitivity of $\gamma(B)$ at high fields and the insensitivity of the $\gamma(T)$ curve for B applied in the basal (a, b) plane up to 7.5 T seemingly lack any manifestation of the scale T^*. In this connection one may cite two typical speculations about the role of anisotropies and the features of a realistic material:

(i) A destruction of the Kondo-compensation mechanism by an applied field may induce anisotropic magnetic correlations and may increase the γ-value.

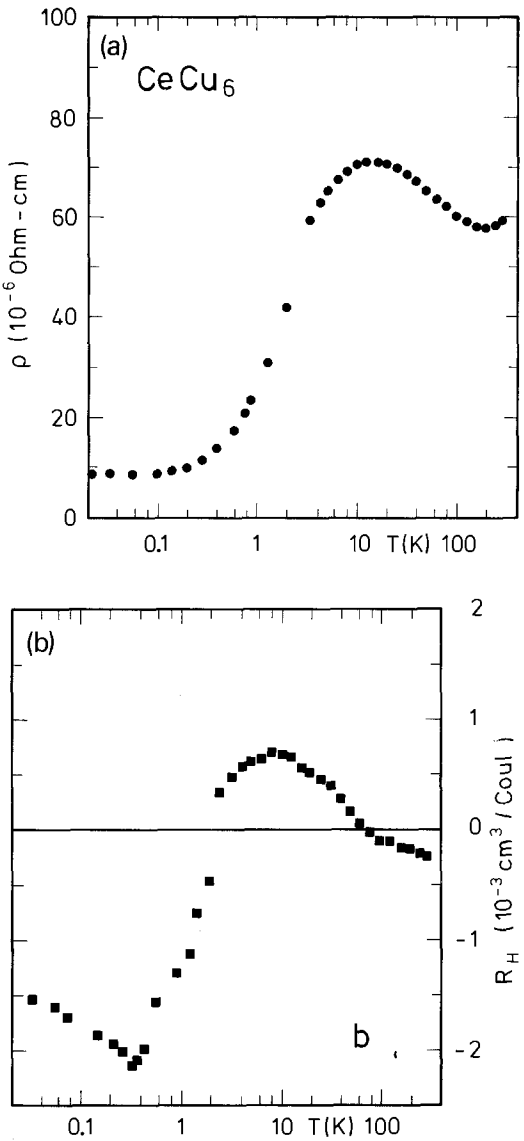

Fig. 21. Temperature dependences on logarithmic scales of (a) resistivity and (b) Hall constant for single crystalline $CeCu_6$ with current in the orthorhombic *b*-direction and field applied parallel to the *c*-direction (Milliken et al. 1988).

(ii) For a renormalized Fermi surface with strongly anisotropic effective masses the response to an applied field in particular directions mainly involves light carriers and does not affect the anisotropic moment compensation and the large γ-value.

Altogether the competition between moment compensation and magnetic correlations for a highly anisotropic material could well lead to strong directional dependences of the characteristic energy scales.

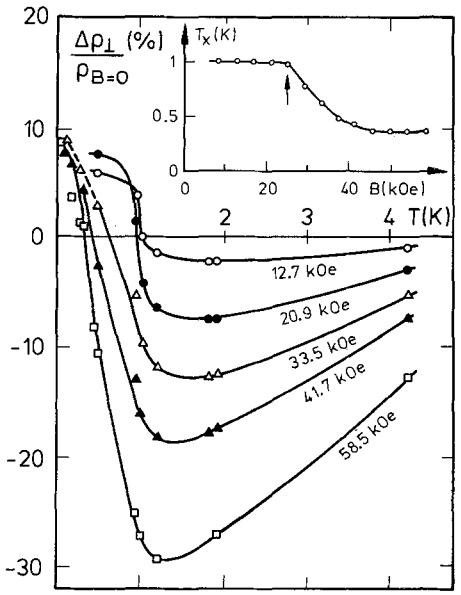

Fig. 22. Relative transverse magnetoresistivity $\Delta\tilde{\rho}(B) \equiv \Delta\rho_{\perp}/\rho_{B=0} = (\rho_{B\perp} - \rho_{B=0})/\rho_{B=0}$ as a function of temperature. Inset: temperature T_x, at which $\Delta\rho_{\perp}(T)$ changes sign, as a function of magnetic field B (Remenyi et al. 1983). Lines through data points are guides to the eye.

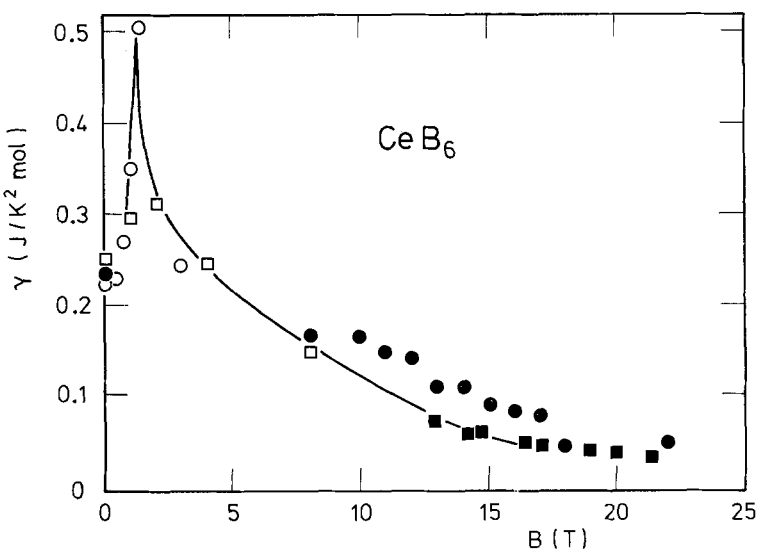

Fig. 23. Magnetic-field dependence of the enhanced linear specific-heat coefficient γ. Open circles were taken from Marcenat (1986) and squares from Bredl (1987). The peak in γ near 2 T is related to the phase transition from the paramagnetic (i.e., antiferroquadrupolar) to the modulated antiferromagnetic phase. The line is a guide to the eye. Filled squares result from de Haas–van Alphen measurements (Joss et al. 1978). The points were calculated from the measured cyclotron masses on the assumption that the mass enhancement going from LaB_6 to CeB_6 is roughly isotropic over the Fermi surface and scaling the mass $m^* = 0.61$ for LaB_6 as $\gamma = m^*\gamma_{La}/m^*_{La}$ to CeB_6 (Müller et al. 1988).

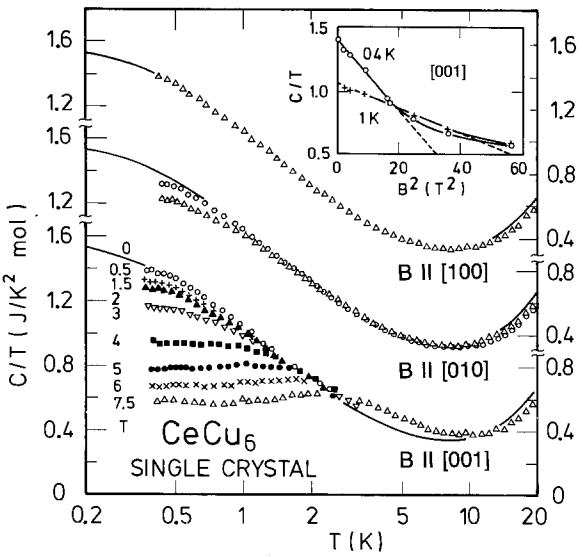

Fig. 24. Field dependence of $C(B)/T$ for $CeCu_6$, with B applied along [100], [010] and [001] axes. Solid lines indicate the $B = 0$ results. Inset shows variation of $C(B)/T$ with B^2 at constant T (Amato et al. 1987b).

2.4. *Transport phenomena*

Among transport coefficients the resistivity most clearly reflects the basic physics of heavy-fermion compounds. For a discussion we refer to the experimental results (Assmus et al. 1984) on two $CeCu_2Si_2$ single crystals (fig. 25) which had been subject to different heat treatments. The significant differences introduced by disorder are a drastically higher residual resistivity and a more pronounced maximum near $T = 20\,\mathrm{K}$, which agrees with the characteristic temperature T^* to within a factor of two. Similar differences are observed if $CeCu_2Si_2$ is doped in a controlled way by either La or Y (Steglich et al. 1987b). These experiments demonstrate, in particular, the sensitivity of the low-temperature resistivity against disturbances of the coherent state at the Ce sites. The corresponding changes can apparently be of the same order of magnitude as the increment in resistivity due to scattering from single Kondo impurities. Regarding the coherence in the low-temperature state of the Kondo lattice, this effect caused by the absence of 4f-scatterers on Ce sites has been labelled "Kondo-hole" scattering (Lawrence et al. 1985, Pethick and Pines 1986, Hirschfeld et al. 1986, Schmitt-Rink et al. 1987, Miyake 1987). The picture implied rests upon the following observation (Cox and Grewe 1988): the imaginary part of the self-energy

$$\mathrm{Im}\,\Sigma(z) \sim \mathrm{Im}\,\Sigma_\alpha^{\mathrm{eff}} - \Delta$$

of band electrons in a Kondo lattice near the Fermi energy $z = \epsilon - i\eta$, $\epsilon \approx E_F$ is sensitive to lattice imperfections at low temperatures, because of a cancellation which guarantees the proper Fermi-liquid behaviour $\mathrm{Im}\,\Sigma(z) \to 0$ $(\epsilon \to \epsilon_f)$ in the fully periodic system. The constant part $-\Delta$ serves to eliminate an equally large contribution in $\mathrm{Im}\,\Sigma_\alpha^{\mathrm{eff}}$ that is due to resonant scattering and leads to the ASR of

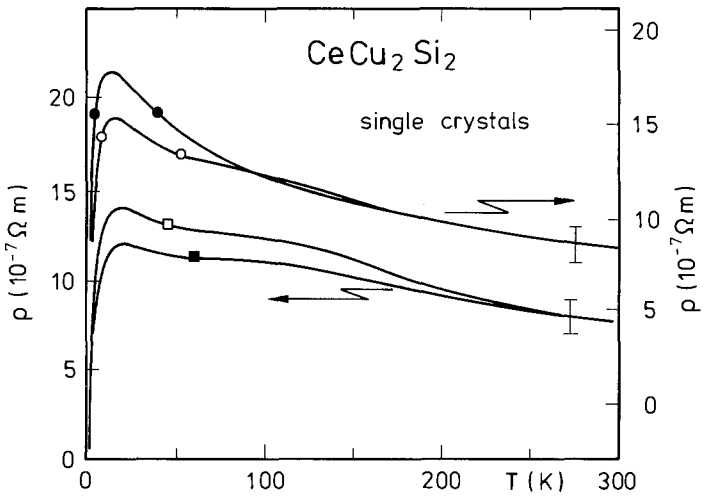

Fig. 25. Temperature dependence of the electrical resistivity for two $CeCu_2Si_2$ single crystals, one mesured unannealed (●, ○) and the other one after annealing (4 days, 1000°C: ■, □). Residual resistivities ρ_0 in μΩ cm: 53 (●), 51 (○) and 4.5 (□). Closed (open) symbols: current parallel (perpendicular) to tetragonal c-axis (Assmus et al. 1984).

the impurity problem. It is, according to eqs. (10) and (11), due to propagation through the periodic lattice and is efficiently reduced by any inhomogeneity in the coherent pattern of scattering. As a result of a fractional Ce-deficiency x, a Nordheim relation for the residual resistivity arises, e.g., $\Delta\rho \sim x(1-x)$, which for small x has a coefficient as large as that observed for the Ce impurities, i.e., $x \lesssim 1$, due to the Kondo effect in a reference system.

The drastic differences between La and Y doping in $CeCu_2Si_2$, which have been observed near the resistivity maximum (Steglich et al. 1987b), may have to be attributed to the different electronic structures of these impurities: whereas both La and Y likewise do not contribute 4f-conduction band mixing, Y with 4d-valence states in addition causes drastic changes in the anisotropic local band structure based upon 5d-states. We would like to propose that the effect is not due to ordinary additional impurity-potential scattering, but rather that the resonant scattering off the Kondo-hole is altered by the change in anisotropy (Ahlheim et al. 1988a).

Above the low-temperature region, two maxima are recognized in $\rho(T)$. The first one can be attributed to the transition from coherent to incoherent scattering off the Ce sites (cf. sect. 2.2), whereas the second one reflects the excited CF states of Ce^{3+} ($J = \frac{5}{2}$) with a total splitting of 360 K (Horn et al. 1981a). The latter effect may be understood in the following way (Cornut and Coqblin 1972, Kashiba et al. 1986). Coming from high temperatures, a logarithmic increase of the resistivity corresponding to the fully degenerate lowest spin–orbit level is found. In the vicinity of the CF-splitting energy, transitions from the CF ground state into excited CF levels gradually become frozen out. They continue, via

virtual processes, to renormalize the coupling constant and the band structure (Yamada et al. 1984, Hanzawa et al. 1985), but at lowest temperatures the results essentially correspond to Kondo scattering from the lowest CF doublet only. This has reduced degeneracy leading to a reduced logarithmic slope compared to the behaviour at high temperatures (Tsvelik and Wiegmann 1983).

The thermoelectric power, $S(T)$, furnishes very useful additional information about the nature of heavy-fermion systems (Brandt and Moshchalkov 1984), since it is proportional to a higher transport integral, i.e., an energy-weighted average over the scattering rate, see eq. (12). For a typical system like $CeCu_2Si_2$ this reveals (Franz et al. 1978) an even more detailed structure than the resistivity according to figs. 20 and 26. The most remarkable facts, in addition to a CF-derived positive peak at elevated temperatures, are the two pronounced extrema in the low-temperature region: a positive maximum (Steglich et al. 1984) at about 0.2 K, which is well below $T^* \approx 10$ K, followed by a change of sign and a minimum near 20 K. Quite similar results, i.e., a positive maximum at $T \ll T^*$ and an extremum in a range near T^* are obtained for, e.g., paramagnetic $CeAl_3$ (Steglich et al. 1984, Jaccard and Flouquet 1985), and antiferromagnetic $CePb_3$ (Gottwick et al. 1987) as well as $CeCu_6$ and $CeRu_2Si_2$ (Steglich et al. 1985). In the last two systems a third positive maximum is observed instead of the negative minimum. Due to the enhanced scattering above the Fermi energy in the vicinity of the ASR, existing calculations (Sparn et al. 1985, Kawakami and Okiji 1987, Cox and Grewe 1988) for simple models furnish positive-definite thermoelectric powers increasing from $S = 0$ at $T = 0$ to a peak at about T^*. Coherence only modifies the low-temperature increase somewhat (Cox and Grewe 1988). For an explanation of the second extremum near T^*, band-structure effects have been invoked, such as excitations involving the bare f-states considerably below E_F and the energy dependence of, as well as the anisotropy in, the hybridization matrix elements (Keiter and Kurkijärvi 1977, Cox and Grewe 1988). One could also think of interaction effects, i.e., finite-U or f-hole screening (the calculations cited are for the $U = \infty$) and of CF excitations (Kawakami and Okiji 1987), the latter certainly being responsible for the high-temperature structure of the thermopower. Theoretical calculations for transport coefficients, based on a perturba-

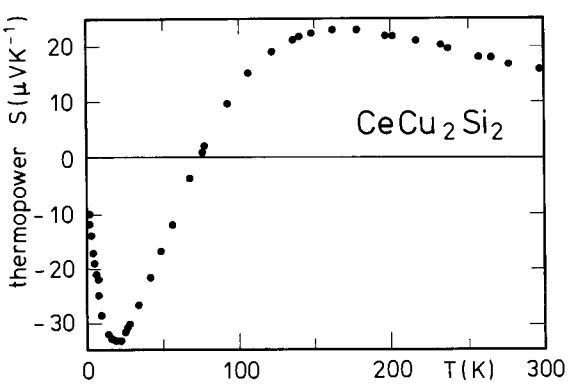

Fig. 26. Temperature dependence of thermopower, S against T, for $CeCu_2Si_2$ for $T > 1.5$ K (Franz et al. 1978). Low-T (<1 K) data in the normal state (not shown) exhibit an additional anomaly similar to that in fig. 20 (Steglich et al. 1984).

tional treatment of the six-fold degenerate Anderson model with $U = \infty$, are presented in fig. 27. They show the different influence of coherence on resistivity, thermopower and Lorenz number (Cox and Grewe 1988).

Magnetic-field effects in the transport coefficients are of particular interest because of the magnetic character of the f-scattering. Due to the enhanced local susceptibility, the Hall effect and the magnetoresistance can be of anomalous size. Figure 21 shows the Hall coefficient $R_H(T)$ of $CeCu_6$ in comparison with the resistivity $\rho(T)$ (Milliken et al. 1988). Two main features are intriguing besides the larger size of R_H:

(i) $R_H(T)$ peaks near the characteristic temperature as does $\rho(T)$, thereby presumably separating an incoherent scattering regime at high T from a Fermi-liquid regime for $T \to 0$.

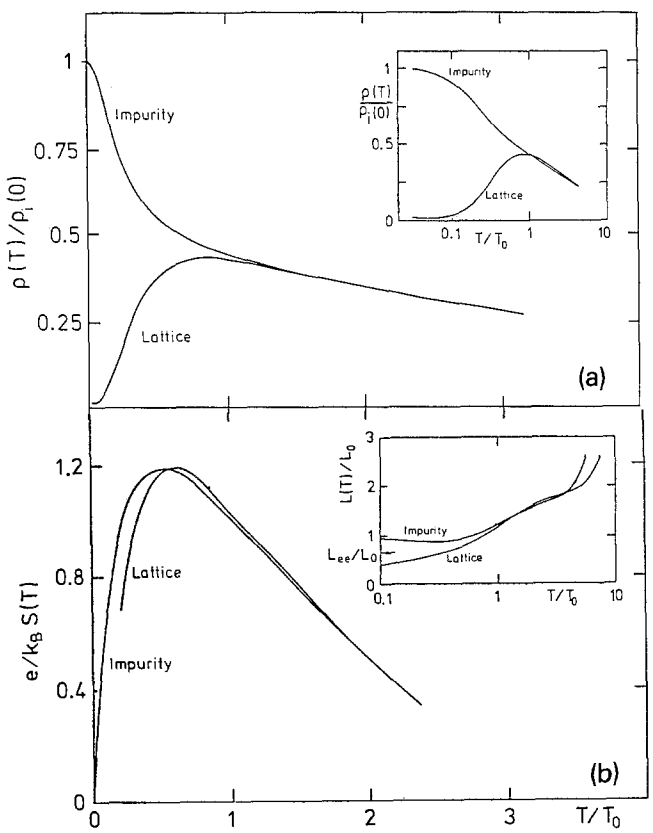

Fig. 27. Resistivity $\rho(T)$ (a), thermoelectric power $S(T)$ and Lorenz number $L(T)$ (b), calculated with LNCA techniques for a sixfold degenerate Anderson lattice model in the Kondo regime (Cox and Grewe 1988). Impurity results, scaled with concentration are shown for comparison. The resistivity results exhibit the logarithmic increase with decreasing temperature and the coherence-derived decrease below $T^* \equiv T_0$ to the residual value due to impurities, which is quadratic in the Fermi liquid regime $T \ll T^*$. $S(T)$ is positive definite for the simple model situation chosen.

(ii) Two changes of sign and an additional peak near 0.3 K indicate a more complex structure of the Hall coefficient.

The coherence effect is well substantiated by La doping (Onuki and Komatsubara 1987). Whereas the sign and the particular temperature dependence of R_H at low temperatures is strongly sensitive to the material, the large maximum near T^* and the positive sign for $T \geqslant T^*$ appear to be a universal feature for both Ce- and U-based compounds (Fert and Levy 1987).

Theoretical explanations for the complex behaviour of $R_H(T)$ have been proposed on the basis of impurity models and, thus, may be applied to the region $T > T^*$ only (Lorek (1990) has made a first step towards a lattice theory). They are based on a linear approximation with respect to the magnetic field and invoke an interference between $l = 2$ and $l = 3$ scattering channels. The well-established skew-scattering mechanism (Fert and Jaoul 1972, Fert 1973, Ballentine and Hubermann 1977) incorporates changes of the z-component of the angular momentum by one unit during the scattering event via the action of the magnetic field. It typically involves the interference between f- and d-channels through a term proportional to $\sin(2\delta_3 - \delta_2)$ in the expression for R_H. A large prefactor reflects the drastic changes in the DOS caused by a splitting of the ASR in the magnetic field (Coleman et al. 1985, Fert and Levy 1987, Levy et al. 1988).

It has been pointed out (Levy 1988) that the effect linear in B also includes extraordinary contributions to the current operator. These can arise via strongly anisotropic mixing matrix elements and via spin–orbit coupling. An analogous possibility has been mentioned above in connection with structure in the thermopower $S(T)$. In the final result for $R_H(T)$, the extraordinary contributions also show up via an interference of the $l = 2$ and $l = 3$ channels, but with different combinations of the two phase shifts, e.g., $\cos(\alpha\delta_3 - \delta_2)$ with $\alpha = 1$, 2 and 3 (Levy 1988). The strong dependence of the f-channel phase shift on temperature and degeneracy of the lowest spin–orbit multiplet can in principle account for much of the rich structure of $R_H(T)$.

The change in resistivity parallel or perpendicular to an applied magnetic field

$$[\rho(B) - \rho(0)]/\rho(0) = \Delta\tilde{\rho}(B)\,,$$

commonly known as the magnetoresistivity, establishes another sensitive probe for the electronic structure of heavy-fermion systems. The reason lies in the fact that the magnetic field affects the fine details of the DOS near E_F. In general, the resistivity of a Kondo impurity decreases monotonically in a magnetic field (Okiji and Kawakami 1982, Horvatić and Zlatić 1984, Hanzawa et al. 1987, Schlottmann 1987). A good example is shown in fig. 28a. $\Delta\tilde{\rho}(B) + 1$ for Ce^{3+} impurities in LaB_6 (Samwer and Winzer 1976) approaches zero rapidly when the Kondo magnetic field B_K is exceeded. In a field of this magnitude, scattering of conduction electrons is suppressed: the lowest Zeeman level of the impurity f-shell is being populated much stronger than the others, and the density of low-energy excitations between the different spin channels decreases. This is borne out by the NCA calculations shown in fig. 28b–d, implying not only a

splitting of the ASR but also an essential reduction of its height, with B increasing beyond B_K. The occupation numbers shown in fig. 28b agree well with those derived from the Bethe-ansatz [Schlottmann (1985b); see also Cox (1987a)], and in addition a slow logarithmic saturation of the majority occupation is recovered (Cox 1987a), as opposed to the exponential saturation of a free ion.

Even for a concentrated system like UBe_{13} this picture seems qualitatively appropriate as apparent from the Bethe-ansatz fit in fig. 29a. For a compound, $\Delta\tilde{\rho}$ is also defined as above; all resistivities appearing, however, are corrected by the ordinary residual value $\rho_0 = \rho(B = 0, T = 0)$, i.e., $\rho \to \rho - \rho_0$ (Steglich et al. 1987c, Rauchschwalbe 1987). For $T > T^* \simeq 8\,\mathrm{K}$ (Felten et al. 1986), the results can well be described by the universal curve

$$\Delta\tilde{\rho} = \Delta\rho(T/T^*, B/B^*)$$

of the impurity model where $B^* = (\mu/k_B)T^*$ and μ is the saturation moment of U^{3+} in the CF doublet ground state. For a fixed temperature T, the functional dependence on magnetic field is correspondingly

$$\Delta\tilde{\rho} = \Delta\tilde{\rho}\left(\frac{B}{B^*(1 + T/T^*)}\right).$$

With the denominator $B_{\mathrm{eff}} = B^*(1 + T/T^*)$ treated as a fit parameter, the experimental data of fig. 29a are well described. The curve of B_{eff} plotted against T thus obtained, however, goes to zero with decreasing T at about 0.2 K (fig. 29b). This can be taken as a signature of coherence in the following way: the decrease of the temperature-dependent resistivity of a Kondo lattice below T^* that results from the decrease of elastic scattering can formally be described via a curve

$$\Delta\tilde{\rho} = \Delta\tilde{\rho}\left(\frac{T}{T^*(T)}\right)$$

with $T^*(T)$ going to zero with T. Using this $T^*(T)$, B^* and B_{eff} also decrease with T, which is consistent with the results shown. There are no data at small B_{eff} due to the superconducting transition. Extrapolation hints at the existence of a region of positive magnetoresistivity at low temperature, cf. also Rauchschwalbe et al. (1986), and thus to an even more fundamental difference between dilute and lattice-periodic Kondo systems than would be apparent from the assumption of this temperature-dependent T^* only. Existing theoretical investigations (Ohkawa 1986, Kawakami and Okiji 1986) are not able to explain this detailed behaviour, although at higher temperatures qualitative agreement is obtained. In particular, the negative maximum of $\Delta\tilde{\rho}(T)$ seems to be another good empirical measure of the lattice Kondo temperature T^*. The continuation to a positive magnetoresistivity at the lowest temperatures is consistent with a temperature-induced increase of the magnetoresistance in a lattice-periodic Fermi-liquid. It is well known (see, e.g., Kittel 1963) that the carriers are forced onto closed or open orbits in transverse directions, which increases the resistivity as long as scattering is small. We take this behaviour as further evidence for the formation of a coherent Fermi-liquid state in these systems at the lowest temperatures.

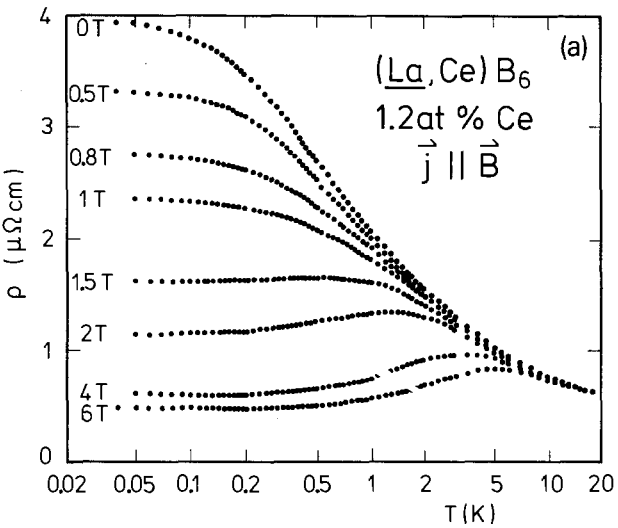

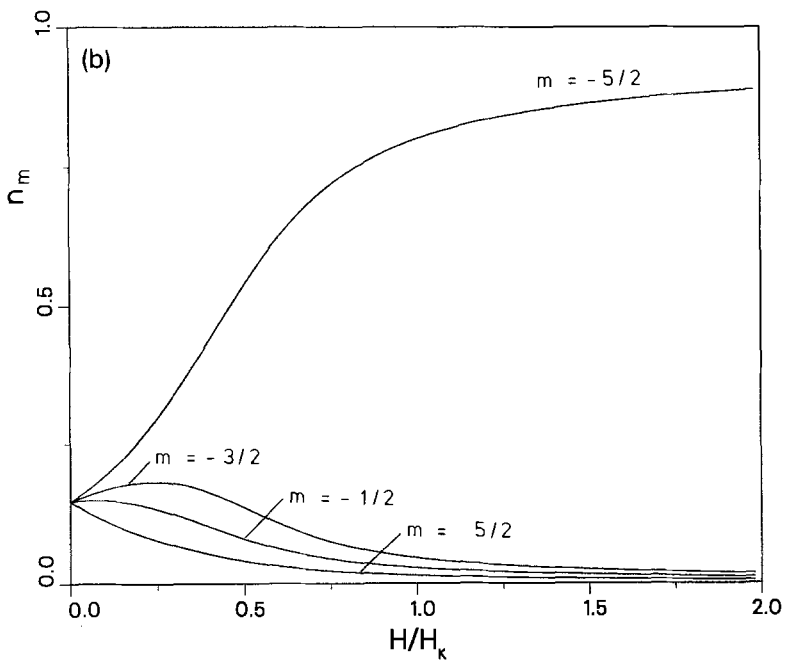

Fig. 28. Magntoresistivity of independent Kondo ions. (a) Experimental data of total resistivity, ρ, as a function of T (on a logarithmic scale) for LaB_6 doped with 1.2 at.% Ce (Samwer and Winzer 1976). (b) Ground-state occupancy of Zeeman-split local levels, calculated with the NCA for a sixfold degenerate Anderson model with $U = \infty$. Parameter values are $\epsilon_1(B=0) = -7.5\Delta$, $k_B T_K = 0.15\Delta$, $T = 0.1\ T_K$. The Kondo field is defined via $g\mu_B H_K = k_B T_K$. (c) Spectrum of majority-spin electrons ($m = -\frac{5}{2}$) for different magnetic fields. Temperature is $T = 0.33\ T_K$, other parameter values as in (b). (d) Spectrum of electrons in the second lowest Zeeman level $m = -\frac{3}{2}$, parameter values as in (c).

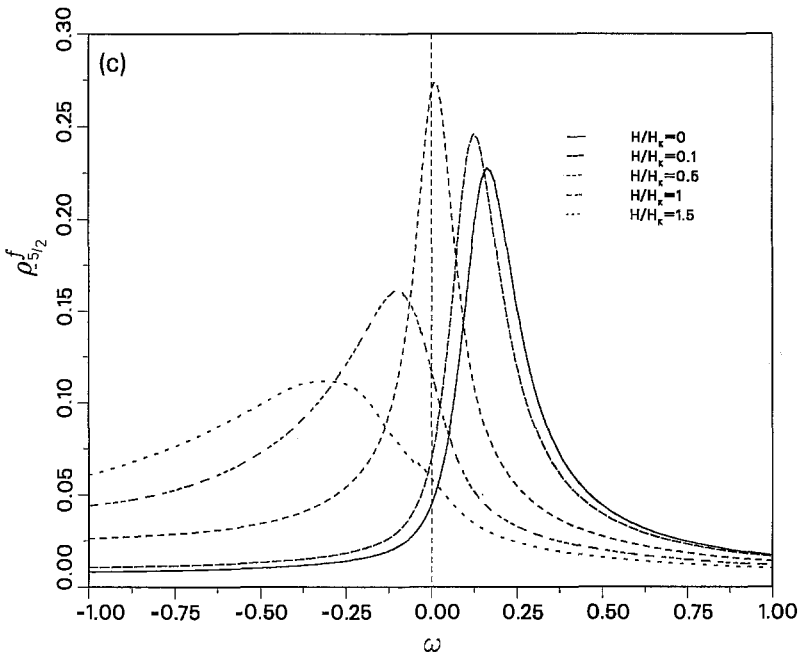
(c)
$\rho^f_{5/2}$
ω
H/H$_K$=0
H/H$_K$=0.1
H/H$_K$=0.5
H/H$_K$=1
H/H$_K$=1.5
0.00
0.05
0.10
0.15
0.20
0.25
0.30
-1.00
-0.75
-0.50
-0.25
0.00
0.25
0.50
0.75
1.00

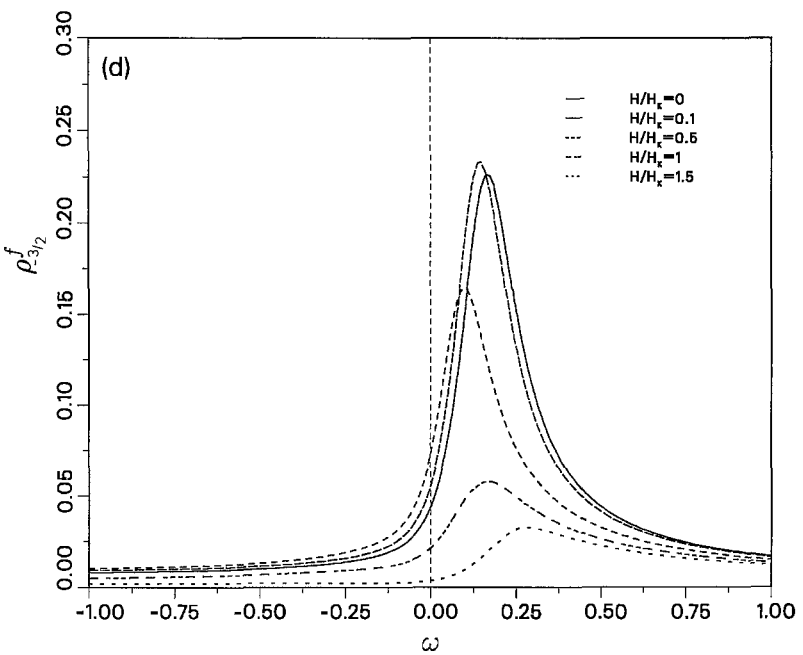
(d)
$\rho^f_{3/2}$
ω
H/H$_K$=0
H/H$_K$=0.1
H/H$_K$=0.5
H/H$_K$=1
H/H$_K$=1.5
0.00
0.05
0.10
0.15
0.20
0.25
0.30
-1.00
-0.75
-0.50
-0.25
0.00
0.25
0.50
0.75
1.00

Fig. 28. (cont'd)

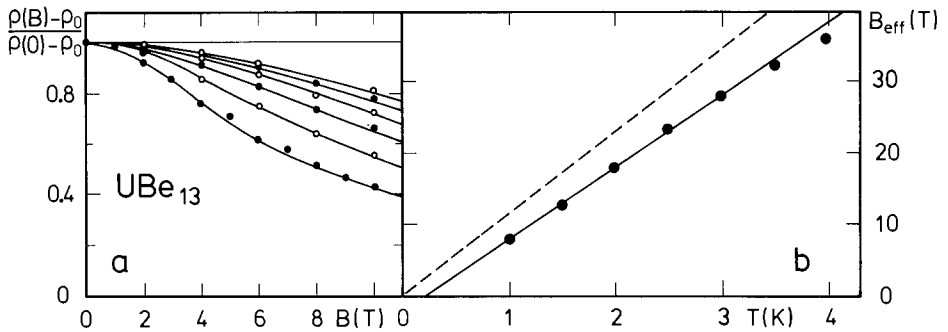

Fig. 29. Magnetoresistivity of UBe_{13}. (a) Fit of Bethe-ansatz results by Schlottmann (1983) to $\Delta\rho$ against B curves for differing temperatures (top–bottom): 4.0 K, 3.5 K, 3.0 K, 2.5 K, 2.0 K, 1.5 K (Steglich et al. 1987c, Rauchschwalbe 1987). (b) Effective magnetic field $B_{\text{eff}} = (k_B/\mu)T^*(1 + T/T^*)$ as a function of temperature (Steglich et al. 1987c, Rauchschwalbe 1987). Dashed line gives result by Batlogg et al. (1987) as obtained from $\Delta\tilde{\rho}(T, B)$, see text.

This interpretation of the magnetoresistivity data of UBe_{13} is in accord with measurements on $CeCu_6$ (Onuki and Komatsubara 1987) and $CeAl_3$ (see fig. 22, Remenyi et al. 1983). With the application of pressure to $CeCu_6$ the negative maximum of $\Delta\tilde{\rho}(T)$ shifts to higher values of T, see fig. 30, as does the characteristic temperature T^*. At the same time the crossing temperature T_x, at which $\Delta\tilde{\rho}(T)$ becomes positive at low B, and B_x, at which the decrease of T_x sets in (see inset), both increase indicating a more band-like behaviour.

Measuring in the low-temperature regime (tens of millikelvins) where, most of the scattering is frozen out by coherence, and using high-purity single crystals, a few groups succeeded in resolving de Haas–van Alphen (dHvA) oscillations in UPt_3 (Taillefer et al. 1987, Taillefer and Lonzarich 1988, Lonzarich 1988), $CeCu_6$ (Reinders et al. 1986, Springford and Reinders 1988), $CeRu_2Si_2$ (Lonzarich 1988), $CeAl_2$ (Lonzarich 1988, Springford and Reinders 1988, Reinders and Springford 1989) and most recently, $CeCu_2Si_2$ (Hunt et al. 1990), CeB_6 (Joss et al. 1987; Müller et al. 1988, Springford and Reinders 1988, Wasserman et al. 1989, Onuki et al. 1989). According to the standard result for the oscillatory variation of the magnetization (Lifshitz and Kosevich 1956, Stamp 1987, Rasul 1989),

$$\Delta M = \frac{T}{\sqrt{B}} \exp\left(\frac{-\pi}{\omega_c \tau}\right) \sin\left(\frac{\pi k_F l}{\omega_c \tau}\right) \left[\sinh\left(\frac{2\pi^2 k_B T}{\hbar \omega_c}\right)\right]^{-1}, \tag{15}$$

the signal is severely weakened by the heavy mass, $m^* = eB/\omega_c c$, in the denominator. The product $\omega_c \tau = eBl/c\hbar k_F$, on the other hand, does not contain the heavy mass. In order to obtain the necessary condition $\omega_c \tau \gg 1$ for the observability of dHvA oscillations, a mean free path of order $l \geqslant 1000$ Å is required as usual. The particular difficulty in heavy-fermion systems is, however, that apart from a small prefactor the predominant inelastic scattering contribution due to electron–electron interactions has to be strongly reduced, in addition to a very low residual resistivity, in order to obtain such large values of l.

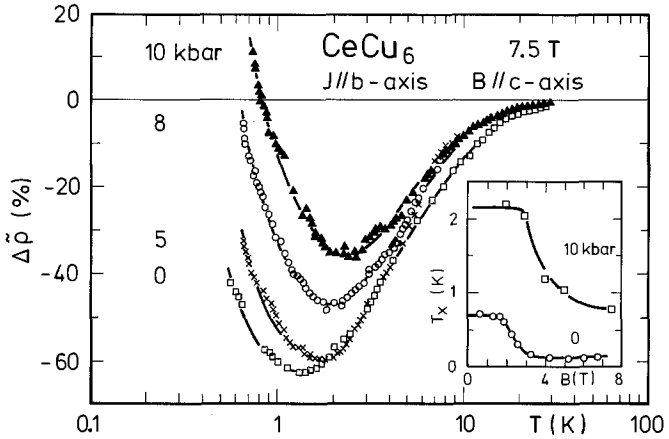

Fig. 30. Transverse magnetoresistivity $\Delta\tilde{\rho}$ against T (on logarithmic scale) for $CeCu_6$ at $B = 7.5$ T for different pressures. Inset shows magnetic-field dependence of T_x, the temperature at which $\Delta\tilde{\rho}$ changes sign, for $p = 0$ and 10 kbar, respectively (Onuki and Komatsubara 1987). Lines through data points are guides to the eye.

The analysis of dHvA amplitudes, as plotted in figs. 31 and 32, for both UPt_3 and $CeCu_6$ reveals detailed information. In particular the effective masses, as extracted from the slopes of the curves in figs. 31a and 32, are highly anisotropic and largely enhanced; the mean free paths, as read off from the inverse slopes of the curves in fig. 31b, are actually quite large, i.e., of order $l \geq 1000$ Å. From these data Fermi surfaces can be mapped out, see fig. 33. These results are remarkable at least in two respects:

(i) The detailed anisotropic Fermi surface agrees well with the band structure results by Oguchi et al. (1986). Consequently, the strong quasiparticle renormalization at low temperature already seems to be compatible with the crystalline symmetries as incorporated in the LDA formalism. This is not necessarily so in the renormalized band calculations where the low-energy dynamics are added via phase shifts with symmetry appropriate to the f-electron ground state. As has been pointed out recently (Zwicknagl 1988), interference of CF excitations on the energy scale $k_B T^*$ may change such results drastically. The latter formalism, however, accounts for the magnitude of the effective masses in a better way.

(ii) The masses actually measured are strongly enhanced, being much larger than the ones calculated within the LDA formalism (Sticht and Kübler 1985, Wang et al. 1987), but do not quite reach the high values extracted from thermodynamic measurements and expected from renormalized band theory. This latter discrepancy is particularly pronounced in $CeCu_6$, reaching a factor of six (Reinders et al. 1986). It can, to a large extent, be traced back to the strong magnetic-field dependence of the specific-heat-derived effective mass (see fig. 24). This reduction has been demonstrated by several groups, cf. Stewart et al. (1988) and Satoh et al. (1988). The mass enhancement found for $CeCu_6$ is well described

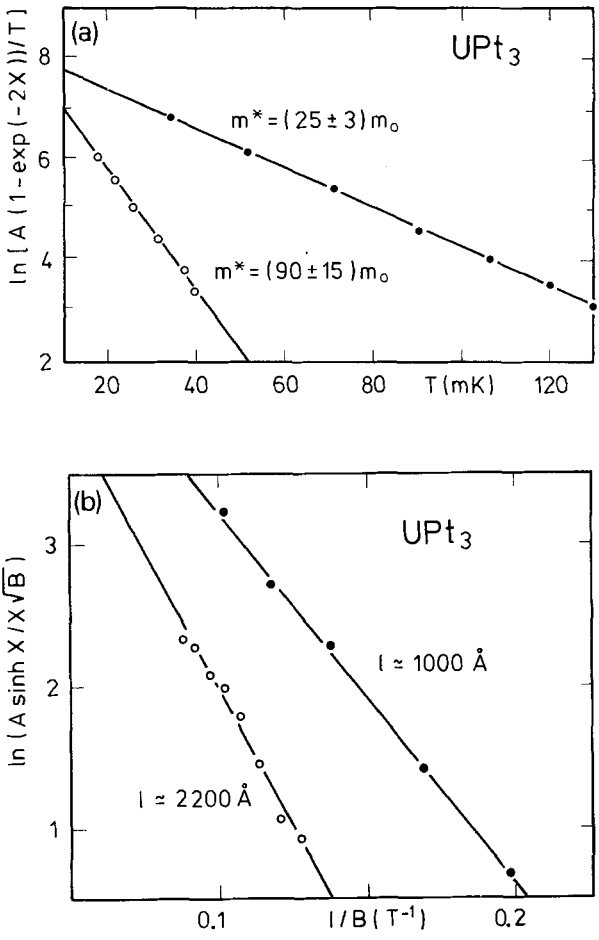

Fig. 31. de Haas–van Alphen amplitude for two oscillatory components of the magnetization of UPt_3 as (a) a function of temperature and (b) inverse magnetic field. The components with the lowest (4.8 MG) and highest (59.5 MG) frequencies are chosen (Taillefer et al. 1987). X is the argument of the sinh in eq. (15). The low-T slope of the curves is proportional to (a) m^* and (b) l.

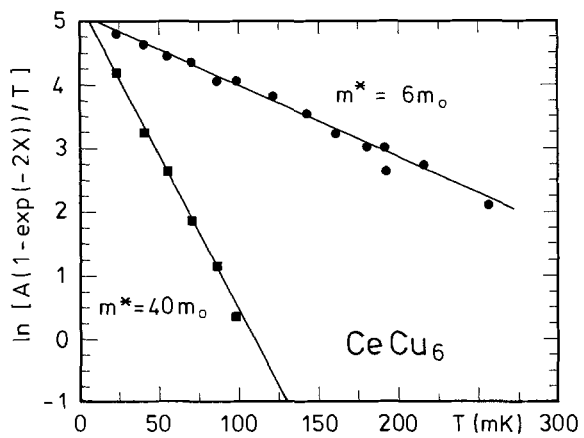

Fig. 32. de Haas–van Alphen amplitude as a function of temperature for two oscillatory components of the magnetization of $CeCu_6$ in the same plot as in fig. 31a (Reinders et al. 1986).

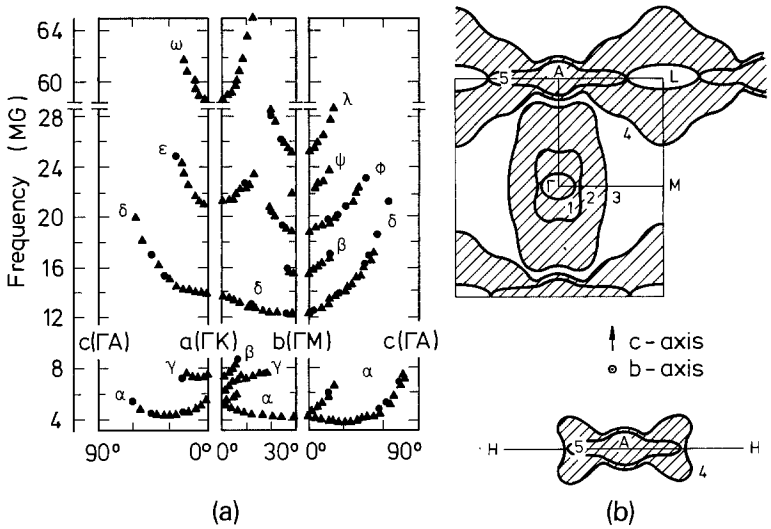

Fig. 33. (a) Dependence of de Haas–van Alphen frequencies on orientation of the external magnetic field in the crystallographic planes a–b, a–c and b–c for UPt_3 (Taillefer and Lonzarich 1988). (b) ΓALM section through the Fermi surface of UPt_3 as derived from an LDA calculation (Oguchi et al. 1986).

by a uniform coefficient for the whole Fermi surface in seeming contrast, however, to conclusions from specific-heat measurements (fig. 24).

2.5. *Elastic effects*

Electronic excitations involving 4f/5f-states can lead to interesting elastic anomalies as a consequence of strong coupling to lattice degrees of freedom. Even though these states are well localized, the f-electrons determine the ionic radius and the bonding to nearest-neighbour atoms in the crystal to a large extent. They influence the anisotropic potential felt by the outer valence electrons very strongly. These facts are well known in the field of IV physics (Grewe et al. 1980, Kuramoto and Müller-Hartmann 1981): real charge fluctuations on the f-shells can cause phase transitions with considerable volume changes (Falicov and Kimball 1969, Hirst 1974, Varma 1976, Grewe and Entel 1979) and anomalies in phonon dispersions and elastic constants (Güntherodt et al. 1978, Mook et al. 1978, Ghatak and Bennemann 1978, Grewe et al. 1978, Bilz et al. 1979, Entel et al. 1979). In compounds with stable 4f-shells magnetoelastic effects are observed and can be explained via directional reorientations of electronic states (Lüthi 1985). Between the two extremes, heavy-fermion compounds exhibit the full scale of these phenomena, though in weaker form: charge fluctuations are mainly virtual and the CF levels are less well defined. We do not want to give a broad discussion here (which is found in chapter 96 of this volume), but to point to some basic and characteristic features, which can shed some light on the nature of heavy fermions and their collective behaviour.

In the spirit of a unified picture for IV and heavy-fermion phenomena, which has been promoted above, we ascribe elastic anomalies in these systems to a dependence of basic electronic parameters, like the position of f-levels and their hybridization strength with band states, upon the location of neighbouring atoms in the crystal. An expansion of the form (Grewe et al. 1980)

$$V = V_0 + \sum_j g_j \Delta X_j , \quad \Delta X_j \sim b_{\lambda q} + b^{\dagger}_{\lambda -q} , \tag{16}$$

e.g., accounts for changes of the hybridization due to displacements ΔX_j of the neighbours, expressed via phonon operators $b_{\lambda q}$ and multiplied by directional coupling constants g_j. For a so-called "breathing-interaction" the g_j point along the equilibrium bonding directions and lead to a change of V with the volume of the local unit cell. The electron–phonon coupling mechanism introduced via eq. (16) in a Hamiltonian

$$H \sim V f^{\dagger} c \sim V_0 f^{\dagger} c + G f^{\dagger} c (b + b^{\dagger})$$

induces a local interplay of lattice deformations and electronic excitations with characteristic energies like the Anderson width $\Delta = \pi V^2 N_F$ or the Kondo-lattice temperature $T^* \sim \exp(-\gamma |\epsilon_1| / \Delta)$, which rule the quasiparticle renormalizations in IV or heavy-fermion systems. Thus, one can expect a strong effective deformation-potential coupling: roughly speaking, local lattice deformations change, via $\Delta \sim V^2$, the quasiparticle DOS $T^{*-1} \sim N_F^*$. For heavy-fermion systems pronounced effects are therefore to be expected at temperatures $T < T^*$ (Grewe 1985).

A phenomenological coupling between heavy quasiparticles and lattice degrees of freedom can in fact be described via the following Grüneisen-type parameter (Lüthi 1985)

$$\eta_v = -\frac{\partial \ln T^*}{\partial \,\mathrm{Vol}} = \frac{\partial \ln N_F^*}{\partial \,\mathrm{Vol}} . \tag{17}$$

This assumes exceptionally large values of order 10^2 in some heavy-fermion compounds (Razafimandimby et al. 1984). The logarithm of the characteristic lattice temperature T^* involves the bare breathing-interaction coupling constants defined in eq. (16) via the one-particle resonance width $\Delta \sim V^2$. The precise connection is clarified by microscopic investigations of an extended Anderson model (Grewe 1984b, Keller et al. 1989): a local lattice deformation modifies the ASR near the Fermi level, thus changing the local scattering potential. A phonon with well defined wave number thereby couples coherently to the quasiparticle bands. The effect is a deformation potential for the heavy quasiparticles. The same local mechanism lies at the heart of the so-called "Kondo volume collapse" (Allen and Martin 1982, Lavagna et al. 1982b). It refers, with the Ce metal as the classical example, to a spontaneous change of the lattice constant upon variation of, i.e., pressure, which is accompanied by a drastic modification of the quasiparticle properties. It includes changes of the residual interactions, e.g., additional contributions from magnetic short-range correlations due to the RKKY interaction in the phase with more stable moments. In the extreme, a transition

between a heavy-fermion and an IV regime occurs, corresponding to a change of the energy scale $k_B T^* \leftrightarrow \Delta$, which rules the scattering resonances. The energy balance responsible for this transition, which may be discontinuous or of a smooth nature, acquires highly non-linear contributions from the complicated way in which the bare coupling [see eq. (16)] enters the quasiparticle-band structure and the contribution of effective interactions (Grewe 1985).

$CeBe_{13}$ and $Ce_{1-x}La_xBe_{13}$ are compounds in which a softening of the Γ_1^+ mode, corresponding to a breathing deformation of the unit cell, is detected by Raman spectroscopy (Blumenröder et al. 1985). A comparative study of the bulk moduli c_B for various RE compounds via Brillouin scattering (Mock et al. 1985) reveals a strong softening in the IV systems $EuCu_2Si_2$ and $YbCu_2Si_2$, see fig. 34. The heavy-fermion compound $CeCu_2Si_2$ still shows a considerable effect, whereas systems with stable valency like $GdCu_2Si_2$ follow strictly a universal linear connection between c_B and the local charge per unit-cell volume. Particular anomalies at low temperatures, which are presumably connected with the formation of coherent heavy-fermion bands, are observed in $CeSn_3$ and $CeAl_3$: the bulk modulus rapidly decreases near T^* and can exhibit a minimum for $T \ll T^*$, see fig. 35a for $CeAl_3$ (Lüthi and Yoshizawa 1987). Strong Fermi-surface anisotropies may be the reason for anomalies seen in other elastic constants such as in $CeSn_3$ (Niksch et al. 1985), $CeCu_6$ (Suzuki 1985), and CeB_6 (Lüthi 1985), see fig. 35b. The last two materials exhibit structural phase transitions at temperatures below 150 K. For $CeCu_6$ also a softening of the corresponding transverse phonons is observed (Noda et al. 1985).

Elastic anomalies in actinide-based heavy-fermion systems are most pronounced for UPt_3. The temperature dependences of two representative elastic modes are shown in fig. 36 (Yoshizawa et al. 1985). Unlike the case of UPd_3, CF effects as a possible source do not seem very likely. The phonon dispersions of UBe_{13}, as measured by neutron scattering (Robinson et al. 1986), do not show strong anomalies. The elastic constant c_{12}, however, is negative at low temperatures, similar to some IV compounds. Remarkably, UBe_{13} possesses a low Debye

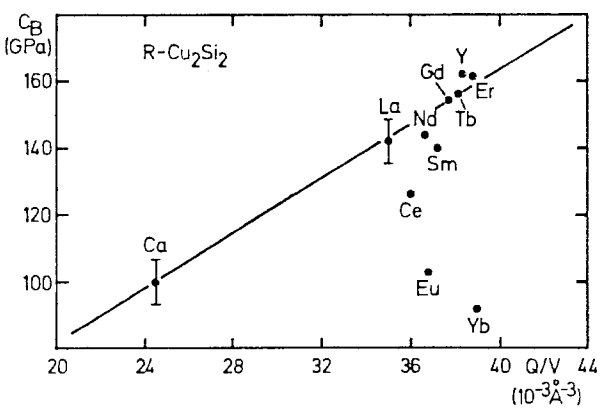

Fig. 34. Bulk modulus c_B of RCu_2Si_2 plotted against the ratio Q/V of the valency Q of the rare earth (R) ion and the unit-cell volume V of the lattice (Mock et al. 1985). The stable-valent RCu_2Si_2 follow a linear c_B against Q/V relation.

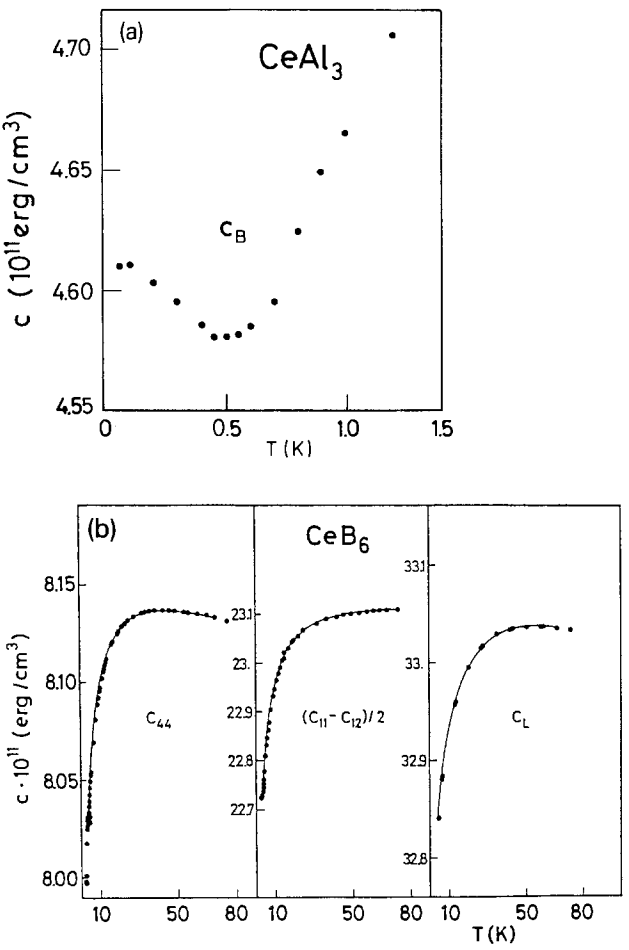

Fig. 35. Elastic constants of (a) $CeAl_3$ (Lüthi and Yoshizawa 1987) and (b) CeB_6 (Niksch et al. 1980) showing pronounced low-temperature anomalies. The softening observed is explained via the action of the Kondo effect on the lattice.

temperature (Goldman et al. 1985) similar to the isostructural IV compound $CeBe_{13}$, which is consistent with speculations about a low U–Be potential due to a strong hybridization between U-5f and the neighbouring Be-s orbitals (Overhauser and Appel 1985).

The negative coefficient α of thermal expansion in $CeAl_3$ (Andres et al. 1975, Ribault et al. 1979) establishes another interesting elastic anomaly connected with the heavy-fermion state at low temperatures. In a study of $Ce_{1-x}Y_xAl_2$ this negative value disappears in the IV regime that is approached for large y-concentrations, see fig. 37 (Schefzyk et al. 1985c). It therefore seems to be characteristic for the Kondo regime. The volume dependence of the quasiparticle-DOS N_F^* alone cannot account for the phenomenon: N_F^* presumably decreases with decreasing volume, i.e., the hybridization increases, and thus $\alpha/T \sim \eta_v > 0$. Several explanations have been put forward: exchange of particles with additional bands (Fetisov and Khomskii 1985), pseudogap formation at low temperatures

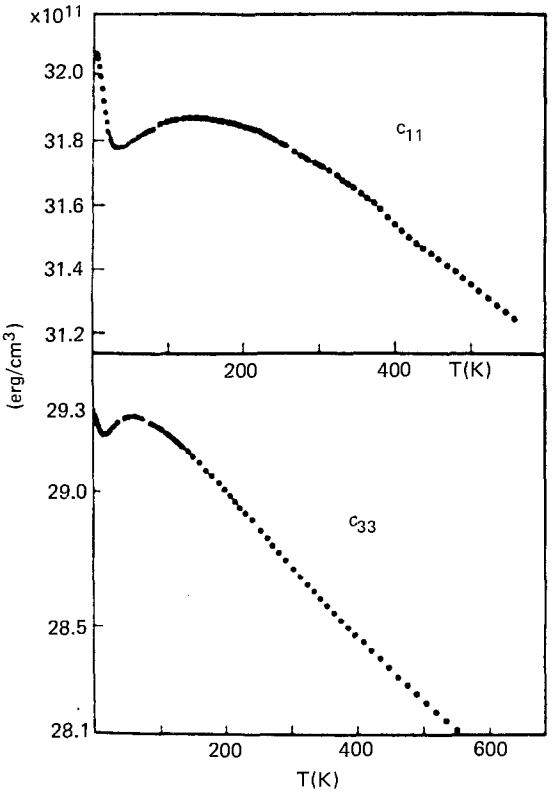

Fig. 36. Elastic constants of UPt_3 show similar low-temperature anomalies to those of Ce compounds, cf. fig. 35 (Yoshizawa et al. 1985).

(Bastide and Lacroix 1986), local quasiparticle interactions as established in the case of liquid He^3 (Misawa 1986), and finally the zero-point pressure of the local Fermi liquid of heavy quasiparticles as being formed with the growth of the ASR near the Fermi energy (Lang et al. 1987). The last two possibilities are in accord with measurements on the Kondo system $Ce_{1-x}La_xAl_2$ in the dilute Ce limit (Lang et al. 1987), which suggests that the negative value of α is a single-site phenomenon. In general, a competition between the different effects mentioned would lead to both signs of α. In normal (n)-state $CeCu_2Si_2$, e.g., α is positive and very anisotropic (Assmus et al. 1990, Steglich et al. 1990) and becomes rather small in the c-direction, similar to UCd_{11} and U_2Zn_{17}, where however magnetic phase transitions may dominate the thermal expansion (Fisk et al. 1984).

The Kondo-volume collapse effect in Ce metal involves a discontinuous transition between the α-phase and the γ-phase (Coqblin 1982, Allen and Martin 1982, Lavagna et al. 1982a, b), see fig. 38c. The Ce valency stays close to 3+ so that promotional models, favouring considerable changes in the f-occupation (Falicov and Kimball 1969, Ramirez et al. 1970, Hirst 1974), can be excluded. Current explanations aim at correlation effects and are based on the volume dependence of the effective exchange integral $\mathcal{J} \sim \Delta/|\epsilon_1|$ between localized and delocalized electrons, which determines both T^* and the RKKY-interaction strength

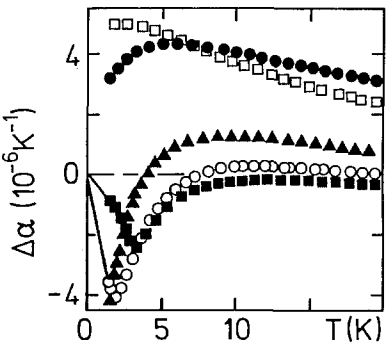

Fig. 37. The 4f-derived contribution, $\Delta\alpha$, to the thermal expansion of $Ce_{1-x}Y_xAl_2$ against temperature for various concentrations x (Schefzyk et al. 1985c). Full squares, $x = 0.05$; empty circles, $x = 0.2$; full triangles, $x = 0.35$; empty squares, $x = 0.5$; full circles, $x = 0.6$. The formation of a heavy Fermi liquid with large zero-point pressure is signalled by the negative sign of $\Delta\alpha$ at low temperatures. For $x \geq 0.6$ the compound approaches the IV regime.

(Thompson et al. 1983, Martin and Allen 1985). In general, such "volume-collapse" transitions occur in a variety of lanthanide and actinide materials (Benedict et al. 1986, Franceschi and Olcese 1969), see figs. 38a and b, with IV SmS as a different characteristic case, where real charge fluctuations play a more important role (Grewe et al. 1980). In $CeCu_6$ (Thompson and Fisk 1985) the f-occupation in the Kondo-lattice state is mildly reduced by pressure. Here, as in a number of other cases (Lawrence et al. 1984), external or lattice pressure can also cause continuous transitions with considerable volume changes as is, e.g., apparent from fig. 38d.

Absorption of ultrasound can be used to probe the electron–lattice coupling and the quasiparticle DOS (Abrikosov 1972). Although the attenuation coefficient in the normal state of UPt_3 and UBe_{13} close to the superconducting transition temperature is not drastically enhanced compared to ordinary metals (Batlogg et al. 1986), it exhibits, at least in UPt_3, interesting temperature-dependent anomalies for higher T (Müller et al. 1986a). In particular, a pronounced longitudinal absorption peak is observed at about 12 K, see fig. 39. Since the transverse absorption does not show this effect, it points to dissipation of energy via coupling of a breathing mode to electronic excitations. The scale of 12 K lies below the characteristic temperature of UPt_3, ranging from 26 K up to 80 K (Rietschel et al. 1988), so that it is natural to involve the heavy fermions and the coupling mechanism discussed above in connection with other elastic anomalies. A straightforward extension of a Boltzmann-equation treatment of ultrasound absorption to this type of coupling (Schotte et al. 1986) can reproduce the peak structure. The physical picture envisages the sound wave changing the height and width of the ASR locally, which leads to a relaxation via f-electron density excitations. Again, a measure for the coupling strength is the change of the characteristic energy scale for the many-body effects with varying lattice

constant, thus involving the Grüneisen-type parameter eq. (17) (Lüthi 1985, Yoshizawa et al. 1986, Grolle et al. 1987).

The particular kind of relaxation discusssed above becomes ineffective at higher temperatures, $T > T^*$, so that the enhanced absorption decreases. At low temperatures, deformation of the ASR by the sound wave has no great effect on the

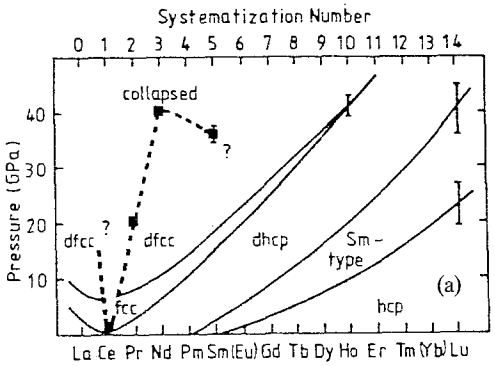

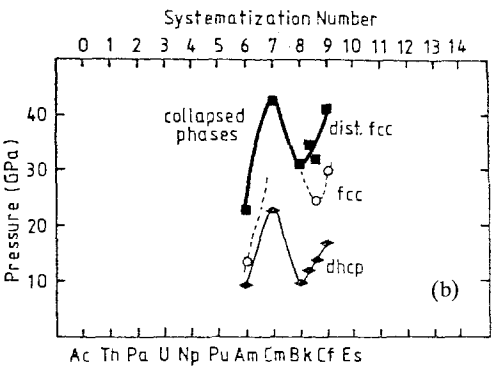

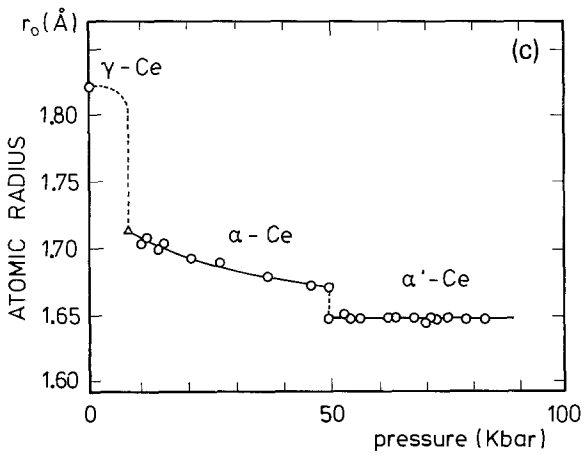

Fig. 38. Isothermal sections at 25°C of (a) intra-lanthanide and (b) intra-actinide generalized binary phase diagrams, showing equilibrium phase boundaries [with estimated hysteresis for (a)] as full lines (Benedict et al. 1986). The broken line in (a) indicates the interpolated boundary for the volume collapse transition of the lanthanides. The atomic radius of Ce at room temperature as a function of pressure is shown in (c) (Franceschi and Olcese 1969), with the Kondo-volume collapse transition at about 7 kbar. This transition can be traced to negative pressures by alloying (Lawrence et al. 1984), as seen in (d) via the temperature dependence of the resistance.

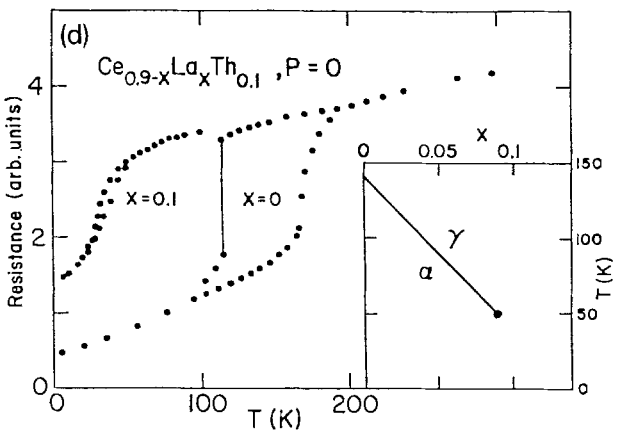

Fig. 38. (cont'd)

remaining quasiparticles near E_F. This leads to a decrease of absorption and qualitatively explains the maximum (Schotte et al. 1986). The magnitude of the absorption coefficient and the importance of a coupling to the density fluctuations compared to a relaxation via heat transfer has been elucidated recently by a direct inspection of the phonon self-energies (Becker and Fulde 1987). In the hydrodynamic regime, the self-energy can be completely reduced to thermodynamic

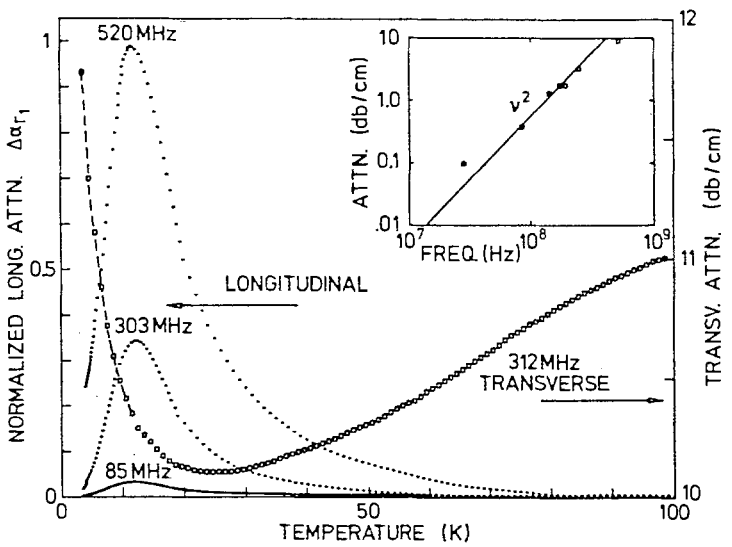

Fig. 39. Temperature dependences of the transverse (312 MHZ and $q \| b$, $u \| c$) and longitudinal (various frequencies and q, $u \| b$) electronic ultrasound-attenuation coefficients of UPt_3 (Müller et al. 1986a). The most striking feature is the pronounced longitudinal attenuation peak at about 12 K, which is ascribed to a deformation-potential coupling to the heavy-fermion bands. The inset proves the quadratic frequency dependence of the longitudinal peak height as expected from theory, solid line (Müller and Bartell 1979).

coefficients, although contact can be made to microscopic calculations, as well. An interesting result of this calculation is the existence of a second quasi-elastic peak in the phonon DOS (besides the usual Rayleigh line due to heat conduction) that is produced by the slow density fluctuations of the heavy Fermi liquid and should be appreciably wider than the first peak by a factor of order m^*/m_0. For large enough wave number this mode can be characterized as propagating instead of diffusing. Such a quasi-elastic peak has recently been found in UPt_3 and was interpreted along these lines (Mock and Güntherodt 1989). The situation reminds one of the coupled electron–phonon excitation found in the IV regime (Grewe et al. 1978). Collective modes in the heavy-fermion liquid are quite generally an interesting subject of current studies. In particular, different kinds of plasmons are being investigated (Becker and Fulde 1987, Höhn and Keller 1988).

The influence of high magnetic fields on elastic properties of heavy-fermion materials can lead to interesting effects. One might think of three possible sources for anomalous behaviour:

(i) The magnetoelastic coupling can become quite strong at the verge of stability of the f-shell. On the one hand, CF levels are then still well defined reflecting the pronounced anisotropies, and coupling to elastic degrees of freedom should be strong. On the other hand, virtual charge excitations of the f-shell are not completely prohibited and can contribute considerably to the response to magnetic fields. An interesting interplay might result.

(ii) The magnetic field may break the Kondo singlets in the Fermi-liquid regime at low temperatures and thereby, via the breathing-mode coupling, cause anomalies in longitudinal elastic constants, i.e., a pronounced magnetic field dependence.

(iii) The nature of the low-temperature phase might change in a more drastic way in strong magnetic fields. Transitions to magnetic phases or the formation of SDW can be induced.

Apparently all of these effects have been observed experimentally: CF transitions seem to determine the peculiar magnetoelastic effects in $Ce_xLa_{1-x}Cu_6$ at intermediate temperatures $T > T_K$ (Winter et al. 1986). The anomalously large volume magnetostriction of a number of Ce, Eu and Yb systems with a weakly unstable or nearly stable 4f-shell displays scaling properties in strong magnetic fields and at low temperatures, which depend on the low-energy scale in a characteristic way (Zieglowski et al. 1985), see fig. 40. In UPt_3 a pronounced softening of the c_{11} mode at a few kelvins is observed near $B = 20$ T, and a similar result holds for $CeRu_2Si_2$ (Kouroudis et al. 1987), see fig. 41. The magnetic Grüneisen-type parameter

$$\eta_B = -\frac{\partial \ln B^*}{\partial \mathrm{Vol}}\,, \tag{18}$$

where B^* is the characteristic field analogous to T^*, corresponds to η_v, see eq. (17), as is to be expected from the theory of the Kondo effect (Tsvelik and Wiemann 1983). An interesting novel feature is the magnetoacoustic quantum

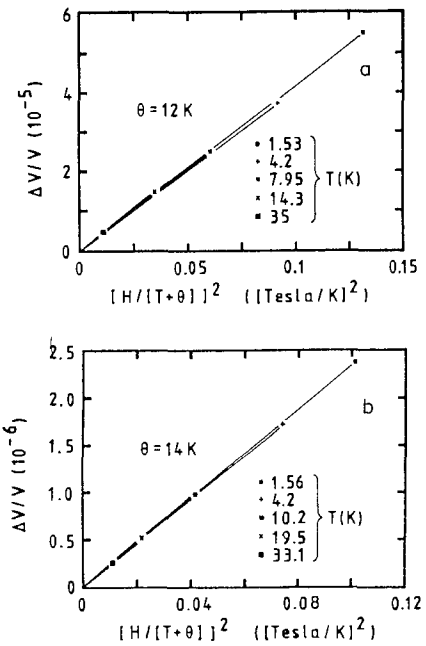

Fig. 40. Scaling of the volume magnetostriction of (a) $CeCu_6$, and (b) mixed-phase $CeCu_2Si_2$ with $[H/(T+\Theta)]^2$ at different temperatures (Zieglowski et al. 1986). H is the applied magnetic field and Θ a characteristic temperature chosen to make all the isotherms coincide as well as possible. Large differences between superconducting and non-superconducting $CeCu_2Si_2$ are found.

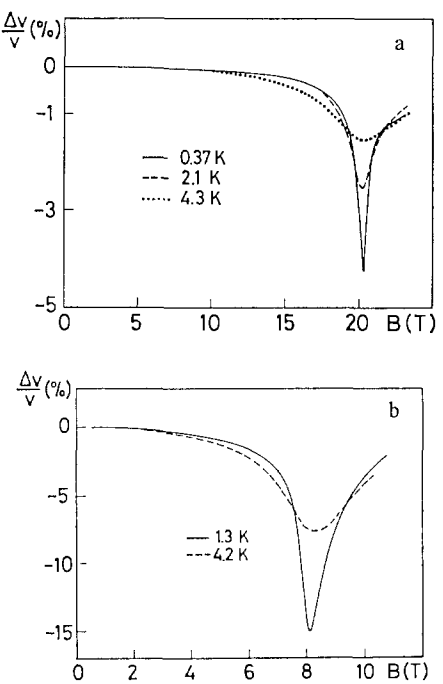

Fig. 41. Magnetoacoustic effects in (a) UPt_3 and (b) $CeRu_2Si_2$ (Kouroudis et al. 1987). An anomalous softening of the c_{11} mode at a characteristic field $B^* \approx 20$ T for UPt_3 and of the c_{33} mode at $B^* \approx 8$ T for $CeRu_2Si_2$ correlates well with metamagnetic phenomena in these systems. The magnitude of B^* reflects well the characteristic temperatures T^*.

oscillations of the elastic constants as a function of the applied magnetic field in UPt_3 and several Ce systems (Lüthi 1985, Kouroudis et al. 1987, Nikl et al. 1987, Thalmeier et al. 1987, Goto et al. 1988).

3. Magnetism

3.1. *The competition between Fermi-liquid formation and magnetic order*

In order to clarify the role which magnetic phenomena play in heavy-fermion systems one may start from two well defined limiting cases: stable-moment behaviour and intermediate valence. In the first case, the energy gained by moment compensation is so small that in the observable temperature range the magnetic degrees of freedom are stable and well defined. The corresponding moments comply with the CF effects, and their dynamics is ruled by indirect exchange interactions. Typically the RKKY interactions then lead to magnetic order that, depending on Fermi momentum and lattice structure, is usually antiferromagnetic. In IV systems, on the other hand, the hybridization broadening of localized f-states is large and prevents, via real charge fluctuations, the formation of a local magnetic moment at all temperatures of interest. Here no natural distinction between local and itinerant degrees of freedom exists, and a Fermi-liquid description is appropriate from the outset.

The interesting regime, in which heavy-fermion behaviour and magnetism can compete, lies in between these two extremes. A continuous lowering of the magnetic transition temperature relative to the low-energy scale, determining the energetics of moment compensation, is to be expected when leaving the stable-moment regime (Doniach 1977). Two qualitatively different situations can be visualized using long-existing experimental information on the compounds $NpSn_3$ (Trainor et al. 1976) and $CeAl_2$ (Barbara et al. 1977, Bredl et al. 1978a). In the first mentioned actinide compound a magnetic phase is formed in the heavy Fermi-liquid. According to fig. 42, the Sommerfeld coefficient in the paramagnetic regime just above the Néel temperature of 10 K is already constant at a large value of about $250\,\mathrm{mJ\,K^{-2}\,mol^{-1}}$. The ordered moment is, according to neutron-diffraction studies (Trainor et al. 1976), largely compensated down to a value of about $0.3\,\mu_B$/Np atom. The large γ-value of about $100\,\mathrm{mJ\,K^{-2}\,mol^{-1}}$ in the ordered phase as $T \to 0$ points to an interpretation of this phenomenon in terms of the band magnetism of heavy quasiparticles (Trainor et al. 1976). In $CeAl_2$ the ratio T_N/T^* is of order one, i.e., much higher than in $NpSn_3$. Above the transition at $T_N \simeq 4\,\mathrm{K}$, the γ-value still shows a considerable increase which extrapolates to $\gamma^* \simeq 1.7\,\mathrm{J\,K^{-2}\,mol^{-1}}$, fig. 43. Such an extrapolation simulating a fictitious Fermi-liquid with compensated moments can be made using $T^* \simeq 5\,\mathrm{K}$ from, e.g., neutron-scattering results (Steglich et al. 1979b), and correcting for short-range order effects via the theoretical curve for $S = \frac{1}{2}$ obtained by means of the Bethe-ansatz technique (Andrei et al. 1983). Compared with this value of γ^*, the observed γ-value as $T \to 0$ is reduced by an order of magnitude, consistent

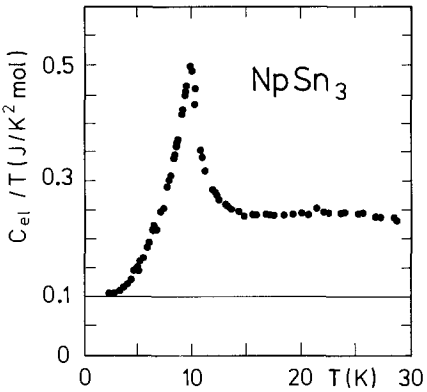

Fig. 42. Electronic specific heat as C_{el}/T against T for $NpSn_3$ (Trainor et al. 1976). Thin horizontal line indicates low-temperature value, $\gamma_0 \simeq 0.1\,\mathrm{J\,K^{-2}\,mol^{-1}}$.

with only a small reduction (about 10%) of the average ordered moment (Barbara et al. 1977). The magnetically ordered phase still involves the original magnetic degrees of freedom frozen into the magnetic state via the intervention of the original band electrons. Both sets of degrees of freedom show some renormalization due to their mutual influence.

Information about the magnetic behaviour of heavy-fermion systems is contained in the wavenumber- and frequency-dependent magnetic susceptibility $\chi(\boldsymbol{q}, \nu)$. In less strongly correlated metals, χ is usually expressed via Stoner's formula [for critical reviews on itinerant magnetism and Stoner theory see, e.g., Moriya (1979), Gautier (1982), Stamp (1985)],

$$\chi(\boldsymbol{q}, \nu)^{-1} = \chi_0(\boldsymbol{q}, \nu)^{-1} - K(\boldsymbol{q}, \nu)\,, \tag{19}$$

where χ_0 is appropriate for a non-interacting gas of quasiparticles and K accounts for the quasiparticle interactions as a result of an RPA treatment. Such an expression has been used in a phenomenological way for a description of the

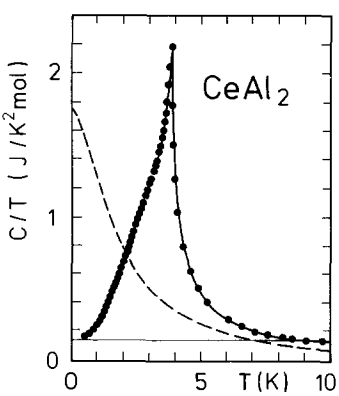

Fig. 43. Specific heat as C/T against T for $CeAl_2$ (Bredl et al. 1978b). Solid line through data points is guide to the eye. Thin horizontal line indicates low-temperature value, $\gamma_0 = 0.135\,\mathrm{J\,K^{-2}\,mol^{-1}}$. Dashed line is Bethe-ansatz result for $S = \frac{1}{2}$ Kondo impurity with $T_K = 0.68\,T^* = 3.5\,\mathrm{K}$ (Andrei et al. 1983).

magnetic response of heavy-fermion systems, as well (Pethick and Pines 1988). In fact, it can be shown that the LNCA version of perturbation theory (Grewe and Pruschke 1985, Grewe 1987, Grewe et al. 1988, Kuramoto and Watanabe 1987, Kuramoto 1989, see also: Lee 1985, Zhang et al. 1987, Auerbach et al. 1988) furnishes a justification for this approximation as well as a definition for the quantities χ_0 and K; compared to the theory of conventional band magnetism they have, however, a somewhat different meaning (Grewe et al. 1988): $\chi_0 \to \chi^{\mathrm{eff}}(\nu)$ is the local susceptibility of an effective site in the lattice, and

$$K(\boldsymbol{q}, \mathrm{i}\nu) = \gamma \frac{1}{\beta N} \sum_{\mathrm{i}\omega, \boldsymbol{k}} T_{\boldsymbol{k}}^{\mathrm{eff}}(\mathrm{i}\omega) G_{\boldsymbol{k}}^{\mathrm{c}}(\mathrm{i}\omega) G_{\boldsymbol{k}+\boldsymbol{q}}^{\mathrm{c}}(\mathrm{i}\omega + \mathrm{i}\nu) T_{\boldsymbol{k}+\boldsymbol{q}}^{\mathrm{eff}}(\mathrm{i}\omega + \mathrm{i}\nu) \tag{20}$$

results from correlations between lattice sites. χ^{eff} is already renormalized as a result of local and quasilocal processes, as are the one-particle band Green functions G^{c} [the superscript stands for a cumulant subtraction due to site exclusion (Grewe 1987)] and the local scattering matrix

$$T_{\boldsymbol{k}}^{\mathrm{eff}}(\mathrm{i}\omega) = |V_{\boldsymbol{k}}|^2 G^{\mathrm{eff}}(\mathrm{i}\omega) .$$

The indices α and σ are left out here for convenience. γ is a constant of order one (we have extracted a common factor $(g\mu_{\mathrm{B}})^2$ in order to deal with energy units only), originating from an approximate treatment of the fully retarded local quasiparticle repulsion, $\mathrm{i}\nu$ and $\mathrm{i}\omega$ are Bose and Fermi frequencies, respectively, $\beta = (k_{\mathrm{B}}T)^{-1}$ and N is the number of lattice sites. Equation (20) has a straightforward interpretation: non-local magnetic correlations arise as a result of local spin-flip excitations, coupled via itinerant electron–hole pairs. The amplitude K contains an electron–hole propagator $G^{\mathrm{c}}G^{\mathrm{c}'}$ and one T-matrix, T^{eff} for spin-flip scattering at each of the two lattice sites. A chain of repeated local interactions of an electron–hole pair at intermediate sites involves powers of $\Pi^{\mathrm{c}}G^{\mathrm{c}}G^{\mathrm{c}'}$, Π^{c} being the local quasiparticle vertex. Equation (19) is the result of a mean-field-like decoupling of this retarded interaction, i.e., $\Pi^{\mathrm{c}} \to \gamma\chi^{\mathrm{eff}}T^{\mathrm{eff}}T^{\mathrm{eff}}$, and of a summation of the resulting geometric series.

An evaluation of K (Grewe 1988a, b) uses the spectral representations

$$G^{\mathrm{eff}}(\mathrm{i}\omega) = \int \mathrm{d}\omega' \frac{\rho^{\mathrm{eff}}(\omega')}{\mathrm{i}\omega - \omega'} , \qquad G_{\boldsymbol{k}}^{\mathrm{c}}(\mathrm{i}\omega) = \int \mathrm{d}\omega' \frac{\rho_{\boldsymbol{k}}^{\mathrm{c}}(\omega')}{\mathrm{i}\omega - \omega'} , \tag{21}$$

and the well-known structure of the spectra ρ^{eff} (Grewe et al. 1988) and $\rho_{\boldsymbol{k}}^{\mathrm{c}}$, see also fig. 9a. Thereby different contributions to K can be identified, i.e., high-energy processes, characteristic of an RKKY-type interaction between local moments, and low-energy processes, producing exchange interactions between the heavy quasiparticles (Grewe 1988a, Kuramoto 1988). The high-energy processes alone would favour a modulated magnetic state with wavevector $\boldsymbol{q}$ and hypothetical transition temperature $T_{\mathrm{m}}^{(\mathrm{h})}$

$$0 = k_{\mathrm{B}}T_{\mathrm{m}}^{(\mathrm{h})} - K^{(\mathrm{h})}(\boldsymbol{q}, \mathrm{i}\nu)\big|_{\substack{\mathrm{i}\nu \to 0 \\ T = T_{\mathrm{m}}^{(\mathrm{h})}}} , \tag{22}$$

where $\chi^{\text{eff}} \sim 1/k_B T$ has been used in this range. Such an RKKY instability actually occurs for stable-moment systems where T^* is low and $T_m^{(h)} \gg T^*$. The relative order of these two characteristic energies is determined in general by a number of factors, in particular the position of the bare f-resonance, hybridization strength, orbital degeneracy and crystal anisotropies (Coleman 1983, Read et al. 1984, Varma et al. 1986, Rice and Ueda 1985, 1986, Fazekas 1987, Doniach 1987a, b, Vulović and Abrahams 1987, Fazekas and Brandow 1987). In the heavy-fermion regime T^* and $T_m^{(h)}$ become comparable. Then the saturation of the susceptibility χ^{eff} at a value of order $1/T^*$ due to moment compensation can lead to a situation in which $T^* > T_m^{(\ell)} > T_m^{(h)}$, where $T_m^{(\ell)}$ is calculated analogously to $T_m^{(h)}$, via the low-energy processes only and using $\chi^{\text{eff}} \sim 1/k_B T^*$ for $T < T^*$. The condition, $T^* \approx T_m^{(\ell)} \approx T_m^{(h)}$, defines the crossover to a different kind of magnetic instability, that is connected with an exchange splitting of the heavy-fermion bands, i.e., to true magnetism of the heavy fermions (Grewe 1988a, Kuramoto 1989). Given the peculiar dispersion of the hybridized quasiparticle bands and the underlying strong anisotropy of the original band structure, the q-dependence of K is important and should lead, as is observed, to inhomogeneous forms of magnetism. In particular, low-energy excitations near the hybridization points of the quasiparticular band structure, see fig. 44, would favour small q-vectors (Grewe and Welslau 1988). A competition of small q-instabilities with $q = 2k_F$ modes, which are characteristic for RKKY magnetism and heavy-fermion magnetism as well (Tsvelik 1979, Grewe and Keiter 1981, Lee 1985), could help to explain the tendencies for complicated magnetic structures in heavy-fermion systems at low temperatures.

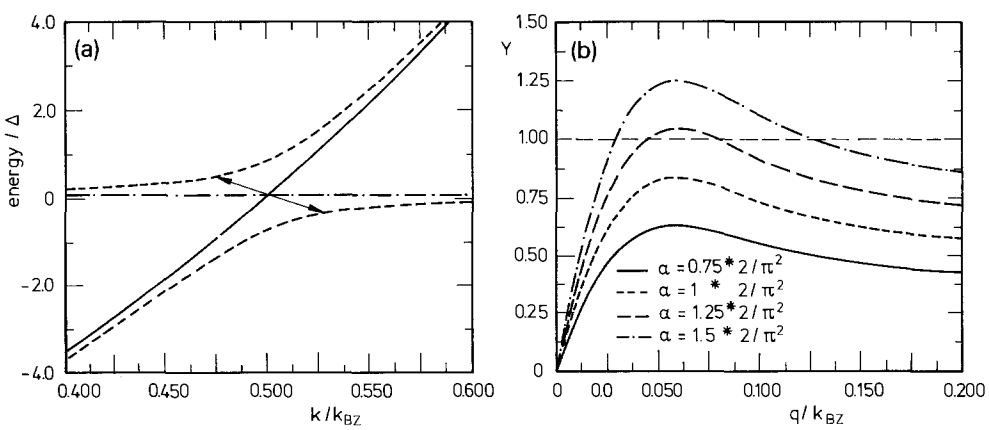

Fig. 44. Transitions across hybridization gaps of the quasiparticle band structure (a) can, depending on the position of the chemical potential (assumed inside the pseudogap for this calculation), and on the other band-structure features, give rise to pronounced structures in the non-local interaction part $Y = \chi^{\text{eff}} K$ of the Stoner denominator [compare eqs. (19) and (20)] at small wavevectors (b). In (b) $\alpha = \gamma/\pi^2$ with γ defined in eq. (20) is varied somewhat around its proper value of $2/\pi^2$ (Grewe and Welslau 1988) to exhibit the strong tendency towards a magnetic instability occurring for $Y(\boldsymbol{q}_{\text{crit}}, \nu = 0) = 1$.

Characteristic differences arise in the electronic excitation spectrum of heavy-fermion magnets in the different regimes. For a magnetic state with well localized moments and only moderate enhancement of γ (i.e., of order $0.1\,\mathrm{J\,K^{-2}\,mol^{-1}}$) as in $CeAl_2$, the following picture has been proposed (Doniach 1977, Nozières 1985): starting from band electrons and ionic f-states, the quasiparticle renormalizations stop when spin order of somewhat renormalized moments occurs. The corresponding RKKY interactions with energy scale T_{RKKY} are mediated by moderately renormalized band electrons. Note that the relevant saturation temperature is usually the one at which short-range magnetic clusters are formed above the cooperative phase-transition temperature $T_N \equiv T_m^{(h)}$. For $CeAl_2$, e.g., T_{RKKY} exceeds $T_N \approx 4\,\mathrm{K}$ by more than an order of magnitude (Steglich et al. 1979b). From then on, spin-flip scattering is frozen out and the band electrons move in the fixed modulated exchange field provided by the moments. Although the DOS near E_F changes due to an exchange-split incipient ASR, see fig. 28, no electronic excitation gap develops anywhere on the Fermi surface. Typically the specific heat well below T_N follows $C = \gamma T + \beta T^3$ with a cubic magnon contribution. For a heavy-fermion magnet in the itinerant regime, on the other hand, the magnetism can be described in the language of quasiparticle-band theory. In particular a spin density wave (SDW) instability (Doniach 1987a) may open an electronic excitation gap on parts of the Fermi surface, a situation strongly favoured by the nesting properties (Fawcett 1988). In such strongly anisotropic cases the density of quasiparticle excitations is reduced at low temperature and an exponential decrease of $\gamma(T)$ can result below T_N. In pure compounds like UPt_3, where this type of phase transition possibly occurs, no $C(T)$ anomaly has been observed, in accord with the small entropy connected with the tiny ordered moments. In the disordered systems $U(Pt_{1-x}Pd_x)_3$ (de Visser et al. 1986), $(U_{1-x}Th_x)Pt_3$ (Ramirez et al. 1987, Stewart et al. 1986) and $Ce(Cu_{1-x}Ag_x)_6$ (Gangopadhyay et al. 1988, Fraunberger et al. 1989, Germann and von Löhneysen 1989), on the other hand, a distinct anomaly is observed. This hints at disorder-induced formation of large local moments, which, in fact, have been observed for the (U, Th)Pd_3 system via neutron diffraction (Aeppli et al. 1988). Concerning a reduction of the one-particle DOS due to SDW formtion, it may be difficult to discriminate this experimentally from a gap in the magnetic excitation spectrum, as characteristic of anisotropic local-moment magnets. The latter has been observed, e.g., for $CeCu_2$ (Gratz et al. 1985).

Realistic heavy-fermion systems are typically situated in a crossover regime between these two limiting cases. We shall nevertheless try to stress certain tendencies observed by assigning, e.g., $CeAl_2$ to the class of local-moment systems and discussing (U, Th)Pt_3 as an itinerant system. One should realize, however, that these tendencies, as resulting from a balance between energies like T_{RKKY} and T^*, can be influenced, e.g., by alloying. We shall discuss the situation within a somewhat broader context by considering the influence of composition changes on energy scales in general.

A particularly simple case, where no cooperative magnetic order is involved, is furnished by $UPt_{5-x}Au_x$ (Ott et al. 1987a, Quitmann et al. 1988). Substitution of Pt by Au up to $x = 1$ leads to an increase of the low-T effective mass as shown by

$\gamma(T \to 0)$, i.e., from 85 mJ K^{-2} mol^{-1} ($x = 0$) to approximately 900 mJ K^{-2} mol^{-1} ($x = 1$) (Quitmann et al. 1988). In principle, alloying can have a twofold effect on T^*. Variations of the band structure and of the chemical potential cause changes of the DOS at E_F, and variations of the average lattice spacing may, in addition, alter the hybridization. In $UPt_{5-x}Au_x$, Quitmann et al. (1988) ascribe the apparent decrease of T^* to a decrease of the DOS at E_F.

More typical for heavy-fermion systems are those cases where composition changes induce a transition between the magnetic and the non-magnetic regimes. A recent example is $UCu_{4+x}Al_{8-x}$ for which T_N ($\simeq$29 K for $x = 0$) vanishes with increasing Cu content near $x = 1.5$ (Geibel et al. 1990). Beyond this composition the ground state is a heavy Fermi-liquid with $\gamma \simeq 800$ mJ K^{-2} mol^{-1} ($x = 1.75$). A reduction of the unit-cell volume with increasing x suggests a growing value of the characteristic temperature T^* and an explanation of the transition in terms of the composition dependence of two characteristic energy scales, T^* and T_{RKKY}. Further evidence is furnished by the system $Ce_{1-x}Y_xAl_2$ (see fig. 3). This idea fits well into the theoretical discussion given above, which will be summarized in a theoretical phase diagram at the beginning of the next section.

The case of $CeCu_2Si_2$ demonstrates the usefulness of the unit-cell volume as a parameter discriminating different ground states in a particularly clear fashion. Figure 45 incorporates the effect of three different ways of changing the volume:

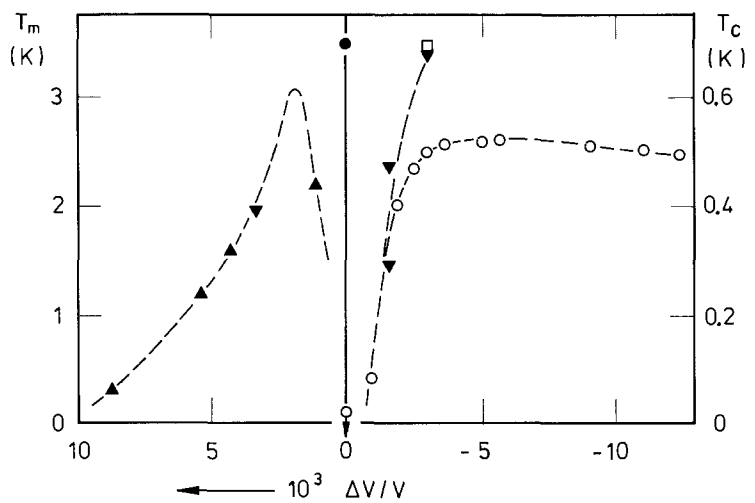

Fig. 45. Magnetic-ordering temperatures T_m (closed symbols, left-hand scale) and superconducting transition temperatures T_c (open symbols, right-hand scale) of $CeCu_2Si_2$ and homologues as a function of relative volume change $\Delta V/V_0 = (V - V_0)/V_0$ with $V = a^2c$. $V_0 = 167.43$ Å^3 is the unit-cell volume of "stoichiometric" single crystals at ambient pressure (Assmus et al. 1984): ●, ○, "stoichiometric" single crystals at $p \geq 0$ (Aliev et al. 1983, Assmus et al. 1984); □, single crystal grown from 26 at.% Cu excess; ▽, polycrystals prepared either with 10 at.% Cu excess ($T_c = 0.68$ K) or stoichiometrically ($T_c < 0.5$ K); ▼, polycrystal of $CeCu_{1.9}Si_2$; ▲, polycrystals of $Ce_{1-x}La_xCu_2Si_2$; V, interpolated between $V = 169.25$ Å for $LaCu_2Si_2$ and V_0 (Aliev et al. 1984). Dashed lines are intended as guides to the eye. Note that a "stoichiometric" single crystal shows a antiferromagnetic transition at $T_m = 3.5$ K, but no superconductivity at $T > 20$ mK (Steglich 1985a).

La doping and Cu deficit ($\Delta V/V_0$ between 0 and 10^{-2}), Cu excess ($-0.3\times10^{-2}\leq\Delta V/V_0\leq0$) and hydrostatic pressure ($-1.2\times10^{-2}\leq\Delta V/V_0\leq0$). Again, decreasing unit-cell volume can be associated with an increasing T^*, as supported by resistivity measurements under pressure (Aliev et al 1983, Bellarbi et al. 1984). The samples with large volume and lower T^* are magnetic. The apparent spin-glass properties (Aliev et al. 1984, Rauchschwalbe et al. 1985a) may be explained by dilute magnetic moments induced by disorder. The samples with low volume and higher T^* exhibit heavy-fermion superconductivity and, in addition, pronounced coherence effects in n-state properties (cf. fig. 72 and the corresponding discussion). Many open questions associated with the complex ternary Ce–Cu–Si phase diagram remain (Ishikawa et al. 1983, Spille et al. 1983, Braun and Jorda 1985, Sun et al. 1990), such as the unusual pressure dependence of the superconducting transition temperature T_c (Aliev et al. 1983, Bellarbi et al. 1984, Bleckwedel and Eichler 1985) and the possible coexistence between superconductivity and itinerant antiferromagnetism, which will be resumed in sect. 4 (cf. fig. 64). Note that single crystals grown from stoichiometric melts ($\Delta V/V_0=0$) still show unexplained features in the susceptibility (fig. 62) and the specific heat, suggesting an antiferromagnetic transition near 3.5 K, but no superconductivity (Steglich 1985a).

A change from a non-magnetic heavy Fermi liquid to a ferromagnetically ordered ground state was found in $CeSi_x$ upon decreasing the Si concentration near $x=1.85$, i.e., precursive to a tetragonal to orthorhombic transition at $x=1.80$ (Yashima et al. 1982), as summarized in fig. 46. In this case, the increase of T^* with x is not connected with a volume compression in any obvious way (Lee et al. 1987).

A particularly interesting phase diagram has recently been established for the system $Ce(Cu_{1-x}Ni_x)_2Ge_2$. Whereas the system $CeCu_2Ge_2$ fits well into the class of local-moment systems with a low $T^*\simeq7$ K, coinciding with T_{RKKY}, the

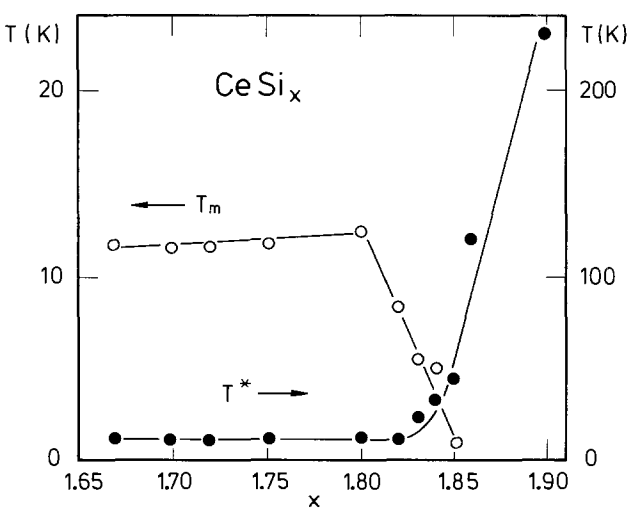

Fig. 46. Lattice Kondo temperature, T^*(●), and magnetic-ordering (Curie) temperature, T_m(○), plotted against composition in the system $CeSi_x$ (Lee et al. 1987).

temperature at which short-range ordering effects become noticeable (de Boer et al. 1987, Knopp et al. 1989), $CeNi_2Ge_2$ is a Kondo lattice with a non-magnetic ground state ($\gamma \simeq 0.4\,J\,K^{-2}\,mol^{-1}$) and $T^* \simeq 30\,K$ (Knopp et al. 1988). Figure 47a shows the Ni-induced increase of T^* in $Ce(Cu_{1-x}Ni_x)_2Ge_2$, which becomes particularly pronounced for $x \geq 0.75$, possibly related to both a volume compression and a DOS increase. Depending on composition, two very different spin structures have been discovered for $Ce(Cu_{1-x}Ni_x)_2Ge_2$. A combination of various bulk measurements (Sparn et al. 1988, Steglich et al. 1989) has established (fig. 47b) the following facts:

(i) a strong depression of the Néel temperature T_{N_1} that is 4.1 K for $CeCu_2Ge_2$ and extrapolates to $T_{N_1} = 0$ for $x \simeq 0.2$;

(ii) at this concentration the evolution of a second type of antiferromagnetic order below $T_{N_2}(x)$ that becomes a maximum ($\simeq 4\,K$) near $x = 0.5$ and can be followed up to a Ni concentration of approximately $x = 0.75$, beyond which magnetic order seems to be absent;

(iii) the occurrence of two phase-transition anomalies in the intermediate composition regime $0.02 \leq x \leq 0.3$.

Neutron diffraction measurements have, in fact, identified two incommensurate antiferromagnetic structures, one with a long modulation vector $q_1 = (0.28, 0.28,$

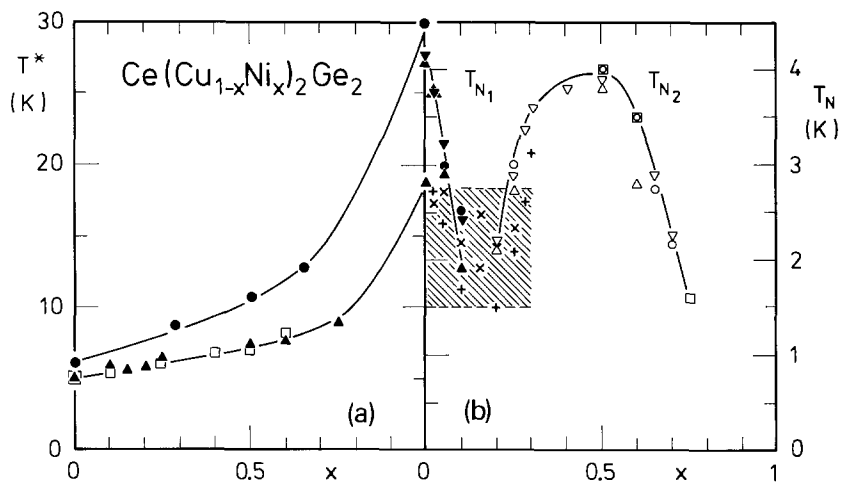

Fig. 47. (a) Lattice Kondo temperature T^* read off positions of broad peaks in both the thermal expansion, $\alpha(T)$ (□), and resistivity, $\rho(T)$ (▲), as well as residual quasielastic linewidths (HWHM), $\Gamma(T)$, extrapolated from $T > 50\,K$ to $T = 0\,K$ (●). In order to match the $\alpha(T)$ and $\rho(T)$ results, $\rho(T)$ peak positions are scaled by a factor of 1.25. (b) Positions of extrema, indicating antiferromagnetic phase transitions, in $\alpha(T)$ (▲, △, ×), specific heat, $C(T)$ (▼, ▽, +), $\rho(T)$ (□) and DC susceptibility (●, ○). Closed symbols refer to onset of "local-moment ordering" below $T_{N_1}(x)$, open symbols indicate formation of "itinerant magnetism" below $T_{N_2}(x)$, crosses are ascribed to the superposition of two modulated structures at intermediate composition (hatched) (Steglich et al. 1990, Loidl et al. 1990b).

0.54) for $x = 0$, the other one with a short $\boldsymbol{q}$-vector, $\boldsymbol{q}_2 = (0, 0, 0.14)$ for $x = 0.5$ (Steglich et al. 1990, Loidl et al. 1990). For the intermediate composition $x = 0.1$, the low-T spin structure is best described by $\boldsymbol{q} = \boldsymbol{q}_1 - \boldsymbol{q}_2 = (0.28, 0.28, 0.41)$, which suggests that both structures may be superposed in the intermediate regime $0.02 \leqslant x \leqslant 0.3$. A steady reduction of the ordered moment from $0.74\ \mu_B$/Ce for $x = 0$ to $\leqslant 0.3\ \mu_B$/Ce for $x \geqslant 0.65$ supports the interpretation that for $Ce(Cu_{1-x}Ni_x)Ge_2$ the alloying-induced transition, between a local-moment-type magnetic ordering (with long $\boldsymbol{q}$) and a non-magnetic Fermi liquid, passes through an itinerant type of antiferromagnetic state characterized by a short $\boldsymbol{q}$-vector (Welslau and Grewe 1990).

3.2. *The role of magnetic correlations in the heavy-fermion liquid*

The preceding considerations stress the importance of magnetic correlations in heavy-fermion systems. Though being generated naturally in the formation of heavy quasiparticles they do not necessarily lead to magnetic ground states (Jullien et al. 1979, Jullien and Martin 1982, Scalettar et al. 1985). Short-range correlations, however, should always be present, even if the Fermi-liquid remains stable at low temperatures (Grewe and Keiter 1981, Rasul 1986, Saso and Seino 1986, Shiba 1986, Auerbach et al. 1988, Chen and Callaway 1988, Norman et al. 1988, Fazekas 1988, Fye and Hirsch 1988). They are necessary for a complete quenching of local moments in the lattice (Nozières 1985). This quenching is initiated at high temperatures $T \gg T^*$ by the local action of the Kondo effect alone. Gradually with decreasing temperature the quenching is supported by the antiferromagnetic couplings developing via the RKKY mechanism. There seems to exist a rather detailed balance between these two main influences: if the itinerant degrees of freedom near the Fermi surface become exhausted too early, RKKY correlations finally grow in distance and lead to a magnetic instability with well defined local moments. If the growth of local compensation is dominant, non-local RKKY correlations do not develop beyond a short-ranged distance. The compensation process may, as is the case near the IV regime, be complemented by real charge fluctuations, so that even fictitious local moments are destabilized at higher temperatures. The different regimes are sketched in fig. 48. In the stable-moment regime a rough estimate of the quantity $Y = \chi^{\mathrm{eff}} K$, which determines the susceptibility-enhancement factor $(1 - Y)^{-1}$ in eqs. (19) to (20), has the form $Y = Cx^2 e^{1/x}$, with the dimensionless indirect local exchange coupling $x = N_F \mathcal{J}$ and a constant C, somewhat smaller than, but of the order of, one (Kuramoto 1981, Grewe and Pruschke 1985). This functional form of Y reflects the competition between the RKKY exchange energy of order x^2 and the singlet binding energy $e^{-1/x}$ due to the Kondo effect (Doniach 1977). The intersection point $Y = 1$ roughly marks the transition from a magnetic ground state of RKKY type at small x to a region where the two competing energy contributions are typically of the same order of magnitude and where the nature of the ground state depends critically on the detailed form of the renormalizations, band structure and critical wavevectors. We idenfity this range of small, but not too small, $x < 1$

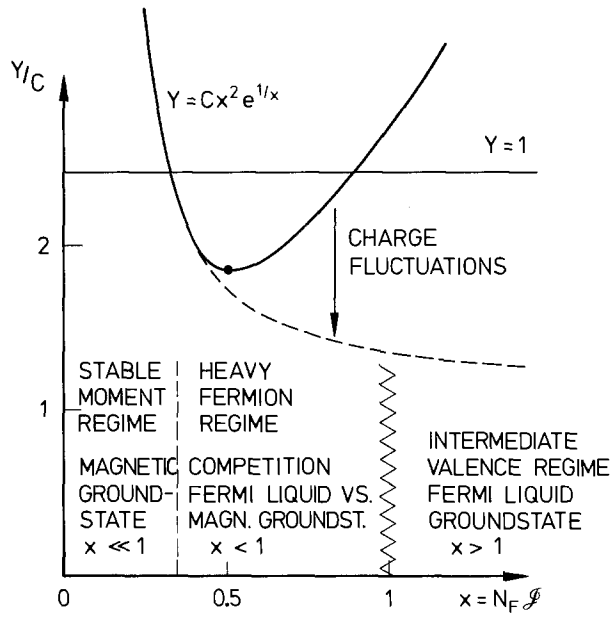

Fig. 48. Depending on the value of the dimensionless indirect local exchange coupling constant $x = N_F \mathcal{J}$ three different types of low-temperature behaviour are encountered: for $x \ll 1$ RKKY magnetism with stable moments occurs, indicated by a non-local interaction part $Y = \chi^{\text{eff}} K > 1$ of the Stoner denominator [compare eqs. (19) and (20)] that is roughly of the form given by Doniach (1977) (full curve). In the heavy-fermion regime (intermediate values $x < 1$), Y remains typically of order one, indicating a tendency towards itinerant magnetism of heavy quasiparticles. The true function $Y(x)$ should decrease montonically (broken curve) for increasing x so that a Fermi liquid ground state always occurs in the IV regime $x > 1$.

as the heavy-fermion regime. Here typically $T_m^{(h)}$ and T^* are comparable to each other and to $T_m^{(\ell)}$, and the collective low-energy scale $T_m^{(\ell)}$ may indeed determine the ground state via an exchange splitting of the heavy quasiparticle bands. Due to the onset of real charge fluctuations, the order-of-magnitude estimate for the true susceptibility-enhancement function Y starts to deviate considerably from Doniach's curve at $x \lesssim 1$. It should decrease monotonically so that in the IV regime for $x > 1$ no magnetic ground state occurs. A clear demonstration of these ideas by experimental observations is given by the phase diagram of $Ce_{1-x}Y_xAl_2$ (fig. 3), which shows a steep decrease of T_N followed by a "spin-glass" regime due to disorder-induced magnetic moments and finally the transition to an intermediate-valence state ($x \gtrsim 0.9$) through a Fermi-liquid regime.

Before actual magnetic ground states of different kinds are discussed in the next two subsections, we want to substantiate the ideas concerning the role of magnetic correlations by referring to neutron-scattering measurements on $CeCu_6$ and $CeRu_2Si_2$ (Rossat-Mignod et al. 1988). These materials are representative of the full span of mass enhancement with $\gamma = 1500\,\text{mJ K}^{-2}\,\text{mol}^{-1}$ and $T^* \approx 4\,\text{K}$ for $CeCu_6$ and $\gamma = 350\,\text{mJ K}^{-2}\,\text{mol}^{-1}$ and $T^* \approx 25\,\text{K}$ for $CeRu_2Si_2$. Among the set of

detailed information obtained (Rossat-Mignod et al. 1988), the following facts seem particularly relevant for the present discussion. Both systems show strong anisotropies in their magnetic response and develop short-range correlations along certain preferred axes with definite q-vectors. At low temperatures the magnetic spectrum shows two contributions, of which one is independent of q. It can be accounted for by a quasielastic Lorentzian and gives the local response of the f-moments. Its half width leads to the Kondo temperature cited above in both cases. The second contribution is peaked at two different characteristic wavevectors in both materials and is, furthermore, concentrated at a characteristic energy transfer ω_0, being of order of the respective $k_B T^*$. This energy $\omega_0 \approx 3k_B$ K for $CeCu_6$ and $\omega_0 \approx 16k_B$ K for $CeRu_2Si_2$ is taken as an effective exchange coupling strength to the nearest neighbours. Since the wavevectors have incommensurate components, anisotropy and band-structure effects should play an important role. Figure 49 shows the temperature dependence of the correlation lengths observed in $CeCu_6$. The strong anisotropy found may be due to an anisotropy of effective exchange interactions and/or of an anisotropy of the moment-compensation mechanism, underlining the discussion at the end of sect. 2.3. A distinct increase of these lengths with decreasing T is recognized for $T \lesssim T^*$, followed by a saturation at typical nearest-neighbour distances. The dominance of the local compensation effect in $CeCu_6$ is further substantiated by the small weigth of about 10% for the non-local magnetic-scattering contribution. The temperature dependences of the energy widths for both contributions in fig. 50 illustrate the freezing of nearest-neighbour magnetic correlations into the ground state, which leads to a strongly temperature-dependent narrowing of the inelastic line below T^*. These correlations can be destroyed by application of a magnetic field with strength of order ω_0/μ. The situation is qualitatively similar for $CeRu_2Si_2$. The

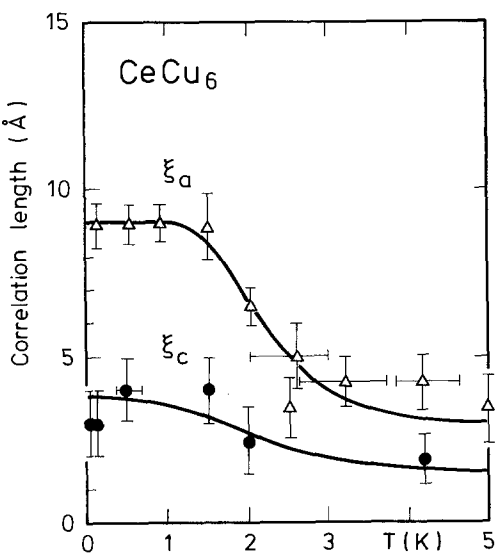

Fig. 49. Magnetic correlation lengths along the a- and c-directions as a function of temperature for $CeCu_6$ (Rossat-Mignod et al. 1988). Lines through data points are guides to the eye.

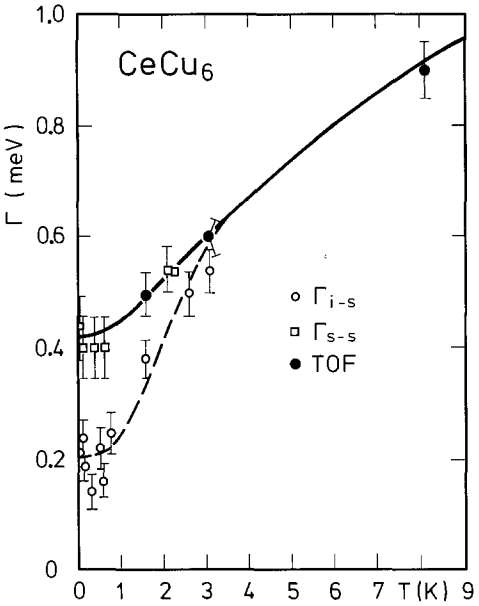

Fig. 50. Temperature dependences of the energy widths deduced from energy scans for single-site (Γ_{ss}) and intersite (Γ_{is}) contributions for single-crystalline $CeCu_6$ (Rossat-Mignod et al. 1988). Also shown are results by Walter et al. (1986) of time-of-flight (TOF) experiments for polycrystalline $CeCu_6$. Solid and dashed lines are guides to the eye.

reduced role of local-moment compensation as compared to $CeCu_6$, shown by the lower γ- and higher T^*-values, also becomes apparent in the increased strength of the non-local magnetic-scattering component, which reaches 40%. Here the Fermi-liquid ground state possesses a considerably larger amount of non-local magnetic correlations.

In view of these non-local magnetic correlations in the ground state of $CeRu_2Si_2$, doping experiments with La find a natural explanation. One observes (Besnus et al. 1987) disorder-induced long-range antiferromagnetism in $Ce_{1-x}La_xRu_2Si_2$ for $x \geqslant 0.08$ with a disorder-independent modulation vector $\boldsymbol{a}_0 = (0.309, 0, 0)$ along the $\boldsymbol{a}$-axis of the tetragonal structure. $\boldsymbol{a}_0$ is the same as the wavevector associated with magnetic correlations in the pure material (Quezel et al. 1988). The itinerant nature of this magnetic instability developing in the heavy-Fermi liquid involves characteristic wavevectors connected with features of the Fermi surface. These do not change essentially with La doping, which mainly has the effect of introducing local magnetic moments by the Kondo-hole mechanism. The resulting increase of magnetic tendencies in the system changes the balance between spin compensation on the one hand and spatial growth of magnetic correlations on the other, and drives the correlation length to infinity. As has been pointed out by Coles (1987), this kind of disorder-induced magnetism reveals an inherent tendency towards formation of a SDW ground state in the heavy-Fermi liquids and bears some resemblance to the situation found in doping pure Y metal with magnetic Gd ions (Sarkissian and Coles 1976). The resulting SDW is of the same type as the one found in pure Cr metal.

An external magnetic field represents another possibility of probing magnetic ground-state correlations. In the presence of non-local antiferromagnetic correla-

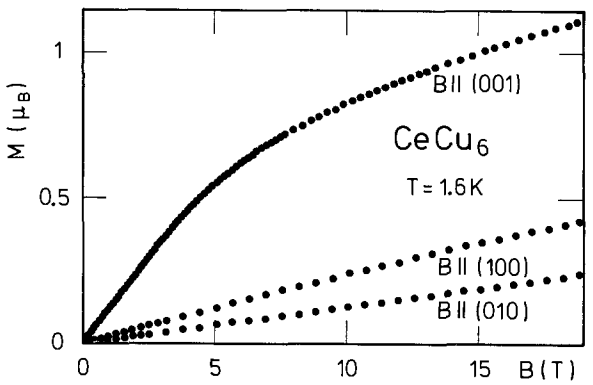

Fig. 51. High-field magnetization, M against B, of $CeCu_6$ for three crystallographic directions at $T = 1.6$ K (Amato et al. 1987b).

tions one expects some kind of spin-flip transition as encountered in ordinary local-moment antiferromagnets (Kosterlitz et al. 1976). This furnishes a possible explanation of the metamagnetic effects observed in $CeRu_2Si_2$ (Besnus et al. 1985, Flouquet et al. 1985) and UPt_3 (Frings et al. 1983). An external field in general polarizes each individual Kondo singlet locally. This effect, related to the increment in the field, is largest for small fields and decreases monotonically until a Zeeman-split local level is recovered for $B > B_K$, whereupon the magnetization has reduced its growth to that of free moments (Schlottmann 1985b, Cox 1987a, b). This behaviour is observed in $CeCu_6$ (Onuki et al. 1985) in agreement with the mainly local correlations of the ground state as discussed above. As seen in fig. 51 the magnetic polarization is strongly anisotropic and largest for B perpendicular to the basal plane. As has been discussed in connection with the anisotropy of energy scales (sect. 2.3) these observations are consistent with the corresponding reduction of effective masses in applied magnetic fields (cf. fig. 24). In UPt_3 (cf. de Visser et al. 1987) and $CeRu_2Si_2$ (cf. Mignot et al. 1988), however, the growth of magnetization in the field has a maximum in a non-zero field, B_M. The anisotropic nature of this effect is demonstrated in fig. 52 (Franse et al. 1984). A pronounced metamagnetic type of field dependence of the low-T magnetization at $B_M \simeq 20$ T results for B applied in the basal hexagonal plane of UPt_3 [and along the c-axis in $CeRu_2Si_2$ at $B_M \simeq 8$ T, Mignot et al. (1988)], see fig. 52. The corresponding maximum in $\chi(B)$ at $B = B_M$ finds its analogue in a maximum of $\chi(T)$ at $T_M \simeq 17$ K (fig. 53). The obvious interpretation is that B_M corresponds to the characteristic energy for antiferromagnetic coupling of neighbouring spins. Breaking these correlations leads to a maximum increment in the magnetization. Particularly clear evidence for the ideas explained above, i.e., that different types of correlations are frozen into a Fermi-liquid-like ground state of the Kondo lattice with essentially the same energy scale T^*, is provided by fig. 54 for $CeRu_2Si_2$ (Mignot et al. 1988): one observes a universal pressure dependence of such different quantities as the inverse susceptibility for $T \to 0$, the inverse effective mass, deduced from the aT^2 term in the low-T resistivity, as well as of B_M and T_M ($\simeq$10 K for $p = 0$).

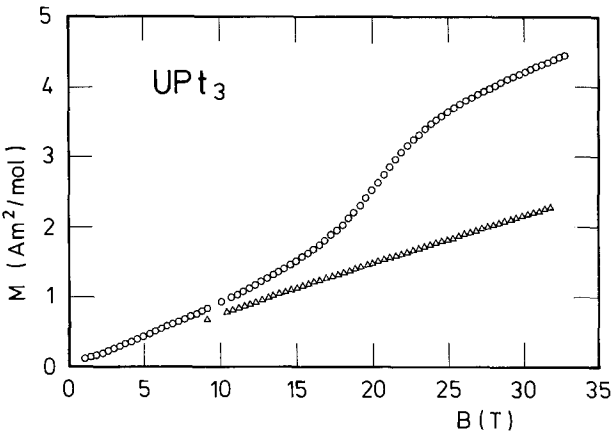

Fig. 52. Magnetization plotted against magnetic field, applied parallel to the hexagonal (a, b) plane, for UPt_3 at $T = 4.2$ K (○) and 77 K (△). Note that in the 4.2 K data, there is no anisotropy within the (a, b) plane (cf. fig. 53), while $M(B)$ for $B \perp (a, b)$ is almost linear, with a slope even somewhat smaller than for the a-axis data at 77 K (Franse et al. 1984).

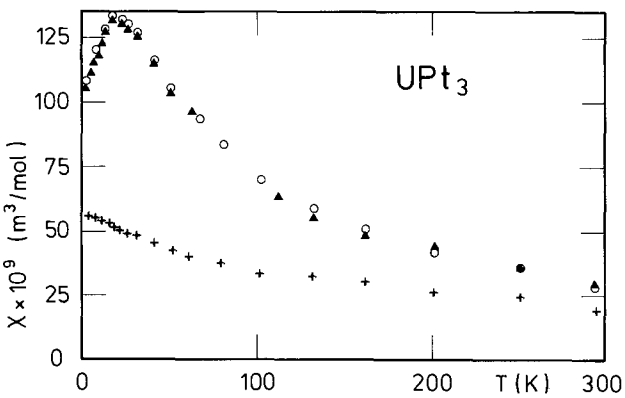

Fig. 53. Susceptibility, $\chi(T)$, of UPt_3, measured in magnetic fields up to 1.3 T along the a-axis (○), the b-axis (▲) and the c-axis (+) (Franse et al. 1984).

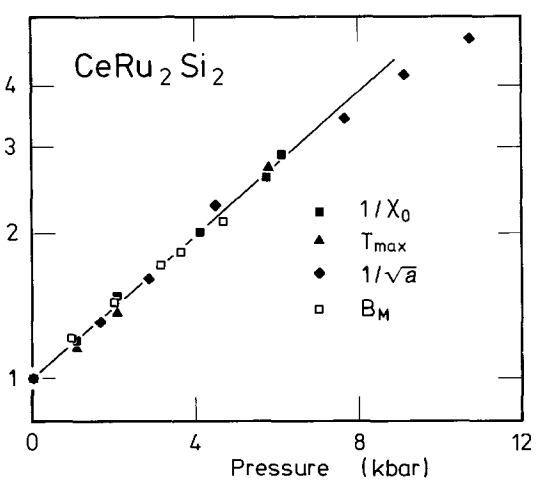

Fig. 54. Normalized pressure dependences of inverse (as $T \to 0$) susceptibility χ_0^{-1}, position of $\chi(T)$ maximum, T_{max}, inverse square root of low-T resistivity coefficient, $a^{-1/2}$, and metamagnetic field, B_M, for $CeRu_2Si_2$. Solid line indicates $\partial \ln T^* / \partial p = 171\ \text{Mbar}^{-1}$. Note logarithmic scale on vertical axis (Mignot et al. 1988).

3.3. *Local-moment magnetism* ($T_m > T^*$)

Although heavy-fermion systems display a whole variety of magnetic phenomena in the full span between the two characteristic cases discussed above, one can assign many of the systems roughly to one of them. Table 2 lists some typical properties of local-moment systems. The intermediate γ-values above the magnetic transition temperature T_m point to moderate renormalizations for band electrons well above $T^*(<T_m < T_{RKKY})$. γ (as $T \to 0$) is usually somewhat lower due to the reduced density of excitations in the magnetically ordered phase. The ordered moments are correspondingly smaller than the free-ion values in the proper CF ground state.

TABLE 2

Characteristics of some "local-moment" magnets: T^*, lattice-Kondo temperature; a-T_m, f-T_m, antiferromagnetic, ferromagnetic ordering temperatures; $\gamma(2T_m)$ and $\gamma(T \to 0)$, Sommerfeld coefficients in the paramagnetic and magnetically ordered phases; $\bar{\mu}_s/\mu_B$, averaged ordered moment per f-ion, in units of μ_B; nd, not determined.

System	T^* (K)	T_m (K)	$\gamma(2T_m)$ (J/K^2 mol f-ion)	$\gamma(T \to 0)$	$\bar{\mu}_s/\mu_B$
$CeAl_2$	3.5[a,*]	a-3.9[a]	0.16[b]	0.135[a]	0.63[c]
CeB_6	3[d]	a-2.35[e,f,g]	0.60[h,§]	0.26[i]	0.65[d]
$CeIn_3$	100[j,**]	a-10.2[j]	0.04[k]	0.05[k]	0.48[l]
$CeCu_2$	10[m]	a-3.5[m]	0.20[n]	0.082[m]	nd
$CeSi_x$ $x = 1.7$	17[o]	f-10.9[o]	nd	0.075[o]	0.5[p]
$CeSi_x$ $x = 1.8$	17[o]	f-9.0[o]	nd	0.23[o]	nd
CeT_2Si_2 T = Ag	5[q]	a-10[r]	nd	nd	nd
CeT_2Si_2 T = Au	nd	a-10[r]	nd	nd	1.29[r]
CeT_2Si_2 T = Pd	nd	a-10[r]	nd	nd	0.62[r]
CeT_2Ge_2 T = Cu	7[s]	a-4.1[t]	0.09[s]	0.10[t]	0.74[u]
CeT_2Ge_2 T = Ag	3[q]	a-5[v]	nd	0.033[w]	nd
CeT_2Ge_2 T = Au	<2[q]	a-15[v]	0.10[s,**]	0.02[w]	nd
CeT_2Ge_2 T = Ru	<2[q]	f-7.5[v]	0.04[s]	0.02[v]	nd
UCd_{11}	nd	a-5[x]	1.42[x,**]	0.25[x]	nd
U_2Zn_{17}	nd	a-9.5[y]	0.42[y,†] 0.24[z,††]	0.20[y]	0.8[α]

[a]Bredl et al. (1978a); [b]Bredl et al. (1978b); [c]Barbara et al. (1977); [d]Horn et al. (1981b); [e]Felsch and Winzer (1978); [f]Kawakami et al. (1980); [g]Schefzyk et al. (1985b); [h]Komatsubara et al. (1980); [i]Bredl (1987); [j]Lawrence (1982); [k]Elenbaas (1980); [l]Benoit et al. (1980); [m]Gratz et al. (1985); [n]Gratz et al. (1988); [o]Satoh et al. (1982); [p]Sato et al. (1985); [q]Loidl et al. (1989a); [r]Grier et al. (1984); [s]Felten (1987b); [t]de Boer et al. (1987); [u]Knopp et al. (1989); [v]Böhm et al. (1988); [w]Caspary (1988); [x]Fisk et al. (1984); [y]Ott et al. (1984a); [z]Gschneidner et al. (1989); [α]Broholm et al. (1987a).

* Derived from $T^* = 5$ K [as obtained from the residual quasielastic neutron line width (HWHM) as well as by using a resonance level model[a] via $T^* = T_K/0.68$, T_K corresponding to the Bethe-ansatz results, see Andrei et al. (1983)], in line with the definition used throughout this article.

** Probably masked by CF effects.

§ Influenced by quadrupolar ordering at 3.3 K.

† From $C_{U_2Zn_{17}} - C_{Th_2Zn_{17}}$.

†† From $C_{U_2Zn_{17}} - C_{Th_2Zn_{17}} - C_{Schottky}$.

Heavy-fermion magnets with well defined local moments usually exhibit some antiferromagnetic type of order. This fact is in accord with the considerable band-electron contributions to the effective exchange interactions. There is no a priori reason, however, to exclude ferromagnetism, and, in fact, a few heavy-fermion ferromagnets exist, e.g., $CeSi_x$, $x < 1.85$ (Yashima et al. 1982), $CeCu_2$ (Gratz et al. 1985) and $CeRu_{2.16}Ge_2$ (Böhm et al. 1988). Recently, even spin-glass behaviour in two heavy-fermion systems containing a periodic array of magnetic moments on the 4f-shells, i.e., $CePd_3B_{0.3}$ with $\gamma \simeq 250\,\mathrm{mJ\,K^{-2}\,mol^{-1}}$ (Dhar et al. 1990) and $CePtGa_3$ with $\gamma \simeq 120\,\mathrm{mJ\,K^{-2}\,mol^{-1}}$ (Tang et al. 1990) has been reported. It is ascribed to variations in the exchange interactions due to disorder on neighbouring non-magnetic lattice or institial sites, similar to what was found earlier for $CeCu_{6.5}Al_{6.5}$ (Rauchschwalbe et al. 1985c).

The anisotropy of the RKKY interaction usually leads to rather complex magnetic structures. In particular, nesting of the Fermi surface can have dramatic effects. An exemplary system is $CeAl_2$ (Steglich et al. 1979b): its spin arrangement displays a type-II antiferromagnetic structure in which the magnetic moments are parallel to [111] and point into opposite directions on the lattice sites $(0,0,0)$ and $(\frac{1}{4},\frac{1}{4},\frac{1}{4})$. The moments are modulated by an incommensurate wavevector $(\frac{1}{2}+\tau,\frac{1}{2}-\tau,\frac{1}{2})$ with $\tau = 0.11$ (Barbara et al. 1977).

High-resolution measurements of the thermal-expansion coefficient $\alpha(T)$, see fig. 55, revealed two closely spaced phase transitions of second order (Schefzyk, et al. 1985a). A positive jump $\Delta\alpha_1 = \alpha(T_{N_1} - \delta) - \alpha(T_{N_1} + \delta) > 0$ is recognized

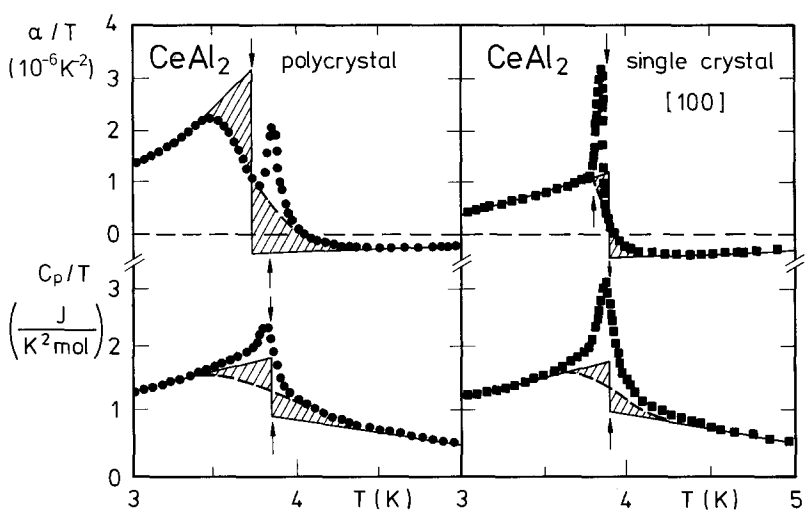

Fig. 55. Thermal expansion as α/T plotted against T (top) and specific heat as C_p/T plotted against T (bottom) for polycrystalline (left) and single-crystal (right) $CeAl_2$ samples. The measurement of α on a single crystal was done along [100]. Dashed lines give interpolations between high- and low-temperature data points, and solid lines are used to replace broad transitions by idealized sharp ones at T_{N_1} (with positive jumps $\Delta\alpha_1$ and ΔC_{p1}), respectively. A second sharper transition at T_{N_2} is characterized by $\Delta\alpha_2 < 0$ and $\Delta C_{p_2} > 0$. T_{N_1} and T_{N_2} are indicated by arrows pointing downwards and upwards, respectively (Schefzyk et al. 1985a).

for the broader transition at T_{N_1}, whereas the sharper transition at T_{N_2} leads to a negative jump $\Delta\alpha_2 < 0$. A corresponding structure in the specific heat (Schefzyk et al. 1985a) can be decomposed into two phase transition anomalies with positive ΔC_1 and ΔC_2. Ehrenfest's relation

$$t_p \equiv \frac{1}{T_N}\left(\frac{dT_N}{dp}\right)_{p=0} = \frac{3\,\mathrm{Vol}\,\Delta x}{\Delta C_p} \tag{23}$$

predicts an increase of T_{N_1} under low pressure and a decrease of T_{N_2}. Thereby a puzzle is resolved concerning the pressure dependence of the magnetic phase transition of $CeAl_2$: whereas specific-heat measurements (Berton et al. 1977) yielded a positive pressure derivative of the phase-transition temperature with t_p close to t_{p1} as derived from $\Delta\alpha_1$, susceptibility data (Barbara et al. 1979, Croft et al. 1979) furnished a negative derivative with t_p close to t_{p2}. Neutron diffraction finally proved (Barbara et al. 1980) that T_{N_2} is associated with the formation of a sinusoidal wave. Lattice defects destroy this modulation as seen from the disappearance of the corresponding satellites. Instead, a magnetic Bragg reflex appears which is associated with the underlying type-II structure. As a result of non-hydrostatic pressure conditions the same happens for pressures $p > 10$ kbar, proving again the high sensitivity of the modulation to lattice imperfections (Barbara et al. 1980). Similar observations in the thermal-expansion measurements led to the characterization of T_{N_1} as the transition temperature for type-II ordering and to the schematic phase diagram shown in fig. 56. The phase diagram is surprisingly consistent with recent specific-heat measurements under external pressures up to 16 kbar, which reveal a maximum in $T_{N_1}(p)$ about $p = 8$ kbar (Hanke 1988, Hanke and Eichler 1989). This maximum has been attributed to a competition between a pressure-induced increase in the indirect- exchange-coupling constants and a decrease of the effective Ce moment. There exists, on the other hand, no such simple explanation for the observed depression of T_{N_2}.

Nesting of the Fermi surface, the probable cause for the incommensurate

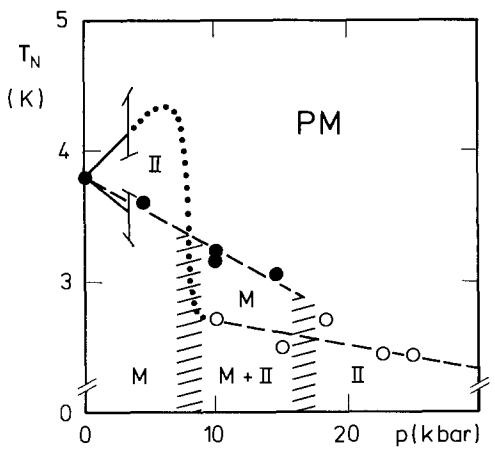

Fig. 56. Magnetic phase diagram of $CeAl_2$ as derived from thermal expansion (solid lines, Schefzyk et al. 1985a) and neutron diffraction (●, ○, dashed lines; Barbara et al. 1980). Dotted line is an interpolation (schematic); II, type-II antiferromagnetic structure; M, modulated structure; PM, paramagnetic phase.

modulated magnetic ground state of $CeAl_2$, has been demonstrated in dHvA measurements for the reference compound $LaAl_2$ (Seitz 1978, Seitz et al. 1979). Long-range antiferromagnetic order in the quasibinary system $La_{1-x}Ce_xAl_2$ already develops at low Ce concentrations: for 10 at.% Ce a T_N of 80 mK is observed (Felsch et al. 1975). It has to be attributed to interactions between random short-range pairs of Ce ions since T_N scales with x^2. For such paired ions, Kondo compensation seems to be suppressed due to mutual interactions and a net moment remains (cf. Tournier 1974). A highly diluted random system of magnetic moments could presumably not establish a regular magnetic structure without a prescribed modulation in the system of band electrons. It thus seems probable that the observed nesting is important and persists even for increasing Ce concentration x when the magnetic state of stoichiometric $CeAl_2$ forms.

We now come to actinide-based compounds. Although UCd_{11} (Fisk et al. 1984) and U_2Zn_{17} (Ott et al. 1984a) have traditionally been discussed in terms of 5f-band formation, we would rather put them into the class of metals with an spd-conduction band hybridizing with well localized 5f-states (Siegrist et al. 1986, Fischer et al. 1987, Olivier et al. 1987, Broholm et al. 1987a). We suggest that this hybridization is not well taken into account by transforming to new conduction bands in order to diagonalize the one-particle part of the Hamiltonian alone. Instead, the essential point for the low-temperature behaviour seems to be, in fact, the generation of a new energy scale k_BT^* via many-body effects. Despite some earlier experimental evidence (Schlabitz et al. 1980, Frick et al. 1982, 1985), this T^* has traditionally not been investigated in these compounds, but there exist some positive indications from theoretical studies including the concept of an "intrinsic" f-band width from a many-body point of view (Pruschke 1989).

It, therefore, seems appropriate to use the same classification scheme as outlined above for actinide systems. According to the specific-heat data above the Néel temperature short-range correlations, as indicative of local-moment behaviour, seem to be present in UCd_{11}, see fig. 57 (Fisk et al. 1984). Similar to $CeAl_2$ (cf. fig. 43), one observes a shoulder in $C(T)/T$ on the low-T side of the phase-transition anomaly that supports an interpretation in terms of a more

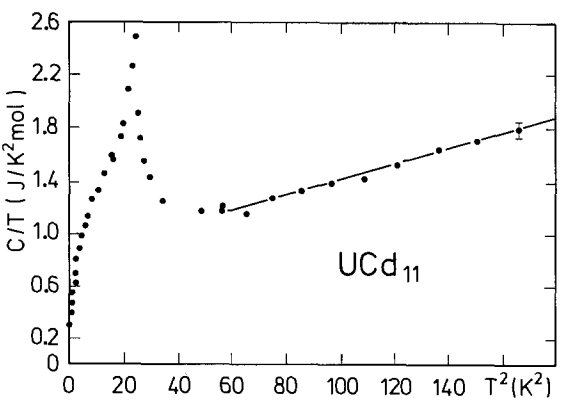

Fig. 57. Specific heat of UCd_{11} as C/T plotted against T^2 (Fisk et al. 1984). Straight solid line indicates a temperature dependence of the specific heat following $C = \gamma T + \beta T^3$ ($T > 7.5$ K).

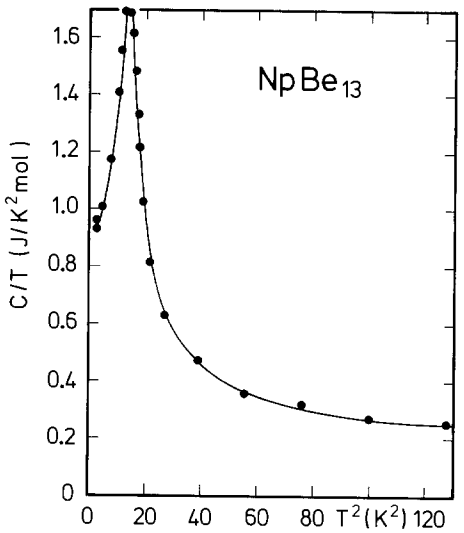

Fig. 58. Specific heat of $NpBe_{13}$ as C/T against T (Stewart et al. 1984b). Solid line is guide to the eye.

complicated magnetic structure. We, thus, assume that the yet unknown value of T^* is smaller than $T_m^{(h)}$ and put UCd_{11} in the class of local-moment magnets.

Considering the specific-heat results of $NpBe_{13}$ (Stewart et al. 1984b) in fig. 58, it seems to be difficult to distinguish any T-dependence of γ from the initial increase above the magnetic phase transition at $T_N = 3.4$ K. This compound seems to be similar to UCd_{11}. The record value of γ (as $T \to 0$) $= 0.9\,\mathrm{J\,K^{-2}\,mol^{-1}}$ implies a rather low T^* value ($\lesssim T_N$) and a considerable admixture of local degrees of freedom to the quasi-particles. Therefore it is listed in table 3. An entropy of about 40% of $R \ln 2$ is released at the phase transitions (Stewart et al. 1984b).

At a first inspection of the specific-heat results for U_2Zn_{17} (fig. 59), i.e., the nearly T-independent value of $\gamma \simeq 500\,\mathrm{mJ/K^2}$ mol-U above $T_N = 9.5$ K, seem to

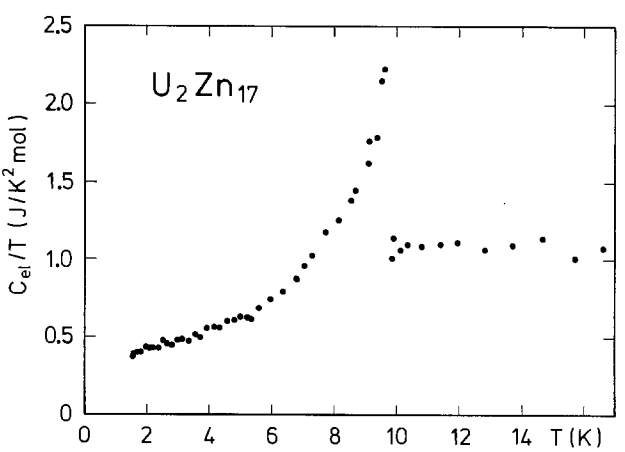

Fig. 59. Electronic specific heat of U_2Zn_{17} as C_{el}/T plotted against T (Ott et al. 1984a).

TABLE 3
Characteristics of "heavy-fermion antiferromagnets". Symbols as in table 2, with T_N instead of T_m.

System	T^* (K)	T_N (K)	$\gamma(2T_N)$ (J/K^2 mol f-ion)	$\gamma(T\to 0)$	$\bar{\mu}_S/\mu_B$
$CePb_3$	15[a]	1.1[a]	0.83[a]	1.00[a]	<0.55[b]
$CeAl_3$	4[c,*]	1.6[d]	0.67[c]	1.25[e]	0.5[f]
non-superconducting +	7[g,*]	3.5[h]	<0.2[h]	0.3[h]	nd
$CeCu_2Si_2$ superconducting	10[g,*]	0.6[i]–0.8[j]	0.60[h]	0.60*	≃0.1[j]
$Ce_{0.9}La_{0.1}Ru_2Si_2$	11[k]	2.7[l]	0.34[k]	>0.63[k]	0.85[l]
$Ce(Cu_{0.9}Ag_{0.1})_6$	nd	0.65[m]	0.70[m]	nd	nd
U_2Zn_{17}	nd	9.5[n]	0.42[n]	0.20[n]	0.8[o]
URu_2Si_2	70[p]	17[q,r,s]	0.12[t]	0.065(0.55^{++})[q]	0.03[u]
UPt_3	80[v]	5[w]	0.36[x]	0.425^{+++}	0.02[w]
$U(Pt_{0.95}Pd_{0.05})_3$	nd	5.8[x]	0.32[x]	≃0.48[x]	0.6[y]
$(U_{0.95}Th_{0.05})Pt_3$	nd	6.5[z]	0.36[z]	≃0.48[z]	0.65[w]
$(U_{0.97}Th_{0.03})Be_{13}$	nd	0.4[α]	0.80[β,δ]	≃2.30[ε,†]	<0.01[α]
$NpSn_3$	nd	10[φ]	0.245[φ]	0.10[φ]	0.3[φ]
$NpBe_{13}$	nd	3.4[λ]	0.40[λ]	0.90[λ]	nd

[a]Lin et al. (1985); [b]Vettier et al. (1986); [c]deBoer et al. (1985); [d]Jaccard et al. (1988); [e]Bredl et al. (1984a); [f]Schenck (1988); [g]Bredl et al. (1985); [h]Steglich (1985a); [i]Nakamura et al. (1988); [j]Uemura et al. (1989); [k]Besnus et al. (1987); [l]Quezel et al. (1988); [m]Fraunberger et al. (1989); [n]Ott et al. (1984a); [o]Broholm et al. (1987a); [p]Rauchschwalbe (1987);[q]Schlabitz et al. (1986); [r]Palstra et al. (1985); [s]Maple et al. (1986); [t]Renker et al. (1987b); [u]Broholm et al. (1987b); [v]Rietschel et al. (1988); [w]Aeppli et al. (1988); [x]de Visser et al. (1987); [y]Frings et al. (1987); [z]Batlogg et al. (1987); [α]Heffner et al. (1989); [β]Ott et al. (1985a); [δ]Mayer et al. (1986b); [ε]Rauchschwalbe et al. (1987c); [φ]Trainor et al. (1976); [λ]Stewart et al. (1984b).

[+] Single crystal.

[++] Extrapolated from the paramagnetic regime.

[+++] See table 1.

[†] Extraploated from finite-field data to $B = 0$ T.

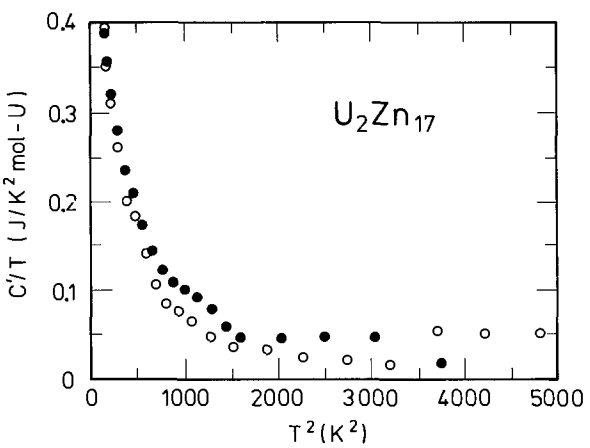

Fig. 60. C'/T plotted against T for two U_2Zn_{17} samples at $T > 11$ K. $C' = C_{U_2Zn_{17}} - C_{Th_2Zn_{17}} - C_{Schottky}$ (Gschneidner et al. 1990).

contradict the relatively large ordered moments ($0.8\ \mu_B$/U) and the considerable transition entropy found in the magnetically ordered low-temperature state: a saturated $\gamma(T)$ would suggest that Fermi-liquid formation is complete and that the moments are screened. This discrepancy has recently been resolved via specific-heat experiments to elevated temperatures (Fischer et al. 1987). These suggest the existence of CF levels (two doublets at $0k_B$ K and $91k_B$ K, and an excited sextet at $164k_B$ K). Subtraction of the corresponding Schottky contribution and the phonon term, as obtained for Th_2Zn_{17} (Fischer et al. 1987), leaves a $\gamma(T)$ curve (Gschneidner et al. 1990) that just above T_N has a negative slope as pronounced as for typical Ce-based heavy-fermion compounds, fig. 60. In conclusion, we also assign U_2Zn_{17} to the class of local-moment magnets. One has to realize, however, that the case of U_2Zn_{17} also features some signs of itinerancy, i.e., the mean-field-like transition and the extreme sensitivity to impurities (Ott 1987), so that as in other cases an intermediate picture might be appropriate.

3.4. *Magnetism of heavy quasiparticles* ($T^* > T_m$)

In this section, heavy-fermion magnets are discussed that show a considerable influence of quasiparticle renormalization. The magnetic degrees of freedom, originally connected with the local moments have, to a large extent, been transferred to the itinerant heavy quasiparticles. Thus, the signature of the materials listed below is a strongly reduced magnetic moment and a large γ-coefficient in the electronic specific heat. We list some of the interesting materials in table 3.

Among Ce compounds, $CePb_3$ seems to provide an excellent example for the scenario outlined above: $T^* \simeq 15$ K (Renker et al. 1987a) is larger than $T_m \simeq 1$ K (Lin et al. 1985), the moment is reduced by about an order of magnitude (Vettier et al. 1986), and $\gamma \simeq 1\ \mathrm{J\ K^{-2}\ mol^{-1}}$ as $T \to 0$ is very large and only slightly reduced compared to the low-T paramagnetic value, see fig. 61. The magnetic order found by neutron diffraction is anisotropic and modulated as is the magnitude of the small ordered moments (Vettier et al. 1986).

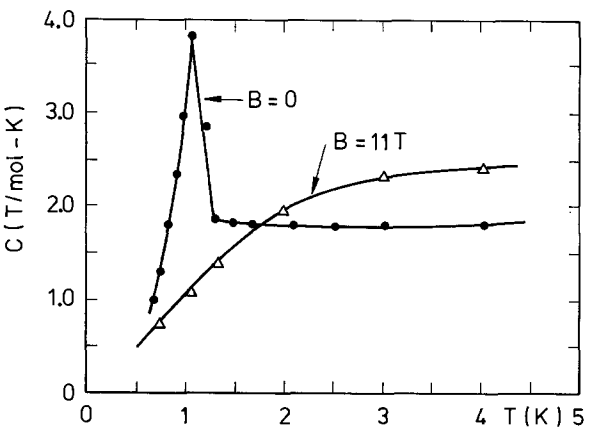

Fig. 61. Specific heat of $CePb_3$ as a function of temperature at B = 0 and 11 T (Lin et al. 1985). Lines through data points are guides to the eye.

For stoichiometric non-superconducting $CeCu_2Si_2$ single crystals the situation is not so clear. A rounded peak in the specific heat near 3.5 K seems indicative of an inhomogeneously broadened magnetic bulk ordering phenomenon (Stewart et al. 1983, Steglich 1985a). The form of the DC susceptibility peak and its intensitivity against applied magnetic fields of order 1 T seem to exclude a spin-glass phenomenon, see fig. 62. Spin-glass effects, on the other hand, may easily be generated by substituting La for Ce (Aliev et al. 1984) or by removing a few at.% of Cu (Rauchschwalbe et al. 1985a). Measurements of the specific-heat in fields as high as 10 T point to the importance of ferromagnetic short-range order (presumably in the basal Ce planes) up to approximately $T \simeq 15$ K ($\simeq T^*$) (Andraka et al. 1989). We suggest that the $C(T)$ and $\chi(T)$ peaks near 3.5 K are connected with the three-dimensional antiferromagnetic alignment of the ferromagnetically ordered sheets. In our rough classification scheme of magnetic phenomena these $CeCu_2Si_2$ single crystals should be assigned to the crossover region.

A similar statement could be made for the system CePtSi, where however a low-T $\gamma(T)$ peak near 0.35 K indicates the formation of coherent heavy-fermion bands (Rebelsky et al. 1988). The maximum near 2 K and a peak in χT at the same temperature was attributed again to an interplay between ferromagnetic and antiferromagnetic ordering tendencies in the system (Rebelsky et al. 1988, Hamzic et al. 1988).

Recently, magnetic behaviour has also been detected in $CeAl_3$, which was formerly considered to provide the prototype of a heavy Fermi-liquid ground state (Barth et al. 1987). So far, one has the following three indications:

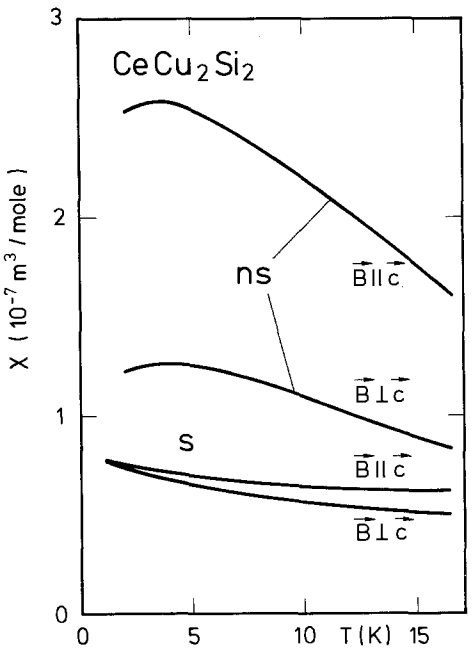

Fig. 62. DC susceptibility as a function of temperature of non-superconducting (ns) and superconducting (s) $CeCu_2Si_2$ single crystals measured with the magnetic field parallel and perpendicular to the tetragonal c-axis (Steglich 1985a).

(i) A maximum at 0.7 K occurs in the susceptibility (Andres et al. 1975), see fig. 63.

(ii) At this temperature, transverse muon-spin rotation (μSR) reveals a "quasi static" magnetic field of 220 G originating from the Ce atoms in the neighbourhood of the interstitial muon. This translates into an average magnetic moment of 0.5 μ_B/Ce (Schenck 1988). A μSR line symmetric to the muon Larmor frequency $\nu_\mu = 0$ develops already at 1.5 K and has been ascribed to "short-range order effects" (Barth et al. 1987, 1988).

(iii) A T^3-dependence of the electrical resistivity between 0.3 K and 1 K for one $CeAl_3$ single crystal is observed and may be interpreted via scattering off spin-wave excitations in a modulated structure (Jaccard et al. 1987), similar to earlier observations with $CeAl_2$ (Sparn et al. 1985).

The absence of a phase-transition anomaly in the specific heat could be explained in two ways:

(a) $CeAl_3$ may be a clear-cut example of itinerant antiferromagnetism of heavy quasiparticles that is supported by a "coherence"-derived peak in $\gamma(T)$ (Benoit et al. 1981, Bredl et al. 1984a) and a T^2-dependence of the resistivity below 0.3 K (Andres et al. 1975) and, thus, may not set free enough entropy at the phase transition. The size of the saturated moment (0.5 μ_B: Schenck 1988) makes this picture somewhat fortuitous, however.

(b) $CeAl_3$ may display a competition between different magnetic tendencies in a way similar to the materials discussed before and, thus, may not develop long-range order at all. As a final caveat we mention the possibility of spin-glass effects contributing to these experimental data.

Zero-field and longitudinal-field μSR measurements on $CeCu_2Si_2$ (Uemura et al. 1989) have indicated the onset of static magnetic correlations below $T_m \simeq 0.8$ K. A sharp disappearence of the ^{63}Cu-NMR line near 0.6 K for magnetic fields $B \geqslant 1.2$ T points to a kind of transition, possibly to a magnetic state with short- or

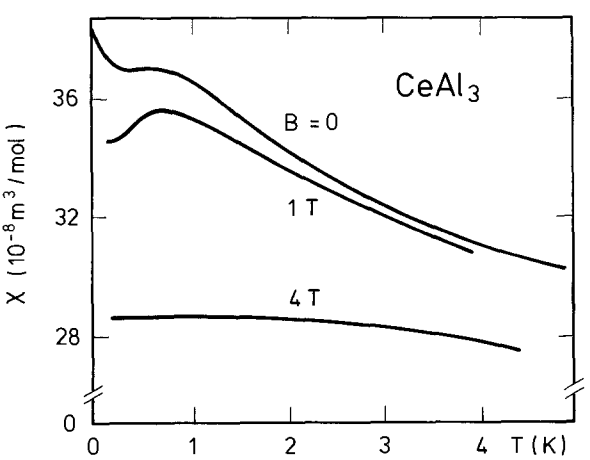

Fig. 63. Zero-field, low-frequency AC susceptibility of $CeAl_3$ at $B = 0$, 1 at 4 T. The low-T upturn in the $B = 0$ results is due to a Ce^{3+} "impurity contribution" which is saturated in a field of 1 T (de Boer et al. 1985).

long-range order and coexisting with superconductivity (Nakamura et al. 1988, 1990). Ultrasound (Bruls et al. 1990) and dilatation (Steglich et al. 1990, Assmus et al. 1990) studies on new $CeCu_2Si_2$ single crystals (Sun et al. 1990) reveal a surprising sample independence of the corresponding transition temperature T_m ($\simeq 0.63$ K) for $B = 0$, which coincides with T_c for the best superconducting samples. For other samples, $T_c < T_m$. Figure 64 shows the phase diagram of $CeCu_2Si_2$ in a T against B representation. It suggests that an anomalous and hitherto unexplained feature, as discovered in the isothermal magnetoresistivity curves (Rauchschwalbe et al. 1987a), is connected with this new transition in n-state $CeCu_2Si_2$. In a similar way anomalies in the resistivity as a function of magnetic field in $CeAl_3$ give rise to a kind of B–T diagram (Jaccard et al. 1988). This example shows that such lines should not necessarily be considered as separating thermodynamic phases. They may also reflect the freezing of short-range order correlations.

Some speculation may arise from the fact that in $CeCu_2Si_2$ the two lines separating normal Pauli paramagnetic states from magnetic and superconducting states for $B \to 0$ approach each other at 0.63 K. Furthermore, the peak in the coefficient γ of the n-state specific-heat occurs in the same temperature regime, i.e., at 0.4 K, see fig. 64. In $CeAl_3$ there is a similar but somewhat larger difference between the position of this $\gamma(T)$ peak (Bredl et al. 1984) and the temperature at which the magnetism-related features are observed (Barth et al. 1987, Jaccard et al. 1988). This order-of-magnitude agreement between the two temperatures could be used as an argument for the idea (Doniach 1987b) that the $\gamma(T)$ peak is caused by freezing of magnetic fluctuations in the vicinity of a

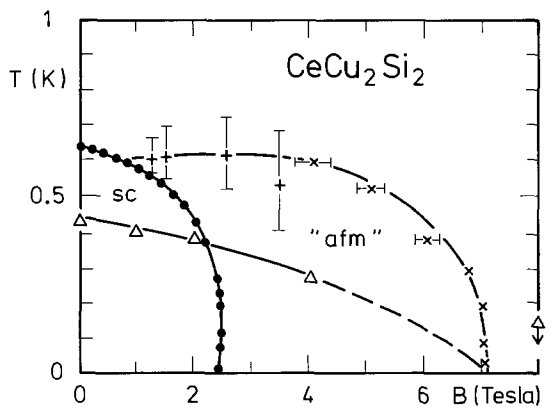

Fig. 64. Temperature–magnetic-field diagram for $CeCu_2Si_2$ indicating superconducting (sc) (●; Steglich et al. 1984) and cooperative magnetic ("afm") regimes as deduced from NMR (+, Nakamura et al. 1988) and magnetoresistivity (×, Rauchschwalbe et al. 1987a) results. Also shown are positions of the $\gamma(T)$ maxima for a bulk superconducting sample (according to its Meissner effect) that is lacking any specific-heat anomaly at T_c and, therefore, exhibits a quasiparticle DOS that is almost identical with that in the normal heavy-fermion state (△, Bredl 1985). Results of single crystals (●, ×) and polycrystalline samples (+, △) are included.

magnetic SDW phase transition. We would, however, prefer an interpretation of the order-of-magnitude agreement which is not built on magnetic long-range order as a driving mechanism. Instead, we stress again the importance of coherence and the common role of the underlying energy scale T^* for all of these phenomena. Certainly, superconductivity and the hypothetical SDW phase both need the Fermi-liquid regime with well defined itinerant quasiparticles as a prerequisite. In forming the Kondo-lattice ground state, local Kondo fluctuations and non-local magnetic fluctuations are typically frozen in on the same temperature scale (cf. fig. 54). Only then is the coherent regime reached. An applied external magnetic field consequently perturbates the ordering phenomena roughly in the same way as demonstrated by the similar shape of the curves in fig. 64.

Like $CeAl_3$ and $CeCu_2Si_2$, UPt_3 has been viewed until recently as a non-magnetic heavy-fermion system. Thorough neutron-diffraction measurements (Aeppli et al. 1988) have revealed, however, the development of antiferromagnetic long-range order starting at $T_N \simeq 5\,K$. The magnetic order parameter, as taken from the $(\frac{1}{2}, 0, 1)$ scattering intensity, levels out at the superconducting transition temperature with a value corresponding to an ordered moment of $0.02\,\mu_B/U$. For the $(1, \frac{1}{2}, 0)$ scattering intensity at $B < 1\,T$, even the destructive influence of superconductivity on the magnetic order parameter can be found (Aeppli et al. 1989), fig. 65. Whether the same electrons can provide both phenomena, implying that magnetic order can sustain an incomplete pseudo-gap

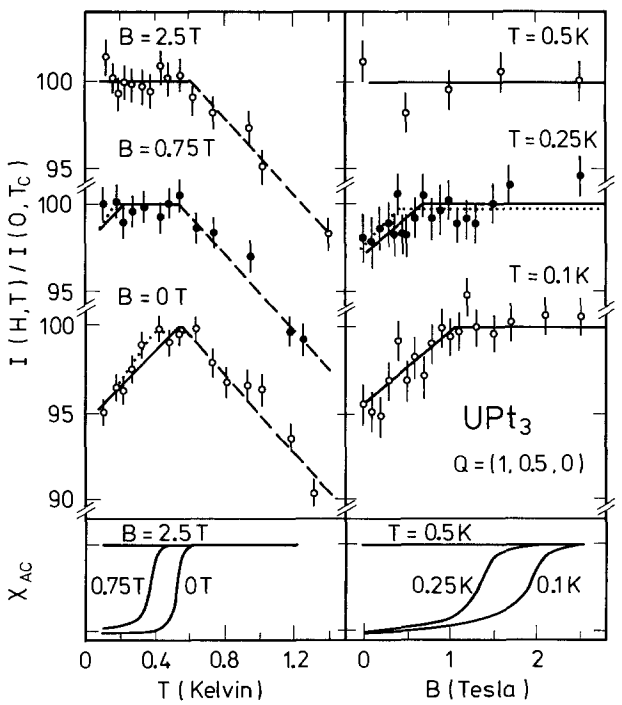

Fig. 65. Normalized and background-corrected temperature (left) and field-dependent (right) $(1, \frac{1}{2}, 0)$ magnetic Bragg intensities (top) and ac susceptibilities (bottom) (Aeppli et al. 1989).

in the quasiparticle-excitation spectrum or whether the coexistence rests upon the formation of a SDW connected with the opening of a gap on one part of the Fermi surface and superconductivity using the rest of the Fermi surface is not known today. Whereas this is a speculation in the case of UPt_3, one has more reason to believe in such a scenario for URu_2Si_2, as discussed below.

Information about the influence of various kinds of dopants on the ground-state properties of UPt_3 is contained in fig. 66 (Batlogg et al. 1987). An increase in the hexagonal distortion as measured by the c/a ratio leads to weaker quasiparticle renormalization and to a suppression of both types of order. A reduction of c/a, on the other hand, favours the SDW instability at the cost of superconductivity. At the same time magnetism gains a more localized character as indicated by the growth of both the ordered moment up to $0.6\,\mu_B$/U (Aeppli et al. 1988) and the change of entropy at the magnetic transition up to approximately $0.1R\ln 2$ (Batlogg et al. 1987, de Visser et al. 1987). We believe that, consistent with the behaviour under pressure, an increase of c/a (meaning a smaller unit-cell volume) is the predominant effect for Ir doping. It raises T^* as shown by the decrease of both the susceptibility and γ ($260\,\mathrm{mJ\,K^{-2}\,mol^{-1}}$), and partially strips the quasiparticles of their heavy masses. Th, Au and Pd (de Visser et al. 1986, Stewart et al. 1986, Batlogg et al. 1987) impurities predominantly seem to lead to the formation of localized moments and thus increase the tendency towards magnetism. In this case coherence and thus superconductivity is suppressed. The specific-heat curve of Th-doped UPt_3 is mean-field like at the transition (Ramirez et al. 1986) so that presumably the itinerant regime applies and the exponential decay seen at the low-T side of the phase-transition anomaly should be assigned to a SDW gap on part of the Fermi surface (fig. 67). This point of view is supported by a slight increase in the resistivity upon cooling through T_N (Ramirez

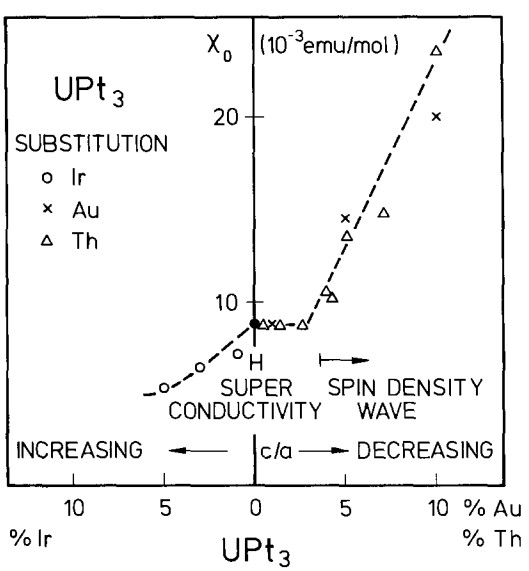

Fig. 66. Intrinsic low-temperature susceptibility of UPt_3 (●) and of quasibinary $(U_{1-x}M_x)Pt_3$ alloys for different dopants as a function of concentration x (in at.%) (Batlogg et al. 1987).

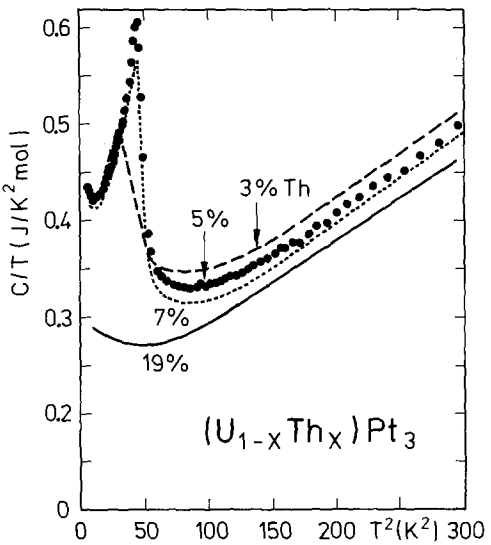

Fig. 67. Specific heat of $(U_{1-x}Th_x)Pt_3$ as C/T plotted against T^2 for different Th concentrations (in at.%) (Ramirez et al. 1986).

et al. 1986) similar to the well-known itinerant antiferromagnet Cr. It is remarkable and consistent with the itinerant picture that this influence of impurities in UPt_3 essentially concerns the formation of local magnetic moments and preserves the characteristic wavevector recognized in the pure material (Aeppli et al. 1988). A similar observation was made in $CeRu_2Si_2$, in which the wavevector characteristic for short-range correlations also characterizes the long-range antiferromagnetic order as induced by doping with La (Quezel et al. 1988).

For UBe_{13}, specific-heat results support the existence of an antiferromagnetically ordered state below about $T = 150$ mK and at fields $B \gtrsim 2$ T (Brison et al. 1988). The observed low-T upturn in $C(T)/T$ strongly increases with magnetic field suggesting that the antiferromagnetic state develops in the normal regions, i.e., in the vortex cores of the Shubnikov phase. Ending in a true maximum at 95 mK for $B = 6$ T, the upturn is likely to balance the enhanced entropy in the superconducting state as inferred from previous results (Ott et al. 1984b, Mayer et al. 1986a). Thermopower experiments (Jaccard et al. 1988) on UBe_{13} indicate that under pressure the magnetically ordered state spreads out over several kelvins (for 67 kbar), while both the Sommerfeld coefficient γ and T_c become depressed. This in accord with the observation by Fisk et al. (1985) that large γ_v-values (per volume) are characteristic of heavy-fermion superconductors, while magnetic ordering is favoured for somewhat reduced values of γ_v. It should be noted that for UBe_{13} doped at 3 at.% Th, according to μSR results (Heffner et al. 1987, 1989) an extremely small ordered magnetic moment μ_S ($<10^{-2}\,\mu_B/U$) and a mean-field-type T-dependence of $\mu_S(T)$ appears below a temperature coinciding with the lower superconducting transition temperature (Ott et al. 1985a), see sect. 4.4. Finally, the situation has become even more bizar by a recent report of antiferromagnetism, presumably also with very small μ_s in pure UBe_{13} at T_{max} as high as 8.8 K (Kleiman et al. 1990).

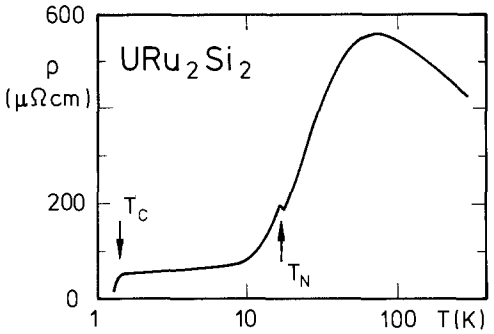

Fig. 68. Electrical resistivity of URu_2Si_2 as a function of temperature (on a logarithmic scale). Arrows mark onset of antiferromagnetism (T_N) and superconductivity (T_c) (Schlabitz et al. 1986).

The resistivity curve of URu_2Si_2 in fig. 68 displays three distinct anomalies associated with different energy scales: $T_{max} \approx 50$ K indicates the gradual transition from incoherent to coherent scattering, below $T_N = 17$ K an antiferromagnetically ordered state is formed, whereas superconductivity develops and coexists (Schlabitz et al. 1986, Palstra et al. 1985, Maple et al. 1986) with antiferromagnetism below $T_c \approx 1$ K. The specific-heat results of fig. 69 (Renker et al. 1987b) imply two additional features, i.e., a broad maximum near 30 K and a nearly exponential decay of $\Delta C(T)$, the 5f-derived contribution, below T_N. These results are utilized to support two conflicting interpretations of the extremely low ordered U moments, $\mu \approx 0.03\ \mu_B$/U, derived from neutron diffraction results on single crystals (Broholm et al. 1987b). The most frequently used interpretation relates the exponential T-dependences of the specific-heat below T_N to a SDW state associated with a gap on part of the Fermi surface (Maple et al. 1986). It is

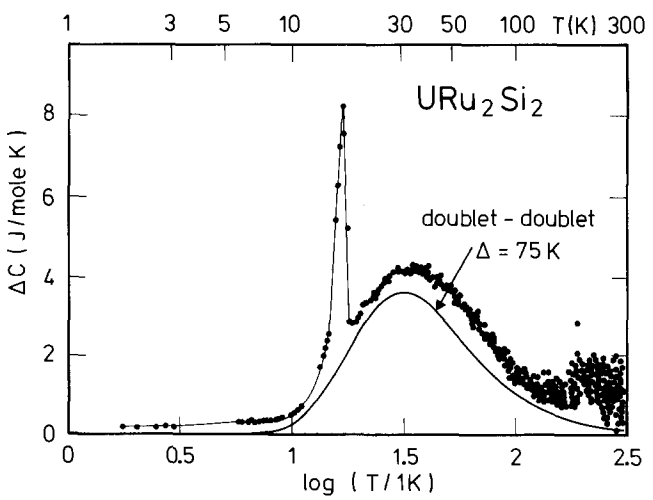

Fig. 69. The 5f-derived specific heat of URu_2Si_2, ΔC, as a function of temperature (on a logarithmic scale) (Renker et al. 1987b). Thick line shows Schottky anomaly for doublet–doublet CF system with a splitting of $k_B \cdot 75$ K. Thin line is guide to the eye.

assumed that superconductivity develops on the remaining section of the Fermi surface (Schlabitz et al. 1986). Regarding the smallness of the ordered magnetic moments, there seems to exist a problem concerning the rather large entropy change connected with the phase transition at 17 K. It is probable that most of this entropy belongs to an additional ordering phenomenon, such as a charge-density wave (CDW), which appears along with the SDW formation (Maple et al. 1986). The alternative picture (Rauchschwalbe 1987) involves a localized 5f-shell in a U^{4+} ($J = 4$) Hund's rule ground state, which appears to be supported by the variation with momentum transfer of the magnetic Bragg intensity following the U^{4+} form factor (Kjems and Broholm 1988). According to the specific-heat maximum near 30 K (fig. 69), with an entropy of about $0.5R \ln 2$ at T_{max}, two low-lying CF doublets separated by $75k_B$ K have been assumed (Renker et al. 1987b). Alternatively, one may consider two low-lying singlets separated by the same CF energy (Rauchschwalbe 1987). In this situation no direct connection to the physics of the Kondo effect or to ordered local magnetic moments seems obvious. It is, however, argued that virtual CF transitions, possibly also involving higher levels, which are induced by hybridization, can lead to effective magnetic moments, in particular small ones, and also to a negative temperature coefficient of the resistivity at elevated temperatures, cf. fig. 68. Thereby, the peak in $\rho(T)$ at 50 K could possibly be ascribed to a spin-fluctuation temperature T^*. For URu_2Si_2 this T^* would have to assume a value of about 70 K (Rauchschwalbe 1987), whereas an interpretation of data for UPt_3 along the same lines, assuming again a U^{4+} state and two low-lying singlets and an excited doublet $80k_B$ K above the ground state (Felten 1987), leads to an effective $T^* \simeq 80$ K.

4. Superconductivity

4.1. *Thermodynamics*

The discovery of heavy-fermion superconductivity below $T_c = 0.7$ K in $CeCu_2Si_2$ (Steglich et al. 1979a) created much excitement among theorists and controversy among experimentalists. The main observation was that superconductivity is a cooperative phenomenon in the system of heavy quasiparticles: in the first place, $LaCu_2Si_2$ is not a superconductor down to the millikelvin range (Steglich et al. 1979a). Notably the specific-heat jump at T_c scales with γT_c, the huge electronic specific-heat of the normal state of $CeCu_2Si_2$ at T_c, see fig. 70a. Further evidence comes from the steep increase of the upper critical magnetic field $B_{c2}(T)$ at T_c (Rauchschwalbe et al. 1982), see fig. 70b. A number of fundamental questions are immediately at hand:

(i) How can superconductivity cope with a concentrated system of magnetic Ce^{3+} ions, which in ordinary superconductors like (La, Ce)Al_2 already leads to a destruction of superconductivity at low doping (Riblet and Winzer 1971)?

(ii) Which kind of interaction, specifically related to the strong mass renormalizations, might lead to the necessary net attraction between quasiparticles?

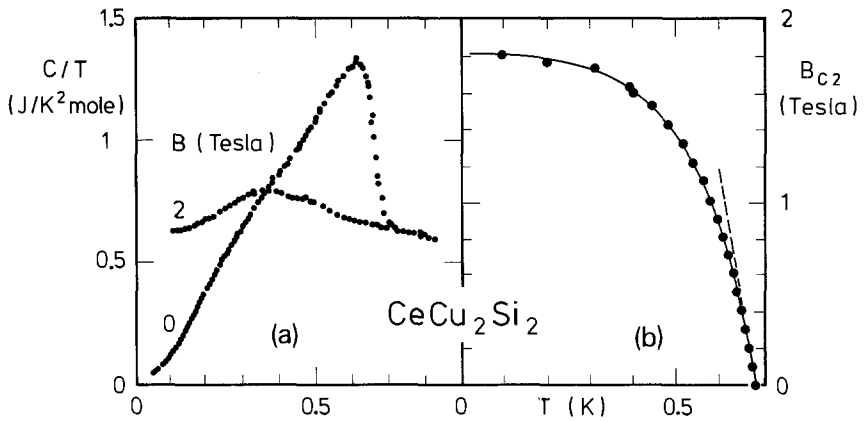

Fig. 70. (a) Specific heat of $CeCu_2Si_2$ C/T plotted against T and (b) upper critical magnetic field B_{c2} plotted against T. Solid line in (b) is guide to the eye, and dashed line indicates slope of $B_{c2}(T)$ at $T_c(-13\,\mathrm{T\,K^{-1}})$. Data in (a) and (b) taken from the same polycrystalline sample (Steglich et al. 1984).

Thinking of phonons or even spin fluctuations as providing the attractive force, there is an immediate question concerning the order of energy scales: The quasiparticle-energy scale T^* ($\approx$15 K) or the corresponding small Fermi energy E_F^* ($\approx$500 K) is apparently *not* much larger than the characteristic scale of the attractive interaction, i.e., the Debye temperature θ_D ($\approx$300 K) in the case of phonons or the singlet–triplet excitation energy that is again roughly T^*. Is, thus, the standard theory of superconductivity applicable?

(iii) Given that the usual assumptions for the standard theory of superconductivity do not work and that anisotropies play a much more important role, which are the right physical terms to think about heavy-fermion superconductivity and what is the appropriate formal framework to describe it?

(iv) Could it be that heavy-fermion superconductivity, in view of similarities to ^{3}He (cf. Leggett 1975), involves an unconventional order parameter, in particular with spin triplet symmetry?

While a few such questions have been clarified by experimental investigations, other have remained open up to now. We shall take up this discussion below in connection with the particular experimental results, see table 4. Starting with the specific-heat results one recognizes that, in spite of the unusually large scales, BCS-type relations can well be preserved. For $CeCu_2Si_2$ samples, $\Delta C/\gamma T_c$ ratios of about 1.4 have been reported (Steglich et al. 1979a). This points to the possibility that the phenomenon might be describable in terms of well-known phenomenological theories, such as the BCS theory, applied to the heavy Fermi-liquid (Parks 1969, Allen and Mitrović 1982, Rainer 1986, 1988). On the other hand, the measured $\Delta C/\gamma T_c$ ratios display considerable variations for the different heavy-fermion superconductors and even for different samples of the same material.

The sample dependence of the specific-heat jump as illustrated in fig. 71 for UPt_3 points to the importance of lattice imperfections [i.e., impurities in the

TABLE 4

Properties and microscopic parameters characterizing the normal and superconducting states of polycrystalline heavy-fermion superconductors: T_c, from specific-heat measurements; B'_{c2} and B'_{c1}, slopes of upper and lower critical-field curves at T_c; ρ_0, normal-state ($T \to 0$) resistivity; l_{tr}, total mean free path; ξ, Ginzburg–Landau coherence length; λ, London penetration depth; κ, Ginzburg–Landau parameter; $B_{c2,0}$, $B_{c2}(T \to 0)$; $B_{c1,0}$, $B_{c1}(T \to 0)$. The other symbols have their usual meanings. nd, not determined.

System	$\gamma(T_c)$ ($J K^{-2} mol^{-1}$)	m^*/m_0	v_F ($m s^{-1}$)	ρ_0 ($10^{-8} \Omega m$)	l_{tr} (10^{-10} m)	T_c (K)	$\Delta C/\gamma(T_c)T_c$	B'_{c2} ($T K^{-1}$)	$B_{c2,0}$ (T)	B'_{c1} ($10^{-3} T K^{-1}$)	$B_{c1,0}$ (10^{-3} T)	λ (10^{-10} m)	ξ (10^{-10} m)	κ
$CeCu_2Si_2$	0.7–1.1[a]	380[a]	4500[a]	1.5–65[a]	≥20[a]	0.11–0.7[a,b,c]	0–1.36[b,c,d,+]	10–23[a]	1.5–2,5[a]	8[a]	2.3[a]	4500[a]	90[a]	50–56[a]
UBe_{13}	0.72[a]	260[a]	6500[a]	17[a]	75[a]	0.87[a]	2.4[e,f]	14[a,§]	10.2[a]	8.6[a]	4.6[a]	3900[a]	95[a]	60–80[a]
$U_{0.97}Th_{0.03}Be_{13}$	1.2[a]	nd	nd	105[a]	nd	0.48[g,§§]	1.95[g,§§]	25–29[a,*]	3.75[a]	9.9[a]	3.75[a]	nd	nd	37[a]
UPt_3	0.42[a]	180[h]	6800[h]	3[h]	360[h]	0.48[h]	0.4–1.6[i,j,k,l,**]	4–6[a]	1.5[a]	nd	nd	3600[h]	200[h]	23[h]
URu_sSi_2	0.065[a,***]	140[a]	10 000[a]	40[a]	150[a]	1.20[a]	0.6[m]	7.6[a]	8[a]	3.2[a]	1.6[a]	7000[a]	100[a]	105[a]

[a]Rauchschwalbe (1987); [b]Steglich et al. (1979b); [c]Bredl et al. (1983); [d]Bredl (1985); [e]Ott et al. (1983); [f]Mayer et al. (1986a); [g]Rauchschwalbe et al. (1987c); [h]de Visser et al. (1987); [i]Stewart et al. (1984a); [j]Franse et al. (1985); [k]Sulpice et al. (1986); [l]Fisher et al. (1989); [m]Schlabitz et al. (1986).

[+] "Gapless superconductors" show $\Delta C/\gamma(T_c)T_c \lesssim 0.1$ (Bredl et al. 1983).

[§] As calculated from C and B'_{c1}; measured values[a]: 200 $T K^{-1}$($B \to 0$), 25 $T K^{-1}$ (0.25 T < B < 2 T), 11 $T K^{-1}$(2 T < B < 10 T).

[§§] $T = T_{ca}$ (upper transition).

[*] Determined resistively, value determined calorimetrically is 75 $T K^{-1}$.

[**] Two closely-spaced transitions replaced by a single one.

[***] Measured value, while for fictitious paramagnetic URu_2Si_2 $\gamma \approx 0.55$ $J K^{-2} mol^{-1}$ is estimated[a].

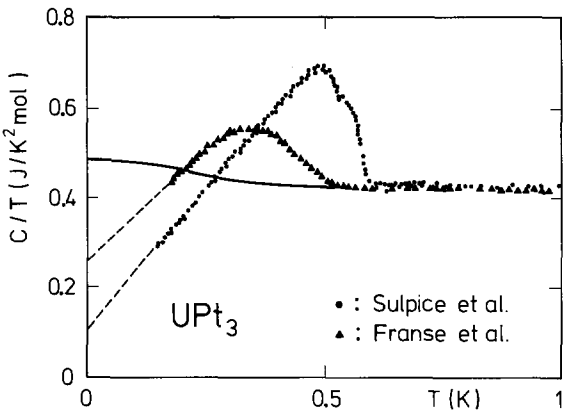

Fig. 71. Specific heat of two UPt_3 samples as C/T plotted against T (Franse et al. 1985, Sulpice et al. 1986). Sample with higher T_c prepared from purer U "starting" material. Dashed lines are extrapolations of data points in the superconducting state. Solid line is a schematic extrapolation of n-state data to meet the entropy balance. Note that the "sample dependence" in the specific heat is confined to the superconducting state (Rauchschwalbe et al. 1987b).

uranium "starting" material, see Rauchschwalbe et al. (1987b)]. The purer sample, i.e., the one prepared from the purer "starting" material, displays a higher value of T_c to begin with, and a higher and more pronounced specific-heat anomaly (Sulpice et al. 1986). In the less pure sample (Franse et al. 1985) pair breaking apparently reduces both T_c and ΔC, see below. These data show further interesting features, e.g., a double-peak structure of the transition anomaly and finite intercepts at $T = 0$, i.e., specific-heat terms linear in T, which will be addressed later. For $CeCu_2Si_2$ there are even more pronounced differences in the specific-heat jump height (fig. 72) (Steglich et al. 1987a). Interestingly enough, part of the results seems to be counterintuitive. Some samples that appear to be of better quality, as checked, e.g., by the residual resistivity and X-ray diffrac-

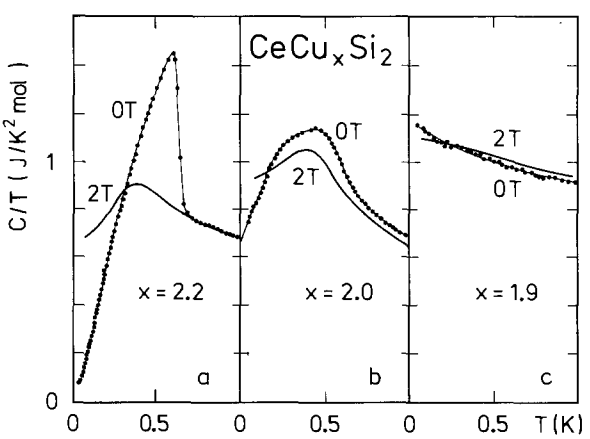

Fig. 72. Specific heat of $CeCu_xSi_2$ as C/T plotted against T at $B =$ 0 T and 2 T (Steglich et al. 1987a). Data points in (b) refer to $CeCu_2Si_2$ sample No 10 (Bredl et al. 1983). Thin solid lines through $B = 0$ T data points are guides to the eye.

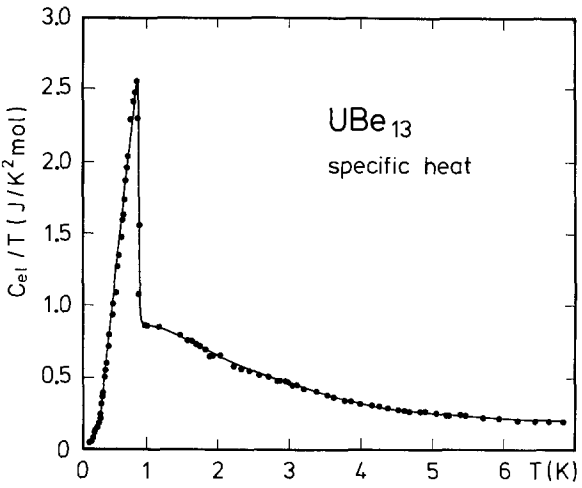

Fig. 73. Electronic part of the specific heat of UBe_{13} as C_{el}/T plotted against T (Ott et al. 1983). Solid line is guide to the eye.

tometry, display nevertheless no specific-heat jump at all when they become superconducting (Bredl et al. 1983). This reminds one strongly of gapless superconductivity (cf. Maki 1969, Steglich 1976). A possible interpretation points to a competition between different contributions to the ground-state energy. The formation of a coherent and correlated Fermi-liquid state could be in conflict with, and thus suppress, an excitation gap in the superconducting state. It can be checked by application of an overcritical magnetic field of 2 T that the $\gamma(T)$ dependence for the superconducting sample with better coherence properties resemble that of the normal state much closer (fig. 72b).

As is displayed by table 4, the specific-heat jump ratios of $CeCu_2Si_2$ and UPt_3 do not seem to be considerably enhanced over the conventional BCS value, i.e., they are even smaller for most samples. In contrast, UBe_{13} (Ott et al. 1983) shows an enhanced value of $\Delta C/\gamma T_c = 2.4$ (fig. 73). This is comparable to the value for Pb and has, likewise, been ascribed to strong-coupling effects (cf. Scalapino 1969).

4.2. *Critical fields and the penetration depth*

Critical fields give important information about the parametes characterizing the normal Fermi-liquid and the superconducting states [see, e.g., Fetter and Hohenberg (1969)]. The slope of $B_{c2}(T)$ at T_c, B'_{c2}, is influenced by the quasiparticle-band structure of the clean material and by impurities. $B_{c2}(T)$ itself is determined by diamagnetic pair breaking near T_c, and the possible presence of Pauli limiting at lower temperatures, i.e., the breaking of spin alignments preferred by the superconducting state, allows for conclusions concerning the symmetry type of the superconducting order parameter. The slope $B'_{c2} = -(\mathrm{d}B_{c2}/\mathrm{d}T)_{T_c}$ is directly connected with the superconducting coherence length, ξ. The Ginzburg–Landau parameter $\kappa = \lambda/\xi$, which can be deduced from the ratio of B'_{c2}

and the lower slope (at T_c) of the critical field B'_{c1}, thus allows for the determination of the penetration depth λ, which will be addressed at the end of this section. λ yields information about quasiparticle masses and about the temperature-dependent magnitude of the superconducting order parameter.

In general, the large slopes of $B_{c2}(T)$ at T_c prove the existence of large effective masses (Rauchschwalbe et al. 1982). Experimental values of B'_{c2} for the different systems are listed in table 4. In particular, for $CeCu_2Si_2$ the increase of B'_{c2} due to crystal imperfections as indicated by the residual resistivities can amount to a factor of about two (Rauchschwalbe 1987). An unexplained feature up to now is the nearly divergent slope of $B_{c2}(T)$ at T_c of UBe_{13} (Maple et al. 1985, Rauchschwalbe et al. 1985b) (fig. 74b). It arose, in connection with the pronounced flattening of $B_{c1}(T)$ near T_c (Rauchschwalbe et al. 1987d), speculations about an anomalous temperature dependence of $\kappa(T)$ and, thus, the penetration depth. The flat minimum in $B_{c2}(T)$ near 0.4 K (fig. 74a) may be traced back to the existence of a second superconducting transition at 0.6 K as is discussed in more detail below. In contrast to $CeCu_2Si_2$ single crystals (Assmus et al. 1984), a pronounced anisotropy of B'_{c2} is observed for UPt_3 crystals (Chen et al. 1984, Rauchschwalbe et al. 1985b), see fig. 75. The reduced slope for the magnetic field applied parallel to the basal plane can be understood from the assumption of zeros in the superconducting gap: a line of nodes in the basal plane as suggested by ultrasound attenuation data (see below) enables the system to respond with a large screening current to a field parallel to the hexagonal *c*-axis in the absence of too much pair breaking. For a field in the basal plane, these nodes are not effective and the screening current leads to a rapid decrease in the condensation energy, indicated by a reduced critical-field slope. As proposed by Rauchschwalbe et al. (1985b), the order parameter may reorient correspondingly when the field becomes large enough and may restore nearly the same large large

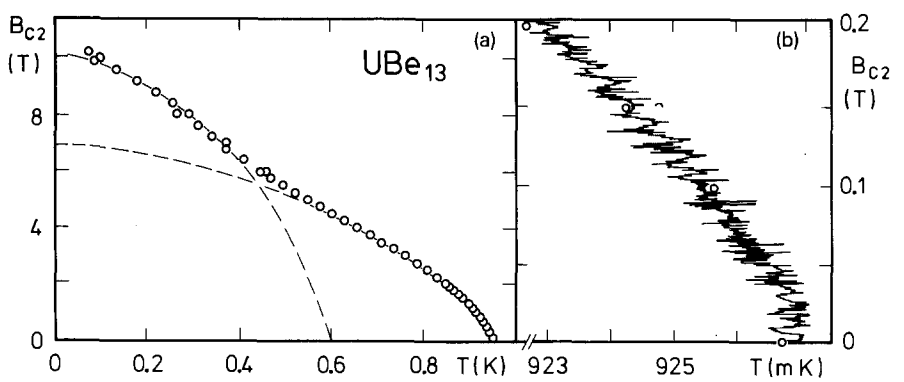

Fig. 74. Upper critical magnetic field, B_{c2} plotted against T, of polycrystalline UBe_{13} as determined (a) from the midpoints of resistive transitions (Rauchschwalbe et al. 1987b) and (b) continuously (Rauchschwalbe et al. 1985b). Open circles in (b) correspond to discrete $B_{c2}(T)$ values from (a). Dashed curves in (a) are extrapolations of experimental data points. They suggest the existence of two superconducting order parameters.

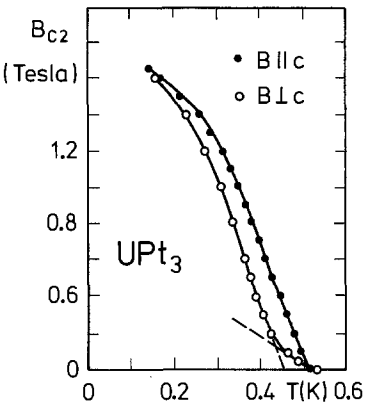

Fig. 75. B_{c2} plotted against T for a UPt_3 single crystal for B parallel and perpendicular to the hexagonal c-axis (Chen et al. 1984). Dashed extrapolations indicate an abrupt change of slope (Rauchschwalbe et al. 1985b).

slope for $B \perp c$ as originally seen for $B \| c$. This would explain the kink in $B_{c2}(T)$ for $B \perp c$. Note that the $B_{c2}(T)$ curves for $B \perp c$ and $B \| c$ were even found to intersect at low temperatures (Shivaram et al. 1986b, DeLong 1987). Recent investigations ascribe the break in the $B_{c2}(T)$-slope for $B \perp C$ to a multicritical point, as discussed at the end of the following subsection.

Consistent with the assumption of an anisotropic order parameter in UPt_3, Pauli limiting does not play any role, unlike $CeCu_2Si_2$. In the latter system (fig. 70b), the $B_{c2}(T)$ curve shows a remarkable flattening at low temperatures that, on the basis of a comparative model study, could be uniquely ascribed to a strong Pauli-limiting effect (Rauchschwalbe et al. 1985b). Even a flat maximum in $B_{c2}(T)$ near $T = 0.2$ K has been resolved and was explained by structure in the normal DOS as resulting from coherence effects (Rauchschwalbe et al. 1985b). An immediate conclusion was that $CeCu_2Si_2$ probably has no order parameter of odd parity. Also in the case of UBe_{13}, $B_{c2}(T)$ curves including strong Pauli-limiting effects gave by far the closest fits to the data (Rauchschwalbe et al. 1985b). The original data by Maple et al. (1985) have been completed by more data points (Rauchschwalbe et al. 1987d, Schmiedeshoff et al. 1988) showing a conspicuous flattening of $B_{c2}(T)$ in an intermediate temperature range. This gives rise to the idea (Rauchschwalbe et al. 1987d) of two consecutive superconducting phase-transitions contributing to $B_{c2}(T)$ in a fashion as indicated by the dashed curves in fig. 74a. The concept of different superconducting phase-transitions seems to be further supported by an analysis of the low-temperature specific-heat results on pure and Th-doped UBe_{13}, as discussed below.

Measurements of the London penetration depth $\lambda(T)$ point to the existence of aniostropic superconducting phases in UBe_{13} (Einzel et al. 1986) and $CeCu_2Si_2$ (Gross et al. 1988), as well. Figure 76 demonstrates for the former system clear deviations from the temperature dependence expected for an ordinary, isotropic superconductor. As an explanation, it has been proposed (Gross et al. 1986, Millis 1987) to use the standard connection between the condensate velocity and the electromagnetic potentials,

$$\boldsymbol{v}^{\mathrm{s}} = \frac{\hbar}{2m^*} \nabla\varphi + \frac{e}{m^* c} \boldsymbol{A}\,, \tag{24}$$

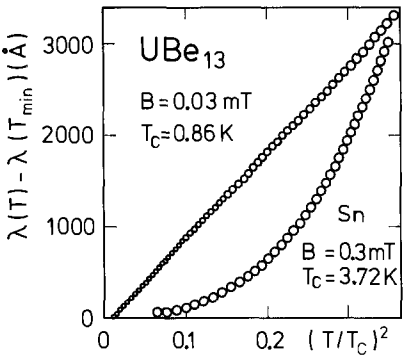

Fig. 76. Increment of the penetration depth of UBe_{13} as a function of $(T/T_c)^2$. For comparison, data for an Sn reference sample are also shown (Einzel et al. 1986).

thereby assuming unitary states with only one free phase and finite excitation gaps for all other intrinsic collective modes of the order parameter. The latter assumption is justified through a possible preferred axis $\boldsymbol{l}$ of the anisotropic order parameter in the crystal structure. Connecting $\boldsymbol{v}^s$ with the screening current density via the tensor of the condensate density, $\boldsymbol{j}^s = e\boldsymbol{n}^s\boldsymbol{v}^s$, and employing the transversality of the current in a static situation, the response kernel $\boldsymbol{K}$ is explicitly expressed via $\boldsymbol{n}^s$ (Einzel et al. 1986):

$$\boldsymbol{j}^s = -\frac{e^2}{m^* c}\left(\boldsymbol{n}^s - \frac{(\boldsymbol{q}\boldsymbol{n}^s)\otimes(\boldsymbol{n}^s\boldsymbol{q})}{\boldsymbol{q}\boldsymbol{n}^s\boldsymbol{q}}\right)\boldsymbol{A}\,. \tag{25}$$

$\boldsymbol{n}^s = \mathrm{n}\mathbf{1} - \boldsymbol{n}^n$ ($\boldsymbol{n}^n$: density of quasiparticle excitations in the presence of the anisotropic condensate; n: (isotropic) density of conduction electrons) is then calculated using the standard weak-coupling formulae for an isotropic order parameter.

$\boldsymbol{K} = -(c/4\pi)(\boldsymbol{P}_{\|}/\lambda_2^2 + \boldsymbol{P}_{\perp}/\lambda_1^2)$ is characterized in general by two different penetration depths perpendicular and parallel to the projection of $\boldsymbol{l}$ on the surface ($\boldsymbol{P}_{\|,\perp}$ are the corresponding projection operators). From the results for $\boldsymbol{n}^n$, that, in the case of zeros of the order parameter on the Fermi surface, exhibit simple power laws as explained in the next subsection, it can be deduced that an axial state, with isolated points of zeros, is consistent with the observed T^2-law for the effective penetration depth. A polar state, on the other hand, with lines of zeros, would give a different power law and, thus, would fail (Gross et al. 1986).

Within this simple theory, which is based on an isotropic effective mass m^* in eq. (24), a large absolute value

$$\lambda(0) = \left(\frac{m^* c^2}{4\pi n^s(0) e^2}\right)^{1/2} \simeq 5000\ \text{Å} \tag{26}$$

is consistently obtained, confirming (cf. table 4) independent estimates for UBe_{13} (MacLaughlin et al. 1984) and $CeCu_2Si_2$ (Rauchschwalbe et al. 1982). It is not clear whether these conclusions are still justified when the anisotropic band structure is properly taken into account. A particularly serious objection concerning the conclusiveness of the above argument against a polar state has been raised by a recent calculation (Klemm et al. 1988) that includes the effect of resonant

impurity scattering. Already for small scattering rates $\hbar\Gamma = 0.1\pi k_B T$ and the phase shift $\sigma = \frac{1}{2}\pi$, the polar state exhibits a near T^2 law for the effective penetration depth. Apart from small differences in the prefactor it thus becomes indistinguishable from the axial state.

4.3. *Power laws: specific heat and transport properties*

An intensively debated topic is the presence of simple power laws in the specific heat and the transport properties of heavy-fermion superconductors (Steglich 1985b, Varma 1985b, Alekseevskii and Khomskii 1985). A simple exponential T-dependence, as predicted by BCS theory for an isotropic spin-singlet state and as observed for many conventional weak- and strong-coupling superconductors, seems exceptional [one example has been reported for UBe_{13} by Ravex et al. (1987)]. It is well established that pair-breaking effects in superconductors can enhance the low-temperature specific-heat and destroy the exponential law (cf. Maki 1969, Müller-Hartmann 1973, Abrikosov and Gorkov 1960, 1961, Shiba 1968), but the existence of a simple power law describing the temperature dependence is usually taken as a signature of anisotropic order parameters of a well defined symmetry type. The exponents in such power laws can be traced back uniquely to the dimensions of that part of the Fermi surface on which the gap vanishes (Volovik and Gorkov 1985, Varma 1985a). This dimension, on the other hand, can at best be inferred from a group-theoretical classification of the superconducting order parameters.

Given that the gap vanishes only on points on the Fermi surface, the number of excited one-particle states available at temperature T is proportional to a small $\boldsymbol{k}$-space volume of diameter proportional to $k_B T$. The total energy of all excitations, E, is thus proportional to T^4 and the specific heat is $C_v \sim dE/dT \sim T^3$. Likewise for a gap vanishing along a line on the Fermi surface the corresponding $\boldsymbol{k}$-space volume is generated by a small cross-section with diameter of order $k_B T$ via parallel transport along this line. Thus, one factor $k_B T$ is replaced by the constant length of a closed curve around the Fermi surface, leading to a T^2-dependence of the specific heat.

The existence and positions of zeros of the superconducting gap on the Fermi surface is intimately connected with its symmetry group. [There exists a vast literature elucidating this fact in connection with the phases of superfluid ^{3}He, see, e.g., Leggett (1975). For an early application to solid-state physics, see Scharnberg and Klemm (1980) and Klemm and Scharnberg (1981).] The gap or equivalently the pair wavefunction is in principle derived from an anomalous expectation value over a product of two fermion operators creating the correlated particles in a Cooper pair. In general such pairing for a crystal with inversion symmetry P in a situation with time-reversal symmetry T takes place between the four degenerate states $\alpha = (\boldsymbol{k}, \uparrow)$, $P\alpha = (-\boldsymbol{k}, \uparrow)$, $T\alpha = (-\boldsymbol{k}, \downarrow)$ and $PT\alpha = (\boldsymbol{k}, \downarrow)$ (Anderson 1984b). $\boldsymbol{k}$ is Bloch's momentum and $\sigma = \uparrow, \downarrow$ a pseudospin, i.e., an observable that replaces the z-component of the quasiparticle spin in the presence of spin–orbit coupling as a good quantum number and transforms like it under the action of P and T (Ueda and Rice 1985, Blount 1985). The definite

transformation properties of the four degenerate states, together with the anticommutativity of the two fermion operators, make it possible to classify the order parameter as pseudospin singlet or triplet: the pair wavefunction, being antisymmetric with respect to particle exchange then has even parity in the singlet and odd parity in the triplet state.

In addition to P and T the total group G of possible symmetry transformations for the order parameter also contains proper point group and gauge transformations (Volovik and Gorkov 1985). Concerning these, the effective pair potential, i.e., the integral kernel entering a self-energy equation like the one obtained in Eliashberg theory, can be decomposed into parts acting on each of the irreducible representations separately [Allen and Mitrović (1982); for a discussion of the peculiarities connected with non-symmorphic lattices, see Blount (1985) and Appel and Hertel (1987)]. This decomposition furnishes an ordering principle for the different possible superconducting phases in the following natural way: if the highest T_c is calculated for the trivial representation, then the order parameter is unchanged under the action of all of these transformations. It thus represents a superconducting phase that has the full crystal symmetry. Although of even parity, the order parameter is thereby not confined to a simple constant, since the crystal group contains only a finite number of rotations. A pure s-wave state would be a special case, which however seems to be realized to a good approximation in most known superconductors. A strongly anisotropic band structure, on the other hand, could mix in higher angular momenta and still preserve a conventional order parameter in the general sense defined above (Fulde et al. 1988). If, however, one of the non-trivial representations is realized, via the highest T_c, then the order parameter resulting is left invariant only by part of the transformations and, thus, has only a subgroup of G as the symmetry group. In this case a breaking of the full crystal symmetry by the superconducting phase-transition is encountered. Such unconventional superconducting phases may possibly even break time reversal symmetry and may thus be connected with magnetic moments originating from supercurrents (Volovik and Gorkov 1985). They arose particular interest which led to extensive studies (Volovik and Gorkov 1985, Ozaki et al. 1985, 1986, Ueda and Rice 1985, Blount 1985, Appel and Hertel 1987) of the set of all the subgroups of G for any of the known heavy-fermion superconductors, i.e., cubic UBe_{13}, hexagonal UPt_3 and tetragonal $CeCu_2Si_2$ and URu_2Si_2. The authors agree that for these structures triplet superconductors should only have isolated zeros (as opposed to lines of zeros) of the order parameter on the Fermi surface. Singlet superconductors, on the other hand, include phases with isolated zeros and/or lines of zeros.

It must be emphasized that anisotropic order parameters can be formed in conventional and unconventional scenarios according to this classification. The conventional case includes the possibility of an isotropic order parameter that may, however, be supplemented by more or less anisotropic components. An important feature is that conventional anisotropic components are to obey faithfully all crystal symmetries and thus inevitably will merely reflect the shape of the Fermi surface. This generally favors higher angular momenta in the systems under consideration, possibly $l = 4$ or $l = 6$ waves (Fulde et al. 1988). For an

unconventional phase, on the other hand, a less structured order parameter, e.g., with a large content of $l=1$ or $l=2$, can be realized. As an argument against a considerable constant (i.e., $l=0$) contribution to the order parameter the strong local repulsion between quasiparticles has frequently been used (Anderson 1984a, Varma 1985a, Lee 1985, Šimanek 1985, Miyake et al. 1986, Rice et al. 1986). If this would be the only point of view to be accommodated, unconventional phases with smaller l might be preferred for phase-space reasons (Zhang et al. 1987). An anisotropic conventional order parameter, on the other hand, can best take advantage of the existing $\boldsymbol{k}$-space anisotropy of one-particle states, i.e., the quasiparticle band structure, and of the effective interactions. This line of reasoning has led to arguments in favor of conventional, though anisotropic order parameters in heavy-fermion superconductors (Miyake et al. 1984, Ohkawa and Fukuyama 1984, Ohkawa 1986, Scalapino et al. 1986, 1987, Miyake 1987, Fulde et al. 1988). Note, however, that a triplet state of A_{1u}-symmetry is suggested by recent model calculations for UPt_3 (Norman 1988, 1989, Putikka and Joynt 1989). As a cautionary remark against an a priori exclusion of an order parameter component with $l=0$ the reduced strength of quasiparticle repulsion should be mentioned: quasiparticles do not derive their heavy mass from band-structure effects but rather from many-body renormalizations which also affect the Coulomb matrix elements (Fenton 1986, 1987). The local quasiparticle repulsion is found to be of the order of the quasiparticle band width T^* only (Tachiki and Maekawa 1984, Matsuura et al. 1984, Grewe and Pruschke 1985, Lee 1985, Grewe 1988b).

The situation in real materials is complicated through the existence of multi-sheeted Fermi surfaces and impurity scattering. Simple-power-law behaviour, as characteristic for a particular anisotropic superconducting state, may suffer drastic changes from resonant impurity scattering (Coffey et al. 1985, Schmitt-Rink et al. 1986, Pethick and Pines 1986, Hirschfeld et al. 1986, Monien et al. 1987a, b, Coffey 1987, Hirschfeld et al. 1988, Klemm et al. 1988). The influence of impurity scattering is twofold, in principle: it introduces lifetime effects and thus may smear out energy-dependent fine structure in the DOS, and it connects different points on the Fermi surface and may thus disturb the $\boldsymbol{k}$-space structure of an anisotropic order parameter. The latter effect could be of particular importance in the presence of an anisotropic Fermi surface with disconnected parts.

In a pure system one can imagine an order parameter forming only on one sheet of the Fermi surface due to differences in quasiparticle properties, concerning, e.g., their effective-mass tensor and their interactions. This opens the possibility for gradual or abrupt transitions between superconducting phases involving different parts of the Fermi surface. In the presence of crystal imperfections one might argue that the resulting scattering mixes all parts of the Fermi surface strongly enough to exclude such pronounced $\boldsymbol{k}$-space inhomogeneities of the superconducting order parameter. This argument is not conclusive. Whereas it certainly applies for an anisotropic order parameter on a nearly isotropic Fermi surface [for a review of relevant work in the framework of the conventional theory of superconductivity, see Allen and Mitrović (1982), chapters 16 and 17],

order-parameter anisotropies could be stabilized by corresponding anisotropies of the Fermi surface and/or of the scattering matrix elements. In particular, it has been argued that the electronic structure of certain impurities can be compatible enough with that of the host metal to preserve to a good approximation even a subdivision of the Fermi surface in disconnected pieces concentrated along symmetry lines (Ahlheim et al. 1988a).

As a result of the arguments given above, two somewhat different points of view concerning transitions between superconducting phases in heavy-fermion systems may be advocated: the first stresses the influence of thermal fluctuations and/or impurity scattering on the relative stability of phases belonging to different representations of the symmetry group G. The second aims at the strong anisotropy and possible multiconnectedness of the Fermi surface with varying quasiparticle properties. Based on these two points of view, a discussion of experimental results on the one hand involves Ginzburg–Landau theory with different group representations and their couplings (Kumar and Wölfle 1987, Sigrist and Rice 1989), and on the other the variation of quasiparticle properties, including the matrix elements for their coupling to specific experimental probes, over the whole Fermi surface and the resulting differences in possible pair correlations (Rauchschwalbe et al. 1987c).

The discussion of power laws has entailed the following experimental probes: specific heat $C(T)$ (fig. 77a–c), thermal conductivity $\kappa(T)$ (fig. 78a–c), spin–lattice relaxation rate by NMR $T_1(T)$ (fig. 79a–c), and ultrasound attenuation $\alpha(T)$ (fig. 80a–c), in addition to the penetration depth $\lambda(T)$ (fig. 76). The first three probes reveal information about the DOS of one-particle excitations in the superconducting state in the most direct way.

Most clearly, the spin–lattice relaxation shows a T^3-dependence for UBe_{13} (MacLaughlin et al. 1984), $CeCu_2Si_2$ and UPt_3 (Asayama et al. 1988). This would be consistent with a T^2-dependence of the specific heat and a corresponding linear dependence $N(E) \sim E^\alpha$ with $\alpha = 1$ for the DOS, since then $(T_1)^{-1} \sim N(|E - E_F| \approx k_B T) C(T) \sim T^3$. This implies zeros of the gap along lines on the Fermi surface. There are, however, some indications in the data which point to the possible existence of (i) a constant DOS at low energies and (ii) a second phase transition below T_c: for $CeCu_2Si_2$ and UBe_{13} the curve at low temperature flattens, indicating increased spin–lattice relaxation, and for UBe_{13} and UPt_3 the slope of $T_1^{-1}(T)$ changes distinctly below T_c.

For the specific-heat, power laws do not appear to be so well defined. In particular, contributions linear in temperature seem to be present at low T. It is instructive to discuss the results in connection with the corresponding data for the thermal conductivity. The case of UPt_3 is particularly revealing: measurements of the specific-heat of UPt_3 samples with differing purity all show a good T^2-dependence, but some variation in the size of the $\gamma_s T$ term of about 130–260 mJ K^{-2} mol^{-1} (cf. fig. 71). The most direct interpretation at hand involves pair breaking which, in an anisotropic superconductor, already results from normal impurities. The size of the effect makes it clear that the resulting impurity bands involve heavy quasiparticles. At first glance the thermal-conductivity data

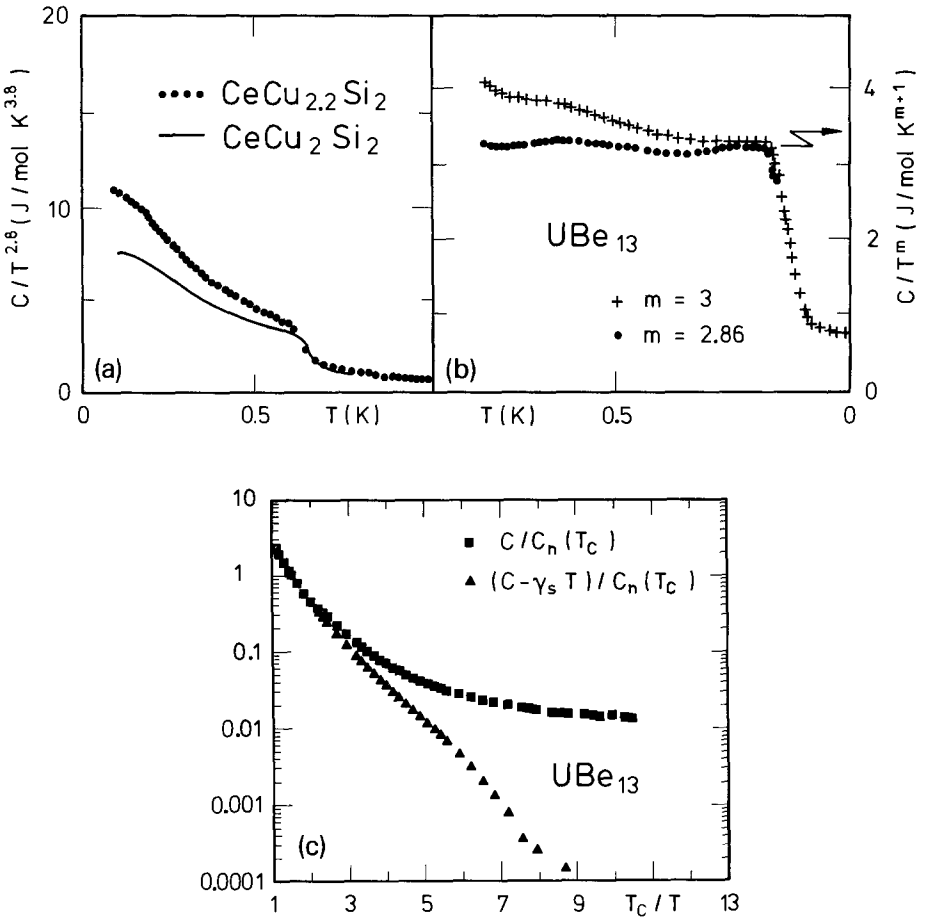

Fig. 77. Temperature dependence of the specific heat, $C(T)$, of polycrystalline samples of (a) $CeCu_{2.2}Si_2$ and $CeCu_2Si_2$, and (b, c) of UBe_{13}. In (a) and (b) C/T^m against T is plotted to check for power laws. In (c) C and $C-\gamma_s T$ ($\gamma_s = 0.11\,J\,K^{-2}\,mol^{-1}$), normalized by $C_n(T_c)$, are plotted on a logarithmic scale as a function of T_c/T. Data in (a) and (b) are from Steglich (1985); data in (c) are from Ravex et al. (1987).

consistently show that this transport coefficient is small and linear in T. Because of their reduced velocity, heavy quasiparticles are far less efficient for the thermal transport compared to light band states. Note that the reduction is not compensated for by the high DOS: most of this DOS is of local character and does not contribute to transport. The linear section above 0.13 K in the $\kappa(T)/T$ data of the pure UPt_3 crystal (Ott et al. 1987b) (see fig. 78b) that gives, when extrapolated to $T=0$, a large value of the linear coefficient $\lambda_s = 2\,mW\,K^{-2}\,cm^{-1}$, can therefore only be explained in terms of such light states. This would lead in a straightforward way to the following picture underlying the thermal transport in superconducting UPt_3: the superconducting transition at 0.5 K involves only part of the

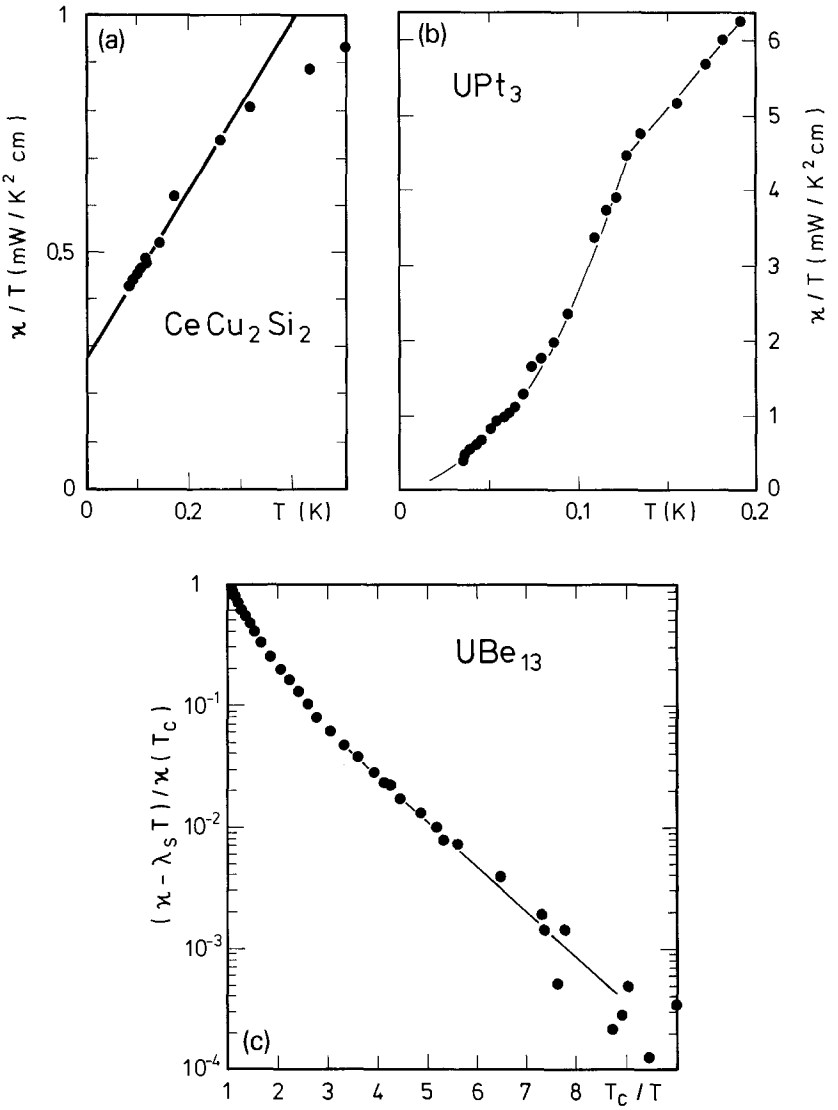

Fig. 78. Temperature dependence of the thermal conductivity of (a) $CeCu_2Si_2$, (b) UPt_3 as κ/T plotted against T and (c) UBe_{13} as $\kappa - \lambda_s T$ ($\lambda_s = 0.03\,\mathrm{mW\,K^{-2}\,cm^{-1}}$), normalized by $\kappa(T_c)$ and plotted as a function of T_c/T (on a logarithmic scale). Data in (a) are from Steglich (1985), data in (b) are from Ott et al. (1987b) and those in (c) are from Ravex et al. (1987). Solid line in (a) indicates low-T behaviour $\kappa = \lambda_s T + \alpha_s T^2$. Solid lines in (b) and (c) are guides to the eye.

Fermi surface and leaves another part with light electrons unchanged. The light electrons make a considerable contribution to $\kappa(T)$ as measured by $\lambda_s T$, which then decreases strongly below 0.13 K. These data, therefore, suggest that due to an induced net attraction there is a second transition at this temperature involving the light electrons and thus having no correspondence in the specific-heat results

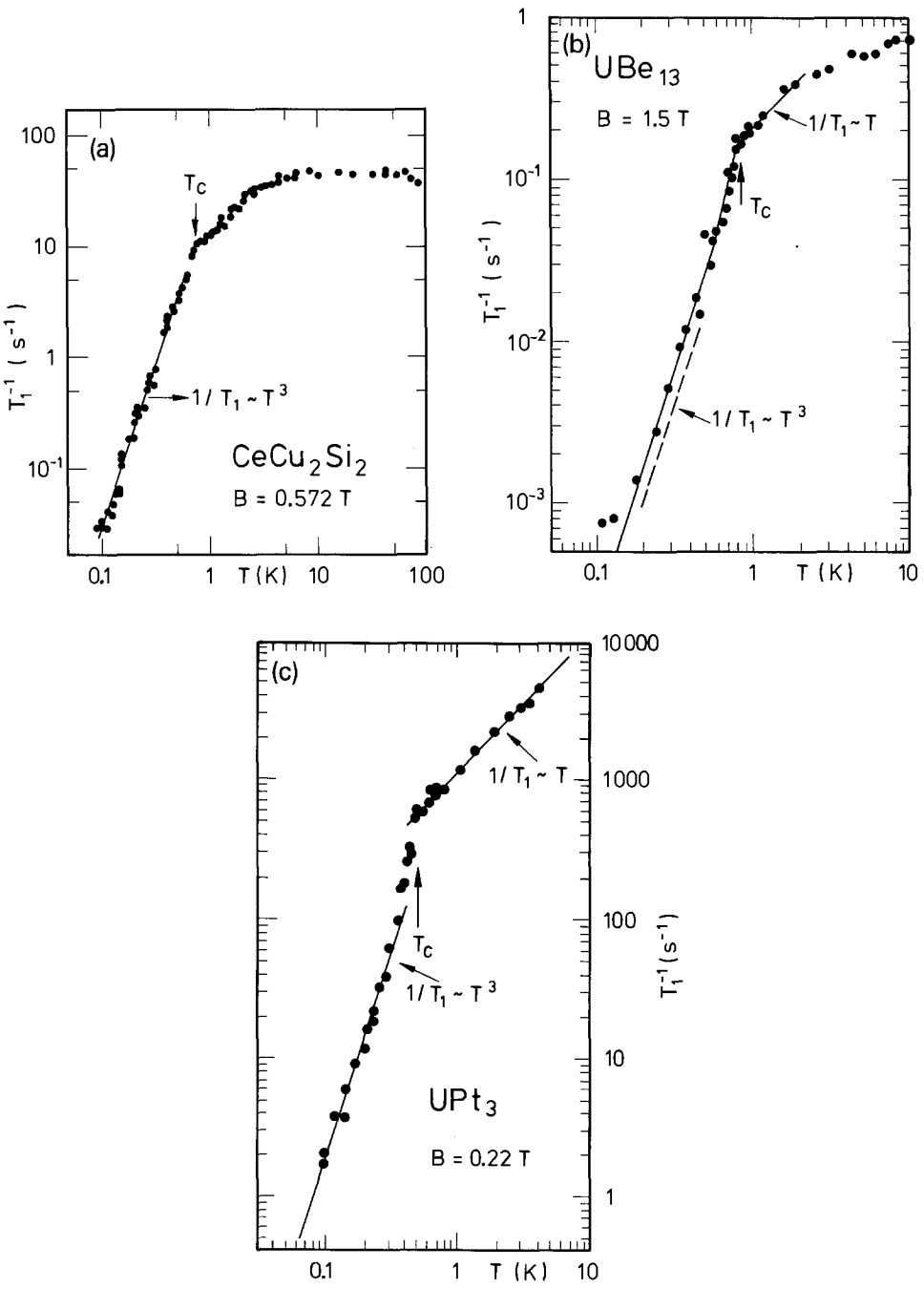

Fig. 79. Temperature dependences of the nuclear spin–lattice relaxation rate in a double-logarithmic plot T_1^{-1} against T for (a) ^{63}Cu in $CeCu_2Si_2$, (b) ^{9}Be in UBe_{13} and (c) ^{195}Pt in UPt_3. Data in (a) and (c) are from Asayama et al. (1988); data in (b) are from MacLaughlin et al. (1984).

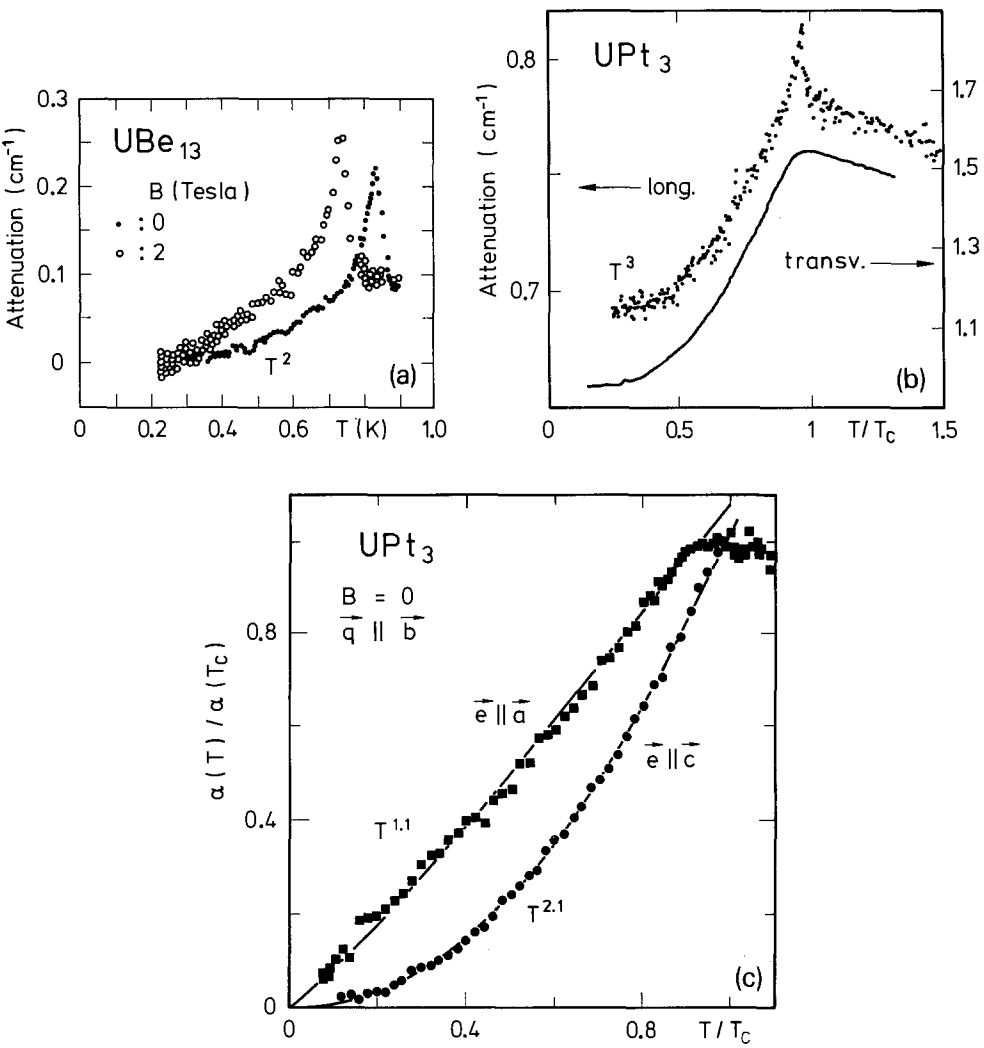

Fig. 80. Temperature dependence of the ultrasound attenuation: (a), α against T for longitudinal sound (1.7 GHz) at $B = 0$ and 2 T in UBe_{13} (Golding et al. 1985); (b), α against T/T_c for longitudinal (0.92 GHz) and transverse (0.67 GHz) sound at $B = 0$ in UPt_3 (Müller et al., 1986b); (c), $\alpha/\alpha(T_c)$ against T/T_c at $B = 0$ for transverse sound (0.132 GHz) along b-axis with polarizations parallel to the a- and c-axes in UPt_3. Solid lines in (c) are power-law fits to the entire data (Shivaram et al. 1986a).

[cf. Ott et al. (1987b) and figs. 71 and 81]. Well below $T = 0.13$ K, almost the whole Fermi surface seems to be involved in an anisotropic superconducting state as inferred from an apparent T^2-dependence with no linear term in $\kappa(T)$. The large linear term $\gamma_s T$ in the specific would then be due to pair breaking – as argued above. New calorimetric studies at ultralow temperatures even reveal an increasing $C(T)/T$ upon cooling below 50 mK (Schuberth et al. 1990). A T^2 law

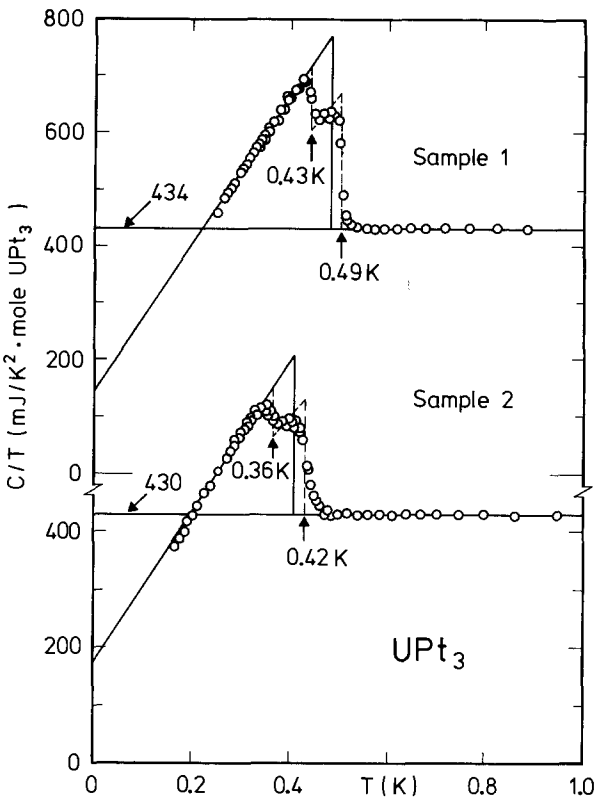

Fig. 81. Specific heat of UPt_3 near the superconducting transition for two different samples (Fisher et al. 1989). Dashed lines represent two idealized transitions at T_a and T_b. Thick solid lines represent one idealized transition, with the same total entropy, at T_c. Thin solid lines are linear extrapolations of measured data that fail entropy balance (cf. fig. 71).

for $C(T)$, i.e., no measureable linear term, has also been observed for URu_2Si_2 (Schlabitz et al. 1986).

In the light of this discussion it would be important to identify the existence of linear terms in $\kappa(T)$ for the two other systems. Looking at the specific-heat, pair-breaking effects are apparently not as strong as in UPt_3. Since, however, controlled alloying with non-magnetic dopants introduces a considerable γ_s in $CeCu_2Si_2$ (Steglich et al. 1987b, Ahlheim et al. 1988a), an anisotropic superconducting order parameter is probable in this material as well. The nature of the corresponding order parameter is, however, not revealed by any clear power law in the specific-heat (Steglich et al. 1984, Steglich 1985a, Assmus et al. 1990). As fig. 77a suggests, an asymptotic $T^{2.8}$ law may be approached as $T \rightarrow 0$. The presence of light quasiparticles contributing to the thermal transport above 80 mK can be inferred from fig. 78a in the case of $CeCu_2Si_2$. Whether these result from pair breaking on parts of the Fermi surface that are not involved in superconductivity or even from a small amount (~3%) of a normal impurity phase is not yet clear.

UBe_{13} shows a linear as well as a cubic contribution to the low-temperature specific-heat (Ott 1987). The thermal conductivity in the same low-T regime is also consistent with the existence of a linear term (Ravex et al. 1987). Significant deviations from any assumed power law are found for both quantities at elevated temperatures (Ravex et al. 1987, Rauchschwalbe et al. 1987b). It has even been suggested (Ravex et al. 1987) that after subtraction of the linear term, exponential BCS-like behaviour results, see figs. 77c and 78c. In addition, an antiferromagnetic transition near 0.15 K was recently suggested on the basis of low-T specific-heat experiments (Brison et al. 1988). The existence of a magnetic phase transition would also solve the puzzle connected with the entropy balance, see sect. 3: the superconducting phase of UBe_{13} possesses far more entropy than is calculated for the normal state with a constant γ. Taking into account the corresponding increase in $C(T)/T$ below 0.25 K as measured at finite field (Brison et al. 1988) one arrives at a considerably improved entropy balance. Model calculations for the thermodynamics of different (isotropic and anisotropic) superconducting phases reveal a difficulty: the severe discrepancy between experimental and theoretical data may be ascribed to a second superconducting phase transition in UBe_{13} near 0.6 K (fig. 82), which appears even more probable in view of the observed structure in $B_{c2}(T)$ (fig. 74a). The relevance of this second transition will become apparent when discussing the phase diagram of $U_{1-x}Th_xBe_{13}$ below, see fig. 88 (Rauchschwalbe et al. 1987d).

The ultrasonic attenuation of the heavy-fermion superconductors UBe_{13} (Golding et al. 1985) and UPt_3 (Müller et al. 1986b, Shivaram et al. 1986a) as seen in figs. 80a–c is generally characterized by an increase in the normal state with

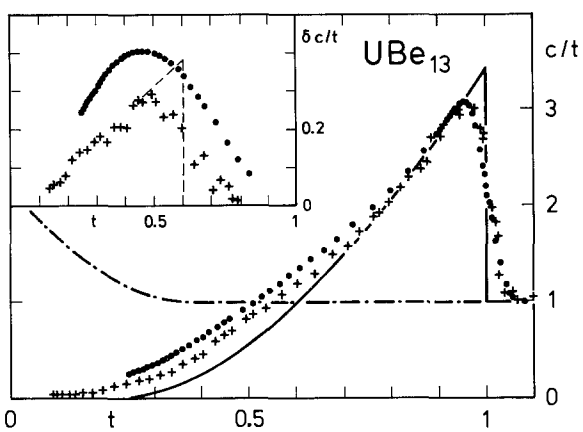

Fig. 82. Specific heat of two UBe_{13} samples (+, Ott et al. 1984b; ●, Mayer et al. 1986a) in a plot of c/t against t; $c = C/C_n(T_c)$, $t = T/T_c$. Solid line is theoretical result for a strong-coupling superconductor with isotropic gap. Inset shows difference between experimental data and the theoretical result in a plot of $\delta c/t$ against t. Dashed curve represents idealized second-order phase transition at 0.6 K. Note that a similar peak is obtained if the theoretical result for a strong-coupling superconductor with axial gap is chosen (Steglich et al. 1987c). Dash-dotted line is a schematic extrapolation of the normal-state data necessary to meet entropy balance at T_c.

decreasing temperature, a characteristic decrease at the low-temperature end, a broad maximum for transverse sound and a spike for longitudinal sound at T_c. The increase above T_c can be explained via an increase in the mean free path of the normal quasiparticles. This mean free path, limited by crystal imperfections and the electron–electron interaction, is too small to allow for considerable attenuation via collective modes of the order parameter in the superconducting state (Wölfle 1986). Thus, the low-temperature curves do, in general, not display the rich dynamics connected with an anisotropic order parameter (Monien et al. 1986a, b, Rodriguez 1987), but to a large degree only the changed excitation spectrum of the normal component. Coupling of ultrasound to a purely relaxational motion of the order-parameter amplitude could, however, contribute to the attenuation peak near T_c where critical slowing down occurs (Miyake and Varma 1986, Monien et al. 1989). Whereas in UPt_3 residual elastic scattering is already dominant at T_c, the low characteristic temperature of UBe_{13}, as, e.g., reflected in the large maximum of the n-state resistivity near 2 K, includes large inelastic electron–electron scattering at T_c, so that the Fermi-liquid regime is not even reached. The experimentally observed T-dependences for the attenuation are not conclusive: whereas for UPt_3, the longitudinal attenuation varies approximately as T^3 (Müller et al. 1986b), a polar state would give a T- and an axial state a T^2-dependence (Rodriquez 1985, Coppersmith and Klemm 1986). For UBe_{13}, on the other hand, theory for the axial state and experiment both yield a T^2-law (Golding et al. 1985). Transverse sound attenuation in UPt_3 likewise shows a correspondence between experiment (Shivaram et al. 1986a) and theory (Hirschfeld et al. 1986, Scharnberg et al. 1986), favouring a polar state. These last results also gave rise to the suggestion that the line of gap zeros lies in the basal hexagonal plane UPt_3 (Shivaram et al. 1986a). Extensive model studies (Coffey 1987, Monien et al. 1987a, b), which include the effect of impurity scattering, show that clear-cut power laws in $\alpha(T)$ can be expected only under very fortunate conditions. A maximum in the ultrasonic-attenuation coefficient at T_c can be expected from the competition (upon cooling) between the increasing mean free path and the decreasing quasiparticle DOS. The additional spike at T_c seen for both compounds in the longitudinal $\alpha(T)$ dependence is likely to result from the particularly strong coupling of longitudinal density fluctuations to electronic energies: it thus reflects the specific-heat jump at the superconducting transition resulting from the reordering of one-particle states. In formal expressions for α, the strong interplay between longitudinal sound and electronic excitations (of incoherent or collective nature) near T_c enters via a large ratio v_s/v_F of the sound velocity to the Fermi velocity that is increased in heavy-fermion systems reflecting a larger accessible phase-space volume (Coffey 1989). This view is supported by the downward shift of this anomaly in magnetic field, which in the case of UBe_{13} is in accord with the upper critical field curve (see fig. 74). For UPt_3 a new phase boundary *below* $B_{c2}(T)$ in the B–T phase diagram as defined by this $\alpha(T)$ anomaly points to either an additional superconducting phase with lower symmetry, similar to the A1 phase in superfluid ^{3}He, or to a magnetically ordered phase, see below.

Previous indications of a double transition in the specific-heat data of UPt_3 for $B = 0$ (fig. 71) seem to be confirmed by sharp structures in new polycrystalline (Fisher et al. 1989) and single-crystal (Hasselbach et al. 1989) samples, although they are not found in other experiments on similar samples (Stewart 1989). In fig. 81 two samples of differing quality, as proven by the differing values of the corresponding transition temperatures, are shown. The deviation ΔT_c of the two transition temperatures remains approximately 60 mK whereas each of the T_c''s is shifted by 70 mK. This was taken as an indication for both transitions being of the same, i.e. superconducting nature (Fisher et al. 1989). Upon applying a magnetic field ($B \perp c$), both T_c''s seem to approach each other and finally not only to merge near $B = 0.5\ T$ (fig. 83), but also to reach the aforementioned phase boundary obtained from the ultrasound data (Schenstrom et al. 1989). The B–T phase diagram of UPt_3 may thus contain three superconducting phases in addition to the normal Fermi liquid, possibly with an antiferromagnetic modulation. Most interesting is the existence of a multicritical point near 370 mK and 0.5 T, at which all four phases seem to coexist. In fact, this has been observed first (Rauchswalbe et al. 1985b, cf. fig. 75) in the resistively determined $B_{c2}(T)$ curve for $B \perp c$ in fig. 75. Concerning the shift of the data in fig. 83, note that the resistively determined T_c is usually somewhat higher than the bulk-T_c determined by specific-heat.

Interestingly enough, this change of slope is also found (Taillefer 1990) in the lower critical field curve shown in fig. 84, which confirms the picture of different superconducting phases. The low-field, high-temperature phase A is extremely sensitive to pressure: the change of slope in $B_{c2}(T)$ disappears under an external hydrostatic pressure as low as 1.4 kbar (fig. 85). It has recently been established,

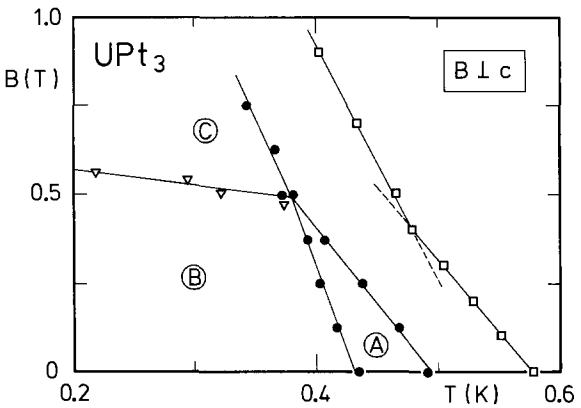

Fig. 83. Proposed phase diagram of the superconducting states in UPt_3 for a magnetic field perpendicular to the c-axis. The existence of two phases at low fields (i.e. for $0 \leq B < 0.5$ T), labelled A and B, is established by the specific-heat measurements of Hasselbach et al. (1989) (closed circles). The transition from phase A to some other high-field phase at $B \simeq 0.5$ T is confirmed by the upper critical-field curve for $B \perp c$ [open squares, taken from Taillefer et al. (1988)]. The fact that this high-field phase, labelled C, is distinct from phase B, is demonstrated by the recent measurements of the ultrasonic attenuation by Schenstrom et al. (1989) (open triangles).

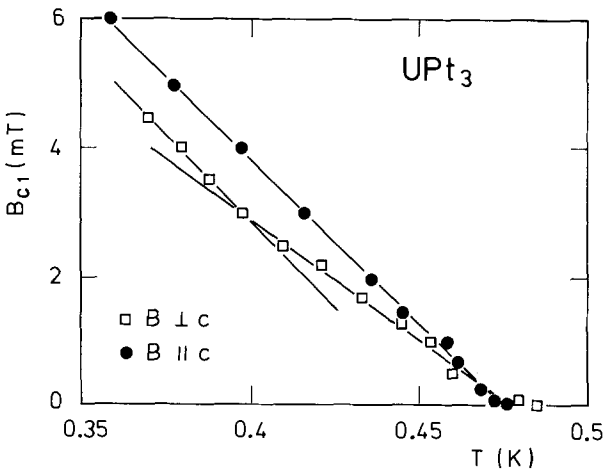

Fig. 84. Lower critical field B_{c1} of UPt_3 near T_c for directions of the magnetic field in the basal plane (parallel to the b-axis, open squares) and parallel to the hexagonal c-axis (closed circles), as determined by magnetization measurements. Note, respectively, the presence and the (apparent) absence of a break in slope around $B = 3$ mT for the two different directions (Taillefer 1990).

too, by measurements of the orientation dependence of the $B_{c2}(T)$ slope for UPt_3 whiskers that at least phase B exhibits the 60° anisotropy of the hexagonal basal plane (Taillefer 1990). Any admixture of anisotropic components to a conventional superconducing order parameter is likely to be reduced by pressure. An explanation of the suppression of phase A, given, e.g., that it is even more

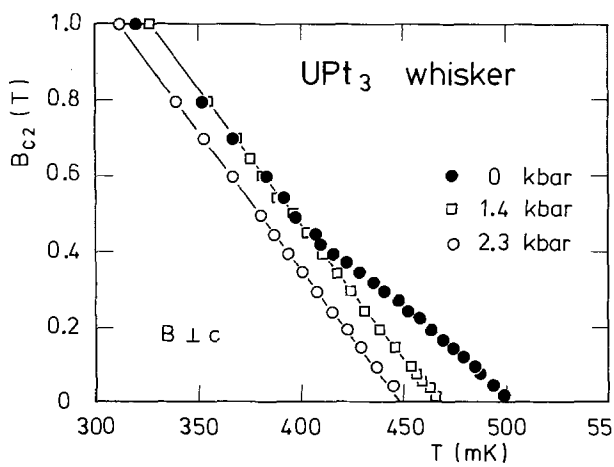

Fig. 85. Temperature dependence of the upper critical field of UPt_3 for three values of the applied hydrostatic pressure in the regime near $T_c(p = 0, B = 0)$ and for a field in the basal plane. Note the complete disappearance of the sharp break in slope of 0.4 T in going from ambient pressure to $p = 1.4$ kbar. This suggests a very rapid suppression of phase A (cf. fig. 83) under pressure (Taillefer 1990).

anisotropic than phase B, seems possible along these lines. Since, however, a $B_{c2}(T)$ anisotropy in the basal plane of the hexagonal structure is not supported by existing group theoretical arguments for unconventional order parameters (Burlachkov 1985), the presence of a symmetry-breaking field is postulated (Taillefer 1990). As a possible source the antiferromagnetic order, discovered by neutron diffractometry (Aeppli et al. 1988), has been inferred. A dependence of the corresponding coupling terms on pressure could lead to the observed disappearance of phase A, as shown in the framework of Ginzburg–Landau theory by Joynt (1988), Hess et al. (1989) and Machida et al. (1989). Surprisingly, however, recent sound-propagation measurements for $B \parallel C$ yield qualitatively the same phase diagram (Bruls et al. 1990), with the A–B phase boundary shifted towards higher-fields. The corresponding shift of the multicritical point obscures the observation of a break in the slope of $B_{c2}(T)$ for this orientation, cf. fig. 75.

Obviously the B–T phase diagram of UPt_3, the x–t diagram of $U_{1-x}Th_xBe_{13}$, see below, and the p–T diagram of ^{3}He share striking similarities. This fact may, however, be fortuitous in view of the pronounced differences with respect to, e.g., symmetry and purity.

4.4. *Impurities in heavy-fermion superconductors*

In the presence of an anisotropic order parameter, impurities in general cause a strong decrease of the transition temperature T_c [see, e.g., Allen and Mitrović (1982) chapters 16 and 17]. Therefore the influence of impurities on heavy-fermion superconductors is particularly intriguing. The situation is different from ordinary superconductors with an isotropic gap, where elastic impurity scattering only renormalizes the normal DOS and does not alter T_c nor lead to a qualitative change of the one-particle excitation spectrum (Anderson 1959). Indeed, this folklore could for the first time be substantiated with doped heavy-fermion superconductors. The depression in T_c for both $Ce_{1-x}M_xCu_{2.2}Si_2$ (fig. 86a) and $U_{1-x}M_xBe_{13}$ (Ahlheim et al. 1988b) turns out to be strong and, furthermore, shows a dependence on the particular dopants. Even for non-magnetic M = La and Y, plots of $\Delta C/\Delta C_0$ against T_c/T_{c0} (fig. 86b) remind us of the pair-breaking phenomenon encountered in BCS superconductors containing paramagnetic impurities (cf., e.g., Steglich 1976): the results lie considerably below the straight line representing the BCS-law of the corresponding states. The corresponding increase of the DOS at low energies seems to be even somewhat more pronounced than that obtained with the Abrikosov–Gorkov theory (Abrikosov and Gorkov 1960, 1961) for stable impurity moments in ordinary superconductors (Skalski et al. 1964). Similar behaviour is well known to result from the Kondo effect associated with moment instabilities (Müller-Hartmann 1973). This raises the suspicion that the "Kondo-hole" picture (Lawrence et al. 1985, Pethick and Pines 1986, Hirschfeld et al. 1986, Miyake 1987, Schmitt-Rink et al. 1987, Cox and Grewe 1988) may also be applicable to impurity scattering in the superconducting state of heavy-fermion systems. Interestingly enough, Gd impurities that, due to their magnetic moment, do not only break the orbital symmetry, but also

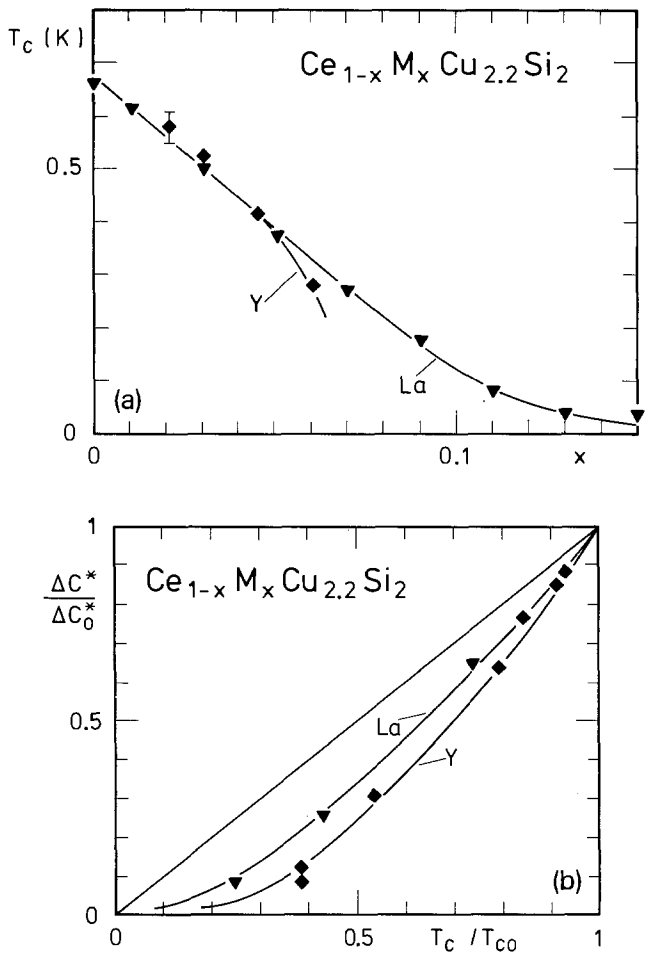

Fig. 86. "Pair breaking" by non-magnetic dopants in $Ce_{1-x}M_xCu_{2.2}Si_2$; M = La (▼), Y(◆) (Ahlheim et al. 1990). (a) Concentration dependence of transition temperature, T_c, plotted against x. Lines are guides to the eye. (b) Reduced specific heat jump,

$$\Delta C^*/\Delta C_0^* = [\Delta C_x/\gamma_x(T_c)]/[\Delta C_{x=0}/\gamma_{x=0}(T_c)]\,,$$

against reduced transition temperature, $T_c/T_{c0} \equiv T_{c,x}/T_{c,x=0}$. Straight line indicates BCS-law of corresponding states ("pair weakening"), the other lines are guides to the eye.

have an influence on the spin pairing, show the strongest effect (Ahlheim et al. 1988b). Superconductivity in $Ce_{1-x}Th_xCu_{2.2}Si_2$ persists up to $x \approx 0.2$ (Ahlheim et al. 1990), and for $x > 0.1$ seems even to coexist with antiferromagnetic order developping below $T_m \simeq 2$–3 K (Jee et al. 1990).

A particularly interesting discovery concerns the existence of a double-peak structure in the specific heat of the $U_{1-x}Th_xBe_{13}$ system in the concentration range 0.02 to 0.04, see fig. 87 (Ott et al. 1985a). The situation is described by the

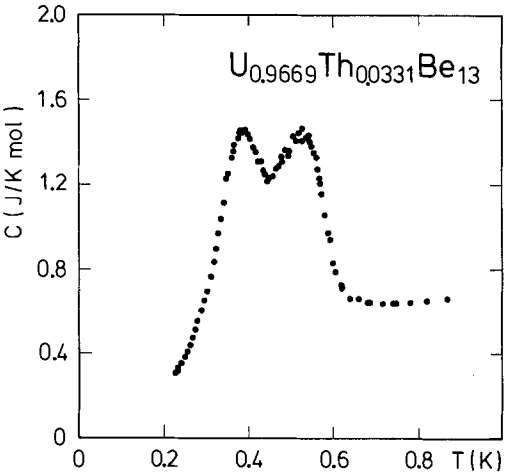

Fig. 87. Specific heat of $U_{1-x}Th_xBe_{13}$ with $x = 3.31$ at.% as C against T (Ott et al. 1985a).

phase diagram of fig. 88 (Rauchschwalbe et al. 1987d). In this concentration range, an upper and lower phase transition line is assumed. The following additional experimental information is available: sound absorption (Batlogg et al. 1985) and thermal expansion (Ott et al. 1986) at the lower transition are anomalously large. μSR experiments point to the onset of antiferromagnetism with an extremely small ordered moment, i.e., less than 10^{-2} μ_B/U (Heffner et al. 1987, 1989). It has been suggested that the lower transition may be of essentially magnetic origin (Batlogg et al. 1985, Moshchalkov 1988).

A discontinuous increase in the slope of the lower critical field, $B_{c1}(T)$, along with the absence of any change in the upper critical field $B_{c2}(T)$ at the lower transition temperature T_{cb} (figs 89a, b) indicates an increase in the superconducting condensation energy (Rauchschwalbe et al. 1987c). These data thus suggest

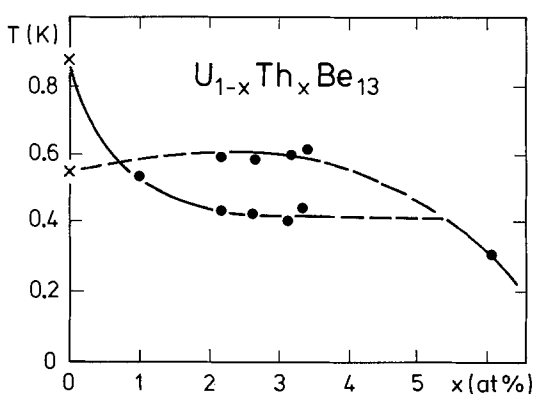

Fig. 88. Phase diagram, T against x, of the superconducting states in $U_{1-x}Th_xBe_{13}$. Dots refer to calorimetric transitions found by Ott et al. (1985a). Crosses are taken from the data in fig. 82. Solid lines are guides to the eye. Dashed lines are interpolations (Rauchschwalbe et al. 1987d).

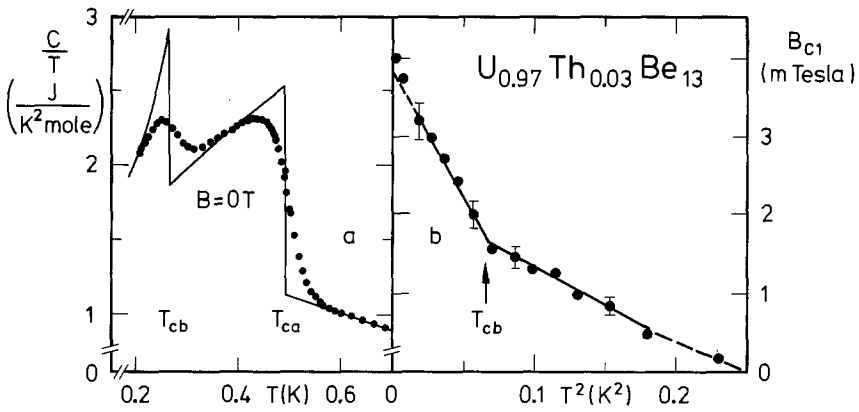

Fig. 89. (a) C/T against T and (b) lower critical field as B_{c1} against T^2 for the same $U_{0.97}Th_{0.03}Be_{13}$ sample (Rauchschwalbe et al., 1987c). Solid lines in (a) represent idealized transitions. Lines in (b) are guides to the eye.

that the lower transition is of superconducting nature, i.e., leads to a different superconducting order parameter. Three alternative methods of explanation have been proposed. The first is inspired by a two-band model and assumes the participation of additional parts of the Fermi surface in the superconducting order parameter at the lower transition. Since scattering in general renders the system more isotropic, impurities mix the two types of order parameter efficiently to a new, more uniform order parameter. Th-dopant atoms, on the other hand, might have an anisotropic scattering potential, matching the anisotropy of the superconducting order parameter to a large extent. This would fit into the general systematics found by Smith et al. (1985). Since both specific-heat jumps are of comparable size, the different portions of the Fermi surface would all contain heavy quasiparticles (Rauchschwalbe et al. 1987c). The two other explanations rest upon the participation of different irreducible symmetry-group representations that are affected by the presence of impurities in different ways. One of them postulates a crossing of the T_c curves of two group representations connected with different anisotropic order parameters near $x \leqslant 0.02$ (Joynt et al. 1986) and a mixing of both representations at the lower transition T_{cb} for larger x (Sigrist and Rice 1989). The other model is based on a sequence of two phase transitions of pure UBe_{13} (cf. figs. 74 and 82), which leads at $T_c = 0.9$ K first to an unconventional phase. Then a mixing of the representations of the original symmetry group results via the feedback of the anisotropic order parameter on the pairing interaction. This non-linear coupling can, even in the set of possible conventional order parameters with respect to the new reduced symmetry, lead to a transition near 0.6 K involving the admixture of an s-wave (Kumar and Wölfle 1987). As a consequence of Th-induced scattering, the relative order of these phase transitions can change. This model needs the existence of a lower superconducting transition of the pure system, and is thus in accord with experimental indications in both the specific heat and $B_{c2}(T)$ (Rauchschwalbe et al. 1987d). All

three different pictures are consistent with the observation that the observed phase transitions are of second order (Rauchschwalbe 1987) and do not separate regions with incompatible order parameters.

Regarding the very small ordered magnetic moment observed below the lower superconducting transition, one might think of four possibilities that are immediately at hand:

(i) Th doping, hindering the formation of a low-T coherent state as inferred from the depression of $T^{\rho}(x)$, the position of the low-T $\rho(T)$ peak, may induce magnetic moments near the Th "Kondo holes" (Moshchalkov 1988). In a way discussed in sect. 3.4 this may lead to a long-range polarization of the heavy Fermi liquid. Interestingly enough, $T^{\rho}(x)$ comes close to $T_c(x)$ near the "multicritical" point at $x \simeq 1.7$ at.% Th (Fisk et al. 1988). Pressure experiments indicate that the effect of Th doping can in part be understood via a "negative lattice pressure" (Lambert et al. 1986, Borges et al. 1988).

(ii) Magnetic degrees of freedom act in some unusual way as a necessary ingredient to superconductivity and are frozen out at the transition.

(iii) Superconducting order prevents total screening of the magnetic U moments and allows them to order magnetically as described in sect. 3.

(iv) A non-unitary order parameter (Volovik and Gorkov 1984, 1985) forms as proposed recently (Sigrist and Rice 1989).

4.5. *Tunnel phenomena*

Tunnel experiments based on proximity effects, quasiparticle and Josephson currents have furnished detailed information about the nature of classical superconductors [see, e.g., the articles by Josephson, McMillan and Rowell, Deutscher and de Gennes in Parks (1969)]. For heavy-fermion superconductors not only the experimental verification but also the theoretical interpretation of such data is more difficult and less unique. In particular, the preparation and characterization of the interfaces and the corresponding transmission properties for quasiparticles and Cooper pairs of non-trivial structure are sources of uncertainty. Only a few relevant theoretical results are known. The classical investigation (Pals et al. 1977) shows that in leading order no Josephson current between a singlet and a triplet superconductor exists and the Josephson frequency arising form the next higher order is $U/(h/4e)$ instead of $U/(h/2e)$. It, however, rests upon the assumption that the tunnel process conserves the one-particle symmetries. Within the same reasoning a proximity contact should reduce the order parameters. One has to face, however, the possibility that the tunnel rate may be substantially suppressed by properties of the barrier alone, which could reduce possible anisotropic Cooper-pair correlations more strongly than isotropic ones (Ambegaokar et al. 1974). This spoils somewhat the prospect of attributing destructive effects to different symmetries on both sides of the interface. Such considerations may be relevant for understanding the observed lack of any Josephson current through weak links between two pieces of UPt_3 (Steglich et al. 1985, Poppe 1985).

In general, those experimental situations seem to be most conclusive in which a definite coupling through an interface can be observed. In particular, two experiments are of relevance here: (i) The observation of a large DC Josephson current through a weak link between $CeCu_2Si_2$ and Al as a counterelectrode, which exhibits ordinary s-wave superconductivity (Steglich et al. 1985, Poppe 1985). (ii) The weakening of an ordinary proximity-induced superconductivity in UBe_{13} below its transition to a state of heavy-fermion superconductivity (Han et al. 1986).

Figure 90 shows the I–V chracteristics of a $CeCu_2Si_2$/Al contact for different temperatures (Steglich et al. 1985, Poppe 1985). The fact that the observed Josephson effect is due to superconductivity through the weak link between Al and $CeCu_2Si_2$ can be inferred from the following observations: (a) the effect disappears in a magnetic field which is overcritical for Al but not for $CeCu_2Si_2$, (b) the effect sets in at the critical temperature of $CeCu_2Si_2$. The equation (Ambegaokar and Baratoff 1963a, b),

$$I_c(T) = R_n^{-1} \Delta_1(T) K([1 - \Delta_1^2/\Delta_2^2]^{1/2}) , \tag{27}$$

that applies for a Josephson contact with n-state resistance R_n between two ordinary superconductors with gaps Δ_1 and Δ_2 (K is the complete elliptical integral of the first kind), reproduces well the order of magnitude of the measured DC Josephson current. Here the BCS relation $2\Delta = 3.5kT_c$ is used for both superconductors. Whereas we believe that this result strongly supports singlet superconductivity in $CeCu_2Si_2$, it should not be taken as proof for an $l = 0$ orbital state: the influence of the barrier may well cause a strong mixing of the different orbital representations of the order parameter. In the case of triplet superconductivity,

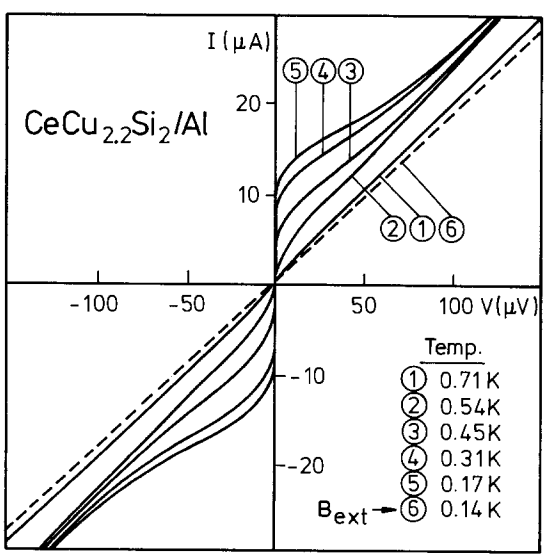

Fig. 90. Current–voltage characteristics of a $CeCu_{2.2}Si_2$/Al Josephson contact ("weak link") at different temperatures (Steglich et al. 1985). Solid lines are for $B = 0$ T, dashed line holds for $B = 25$ mT, a field that is overcritical for Al and comparable to B_{c1} (as $T \to 0$) of $CeCu_2Si_2$.

on the other hand, the tunnelling process would have to strongly violate pseudo-spin conservation, which seems unlikely to us.

In the same spirit, the temperature dependence of the critical currents through weak links between UBe_{13} and Ta as displayed in fig. 91 (Han et al. 1986) can be understood. Since the effect sets in at $T_c^* = 3.23\,K$, i.e., not too far below $T_c = 4.47\,K$ for Ta but way above $T_c = 0.92\,K$ for UBe_{13}, it must be caused by proximity-induced superconductivity in the heavy-fermion system at this temperature. This is substantiated by the detection of an AC Josephson effect. The height of the "Shapiro steps" of $\Delta U = h\nu/2e$ indicates that this effect is of leading order (Han et al. 1986). If it is again assumed that the barrier cannot work constructively between two different superconducting symmetries, the proximity-induced order should be of the same classical type as that of Ta. The critical current rises with decreasing temperature, in rough agreement with what is expected from such a proximity contact (Han et al. 1985). Near the onset of heavy-fermion superconductivity in UBe_{13}, however, the critical current starts to fall, which is different from what is seen for Mo. This is a clear hint at a different symmetry type of the new order parameter. We thus conclude that the order parameter of UBe_{13} cannot be isotropic. Triplet superconductivity is not necessarily involved, however, as was suggested by Han et al. (1986). The strong anisotropies connected with the heavy quasiparticles and their interactions alone could produce this destructive effect.

For a unique interpretation of these interesting experimental results, some new developments in theory would be highly desirable. These concern a realistic description of tunnel barriers within the semiclassical approach to superconductivity. Although it is possible within this theory to treat the standard surface model for the proximity effect with help of a sensible phenomenological boundary condition (Ashauer et al. 1986), tunnelling through a barrier is usually described

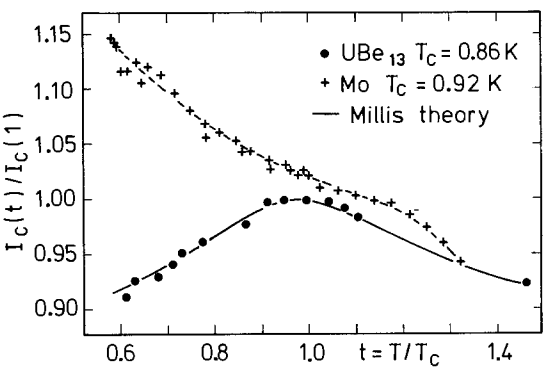

Fig. 91. Normalized critical current, $I_c(t)/I_c(1)$, as a function of reduced temperature, $t = T/T_c$, for junctions of Mo–Ta and UBe_{13}–Ta. Dashed line is a guide to the eye. Solid curve is a fit to the data of a model that explains the reduction of Δ_s, the singlet order parameter of the "proximity-induced surface superconductivity", by the development of a triplet order parameter below the bulk-T_c of UBe_{13}. In this model $I_c \sim \Delta_s \Delta_{Ta}$ is assumed (Han et al. 1986).

via a set of hypothetical matrix elements $M_{\alpha\beta}$. They transform a quasiparticle with Bloch momentum $\boldsymbol{k}$ and pseudospin α on side A into one with $\boldsymbol{q}$ with β on side B (Ambegaokar and Baratoff 1963a, b, Sauls et al. 1986). In the framework of BCS theory it is straightforward to express the Josephson current through the barrier

$$I_c(t) = \frac{2e}{\hbar}\,\mathrm{Im}\{\langle\!\langle v|v\rangle\!\rangle(eU + i\eta)e^{i\omega_0 t}\}\,, \quad \omega_0 = \frac{2eU}{\hbar} \tag{28}$$

via the anomalous velocity correlation

$$\langle\!\langle v|v\rangle\!\rangle(eU + i\eta) = \sum_{k,q} \frac{g_{k,q}}{4E_k^A E_q^B}\,\mathrm{Tr}\{\hat{M}_{k,q}\hat{\Delta}_q^B \hat{M}^T_{-k,-q}\hat{\Delta}_k^{A\dagger}\}\,,$$

$$g_{k,q} = \int_{-\infty}^{\infty} d\omega \int_{-\infty}^{\infty} d\omega'\, \frac{f^A(\omega) - f^B(\omega')}{\omega_0 - \omega + \omega' + i\eta}\,[\delta(\omega + E_k^A] - \delta(\omega - E_k^A)]$$

$$\times [\delta(\omega' + E_q^B) - \delta(\omega' - E_q^B)]\,, \tag{29}$$

where $\hat{\Delta} = [\Delta_0 \hat{1} + \boldsymbol{\Delta}\hat{\boldsymbol{\sigma}}]i\hat{\sigma}_y$ is the usual (wavevector-dependent) order parameter matrix in pseudospin space for side A or B,

$$E_k = (\epsilon_k^2 + |\Delta_{0k}|^2 + |\boldsymbol{\Delta}_k|^2)^{1/2}\,,$$

for unitary states with one particle energies ϵ_k, and $\hat{M} = m_0\hat{1} + \boldsymbol{m}\hat{\boldsymbol{\sigma}}$ is the matrix of tunnel matrix elements with pseudospin-conserving part m_0. $\boldsymbol{m}$ incorporates those tunnelling processes that can mix singlet and triplet representations of the order parameter. The superscripts T and † indicate transposed and Hermitean conjugate matrices, respectively. Straightforward evaluation of the trace in pseudospin space in eq. (29) gives the following results in the presence of time-reversal invariance (Sauls et al. 1986, Grewe 1986):

(i) A singlet-to-singlet current ($\boldsymbol{\Delta}_A = \boldsymbol{\Delta}_B = 0$) is caused by both pseudospin conserving and non-conserving transfers, i.e.,

$$I_c^{ss} \sim 2(|m_0|^2 + |\boldsymbol{m}|^2)\Delta_{0B}\Delta_{0A}^*\,. \tag{30a}$$

(ii) A singlet-to-triplet current ($\boldsymbol{\Delta}_A = \Delta_{0B} = 0$) does not occur for pseudospin conserving tunnelling processes only ($\boldsymbol{m} = 0$), since

$$I_c^{st} \sim 2[2\,\mathrm{Re}(m_0^*\boldsymbol{m}) - i\boldsymbol{m} \times \boldsymbol{m}^*]\boldsymbol{\Delta}_B\Delta_{0A}^*\,. \tag{30b}$$

It also vanishes, if tunnelling conserves parity, since then m_0 and $\boldsymbol{m}$ are purely real and imaginary, respectively.

(iii) For a triplet-to-triplet current ($\Delta_{0A} = \Delta_{0B} = 0$) again all the tunnelling matrix elements can contribute:

$$I_c^{tt} \sim 2\boldsymbol{\Delta}_B[(|m_0|^2 - |\boldsymbol{m}|^2) + 2\,\mathrm{Re}(\boldsymbol{m}\cdot\boldsymbol{m}^*)]\boldsymbol{\Delta}_A^* - 4i\,\mathrm{Re}(m_0\boldsymbol{m}^*)\cdot(\boldsymbol{\Delta}_B \times \boldsymbol{\Delta}_A^*)\,. \tag{30c}$$

More detailed information about a possible mixing of different symmetry-group representations of pseudo-spin singlet or triplet order parameters can in principle be obtained by inspection of the wave-vector dependence in eq. (29).

This kind of semi-phenomenological theory is unsatisfactory from at least two points of view: (1) No theory exists for the tunnel matrix elements that would take the complex quasiparticle structure on both sides in account; and (2) the order parameter near the physical barrier behaves inhomogenously so that – if the corresponding regions are not formally included into the "barrier" – only the semiclassical theory of superconductivity appears appropriate (Ashauer et al. 1986). Furthermore, for reliable estimates of the size of tunnel currents, the orientation of interfaces relative to the crystal axes (Geshkenbein and Larkin 1986) and the influence of inhomogeneity on the spin–orbit coupling (Fenton 1985) may have to be taken properly into account.

4.6. *Some conclusions concerning the nature of heavy-fermion superconductivity*

The detailed experimental investigations have, at least for $CeCu_2Si_2$ and UBe_{13}, spoiled the original hope of finding triplet superconductivity in metals similar to the known case of superfluid ^3He. Apparently the lower symmetry and the lower purity of crystals play an essential role for the superconducting states found in heavy-fermion compounds. We would like to recall a few key observations which underline this conclusion:

(i) the rather weak "pair-breaking" effect of non-magnetic dopants (Ahlheim et al. 1988a,b);

(ii) the strong Pauli limiting in $B_{c2}(T)$ that is particularly pronounced for $CeCu_2Si_2$ but also occurs for UBe_{13} (Rauchschwalbe et al. 1985b);

(iii) the large DC Josephson current through weak links formed between $CeCu_2Si_2$ and Al (Steglich et al. 1985, Poppe 1985); and

(iv) a 50% reduction in the local spin susceptibility of UBe_{13} upon cooling through T_c, as measured by the μSR-Knight shift (Heffner et al. 1986).

In the light of the existing experimental evidence the occurrence of anisotropic order parameters is possible. Whether these are conventional, i.e., crystal symmetry preserving, or unconventional is unknown. In particular, it cannot be decided at present which of the possible order parameters is realized in any of the four materials $CeCu_2Si_2$, UBe_{14}, UPt_3 and URu_2Si_2. Power laws measured in a number of experimental quantities do not give a consistent picture. The behaviour is not unique for any of these substances, and the question must be allowed whether such power laws are at all genuine traces of an underlying low-temperature symmetry of the pure superconductors.

This last point may be elucidated by considering a spin-fluctuation mechanism for Cooper pairing (Millis et al. 1988). Given that short-range antiferromagnetic spin fluctuations actually cause pairing, considerable pair breaking would result at the same time for an anisotropic order parameter. This is due to inelastic scattering of quasiparticles by the spin fluctuations that would also in this theory account for the large normal-state resistivity near T_c as observed for $CeCu_2Si_2$ and, in particular, UBe_{13}. The essential point is that, due to this strong pair breaking, strong-coupling effects are present below T_c. Any signature of a possible anisotropic order parameter in the DOS is, thus, wiped out. At the

lowest temperatures, inelastic scattering is frozen out, but residual elastic scattering is still present and can be large, as is likely in, e.g., the case for UBe_{13} and for $CeCu_2Si_2$ with residual resistivities as large as 15 $\mu\Omega$ cm and 65 $\mu\Omega$ cm (Rauchschwalbe 1987), respectively. In general, strong-coupling effects should be considerable, no matter what microscopic mechanism is assumed, since the stability of the quasiparticles is not large: itinerant quasiparticles form typically at temperatures comparable to the superconducting transition temperature. One wonders how, under these circunstances, an anisotropic order parameter can be maintained at all. The evidence for a multiphase diagram of UPt_3 and $U_{1-x}Th_xBe_{13}$ as discussed above, however, supports such an appealing possibility. In our opinion, the size of the coherence length ($\xi \sim 100$ Å), which is smaller than in classical superconductors by up to two orders of magnitude, plays an important role. ξ is still much larger than the lattice constant, so that the pair wavefunction is in fact well defined in $\boldsymbol{k}$-space instead of real space. Therefore the observed order parameter anisotropies are to be connected with extreme Fermi surface anisotropies: it is conceivable that there is either a lack of heavy quasiparticles in certain $\boldsymbol{k}$-space directions, as suggested by some band-structure calculations, or an opening of a gap in particular sections of the Brillouin zone, as is to be expected in connection with SDW formation. This latter possibility is in accord with neutron diffraction and μSR results on URu_2Si_2 (Broholm et al. 1987b), $U_{1-x}Th_xBe_{13}$ (Heffner et al. 1987, 1989) and, presumably, UPt_3 (Aeppli et al. 1988).

Not only the symmetry of the order parameter but, more fundamentally, the true nature of the interactions responsible for Cooper-pair formation is still unknown. On the one hand, there is a theoretical prejudice, based on the apparent importance of the magnetic degrees of freedom in the heavy Fermi-liquid state and some similarities to ^{3}He, i.e., strong local repulsion of quasiparticles, that the mechanism involves magnetic fluctuations (Fay and Appel 1985, Béal-Monod 1985, Šimanek 1985, Schuh 1985, Béal-Monod et al. 1986, Cyrot 1986, Miyake et al. 1986, Scalapino et al. 1987, Norman 1987, Grabowski 1987, Zhang et al. 1987, Dolgov et al. 1987, Zhang and Lee 1988, Putikka and Joynt 1989). Due to this repulsion and the expected weak quasiparticle dispersion, anisotropic superconducting phases and reduced coherence lengths seem probable, which is in accord with experiments. On the other hand, there does not really exist any conclusive correlation between an enhanced tendency towards magnetism and the occurrence of such superconductivity, see sect. 3. The conventional deformation-potential coupling mechanism, applied to the itinerant states alone, however, can apparantly not account for pairing between heavy fermions (Entel et al. 1985, Pickett et al. 1986, Fenton 1987, Normal 1988).

There are a number of experimental clues hinting at a strong coupling of the heavy quasiparticles to elastic degrees of freedom. We have discussed them in connection with ultrasonic attenuation (Müller et al. 1986a), anomalies in elastic constants (Lüthi and Yoshizawa 1987) and thermal expansion (Ribault et al. 1979, Lang et al. 1987). The salient interpretation of the Kondo-volume collapse in Ce compounds in particular invokes this mechanism. The coupling strength is likely

to be comparable to any interaction among heavy quasiparticles. Consequently, this particular kind of electron–phonon interaction also has to be considered as a possible source of heavy-fermion superconductivity (Razafimandimby et al. 1984, Grewe 1984b, Miyake et al. 1984, Entel and Matschke 1986, Ohkawa 1987, Jichu et al. 1987, Keller et al. 1988). Although the local nature of the quasiparticle–phonon interaction as opposed to a conventional deformation-potential coupling could favour an anisotropy by its own, it is not likely that unconventional superconducting order parameters can arise without the effect of local quasiparticle repulsion. In conclusion, we want to advocate the following point of view: heavy-fermion superconductivity is produced by an interplay of elastic- and electronic-coupling mechanisms that are peculiar to the nature of the heavy Fermi-liquid (Grewe 1988b). The variety of experimental data, which cannot be interpreted consistently with any one of the existing theoretical models, is probably caused by a sensitive balance between such different sources of interaction and, most probably, by their interference. The situation is further complicated by the strongly frequency-dependent renormalizations of the quasiparticles and the pronounced wavevector dependences of the two contributing interactions, which are characteristically different. The electron–phonon interaction is generally attractive and involves the local breathing modes, whereas the exchange of spin flutuations generates a q-dependent repulsion that may, however, favour superconductivity due to pronounced structure at $q \approx 2k_F$ and, possibly, also at small q-values. Thus, no easy answers to the fundamental questions raised in this field may exist at all.

5. Epilogue

Viewing the field of heavy-fermion physics as a whole, several observations can be made, which concern the impact of this new field of research on our understanding of solid-state physics.

A number of exciting phenomena have enriched solid-state physics, e.g., strongly enhanced and temperature-dependent thermodynamic coefficients, coherent heavy Fermi liquids with well defined, highly anisotropic Fermi surfaces as measured by the de Haas–van Alphen effect, anisotropic superconducting order parameters and itinerant magnetic phases with small moments, formed in the low-temperature Fermi-liquid state. The wealth of experimental data is at least partially understood. In a qualitative sense new concepts that have been derived from the many-body properties of simple models have clarified some basic features. These concern the existence of heavy masses, the influence of coherence and an initial insight into cooperative mechanisms. Heavy-fermion physics has, however, brought some basic problems of solid-state theory into focus. In spite of qualitative progress in strong-correlation physics, no general concept for quantitative calculations has been developed so far which is comparable to band-structure theory for simpler metals. It is certainly important to implement modern many-body methods for strong correlations into a realistic calculation scheme for

general response functions, which yields one-particle spectra only as a special case. One example that has to be seen in this context is the ongoing discussion about the validity of a band picture for U compounds. The actinide systems with their peculiar, not well understood, behaviour clearly demonstrate that the solution, in general, cannot be found by semi-phenomenological approaches that have to be based on a clear hierarchy of characteristic energies. Within this context, the heavy-fermion systems are a "simple" prototype for a new generation of materials with strong influence of crystal structures and local correlations. Other prominent examples are the intermediate-valence compounds and the high-T_c superconductors.

In its initial stages heavy-fermion research has mainly been concentrated on the phenomenon of superconductivity. In a few years, a considerable repertoire of experimental methods and theoretical models, some of them with new features, has been applied. Soon, however, it was realized that important questions remained open: experimental results proved inconclusive regarding the pairing mechanism and the nature of the superconducting phases. Truly microscopic theories were limited in their scope by technical problems that already apply in a study of the normal state in the presence of correlations. An important lesson to be learned concerns the extreme sensitivity of heavy-fermion properties on lattice disorder, which seems to be a general phenomenon for strongly correlated materials. It is, therefore, remarkable that after the first active period and the advent of high-T_c superconductivity the field of heavy-fermion physics has retained its appeal. The reason is primarily to be found in new exciting discoveries that bring interesting magnetic states and even the normal Fermi-liquid phase into focus. For theoreticians the normal state of heavy-fermion systems certainly poses an ongoing challenge and serves as a good model to study strong local correlations in a broader context. It can be hoped that the knowledge gathered here will also prove useful for 5f and 3d materials in general as far as the role of correlations is concerned. As has become clear in the last three years in connection with high-T_c superconductors, additional aspects are important in all of these interesting new materials. We mention, in particular, the role of dimensionality and crystal structure, and the antagonism between the localized and the delocalized pictures, which becomes more relevant with increasing spatial extent of the f- and d-wavefunctions.

Acknowledgements

We have largely benefitted over the years from collaborations and discussions with many colleagues, in particular, with the members of the Sonderforschungsbereich (SFB) 252 "Elektronisch Hochkorrelierte Metallische Materialien", Darmstadt/Frankfurt/Mainz/Stuttgart. Part of this review was drafted during our stay at the University of Florida, Gainesville, and we would like to thank G.R. Stewart and P. Wölfle for their warm hospitality. We are also very grateful to T. Pruschke for contributing numerical results and figures.

Excellent technical assistance by A. Hanna-Daoud, B. Knell, C. Castel and R. Geibel is gratefully acknowledged. We have received support by the Deutsche Forschungsgemeinschaft, in part under the auspices of the SFB 252, and one of us (F.S.) also by the Stiftung Volkswagenwerk.

References

Aarts, J., F.R. de Boer, S. Horn, F. Steglich and D. Meschede, 1981, in: Valence Fluctuations in Solids, eds L.M. Falicov, W. Hanke and M.B. Maple (North-Holland, Amsterdam) p. 301.

Abrikosov, A.A., 1965a, Physics **2**, 5.

Abrikosov, A.A., 1965b, Physics **2**, 61.

Abrikosov, A.A., 1972, Solid State Phys., Suppl. **12**.

Abrikosov, A.A., and L.P. Gorkov, 1960, Zh. Eksp. Teor. Fiz. **39**, 1781.

Abrikosov, A.A., and L.P. Gorkov, 1961, Sov. Phys.-JETP **12**, 1243.

Abrikosov, A.A., L.P. Gorkov and J.E. Dzyaloshinsky, 1963, Methods of Quantum Field Theory in Statistical Physics (Prentice-Hall, Englewood Cliffs, New York).

Aeppli, G., E. Bucher, A.I. Goldman, G. Shirane, C. Broholm and J.K. Kjems, 1988, J. Magn. & Magn. Mater. **76&77**, 385.

Aeppli, G., D. Bishop, C. Broholm, E. Bucher, K. Siemensmeyer, M. Steiner and N. Stüsser, 1989, Phys. Rev. Lett. **63**, 676.

Ahlheim, U., P. van Aken, H. Spille and F. Steglich, 1988a, Helv. Phys. Acta **61**, 518.

Ahlheim, U., M. Winkelmann, P. van Aken, C.D. Bredl, F. Steglich and G.R. Stewart, 1988b, J. Magn. & Magn. Mater. **76&77**, 520.

Ahlheim, U., M. Winkelmann, C. Schank, C. Geibel, F. Steglich and A.L. Giorgi, 1990, Physica B **163**, 391.

Alekseevskii, N.E., and D.I. Khomskii, 1985, Sov. Phys. Usp. **28**, 1136.

Aliev, F.G., N.B. Brandt, V.V. Moshchalkov and S.M. Chudinov, 1983, Solid State Commun. **45**, 215.

Aliev, F.G., N.B. Brandt, V.V. Moshchalkov and S.M. Chudinov, 1984, J. Low Temp. Phys. **57**, 61.

Allen, J.W., and R.M. Martin, 1982, Phys. Rev. Lett. **49**, 1106.

Allen, P.B., and B. Mitrović, 1982, Solid State Phys. **37**, 1.

Amato, A., D. Jaccard, E. Walker, J. Sierro and J. Flouquet, 1987a, J. Magn. & Magn. Mater. **63&64**, 300.

Amato, A., D. Jaccard, J. Flouquet, F. Lapierre, J.L. Tholence, R.A. Fisher, S.E. Lacy, J.A. Olsen and N.E. Phillips, 1987b, J. Low Temp. Phys. **68**, 371.

Ambegaokar, V., and A. Baratoff, 1963a, Phys. Rev. Lett. **10**, 486.

Ambegaokar, V., and A. Baratoff, 1963b, Phys. Rev. Lett. **11**, 104.

Ambegaokar, V., P.G. de Gennes and D. Rainer, 1974, Phys. Rev. A **9**, 2676.

Ambrüster, H., W. Franz, W. Schlabitz and F. Steglich, 1979, J. Phys. (Paris) **40**, C4-150.

Anderson, P.W., 1959, J. Phys. Chem. Solids **11**, 26.

Anderson, P.W., 1961, Phys. Rev. **124**, 41.

Anderson, P.W., 1984a, Phys. Rev. B **30**, 1553.

Anderson, P.W., 1984b, Phys. Rev. B **30**, 4000.

Andraka, B., G. Fraunberger, J.S. Kim, C. Quitmann and G.R. Stewart, 1989, Phys. Rev. B **39**, 64020.

Andrei, N., K. Furuya and J.K. Loewenstein, 1983, Rev. Mod. Phys. **55**, 331.

Andres, K., J.E. Graebner and H.R. Ott, 1975, Phys. Rev. Lett. **35**, 1779.

Appel, J., and P. Hertel, 1987, Phys. Rev. B **35**, 155.

Asayama, K., Y. Kitaoka and Y. Kohori, 1988, J. Magn. & Magn. Mater. **76&77**, 449.

Ashauer, B., G. Kieselmann and D. Rainer, 1986, J. Low Temp. Phys. **63**, 349.

Assmus, W., M. Herrmann, U. Rauchschwalbe, S. Riegel, W. Lieke, H. Spille, S. Horn, G. Weber, F. Steglich and G. Cordier, 1984, Phys. Rev. Lett. **52**, 469.

Assmus, W., W. Sun, G. Bruls, D. Weber, B. Wolf, B. Lüthi, M. Lang, U. Ahlheim, A. Zahn and F. Steglich, 1990, Physica B **165&166**, 379.

Auerbach, A., and K. Levin, 1986, Phys. Rev. Lett. **57**, 877.

Auerbach, A., Ju.H. Kim, K. Levin and M.R. Norman, 1988, Phys. Rev. Lett. **60**, 623.

Ballentine, J.E., and M. Hubermann, 1977, J. Phys. C **10**, 4991.

Barbara, B., J.X. Boucherle, J.L. Buevoz, M.F. Rossignol and J. Schweizer, 1977, Solid State Commun. **24**, 481.

Barbara, B., M. Cyrot, C. Lacroix-Lion-Caen and M.F. Rossignol, 1979, J. Phys. (Paris) **40**, C5-340.

Barbara, B., M.F. Rossignol, J.X. Boucherle and C. Vettier, 1980, Phys. Rev. Lett. **45**, 938.

Barth, S., H.R. Ott, F.N. Gygax, B. Hitti, E. Lippelt, A. Schenck, C. Baines, B. van den Brandt, T. Konter and S. Mango, 1987, Phys. Rev. Lett. **59**, 2991.

Barth, S., H.R. Ott, F.N. Gygax, B. Hitti, E. Lippelt and A. Schenck, 1988, J. Magn. & Magn. Mater. **76&77**, 455.

Bastide, C., and C. Lacroix, 1986, Solid State Commun. **59**, 121.

Batlogg, B., D.J. Bishop, B. Golding, C.M. Varma, Z. Fisk, J.L. Smith and H.R. Ott, 1985, Phys. Rev. Lett. **55**, 1319.

Batlogg, B., D.J. Bishop, B. Golding, E. Bucher, J. Hufnagl, Z. Fisk, J.L. Smith and H.R. Ott, 1986, Phys. Rev. B **33**, 5906.

Batlogg, B., D.J. Bishop, E. Bucher, B. Golding Jr, A.P. Ramirez, Z. Fisk, J.L. Smith and H.R. Ott, 1987, J. Magn. & Magn. Mater. **63&64**, 441.

Baym, G., and C. Pethick, 1978, in: The Physics of Liquid and Solid Helium, part II, eds K.H. Bennemann and J.B. Ketterson (Wiley, New York) ch. 1.

Béal-Monod, M.T., 1985, Phys. Rev. B **31**, 1647.

Béal-Monod, M.T., C. Bourbonnais and V.J. Emery, 1986, Phys. Rev. B **34**, 7716.

Becker, K.W., and P. Fulde, 1987, Z. Phys. B **67**, 35.

Bellarbi, B., A. Benoit, D. Jaccard, E. Walker, J. Sierro and J. Flouquet, 1984, Phys. Rev. B **30**, 1182.

Benedict, U., W.A. Grosshaus and W.B. Holzapfel, 1986, Physica B **144**, 14.

Benoit, A., J.X. Boucherle, P. Convert, J. Flouquet, J. Palleau and J. Schweizer, 1980, Solid State Commun. **34**, 293.

Benoit, A., A. Berton, J. Chaussy, J. Flouquet, J.C. Lasjaunias, J. Odin, J. Palleau, J. Peyrard and M. Ribault, 1981, in: Valence Fluctuations in Solids, eds L.M. Falicov, W. Hanke and M.B. Maple (Noi Holland, Amsterdam) p. 283.

Berton, A., J. Chaussy, G. Chouteau, B. C nut, J. Peyrard and R. Tournier, 1977, in: Valence Instabilities and Related Narrow-Band Phenomena, ed. R.D. Parks (Plenum Press, New York) p. 471.

Besnus, M.J., J.P. Kappler, P. Lehmann and A. Meyer, 1985, Solid State Commun. **55**, 779.

Besnus, M.J., P. Lehmann and A. Meyer, 1987, J. Magn. & Magn. Mater. **63&64**, 323.

Bickers, N.E., 1987, Rev. Mod. Phys. **59**, 845.

Bickers, N.E., D.L. Cox and J.W. Wilkins, 1985, Phys. Rev. Lett. **54**, 230.

Bickers, N.E., D.L. Cox and J.W. Wilkins, 1987, Phys. Rev. B **36**, 2036.

Bilz, H., G. Güntherodt, W. Kleppmann and W. Kress, 1979, Phys. Rev. Lett. **43**, 1998.

Bleckwedel, A., and A. Eichler, 1985, Solid State Commun. **56**, 693.

Blount, E.I., 1985, Phys. Rev. B **32**, 2935.

Blumenröder, S., E. Zirngiebl, G. Güntherodt, A. Jayaraman, B. Batlogg, A. Meyer and Z. Fisk, 1985, J. Magn. & Magn. Mater. **47&48**, 318.

Böhm, A., R. Caspary, U. Habel, L. Pawlak, A. Zuber, F. Steglich and A. Loidl, 1988, J. Magn. & Magn. Mater. **76&77**, 150.

Borges, H.A., J.D. Thompson, M.C. Aronson, J.L. Smith and Z. Fisk, 1988, J. Magn. & Magn. Mater. **76&77**, 235.

Brandow, B.H., 1977, Adv. Phys. **26**, 651.

Brandow, B.H., 1986, Phys. Rev. B **33**, 215.

Brandow, B.H., 1988, Phys. Rev. B **37**, 250.

Brandt, N.B., and V.V. Moshchalkov, 1984, Adv. Phys. **33**, 373.

Braun, H.F., and J.L. Jorda, 1985, Physica B **135**, 72.

Bredl, C.D., 1985, Dissertation, TH Darmstadt, unpublished.

Bredl, C.D., 1987, J. Magn. & Magn. Mater. **63&64**, 355.

Bredl, C.D., F. Steglich and K.D. Schotte, 1978a, Z. Phys. B **29**, 327.

Bredl, C.D., F. Steglich and K.D. Schotte, 1978b, J. Magn. & Magn. Mater. **9**, 17.

Bredl, C.D., H. Spille, U. Rauchschwalbe, W. Lieke, F. Steglich, G. Cordier, W. Assmus, M. Herrmann and J. Aarts, 1983, J. Magn. & Magn. Mater. **31–34**, 373.

Bredl, C.D., S. Horn, F. Steglich, B. Lüthi and R.M. Martin, 1984a, Phys. Rev. Lett. **52**, 1982.

Bredl, C.D., N. Grewe, F. Steglich and E. Umlauf, 1984b, in: Proceedings of LT-17, eds U. Eckern, A. Schmid, W. Weber and H. Wühl (Elsevier, Amsterdam) p. 327.

Bredl, C.D., W. Lieke, R. Schefzyk, M. Lang, U. Rauchschwalbe, F. Steglich, J.C.P. Klaasse, J. Aarts and F.R. de Boer, 1985, J. Magn. & Magn. Mater. **47&48**, 30.

Brison, J.P., A. Ravex, J. Flouquet, Z. Fisk and J.L. Smith, 1988, J. Magn. & Magn. Mater. **76&77**, 525.

Brodale, G.E., R.A. Fisher, N.E. Phillips and J. Flouquet, 1986, Phys. Rev. Lett. **56**, 390.

Broholm, C., J.K. Kjems, G. Aeppli, Z. Fisk, J.L. Smith, S.M. Shapiro, G. Shirane and H.R. Ott, 1987a, Phys. Rev. Lett. **58**, 917.

Broholm, C., J.K. Kjems, W.J.L. Buyers, P. Matthews, T.T.M. Palstra, A.A. Menovsky and J.A. Mydosh, 1987b, Phys. Rev. Lett. **58**, 1467.

Bruls, G., B. Lüthi, D. Weber, B. Wolf and P. Thalmeier, 1990a, Phys. Scr., in press.

Bruls, G.J.C.L., D. Weber, B. Wolf, B. Lüthi, A.A. Menovsky, A. de Visser and J.J.M. Franse, 1990b, Physica B **165&166**, 369.

Burlachkov, L.I., 1985, Sov. Phys.-JETP **62**, 800.

Caspary, R., 1988, H. Diploma (TH Darmstadt) unpublished.

Chan, S.K., and D.J. Lam, 1974, The Actinides - Electronic Structure and Related Properties, Vol. 1, eds A.J. Freeman and J.B. Darby Jr (Academic Press, New York) p. 1.

Chen, D.P., and J. Callaway, 1988, Phys. Rev. B **38**, 11869.

Chen, J.W., S.E. Lambert, M.B. Maple, Z. Fisk, J.L. Smith, G.R. Stewart and J.O. Willis, 1984, Phys. Rev. B **30**, 1583.

Coffey, L., 1987, Phys. Rev. B **35**, 8440.

Coffey, L., 1989, Phys. Rev. B **40**, 715.

Coffey, L., T.M. Rice and K. Ueda, 1985, J. Phys. C **18**, L813.

Coleman, P., 1983, Phys. Rev. B **28**, 5255.

Coleman, P., 1984, Phys. Rev. B **29**, 3035.

Coleman, P., and N. Andrei, 1986, J. Phys. C **19**, 3211.

Coleman, P., P.W. Anderson and T.V. Ramakrishnan, 1985, Phys. Rev. Lett. **55**, 414.

Coles, B.R., 1987, Contemp. Phys. **28**, 143.

Coppersmith, S.N., and R.A. Klemm, 1986, Phys. Rev. Lett. **56**, 1870.

Coqblin, B., 1982, in: Magnetism of Metals and Alloys, ed. M. Cyrot (North-Holland, Amsterdam) p. 295 ff.

Cornut, B., and B. Coqblin, 1972, Phys. Rev. B **5**, 4541.

Cox, D.L., 1987a, Phys. Rev. B **35**, 4561.

Cox, D.L., 1987b, Phys. Rev. Lett. **59**, 1240.

Cox, D.L., 1988, Physica C **153**, 1642.

Cox, D.L., and N. Grewe, 1988, Z. Phys. B **71**, 321.

Cox, D.L., N.E. Bickers and J.W. Wilkins, 1985, J. Appl. Phys. **57**, 3166.

Cox, D.L., N.E. Bickers and J.W. Wilkins, 1986, J. Magn. & Magn. Mater. **54–57**, 333.

Crabtree, G.W., 1985, J. Magn. & Magn. Mater. **52**, 169.

Croft, M.C., R.P. Guertin, L.C. Kupferberg and R.D. Parks, 1979, Phys. Rev. B **20**, 2073.

Cyrot, M., 1986, Solid State Commun. **60**, 253.

de Boer, F.R., J.C.P. Klaasse, J. Aarts, C.D. Bredl, W. Lieke, U. Rauchschwalbe, F. Steglich, R. Felten, U. Umhofer and G. Weber, 1985, J. Magn. & Magn. Mater. **47&48**, 60.

de Boer, F.R., J.C.P. Klaasse, P.A. Veenhuizen, A. Böhm, C.D. Bredl, U. Gottwick, H.M. Mayer, L. Pawlak, U. Rauchschwalbe, H. Spille and F. Steglich, 1987, J. Magn. & Magn. Mater. **63&64**, 91.

de Visser, A., J.C.P. Klaasse, M. van Sprang, J.J.M. Franse, A. Menovsky and T.T.M. Palstra, 1986, J. Magn. & Magn. Mater. **54–57**, 375.

de Visser, A., A. Menovsky and J.J.M. Franse, 1987, Physica B **147**, 81.

DeLong, L.E., 1987, in: Theoretical and Experimental Aspects of Valence Fluctuations and Heavy Fermions, eds L.C. Gupta and S.K. Malik (Plenum Press, New York) p. 65.

Desgranges, H.U., 1987, Solid State Commun. **61**, 491.

Desgranges, H.U., and J.W. Rasul, 1985, Phys. Rev. B **32**, 6100.

Desgranges, H.U., and J.W. Rasul, 1987, Phys. Rev. B **36**, 328.

Dhar, S.K., K.A. Gschneidner Jr, C.D. Bredl and F. Steglich, 1989, Phys. Rev. B **39**, 2439.

Dolgov, O.V., E.P. Fetisov, D.I. Khomskii and S. Svozil, 1987, Z. Phys. B **67**, 63.

Doniach, S., 1977, Physica B **91**, 231.

Doniach, S., 1987a, Phys. Rev. B **35**, 1814.

Doniach, S., 1987b, in: Theoretical and Experimental Aspects of Valence Fluctuations and Heavy Fermions, eds L.C. Gupta and S.K. Malik (Plenum Press, New York) p. 179.

Edelstein, A.S., R.E. Majewski and T.H.

Blewitt, 1977, in: Valence Instabilities and Related Narrow-Band Phenomena, ed. R.D. Parks (Plenum Press, New York) p. 115.
Einzel, D., P.J. Hirschfield, F. Gross, B.S. Chandrasekhar, K. Andres, H.R. Ott, J. Beuers, Z. Fisk and J.L. Smith, 1986, Phys. Rev. Lett. **56**, 2513.
Elenbaas, R., 1980, Dissertation, University of Amsterdam, unpublished.
Elliott, R.J., J.A. Krumhansl and P.L. Leath, 1974, Rev. Mod. Phys. **46**, 465.
Entel, P., and M. Matschke, 1986, NSF-ITP Preprint.
Entel, P., N. Grewe, M. Sietz and K. Kowalski, 1979, Phys. Rev. Lett. **43**, 2002.
Entel, P., Z. Zielinski and M. Matschke, 1985, Z. Phys. B **60**, 283.
Falicov, L.M., and J.C. Kimball, 1969, Phys. Rev. Lett. **22**, 997.
Fawcett, E., 1988, Rev. Mod. Phys. **60**, 209.
Fay, D., and J. Appel, 1985, Phys. Rev. B **32**, 6071.
Fazekas, P., 1987, J. Magn. & Magn. Mater. **63&64**, 545.
Fazekas, P., 1988, in: Recent Progress in Many-Body Theories, Vol. I, eds A.J. Kallio, E. Pajanne and R.F. Bishop (Plenum Press, New York) p. 143 ff.
Fazekas, P., and B.H. Brandow, 1987, Phys. Scr. **36**, 809.
Felsch, W., and K. Winzer, 1978, J. Phys. (France) **39**, C6-832.
Felsch, W., K. Winzer and G. v. Minnigerode, 1975, Z. Phys. B **21**, 151.
Felten, R., 1987, Dissertation, TH Darmstadt, unpublished.
Felten, R., F. Steglich, G. Weber, H. Rietschel, F. Gompf, B. Renker and J. Beuers, 1986, Europhys. Lett. **2**, 323.
Felten, R., G. Weber and H. Rietschel, 1987, J. Magn. & Magn. Mater. **63&64**, 383.
Fenton, E.W., 1985, Solid State Commun. **54**, 709.
Fenton, E.W., 1986, Solid State Commun. **60**, 351.
Fenton, E.W., 1987, in: Novel Superconductivity, eds S.A. Wolf and V.Z. Kresin (Plenum Press, New York) p. 279 ff.
Fert, A., 1973, J. Phys. F **3**, 2126.
Fert, A., and O. Jaoul, 1972, Phys. Rev. Lett. **28**, 303.
Fert, A., and P.M. Levy, 1987, Phys. Rev. B **36**, 1907.
Fetisov, E.P., and D.I. Khomskii, 1985, Solid State Commun. **56**, 403.
Fetter, A.L., and P.C. Hohenberg, 1969, in: Superconductivity, Vol. 2, ed. R.D. Parks (Marcel Dekker, New York) p. 817.
Fischer, H.E., E.T. Swartz, R.O. Pohl, B.A. Jones, J.W. Wilkins and Z. Fisk, 1987, Phys. Rev. B **36**, 5330.
Fisher, R.A., S. Kim, B.F. Woodfield, N.E. Phillips, L. Taillefer, K. Hasselbach, J. Flouquet, A.L. Giorgi and J.L. Smith, 1989, Phys. Rev. Lett. **62**, 1411.
Fisk, Z., G.R. Stewart, J.O. Willis, H.R. Ott and F. Hulliger, 1984, Phys. Rev. B **30**, 6360.
Fisk, Z., J.L. Smith, H.R. Ott and B. Batlogg, 1985, J. Magn. & Magn. Mater. **52**, 79.
Fisk, Z., H. Borges, M. McElfresh, J.L. Smith, J.D. Thompson, H.R. Ott, G. Aeppli, E. Bucher, S.E. Lambert, M.B. Maple, C. Broholm and J.K. Kjems, 1988, Physica C **153–155**, 1728.
Flouquet, J., P. Haen, C. Marcenat, P. Lejay, A. Amato, D. Jaccard and E. Walker, 1985, J. Magn. & Magn. Mater. **52**, 85.
Franceschi, E., and G.L. Olcese, 1969, Phys. Rev. Lett. **22**, 1299.
Franse, J.J.M., P.H. Frings, A. de Visser, A. Menovsky, T.T.M. Palstra, P.H. Kes and J.A. Mydosh, 1984, Physica B **126**, 116.
Franse, J.J.M., A. Menovsky, A. de Visser, C.D. Bredl, U. Gottwick, W. Lieke, H.M. Mayer, U. Rauchschwalbe, G. Sparn and F. Steglich, 1985, Z. Phys. B **59**, 15.
Franz, W., E. Griessel, F. Steglich and D. Wohlleben, 1978, Z. Phys. B **31**, 7.
Fraunberger, G., B. Andraka, J.S. Kim, U. Ahlheim and G.R. Stewart, 1989, Phys. Rev. B **40**, 4735.
Freeman, A.J., and J.B. Darby Jr, eds, 1974, The Actinides, Vols. I and II (Academic Press, New York).
Frick, B., J. Schoenes, O. Vogt and J.W. Allen, 1982, Solid State Commun. **42**, 331.
Frick, B., J. Schoenes and O. Vogt, 1985, J. Magn. & Magn. Mater. **47&48**, 549.
Friedel, J., 1952, Philos. Mag. **43**, 153.
Frings, P.H., J.J.M. Franse, F.R. de Boer and A. Menovsky, 1983, J. Magn. & Magn. Mater. **31–34**, 240.
Frings, P.H., B. Renker and C. Vettier, 1987, J. Magn. & Magn. Mater. **63&64**, 202.
Fulde, P., and M. Loewenhaupt, 1985, Adv. Phys. **34**, 589.

Fulde, P., J. Keller and G. Zwicknagl, 1988, Solid State Phys. **41**, 1.
Fye, R.M., and J.E. Hirsch, 1988, preprint.
Gangopadhyay, A.K., J.S. Schilling, E. Schuberth, P. Gutsmiedl, F. Gross and K. Andres, 1988, Phys. Rev. B **38**, 2603.
Gautier, F., 1982, in: Magnetism of Metals and Alloys, ed. M. Cyrot (North-Holland, Amsterdam) p. 1 ff.
Geibel, C., U. Ahlheim, A.L. Giorgi, G. Sparn, H. Spille, F. Steglich and W. Suski, 1990, Physica B **163**, 194.
Germann, A., and H. v. Löhneysen, 1989, Europhys. Lett. **9**, 367.
Geshkenbein, V.B., and A.I. Larkin, 1986, Sov. Phys.-JETP Lett.
Ghatak, S.R., and K.H. Bennemann, 1978, J. Phys. F **8**, 57.
Golding, B., D.J. Bishop, B. Batlogg, W.H. Haemmerle, Z. Fisk, J.L. Smith and H.R. Ott, 1985, Phys. Rev. Lett. **55**, 2479.
Goldman, A.I., S.M. Shapiro, D.E. Cox, J.L. Smith and Z. Fisk, 1985, Phys. Rev. B **32**, 6042.
Goldman, A.I., S.M. Shapiro, G. Shirane, J.L. Smith and Z. Fisk, 1986, Phys. Rev. B **33**, 1627.
Goncalves da Silva, C.E.T., and L.M. Falicov, 1972, J. Phys. C **5**, 63.
Goto, T., T. Suzuki, Y. Ohe, T. Fujimura and A. Takami, 1988, J. Magn. & Magn. Mater. **76&77**, 305.
Gottwick, U., R. Held, G. Sparn, F. Steglich, K. Vey, W. Assmus, H. Rietschel, G.R. Stewart and A.L. Giorgi, 1987, J. Magn. & Magn. Mater. **63&64**, 341.
Grabowski, M., 1987, J. Phys. C **20**, L735.
Gratz, E., E. Bauer, B. Barbara, S. Zemirli, F. Steglich, C.D. Bredl and W. Lieke, 1985, J. Phys. F **15**, 1975.
Gratz, E., E. Bauer, R. Hauser, N. Pillmayr, G. Hilscher, H. Müller and B. Barbara, 1988, J. Magn. & Magn. Mater. **76&77**, 275.
Grewe, N., 1982, in: Valence Instabilities, eds P. Wachter and H. Boppart (North-Holland, Amsterdam) p. 21.
Grewe, N., 1983a, Z. Phys. B **52**, 193.
Grewe, N., 1983b, Z. Phys. B **53**, 2711.
Grewe, N., 1984a, Solid State Commun. **50**, 19.
Grewe, N., 1984b, Z. Phys. B **56**, 111.
Grewe, N., 1985, J. Magn. & Magn. Mater. **47&48**, 20.
Grewe, N., 1986, paper presented at the Heavy-Fermion Symposium, Bischofsgrün, F.R.G., unpublished.
Grewe, N., 1987, Z. Phys. B **67**, 323.
Grewe, N., 1988a, Solid State Commun. **66**, 1053.
Grewe, N., 1988b, Solid State Commun. **67**, 1053.
Grewe, N., and P. Entel, 1979, Z. Phys. B **33**, 331.
Grewe, N., and H. Keiter, 1981, Phys. Rev. B **24**, 4420.
Grewe, N., and T. Pruschke, 1985, Z. Phys. B **60**, 311.
Grewe, N., and B. Welslau, 1988, Solid State Commun. **65**, 437.
Grewe, N., P. Entel and H.J. Leder, 1978, Z. Phys. B **30**, 393.
Grewe, N., H.J. Leder and P. Entel, 1980, in: Festkörperprobleme XX, Advances in Solid State Physics, ed. J. Treusch (Vieweg, Braunschweig) p. 413.
Grewe, N., T. Pruschke and H. Keiter, 1988, Z. Phys. B **71**, 75.
Grier, B.H., J.M. Lawrence, V. Murgai and R.D. Parks, 1984, Phys. Rev. B **29**, 2664.
Grolle, J., V. Müller and K.H. Bennemann, 1987, Phys. Rev. B **35**, 4493.
Gross, F., B.S. Chandrasekhar, D. Einzel, K. Andres, P.J. Hirschfeld, H.R. Ott, J. Beuers, Z. Fisk and J.L. Smith, 1986, Z. Phys. B **64**, 175.
Gross, F., B.S. Chandrasekhar, K. Andres, U. Rauchschwalbe, E. Bucher and B. Lüthi, 1988, Physica C **153–155**, 439.
Grüner, G., and A. Zawadowski, 1972, Solid State Commun. **11**, 663.
Grüner, G., and A. Zawadowski, 1974, Rep. Prog. Phys. **37**, 1497.
Gschneidner Jr, K.A., J. Tang, S.K. Dhar and A. Goldman, 1990, Physica B **163**, 507.
Gunnarsson, O., and K. Schönhammer, 1983, Phys. Rev. B **28**, 4315.
Gunnarsson, O., and K. Schönhammer, 1987, in: Handbook of the Physics and Chemsitry of Rare Earths, Vol. 10, eds K.A. Gschneidner Jr, L. Eyring and S. Hüfner (Elsevier, Amsterdam) ch. 64.
Güntherodt, G., R. Merlin, A. Frey and M. Cardona, 1978, Solid State Commun. **27**, 551.
Haensel, R., G. Keitel, P. Schreiber, B. Sonntag and C. Kunz, 1969, Phys. Rev. Lett. **23**, 528.

Haensel, R., G. Keitel, B. Sonntag, C. Kunz and P. Schreiber, 1970, Phys. Status Solidi A **2**, 85.

Haldane, F.D.M., 1981, in: Valence Fluctuations in Solids, eds L.M. Falicov, W. Hanke and M.B. Maple (North-Holland, Amsterdam) p. 153.

Hamzic, A., A. Fert, M. Miljak and S. Horn, 1988, Phys. Rev. B **38**, 7141.

Han, S., K.W. Ng, E.L. Wolf, H.F. Braun, L. Tanner, Z. Fisk, J.L. Smith and M.R. Beasley, 1985, Phys. Rev. B **32**, 7567.

Han, S., K.W. Ng, E.L. Wolf, A. Millis, J.L. Smith and Z. Fisk, 1986, Phys. Rev. Lett. **57**, 238.

Hanke, E., 1988, Diploma thesis (TU Braunschweig) unpublished.

Hanke, E., and A. Eichler, 1989, to be published.

Hanzawa, K., K. Yamada and K. Yoshida, 1985, J. Magn. & Magn. Mater. **47&48**, 357.

Hanzawa, K., K. Yamada and K. Yoshida, 1987, J. Phys. Soc. Jpn. **56**, 678.

Hasselbach, K., L. Taillefer and J. Flouquet, 1989, Phys. Rev. Lett. **63**, 93.

Heffner, R.H., D.W. Cooke, Z. Fisk, R.L. Hutson, M.E. Schillaci, J.L. Smith, J.O. Willis, D.E. MacLaughlin, R.E. Lichti, A.B. Denison and J. Oostens, 1986, Phys. Rev. Lett. **57**, 1255.

Heffner, R.H., D.W. Cooke and D.E. MacLaughlin, 1987, in: Theoretical and Experimental Aspects of Valence Fluctuations and Heavy Fermions, eds L.C. Gupta and S.K. Malik (Plenum Press, New York) p. 319.

Heffner, R.H., D.W. Cooke, A.L. Giorgi, R.L. Hutson, M.E. Schillaci, H.D. Rempp, J.L. Smith, J.O. Willis, D.E. MacLaughlin, C. Boekema, R.L. Lichti, J. Oostens and A.B. Denison, 1989, Phys. Rev. B **39**, 11345.

Hess, D.W., T.A. Tokuyasu and J.A. Sauls, 1989, J. Phys. Condens. Matter **1**, 8135.

Hill, H.H., 1970, in: Plutonium 1970 and Other Actinides, Part I, Nuclear Metallurgy, Vol. 17, ed. W.M. Miner (Metallurgical Society AIME, New York) p. 2.

Hirschfeld, P., D. Vollhardt and P. Wölfle, 1986, Solid State Commun. **59**, 111.

Hirschfeld, P.J., P. Wölfle and D. Einzel, 1988, Phys. Rev. B **37**, 83.

Hirst, L.L., 1974, J. Phys. Chem. Solids **35**, 1285.

Hirst, L.L., 1978, Adv. Phys. **27**, 231.

Hofmann, U., and J. Keller, 1989, Z. Phys. B **74**, 499.

Höhn, T., and J. Keller, 1988, J. Magn. & Magn. Mater. **76&77**, 343.

Horn, S., E. Holland-Moritz, M. Loewenhaupt, F. Steglich, H. Scheuer, A. Benoit and J. Flouquet, 1981a, Phys. Rev. B **23**, 3171.

Horn, S., F. Steglich, M. Loewenhaupt, H. Scheuer, W. Felsch and K. Winzer, 1981b, Z. Phys. B **42**, 125.

Horvatič, B., and V. Zlatič, 1984, Phys. Rev. B **30**, 6717.

Hunt, M., P. Meeson, P.-A. Probst, P. Reinders, M. Springford, W. Assmus and W. Sun, 1990, Physica B **165&166**, 323, 337.

Hunt, M., P. Meeson, P.-A. Probst, P. Reinders, M. Springford, W. Assmus and W. Sun, 19xx, J. Magn. & Magn. Mater., in press.

Ishikawa, M., H.F. Braun and J.L. Jorda, 1983, Phys. Rev. B **27**, 3092.

Jaccard, D., and J. Flouquet, 1985, J. Magn. & Magn. Mater. **47&48**, 45.

Jaccard, D., R. Cibin, J.L. Jorda and J. Flouquet, 1987, Jpn. J. Appl. Phys. **26**, Suppl. 26-3, 517.

Jaccard, D., J. Sierro, J.P. Brison and J. Flouquet, 1988, J. Phys. (France) **49**, C8-741.

Jarlborg, T., H.F. Braun and M. Peter, 1983, Z. Phys. B **52**, 295.

Jee, C.S., B. Andraka, J.S. Kim, H. Li, H.W. Meisel and G.R. Stewart, 1990, preprint.

Jefferson, J.M., and K.W.H. Stevens, 1978, J. Phys. C **11**, 3919.

Jichu, H., A.D.S. Nagi, B. Jin, T. Matsuura and Y. Kuroda, 1987, Phys. Rev. B **35**, 1692.

Joss, W., J.M. van Ruitenbeek, G.W. Crabtree, J.L. Tholence, A.P.J. van Deursen and Z. Fisk, 1987, Phys. Rev. Lett. **59**, 1609.

Joynt, R., 1988, Supercond. Sci. Technol. **1**, 210.

Joynt, R., T.M. Rice and K. Ueda, 1986, Phys. Rev. Lett. **56**, 1412.

Julien, R., and R.M. Martin, 1982, Solid State Commun. **41**, 967.

Julien, R., P. Pfeuty, J.N. Fields and S. Doniach, 1979, J. Phys. (France) **C5**, 297.

Kaga, H., and H. Kubo, 1988, Solid State Commun. **65**, 257.

Kashiba, S., S. Maekawa, J. Takahashi and M. Tachiki, 1986, J. Phys. Soc. Jpn. **55**, 1341.

Kasuya, T., 1956, Prog. Theor. Phys. **16**, 45.

Kawakami, M., S. Kunii, T. Komatsubara and T. Kasuya, 1980, Solid State Commun. **36**, 435.
Kawakami, N., and A. Okiji, 1986, J. Phys. Soc. Jpn. **55**, 2114.
Kawakami, N., and A. Okiji, 1987, Jpn. J. Appl. Phys. **26**, Suppl. 26-3, 499.
Keiter, H., and G. Czycholl, 1983, J. Magn. & Magn. Mater. **31–34**, 477.
Keiter, H., and J.C. Kimball, 1971, Int. J. Magn. **1**, 233.
Keiter, H., and J. Kurkijärvi, 1977, Z. Phys. B **26**, 169.
Keiter, H., and G. Morandi, 1984, Phys. Rep. **109**, 227.
Keller, J., R. Bulla, T. Höhn and K.W. Becker, 1990, Phys. Rev. B **41**, 1878.
Kim, C.-I., Y. Kuramoto and T. Kasuya, 1987, Solid State Commun. **62**, 627.
Kittel, C., 1963, Quantum Theory of Solids (Wiley, New York).
Kjems, J.K., and C. Broholm, 1988, J. Magn. & Magn. Mater. **76&77**, 371.
Kleiman, R.N., D.J. Bishop, H.R. Ott, Z. Fisk and J.L. Smith, 1990, Phys. Rev. Lett. **64**, 1975.
Klemm, R.A., and A. Scharnberg, 1981, Phys. Rev. B **24**, 6361.
Klemm, R.A., K. Scharnberg, D. Walker and C.T. Rieck, 1988, Z. Phys. B **72**, 139.
Knopp, G., A. Loidl, R. Caspary, U. Gottwick, C.D. Bredl, H. Spille, F. Steglich and A.P. Murani, 1988, J. Magn. & Magn. Mater. **74**, 341.
Knopp, G., A. Loidl, K. Knorr, L. Pawlack, M. Duczmal, R. Caspary, U. Gottwick, H. Spille, F. Steglich and A.P. Murani, 1989, Z. Phys. B **77**, 95.
Koelling, D.D., B.D. Dunlap and G.W. Crabtree, 1985, Phys. Rev. B **31**, 4966.
Kojima, H., Y. Kuramoto and M. Tachiki, 1984, Z. Phys. B **54**, 293.
Komatsubara, T., T. Suzuki, M. Kawakami, S. Kunii, T. Fujita, Y. Ishikawa, A. Takase, K. Kojima, M. Suzuki, Y. Aoki, K. Takegahara and T. Kasuya, 1980, J. Magn. & Magn. Mater. **15–18**, 963.
Kondo, J., 1964, Prog. Theor. Phys. **32**, 37.
Kondo, J., 1966, J. Appl. Phys. **37**, 1177.
Kosterlitz, J.M., D.R. Nelson and M.E. Fisher, 1976, Phys. Rev. B **13**, 412.
Kouroudis, I., D. Weber, M. Yoshizawa, B. Lüthi, L. Puech, P. Haen, J. Flouquet, G. Bruls, U. Welp, J.J.M. Franse, A. Menovsky, E. Bucher and J. Hufnagl, 1987, Phys. Rev. Lett. **58**, 820.
Kozarzewski, B., 1973, Acta Phys. Pol. A **44**, 237.
Krishna-murthy, H.R., K.G. Wilson and J.W. Wilkins, 1975, Phys. Rev. Lett. **35**, 1101.
Krishna-murthy, H.R., J.W. Wilkins and K.G. Wilson, 1980a, Phys. Rev. B **21**, 1003.
Krishna-murthy, H.R., J.W. Wilkins and K.G. Wilson, 1980b, Phys. Rev. B **21**, 1044.
Kumar, P., and P. Wölfle, 1987, Phys. Rev. Lett. **59**, 1954.
Kuramoto, Y., 1981, Z. Phys. B **40**, 4.
Kuramoto, Y., 1983, Z. Phys. B **53**, 37.
Kuramoto, Y., 1985, in: Theory of Heavy Fermions and Valence Fluctuations, eds. T. Kasuya and T. Saso (Springer, Heidelberg) p. 152.
Kuramoto, Y., 1989, Physica B **156&157**, 789.
Kuramoto, Y., and H. Kojima, 1984, Z. Phys. B **57**, 95.
Kuramoto, Y., and H. Kojima, 1985, J. Magn. & Magn. Mater. **47&48**, 329.
Kuramoto, Y., and E. Müller-Hartmann, 1981, in: Valence Fluctuations in Solids, eds L.M. Falicov, W. Hanke and M.B. Maple (North-Holland, Amsterdam) p. 139.
Kuramoto, Y., and E. Müller-Hartmann, 1985, J. Magn. & Magn. Mater. **52**, 122.
Kuramoto, Y., and T. Watanabe, 1987, Physica B **148**, 80.
Lambert, S.E., Y. Dalichaouch, M.B. Maple, J.L. Smith and Z. Fisk, 1986, Phys. Rev. Lett. **57**, 1619.
Lang, M., R. Schefzyk, F. Steglich and N. Grewe, 1987, J. Magn. & Magn. Mater. **63&64**, 79.
Langer, J.S., and V. Ambegaokar, 1961, Phys. Rev. **121**, 1090.
Langreth, D.C., 1966, Phys. Rev. **150**, 516.
Lavagna, M., C. Lacroix and M. Cyrot, 1982a, J. Phys. F **12**, 745.
Lavagna, M., C. Lacroix and M. Cyrot, 1982b, Phys. Lett. A **90**, 210.
Lawrence, J.M., 1982, J. Appl. Phys. **53**, 2117.
Lawrence, J.M., P.S. Riseborough and R.D. Parks, 1981, Rep. Progr. Phys. **44**, 1.
Lawrence, J.M., J.D. Thompson, Z. Fisk, J.L. Smith and B. Batlogg, 1984, Phys. Rev. B **29**, 4017.
Lawrence, J.M., J.D. Thompson and Y.Y. Chen, 1985, Phys. Rev. Lett. **54**, 2537.

Lee, P.A., T.M. Rice, J.W. Serene, L.J. Sham and J.W. Wilkins, 1986, Comments Condens. Matter Phys. **XII**, 99.
Lee, T.K., 1985, J. Phys. C **18**, L31.
Lee, T.K., and F.C. Zhang, 1984, J. Appl. Phys. **55**, 1936.
Lee, W.H., R.N. Shelton, S.K. Dhar and K.A. Gschneidner Jr, 1987, Phys. Rev. B **35**, 8523.
Leggett, A.J., 1975, Rev. Mod. Phys. **47**, 331.
Levy, P.M., 1988, Phys. Rev. B **38**, 6779.
Levy, P.M., Wei Guo and D.L. Cox, 1988, J. Appl. Phys. **63**, 3896.
Lieke, W., U. Rauchschwalbe, C.D. Bredl, F. Steglich, J. Aarts and F.R. de Boer, 1982, J. Appl. Phys. **53**, 2111.
Lifshitz, I.M., and A.M. Kosevich, 1956, Sov. Phys.-JETP **2**, 636.
Lin, C.L., J. Teter, J.E. Crow, T. Mihalisin, J. Brooks, A.I. Abou-Aly and G.R. Stewart, 1985, Phys. Rev. Lett. **54**, 2541.
Loewenhaupt, M., and E. Holland-Moritz, 1979, J. Appl. Phys. **50**, 7456.
Loewenhaupt, M., S. Horn, F. Steglich, E. Holland-Moritz and G.H. Lander, 1979, J. Phys. (France) **40**, C4-142.
Loidl, A., G. Knopp, H. Spille, F. Steglich and A.P. Murani, 1989, Physica B **156&157**, 794.
Loidl, A., A. Krimmel, K. Knorr, A. Grauel, S. Horn, M. Lang, G. Sparn, F. Steglich and A.P. Murani, 1990, to be published.
Lonzarich, G.G., 1988, J. Magn. & Magn. Mater. **76&77**, 1.
Lorek, A., 1990, Diploma thesis, TH Darmstadt, and to be published.
Lüthi, B., 1985, J. Magn. & Magn. Mater. **52**, 70.
Lüthi, B., and M. Yoshizawa, 1987, J. Magn. & Magn. Mater. **63&64**, 274.
Luttinger, J.M., 1960, Phys. Rev. **119**, 1153.
Luttinger, J.M., and J.C. Ward, 1960, Phys. Rev. **118**, 1417.
Machida, K., M. Ozaki and T. Ohmi, 1989, J. Phys. Soc. Jpn. **58**, 4116.
MacLaughlin, D.E., C. Tien, W.G. Clark, M.D. Lan, Z. Fisk, J.L. Smith and H.R. Ott, 1984, Phys. Rev. Lett. **53**, 1833.
Maki, K., 1969, in: Superconductivity, Vol. 2, ed. R.D. Parks (Marcel Dekker, New York) p. 1035.
Maki, K., and X. Huang, 1988, J. Magn. & Magn. Mater. **76&77**, 499.
Maple, M.B., J.W. Chen, S.E. Lambert, Z. Fisk, J.L. Smith, H.R. Ott, J.S. Brooks and M.J. Naughton, 1985, Phys. Rev. Lett. **54**, 477.
Maple, M.B., J.W. Chen, Y. Dalichaouch, Y. Kohara, C. Rossel, M.S. Torikachivili, H.W. McElfresh and J.D. Thompson, 1986, Phys. Rev. Lett. **56**, 185.
Marcenat, C., 1986, Dissertation, University of Grenoble, unpublished.
Martin, R.M., 1982, Phys. Rev. Lett. **48**, 362.
Martin, R.M., and J.W. Allen, 1985, J. Magn. & Magn. Mater. **47&48**, 257.
Matsuura, T., K. Miyake, H. Jichu and Y. Kuroda, 1984, Prog. Theor. Phys. **72**, 402.
Mayer, H.M., 1986, Diploma thesis, TH Darmstadt, unpublished.
Mayer, H.M., U. Rauchschwalbe, F. Steglich, H. Rietschel, H. Schmidt, H. Wühl and J. Beuers, 1986a, Phys. Rev. B **33**, 3168.
Mayer, H.M., U. Rauchschwalbe, F. Steglich, G.R. Stewart and A.L. Giorgi, 1986b, Z. Phys. B **64**, 299.
Menge, B., and E. Müller-Hartmann, 1988, Z. Phys. B **73**, 225.
Mignot, J.-M., J. Flouquet, P. Haen, F. Lapierre, L. Puech and J. Voiron, 1988, J. Magn. & Magn. Mater. **76&77**, 97.
Milliken, F.P., T. Penney, F. Holtzberg and Z. Fisk, 1988, J. Magn. & Magn. Mater. **76&77**, 201.
Millis, A.J., 1987, Phys. Rev. B **35**, 151.
Millis, A.J., and P.A. Lee, 1987, Phys. Rev. B **35**, 3394.
Millis, A.J., S. Sachdev and C.M. Varma, 1988, Phys. Rev. B **37**, 4975.
Misawa, S., 1986, Solid State Commun. **58**, 63.
Miyake, K., 1987, J. Magn. & Magn. Mater. **63&64**, 411.
Miyake, K., and C.M. Varma, 1986, Phys. Rev. Lett. **57**, 1627.
Miyake, K., T. Matsuura, H. Jichu and Y. Nagaoka, 1984, Progr. Theor. Phys. **72**, 1063.
Miyake, K., S. Schmitt-Rink and C.M. Varma, 1986, Phys. Rev. B **34**, 6554.
Mock, R., and G. Güntherodt, 1989, Z. Phys. B **74**, 315.
Mock, R., B. Hillebrands, H. Schmidt, G. Güntherodt, Z. Fisk and A. Meyer, 1985, J. Magn. & Magn. Mater. **47&48**, 312.
Monien, H., K. Scharnberg, L. Tewordt and W. Schopohl, 1986a, J. Low Temp. Phys. **65**, 13.
Monien, H., K. Scharnberg, L. Tewordt and W. Schopohl, 1986b, Phys. Rev. B **34**, 3487.

Monien, H., K. Scharnberg, L. Tewordt and D. Walker, 1987a, Solid State Commun. **61**, 581.
Monien, H., K. Scharnberg and D. Walker, 1987b, Solid State Commun. **63**, 263.
Monien, H., L. Tewordt and K. Scharnberg, 1989, preprint.
Mook, H.A., R.M. Nicklow, T. Penney, F. Holtzberg and M.W. Shafer, 1978, Phys. Rev. B **18**, 2925.
Moriya, T., 1979, J. Magn. & Magn. Mater. **14**, 1.
Moshchalkov, V.V., 1987, Sov. Phys.-JETP Lett. **45**, 226.
Moshchalkov, V.V., 1988, J. Magn. & Magn. Mater. **76&77**, 213.
Mott, N.F., 1974, Metal-Insulator Transitions (Taylor & Francis, London).
Mühlschlegel, B., 1968, Z. Phys. **208**, 94.
Müller, T., W. Joss, J.M. van Ruitenbeek, U. Welp, P. Wyder and Z. Fisk, 1988, J. Magn. & Magn. Mater. **76&77**, 35.
Müller, V., and K. Bartell, 1979, Z. Phys. B **22**, 271.
Müller, V., D. Maurer, K. de Groot, E. Bucher and H.E. Bömmel, 1986a, Phys. Rev. Lett. **56**, 248.
Müller, V., D. Maurer, E.W. Scheidt, C. Roth, K. Lüders, E. Bucher and H.E. Bömmel, 1986b, Solid State Commun. **57**, 319.
Müller, V., C. Roth, D. Maurer, E.W. Scheidt, K. Lüders, E. Bucher and H.E. Bömmel, 1987, Phys. Rev. Lett. **58**, 1224.
Müller-Hartmann, E., 1973, in: Magnetism V, ed. H. Suhl (Academic Press, New York) p. 353 ff.
Müller-Hartmann, E., 1984, Z. Phys. B **57**, 281.
Murani, A.P., K. Knorr and K.H.J. Buschow, 1977, in: Crystal Field Effects in Metals and Alloys, ed. A. Furrer (Plenum Press, New York) p. 268.
Murani, A.P., K. Knorr, K.H.J. Buschow, A. Benoit and J. Flouquet, 1980, Solid State Commun. **36**, 523.
Nakamura, H., Y. Kitaoka, H. Yamada and K. Asayama, 1988, J. Magn. & Magn. Mater. **76&77**, 517.
Nakamura, H., T. Iwai, Y. Kitaoka and K. Asayama, 1990, J. Magn. & Magn. Mater., in press.
Newns, D.M., and N. Read, 1987, Adv. Phys. **36**, 799.
Nikl, D., I. Kouroudis, W. Assmus, B. Lüthi, G. Bruls and U. Welp, 1987, Phys. Rev. B **35**, 6864.
Niksch, M., B. Lüthi and K. Andres, 1980, Phys. Rev. B **22**, 5774.
Niksch, M., I. Kouroudis, W. Assmus and B. Lüthi, 1985, J. Magn. & Magn. Mater. **47&48**, 297.
Noda, Y., K. Yamada, I. Hirosawa, Y. Endoh, Y. Onuki and T. Komatsubara, 1985, J. Phys. Soc. Jpn. **54**, 4486.
Norman, M.R., 1987, Phys. Rev. Lett. **59**, 232.
Norman, M.R., 1988, Phys. Rev. B **37**, 4987.
Norman, M.R., 1989, Phys. Rev. B **39**, 7305.
Norman, M.R., T. Oguchi and A.J. Freeman, 1988, Phys. Rev. B **38**, 11193.
Nozières, P., 1964, Theory of Interacting Fermi Systems (W.A. Benjamin, New York).
Nozières, P., 1974, J. Low Temp. Phys. **17**, 31.
Nozières, P., 1978, J. Physique **39**, 1117.
Nozières, P., 1985, Ann. Phys. Fr. **10**, 19.
Nozières, P., and C.T. de Dominicis, 1969, Phys. Rev. **178**, 1097.
Oguchi, T., and A.J. Freeman, 1986, J. Magn. & Magn. Mater. **61**, 233.
Oguchi, T., A.J. Freeman and G.W. Crabtree, 1986, Phys. Lett. A **117**, 428.
Ohkawa, F.J., 1984, J. Phys. Soc. Jpn. **53**, 1389.
Ohkawa, F.J., 1986, J. Phys. Soc. Jpn. **55**, 2527.
Ohkawa, F.J., 1987, J. Phys. Soc. Jpn. **56**, 713.
Ohkawa, F.J., and H. Fukuyama, 1984, J. Phys. Soc. Jpn. **53**, 4344.
Okiji, A., and N. Kawakami, 1982, J. Phys. Soc. Jpn. **51**, 3192.
Okiji, A., and N. Kawakami, 1986, J. Magn. & Magn. Mater. **54–57**, 327.
Olivier, M., T. Siegrist and S.P. McAlister, 1987, Phys. Rev. B **35**, 5025.
Onuki, Y., and T. Komatsubara, 1987, J. Magn. & Magn. Mater. **63&64**, 281.
Onuki, Y., Y. Shimizu and T. Komatsubara, 1984, J. Phys. Soc. Jpn. **53**, 1210.
Onuki, Y., Y. Shimizu and T. Komatsubara, 1985, J. Phys. Soc. Jpn. **54**, 304.
Onuki, Y., T. Komatsubara, P.H.P. Reinders and M. Springford, 1989, J. Phys. Soc. Jpn., in press.
Ott, H.R., 1987, in: Progress in Low Temperature Physics, Vol. XI, ed. D.F. Brewer (Elsevier, Amsterdam) p. 215.

Ott, H.R., H. Rudigier, Z. Fisk and J.L. Smith, 1983, Phys. Rev. Lett. **50**, 1595.
Ott, H.R., H. Rudigier, P. Delsing and Z. Fisk, 1984a, Phys. Rev. Lett. **52**, 1551.
Ott, H.R., H. Rudigier, T.M. Rice, K. Ueda, Z. Fisk and J.L. Smith, 1984b, Phys. Rev. Lett. **52**, 1915.
Ott, H.R., H. Rudigier, Z. Fisk and J.L. Smith, 1985a, Phys. Rev. B **31**, 1651.
Ott, H.R., H. Rudigier, Z. Fisk, J.O. Willis and G.R. Stewart, 1985b, Solid State Commun. **53**, 235.
Ott, H.R., H. Rudigier, E. Felder, Z. Fisk and J.L. Smith, 1986, Phys. Rev. B **33**, 126.
Ott, H.R., H. Rudigier, E. Felder, Z. Fisk and J.D. Thompson, 1987a, Phys. Rev. B **35**, 1452.
Ott, H.R., E. Felder, A. Bernasconi, Z. Fisk, J.L. Smith, L. Taillefer and G.G. Lonzarich, 1987b, Jpn. J. Appl. Phys. **26**, Suppl. 26–3, 1217.
Overhauser, A.W., and J. Appel, 1985, Phys. Rev. B **31**, 193.
Ozaki, M., K. Machida and T. Ohmi, 1985, Prog. Theor. Phys. **74**, 221.
Ozaki, M., K. Machida and T. Ohmi, 1986, Prog. Theor. Phys. **75**, 442.
Pals, J.A., W. v. Haeringen and M.H. v. Maaren, 1977, Phys. Rev. B **15**, 2592.
Palstra, T.T.M., A.A. Menovsky, J. van den Berg, A.J. Dirkmaat, J.G. Niewenhuys and J.A. Mydosh, 1985, Phys. Rev. Lett. **55**, 2727.
Parks, R.D., ed., 1969, Superconductivity (Marcel Dekker, New York) Vols. 1 & 2.
Patthey, F., W.-D. Schneider, Y. Baer and B. Delley, 1987, Phys. Rev. Lett. **58**, 2810.
Pethick, C.J., and D. Pines, 1986, Phys. Rev. Lett. **57**, 118.
Pethick, C.J., and D. Pines, 1988, in: Proc. 5th Int. Conf. on Recent Progress in Many Body Theories, eds R. Bishop, A. Kallio and E. Pajanne (Plenum Press, New York).
Pickett, W.E., H. Krakauer and C.S. Wang, 1986, Phys. Rev. B **34**, 6546.
Poppe, U., 1985, J. Magn. & Magn. Mater. **52**, 157.
Pruschke, T., 1989, Dissertation, TH Darmstadt, unpublished.
Pruschke, T., and N. Grewe, 1989, Z. Phys. B **74**, 439.
Putikka, W.O., and R. Joynt, 1989, Phys. Rev. B **39**, 701.
Quezel, S., P. Burlet, J.L. Jacoud, L.P. Regnault, J. Rossat-Mignod, C. Vettier, P. Lejay and J. Flouquet, 1988, J. Magn. & Magn. Mater. **76&77**, 403.
Quitmann, C., B. Andraka, J.S. Kim, B. Treadway, G. Fraunberger, G.R. Stewart and J. Sticht, 1988, J. Magn. & Magn. Mater. **76&77**, 91.
Rainer, D., 1986, in: Progress in low Temperature Physics, Vol. X, ed. D.F. Brewer (Elsevier, Amsterdam) p. 371.
Rainer, D., 1988, Phys. Scr. **T23**, 106.
Ramirez, A.P., B. Batlogg, E. Bucher and A.S. Cooper, 1986, Phys. Rev. Lett. **57**, 1072.
Ramirez, R., L.M. Falicov and J.C. Kimball, 1970, Phys. Rev. B **2**, 3383.
Rasul, J.W., 1986, J. Magn. & Magn. Mater. **54–57**, 403.
Rasul, J.W., 1989, Phys. Rev. B **39**, 663.
Rauchschwalbe, U., 1987, Physica B **147**, 1.
Rauchschwalbe, U., W. Lieke, C.D. Bredl, F. Steglich, J. Aarts, K.M. Martini and A.C. Mota, 1982, Phys. Rev. Lett. **49**, 1448.
Rauchschwalbe, U., W. Baus, S. Horn, H. Spille, F. Steglich, F.R. de Boer, J. Aarts, W. Assmus and M. Herrmann, 1985a, J. Magn. & Magn. Mater. **47&48**, 33.
Rauchschwalbe, U., U. Ahlheim, F. Steglich, D. Rainer and J.J.M. Franse, 1985b, Z. Phys. B **60**, 379.
Rauchschwalbe, U., U. Gottwick, U. Ahlheim, H.M. Mayer and F. Steglich, 1985c, J. Less Common Metal **111**, 265.
Rauchschwalbe, U., F. Steglich and H. Rietschel, 1986, Europhys. Lett. **1**, 71.
Rauchschwalbe, U., F. Steglich, A. de Visser and J.J.M. Franse, 1987a, J. Magn. & Magn. Mater. **63&64**, 347.
Rauchschwalbe, U., U. Ahlheim, H.M. Mayer, C.D. Bredl and F. Steglich, 1987b, J. Magn. & Magn. Mater. **63&64**, 447.
Rauchschwalbe, U., F. Steglich, G.R. Stewart, A.L. Giorgi, P. Fulde and K. Maki, 1987c, Europhys. Lett. **3**, 751.
Rauchschwalbe, U., C.D. Bredl, F. Steglich, K. Maki and P. Fulde, 1987d, Europhys. Lett. **3**, 757.
Ravex, A., J. Flouquet, J.L. Tholence, D. Jaccard and A. Meyer, 1987, J. Magn. & Magn. Mater. **63&64**, 400.
Razafimandimby, H., P. Fulde and J. Keller, 1984, Z. Phys. B **54**, 111.

Read, N., D.M. Newns and S. Doniach, 1984, Phys. Rev. B **30**, 3841.
Rebelsky, L., K. Reilly, S. Horn, H. Borges, J.D. Thompson, J.O. Willis, R. Aikin, R. Caspary and C.D. Bredl, 1988, J. Appl. Phys. **63**, 3405.
Reinders, P.H.P., and M. Springford, 1989, J. Magn. & Magn. Mater. **79**, 295.
Reinders, P.H.P., M. Springford, P.T. Coleridge, R. Boulet and D. Ravot, 1986, Phys. Rev. Lett. **57**, 1631.
Remenyi, G., A. Briggs, J. Flouquet, O. Laborde and F. Lapierre, 1983, J. Magn. & Magn. Mater. **31–34**, 407.
Renker, B., E. Gering, F. Gompf, H. Schmidt and H. Rietschel, 1987a, J. Magn. & Magn. Mater. **63&64**, 31.
Renker, B., F. Gompf, E. Gering, P. Frings, H. Rietschel, R. Felten, F. Steglich and G. Weber, 1987b, Physica B **148**, 41.
Ribault, M., A. Benoit, J. Flouquet and J. Palleau, 1979, J. Phys. (Paris) **40**, L413.
Riblet, G., and K. Winzer, 1971, Solid State Commun. **9**, 1663.
Rice, T.M., and K. Ueda, 1985, Phys. Rev. Lett. **55**, 995.
Rice, T.M., and K. Ueda, 1987, Phys. Rev. B **34**, 6420.
Rice, T.M., K. Ueda and H.R. Ott, 1986, J. Magn. & Magn. Mater. **54–57**, 317.
Rietschel, H., B. Renker, R. Felten, F. Steglich and G. Weber, 1988, J. Magn. & Magn. Mater. **76&77**, 105.
Robinson, J.M., 1979, Phys. Rep. **51**, 1.
Robinson, R.A., J.D. Axe, A.I. Goldman, Z. Fisk, J.L. Smith and H.R. Ott, 1985, Phys. Rev. B **33**, 6488.
Rodriguez, J.P., 1985, Phys. Rev. Lett. **55**, 250.
Rodriguez, J.P., 1987, Phys. Rev. B **36**, 168.
Rossat-Mignod, J., L.P. Regnault, J.L. Jacoud, C. Vettier, P. Lejay, J. Flouquet, E. Walker, D. Jaccard and A. Amato, 1988, J. Magn. & Magn. Mater. **76&77**, 376.
Rudermann, M.A., and C. Kittel, 1954, Phys. Rev. **96**, 99.
Samwer, K., and K. Winzer, 1976, Z. Phys. B **25**, 269.
Sarkissian, B.V.B., and B.R. Coles, 1976, Communications on Physics **1**, 17.
Saso, T., and Y. Seino, 1986, J. Phys. Soc. Jpn. **55**, 3729.
Sato, N., M. Kohgi, T. Satoh, Y. Ishikawa, H. Hiroyoshi and H. Takei, 1985, J. Magn. & Magn. Mater. **52**, 360.
Satoh, K., T. Fujita, Y. Maeno, Y. Onuki and T. Komatsubara, 1988, J. Magn. & Magn. Mater. **76&77**, 128.
Satoh, T., H. Yashima and H. Mori, 1982, in: Valence Instabilities, eds P. Wachter and H. Boppart (North-Holland, Amsterdam) p. 533.
Sauls, J.A., Z. Zhou and P.W. Anderson, 1986, preprint.
Scalapino, D., 1969, in: Superconductivity, Vol. 1, ed. R.D. Parks (Marcel Dekker, New York) p. 449.
Scalapino, D.J., E. Loh Jr and J.E. Hirsch, 1986, Phys. Rev. B **34**, 8190.
Scalapino, D.J., E. Loh Jr and J.E. Hirsch, 1987, Phys. Rev. B **35**, 6694.
Scalettar, R.T., D.J. Scalapino and R.L. Sugar, 1985, Phys. Rev. B **31**, 7316.
Scharnberg, K., and R.A. Klemm, 1980, Phys. Rev. B **22**, 5233.
Scharnberg, K., D. Walker, H. Monien, L. Tewordt and R.A. Klemm, 1986, Solid State Commun. **60**, 535.
Schefzyk, R., W. Lieke and F. Steglich, 1985a, Solid State Commun. **54**, 525.
Schefzyk, R., M. Peschke, F. Steglich, K. Winzer and W. Assmus, 1985b, Z. Phys. B **60**, 373.
Schefzyk, R., J. Heibel, F. Steglich, R. Felten and G. Weber, 1985c, J. Magn. & Magn. Mater. **47&48**, 83.
Schenck, A., 1988, private communication.
Schenstrom, A., M.F. Xu, Y. Hong, D. Bein, M. Levy, B.K. Sarma, S. Adenwalla, Z. Zhao, T. Tokusayu, D.W. Hess, J.B. Ketterson, J.A. Sauls and D.G. Hinks, 1989, Phys. Rev. Lett. **62**, 332.
Schlabitz, W., F. Steglich, C.D. Bredl and W. Franz, 1980, Physica B **102**, 321.
Schlabitz, W., J. Baumann, B. Pollit, U. Rauchschwalbe, H.M. Mayer, U. Ahlheim and C.D. Bredl, 1986, Z. Phys. B **62**, 171.
Schlottmann, P., 1983, Z. Phys. B **51**, 223.
Schlottmann, P., 1984a, Phys. Rev. B **30**, 1454.
Schlottmann, P., 1984b, Z. Phys. B **55**, 213.
Schlottmann, P., 1985a, J. Magn. & Magn. Mater. **52**, 211, 214.
Schlottmann, P., 1985b, J. Magn. & Magn. Mater. **47&48**, 367.
Schlottmann, P., 1987, Phys. Rev. B **35**, 5279.
Schmiedeshoff, G.M., Y.P. Ma, J.S. Brooks,

M.B. Maple, Z. Fisk and J.L. Smith, 1988, Phys. Rev. B **38**, 2934.
Schmitt-Rink, S., K. Miyake and C.M. Varma, 1986, Phys. Rev. Lett. **57**, 2575.
Schmitt-Rink, S., K. Miyake and C.M. Varma, 1987, Phys. Rev. Lett. **57**, 2575.
Schotte, K.D., D. Förster and U. Schotte, 1986, Z. Phys. B **64**, 165.
Schrieffer, J.R., and D.C. Mattis, 1965, Phys. Rev. A **140**, 1412.
Schrieffer, J.R., and P.A. Wolff, 1966, Phys. Rev. **149**, 491.
Schuberth, E., G. Hofmann, F. Gross, K. Andres and J. Hufnagl, 1990, Europhys. Lett. **11**, 249.
Schuh, B., 1985, Phys. Status Solidi B **131**, 342.
Seitz, E., 1978, J. Phys. F **8**, L189.
Seitz, E., B. Lengeler, G. Kamm and J. Kopp, 1979, J. Phys. (Paris) **40**, C5-76.
Shiba, H., 1968, Prog. Theor. Phys. **40**, 435.
Shiba, H., 1975, Prog. Theor. Phys. **54**, 967.
Shiba, H., 1986, J. Phys. Soc. Jpn. **55**, 2765.
Shivaram, B.S., Y.H. Jeong, T.F. Rosenbaum and D.G. Hinks, 1986a, Phys. Rev. Lett. **56**, 1078.
Shivaram, B.S., T.F. Rosenbaum and D.G. Hinks, 1986b, Phys. Rev. Lett. **57**, 1259.
Siegrist, T., M. Olivier, S.P. McAlister and R.W. Cochrane, 1986, Phys. Rev. B **33**, 4370.
Sigrist, M., and T.M. Rice, 1989, Phys. Rev. B **39**, 2200.
Šimanek, E., 1985, Phys. Rev. B **31**, 3172.
Skalski, S., O. Betbeder-Matibet and P.R. Weiss, 1964, Phys. Rev. **136**, 1500.
Smith, J.L., Z. Fisk, J.O. Willis, B. Batlogg and H.R. Ott, 1984, J. Appl. Phys. **55**, 1996.
Smith, J.L., Z. Fisk, J.O. Willis, A.L. Giorgi, R.B. Roof, H.R. Ott, H. Rudigier and E. Felder, 1985, Physica B **135**, 3.
Sparn, G., W. Lieke, U. Gottwick, F. Steglich and N. Grewe, 1985, J. Magn. & Magn. Mater. **47&48**, 521.
Sparn, G., R. Caspary, U. Gottwick, A. Grauel, U. Habel, M. Lang, M. Nowak, R. Schefzyk, W. Schiebeling, H. Spille, M. Winkelmann, A. Zuber, F. Steglich and A. Loidl, 1988, J. Magn. & Magn. Mater. **76&77**, 153.
Spille, H., U. Rauchschwalbe and F. Steglich, 1983, Helv. Phys. Acta **56**, 165.
Springford, M., and P.H.P. Reinders, 1988, J. Magn. & Magn. Mater. **76&77**, 11.
Stamp, P.C.E., 1985, J. Phys. F **15**, 1829.
Stamp, P.C.E., 1987, Europhys. Lett. **4**, 453.
Steglich, F., 1976, Z. Phys. B **23**, 331.
Steglich, F., 1985a, Springer Series in Solid-State Sciences **62**, 23.
Steglich, F., 1985b, Physica B **130**, 145.
Steglich, F., 1989, J. Phys. Chem. Solids **50**, 225.
Steglich, F., J. Aarts, C.D. Bredl, W. Lieke, D. Meschede, W. Franz and H. Schäfer, 1979a, Phys. Rev. Lett. **43**, 1892.
Steglich, F., C.D. Bredl, M. Loewenhaupt and K.D. Schotte, 1979b, J. Phys. (Paris) **40**, C5-301.
Steglich, F., J. Aarts, C.D. Bredl, G. Cordier, F.R. de Boer, W. Lieke and U. Rauchschwalbe, 1982, in: Superconductivity in d-Band and f-Band Metals, eds W. Buckel and W. Weber (Kernforschungszentrum Karlsruhe) p. 145.
Steglich, F., C.D. Bredl, W. Lieke, U. Rauchschwalbe and G. Sparn, 1984, Physica B **126**, 82.
Steglich, F., U. Rauchschwalbe, U. Gottwick, H.M. Mayer, G. Sparn, N. Grewe, U. Poppe and J.J.M. Franse, 1985, J. Appl. Phys. **57**, 3054.
Steglich, F., C.D. Bredl, F.R. de Boer, M. Lang, U. Rauchschwalbe, H. Rietschel, R. Schefzyk, G. Sparn and G.R. Stewart, 1987a, Phys. Scr. **T19**, 253.
Steglich, F., U. Ahlheim, U. Rauchschwalbe and H. Spille, 1987b, Physica B **148**, 6.
Steglich, F., C.D. Bredl, U. Rauchschwalbe, P. Fulde, K. Maki, H. Rietschel and G.R. Stewart, 1987c, in: Theoretical and Experimental Aspects of Valence Fluctuations and Heavy Fermions, eds L.C. Gupta and S.K. Malik (Plenum Press, New York) p. 17.
Steglich, F., G. Sparn, R. Moog, S. Horn, A. Grauel, M. Lang, M. Nowak, A. Loidl, A. Krimmel, K. Knorr, A.P. Murani and M. Tachiki, 1990a, Physica B **163**, 19.
Steglich, F., C. Geibel, S. Horn, U. Ahlheim, M. Lang, G. Sparn, A. Loidl, A. Krimmel and W. Assmus, 1990b, J. Magn. & Magn. Mater., in press.
Stewart, G.R., 1984, Rev. Mod. Phys. **56**, 755.
Stewart, G.R., 1989, private communication.
Stewart, G.R., Z. Fisk and J.O. Willis, 1983, Phys. Rev. B **28**, 172.
Stewart, G.R., Z. Fisk, J.O. Willis and J.L. Smith, 1984a, Phys. Rev. Lett. **52**, 679.
Stewart, G.R., Z. Fisk, J.L. Smith, J.O. Willis and M.S. Wire, 1984b, Phys. Rev. B **30**, 1249.

Stewart, G.R., A.L. Giorgi, J.O. Willis and J. O'Rourke, 1986, Phys. Rev. B **34**, 4629.
Stewart, G.R., B. Andraka, C. Quitmann, B. Treadway, Y. Shapira and E.J. McNiff Jr, 1988, Phys. Rev. B **37**, 3344.
Sticht, J., and J. Kübler, 1985, Solid State Commun. **54**, 389.
Sticht, J., N. d'Ambrumenil and J. Kübler, 1986, Z. Phys. B **65**, 149.
Strange, P., and D.M. Newns, 1986, J. Phys. F **16**, 335.
Suhl, H., 1965, Phys. Rev. A **138**, 515.
Sulpice, A., P. Gandit, J. Chaussy, J. Flouquet, D. Jaccard, P. Lejay and J.L. Tholence, 1986, J. Low Temp. Phys. **62**, 39.
Sun, W., M. Brand, G. Bruls and W. Assmus, 1990, Z. Phys. B **80**, 249.
Suzuki, T., 1985, J. Phys. Soc. Jpn. **54**, 2367.
Tachiki, M., and S. Maekawa, 1984, Phys. Rev. B **29**, 2497.
Taillefer, L., 1990, Physica B **163**, 278.
Taillefer, L., and G.G. Lonzarich, 1988, Phys. Rev. Lett. **60**, 1570.
Taillefer, L., R. Newbury, G.G. Lonzarich, Z. Fisk and J.L. Smith, 1987, J. Magn. & Magn. Mater. **63&64**, 372.
Taillefer, L., F. Piquemal and J. Flouquet, 1988, Physica C **153–155**, 451.
Tang, J., K.A. Gschneidner Jr, R. Caspary and F. Steglich, 1990, Physica B **163**, 201.
Thalmeier, P., P. Lemmens, S. Ewert, D. Lenz and K. Winzer, 1987, Europhys. Lett. **4**, 1177.
Thompson, J.D., 1987, J. Magn. & Magn. Mater. **63&64**, 358.
Thompson, J.D., and Z. Fisk, 1985, Phys. Rev. B **31**, 389.
Thompson, J.D., Z. Fisk, J.M. Lawrence, J.L. Smith and R.M. Martin, 1983, Phys. Rev. Lett. **50**, 1081.
Thompson, J.D., J.O. Willis, C. Godart, D.E. MacLaughlin and L.C. Gupta, 1985, J. Magn. & Magn. Mater. **47&48**, 281.
Tournier, R., 1974, in: Low Temperature Physics - LT 13, Vol. 2, eds K.D. Timmerhaus, W.J. O'Sullivan and E.F. Hammel (Plenum Press, New York) p. 257.
Trainor, R.J., M.B. Brodsky and H.V. Culbert, 1975, Phys. Rev. Lett. **34**, 1019.
Trainor, R.J., M.B. Brodsky, B.D. Dunlap and G.K. Shenoy, 1976, Phys. Rev. Lett. **37**, 1511.
Tsvelik, A.M., 1979, Zh. Eksp. Teor. Fiz. **76**, 2260 [Sov. Phys.-JETP **49**, 1142].
Tsvelik, A.M., and B.P. Wiegmann, 1983, Adv. Phys. **32**, 453.
Ueda, K., and T.M. Rice, 1985, Phys. Rev. B **31**, 7114.
Uemura, Y.J., W.J. Kossler, X.H. Yu, H.E. Schone, J.R. Kempton, C.E. Stronach, S. Barth, F.N. Gygax, B. Hitti, A. Schenck, C. Baines, W.F. Lankford, Y. Onuki and T. Komatsubara, 1989, Phys. Rev. B **39**, 4726.
Varma, C.M., 1976, Rev. Mod. Phys. **48**, 219.
Varma, C.M., 1985a, Comments Solid State Phys. **11**, 221.
Varma, C.M., 1985b, J. Appl. Phys. **57**, 3064.
Varma, C.M., W. Weber and L.J. Randall, 1986, Phys. Rev. B **33**, 1015.
Vettier, C., P. Morin and J. Flouquet, 1986, Phys. Rev. Lett. **56**, 1980.
Volovik, G.E., and L.P. Gorkov, 1984, Zh. Eksp. Teor. Fiz. **39**, 550 [Sov. Phys.-JETP **39**, 674].
Volovik, G.E., and L.P. Gorkov, 1985, Zh. Eksp. Teor. Fiz. **88**, 1412 [Sov. Phys.-JETP **61**, 843].
Vulović, V.Z., and E. Abrahams, 1987, Phys. Rev. B **36**, 2614.
Walter, U., D. Wohlleben and Z. Fisk, 1986, Z. Phys. B **62**, 235.
Wang, C.S., M.R. Norman, R.C. Albers, A.M. Boring, W.E. Pickett, H. Krakauer and N.E. Christensen, 1987, Phys. Rev. B **35**, 7260.
Wasserman, A., M. Springford and A.C. Hewson, 1989, J. Phys. **1**, 2669.
Welslau, B., and N. Grewe, 1990, Physica B **165&166**, 387.
Wilson, K.G., 1975, Rev. Mod. Phys. **47**, 733.
Winter, K.M., D. Lenz, H. Schmidt, S. Ewert, S. Blumenröder, E. Zirngiebl and K. Winzer, 1986, Solid State Commun. **59**, 117.
Wohlleben, D., 1976, J. Phys. (Paris) C **4**, 231.
Wohlleben, D.K., and B.R. Coles, 1973, in: Magnetism V, ed. H. Suhl (Academic Press, New York) p. 3 ff.
Wölfle, P., 1986, Phys. Lett. A **119**, 40.
Yamada, K., 1974, Prog. Theor. Phys. **53**, 970.
Yamada, K., 1975, Prog. Theor. Phys. **54**, 316.
Yamada, K., K. Yosida and K. Hanzawa, 1984, Prog. Theor. Phys. **71**, 450.
Yamada, K., K. Okada, K. Yosida and K. Hanzawa, 1987, Prog. Theor. Phys. **77**, 1097.
Yashima, H., N. Sato, H. Mori and T. Satoh, 1982, Solid State Commun. **43**, 595.
Yoshimori, A., 1976, Prog. Theor. Phys. **55**, 67.

Yoshimori, A., and H. Kasai, 1983, J. Magn. & Magn. Mater. **31–34**, 475.
Yoshimori, A., and H. Kasai, 1986, Solid State Commun. **58**, 259.
Yoshimori, A., and A. Zawadowski, 1982, J. Phys. C **15**, 5241.
Yoshizawa, M., B. Lüthi, T. Goto, T. Suzuki, B. Renker, A. de Visser, P. Frings and J.J.M. Franse, 1985, J. Magn. & Magn. Mater. **52**, 413.
Yoshizawa, M., B. Lüthi and K.D. Schotte, 1986, Z. Phys. B **64**, 169.
Yosida, K., 1957, Phys. Rev. **106**, 895.
Yosida, K., and A. Watabe, 1962, Prog. Theor. Phys. **28**, 361.
Yosida, K., and K. Yamada, 1970, Suppl. Prog. Theor. Phys. **46**, 244.
Yosida, K., and K. Yamada, 1974, Prog. Theor. Phys. **53**, 1286.
Zhang, F.C., and T.K. Lee, 1984, Phys. Rev. B **30**, 1556.
Zhang, F.C., and T.K. Lee, 1988, preprint.
Zhang, F.C., T.K. Lee and Z.B. Su, 1987, Phys. Rev. B **35**, 4728.
Zieglowski, J., H.U. Häfner and D. Wohlleben, 1986, Phys. Rev. Lett. **56**, 193.
Zlatić, V., and B. Horvatić, 1983, Phys. Rev. B **28**, 6904.
Zwicknagl, G., 1988, J. Magn. & Magn. Mater. **76&77**, 16.

SUBJECT INDEX